Far-from-equilibrium universality in interacting quantum matter

Dissertation

Tibor Rakovszky

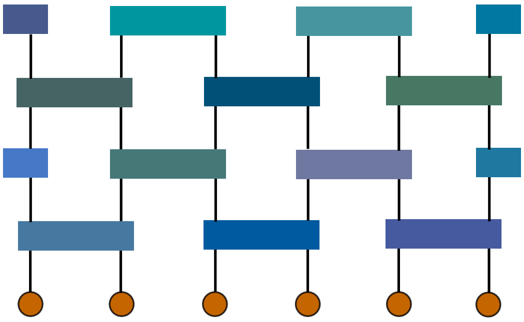

Chair of Theoretical Solid-State Physics
Department of Physics
Technical University of Munich

TECHNISCHE UNIVERSITÄT MÜNCHEN

FAKULTÄT FÜR PHYSIK
LEHRSTUHL FÜR THEORETISCHE FESTKÖRPERPHYSIK

Far-from-equilibrium Universality in Interacting Quantum Matter

Tibor Rakovszky

Vollständiger Abdruck der von der Fakultät für Physik der Technischen Universität München zur Erlangung des akademischen Grades eines **Doktors der Naturwissenschaften (Dr. rer. nat.)** genehmigten Dissertation.

Vorstizender: Prof. Dr. Alexander Holleitner

Prüfer der Dissertation:

1. Prof. Dr. Frank Pollmann
2. Prof. Dr. Johannes Knolle

Die Dissertation wurde am 09.06.2020 bei der Technischen Universität München eingerecht und durch die Fakultät für Physik am 15.07.2020 angenommen

Abstract

The study of far-from-equilibrium quantum systems is a rapidly growing field of condensed matter physics, combining fundamental questions of statistical mechanics with groundbreaking experimental techniques that provide a hitherto unseen degree of control over quantum systems of many particles. Entanglement and other notions of quantum information theory have emerged as important tools in this context, central to understanding the quantum thermalization process. In this thesis, we study the dynamics of such quantities, and uncover many of their interesting universal features. We achieve this by combining the study of simple minimal models, known as random unitary circuits, with extensive numerical simulations. The former, in particular, are crucial in revealing universal behavior, giving rise to a 'hydrodynamics of quantum information' at long length- and time scales.

We focus on the spreading of local operators and the growth of entanglement as two main aspects of how quantum information becomes scrambled on the way to thermalization. We develop a simple theory for the former, in terms of a biased diffusion equation, and show that it applies in generic one-dimensional many-body systems. We then extend this theory to include the effect of local conserved quantities, which lead to novel universal features, such as slow 'hydrodynamic tails'. We find that the same conservation laws also have a profound effect on the dynamics of entanglement. Most strikingly, they turn the growth of certain measures (so-called higher Rényi entropies) from ballistic to sub-ballistic, which we explain in terms of 'rare events' in the quantum evolution.

Understanding these generic aspects of quantum many-body dynamics also paves the way for constructing better tools to study them in the future. We illustrate this by developing a new numerical technique for quantum dynamics, which uses our newfound understanding of operator spreading to circumvent the limitations of previous methods. We show that our algorithm, which we name 'dissipation-assisted operator evolution' (DAOE), can capture transport coefficients of strongly interacting quantum chains with very high precision.

Kurzfassung

Die Untersuchung von Quantensystemen fernab des thermodynamischen Gleichgewichts stellt ein rapide wachsendes Forschungsfeld im Bereich der Physik der kondensierten Materie dar und kombiniert fundamentale Fragen der Statistischen Mechanik mit bahnbrechenden experimentellen Methoden die eine bislang unerreichte Kontrolle über Quantenvielteilchensysteme ermöglichen. In diesem Kontext haben sich Verschränkung und weitere Konzepte der Quanteninformationstheorie als zentrale Werkzeuge zum Verständnis des Quanten-Thermalisierungsprozesses etabliert. In dieser Arbeit untersuchen wir die Dynamik solcher physikalischer Größen und erarbeiten eine Vielzahl der damit in Verbindung stehenden universellen Eigenschaften. Zu diesem Zweck kombinieren wir die Untersuchung simpler minimaler Modelle, bekannt als randomisierte unitäre Quantenschaltkreise, mit extensiven numerischen Simulationen. Insbesondere Erstere erweisen sich als essentiell zur Studie universeller Eigenschaften, gültig auf großen Längen- und Zeitskalen, und führen damit zu einer ‘Hydrodynamik der Quanteninformation’.

Wir befassen uns mit der Ausbreitung lokaler Operatoren und dem Anwachsen von Verschränkung als den beiden Hauptaspekten der Durchmischung von Quanteninformation auf dem Weg ins thermische Gleichgewicht. Insbesondere entwickeln wir eine theoretische Beschreibung für ersteren Aspekt durch eine asymmetrische Diffusionsgleichung und demonstrieren deren Anwendbarkeit für generische, eindimensionale Vielteilchensysteme. Anschließend erweitern wir diese Theorie um die Beschreibung lokaler Erhaltungsgrößen, die zu neuartigen universellen Eigenschaften wie langsamen ‘hydrodynamischen Moden’ führen. Wir finden weiter, dass die Existenz selbiger Erhaltungsgrößen einen tiefgreifenden Einfluss auf die Dynamik von Verschränkung hat. Als markantestes Beispiel demonstrieren wir die Modifikation des zeitlichen Verlaufs bestimmter Messgrößen (sogenannter höherer Rényi Verschränkungen) von ballistischem zu sub-ballistischem Wachstum, und erklären diesen Effekt durch die Präsenz ‘seltener Ereignisse’ in der Quanten-Zeitentwicklung.

Das Verständnis dieser allgemeinen Aspekte der Dynamik von Quantenvielteilchensystemen bereitet darüber hinaus den Weg für die Konstruktion verbesserter Werkzeuge die zu künftigen Untersuchungen selbiger Systeme dienen. Dies illustrieren wir durch die Entwicklung einer neuen numerischen Methode zur Simulation von Quantendynamik, welche, basierend auf unserem neugewonnenen Verständnis der Ausbreitung von Operatoren, die Limitierungen früherer Methoden erfolgreich umgeht. Wir zeigen, dass unser Algorithmus, den wir ‘Dissipations-assistierte Operator-Entwicklung’ (DAOE) nennen, die Transportkoeffizienten stark wechselwirkender eindimensionaler Quantensysteme mit sehr hoher Präzision erfasst.

Contents

List of Publications

This thesis is based on the following publications by the author (we indicate in brackets the chapters which contain most of the results from each paper):

[1] C. W. von Keyserlingk, Tibor Rakovszky, Frank Pollmann, and S. L. Sondhi. Operator hydrodynamics, otocs, and entanglement growth in systems without conservation laws. *Phys. Rev. X*, 8:021013, Apr 2018. doi: 10.1103/PhysRevX.8.021013. URL https://link.aps.org/doi/10.1103/PhysRevX.8.021013 (Chapter 4)

[2] Tibor Rakovszky, Sarang Gopalakrishnan, S. A. Parameswaran, and Frank Pollmann. Signatures of information scrambling in the dynamics of the entanglement spectrum. *Phys. Rev. B*, 100:125115, Sep 2019. doi: 10.1103/PhysRevB.100.125115. URL https://link.aps.org/doi/10.1103/PhysRevB.100.125115 (Chapter 6)

[3] Tibor Rakovszky, Frank Pollmann, and C. W. von Keyserlingk. Diffusive hydrodynamics of out-of-time-ordered correlators with charge conservation. *Phys. Rev. X*, 8:031058, Sep 2018. doi: 10.1103/PhysRevX.8.031058. URL https://link.aps.org/doi/10.1103/PhysRevX.8.031058 (Chapter 8)

[4] Tibor Rakovszky, C. W. von Keyserlingk, and Frank Pollmann. Dissipation-assisted operator evolution method for capturing hydrodynamic transport. ArXiv preprint, 2004.05177, 2020 (Chapter 9)

[5] Tibor Rakovszky, Frank Pollmann, and C. W. von Keyserlingk. Sub-ballistic growth of rényi entropies due to diffusion. *Phys. Rev. Lett.*, 122:250602, Jun 2019. doi: 10.1103/PhysRevLett.122.250602. URL https://link.aps.org/doi/10.1103/PhysRevLett.122.250602 (Chapter 10)

[6] Tibor Rakovszky, C. W. von Keyserlingk, and Frank Pollmann. Entanglement growth after inhomogenous quenches. *Phys. Rev. B*, 100:125139, Sep 2019. doi: 10.1103/PhysRevB.100.125139. URL https://link.aps.org/doi/10.1103/PhysRevB.100.125139 (Chapter 11)

The author has also published the following papers during his doctoral studies, which are independent of the work presented in the thesis:.

[7] Tibor Rakovszky, Pablo Sala, Ruben Verresen, Michael Knap, and Frank Pollmann. Statistical localization: From strong fragmentation to strong edge modes. *Phys. Rev. B*, 101:125126, Mar 2020. doi: 10.1103/PhysRevB.101.125126. URL https://link.aps.org/doi/10.1103/PhysRevB.101.125126

[8] Pablo Sala, Tibor Rakovszky, Ruben Verresen, Michael Knap, and Frank Pollmann. Ergodicity breaking arising from hilbert space fragmentation in dipole-conserving hamiltonians. *Phys. Rev. X*, 10:011047, Feb 2020. doi: 10.1103/PhysRevX.10.011047. URL https://link.aps.org/doi/10.1103/PhysRevX.10.011047

[9] Tibor Rakovszky, János K. Asbóth, and Andrea Alberti. Detecting topological invariants in chiral symmetric insulators via losses. *Phys. Rev. B*, 95:201407, May 2017. doi: 10.1103/PhysRevB.95.201407. URL https://link.aps.org/doi/10.1103/PhysRevB.95.201407

Prior to the beginning of the doctoral studies, the author has published the following two papers:

> [10] Tibor Rakovszky, Márton Mestyán, Mario Collura, Márton Kormos, and Gábor Takács. Hamiltonian truncation approach to quenches in the ising field theory. *Nuclear Physics B*, 911:805 – 845, 2016. ISSN 0550-3213. doi: https://doi.org/10.1016/j.nuclphysb.2016.08.024. URL `http://www.sciencedirect.com/science/article/pii/S0550321316302541`
>
> [11] Tibor Rakovszky and Janos K. Asboth. Localization, delocalization, and topological phase transitions in the one-dimensional split-step quantum walk. *Phys. Rev. A*, 92:052311, Nov 2015. doi: 10.1103/PhysRevA.92.052311. URL `https://link.aps.org/doi/10.1103/PhysRevA.92.052311`

The author has made significant contributions to all of these works, including the development of ideas, analytical calculations, the design and implementation of numerical algorithms, the interpretation of results and the writing of the manuscripts.

Acknowledgements

First and foremost, I would like to thank my advisor, Prof. Frank Pollmann, for his guidance and constant support throughout the years of my PhD. His insight and creativity in physics, his many great advice, and his willingness to let me freely explore various topics, have made working with him a wonderful experience, and much more fruitful than I could have expected in my wildest dreams when I started.

I want to thank Curt von Keyserlingk for our many collaborations, for the countless hours spent discussing physics, and for his friendship and advice throughout the years. I count myself very lucky to have had the opportunity to work with him, and hope that our collaboration with him and Frank will continue for many more years to come.

The work presented in this thesis would have been impossible without the many great discussions with the people that I had the good fortunate to collaborate with, Shivaji Sondhi, Sarang Gopalakrishnan, Siddharth Parameswaran, Michael Knap, Andrea Alberti, Ruben Verresen, Pablo Sala and János Asbóth. I am especially thankful to Shivaji for his wisdom, and to János for first introducing me to the world of condensed matter physics, and for many illuminating discussions since then. I also want to take this opportunity to thank Prof. David Huse for many insightful discussions.

I am extremely thankful for all the members of the condensed matter theory group at TUM, for creating an inspiring and friendly environment. Frank and Michael deserve much praise for maintaining such a stimulating atmosphere. I am grateful for Johannes Hauschild for his infinite patience in explaining things to me, and for letting me stay at his place while I was going through the hurdles of finding an apartment in Munich. I am thankful to Ruben and Pablo for many inspiring discussions about physics, and equally many games of table tennis. I also want to thank Claudine Voelcker for her constant help with all sorts of administrative issues.

I would like to acknowledge the Deutsche Forschungsgemeinschaft (DFG) through Research Unit FOR 1807, for funding my research and visits to various schools and conferences, from which I benefited greatly.

I am grateful to my friends, who helped me keep up my good spirits throughout the years. I am thankful to Péter Kutas for his friendship, and for introducing me to so many other great people. I thank Marci Dücső, Gábor Szűcs and Ildi Czeller, for coming to brighten my days when I first moved to Munich, and for many great discussions, Bálint Hujter for all our stimulating exchanges, had throughout various cities of Europe, Hanna Róza Nemesbüki for many great conversations and for motivating me to finish this thesis on time, and all the others, too many to count. I am especially thankful to my friend, Gergely Bognár, who has probably helped me preserve my sanity more than anyone.

Finally, I would like to thank some of those without whom I could not be where I am today. I thank Péter Antók for first showing me how interesting mathematics can be, and for our countless conversations since then. I am especially grateful to Bálint József, for imparting to me some of his vast knowledge and wisdom. I am thankful to my friend Gábor Kónya for all his clear explanations of physics, and for introducing me to János Asbóth and thus setting me on the path that lead me here. Last, and most importantly, I am most grateful to my mother, Zsuzsa, for helping me realize my interest in physics, and for her enormous love and support.

1. Introduction

While the foundations of quantum mechanics have been laid out almost a century ago, the extremely rich tapestry of physical phenomena that stem from these principles are still actively explored to this day. On the one hand, this includes ongoing research in the field of quantum foundations, where increasingly counter-intuitive features of the quantum world are uncovered every year [12–17]. Closely related to this, *quantum information theory* [18–21] has emerged as an exciting field on its own right, providing a rigorous mathematical understanding of the types of correlations that are absent in the classical world, increasingly with an eye towards practical applications in the form of quantum computing [18, 22, 23]. On another frontier, *quantum many-body systems* [24–28], where a macroscopic number of constituents interact with each other in a quantum coherent way, have provided an inexhaustible source of surprises both for theoretical physicists and experimentalists, leading to the discovery of various quantum phases of matter, such as superfluids [29, 30], superconductors [30–32], fractional quantum Hall phases [33–36] and topological insulators [37–40].

A common thread throughout all of these fields is the necessity for an ever increasing amount of experimental control over quantum systems. While Einstein, Schrödinger or Bell only considered their thought experiments as theoretical tools, not realizable in practice, advances in the last four decades have allowed experimenters to prove them wrong, creating well-isolated quantum systems and probing their properties with incredible accuracy [41–45]. This effort has culminated in a series of increasingly intricate experiments that confirm Bell's predictions about the non-classical nature of quantum correlations [13, 14, 46–51]. The same experimental advances have also opened the way for new questions in quantum many-body physics. An early success in this direction has been the realization of *Bose-Einstein condensates* in dilute gases [52–55], a state of matter predicted by Einstein some 70 years prior [56]. Subsequent breakthroughs have lead to a proliferation of research on 'artificial quantum systems', where properties of quantum coherently interacting particles can be controlled and measured with a precision much higher than in those occurring in nature. These *quantum simulators* [57–61] can even be used to shed light on features of the standard model and other problems in high energy particle physics [62–70]! In recent years, this field of research has become closely tied the effort to build a reliable quantum computer [18, 71–74], which has reached an important milestone last year when the group led by John Martinis at Google announced the achievement of 'quantum supremacy' (the execution of a computation beyond the reach of any existing classical supercomputer) [75].

The ability to create and measure quantum systems of many particles, well separated from their environment, has lead to an important paradigm-shift in condensed matter physics, prompting physicists to ask questions that were beyond their reach previously. Part of this development was the realization that concepts borrowed from quantum information theory, entanglement in particular, can be extremely useful in characterizing quantum states of matter in equilibrium. This includes the discovery of universal properties of entanglement that characterize various topological phases of matter at zero temperature [76–81], and also a breadth of novel numerical methods for studying quantum systems, often formulated in the language of tensor networks, initiated by the celebrated Density Matrix Renormalization Group (DMRG) algorithm [82–85]. Many of these results have been collected in a recent book [28], whose last chapter summarizes the end goal of this research direction: *A unification of* (quantum) *information and matter*. It is worth noting that simultaneously with these developments, notions of entanglement and quantum information have also gained traction in the field of quantum gravity, primarily due to ongoing efforts to solve the infamous black hole information paradox [86–91].

More recently, experiments on artificial quantum systems have given birth to new subfield of many-body physics: the study of closed quantum systems far from equilibrium [92–96]. Due to the aforementioned experimental advances in preparing and manipulating quantum systems of many particles, well separated from their environments, physicists turned their attention towards questions of how such systems evolve under their own dynamics, as they follow Schrödinger's equation. This is closely related to the foundations of (quantum) statistical physics: under what conditions does a system reach an eventual equilibrium state that is described by the usual assumptions of thermal ensembles? This led physicists to develop a theory of the properties that many-body systems need to possess in order for such thermalizing behavior, and explore the conditions under which thermalization can fail to occur [93–102]. From the theory side, these developments relied largely on advances in numerical simulations, both in the form of better hardware, and by developing novel algorithms to tackle many-body dynamics [99, 103–105].

The work presented in this thesis exists at the interface of the two trends described in the previous paragraphs: the increasing importance of quantum information theory to describe many-body systems, and the investigation of far-from-equilibrium unitary dynamics in these systems. It has been realized early on, that quantum information provides an extremely useful perspective into thermalization, which can be understood largely as a 'scrambling' of information between the many degrees of freedom. Entanglement, in particular, has been identified as playing a central role in this process, leading to the emergence of thermal entropy at long times [106]. More recently, the spreading of initially local operators has come to the scientific forefront, as an extremely useful tool in characterizing scrambling [107]. These developments naturally lead to a variety of important questions. Are there universal features in the dynamics of quantum information that emerge at long times? What are the possible universality classes? How are they affected by symmetries, and how does quantum information couple to the dynamics of conserved quantities? What are the relevant time scales for thermalization, and how do they manifest in quantities like entanglement?

In this thesis, we develop a comprehensive understanding of many of these questions. To do so, requires a new set of theoretical tools, as the only existing techniques for treating generic systems out of equilibrium are numerical, and are typically restricted to short time scales, which makes it difficult to discern universal features. We circumvent this problem by constructing solvable minimal models, so-called *random circuits*, that are designed to capture precisely these universal properties. These also allow us to incorporate interesting physical features, such as symmetries, 'step-by-step', while stripping away all unnecessary details.

Let us summarize here some of the main achievements of the random circuit approach presented in the thesis:

- We derive an exact description of operator spreading, given in terms of a biased diffusion equation, and provide evidence that it constitutes generic behavior in one-dimensional systems.

- We use this biased diffusion picture to shed light on entanglement growth; in particular, we argue that the diffusion of the front is necessary to understand why the speed of entanglement growth is slower than one would naively expect.

- We show how this separation of time scales can be observed in the entanglement spectrum of a finite subsystem.

- We extend our theory to include the effect of conserved quantities and their diffusive transport. We find that these give rise to slow hydrodynamic tails in operator spreading.
- We develop a new numerical technique that builds on our operator spreading results to provide a way of precisely calculating transport properties in strongly interacting quantum systems.
- We investigate the effect of diffusive transport on entanglement, and find that it leads to qualitatively new behavior in higher Rényi entropies, which are directly relevant to experiments [108–110], making their growth sub-ballistic.
- We develop a description of entanglement growth in situations where conserved quantities have large-scale inhomogeneities.

To test the generality of our results outside the realm of solvable models, we perform extensive numerical computations. In particular, we apply both an exact numerical evolution of small systems [111–113], as well as *tensor network methods* [84, 85, 105]. Moreover, as stated above, we provide our own contribution to the development of new numerical tools, relying on the insight gained by studying random circuits.

Structure and contents of the thesis

This thesis starts with a concise summary of much of the necessary background that we will rely on in what follows, presented in Chapter 2. We describe the key notions lying behind quantum thermalization, such as the Eigenstate Thermalization Hypothesis (ETH), scrambling of quantum information and the emergence of hydrodynamic theories; we also give a review of some of the most important techniques, both experimental and numerical, that are used to study these questions.

The main part of the thesis is split into two parts. Part I concerns the dynamics in systems with no conserved quantities. In Chapter 3 we construct a *random circuit model* that captures universal features of this class of systems. We then use this model to study operator spreading and entanglement growth, in Chapters 4 and 5, respectively, extracting universal features and contrasting them with numerical results on other models. In Chapter 6 we consider some intricate features of the evolving entanglement spectrum and connect them to operator spreading.

Part II deals with systems that have diffusively transported conserved quantities. Chapter 7 introduces minimal models for this case, by endowing the previous random circuit with a $U(1)$ symmetry. In Chapter 8, we use these models to study the relationship between transport and operator spreading in detail. As a by-product, we devise a numerical method, aimed at calculating transport coefficients, and test it in various strongly interacting quantum systems, which we detail in Chapter 9. The final two chapters are devoted to entanglement growth in diffusive systems. In Chapter 10 we uncover a surprising relationship between transport and the dynamics of higher Rényi entropies, which makes the latter grow sub-ballistically in time. Lastly, in Chapter 11 we consider the fate of inhomogenous initial states, and show how these inhomogeneities leave their mark on the entanglement structure as they smooth out diffusively.

2. Preliminaries: Dynamics in Closed Quantum Systems

Throughout this thesis, we will be concerned with the dynamics of states in closed quantum systems, comprised of a macroscopic number of interacting degrees of freedom. Moreover, we will focus on models, relevant for many condensed matter and cold atomic systems, where the degrees of freedom live on a lattice, rather than in a continuum, although most of the features we discuss are expected to carry over to the latter case. For simplicity, we will often refer to the local degrees of freedom as 'spins', although they need not correspond to physical spins, and can in fact be fermions or bosons as well. A key aspect of these systems is that the dimension of the Hilbert space grows exponentially with the number of spins (bosons/fermions), making their study challenging, but also very interesting.

We consider a situation where an initial many-body wavefunction, $|\Psi_0\rangle$, is evolved in time as $|\Psi(t)\rangle = U(t)|\Psi_0\rangle$. Here $U(t)$ is a unitary time evolution operator, which we assume to be local in space. The simplest case is the evolution with a static local Hamiltonian, $U(t) = e^{-iHt}$, or with a time-dependent one, $U(t) = \mathcal{T}e^{-i\int \mathrm{d}tH(t)}$, (where $\mathcal{T}$ stands for time ordering). Then the locality [114] of the Hamiltonian[1] ensures that dynamics under $U(t)$ has an emergent light cone (characterized by the so-called *Lieb-Robinson velocity*), v_{LR}, such that operators outside each others light cone commute, up to corrections that decay exponentially with their distance [115, 127–129]. We will also consider cases where $U(t)$ is defined in terms of a circuit of local gates (unitary operations acting on a finite region), rather than by reference to a Hamiltonian; these models also share the same notion of a linear light cone.

We will also require that the initial states $|\Psi_0\rangle$ is *short-range correlated*, which is the case for physically relevant states, realizable in experiments. The simplest such case is a simple product state, where the local degrees of freedom on the lattice are completely uncorrelated, i.e. *product states* on the different lattice sites. More generally, one can consider taking a system with a particular initial Hamiltonian H_0 and cooling it down to its ground state. Then one can induce dynamics by suddenly changing the parameters of the system to generate evolution by a modified Hamiltonian H; this is usually referred to as a *quantum quench* [106, 130, 131]. Since the initial state in this case the ground state of H_0, it has correlations that decay exponentially in space [115] and satisfies an *area law* for entanglement [132], provided that the spectrum of H_0 is gapped. As a general conditions, we shall assume that the initial state $|\Psi_0\rangle$ has exponentially decaying correlations. We are therefore interested in *the evolution of initially short-range correlated states under local unitary dynamics.*

The above discussion is in terms of the Schrödinger picture, where the quantum state of the system, $|\Psi(t)\rangle$, is evolving in time. As we know from our undergraduate studies of quantum mechanics, it is often useful to utilize the Heisenberg picture instead, where it is the observables that evolve in time as $U(t)^\dagger \mathcal{O} U(t)$. While the two pictures are equivalent as

---

[1] Here, by *local*, we mean a Hamiltonian that is a sum of *geometrically local* terms, i.e., the size of each term in the Hamiltonian decays at least exponentially with the size of the region that it acts on – although a sufficiently fast power law decay is also sufficient to produce a linear light cone [115–123]. In practice, we mostly consider cases where the terms act strictly within a finite region. Contrast this with the case of k-*local* Hamiltonians, such as the Sachdev-Ye Kitaev model [124–126], where the terms only act on at most k spins, but there is no restriction on spatial locality.

far as expectation values are concerned, there are various quantities (such as entanglement) that only make sense in one or the other. In particular, as we shall see, observables admit a notion of spatial locality that proves very useful when one tries to discern how quantum information gets redistributed between different parts of the system during dynamics. In what follows, we will consider the evolution process in both pictures and observe how they complement each other.

2.1. Thermalization in closed quantum systems

Most of the results below will concern dynamics at intermediate time scales, i.e., time that are long enough such that we can observe universal features that are independent of the microscopic details of $U(t)$ and of the initial state/operator, but short enough that the system is still far from equilibrium. However, before moving on to the discussion of these features, it is useful to discuss the fate of system at very late times, and the equilibrium state that it eventually approaches. The issue of *quantum thermalization* (and lack thereof) has been the object of intense study, with many open question still being investigated to this day, and we an only offer a brief overview here. Detailed reviews are provided by Refs. [94, 95, 100, 101] (see also Refs. [93, 96, 102, 133]).

2.1.1. The Eigenstate Thermalization Hypothesis

Consider now the evolution with a fixed Hamiltonian H, with eigenvalues E_n and eigenstates $H|n\rangle = E_n|n\rangle$. In this basis, the entirety of the quantum dynamics reduces to each state oscillating with the appropriate phase e^{-iE_nt}. The evolution of an arbitrary obrervable $\mathcal{O}$ can be written as

$$\langle\mathcal{O}\rangle(t) \equiv \langle\Psi(t)|\mathcal{O}|\Psi(t)\rangle = \sum_{m,n} e^{-i(E_n-E_m)t} c_n c_m^* \langle m|\mathcal{O}|n\rangle, \tag{2.1}$$

where $c_n \equiv \langle n|\Psi_0\rangle$ are the coefficients of the initial state in the energy eigenbasis. In the absence of fine-tuning, we can assume that the spectrum of H is non-degenerate[2]. In that case, taking the time-average to extract the long-time value we get

$$\lim_{T\to\infty} \frac{1}{T}\int_0^T \mathrm{d}t \langle\mathcal{O}\rangle(t) = \sum_n |c_n|^2 \langle n|\mathcal{O}|n\rangle \equiv \mathrm{tr}(\rho_{\mathrm{DE}}\mathcal{O}), \tag{2.2}$$

where the last equality defines the *diagonal ensemble*, $\rho_{\mathrm{DE}} \equiv \sum_n |c_n|^2 |n\rangle\langle n|$. Clearly, if the time-dependent expectation value $\langle\mathcal{O}\rangle(t)$ relaxes to an equilibrium value at long times, it has to coincide with the diagonal ensemble prediction; in this sense, the equilibration process consists of nothing else, but the dephasing between different eigenmodes. However, this prediction looks very different from what the axioms of statistical physics would suggest: the diagonal ensemble depends on exponentially many parameters of the initial state, given in terms of the coefficients c_n, while a system in thermal equilibrium should admit a description with only a handful of parameters (in the absence of additional symmetries, only one parameter: the total energy or the temperature, depending on our choice of microcanonical vs. canonical ensemble). Therefore, to argue that the system in fact reaches thermal equilibrium, and does not violate the assumptions of statistical physics, two things remain to be done: (1) understanding under what conditions can the diagonal ensemble be replaced by the microcanonical one, and (2) showing that this relaxation indeed happens, i.e. that any potential oscillations around the time-average die out at long times. Both of these are achieved by the *Eigenstate Thermalization Hypothesis* [94, 95, 97–99, 101].

---

[2] Symmetries can impose degeneracies. In this case, one should consider each symmetry sector separately.

The Eigenstate Thermalization Hypothesis (ETH) is an ansatz for the matrix elements of *local* observables $\mathcal{O}$ in the eigenstate basis of the many-body Hamiltonian. It can be stated as

$$\langle m|\mathcal{O}|n\rangle = \mathcal{O}(E)\delta_{nm} + e^{-S(E)/2} f_{\mathcal{O}}(E,\omega) R_{nm}, \tag{2.3}$$

where $E = \frac{E_n+E_m}{2}$ is the average energy of the two states, $\omega = E_n - E_m$ is their difference, $S(E)$ is the thermodynamic entropy (the logarithm of the density of states) at energy E, R_{nm} are independent random variables with zero mean and unit variance and $\mathcal{O}(E)$ and $f_{\mathcal{O}}(E,\omega)$ are some unspecified smooth functions. The two crucial elements of this ansatz are the following: (1) the diagonal matrix elements are *the same* for all eigenstates within a small energy window, up to exponentially small corrections, and (2) all the off-diagonal matrix elements are exponentially suppressed as well. These two properties solve the issues (1) and (2) outlined in the previous paragraph, respectively.

To see how issue (1), namely the discrepancy between the diagonal and microcanonical ensembles, is resolved, note that the types of initial states we consider, namely ones with short-range correlations, are *sharply peaked* in energy for local Hamiltonians. In particular, if the Hamiltonian is a sum of local terms, $H = \sum_j h_j$, then we have for the variance of the energy

$$\Sigma_H^2 \equiv \langle H^2\rangle_{\Psi_0} - \langle H\rangle_{\Psi_0}^2 = \sum_{j,j'} \left[\langle h_j h_{j'}\rangle_{\Psi_0} - \langle h_j\rangle_{\Psi_0}\langle h_{j'}\rangle_{\Psi_0}\right]. \tag{2.4}$$

Assuming, as we did, no long-range correlations in Ψ_0, the only significant contribution to this sum comes from $j \approx j'$ (i.e., cases when the distance between j and j' does not scale with system size). This gives $\Sigma_H^2 \sim V$, where V is the total volume. Given that the total energy itself is extensive, the relative fluctuations are suppressed as $\frac{\Sigma_H}{\langle H\rangle} \sim V^{-1/2}$. A similar clustering holds for other extensive conserved quantities, assuming no long-range correlations. Consequently, in the diagonal ensemble expectation value in Eq. (2.2), all the states that have a significant weight are within the same small energy window, and, by virtue of ETH, have the same expectation values. These expectation values can therefore be taken out of the sum, which thus gives $\mathrm{tr}(\rho_{\mathrm{DE}}\mathcal{O}) = \mathcal{O}(E) = \mathrm{tr}(\rho_{\mathrm{microcan,E}}\mathcal{O})$, where $E = \langle\Psi_0|H|\Psi_0\rangle$ is the only remaining parameter that characterizes the final equilibrium state. One can then apply standard arguments from statistical physics to argue that the microcanonical ensemble can be replaced by the canonical one, with the appropriate temperature $\frac{1}{T} = \frac{\partial S}{\partial E}$.

The resolution of issue (2), on the other hand, is related to the suppression of off-diagonal matrix elements. In particular, the time average of temporal fluctuations on top of the average is given by (see Ref. [94] for details)

$$\lim_{T\to\infty}\frac{1}{T}\int_0^T \mathrm{d}t \left[\langle\mathcal{O}\rangle(t) - \bar{O}\right]^2 = \sum_{\substack{n,m\\ n\neq m}} |c_n|^2|c_m|^2|\langle m|\mathcal{O}|n\rangle|^2, \tag{2.5}$$

which is suppressed by a factor of $e^{-S(E)/2}$ by virtue of Eq. (2.3). The smallness of off-diagonal matrix elements is also important in explaining the observation that local operators typically equilibrate on short (often $O(1)$) time scales. Naively, one might think that the time it takes to reach the diagonal ensemble is the time it takes for neighboring energy levels to loose phase coherence; since the energy level spacing is exponentially small in system size, this would imply that equilibration takes exponentially long times. However, the ETH ansatz ensures that the time-dependent parts of the expectation value, which are related to off-diagonal matrix elements, are suppressed, leading to much faster relaxation in most cases.

It is important to note that Eq. (2.3) can not be true for arbitrary observables. This is because, if one has access to all expectation values, one can always reconstruct the full quantum state, and therefore distinguish the eigenstates at the same energy from each other and from the thermal (mixed) state. What *precisely* is the subset of observables for which the ETH ansatz is valid is not know generically [134, 135]; however, in the thermodynamic limit it is expected to hold for any *local* observable, i.e. ones that act on only a finite region in space. Similarly, therefore, the long-time state $|\Psi(t \to \infty)\rangle$ will be indistinguishable from a thermal ensemble if one only has access to local measurements. In this sense ETH provides a sufficient condition for a system to thermalize for *any* initial state that satisfies the above clustering condition on its conserved quantities[3]. Although, as the name suggests, ETH is only a conjecture, there is a large body of evidence, both numerical [94, 99, 138–148] and analytical [97, 100, 149–153], suggesting that it is indeed the correct mechanism by which generic closed quantum systems thermalize.

2.1.2. Random matrix theory and quantum chaos

Much of the motivation behind the ETH ansatz comes from the field of *random matrix theory* (RMT) [154, 155]. It was realized a long time ago, originally by Wigner in the context of nuclear physics [156–160], that Hamiltonians of sufficiently many, strongly interacting particles tend to exhibit features similar to Hermitian matrices with random entries, particularly regarding the statistics of their eigenvalues and certain properties of their eigenvectors. Later on, it was discovered that the same properties can be used to distinguish (few-body) quantum systems whose classical limits are chaotic from those that are integrable: the chaotic ones correspond to Hamiltonians that have the same spectral properties as random matrices [161–166]. This *pseudo-randomness* is characteristic of chaotic behavior, and can be thought of as analogous to the pseudo-randomness inherent in classical chaos. Indeed, random matrix-like spectral statistics is now usually taken as the definition of what it means for a quantum system to be *chaotic* [94, 165, 166]. Similarly, the ETH ansatz can be understood as saying that eigenstates of the Hamiltonian effectively look like random states (albeit only within a reduced Hilbert space, whose size is measured by the entropy $S(E)$), a statement that was previously known in the context of chaotic semiclassical systems as *Berry's conjecture*[4] [161].

As a consequence of the close relationship between ETH and random matrix theory, many-body systems that obey the former tend to have spectral properties that conform to the predictions of RMT, and vice versa. Indeed, in this context, the words *chaotic* (which is defined in terms of RMT spectral statistics), and *ergodic*, (usually taken to be equivalent to 'ETH-obeying'), are often used interchangeably [94]. This is important for several reasons; one is that the spectral statistics is easier to check in practice, since it only requires knowledge of the eigenvalues, not the eigenvectors. One then studies the correlations between different energy levels, which can be used to distinguish systems that thermalize from ones that do not (see below for examples of the latter). Of course, the level statistics of a local, deterministic system are not exactly the same as that of a matrix whose elements are chosen independently (apart from the restriction of hermiticity), which has no notion of locality. Nevertheless, for generic systems, RMT statistics applies for energy levels that are sufficiently close to one another, below an energy scale known as the *Thouless energy* [94]. While this statement can be argued for rather rigorously in the semiclassical regime [161, 171–174], the first analytical studies in fully quantum many-body systems have only become possible recently, in the kind of random circuit models that are also the focus of this thesis [175–178], as well as in certain deterministic unitary circuits [179, 180]. These studies confirmed earlier intuition, that in systems with

---

[3] There are arguments to the effect that ETH is also a *necessary* condition [136, 137].

[4] Random matrix theory has also found important applications in many other areas of physics, for example in the study of transport in disordered mesoscopic conductors [167–169], and the related classification of noninteracting topological phases [170].

diffusive transport (see Section 2.3), the Thouless energy scales with the linear size of the system L as $E_{\mathrm{Th}} \sim 1/L^2$, making it exponentially larger than the average spacing between energy levels[5] Within this Thouless window, Eq. (2.3) reduces to the RMT prediction that eigenvectors of the Hamiltonian are essentially uncorrelated random vectors; however, ETH is in fact more general than RMT, and applies also outside on energy scales beyond E_{Th}, where the functions $\mathcal{O}(E)$ and $f_{\mathcal{O}}(E,\omega)$ start to play a role.

One particularly important characteristic of quantum chaotic systems that merits a brief discussion here is *level repulsion*[6]. According to this, the probability of two energy levels being very close to each other is strongly suppressed. In particular, the probability of two subsequent eigenvalues having a distance $E_n - E_{n-1} = \omega$ in a random Hermitian matrix with no additional symmetries is given by the *Wigner-Dyson* distribution [94, 154, 155], which is well approximated by $P(\omega) = A\omega^2 e^{-B\omega^2}$ (A and B are constants that can be fixed by normalizing P and fixing units such that the average level spacing is 1). Importantly, this function goes to zero in the limit $\omega \to 0$. One should contrast this with the naive expectation that one would get by assuming that the eigenvalues are all independently chosen random numbers, in which case they have *Poisson* level statistics, $P(\omega) = e^{-\omega}$, which goes to a finite value as $\omega \to 0$. We will later on study level repulsion in a different context, for the *entanglement spectrum* of a time-evolving state, in Chapter 6.

Importantly, not all physical systems satisfy ETH, or have RMT statistics. Quantum integrable models, which possess an extensive number of conserved densities, and consequently have non-diffractive scattering of infinitely long-lived quasiparticles, provide an example of systems that fail to reach thermal equilibrium (instead, in most cases they equilibrate to a so-called *Generalized Gibbs Ensemble*) [94, 99, 103, 181, 182]. Such models, however, are fine-tuned: a generic local perturbation will break integrability and lead to thermalization at sufficiently long times. A more robust counter-example to the ETH is provided by *many-body localization* (MBL) due to strong spatial disorder [93, 96, 102, 133, 183–186], an extension of *Anderson localization* [187, 188] to the interacting regime. In one dimension, MBL has been shown to form a stable non-equilibrium phase of matter, robust against arbitrary local perturbations [189–194]; whether the same is true in higher dimensions is currently debated [195–200]. Since they evade the rules of statistical mechanics, many-body localized systems can exhibit interesting physical phenomena prohibited in equilibrium, such as otherwise forbidden ordering at finite energy densities (e.g., symmetry breaking or symmetry protected topological order in one dimension) [96, 201–204], or entirely new phases of matter particular to *periodically driven* (also known as Floquet) systems [205–211], which would otherwise thermalize to a featureless, entropy-maximizing (‘infinite temperature’) state [212–215]. *Time crystals* provide a particularly striking example of such a genuinely out-of-equilibrium phase of matter [216–221].

In this thesis, we will be concerned with systems that *do* thermalize, and ask questions about the properties of the thermalization process, identifying a variety of relevant time scales and universal exponents that characterize the approach to equilibrium. Dynamics in the MBL phase has also been studied extensively, and has its own universal features [222–224], however these call for a different set of tools and are in some ways simpler than thermalizing ones. Yet another physically interesting regime is the case of moderate disorder, close to, but outside of the MBL phase. While these systems thermalize, the dynamics at earlier times can be dominated by rare localized regions and can look qualitatively different from those of translationally invariant or weakly disordered systems [225–232]. While these are more amenable to the methods we use in this thesis [233],

---

[5] In systems without conserved quantities (which we study in Part I of this thesis), the Thouless energy can be even larger, decaying only logarithmically with L [176, 179].

[6] Another one is *level stiffness* (also known as *spectral rigidity*), which says that the variance of the number of energy levels within an interval of size ΔE grows only as $\sim \log \Delta E$, much more slowly than the $\sim \Delta E$ that one would expect for e.g. independent random numbers.

we will also refrain from discussing them here.

2.2. Quantities of interest

In our discussion of thermalization above, we focused on the evolution of expectation values of (local) observables, $\langle\mathcal{O}\rangle(t)$. These are the simplest to interpret physically, and also the easiest to access in experiments (see below). One could extend this to other one-time observables, such as equal time correlations of the form $\langle\Psi(t)|\mathcal{O}_x\mathcal{O}_y|\Psi(t)\rangle$, where $\mathcal{O}_{x,y}$ are observables localized around positions x, y (while such a 2-point correlator is no longer local in space, it is still 'few-body', and thus expected to satisfy ETH). Another set of observables, that appear naturally, for example in description of transport properties (see Section 2.3), are two-time correlations of the form $\langle\mathcal{O}_x(t_1)\mathcal{O}_y(t_0)\rangle_\beta$, where β is used to denote that these correlations are usually evaluated in some thermal ensemble, characterized by its inverse temperature β. It turns out, however, that these *time-ordered* observables do not tell the whole story: to describe quantum thermalization, it is often useful to consider more intricate objects, which characterize the evolution of quantum information.

2.2.1. Out-of-time-ordered correlators

Common to all time-ordered observables above is that they are 'second order' in the time evolution operator $U(t)$, in the sense that they involve a single forward and a single backward time evolution[7] (consider $\mathcal{O}(t) \equiv U(t)^\dagger\mathcal{O}U(t)$ as the simplest example). Another way of expressing this is that all these quantities can be evaluated by considering the object $U^* \otimes U$, which acts as an evolution operator on a doubled Hilbert space (i.e., the space of operators). However, there are quantities of interest which are higher order function of U. As a particular example, consider the so-called out-of-time-order correlator (OTOC) [234–240] between operators $\mathcal{O}_x$ and $\mathcal{O}_y$:

$$\mathrm{Re}\langle\mathcal{O}_x(t)\mathcal{O}_y(0)\mathcal{O}_x(t)\mathcal{O}_y(0)\rangle = 1 - \frac{1}{2}\langle[\mathcal{O}_x(t),\mathcal{O}_y(0)]^\dagger[\mathcal{O}_x(t),\mathcal{O}_y(0)]\rangle, \tag{2.6}$$

where Re stands for the real part. Such OTOCs were originally introduced due to their connection to classical chaos [241]. In a classical limit (e.g. $\hbar \to 0$, or a large-S limit in a spin model), the commutators in Eq. (4.15) are replaced by Poisson brackets, and the resulting quantity measures the divergence of nearby classical trajectories, which can then be used to define Lyapunov exponents [241–243]. While it was proposed that one can define 'quantum Lyapunov exponents' analogously, using the OTOC in (4.15) [125, 238, 244–248], it appears that this only leads to positive exponents in systems that are close to some classical or mean-field limit [1, 231, 243, 249–253]. Nevertheless, the OTOC is a useful quantity even away from the semiclassical limit, as it can be used to characterize the spreading of information from simple to complicated degrees of freedom during the evolution. In particular, while equal-time correlations of the form $\langle\mathcal{O}_x(t_1)\mathcal{O}_y(t_0)\rangle$ are useful in characterizing the light cone spreading of correlations in integrable systems [130, 254, 255], in generic systems at finite temperatures such correlators decay to zero after the quasiparticle lifetime; OTOCs, on the other hand, can be used to define a propagating wavefront of quantum information for these systems, even at infinite temperature [249]. The speed of this front is known as *the butterfly velocity*, v_B, named in reference to its relationship with classical chaos [234, 237, 256]. At infinite temperature, it is a close relative of the aforementioned Lieb-Robinson velocity[8], but it also allows to probe behavior

---

[7] In a Keldysh path-integral formalism this means that one generically needs two time contours to evaluate these quantities.

[8] Their difference consists in a different choice of norm for the commutator: operator norm or Frobenius norm.

at finite temperatures.

A peculiarity of the OTOC is that, due to the lack of time ordering, it is a higher order function of $U(t)$. On can think of Eq. (4.15) as a function of two copies of the time-evolved operator, $\mathcal{O}_x(t) \otimes \mathcal{O}_x(t)$, which corresponds to a *four-layer* evolution operator $U^* \otimes U \otimes U^* \otimes U$. One could extend this to higher order correlations involving n distinct, un-ordered points in time [257–260], which would evolve according to a $2n$-layer evolution, involving n copies of U and n copies of U^*. These 'higher order' observables can therefore probe structures in $U(t)$ that are not simply accessible from time-ordered measurements[9].

2.2.2. Entanglement and Rényi entropies

Another set of interesting quantities that similarly involve higher moments of U are the *Rényi entropies* [261] of reduced density matrices of various subsystems. Given the reduced density matrix, $\rho_A(t) = \mathrm{tr}_{\bar{A}}(|\Psi(t)\rangle\langle\Psi(t)|)$ ($\bar{A}$ being the complement of A), they are calculated as

$$S_\alpha(t) \equiv \frac{1}{1-\alpha} \log \mathrm{tr}(\rho_A^\alpha), \tag{2.7}$$

for $\alpha \in [0, \infty]$. This definition includes as a special case the von Neumann entropy [262, 263], recovered in the limit $\alpha \to 1$. In a pure state, where the entropy of the whole system vanishes, these entropies can be used to characterize the amount and structure of entanglement between degrees of freedom inside and outside of A. They also play a crucial role in our understanding of quantum thermalization. In particular, for subsystems that are much smaller than the whole system, ETH ensures that at long times $\rho_A(t \to \infty)$ will be indistinguishable from a Gibbs state [135]; consequently, the thermal entropy that characterizes the equilibrium state is the von Neumann entropy of ρ_A in this limit. Therefore *the thermal entropy is equal to the entanglement accumulated during time evolution.* One sometimes formulates this by saying that 'a thermalizing quantum system acts as its own bath' [106, 264, 265].

Thermal entropy is extensive, so a thermalizing system must have $\lim_{t\to\infty} S_1(t) \sim |A|$ (in fact, the same holds for other values of the Rényi index α, due to the Gibbs form of ρ_A). The initial state, $|\Psi(t_0)\rangle \equiv |\Psi_0\rangle$, on the other hand, by our assumptions satisfies an *area law*, $S_1(t_0) \sim |\partial A|$ (where ∂A denotes the boundary of subsystem A). Therefore, in order to approach thermal equilibrium, large amounts of entanglement need to be generated between A and $\bar{A}$. A crucial part of understanding the detailed mechanisms of thermalization is understanding how this entanglement generation occurs. While an appealing theoretical picture was developed early on for integrable systems [106, 131, 264, 266–268], it relies crucially on the notion of long-lived quasiparticles that can act as carriers of entanglement, and it therefore does not generalize to chaotic dynamics. In fact, the physical mechanisms for entanglement growth are qualitatively different in the two cases. In the integrable case, essentially all the entanglement is 'created' at time t_0, in the form of short-distance Bell pairs. The only role of the subsequent dynamics is to move the particles that make up the Bell pair apart from each other (via the ballistic propagation of quasiparticles); the entropy of A grows as more and more particles enter it (with their Bell partners lying in $\bar{A}$). In the chaotic case, on the other hand, entanglement is being continually generated by interactions between particles, which is the main source of entanglement growth, rather than their free propagation. This is exemplified by the fact that

---

[9] One could of course always reconstruct the full evolution if one has access to *all* time-ordered correlations. However, information that is readily available in the OTOC might be hidden in the detailed correlations between a very large number of different such measurements. The difference becomes even clearer when we consider *ensembles* of random evolutions, as we shall do later on; in that case the behavior of higher moments of U, such as $U^* \otimes U \otimes U^* \otimes U$, contains information not accessible by considering lower moments, e.g. $U^* \otimes U$. See also the notion of unitary k-designs [259].

the same interactions generically render transport diffusive (rather than ballistic), while the growth of the von Neumann entropy remains linear [269]. Another, more direct, way to detect this crucial difference is by considering measures of multi-party entanglement, which are small in the integrable case, but large for chaotic systems, signaling the 'all-to-all' nature of entanglement in the latter case, as opposed to the simple Bell-pair picture of integrable dynamics [240, 270–272]. These considerations show that one needs a new theoretical framework for understanding entanglement dynamics in generic systems. As we shall see below, random circuits provide a crucial tool for developing such a framework (see Chapter 5 in particular).

The linear growth of S_1 defines another scale in the system, known as the *entanglement velocity*, v_E [256, 273–276]. It is defined such that $\frac{\partial S_1}{\partial t} = |\partial A| s_\mathrm{eq} v_\mathrm{E}$, where s_eq is the entropy density of the equilibrium state that the system approaches. It can be argued on general grounds that $v_\mathrm{E} \leq v_\mathrm{B}$, with equality occurring only in specific, highly fine-tuned cases [256, 277]. v_B and v_E therefore define two distinct time scales for the scrambling of quantum information. We will discuss an alternative way of addressing these time scales in Chapter 6. Moreover, one could define a separate entanglement velocity for each Rényi entropy S_α, which can give even more insight into the dynamics of thermalization [278]. However, in Chapter 10 we will argue that in a wide class of systems (those with diffusive transport), the velocities associated to entropies with index $\alpha > 1$ are in fact zero, and these Rényi entropies instead grow sub-ballistically.

2.3. Slow variables and hydrodynamic equations

At first glance, saying anything meaningful about even the simplest of such dynamical quantities, such as time-dependent expectation values $\langle \mathcal{O} \rangle(t)$, appears to be an insurmountable task. In an initial state with a high energy density, there is an exponentially large number of processes available for the system to relax towards equilibrium; one would in principle need to keep track of all of these. Indeed, at short times, one can say very little generically, and has to treat systems on a case-by-case basis[10]. Luckily, this is the regime where numerical methods are most reliable.

There is, however, an intermediate time regime, still much before full equilibration, where the dynamics simplifies and universal features can emerge. This has to do with the fact that, precisely because of the huge number of possible processes, most degrees of freedom relax after some quick local thermalization time. The important exception is provided by *conserved quantities*, more precisely their local densities. An excess of such a conserved quantity cannot relax back to equilibrium locally: it has to be transported across the system [279–282]. This is especially important when the density varies slowly in space (compared to microscopic length scales), in which case it is locally close to being in equilibrium and will be almost stationary. In particular, one could consider a plane-wave like sinusoidal modulation of the density, parametrized by its wavenumber k. The conservation law implies that the relaxation time for this mode has to diverge in the limit $k \to 0$. In this sense, the conserved densities define *slow modes* for the dynamics.

2.3.1. Diffusive hydrodynamics of conserved densities

This discussions suggests a two-step picture of equilibration. After the local thermalization time, the system reaches a state of *local equilibrium*. At this point, local 'fluid cells' (parts of the system that are large compared to microscopic scales, but much smaller than the

---

[10] At exceedingly small times, where t is much below the inverse of the typical interaction strength (equivalently, when $v_\mathrm{LR} t \ll 1$), one can use perturbation theory to follow the dynamics of local quantities. These are times where communication between sites beyond nearest neighbors is negligible; as such, they are not very interesting from the perspective of many-body physics.

whole) are well approximated by a thermal states[11]. As such, they are parametrized only by the total amount of each conserved quantity they contain, or, equivalently, the corresponding intensive variables (temperature, chemical potential, etc.). The second part of the thermalization process involves the smoothing of these space-time dependent density profiles, until they become homogenous. Note, however, that while this description (which is essentially unchanged in the case of a classical many-body system) adequately describes the evolution of local observables and their correlations, it misses the non-trivial dynamics of various measures of quantum information, which we discussed above, and which we will be concerned throughout much of this thesis. Nevertheless, we will find it useful to understand the dynamics that emerges from this local equilibrium approximation, for two reasons. First, it provides a blueprint for the appearance of universal features, for which we shall find analogies in other quantities later on. Second, when the aforementioned slow modes are present, they play an important role in determining the dynamics of more involved quantities (OTOCs, Rényi entropies), as we will discuss in Part II.

Consider a system with a single conserved 'charge', $\hat{Q} = \int \mathrm{d}x\, \hat{q}(x)$[12]. As a physical example, one could think of $\hat{q}$ as the energy density. The equilibration of the local density $\hat{q}(x)$ is governed by the continuity equation,

$$\partial_t \hat{q}(x,t) = -\partial_x \hat{j}_q(x,t), \tag{2.8}$$

which defines the associated current $\hat{j}_q$. While this is an exact operator equation, it is in itself not very useful. However, one can simplify it by taking its expectation value and making use of the assumption of local equilibrium. In this case, the state of the system should be characterized by the density profile $\langle \hat{q}(x,t)\rangle$, and thus the current should also be a function of this profile. The relation between the two can still in principle be very complicated; however, one can often make a *linear* approximation, which can be written (assuming space-time translation invariance) as

$$\langle \hat{j}_q(x,t)\rangle = -\int \mathrm{d}x' D(x-x')\partial_{x'}\langle \hat{q}(x',t\rangle. \tag{2.9}$$

The last step is to assume that the density profile is smoothly varying. In this long-wavelength limit, one can perform a gradient expansion of the current (or, equivalently, expand the Fourier transform of $D(x)$ in the wavenumber k) to find

$$\langle \hat{j}_q(x,t)\rangle = -D\partial_x\langle \hat{q}(x,t\rangle + c\partial_x^2\langle \hat{q}(x,t\rangle + \ldots. \tag{2.10}$$

The leading order dynamics of the density is then given by the *diffusion equation*

$$\partial_t\langle \hat{q}(x,t\rangle = D\partial_x^2\langle \hat{q}(x,t\rangle. \tag{2.11}$$

It is characterized by a single transport coefficient, the diffusion constant D.

Part of the assumptions that went into the above hydrodynamic approximation is locality in time: the current follows changes in the density profile instantaneously. A more general version, that takes into account a potential time-delay would read[13]

$$\langle \hat{j}_q(x,t)\rangle = \int \mathrm{d}t' \int \mathrm{d}x' D(x-x',t-t')\partial_{x'}\langle \hat{q}(x',t')\rangle. \tag{2.12}$$

---

[11] In a dilute gas, one can use the Boltzmann equation to motivate the emergence of such local equilibrium states and the subsequent hydrodynamic description [283, 284]. However, we are concerned with the strongly interacting regime where such semi-classical descriptions are of limited use.

[12] In this section we use a continuum notation. On a lattice, integrals and derivatives should be replaced by their discrete counterparts; alternatively one can use sufficiently coarse-grained variables such that the underlying lattice structure becomes unimportant. We also use notation that suggests a one-dimensional system, since these will be at the focus later on, but all the discussions of this section generalize naturally to arbitrary dimensions.

[13] See also our discussion of memory matrices in Section 9.1

The function $D(x,t)$ now incorporates memory effects. These can arise through processes that propagate through the subspace of fast variables. Assuming we have identified the slow subspace appropriately, these processes should have a short relaxation time, making the memory kernel quickly decay in time. On time scales much larger than this microscopic 'memory time', which is the regime typically relevant for hydrodynamic transport, these effects are therefore often negligible, such that to a leading order one canmake a Markov approximation, $D(x,t) = D(x)\delta(t)$, recovering Eq. (2.9). However, these neglected microscopic processes do factor into the value of the diffusion constant (and the coefficients of the subleading terms in the gradient expansion).

From a physical perspective, it is natural to assume that the same transport equation that governs the relaxation of an inhomogenous density profile, shows up also in its spontaneous thermal fluctuations, as measured by the *equilibrium* correlation functions $C_q(x,t) = \langle \hat{q}(x,t)\hat{q}(0,0)\rangle_{\text{eq}}$ (if $\langle q\rangle_{\text{eq}}$ is different from zero, one should of course consider the connected correlation instead). Indeed, this intuition is made rigorous in the linear response regime [279, 285, 286]. We can imagine that the inhomogenous initial profile at time 0 in the non-equilibrium case is prepared by adiabatically applying an appropriate external field which is then switched off. For small fields, linear response theory then tells us that the evolution of the density is, to leading order, governed by the response function, which is indeed the unequal time correlation of the density in equilibrium[14]. Therefore, the universal low-frequency, long-wavelength behavior of the correlation is also governed by the diffusion equation. At high temperatures, where the equal-time correlations decay rapidly, and we can approximate the initial condition at $t = 0$ by a Dirac delta, this suggest a Gaussian shape:

$$C_q(t,x) \approx \frac{e^{-\frac{x^2}{2Dt}}}{\sqrt{2\pi Dt}}. \tag{2.13}$$

The correlations therefore spread out within a *diffusive cone*, of size $\sqrt{t}$, much smaller than the ballistic Lieb-Robinson cone dictated by locality alone. Relatedly, the correlations at a fixed position decay slowly, as a power law $\sim t^{-1/2}$. Indeed, the relationship between such equilibrium correlations and transport gives rise to the usual Kubo formula for calculating the diffusion coefficients:

$$D = \frac{1}{L^d\, k_B T \chi} \int_0^\infty \mathrm{d}t \langle \hat{J}(t)\hat{J}\rangle_{\text{eq}}, \tag{2.14}$$

where $\hat{J} = \int \mathrm{d}x \hat{j}_q(x)$ is the total current, χ is the static susceptibility[15] and L^d is the volume of the system. We mention here that there is yet another different, but related context, where dynamics is governed by the same diffusive transport equation. This is the relaxation of *equal time* 2-point correlations of the density, $\langle\Psi(t)|\hat{q}(x)\hat{q}(0)|\Psi(t)\rangle - \langle\hat{q}(x)\hat{q}(0)\rangle_{\text{eq}}$, after a quantum quench from a *homogenous* initial state $|\Psi_0\rangle$. These show the same diffusive, Gaussian space-time profile [287].

The above treatment easily generalizes to the case of several conserved densities, $\{\hat{q}_i\}$ (for example energy and particle number/electric charge). In this case, the diffusion constant acquires a matrix structure, D_{ij}, which relate currents of the charge $\langle\hat{q}_i\rangle$ to the gradient $\partial_x\langle\hat{q}_j\rangle$. The off-diagonal components measure thermopower-type effects, where e.g. a temperature gradient generates an electric current or, vice versa, a gradient in the electric potential generates a heat current. D_{ij} and D_{ji} are related to each other via the *Onsager relations*[16] [281, 288].

---

[14] While the response function is not exactly the same as C_q, the two are related to each other via the fluctuation-dissipation relation.

[15] χ is defined by the response of the conserved quantity to a change in the associated intensive variable, e.g. a chemical potential: $\chi \equiv \frac{\partial\langle Q\rangle}{\partial\mu}\big|_{\mu=0}$. It can be shown to be equivalent to the spatially averaged correlator, $\chi = k_B T \int \mathrm{d}x C_q(0,x)$ [279]

[16] To write these in the simplest form, one usually replaces gradients of q_i with gradients of the corre-

2.3.2. Going beyond diffusion

Our discussion relied on the notion of local equilibrium. This is expected to be quickly established at finite energy (or particle) densities, by the frequent collisions between particles. The situation is quite different at low densities: Near the ground state, close to zero temperature, most quantum systems exhibit long-lived stable quasiparticles[17]. These quasiparticles, which are effectively non-interacting, propagate ballistically, rather than diffusively[18]. At low but finite temperatures (or particle densities) this results in a crossover: at short times, before collisions can take place, the ballistic behavior dominates, but it crosses over to diffusive transport at the local thermalization time, which diverges as one approaches zero temperature. This is again a manifestation of *dephasing*, which we discussed already in the context of thermalization and the ETH above: the ballistic transport of free quantum particles is a consequence of phase coherence; when coherence is destroyed by the interactions, the motion of particles becomes that of a a classical stochastic random walk. Since the diffusion sets in due to the interactions, whose effective strength depends on the density of the conserved quantities themselves, this also suggests that the transport coefficients themselves should also in general depend on the background value of these charges (or equivalently, their intensive counterparts, such as temperature and chemical potential). This introduces a form of non-linearity to the hydrodynamic description that we ignored in our simplistic derivation.

One can apply renormalization group (RG) methods to argue that the simple diffusive description nevertheless gives the leading order universal behavior, and the neglected contributions (higher derivative terms, nonlinearities and memory effects) are irrelevant perturbations. Nevertheless, they do give rise to interesting physical effects. One of these is that the higher order corrections to the diffusion equation give rise to subleading power laws in the relaxation of correlation functions. For example, the autocorrelations of a single conserved quantity would then decay as

$$C_q(t,0) = (2\pi D t)^{-\frac{d}{2}} + a_1 t^{-\alpha_1} + a_2 t^{-\alpha_2} + \dots,$$

where $\alpha_i > d/2$; these various power laws often go under the name of *hydrodynamic long-time tails*[19] [287, 293–295]. The simplest of these originates from the next order in the gradient expansion, $\partial_x^4 q$, and gives $\alpha_1 = d/2+1$. Another contribution comes from from nonlinearities of the form $\partial_x(q\partial_x q)$[20], which lead to an exponent $\alpha_2 = d$, which becomes the leading correction in $d = 1$ and is of the same order as the higher derivative correction in $d = 2$.

Another important effect is that the interaction between slow and fast variables can be taken into account as a randomly fluctuating force exerted on the former by the latter [279, 293]. This would show up as an additional term on the RHS of Eq. (2.9) (or in Eq. (2.12), if we take into account that the noise has a finite autocorrelation time; see also Section 9.1), which turns the equations of motion for the conserved densities into stochastic equations.

---

sponding intensive variable, the 'chemical potential' μ_i, in the driving force. Then the constitutive relation reads $j_{q_i} = L_{ij}\partial_x \mu_j$, where the Onsager matrix now has to be symmetric, $L_{ij} = L_{ji}$, for systems that are invariant under time reversal.

[17] There are exceptions to this in the case of certain gapless systems in $d \geq 2$ dimensions. These are usually referred to as *strange metals*.

[18] This is the case in a clean system without disorder. In a real sample, impurities are bound to be present. Taking into account the scattering of charge carriers off of these impurities leads to the well known Drude-Sommerfeld theory, which again predicts diffusive transport of charge. This description, however, breaks down in dimensions $d < 3$, where non-interacting electrons tend to become Anderson localized in the presence of arbitrarily weak disorder [188, 289].

[19] A closely related phenomenon is the appearance of power-law tails in *other* correlations functions, most notably in the current-current (or velocity-velocity) autocorrelations [290–292].

[20] Note that this term has to vanish whenever the system has a symmetry $q \to -q$. This occurs for example at infinite temperature / zero chemical potential.

On a formal level, this is completely analogous to the derivation of the Langevin equation for Brownian motion for a heavy particle immersed in a fluid of lighter ones (with the role of the ratio of the two masses played by the momentum k) [279]. The resulting theory is referred to as *nonlinear fluctuating hydrodynamics* [296–299]. A fully systematic effective field theory approach that takes all these various effects into account has been developed only recently, see Refs. [281, 295, 297] for details.

We note, in passing, that a richer form of hydrodynamics emerges in systems which have microscopic translation invariance. In this case, one has to include also the momentum density among the slow variables, which is differentiated from the ones discussed above by the fact that it is asymmetric with respect to time-reversal (and spatial parity). Using approximation similar to the ones above, one ends up with a hydrodynamic description, which in this case takes the form of the Navier-Stokes equation. This includes new transport coefficients, the (shear and bulk) viscosities, which relate the momentum current density to gradients of the momentum density (the local fluid velocity). This leads to a more complicated structure for correlations functions in a fluid, one that also involves ballistically propagating (sound) modes, which are damped by viscosity.

It is also interesting to note, that this picture is modified quantitatively in one spatial dimension. In this case, leading order nonlinearities become relevant perturbations, and, together with the aforementioned noise terms, give rise to a new universality class, characterized by what is known as the *stochastic Burgers equation* [291, 298–302] for the (mass) density of the fluid. After a change of variables (from the density ρ to its derivative, $\partial_x \rho$), this is found to be equivalent to the celebrated Kardar-Parisi-Zhang (KPZ) equation [303] (which we will encounter later on in some very different contexts). This leads, for example, to a $\sim t^{-2/3}$ relaxation for certain modes, as opposed to the $\sim t^{-1/2}$ predicted by diffusive hydrodynamics. Nevertheless, in the strongly interacting lattice systems we will be concerned in this thesis, Umklapp scattering processes provide an efficient way for momentum relaxation, and therefore the simpler, diffusive hydrodynamics outlined above will be sufficient for our purposes when we consider the role of conservation laws in Part II.

The considerations presented here should make it clear that a central ingredient in arriving at the hydrodynamic description is that the system (locally) thermalizes; this is why it is sufficient to keep track of only the conserved quantities at late times[21] It is therefore natural to expect that our approximations should break down in systems that do *not* thermalize. Indeed, in integrable models, the existence of infinitely long-lived quasiparticle excitations usually leads to ballistic transport of at least some of the conserved quantities [286, 304, 305]. An example studied very extensively in recent years is the spin-1/2 XXZ chain, where energy transport is ballistic, while spin transport can be diffusive, ballistic, or even super-diffusive (between diffusive and ballistic)[22], depending on the anisotropy and filling fraction [286, 312–319]. Many of the non-equilibrium properties of integrable systems can nevertheless be captured in the spirit of hydrodynamics, provided that one takes into account the infinite set of extensive quantities, that is, relying on local equilibration to a Generalized Gibbs Ensemble and using Bethe Ansatz technology [320–323] to evaluate the current densities. The resulting coarse-grained description was named *Generalized Hydrodynamics* and has been the object of extensive study in recent years [282, 307, 324–329]. Many-body localization, on the other hand, leads to

---

[21] Let us mention here that slow modes can arise also for reasons other than an explicit conservation law. The most prominent example is the case of a spontaneously broken continuous symmetry, which gives rise to new slow degrees of freedom, closely related to the Goldstone modes [279].

[22] This latter case is realized in the isotropic—$SU(2)$-invariant—point, and there are results suggesting that it is also described by the KPZ universality class, leading to a $\sim t^{2/3}$ spreading of correlations [306–310]. Another recent paper [311] argues that non-Abelian rotation symmetry can also lead to a weak breaking of diffusive scaling, with logarithmic corrections of the form $\sim t^{1/2} \log t$, even in non-integrable systems.

a complete suppression of transport and a state that is insulating at arbitrary temperatures [96]. Are there any systems that *do* thermalize, but do not show diffusive transport, even at high temperatures? It has been suggested that non-Abelian symmetries can lead to logarithmic corrections [311] (see previous footnote[22]), which can make spin transport faster than diffusive. On the other side, there is evidence showing that disordered systems can have a regime of intermediate disorder strength, where the they are not yet MBL, but their dynamics is dominated by rare localized regions, leading tot sub-diffusive transport, with a power-law exponent that continuously interpolates between 1/2 (diffusion) at weak disorder and 0 at the MBL transition [225–233]. Recently, it was demonstrated that sub-diffusive transport can arise also from the conservation of various higher moments of the conserved quantity (e.g. the total dipole moment) [330–333]. We will not discuss these cases further, and will instead focus in the following on systems that either have no conserved quantities or show simple diffusive transport[23].

In the approach we outlined here, the hydrodynamic equations (in the simplest case discussed above, the diffusion equation) follow from general considerations. Connecting them to the microscopic dynamics, on the other hand, is a highly non-trivial matter. One for example would like to confirm the diffusive nature of transport, calculate its subleading corrections, as well as compute the various coefficients associated to these, starting from a particular microscopic model for the evolution, e.g. a particular many-body Hamiltonian. A useful general approach was developed by Zwanzing and Mori, which goes under the name of *memory matrix formalism* [279, 335–339]. In this approach, one takes seriously the splitting of degrees of freedom into slow and fast subspaces, and tries to systematically compute the contributions to the equilibrium dynamical correlations of slow operators from processes that travel through fast modes. Assuming the splitting was done correctly, these corrections should be negligible beyond some short 'memory time'. This leads to physically transparent formulae for various transport properties[24]. However, evaluating the predictions of the memory matrix method in practice is itself no easy task, and is mostly restricted to perturbations around some fine-tuned point [340, 341]. We will return to these issues in Chapter 9.

What the discussion of this section shows is that, focusing on the correct ('slow') variables, one can find relatively simple universal descriptions of various dynamical quantities. Much of what we will be concerned with below is developing similar effective descriptions for the more complicated quantities introduced in Section 2.2 to characterize the scrambling of quantum information. In these cases, identifying the appropriate slow variables and their effective dynamics is less intuitive. For this reason, we will take a different approach. Rather than trying to motivate a description on general grounds, we consider concrete minimal models, which are designed to capture the universal features of the dynamics. One can think of these as effectively projecting out the fast variables (making their relaxation time zero), so that one is left with only the dynamics of the slow modes. We can then use these to extract the universal features that generalize to broader classes of physical systems. Moreover, these minimal models also provide quantitative results which are of interest on their own right.

Finally, before concluding this section, we summarize some of the most relevant time scales for dynamics in generic thermalizing quantum systems with local interactions and

---

[23] Given that diffusion is quite generic in thermalizing systems, and that long-time dynamics in these system is dictated by the ETH, one might naturally wonder if there is a relationship between the two. In fact, diffusion shows up as a subleading correction in the off-diagonal part of ETH [94], making the variance of a conserved density, $\langle n|\hat{q}|m\rangle$, scale, in the regime $|E_n - E_m| < 1/L^2$, as $\sim e^{-S(E)}L$. Note that $S(E) \propto L$, so that the L constitutes a logarithmically small correction [94]. In Ref [334], the authors generalize this relation to disordered systems with sub-diffusive transport, where the subleading L is replaced by $L^{\frac{1-\gamma}{2\gamma}}$, with $\gamma < 1/2$ being the power-law exponent that characterizes the decay of autocorrelations of $\hat{q}$.

[24] See Section 9.1 for a short introduction.

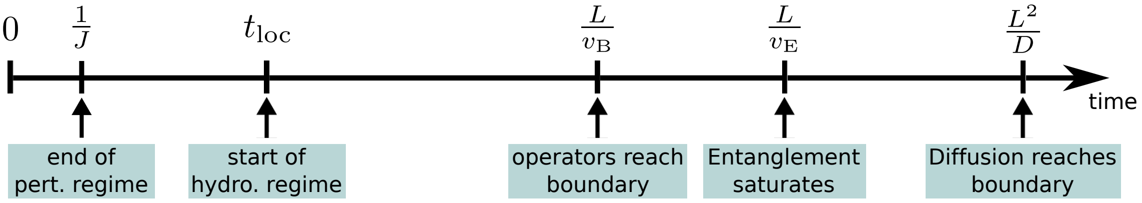

Figure 2.1.: Summary of time scales in generic clean local quantum systems. J is the local interaction strength. t_{loc} is the local equilibration time, after which hydrodynamic approximations become valid. v_{B} and v_{E} are the butterfly and entanglement velocities, introduced in Section 2.2. D is the diffusion constant (assuming a single conserved density).

no (or weak) disorder, in Fig. 2.1. There is some initial local dynamics at times $t \ll 1/J$, where J is some typical local interaction strength. Time-dependent perturbation theory breaks down at times $Jt \approx 1$. At a later time, t_{loc}, the system develops local equilibrium in each 'fluid cell'; at this point universal features can emerge, captured by hydrodynamic theories. For a finite system, or subsystem, of linear size L, the dynamics eventually leads to thermalization. At times $v_{\mathrm{B}}t \approx L$, operators have spread across the (sub)system, and information is largely scrambled on this scale. At a later time, $v_{\mathrm{E}}t \approx 1$, the von Neumann entropy of the subsystem (or half of the chain, if we consider the entire system) saturates to the thermal entropy. Finally, on much longer scales, $Dt \approx L^2$, the diffusive spreading of correlations also reaches the boundaries. If there are multiple diffusively transported quantities, then each defines a separate time scale, set by the associated diffusion constant (i.e., the eigenvalues of the diffusion matrix).

2.4. Overview of numerical methods used in this thesis

Despite their limitations mentioned in the introduction, numerical studies have played a central role in understanding quantum non-equilibrium phenomena. Here, we review the two approaches most relevant for our purposes:: exact diagonalization, and its cousins, and tensor network-based methods. Other numerical techniques include variations of quantum Monte Carlo [342–346], dynamical mean-field theory [347–350], Keldysh diagrammatic techniques [351–354] and recently neural network quantum states [355–358]. The development of new methods is ongoing [359–363], and we will describe a contribution of our own in Chapter 9.

2.4.1. Exact dynamics and quantum typicality

The simplest method is also one of the most widely used. For a sufficiently small lattice system, one can store both quantum states and Hamiltonians exactly on a computer. One can then study their behavior and compare different system sizes in an attempt to extract results about the thermodynamic limit [111, 112]. This approach is almost the only one available[25] if one want to study the highly excited eigenstates directly, for example to verify the ETH ansatz [94, 99, 138–148]. In this case, one constructs a matrix of the Hamiltonian and diagonalizes it numerically, hence the name *exact diagonalization* (ED). The diagonalization is numerically expensive, limiting its applicability to $L \approx 15$ qubits in the general case, which can be improved by exploiting symmetries, such as spin- or momentum conservation [112]. This method has also been used extensively to study the MBL phase and its associated phase transition [184, 365–368]. However, addressing the

---

[25] See Ref. [364] for an exception.

effects of finite size in these studies is often difficult. For example, there are various works suggesting that ED studies might significantly underestimate the critical disorder strength of the MBL transition [369–374].

A closely related method, also sometimes referred to as 'ED', despite the fact that it does not actually involve diagonalizing anything, is to perform the time evolution from a given initial state in a numerically exact fashion. In this case, the finite system size leads to, via the Lieb-Robinson velocity, a finite time scale, at which point results become dominated by finite-size effects. Since these time evolution studies do not require one to diagonalize the Hamiltonian, they are numerically more efficient, and can usually be done for significantly larger systems, up to $L \approx 25$ even in the absence of symmetries. The key feature that allows this is that local Hamiltonians are sparse matrices, with the number of non-zero matrix elements scaling only linearly, rather than quadratically, with the Hilbert space dimension [111, 112]. This means that matrix-vector multiplications can be performerd efficiently. One can then construct the time-evolved state from repeated matrix-vector multiplications[26] [229, 231, 375–377] (the simplest version of this is just a Taylor expansion of e^{-iHt}, but more efficient numerical schemes exist).

A helpful trick, often used in conjunction with these exact methods, is the one provided by *quantum typicality* [378–383]. This allows one to exchange the calculation of thermal correlations with studying ensembles of pure quantum states, which often turns out to be numerically less costly, especially at high temperatures. The basic idea can be explained by considering the infinite temperature case, $\beta = 0$. The key point is that the infinite temperature ensemble can be replaced by a pure quantum state, drawn randomly from the entire Hilbert space (using the unique probability measure specified by invariance under arbitrary basis changes, known ar the *Haar* measure [384]). Indeed, one can show by explicit calculation (see App. A.1), that such a random state $|\Psi_{\text{Haar}}\rangle$ satisfies $\overline{\langle\Psi_{\text{Haar}}|A|\Psi_{\text{Haar}}\rangle} = \langle A\rangle_{\beta=0}$, where $\overline{(\dots)}$ denotes averaging over random states and A is an arbitrary observable. Importantly, one can also show that the fluctuations between different choices of random states are suppressed by a factor of $\mathcal{N}^{-1/2}$, where $\mathcal{N}$ is the Hilbert space dimension, so in practice a single randomly chosen state will give a very good approximation of the thermal value. Note that this is very much similar in spirit to our discussion of quantum thermalization: a pure state can effectively mimic a thermal ensemble. Let us then consider a dynamical correlation function of the form $\langle A(t)B\rangle_{\beta=0}$. By the above argument, this can also be evaluated by taking a random pure state and then computing the overlap between $U(t)B|\Psi_{\text{Haar}}\rangle$ and $AU(t)\Psi_{\text{Haar}}$. This only requires evolving pure states, rather than operators; the latter is much more expensive numerically. This method has been applied succesfully to a variety of problems [113, 385–390], including the calculation of OTOCs [3, 231]; it can also be extended to finite temperatures, by appropriately sampling the states from the Hilbert space, for example by replacing $|\Psi_{\text{Haar}}\rangle$ with $e^{-\beta H/2}|\Psi_{\text{Haar}}\rangle$. This works well for high temperature, with the statistical errors increasing with β [113, 391, 392] (see also Ref. [393]).

2.4.2. Tensor network methods

While exact diagonalization-type studies have played a huge role in uncovering features of quantum dynamics, their fundamental limitation to small systems raises the need for alternative methods. Among the most successful of these are the ones formulated in the language of *tensor networks*. While we certainly cannot do full justice to tensor networks (see Refs. [85, 394–396] for some reviews), we give a brief overview of the most relevant aspects as they pertain to studying dynamics, especially in one spatial dimension. The

---

[26] One can similarly exploit the sparseness of the Hamiltonian if one only wants to compute a few (usually low-energy) eigenstates, rather than perform a full diagonalization. This is the essence of the so-called Lánczos method [112].

key idea behind tensor networks is to utilize locality, and in particular, the local structure of entanglement, to provide a more efficient representation of quantum states. For this reason, they work especially well in capturing states that satisfy an *area law* [394, 397, 398], meaning that the von Neumann entropy S_1 of a subsystem A is proportional to the surface area of A, rather than its volume. Tensor network states are therefore often used as a variational ansatz, which work particularly well for capturing area law states. This includes the ground states of all one-dimensional gapped local Hamiltonians [132, 399–404].

To illustrate these ideas, let us consider the most frequently used type of tensor network, called a *matrix product state* (MPS) [84, 85, 405–410]. Consider a one-dimensional chain of qubits, with sites labeled by $r = 1, 2, \ldots L$. On each site, we can choose a basis $|n_r = 0, 1\rangle$. The full many-body state can then be parametrized by a tensor with L indices of the form $\Psi_{n_1 n_2 \ldots n_L}$, which contains all the 2^L complex coefficients that characterize the state in this basis. The key idea is to rewrite this big tensor as a product of smaller tensors, one for each site. This local tensors, $A^{n_r}_{\alpha_{r-1}\alpha_r}$ have three indices[27] (also called 'legs'): one 'physical' index, n_r, which coincides with the appropriate index of Ψ, and two 'virtual' indices, which are contracted with one of the indices of the neighboring sites. One can think of these as separate matrices for each value of n_r (hence the name). These matrices are then multiplied together, such that the entire state is written as $\Psi_{n_1 n_2 \ldots n_L} = u_{\alpha_0} A^{n_1}_{\alpha_0\alpha_1} A^{n_2}_{\alpha_1\alpha_2} \ldots A^{n_L}_{\alpha_{L-1}\alpha_L} v_{\alpha_L}$, where u, v contain some appropriately chosen boundary conditions[28]. This is illustrated in Fig. 2.2(a). The index α_r goes from 1 to some integer χ_r, which is called the *bond dimension*;, making A^{n_r} a matrix of size $\chi_{L-1} \times \chi_L$. The bond dimensions specify how big a chunk of the Hilbert space we can capture with the MPS ansatz; χ_r limits the amount of entanglement between sites $[1, r]$ and sites $[r + 1, L]$ to be at most $\log \chi_r$. If $\chi_r = 1$ for all r then we are therefore simply describing product states. On the other hand, if $\chi_r = 2^{\min(r, L-r)}$, then we can describe an arbitrary state – this, however, requires an exponentially large bond dimension, $\chi = 2^{L/2}$, in the middle of the chain. For area law states, however, one can approximate the state to arbitrary precision while keeping $\max\{\chi_r\}$ independent of system size[29]. Part of the usefulness of MPS lies in the fact that many features of the state, such as local expectation values, two-point correlations or overlaps between states, can be computed very efficiently, by contracting the appropriate tensors[30] [85, 396]. Importantly, if the state is invariant under translations, one can also write down an MPS directly in the thermodynamic limit [85, 407–409, 413], parametrized by a single three-leg tensor $A^n_{\alpha\beta}$.

Matrix product states are, for the reasons outlined above, a central tool in studying the ground states of one-dimensional quantum systems, where one can variationally optimize the MPS to minimize its energy, using the celebrated density matrix renormalization group [82, 83, 85, 414–416]. However, they also found application in studying dynamics [85, 104, 105, 359, 360, 413, 417–423]. In this case, the entanglement of the state grows with time, approaching a thermal volume law, as discussed above. This implies that for a fixed maximal χ, one is limited to sufficiently early times before the MPS approximation breaks down. Generically, as we shall see, the von Neumann entropy tends to grow linearly in time [269], making the times attainable grow only logarithmically with $\chi_{\max}$. Nevertheless,

---

[27] In principle, these tensors can be different for each site and should have an additional label (not a tensor index!) that labels which site they belong to. Here, we suppress this to keep the notation cleaner.

[28] We are imagining an open chain here. For a closed chain, one can simply take the trace by making $\alpha_L = \alpha_0$. However, in practice, the open chain case is easier to deal with.

[29] Technically, the relevant property is area law for Rényi entropies S_α with index $\alpha < 1$ [132, 400, 411]. However, in most physical situations, area law of S_1 is sufficient.

[30] A key point, that we cannot do full justice here, is the *gauge redundancy* of the MPS description [85, 409, 412]. The matrices A^{n_r} and $M^{r-1} A^{n_r} M^r$ describe the same quantum state, for arbitrary matrices $\{M^r\}$. This can be used to transform any MPS into a *canonical form*; in the canonical form, a local expectation value on site r can be calculated using the matrices A^{n_r} alone, without having to contract the full network.

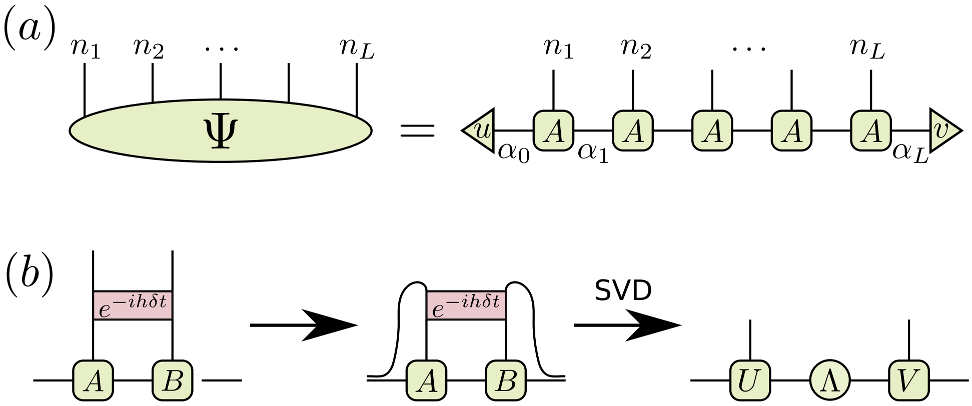

Figure 2.2.: Matrix product states. (a) MPS ansatz for a many-body quantum state. Each site corresponds to a three-leg tensor A (with site label suppressed). (b) Main steps of the TEBD algorithm for time evolving an MPS for a nearest neighbor Hamiltonian. In the 1st step, a pair of neighboring MPS tensors (denoted by A and B) are updated, by evolving them with a local 2-site term h of the Hamiltonian, for a small time step δt. In the 2nd step, the resulting four-leg tensor is re-interpreted as a matrix, by grouping two pairs of legs together. In the 3rd step, an SVD is performed on this matrix, to split it up into single-site tensors again. The singular values are contained in the matrix Λ, which can be truncated if necessary to keep the maximal bond dimension fixed.

the fact that the MPS methods allow one to study dynamics of large systems, or even directly in the thermodynamic limit, make them a useful tool, complementing the ED studies discussed above.

The simplest method to time-evolve an MPS, which we will utilize in this thesis, is called time-evolving block decimation (TEBD) [104, 417]. It relies on breaking up the evolution into an application of 2-site unitary operations, via a Trotter-Suzuki decomposition [104, 421, 424, 425], which works particularly well for Hamiltonians with only nearest-neighbor interactions. Then one can update the MPS tensors for a pair of neighboring sites at a time, by applying the 2-site unitary and then performing a *singular value decomposition* to turn the result back into MPS form (see Fig. 2.2(b)). The singular values that appear are nothing else but the Schmidt values corresponding to the entanglement between the two halves of the chain, separated by the bond that is being updated. Consequently, the new tensors will tend to have an increased bond dimension to reflect the new entanglement generated by the unitary; this would lead to the bond dimensions growing exponentially in time. In practice, one has to cut this off by fixing a maximal χ in the simulation; the MPS tensors are then truncated, by throwing away the smallest singular values to compress the bond dimension back to χ. The error of this approximation is characterized by the sum of squares of the discarded singular values, the *truncation error*. As long as it is sufficiently small, which is the case at early enough times, the MPS gives a good approximation of the true time-evolved state.

There exist a variety of other methods for evolving an MPS in time, some of which also apply easily to longer-range interactions [359, 360, 423]. There are also plenty of numerical approaches that rely on slightly different tensor networks. For example, one can represent operators, rather than states, in a very similar form, the only difference being that the local tensors in this case have four indices, $A^{n_r n'_r}_{\alpha_{r-1}\alpha_r}$, corresponding to the in- and out indices of the operator. One can then use these to represent observables (density matrices), and perform Heisenberg (von Neumann) evolution, for example by an simple modification of the TEBD algorithm[31] [361, 427, 428]. One important aspect, that several recent papers have focused on, is trying to develop tensor network methods that appropriately capture the hydrodynamic behavior discussed in Section 2.3 [361, 429–431]. This would bridge the gap between the microscopic, early-time behavior, and the late-time universal physics, while allowing to calculate the transport coefficients directly from the underlying Hamiltonian. The issue here is that the truncation of Schmidt values in the TEBD scheme leads to a violation of conservation laws, making it ill-suited for capturing transport appropriately. Other methods get around this limitation, either by modifying the truncation scheme appropriately [361], or by replacing it with a projection instead [359, 360, 429]. In these cases, conservation laws are exact, leading to *some* form of transport. However, it is at present unclear, whether these methods actually capture the correct transport coefficients, and there is in fact evidence that they do not, at least in certain cases [430]. We will propose an alternative, more well-controlled method below in Chapter 9. For a recent, comprehensive review of time-evolution using tensor networks, see Ref. [105].

2.5. Experimental platforms

As mentioned already in the introduction, much of the progress in the field of quantum dynamics has to do with the important experimental advances that made it possible to realize quantum many-body systems that are isolated from the environment (at least to a sufficient degree such that any coupling to the outside world is negligible on the time scales on which they are observed) and to probe their various properties, including those discussed in Section 2.2. A variety of different platforms have emerged over the years which allow for such experiments to be performed, each with its own advantages and disadvantages. In particular, different setups offer various degrees of control over initial states, microscopic interactions, dimensionality and number of degrees of freedom, the type of quantities that can be accessed by measurements and the coherence times until which the experiment can be run without encountering the effects of the environment. Here we review the most relevant of these, along with a few key experiments, while an overview of the whole field is of course outside the scope of this thesis.

2.5.1. Ultracold atoms and trapped ions

The two experimental platform most relevant for our purposes are (neutral) *ultracold atoms* [60, 432, 433] and *trapped ions* [43, 61, 434]. Both provide a very high degree of control and tunability, regarding both the interactions between the constituents and the precision with which they can realize particular quantum states. In the case of neutral atoms, the controlling of interactions is achieved by the *Feshach resonance* effect, which allows changing both the magnitude and sign of contact interactions between atoms, by tuning an external magnetic field. External trapping potentials allow experimenters to change the dimensionality of the system, i.e. confining the atoms to lines or planes. In the case of ions, one has access to an array of manipulation techniques that are not available for neutral atoms, making it possible to address individual ions with an extremely high precision. Internal (usually hyperfine) states of the ions can serve as effective spin degrees of freedom and their states can be manipulated with near perfect precision via lasers. A downside is that the charged ions exhibit long-ranged interactions as a consequence of the Coulomb repulsion (unlike their neutral counterparts, which dominantly have contact interactions), which makes it harder to simulate local quantum dynamics, and in general

---

[31] This also provides a natural way of incorporating dissipation effects to perform a non-unitary evolution in case of an open quantum system [420, 426].

makes the finite size effects more significant. Moreover, the sizes attainable in these experiments are generically smaller than those in the neutral atom case.

Many early experiments in the context of quantum dynamics focused on time-of-flight measurements in cold atomic gases [432, 435, 436]. One of the early successes in studying quantum thermalization came from comparing the relaxation of a three dimensional gas of strongly interacting atoms with its one-dimensional counterpart. While the former showed a quick relaxation to thermal equilibrium, the latter exhibited long-lived coherent oscillations (prompting the authors to name the experiment a 'quantum Newton's cradle') [182]. This was explained as a consequence of the near-integrability of the latter setup, and stimulated a great deal of interest in the conditions of thermalization and the unique dynamics of quantum integrable models. The same Newton's cradle setup was revisited recently [437], while other experiments have focused on the emergence of the generalized Gibbs ensemble [438–440].

The cold atom setups can be further pushed in the direction of mimicking condensed matter systems by the introduction of *optical lattices*, which provide periodic potentials, much like the ones experienced by electrons in a crystalline material [441, 442]. These lattices are engineered via the interference pattern created by overlapping laser beams. As the atoms interact with the electric field through a dipole force, they experience the varying intensities of the pattern as a periodic potential. The tunnel coupling, or hopping amplitude, can be tuned by varying the depth of the potential. Thus, one can realize in these systems models of quantum magnetism, such as the Ising model [443–445]. Recently, the invention of *quantum gas microscopy* [446–449] has opened up the possibility of *in-situ*, site-resolved measurements, and even taking complete snapshots of the many-body quantum state (amounting to a projective measurement in the local occupation basis), for example via high-resolution fluorescence imaging. The same techniques can also be used to coherently flip the spin of each atom individually, allowing to create various initial states, and to assemble lattices atom-by-atom [450, 451]. Similar level of control is possible in trapped ion experiments [61].

Such methods have enabled the measurement of the spreading of correlations after a quantum quench in various setups [452–455]. This also includes probing transport properties and thus the emergence of hydrodynamics [330, 453, 456–459]. Similar methods were used to establish experimentally the transition from thermalizing to localized behavior due to disordered [200, 460] or quasi-periodic [186, 461] potentials, and to observe time-crystalline behavior in a trapped ion system [220].

Importantly for our present purposes, the high degree of control available in these experimental setups also opens up the possibility of probing the complicated correlations hidden in some of the 'higher order' observables we defined above in Section 2.2 [462]. In particular, following theoretical proposals [463, 464], a series of ground-breaking experiments has demonstrated the possibility of accessing the second Rényi entropy as a means of probing thermalization [108, 109]. These experiments used the so-called 'replica trick' (see Section 5.2), wherein e^{-S_2} is re-interpreted as an expectation value in a doubled Hilbert space, corresponding to two identical copies of the same quantum system. In the experiments, two copies were indeed prepared and evolved in time in parallel; interfering the two copies can then be used to reveal the Rényi entropy. Two other measures of entanglement, termed the *configurational entropy* and the *number entropy* (see also in Section 10.3) were measured in Ref. [465] to obtain a logarithmic growth, characteristic of many-body localized systems [222, 223]. There exist also both theoretical proposals [249, 466] and experimental results [467, 468] measuring OTOCs. These typically rely on reversing the arrow of time, in a manner similar to spin echo-type experiments. A recent set of experiments [110, 469–471] has demonstrated the possibility of measuring both OTOCs and Rényi entropies in a *single* copy of the system, without the need for time-reversal, by performing local measurements in a randomly chosen basis, and evaluating correlations of the outcomes.

A variation of the neutral atom setups is offered by systems of Rydberg atoms [63, 472]. There, one of the electrons of the atom is excited to a high-lying orbital, which leads to an increased sensitivity towards electric and magnetic fields. It also results in strong van der Waals interactions, that decay rapidly with distance (as $\sim 1/r^6$), and are therefore often well approximated by local models. They can again be trapped by e.g. optical tweezers, and their interactions controlled by varying the distance between atoms, or by coupling them to a different Rydberg state, while fluorescence imaging can be used to detect their distribution. Recently, a chain of 51 Rydberg atoms was used as a programmable quantum simulator and used to study dynamics from various initial states [473], leading to the discovery of so-called *many-body quantum scars* [474, 475].

While we focused on cold atoms and trapped ions, let us emphasize that there also exist setups in more conventional condensed matter systems, in particular those where the microscopic degrees of freedom are nuclear spins of some material. In this case, NMR techniques are used to prepare and measure the quantum states [476, 477]. While not as well controlled as ultracold atoms or ions, they have the advantage of having truly macroscopic number of interacting degrees of freedom, avoiding the finite-size effects that can plague other methods. These were also used to demonstrate localization due to disorder [478] and time crystal-like behavior [479, 480], and to measure OTOCs using spin-echo techniques [478, 481]. Another condensed-matter based platform is provided by nuclear vacancy (NV) centers embedded in diamond, which can be manipulated by using microwave radiation [482–484]. These were used to study thermalization dynamics [485, 486], and were among the first to be shown to exhibit the period doubling (and later, tripling) associated with time crystals [219].

2.5.2. Quantum computers

While the above examples all roughly fall under the idea of (analog) *quantum simulators* [57–59], similar techniques have been central to recent efforts towards realizing a *universal (digital) quantum computer* [18, 71, 72, 74]. In particular, the trapped ion setup, due to its aforementioned controllability, has been used extensively to develop quantum computing hardware [487–491]. The necessary ingredients needed to build a universal quantum computer have been demonstrated with high precision in this setup [492–497]. Moreover, the hyperfine ion qubit states can have very long coherence times, as large as 600s in certain cases [491, 498]. However, scaling up to larger systems remains a challenge, with the currently existing ones limited to ≈ 20 qubits.

Recently, significant progress was achieved in *superconducting circuits*, build out of non-linear superconducting resonators based on the Josephson effect [499–512]. Last year, these efforts culminated in an experiment that claimed to have finally achieved *quantum supremacy* [75]: the accomplishment of a computational task unattainable by even the largest classical supercomputers [22, 513–515]. This was done by sampling from the output distribution of a random circuit of unitary gates applied on a 53-qubit quantum computer[32]. Other promising architectures for quantum computing include electronic semiconductors [519, 520], impurity spins [521] (such as NV center [522]) and linear optics [523, 524], among others [525].

The efforts to build a quantum computer relate to the topic of the present thesis on several levels. On the one hand, one of the most promising application of the type of *noisy intermediate scale quantum* (NISQ) [23] computers that are likely to be available in the

---

[32] Similar setups on a smaller scale have also been used to simulate quantum dynamics [516], for example to demonstrate localization [517, 518].

near-term, is to perform quantum simulation of interesting many-body systems, including their dynamics [57, 63, 434, 526, 527]. In this sense, the digital quantum computers would provide a complementary experimental platform to those outlined above, with potentially much greater control over all the details of the dynamics and the measurement of the final state. These could be used to test theoretical predictions and uncover new features of the time evolution. From a different point of view, the quantum computing hardware are themselves particular quantum many-body systems. Thus, understanding general features of quantum dynamics could be highly useful in improving their design and to understand the types of errors they experience and how to counter them. Dynamics of entanglement plays a particularly important role in this respect, as entanglement provides a crucial resource that leads to a computational advantage compared to classical computers [19, 528]. Moreover, execution of random unitary circuits, similar to the ones we study in this thesis, has emerged as a useful way to test the capabilities of quantum computers [514, 515, 529, 530] (including the aforementioned quantum supremacy experiment [75]). Understanding the features of their dynamics is therefore an important topic on its own right.

Part I.

Quantum Information Dynamics without Conservation Laws

Overview of Part I

As discussed in the Introduction, Part I of this thesis concerns the dynamics of quantum information in closed quantum systems with no additional conserved quantities – this includes energy conservation, which means that we will be focusing on cases that lack (continuous) time-translation invariance.

Chapter 3: Systems without local conservation laws

In Chapter 3 we first give a brief discussion on systems without conservation laws. The simplest such cases are *periodically driven* systems, which break energy conservation by absorbing energy from a drive. These have been a subject of intense study in recent years [531–534]. Another type of system that belongs to this category are those with explicit noise in their dynamics, for example due to some randomly fluctuating external fields. In Section 3.1 we construct a model of the latter kind, a circuit of randomly chosen local unitary gates, which will serve as the basis of our subsequent studies in this part of the thesis. Such random circuit models have received a great deal of attention in recent years, and we will describe our own contributions, while also summarizing some others, when we deem it necessary.

Chapter 4: Operator Spreading

Chapter 4 contains our study of operator spreading in systems with no symmetries. For the most part, we focus on the aforementioned circuit model in one dimension, where one can carry out an exact calculation of many relevant quantities. In Section 4.2 we discuss this calculation in detail, and show that the dynamics of an evolving operator has a simple description in terms of a biased random walk. This is characterized by two relevant parameters, related to two main features of the evolution: a ballistic spreading of the operator wavefront, with the *butterfly velocity* v_{B}, and a *diffusive broadening* of the wavefront, with a diffusion constant D. We also discuss how the same features manifest in out-of-time-order correlators. In Section 4.3 we argue that the biased diffusion description should apply more generally, also to deterministic systems, and support this claim with numerical results on a driven spin chain. Section 4.4 provides a brief description of the higher dimensional case, based on Ref. [253]. In this case, biased diffusion is replaced by the Kardar-Parisi-Zhang (PKZ) equation, leading to a different exponent for front broadening.

Chapter 5: Entanglement Growth

In Chapter 5 we switch our focus to entanglement. In Section 5.1 we show how our results on operator spreading in the random circuit can be turned into a calculation of the annealed average of the second Rényi entropy. We find a linear growth in time, with a *entanglement velocity* v_{E} that is strictly smaller than v_{B}, and discuss the eventual saturation for finite subsystems. An alternative calculation, that does not rely on operator spreading, is presented in Section 5.2. In this description, calculating averages over the random circuit is turned into a problem similar to evaluating a classical partition function in one higher dimension. This method, adapted from Ref. [278], has the advantage of being more generalizable, and we will rely heavily on similar calculations in Part II. In the case of entanglement entropies, it gives rise to a simple physical picture, wherein entanglement growth is associated with the free energy of a polymer (or membrane, in higher dimensions) in spacetime. In Section 5.3 this picture is used to explain the effects of noise on entanglement dynamics, leading to another appearance for the KPZ equation.

Chapter 6: Entanglement spectroscopy after a quench

The last chapter of this part of the thesis offers an alternative view on the scrambling of quantum information, by looking at the fine structure that appears in the statistics of the entanglement spectrum, i.e. the eigenvalues of a reduced density matrix of some finite subsystem (or, more precisely, their logarithms). We find that the spectrum is sensitive to correlations that develop between the two edges of the subsystem. Since these correlations are initially very small (carried only by rare 'tail events' of operators spreading faster than the Lieb-Robinson speed), they show up first at the smallest eigenvalues, where they lead to level repulsion. This shows up as an 'edge' in the spectrum, separating small and large eigenvalues which have different statistics. This edge gradually moves in time, until the entire spectrum develops level repulsion. We provide an analytical argument, which shows that the time scale for this to happen is dictated by the Lieb-Robinson velocity. We support this with numerical results on a variety of systems, which confirm that the appearance of level repulsion corresponds to a separate time scale, smaller than the thermalization time of the subsystem.

3. Systems without local conservation laws

As mentioned above, the physically most natural representation of unitary dynamics is when the system evolves under a particular, time-independent Hamiltonian H. Such systems by definition exhibit *energy conservation* (the Hamiltonian commutes with itself). Moreover, many systems relevant in experiments also possess other extensive conserved quantities, such as particle number of total magnetization. As we discussed in Section 2.3, such extensive conserved quantities play a crucial role in the many-body dynamics: they give rise to slow, hydrodynamic modes that are the only relevant local degrees of freedom at long times.

Precisely for this reason, it is enlightening to consider to systems that have *no conserved quantities*. Conventional wisdom would indicate that these have no slow modes and show no interesting dynamics after the very shortest timescales. On the contrary, we will find that new types of slow, 'hydrodynamic' variables emerge once we shift our attention from simple correlations to more refined quantities that capture the scrambling of quantum information (see the discussion in Sec. 2.2). In particular, we will show that the conservation of information (i.e., unitarity) manifests itself as a new, 'hidden' conservation law and the transport of this conserved quantity admits simple universal descriptions.

Physically, the simplest manifestation of systems without conservation laws is achieved by a periodic drive, i.e. a Hamiltonian with a periodic time-dependence $H(t) = H(t+T)$. Such driven (also known as *Floquet*) systems are relevant for many experimental setups [531–534]. Below we will also consider models where $U(t)$, rather than being periodic, changes randomly in time (while remaining unitary throughout). As we shall see, integrating over the randomness in these models can result in very simple effective descriptions. As we will argue, many of the main conclusions drawn from studying these models apply equally well to deterministic systems.

In the absence of conservation laws, statistical mechanics dictates that the long-time equilibrium state should be one that maximizes entropy, i.e. the maximally mixed state $\rho = \mathbb{1}/\mathcal{N}$ (also known as the 'infinite temperature' ensemble, since it corresponds to a Gibbs state with $\beta = 0$), with $\mathcal{N}$ the Hilbert space dimension. Indeed, the systems we study in this part of the thesis all approach this state locally, which also implies that the Rényi entropies of finite subsystems tend to their maximal values (up to small subleading corrections). In particular, as we discussed in Section 2.4, in a Haar random pure state, the expectation value of any operator is exponentially narrowly peaked around the infinite temperature result [535]. Therefore we expect that the evolving state $|\Psi(t)\rangle$ will increasingly look like such a Haar random state[1]. Haar random states, being basis-independent, have lost all notion of spatial structure; they have information distributed equally between all possible degrees of freedom, irrespective of locality. In this sense (and in ways which we will make clear below when considering evolution in the Heisenberg picture), information becomes 'scrambled' during time evolution; our goal in this part will be to elucidate some general features of this scrambling as they apply to many-body systems with no constraints on their dynamics other than locality.

---

[1] In Floquet systems, which admit an eigendecomposition similar to the Hamiltonian case, this thermalization process can be understood in the language of ETH: eigenstates of $U(T)$ themselves should look like independent Haar random states; this gives a simplified version of Eq. (2.3), where the energy-dependence disappears and all diagonal matrix elements are given by the infinite temperature result, while off-diagonal ones are suppressed by a factor of $\mathcal{N}^{-1/2}$

3.1. Local Haar Random Circuit Model

An alternative to evolving with a time-dependent Hamiltonian, we will consider here a different type of dynamics with no conservation laws, constructed as a circuit of local unitary gates, illustrated in Fig. 3.1. In this setup, the initial state or operator is acted upon by a series of unitaries, each of which is local (i.e., only acts non-trivially on a finite region). Such circuits provide a model for quantum computations [18] and are very natural in that context. They also show up when one discretizes continuous time evolution by e.g. a Trotter scheme [104, 424, 425]. The main difference is that while in the latter case, the gates that appear correspond to infinitesimal steps, and are therefore close to the identity, this does not have to be true in a more general circuit[2]. Physically, the difference between circuit models and other Floquet models is that the former have infinitely sharply defined light cones, where perturbations vanish on the outside, while the latter generically have a non-zero probability of spreading information arbitrarily far even at short times. However, due to the Lieb-Robinson bounds, these probabilities are exponentially small outside of a linear light cone and therefore negligible in most cases. In fact, one can use this fact to approximate continuous dynamics as a unitary circuit [536]. Later, in Section 4.3, we will meet a non-trivial Floquet model where such a representation becomes exact.

While circuit models provide a useful perspective on quantum evolution, generically they are not any more solvable than other forms of many-body dynamics. However, recent years saw the emergence of several different methods for constructing circuit models that are exactly solvable, at lest for certain quantities. These provide a rare example of many-body dynamics that is solvable without being integrable, and as such, they have been central towards gaining a better understanding of many relevant questions. The first of these set of models is provided by so-called *dual-unitary circuits*. These have the defining property that slices of the two-dimensional circuits in the *spatial* direction (rather than time-slices) also define unitary operations. This property simplifies calculations, and has lead to a breadth of recent results for dynamical correlations, spectral form factors and Rényi entropies, among others [179, 180, 537–540]. Other types of quantum circuits that, while are generically not analytically tractable, allow for essentially numerically exact simulations, are *Clifford* and recently introduced *cellular automaton* circuits. The former act as permutations on products of Pauli operators, while inducing non-trivial, yet efficiently simulable, dynamics on quantum states [276, 541–544]. The latter are in some sense the opposite: they perform permutations of basis states in a particular product basis, but can have non-trivial behavior for operators [545–548].

While these systems provide extremely useful tools for studying non-equilibrium dynamics, they are all fine-tuned in various ways, and have features that make them non-generic. An alternative approach to solvable models that can avoid this issue is given by *random circuits*, which are at the focus of this thesis. In this case, the circuit elements (local gates) are chosen from some random ensemble of unitaries. Then it is the averaging over realizations of such a random circuit that serve to simplify the results and allow for an analytical, or semi-analytical, treatment. In particular, as we shall see in detail below, the averaging procedure often allows one to map the calculation of various quantities of interest to a 'classical'[3] stochastic process, or equivalently, to the evaluation of a classical partition function. In many cases, the latter can be computed analytically, at least in some limit, while in others it still allows for a numerical calculation that is significantly more efficient than tackling the original quantum problem directly. Various arguments and numerical results suggest that these random circuits exhibit *universal* features that

---

[2] Of course one could always design a Hamiltonian that reproduces the effects of the circuit, but this would require evolving disconnected regions for long times independently.

[3] The quotation marks refer to the fact that in some of the more complicated cases, the effective model might still contain negative weights, making it not entirely classical.

generalize to a large set of other models, including ones that are not random in time, and even to generic time-independent Hamiltonians [1, 3, 252, 253, 260, 427, 429, 549].

This last point merits some further discussion. It might at first appear surprising that the kind of noisy evolution resulting from a random circuit can capture the behavior of non-random systems. Note, however, that such noisy models have been used for a long time in studies of many-body dynamics [550–552]. As mentioned previously in Section 2.3, such stochastic equations appear naturally in the context of hydrodynamic transport[4] [279, 281, 293, 299]. The idea behind these, is that the degrees of freedom at small scales can effectively serve as a source of noise on the dynamics of the large-scale, 'slow' variables that appear in in the hydrodynamic description, even when the dynamics at the microscopic level is deterministic. A simple intuitive example is provided already by Brownian motion, where the kicks provided by the fluid molecules can be incorporated into a random noise.

There is an alternative way of thinking about the emergence of 'noisiness', that is particular to the quantum setting and makes connection with the notion of equilibration exposed by the eigenstate thermalization hypothesis. Recall, that in the ETH picture, the equilibrium state is already 'there' in the eigenstates: the only necessary ingredient provided by the dynamics is the *dephasing* between the different eigenstates, that brings out their thermal nature. Dephasing also plays a central role in dynamics at intermediate times. A particular example is the *diffusive transport* of conserved quantities, discussed previously in Section 2.3, which is expected to be generic in many-body lattice systems at high temperatures. Such diffusive behavior is exactly what one would find for a classical random walk, as opposed to freely propagating quantum particles. The difference between the two is that of phase coherence: it is the constructive and destructive interference between different paths that leads to a characteristic *ballistic* (rather than diffusive) spreading in the quantum case. The prevalence of diffusive transport in closed (and even translation invariant) many-body quantum systems [249, 269, 279, 285, 294, 553, 554] shows that interactions between particles lead to a loss of phase coherence. Introducing an explicit noise, can play a very similar role, destroying coherence (for instance, adding noise to single-particle quantum dynamics also induces a cross-over towards a classical random walk behavior). For example, while (as we discuss in Section 7.2), a random circuit can give rise to diffusive transport in an almost trivial way, due to the explicit noise, qualitatively the same behavior arises in non-random models simply due to interaction. A similar intuition explains the qualitatively similar behavior between random and non-random models for the other quantities we study below (see also Ref. [260] for a different approach towards justifying the universality of random circuit results).

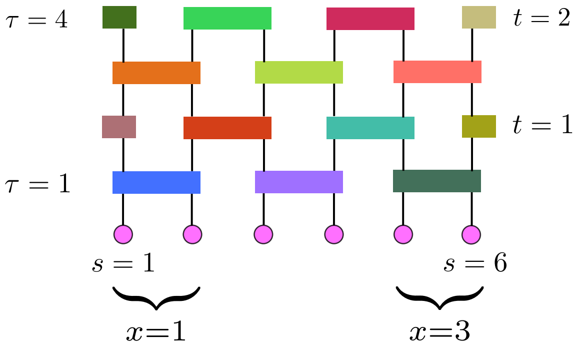

Figure 3.1.: Structure of the local unitary circuits studied in this paper. The on-site Hilbert space dimension is q. Each two-site gate is a $q^2 \times q^2$ unitary matrix, randomly chosen from the Haar distribution.

---

[4] See also Section 9.1 for a more direct derivation of this fact, in the so-called memory matrix formalism.

With these motivations in mind, we now introduce the random circuit model we study in the subsequent questions. We consider a one-dimensional chain of ‘spins’, or qudits, with local Hilbert space dimension $q \geq 2$ (we will briefly discuss higher dimensional generalizations in Section 4.4). The building blocks of the model are 2-site unitary gates, chosen from the *Haar measure*: this is the unique probability distribution over $N \times N$ unitary matrices (in our case, $N = q^2$) that is invariant under left- and right multiplication, that is $p(U) = p(VU) = p(UV)$ for any $N \times N$ unitary V. We evolve states (or operators) by acting on them with such Haar random gates, arranged in a ‘brick-wall’ pattern: odd numbered layers act on all the odd bonds of the chain while even numbered layers act on even bonds[5]. This is shown in Fig. 3.1. This prescription defines an ensemble of local unitary evolutions, with strict light cone speed $v_{\text{LC}} = 1$ due to the geometry. The only parameter, characterizing this ensemble, is the local dimension q. We are interested in the typical behavior of such a circuit, which we will approach by considering the circuit-averaged dynamics of various quantities. As we shall argue below, the results are indicative of the behavior of typical individual realizations of the circuits (modulo some important subleading effects in certain cases, which we discuss in Section 5.3), and also shed light on the dynamics of deterministic systems. We will illustrate this latter point by performing explicit numerical calculations on a particular periodically driven spin chain and showing that it exhibits the same qualitative features of operator spreading that are found in the random circuit model.

---

[5] An alternative construction, considered e.g. in Ref. [276], is to randomize also the geometry of the circuit, for example by choosing a random bond to update in each step. On can interpolate between the two cases, for example by replacing every gate in the brick-wall circuit with an identity with some probability p. Generically, the universal features we discuss below are expected to remain the same throughout this interpolation, including the two limiting cases, at least for $q < \infty$.

4. Operator Spreading

As discussed in Section 2.2, out-of-time-order correlations can be used to study the scrambling of quantum information by the many-body dynamics, that is, how information that is initially contained in simple, local observables, gets redistributed over increasingly complicated operators. Here we discuss various universal features of this phenomenon, relying on our random circuit model. We first show that the spreading of operators can be characterized by a 'hidden' conservation law that arises due to the unitarity of quantum dynamics. In one-dimensional systems, which will be our main focus, this can be incorporated into a local conserved density. As we show, averaging over random circuits endows this quantity with a very simple, exactly solvable dynamics, which is that of a biased random walk. We discuss the resulting behavior in detail and provide evidence that the description in terms of biased diffusion is universal, applicable to chaotic many-body dynamics without conserved quantities in one-dimension. The case of higher dimensions is briefly summarized in Section 4.4, while the extension to systems with conservation laws is postponed until Part II.

4.1. Quantifying operator spreading

Consider a one-dimensional chain of L sites, for which the Hilbert space of a single site is $\mathcal{H}_{\text{site}} = \mathbb{C}^q$. There exist operators X, Z on the single site Hilbert space obeying

$$ZX = e^{2\pi i/q} XZ \tag{4.1a}$$

$$Z^q = X^q = 1\,. \tag{4.1b}$$

These generate a convenient complete basis for all operators on $\mathcal{H}_{\text{site}}$, namely $\{\sigma^\mu \equiv X^{\mu^{(1)}} Z^{\mu^{(2)}} : \mu \in \mathbb{Z}_q^{\otimes 2}\}$. Here μ is shorthand for the doublet $\mu^{(1)}, \mu^{(2)} \in \{0, 1, \ldots, q-1\} = \mathbb{Z}_q$. This basis is orthonormal, such that $\text{tr}(\sigma^{\mu\dagger}\sigma^\nu)/q = \delta_{\mu\nu}$. The operators σ^μ can be regarded as generalizations of Pauli matrices, where the usual Paulis correspond to the $q = 2$ case. Generalizing this to the Hilbert space of a 1D chain, $\mathcal{H}_{\text{chain}} = (\mathbb{C}^q)^{\otimes L}$, a complete orthonormal basis of operators is given by the q^{2L} Pauli *strings*, defined as $\sigma^{\vec{\mu}} \equiv \bigotimes_{r=1}^{L} \sigma_r^{\mu_r}$, where each string is indexed by a vector $\vec{\mu} \in \left(\mathbb{Z}_q^{\otimes 2}\right)^{\otimes L}$.

Our goal is to quantify how an initial Pauli string spreads over the space of all Pauli strings under local unitary time evolution. At time τ the Pauli string $\sigma^{\vec{\mu}}$ becomes

$$\sigma^{\vec{\mu}}(\tau) \equiv U^\dagger(\tau)\sigma^{\vec{\mu}}U(\tau) = \sum_\nu c^{\vec{\mu}}_{\vec{\nu}}(\tau)\, \sigma^{\vec{\nu}}. \tag{4.2}$$

This defines a set of 'operator spreading coefficients' $c^{\vec{\mu}}_{\vec{\nu}}(\tau) \equiv \text{tr}\left(\sigma^{\vec{\nu}\dagger}U^\dagger(\tau)\sigma^{\vec{\mu}}U(\tau)\right)/q^L$. The full set of coefficients, $\{c^{\vec{\mu}}_{\vec{\nu}}(\tau)\}$, encodes all information regarding the unitary time evolution. However, the values of particular coefficients themselves are of limited interest (they are rather like trying to capture the evolution of a gas by keeping track of all the position and momenta of individual particles). It is more useful to consider 'coarse-grained' quantities, that one might hope show up in some effective 'hydrodynamic' description. We will be particularly interested in the total weight on all operators with right endpoint s appearing in $\sigma^\mu(\tau)$, i.e.,

$$\rho^{\vec{\mu}}_R(s,\tau) \equiv \sum_{\vec{\nu}} \left|c^{\vec{\mu}}_{\vec{\nu}}(\tau)\right|^2 \delta(\text{RHS}(\vec{\nu}) = s), \tag{4.3}$$

where RHS($\vec{\nu}$) denotes the rightmost site on which $\vec{\nu}$ is non-zero.[1] Note that the 'density' $\rho_R^{\vec{\mu}}$ is conserved, i.e., $\sum_s \rho_R^{\vec{\mu}}(s) = 1$ at all times. Motivated by this, we refer to $\rho_R^{\vec{\mu}}$ as the (right) *operator density* of the time evolved Pauli string $\sigma^{\vec{\mu}}$. This hidden conservation law plays a crucial role in what follows. In analogy with the discussion of hydrodynamics in Section 2.3, one expects that such conserved quantities provide the important slow variables that characterize the dynamics of the evolving operator on sufficiently long time scales[2]. As we shall see, this statement becomes exact upon averaging in the random circuit.

4.2. Operator spreading in the 1D Haar random circuit

In the following we will quantify how operators spread under the time evolution generated by the random circuit defined above in Chapter 3. We focus on the average of the operator density, defined in Eq. (4.3), for which we derive an exact equation of motion. Upon solving this equation, we find that the operator density moves in a front with velocity $v_{\mathrm{B}} \leq v_{\mathrm{LC}}$, while the width of the moving front increases in time diffusively.

4.2.1. Random walk dynamics of operator density

We start by noting that, under Haar averaging, the operator spreading coefficient $c_{\vec{\nu}}^{\vec{\mu}}(\tau)$ vanishes for any time $\tau \geq 1$, provided that $\vec{\mu}$ is non-trivial, since $c_{\vec{\nu}}^{\vec{\mu}}$ and $-c_{\vec{\nu}}^{\vec{\mu}}$ have equal probability. However, the average of its modulus squared, $\overline{|c_{\vec{\nu}}^{\vec{\mu}}(\tau)|^2}$, can be non-zero. (An explicit expression for this quantity is written down in App. A.3, using a mapping to a classical Ising model, but we will not require it for the subsequent discussion).

Following Eq. (4.3), we define the average operator density as

$$\overline{\rho_R^{\vec{\mu}}}(s,\tau) \equiv \sum_{\vec{\nu}} \overline{|c_{\vec{\nu}}^{\vec{\mu}}(\tau)|^2}\, \delta(\mathrm{RHS}(\vec{\nu}) = s). \tag{4.4}$$

As we show below, this quantity satisfies an equation of motion, Eq. (4.8), which does not depend explicitly on $\vec{\mu}$. Pre-empting this, we drop the explicit $\vec{\mu}$ dependence, $\overline{\rho_R^{\vec{\mu}}} \to \overline{\rho_R}$, to declutter notation. In fact, $\vec{\mu}$ will enter considerations only as an initial condition on the operator density

$$\overline{\rho_R}(s,0) = \delta(\mathrm{RHS}(\vec{\mu}) = s), \tag{4.5}$$

which is the same for all initial operators that share the same right endpoint.

To understand how $\overline{\rho_R}$ evolves in time, consider the effect of applying a single two-site gate on sites s and $s+1$. There are $q^4 - 1$ nontrivial operators acting on this two-site Hilbert space. Of these, $q^2 - 1$ contribute to $\overline{\rho_R}(s,\tau)$ (the ones that are trivial on site $s+1$), while the other $q^2(q^2-1)$ contribute to $\overline{\rho_R}(s+1,\tau)$. Under a two site Haar random unitary transformation all the possible transitions between any of these $q^4 - 1$ operators have, on average, the same probability [555]. The upshot is that after the application of the unitary gate the density $\overline{\rho_R}$ evolves as

$$\overline{\rho_R}(s,\tau+1) = (1-p)\left[\overline{\rho_R}(s,\tau) + \overline{\rho_R}(s+1,\tau)\right]; \tag{4.6a}$$

$$\overline{\rho_R}(s+1,\tau+1) = p\left[\overline{\rho_R}(s,\tau) + \overline{\rho_R}(s+1,\tau)\right], \tag{4.6b}$$

with probabilities $p = \frac{q^2}{q^2+1}$ and $1-p = \frac{1}{q^2+1}$. To apply a similar argument for two subsequent layers of the circuit it is useful to redefine the density by grouping together

---

[1] A similar quantity was defined in Ref. [237]

[2] Of course there is a similar *left* operator density, ρ_L, defined by using the left endpoints. However, the dynamics of the two densities decouple (as one can guess based on locality).

the pairs of sites on which the first layer of the circuit acts. We abuse notation and denote this quantity as

$$\overline{\rho_R}(x,t) \equiv \overline{\rho_R}(s=2x-1,\tau=2t) + \overline{\rho_R}(s=2x,\tau=2t), \tag{4.7}$$

where we now only consider the value of the operator density at even time steps $\tau = 2t$. Applying Eq. (4.6) for two layers we arrive at the equation

$$\overline{\rho_R}(x,t+1) = 2p(1-p)\,\overline{\rho_R}(x,t) + p^2\,\overline{\rho_R}(x-1,t) + (1-p)^2\,\overline{\rho_R}(x+1,t). \tag{4.8}$$

Thus the right endpoints of Pauli strings perform a biased random walk on the lattice, where in each step they move to the right with probability p^2, to the left with probability $(1-p)^2$, and stay on the same site otherwise; this is illustrated in Fig. 4.1. A feature of the above equation is that the time evolution of $\overline{\rho_R}$ is independent of the internal structure of the operator and thus the solution $\overline{\rho_R}(x,t)$ will be the same for all initial Pauli strings, modulo a shift $x \to x - x_0$ where x_0 is defined by the right endpoint of the initial string.

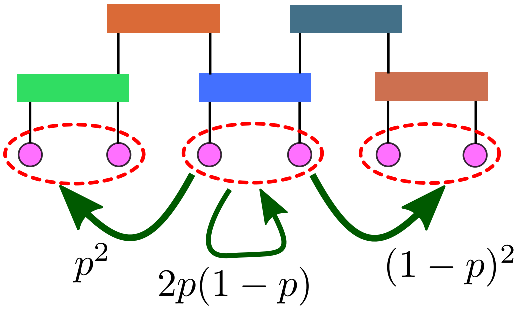

Figure 4.1.: Random walk of the operator's right endpoint in the Haar-averaged random circuit, as described by Eq. (4.8). We group pairs of sites together (red dashed ovals) to define coarse-grained coordinates. A pair of subsequent layers induces a biased random walk in these coordinated, with probabilities indicated in the figure.

The result of this random walk process is a front that propagates to the right from its initial position as $\langle x\rangle - x_0 = v_\mathrm{B} t$ with a *butterfly velocity* $v_\mathrm{B} = p^2 - (1-p)^2 = \frac{q^2-1}{q^2+1}$. Thus the speed at which the operator weight travels is smaller than the light cone velocity: $v_\mathrm{B} < v_\mathrm{LC} = 1$ (see also Ref. [556]). The width of the front increases in time as $\langle x^2\rangle - \langle x\rangle^2 = 2D_\rho t$, with diffusion constant $D_\rho = \sqrt{1-v_\mathrm{B}^2}/4 = \frac{q/2}{q^2+1}$. Note that in the limit $q \to \infty$ the 'particle' described by $\overline{\rho_R}(x,t)$ hops to the right with probability 1 in each step, and consequently the front becomes infinitely sharp with velocity $v_\mathrm{B} \to v_\mathrm{LC} = 1$.

The total weight of left endpoints, $\overline{\rho_L}(x,t)$, obeys a similar equation except that it propagates to the left with velocity $-v_\mathrm{B}$, while diffusing at the same rate[3], as shown in Fig. 4.2. This means that at time t the vast majority of quantum information initially stored in $\sigma^{\vec{\mu}}$ with left (right) endpoint x_l (x_r) is carried by operators with support $[x_l - v_\mathrm{B}t, x_r + v_\mathrm{B}\tau]$, but where the precise position of either endpoint can be uncertain within a region of width $\Delta x \sim \sqrt{D_\rho t}$.

We can find the full distribution of $\overline{\rho_R}(x,t)$ using a standard generating functional method. In the rest of this section we will use coordinates relative to the initial position of the front, i.e. $x - x_0 \to x$. The solution to Eq. (4.8) then reads

$$\overline{\rho_R}(x,t) = \frac{q^{2(t+x)}}{(1+q^2)^{2t}}\binom{2t}{t+x}. \tag{4.9}$$

---

[3] In principle, for systems that are not invariant under spatial reflection, one could have distinct butterfly velocities and distinct diffusion constants for the two front propagating left and right. See also Refs. [557, 558]

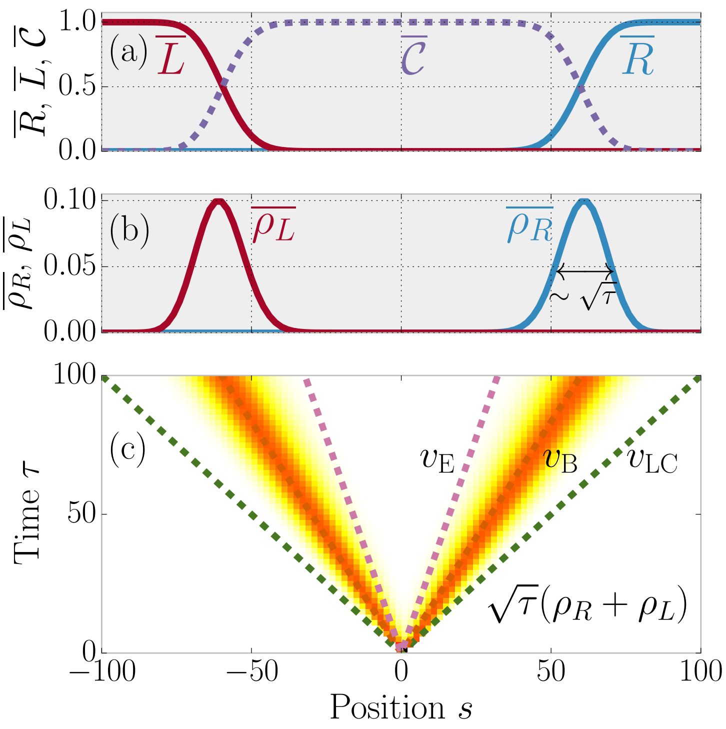

Figure 4.2.: Spreading of a one-site operator averaged over random unitary circuits with $q = 2$. $\overline{\rho_R}(s,\tau)$ ($\overline{\rho_L}(s,\tau)$) is the total weight carried by Pauli strings with right (left) endpoint on site s at time τ. Figure (c) shows the sum of these two functions (multiplied by $\sqrt{\tau}$ to show the position of the front more clearly). Almost all the weight is carried by operators with endpoints at the two fronts propagating out from the initial site with speed $v_{\mathrm{B}} = \frac{q^2-1}{q^2+1}$. These fronts in turn broaden diffusively in time as $\sqrt{\tau}$. The two other velocity scales, the light cone velocity v_{LC} and the entanglement velocity v_{E} (see Eq. (5.6)), are also indicated, satisfying $v_{\mathrm{E}} < v_{\mathrm{B}} < v_{\mathrm{LC}}$. The values of $\overline{\rho_R}$ and $\overline{\rho_L}$ after 100 layers of the circuit are shown in Fig. (b). Fig. (a) shows the integrated operator weights $\overline{R}(s)$ ($\overline{L}(s)$), denoting the total weight left (right) of site s, along with the OTO correlator $\mathcal{C}(s,\tau)$. The OTOC saturates to 1 inside the front and has the value 1/2 exactly at $\tau = s/v_{\mathrm{B}}$

In the scaling limit, taking $t, x \to \infty$ but keeping $x/t \approx v_{\mathrm{B}}$ fixed, this becomes (using Stirling's approximation)

$$\overline{\rho_R}(x = v_{\mathrm{B}}t + O(\sqrt{t})) = \frac{e^{-\frac{(x-v_{\mathrm{B}}t)^2}{(1-v_{\mathrm{B}}^2)t}}}{\sqrt{\pi(1-v_{\mathrm{B}}^2)t}}, \tag{4.10}$$

so that the traveling front has the shape of a Gaussian, as one would expect from the solution of the continuum limit of the lattice diffusion equation Eq. (4.8).

As we shall see in the next section, it is also useful to compute the total weight of all Pauli strings contained entirely to the left of position x. This quantity, which we denote by $R(x)$, is given by

$$R(x) \equiv \sum_{y \leq x} \rho_R(y). \tag{4.11}$$

Around the position of the front, where $x \approx v_\mathrm{B} t$, we can integrate Eq. (4.10) to obtain

$$\overline{R}(x = v_\mathrm{B} t + O(\sqrt{t})) \approx \frac{1}{2}\left[\mathrm{erf}\left(\frac{x - t v_\mathrm{B}}{\sqrt{t(1-v_\mathrm{B}^2)}}\right) + 1\right], \tag{4.12}$$

where $\mathrm{erf}(x)$ is the error function.

Later on we will also need an approximation for R well away from the front. Using the fact that in the large t limit $\overline{\rho_R}(x,t)$ increases sharply with x for $x/t < v_\mathrm{B}$, the sum in Eq. (4.11) is dominated by its largest term (i.e. $y = x$). Using the fact that $\overline{R}\,(x \geq v_\mathrm{LC} t) = 1$ we can similarly approximate $\overline{R}$ for $x/t > v_\mathrm{B}$, to obtain

$$\overline{R}(x) \approx (1 - 2\overline{\rho_R}(x))\Theta(x - v_\mathrm{B} t) + \overline{\rho_R}(x), \tag{4.13}$$

where Θ is the Heaviside step function. This result is accurate up to multiplicative $O(1)$ constants when $|x - v_\mathrm{B} t|/t = O(1)$ in the large t limit. See the discussion in App. A.4.1 for a precise statement and derivation of Eq. (4.13).

Using our results for the coarse-grained density $\overline{\rho_R}(x,t)$ we can also write a formula for the density in terms of the site coordinate s. Note that due to Eq. (4.6), the ratio $\overline{\rho_R}(s = 2x+1)/\overline{\rho_R}(s = 2x) = q^2$ is fixed at any time $\tau = 2t$. Using this, the density on site s after applying an even number of layers becomes

$$\overline{\rho_R}(s = 2x + n, \tau = 2t) = \frac{q^{2(t+x-1+n)}}{(1+q^2)^{2t}}\binom{2t-1}{t+x-1}, \tag{4.14}$$

where $n = 0, 1$. We can use Eq. (4.14) to derive the total operator weight left of site s, i.e. $R(s) = \sum_{r \leq s} \rho(r)$, which, as we will see in the next section, is closely related to the OTOC between sites 0 and s.

4.2.2. Behavior of out-of-time-order correlators

We can relate our results for the time evolution of operator weights to that of the out-of-time-order correlator (OTOC), previously defined in Section 2.2. For concreteness consider the following OTOC between two Pauli operators separated by distance s (in this section we work in a shifted coordinate system where one of the Pauli operators resides at site 0)

$$\mathcal{C}(s,\tau) \equiv \frac{1}{2}\langle [Z_0(\tau), Z_s]\,[Z_0(\tau), Z_s]^\dagger \rangle = 1 - \mathrm{Re}\langle Z_0(\tau)\, Z_s Z_0^{-1}(\tau)\, Z_s^{-1}\rangle, \tag{4.15}$$

where s and τ are the original time/lattice coordinates (as opposed to the coarse grained coordinates t, x below Eq. (4.7)) and we have left unspecified the state (pure or mixed) in which the OTOC is evaluated. Here Z_r denotes the generalized Pauli operator introduced back in Eq. (4.1), situated on site r. We will be mainly interested the behavior of the OTOC $\mathcal{C}(s,\tau)$ in the limit $\tau \gg 1$, along rays with $\kappa \equiv s/\tau$ held fixed. As we detail below, for s outside of the light cone ($\kappa > 1$) it is zero. As s enters the light-cone ($\kappa < 1$ and close to 1) it increases, but sub-exponentially. When s is near the operator front ($\kappa approx v_\mathrm{B} < 1$) the OTOC becomes $O(1)$. After the front has passed ($\kappa < v_\mathrm{B}$), the OTOC exponentially saturates to the value 1 with an exponent that is independent of s. See Fig. 4.3 for a summary.

Let $\overline{\mathcal{C}}$ denote the average of the OTOC over all unitary circuits with geometry shown in Fig. 3.1. Note that, due to the averaging, this quantity is independent of the choice of Pauli operator, i.e., it would be the same if we replaced either or both operators in Eq. (4.15) with another local Pauli different from Z. We will be concerned with the second term in Eq. (4.15) which equals

$$1-\overline{\mathcal{C}}(s,\tau)=\sum_{\mu\nu}\overline{c_0^{\mu}(\tau)c_0^{*\nu}(\tau)}\,\mathrm{Re}\langle\sigma^{\mu}Z_s\sigma^{\dagger\nu}Z_s^{-1}\rangle=\sum_{\mu}\overline{|c_0^{\mu}(\tau)|^2}\cos\theta_{\mu,Z_s},\tag{4.16}$$

where $e^{i\theta_{\mu,Z_s}}$ is a q^{th} root of unity defined by $\sigma^{\mu}Z_s=e^{i\theta_{\mu,Z_s}}Z_s\sigma^{\mu}$, and $c_0^{\mu}(\tau)$ are the operator spreading coefficients of $Z_0(\tau)$. Notice that Haar averaging forces $\mu=\nu$, which removes all dependence on the particular state in which we choose to evaluate the OTOC[4]. In particular, the average OTOC value in any state, pure or mixed, will be identical to the average OTOC value at infinite temperature, i.e., $\mathrm{tr}(\frac{1}{2}|[Z_0(\tau),Z_s]|^2)/2^L$. At this point, we could use the exact expressions for the coefficients $\overline{|c_0^{\mu}(\tau)|^2}$ from App. A.3 to write an exact closed form expression for the OTOC. However, instead of doing that, we will write a more manageable asymptotic expression for Eq. (4.16) using simpler results from Section 4.2.1.

To perform the sum over Pauli strings in Eq. (4.16), we first need to prove the following statement: $\overline{|c_0^{\vec{\mu}}(\tau)|^2}$ depends *only on the position of the two endpoints of the string* $\vec{\mu}$. The proof goes as follows. First, it is easy to verify that under Haar averaging, $\overline{|c_{\vec{\nu}}^{\vec{\mu}}(\tau)|^2}=\overline{|c_{\vec{\mu}}^{\vec{\nu}}(\tau)|^2}$ for any ν. This implies that the average probability of the one-site operator Z_0 evolving into a specific string $\vec{\mu}$ is the same as the probability of string $\vec{\mu}$ evolving into Z_0. In the random walk picture this latter process corresponds to both left and right endpoints ending up on site 0 at time τ during their respective random walks. As we noted previously, these random walks are independent of the internal structure of the initial string. Thus $\overline{|c_0^{\vec{\mu}}(\tau)|^2}$ depends only on where the two endpoints of $\vec{\mu}$ are located. We confirm this argument more concretely with an explicit expression for such operator spread coefficients in App. A.3.

The above statement has important consequences for the OTOC. If site s lives in the support of $\vec{\mu}$ then the contribution to Eq. (4.16) coming from the strings with the same support as $\vec{\mu}$ have an equal weight for each possible value $\theta_{\mu,Z_s}\in\frac{2\pi}{q}\{1,\ldots,q\}$, so that the cosine term averages to zero. The remaining part is the total weight due to Pauli strings which are supported on intervals that do not contain site s (along with some corrections for Pauli strings which border on site s). Deferring the full justification to App. A.4.2, the upshot is that provided $\kappa>0$, in the $\tau\to\infty$ limit, the OTOC behaves as

$$\overline{\mathcal{C}}(s,\tau)\approx 1-\overline{R}\,(s-1,\tau)+q^{-2}\overline{\rho_R}\,(s,\tau)\,,\tag{4.17}$$

up to exponentially small corrections in τ. Hence the OTOC is directly related to the operator density, and changes appreciably at the operator front $s=v_{\mathrm{B}}t$, as we show in Fig. 4.3.

Let us now summarize the behaviour of the OTOC as a function of space and time, as parametrized by the ratio $\kappa\equiv s/\tau$ and taken in the limit $\tau\gg 1$. We distinguish four regimes of OTOC behaviour which we illustrate in Fig. 4.3.

1. Trivial OTOC at early times ($1<\kappa$): In this regime the events $(\tau,0),(0,s)$ are causally disconnected, so the commutator in Eq. (4.15) (and hence the OTOC) is exactly zero.

2. Early OTOC growth ($v_{\mathrm{B}}<\kappa<1$): This regime describes the behaviour after site s has entered the light cone, but before it encounters the main operator front. Here we approximate the OTOC using Eq. (4.13), so that $\overline{\mathcal{C}}(s,\tau)\approx c_1\overline{\rho_R}(s-1,\tau)+\overline{\rho_R}(s,\tau)$,

---

[4] To see that $\overline{c^{\mu}c^{\nu *}(\tau)}\propto\delta_{\mu\nu}$: If $\mu\neq\nu$ there exists a single site Pauli σ_r^{α} such that the group commutators $[\sigma_r^{\alpha}:\sigma^{\mu,\nu}]=e^{i\theta_{\mu,\nu}}$ are unequal. Using the invariance of the two-site Haar measure under multiplication by single site operators, this implies $\overline{c^{\mu}c^{\nu *}(\tau)}=e^{i(\theta_{\mu}-\theta_{\nu})}\overline{c^{\mu}c^{\nu *}(\tau)}$ from whence the result follows.

where $c_1 > 1$ is bounded in the $s, \tau \to \infty$ limit. Fortunately a simple closed form expression already exists for $\overline{\rho_R}$, namely Eq. (4.14). We obtain a more convenient expression for the initial OTOC growth by expanding Eq. (4.14) near the light cone, in the limit $\delta^2/s \to 0$, where $\delta \equiv \tau - s$ is the distance between s and the light cone:

$$\overline{\mathcal{C}}(s,\tau) \approx e^{\frac{1}{2}\delta\log\left(\frac{\gamma s}{\delta}\right)-\frac{1}{6\delta}} \times \left(\frac{q^2}{q^2+1}\right)^s \frac{(1+q^2)\sqrt{\delta}}{2s\sqrt{\pi}}, \tag{4.18}$$

up to multiplicative O(1) constants, where $\gamma = e\left(1-v_{\mathrm{B}}^2\right)/2$. This formula demonstrates that the OTOC will increase with an exponent $\lambda \sim \log s$ for $0 < \delta \ll s$. Due to its dependence on s, and its limited range of validity, we believe that this should *not* be viewed as a Lyapunov exponent as in Ref. [239]. Note that the exponential increase occurs in a regime where the overall scale of the OTOC is still exponentially small in s. In the regime where the OTOC increases to an $O(1)$ value (i.e., when the operator front hits, see next point) its behavior is *not* exponential. Furthermore, we note that $\gamma \sim 1/q^2$ for large q, such that the regime in which the exponential behavior can be observed becomes *smaller* in the large q limit.

3. Near the front ($|\kappa - v_{\mathrm{B}}| = O(1/\sqrt{\tau})$): As mentioned, the above approximation breaks down when the main front, which we recall travels at speed v_{B} and has width $\sim \sqrt{\tau}$, arrives at site s. In this intermediate regime, we estimate the OTOC by combining Eq. (4.17) and Eq. (4.12) into

$$\overline{\mathcal{C}}(s,\tau) \approx \frac{1}{2}\mathrm{erfc}\left(\frac{s - v_{\mathrm{B}}\tau}{\sqrt{2\tau(1-v_{\mathrm{B}}^2)}}\right). \tag{4.19}$$

   This formula describes the behaviour of the OTOC in the regime when it increases from a value exponentially small in s to an $O(1)$ number.

4. Late times ($0 < \kappa < v_{\mathrm{B}}$): After the main front has passed the OTOC relaxes exponentially to 1. Expanding Eq. (4.13) for fixed $s - v_{\mathrm{LC}}\tau$ and large τ we find that the OTOC in this late time regime is

$$1 - \overline{\mathcal{C}}(s,\tau) \approx \frac{(1+q^{-2})q^s}{\sqrt{8\pi\tau}}\left(\frac{2q}{1+q^2}\right)^\tau \tag{4.20}$$

   Thus the OTOC decays to its equilibrium value with an exponent $\log\left(\frac{1+q^2}{2q}\right)$.

Probably the most important feature of this result is the lack of a well-defined Lyapunov exponent that would give an exponential growth of the OTOC near (but outside of) the butterfly front. This distinguishes the random circuit model from other exactly solvable non-integrable many-body systems, most notably the large-N limit of the SYK model and its generalizations [125, 559–561]. Indeed, one can devise a modified random circuit model, in continuous time, which mimicks a chain of coupled SYK models, each consisting of N qubits, with the addition that the couplings fluctuate in time, which makes it more tractable for finite N (and more similar to our random circuit) [252]. In that setting, one can show that while the Lyapunov exponent is well defined in the $N \to \infty$ limit, it disappears when one includes finite N corrections. As shown in Ref. [252], this is in fact closely related to the appearance of diffusive front broadening (which is suppressed at large N): this broadening is responsible for 'washing out' the Lyapunov exponent near the front. Indeed, one can argue more generically, that, assuming that the scaling of the OTOC along the ray $\kappa = v_{\mathrm{B}} + 0^+$ matches smoothing its scaling form in the front regime ($x = v_{\mathrm{B}}t + O(\sqrt{t})$), then its growth should be slower than exponential [251]. This

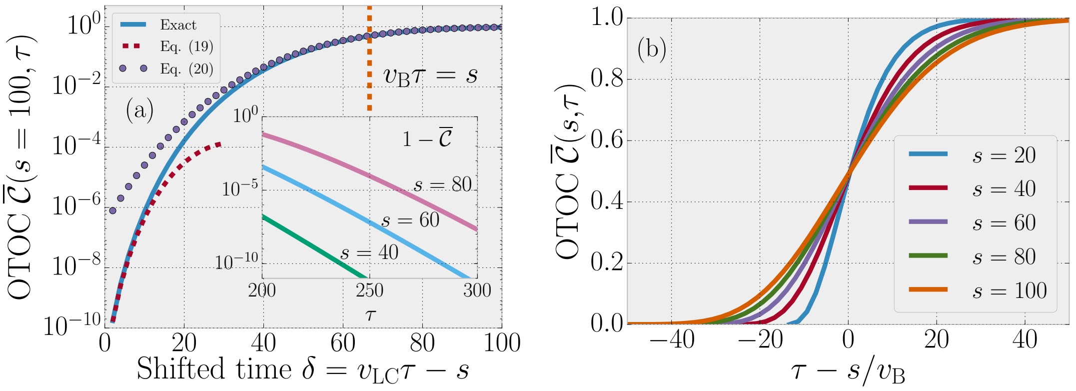

Figure 4.3.: Time dependence of the average OTOC in the random circuit model. (a) Different time regimes for fixed separation $s = 100$. The exact result for the OTOC follows Eq. (4.18) after the light cone hits site s. The behavior then goes over to regime described by Eq (4.19) after the front with speed $v_{\rm B}$ arrives. The inset shows the exponential decay of the OTOC to its final value 1, as described by Eq. (4.20), for different separations. (b): scaling collapse of the OTOC at the front.

indicates that the Lyapunov exponents observed in various models [125, 246, 559, 562] are all consequences of some semiclassical or large-N limit, and are not present for systems in the fully quantum regime, with $O(1)$ local Hilbert spaces and local interactions[5] [250].

4.2.3. Fluctuations between circuit realizations

The results discussed above concern quantities averaged over many different random circuits with the same geometry but different choices of two-site gates. The question remains regarding whether these average quantities are also 'typical', i.e. how large are the fluctuations between different realizations of the random circuit. In this section we investigate this problem numerically. Our numerical method relies on representing the operator $Z_0(t)$ as a matrix product operator (MPO), the operator version of the matrix product state. Both are characterized by their *bond dimension* (often denoted χ), which in the case of states is closely related to the maximal amount of entanglement between two halves of the one-dimensional chain (see Section 2.4 for a brief introduction to 1D tensor networks). The time evolution is performed by the Time Evolving Block Decimation (TEBD) algorithm [84, 85, 104, 105, 417], which applies two-site unitary gates to the MPO and the recompresses the result to the original MPO form with an increased bond dimension. Two layers of the random circuit can be applied by just a single step of the TEBD algorithm, which allows us to go up to bond dimension $\chi \approx 10000$. Both the infinite temperature OTOC and the total operator weight contained in an arbitrary subregion can be extracted straightforwardly from the MPO representation (both calculations are similar to computing the overlap of two matrix product states, but in the computation of $R(s)$ only the legs corresponding to sites $\leq s$ are contracted).

To quantify the fluctuations we look at an ensemble of 100 random circuit realizations (which is enough to reliably reproduce the exact average quantities, see Fig. 4.4) with on-site Hilbert space dimension $q = 2$ and compute a) the OTOC $\mathcal{C}(s, \tau)$ defined in Eq. (4.15) and b) the total operator weight $R(s, \tau)$ of $Z_0(\tau)$ contained in the region left of site s. Both $R(s, \tau)$ and $\mathcal{C}(s, \tau)$ are functions of the distance s and the number of layers τ. We

---

[5] Exponential growth *is* possible, and has been observed, however, in systems with sufficiently long-ranged interactions [107, 118, 125, 252, 563, 564].

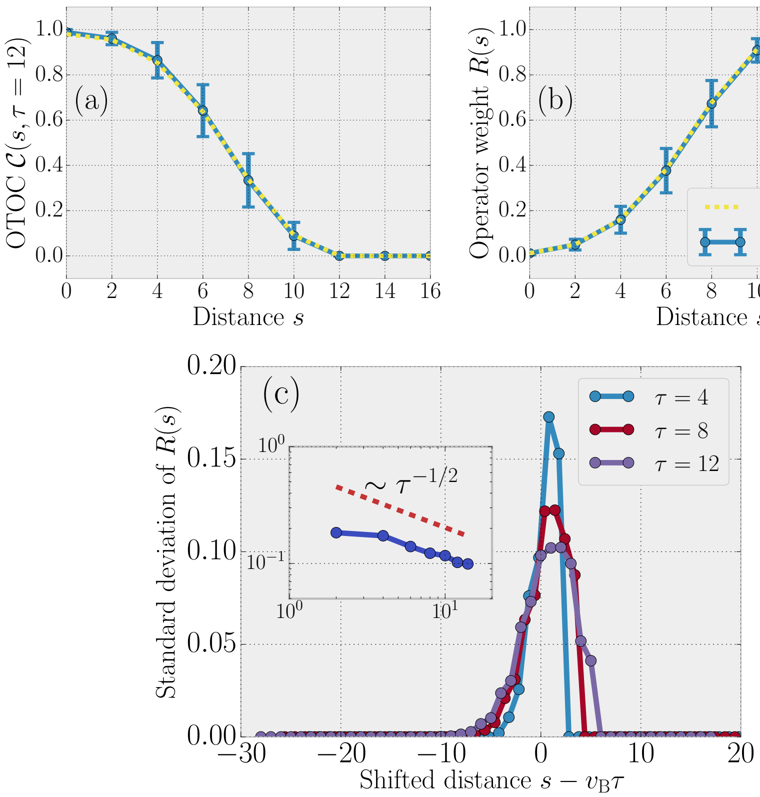

Figure 4.4.: Average values and fluctuations of the (a) OTOC and (b) the total weight left of site s for the time evolved operator $Z_0(\tau)$ after $\tau = 12$ layers of the random circuit. Blue dots correspond to average values of 100 different random circuits while the error bars signify one standard deviation. Figure (c) shows the standard deviations of $R(s)$ for different times. The largest fluctuations decrease in time approximately as $\propto \tau^{-1/2}$, as shown by the inset.

find that for both quantities, the circuit-to-circuit fluctuations are largest at the traveling wavefront and become smaller deep behind it. This is shown in Fig. 4.4. This also shows that there is a well defined front for the information propagation in each individual circuit.

We also find that the fluctuations decrease in time. Fig. 4.4 (c) shows the standard deviation of the weight $R(s)$ for different times. We find that the maximum of this standard deviation over all values of s decreases in time, approximately as $\propto \tau^{-\beta}$ with an exponent $0.4 < \beta < 0.5$.

In Ref. [253], the authors provide an analytical estimate for the size of fluctuations between different circuit realizations, that supports the claim that the results for operator spreading become self-averaging at long times. To arrive at this result, they consider adding noise to the biased diffusion equation (in a continuum formulation), that describes the dynamics of $\rho_R(x,t)$. They only consider noise in the drift term, as this is more relevant (in the RG sense) than noise in the diffusion constant. The resulting equation reads

$$\partial_t \rho_R(x,t) = \partial_x (v_\mathrm{B} + \eta(x,t)) \rho_R(x,t) + D_\rho \partial_x^2 \rho_R(x,t), \tag{4.21}$$

where η is uncorrelated white noise. They then argue that this noise in the drift (i.e., butterfly) velocity introduces fluctuations in the position of the front which are of the order $\sim t^{1/4}$, and are therefore negligible compared to the $\sim t^{1/2}$ width of the front that results from diffusion. The $t^{1/4}$ scaling can be intuitively understood from the fact that the ‘wavepacket’ describing the front visits a space-time volume $V(t) \sim \int^t \mathrm{d}t' \sqrt{t'} \sim t^{3/2}$

up to time t; the noise is averaged out on this scale, resulting in an average contribution to the speed $v_{\mathrm{av}} \sim \int_{V(t)} \eta(x,t) \sim V(t)^{-1/2} \sim t^{-3/4}$, which corresponds to a displacement $\Delta x \sim v_{\mathrm{av}} t \sim t^{1/4}$. This result supports the statement that the effect of circuit-to-circuit fluctuations becomes negligible at long times, and applies to particular realizations as well. An important takeaway from this is that the 'noise' inherent in the diffusion equation does not originate from the randomness of the dynamics, but from quantum fluctuations which gives rise to a distribution over different operators (see also Ref. [252]). Consequently, we conjecture that the biased diffusion equation described the long-time, long-wavelength behavior of operator spreading even in deterministic, translation-invariant systems. We list evidence for this statement in the next section.

4.3. Operator diffusion in deterministic models

A natural question that emerges in relation to the results stated above, is to what extent are they representative of other, more generic thermalizing quantum many-body systems[6]. To address this question we investigate a system with a periodically driven nearest neighbor Hamiltonian. Our model has the same geometry as the random circuit, shown in Fig. 3.1 and it similarly does not conserve energy. However, unlike random circuits, it is periodic in time and its two-site (and one-site) gates take a specific form, rather than randomly chosen. Despite these two significant differences, we find that several details of the operator spreading described in Section 4.2 remain approximately valid. Most importantly, we find evidence of diffusive broadening of the operator wavefront with time. This feature has also appeared in more recent numerical studies of ergodic Hamiltonian spin chains [427, 429, 567].

For concreteness, we consider a model with on-site Hilbert space dimension $q = 2$ that consists of switching back and forth between two Hamiltonians, such that one period of the time evolution (with period time T) is given by

$$\hat{U} = e^{-i\frac{T}{2} g \sum_s X_s} e^{-i\frac{T}{2}\sum_s [Z_s Z_{s+1} + h Z_s]}. \tag{4.22}$$

This system —which we refer to as the 'kicked Ising model' —is known to be ergodic, provided that both g and h are sufficiently large. Since at any given time the terms in the Hamiltonian all commute with each other, the time evolution can be represented as a circuit of two-site unitaries (with the one-site rotations included in the two-site gates) with the same geometry as in Fig. 3.1. As such, it is in fact contained among the ensemble of random circuits considered before. The question is to what extent do the properties of this specific circuit coincide with the average quantities discussed above.

At first, operator spreading in the Floquet system seems very different from the case of the random circuit. There is no inherent randomness and the evolution is completely determined by the internal structure of the initial operator σ^{μ}, while for the random circuit the average behavior was independent of the internal structure. However, it is well known that ergodic systems can behave as baths for themselves [97, 98] and in effect generate their own noise. If the same reasoning can be applied to the question of operator spreading in ergodic systems, then it is plausible that the noise averaged equation Eq. (4.8) holds in deterministic ergodic systems, and as a result the diffusively broadening ballistic front picture continues to apply.

Another way to motivate the same coarse-grained description can be given in a spirit similar to the discussion of Section 2.3. Using the locality of the dynamics, ρ_R not only

---

[6] Later on, in Refs. [565, 566], the same scaling of the operator front was shown to hold in a Heisenberg spin chain subject to a randomly fluctuating magnetic field. However, here we are interested in understanding whether our results are relevant also to systems where the dynamics is completely deterministic.

obeys global conservation law (where we revert to a continuum notation for ease of presentation) $\int \mathrm{d}x \rho_R(x,t) = const.$, it should also obey a local conservation law

$$\partial_t \rho_R(x,t) + \partial_x J_R(x,t) = 0 \tag{4.23}$$

for some local current density $J_R(x,t)$. This conservation law puts severe restrictions on the equation of motion of ρ_R. One then assumes, similarly to the usual derivation of hydrodynamics, that at sufficiently long time scales, the evolving operator relaxes to some form of 'local equilibrium', where it can be described entirely in terms of the conserved density, at least locally. In this case, relying on a long wavelength (gradient) expansion, one can write down the constitutive equation $J_R \sim v\rho_R + D_\rho \partial_x \rho_R + \ldots$; this constitutive relation is exactly the continuum version of the random walk equation we derived for the circuit-averaged ρ_R in Eq. (4.8). This hydrodynamic reasoning also makes it clear that in generic cases, the biased diffusion would only capture the leading order behavior, and a more complete treatment would supplement it with various correction terms, akin to the subleading power laws that appear in usual hydrodynamics. A rigorous treatment of these, in the spirit of Ref. [295], is a very interesting open problem.

Therefore it seems plausible that in a sufficiently coarse grained picture, the dynamics might be well approximated by a biased diffusion similar to the one described in Section 4.2 for the Floquet circuit, with the butterfly velocity and diffusion constant depending on the microscopic couplings. Here we present numerical evidence in support of this conjecture. Our results can be summarized in three points:

- The butterfly velocity v_B depends strongly on the coupling g and can be tuned to be much smaller than the light cone velocity v_LC.
- When tuning the couplings to decrease v_B from its maximal value $v_\mathrm{B} \approx v_\mathrm{LC}$, the front also becomes wider, as expected for a random walk when increasing the probability of hopping to the left at the expense of the probability of hopping right.
- The operator wavefront gets wider during time evolution, with the width increasing in time as $\sim t^\alpha$, with an exponent $0.5 \lesssim \alpha \lesssim 0.6$

We investigate numerically the dynamics of the time evolved operator $Z_0(t)$, using the same MPO-TEBD method as described at the beginning of Section 4.2.3. We find a linearly propagating wavefront, which shows up in both the OTOC and the weight $R(s)$, with the former saturating to 0, and the latter to 1 behind the front. While for the random circuit the speed of the front was set by the on-site Hilbert space dimension q, for the kicked Ising model we find that this speed can be tuned continuously by changing the value of the transverse field[7] g, as shown in Fig. 4.5. Note that changing g does not affect the light cone velocity, which is $v_\mathrm{LC} = 1$ due to the geometry of the circuit that represents the Floquet time evolution. For $g = 0$, an initial operator Z_0 remains localized on the same site. As we make g larger, the butterfly velocity gradually increases and it reaches $v_\mathrm{B} \approx v_\mathrm{LC}$ for $g \approx 0.9$ with period time $T = 1.6$[8]. Looking at Fig. 4.5 we notice that decreasing v_B from its maximum corresponds to an increased front width at any given time. This is consistent with a coarse-grained random walk description, wherein increasing the probability of hopping to the right results in both a larger butterfly velocity and a suppression of the diffusion constant.

---

[7] We have found that the butterfly velocity does not depend significantly on the value of h, provided that it is not too small

[8] We note that this set of parameters, for which v_B is near maximal, is close to the parameter choice found in Ref. [568] to exhibit very fast thermalization. Moreover, there exist a nearby *self-dual* line, $T = \pi/2$, $g = 1$ and h arbitrary, where $v_\mathrm{B} = v_\mathrm{LC} = 1$ exactly and therefore diffusive front broadening is completely suppressed [537].

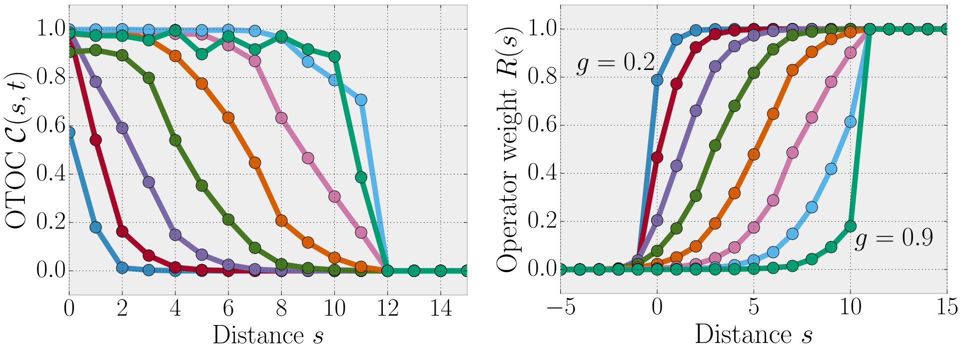

Figure 4.5.: OTOC (left) and operator weight $R(s)$ (right) for different distances s after $t/T = 12$ driving cycles of the kicked Ising model with the strength of the transverse field $g = 0.2, 0.3, \ldots, 0.9$ as indicated in the right figure. The longitudinal field is fixed at $h = 0.809$ while the period time is $T = 1.6$. The butterfly velocity shows a strong dependence on the coupling g, with the front width increasing as one moves away from the limit of maximal velocity.

The most important evidence in support of a hydrodynamic description comes from examining the front width as a function of time. Similarly to the random circuit model, we find the wavefront of the operator spreading broadens as we go to longer times. To quantify the width, we look at the standard deviation of $\rho_R(s) = R(s) - R(s-1)$, i.e.

$$\sigma(t) \equiv \sqrt{\sum_s \rho_R(s) s^2 - \left[\sum_s \rho_R(s) s\right]^2} \tag{4.24}$$

As shown in Fig. 4.6, at long times the width grows algebraically in time as $\sigma(t) \propto t^\alpha$ with an exponent $0.5 \lesssim \alpha \lesssim 0.6$. This is consistent with the random walk description of operator spreading put forward in Section 4.2, and supports our conjecture that the biased diffusion equation captures the universal features of operator spreading in one dimensional systems.

Our hydrodynamic equation for ρ_R relied on having a single conserved density (there is of course also ρ_L, the left endpoint density, but that decouples from ρ_R due to locality). This is true in the systems we studied in this chapter, with no local conserved

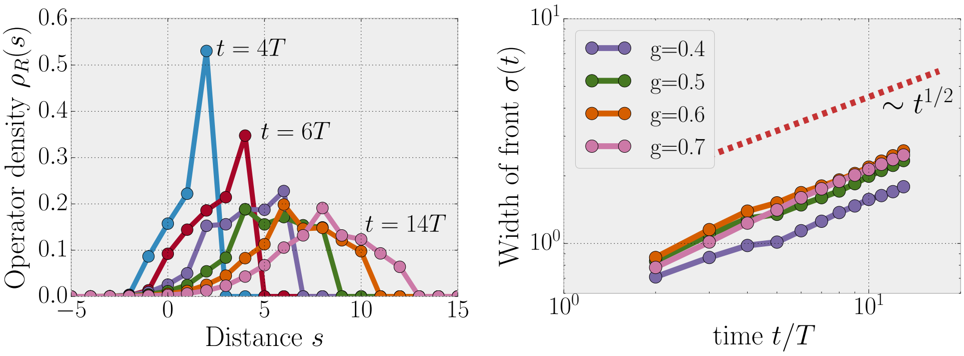

Figure 4.6.: Broadening of the operator wavefront with time in the kicked Ising model for parameters $h = 0.809$ and $T = 1.6$. Left: the weight $\rho(s)$ for transverse field $g = 0.7$ at times $t/T = 4, 6, \ldots, 14$. Right: the width of the front as defined by Eq. (4.24) as a function of time for different g, showing a roughly diffusive broadening of the wavefront.

quantities in the traditional sense (energy, particle number, etc.). In systems that *do* have such conserved quantities, one would have to include these in the hydrodynamic description. This will be the topic of Chapter 8. As we will show there, the coupling to particle/energy density gives rise to various interesting novel features in operator spreading, that do not appear in the models we studied in this chapter. However, the general picture of a diffusively broadening butterfly front remains unchanged (at least in the high temperature / low chemical potential regime). This is also corroborated by various numerical studies, which have shown evidence of a diffusively growing front in energy conserving ergodic spin-chains [427, 429, 567]. Ref. [546] has also found clear evidence of a diffusive broadening operator front in a model based on a classical cellular automaton, despite this particular model being integrable. Indeed, it was subsequently argued, that interacting integrable systems generically also have a diffusive front broadening, which can be explained in the language of generalized hydrodynamics, considering phase shifts in particle trajectories [569].

4.4. Operator spreading in higher dimensions

Before concluding our discussion of operator spreading in the absence of conservation laws, let us give a brief overview of how our results are expected to change in higher spatial dimensions, based on Ref [253]. The crucial difference is that, for $d \geq 2$, the operator wave front can no longer be characterized in terms of its 'endpoint'; instead, one has to deal with a $d-1$ dimensional object, which describes the position of the front, spreading outwards from an initial seed that corresponds to the support of the operator at $t = 0$. As a consequence, OTOCs do not obey a local differential equation. Instead, one can use the same circuit-averaging formulae as before to map operator spreading in a higher dimensional Haar random circuit to a classical surface growth problem.

In this effective description, each site of the lattice can be empty (= identity operator) or occupied (= a non-trivial Pauli) and whenever a local gate (which are now arranged in a higher dimensional circuit) is applied to a pair of sites which are not both empty, the probabilities of being occupied evolve according to a simple counting of the number of non-trivial one- and two-site operators (for example, the probability of both sites being occupied after the application of the gate is $\frac{(q^2-1)^2}{q^4-1} = \frac{q^2-1}{q^2+1}$). The resulting stochastic evolution for the occupations is similar to other well-studied growth models, such as the Eden model [303, 570–573]. The upshot is that, much like in the one-dimensional case, the growing cluster clearly separates into an 'inside' region, where the average occupation (which is proportional to the circuit-averaged OTOC) is $n \approx 1$, and an 'outside' region, where $n \approx 0$, with the size of the former growing ballistically in time. The evolution then reduces to the stochastic dynamics of the $d-1$ dimensional surface between the two regions. The authors of Ref. [253] argue that, in analogy to e.g. the Eden model, the universal features of this effective dynamics for the 'height field' h (i.e., the distance of the interface from the original seed) is given by the Kardar-Parisi-Zhang (KPZ) equation:

$$\partial_t h(x,t) = v_{\mathrm{B}} + \nu \partial_x^2 h(x,t) + \frac{\lambda}{2}(\partial_x h(x,t))^2 + \zeta(x,t), \tag{4.25}$$

where x is the coordinate perpendicular to the surface and ζ is uncorrelated white noise. v_{B} gives the average speed of the ballistic front spreading. Importantly, the coefficient λ, which captures the fact that the local growth rate depends on the slope of the surface, makes the problem non-linear. This leads, under coarse-graining, to a non-trivial fixed point, with its own universal exponents. The most important of these for the operator spreading problem is that the fluctuations in the position of the front, i.e. the size of the front region, grows in time as $\sim t^\beta$ with an exponent β that depends on the dimensionality.

In particular, $\beta = 1/3$ in $d = 2$ and $\beta \approx 0.24$ in $d = 3$, as opposed to the diffusive $\beta = 1/2$ broadening we obtained for the one-dimensional problem. Moreover, in $d \geq 2$ there is also a subleading correction to the *position* of the front, which grows with the same $\sim t^{\beta}$ scaling. In Ref. [253], the authors perform extensive numerical simulations of the classical surface growth dynamics that result from circuit-averaging, which confirm this $t^{1/3}$ scaling in the two-dimensional case. The same universal scaling was also confirmed in a continuous-time spin model subject to a strongly fluctuating magnetic field [565]. Arguments similar to the ones above suggest that these results should be applicable also to deterministic evolutions (note that the space-time volume covered by the front also grows with d, further suppressing the effects of noise).

5. Entanglement Growth

As discussed in Chapter 2, the growth of entanglement is a central feature of many-body quantum dynamics, closely connected to the approach towards thermal equilibrium. In this chapter we show that, similar to the case of operator spreading, the random circuit model can be used to calculate exactly certain measures of entanglement, and the results can be used to motivate a more general long-wavelength 'hydrodynamic' theory of entanglement growth, which captures universal features also in more generic models. We will mostly focus on higher Rényi entropies, S_α with $\alpha = 2, 3, \ldots$, as these are the ones where an exact solution (in a sense clarified below) is feasible. However, there is evidence, both numerical and analytical, that the general picture generalizes also to the case of the von Neumann entropy.

5.1. From operator spreading to entanglement growth

In this section we use our results for operator spreading to compute the time evolution of the second Rényi entropy S_2 between two sides of a spatial entanglement cut and extract the entanglement velocity from it. More precisely, we will calculate the *annealed average* $S_2^{(a)} \equiv -\log \overline{e^{-S_2}}$, i.e., taking the logarithm *after* the circuit-averaging. This is a simpler quantity than the *quenched average*, $\overline{S_2}$. We will comment on the differences later in Section 5.2. We find that the annealed average grows linearly, $S_2^{(a)} = \log q v_\mathrm{E} t$, with an *entanglement velocity* v_E that is smaller than the butterfly velocity for any finite q and approaches the light cone velocity logarithmically slowly, so that $v_\mathrm{LC} - v_\mathrm{E} \propto 1/\log q$ for large q. This (due to the concavity of the logarithm) provides a lower bound for the entanglement velocity of the quenched average, and consequently of the von Neumann entropy: $S_2^{(a)} \leq \overline{S_2} \leq \overline{S_1}$. At long times, $S_2^{(a)}$ saturates to its maximal value with the saturation becoming increasingly sharp as q is increased.

Consider an initial ferromagnetic product state of the 1D chain where the state on site s is an eigenstate of the local Pauli operator Z_s with eigenvalue $+1$ (Note that, for the average behavior of the random circuit, the choice of initial product state is unimportant). The density matrix $\hat{\omega}$ corresponding to this state is then a sum over all possible Z*-strings*, i.e. Pauli strings that only contain powers of the operator Z on each site:

$$\hat{\omega} = \frac{1}{q^L} \prod_{s=1}^{L} \left(\sum_{k=0}^{q-1} Z_s^k \right) = \frac{1}{q^L} \sum_{\vec{\nu} \in \text{Z-strings}} \sigma^{\vec{\nu}}. \tag{5.1}$$

The density matrix at time t is obtained by replacing each Pauli string σ^ν in Eq. (5.1) with its time evolved counterpart $\sigma^{\vec{\nu}}(t)$.

Let us now divide the system into two regions, A and B, the first of which corresponds to sites $1, \ldots, L_\mathrm{A}$. Generalizing the formula of Refs. [256, 574], the second Rényi entropy $S_2 \equiv -\log \mathrm{tr}(\hat{\omega}_\mathrm{A}^2)$ of the reduced density matrix $\hat{\omega}_\mathrm{A} = \mathrm{tr}_\mathrm{B}(\hat{\omega})$ is related to the operator spreading coefficients by

$$e^{-S_2} = \frac{1}{q^{L_\mathrm{A}}} \sum_{\vec{\nu}, \vec{\nu}'} \sum_{\vec{\mu} \subset A} c_{\vec{\mu}}^{\vec{\nu}} c_{\vec{\mu}}^{\vec{\nu}'^*} \approx \frac{1}{q^{L_\mathrm{A}}} \sum_{\vec{\nu}} \sum_{\vec{\mu} \subset A} |c_{\vec{\mu}}^{\vec{\nu}}|^2 \tag{5.2}$$

where the strings $\vec{\nu}$ and $\vec{\nu'}$ are both Z-strings and μ has support entirely in subsystem A. In the last equality of Eq. (5.2) we assumed that the off-diagonal contributions are negligible, which becomes *exactly* true in the random circuit model once we average over different realizations.

Let us assume that L_A is even. Reverting back to the coarse-grained position x (see Eq. (4.7)) we recognize Eq. (5.2) as the total operator weight in region A, $R(x = L_\mathrm{A}/2, t)$, as defined in Eq. (4.11), summed over all initial Z-strings. As we noted previously, this quantity is on average the same for all initial strings with the same endpoints x_0. The number of different Z-strings with right endpoint x_0 is $q^{2(x_0-1)}(q^2-1)$. After averaging over random circuits, and assuming an even number of layers, Eq. (5.2) thus becomes

$$\overline{e^{-S_2(\tau)}} = \frac{1}{q^{L_\mathrm{A}}} + \frac{q^2-1}{q^2} \sum_{x_0=1}^{L/2} \frac{\overline{R}(L_\mathrm{A}/2 - x_0, t = \tau/2)}{q^{L_\mathrm{A}-2x_0}}, \tag{5.3}$$

where we have used that $\overline{\rho_R}(x)$ (and consequently $\overline{R}(x)$) only depends on the position x relative to the initial endpoint x_0. The first term in Eq. (5.3) is the contribution coming from the identity operator, which is responsible for the saturation of the entanglement at long times.

Using the exact solution Eq. (4.9) one can perform the sum over initial positions to find

$$\overline{e^{-S_2(\tau)}} = q^{-L_\mathrm{A}} + [1 - q^{-L_\mathrm{A}}] \frac{q^\tau}{(1+q^2)^\tau} \sum_{x=-\tau/2}^{L_\mathrm{A}/2-1} \binom{\tau}{\frac{\tau}{2}+x}. \tag{5.4}$$

The sum over binomial coefficients can be expressed in terms of a hypergeometric function.

Eq. (5.4) describes an entanglement that initially increases linearly with time and saturates to the maximum value $L_\mathrm{A} \log q$ at long times. For $\tau \ll L_\mathrm{A}$ we find

$$\overline{e^{-S_2(\tau)}} \approx \left(\frac{2q}{1+q^2}\right)^\tau, \tag{5.5}$$

from which we can identify the *entanglement velocity*[1]

$$v_\mathrm{E} \equiv \frac{1}{\log q} \frac{\mathrm{d}S_2^{(a)}(\tau)}{\mathrm{d}\tau} = \frac{\log \frac{q+q^{-1}}{2}}{\log q} = \frac{\log\left(1 - v_\mathrm{B}^2\right)}{\log\left(\frac{1-v_\mathrm{B}}{1+v_\mathrm{B}}\right)}. \tag{5.6}$$

This is a separate velocity scale, distinct from, and smaller than the front speed $v_\mathrm{E} < v_\mathrm{B}$. This difference comes from the diffusive broadening of the operator wavefront. First, it is straightforward to verify that if the wavefront is sharp, i.e., $\overline{R}(x,t) = \Theta(x - v_\mathrm{B}t)$, then Eq. (5.3) gives $v_\mathrm{E} = v_\mathrm{B}$. Second, we have checked that Eq. (5.3) gives $v_\mathrm{E} = v_\mathrm{B}$ even if the wavefront has a width which is finite but independent of time[2]. Hence, we attribute the difference between v_B and v_E to the fact that the operator front broadens with time.

In the right panel of Fig. 5.1 we compare the exact formula Eq. (5.4) to the second Rényi entropy as computed numerically (using a matrix product state representation), averaging over 100 realizations of the circuit and find extremely good agreement. Moreover, the numerical calculation allows us to compare $S_2^{(a)}$ and the quenched average Rényi entropy $S_2^{(q)} \equiv \overline{S_2}$. We find no significant difference between the two values, showing that there are no strong circuit-to-circuit fluctuations in the entropy on the time scales accessible in the numerics. As we discuss later in Section 5.3, the fluctuations do lead to important

---

[1] Intuitively v_E can be thought of as the rate at which a maximally entangled region would need to grow in order to have entropy $S(\tau)$. See also Ref. [256] for a discussion of v_E.

[2] We checked this for front profiles arising from $\rho_R(x,t) \propto e^{-(x-vt)^2/\sigma^2}$ and $\rho_R(x,t) \propto e^{-|x-vt|/\sigma}$.

subleading effects at longer times that are not visible in $S_2^{(a)}$. Nevertheless, our numerics suggest that the analytical solution does capture the leading linear growth correctly, and the entanglement velocity of $S_2^{(q)}$ is not significantly different from the one we derived above for $S_2^{(a)}$. On the other hand, we found numerically that replacing the Rényi entropy with the von Neumann entropy does lead to a slightly larger entanglement velocity.

The entanglement saturates when the contribution of the identity becomes significant (i.e. when all other operators have essentially left the subsystem). Note that the saturation softens, compared to the prediction of the simple operator spreading model of Ref. [574], which is another consequence of the diffusive broadening of the front. This intermediate saturation regime becomes smaller with increasing q, as shown in the left panel of Fig. 5.1.

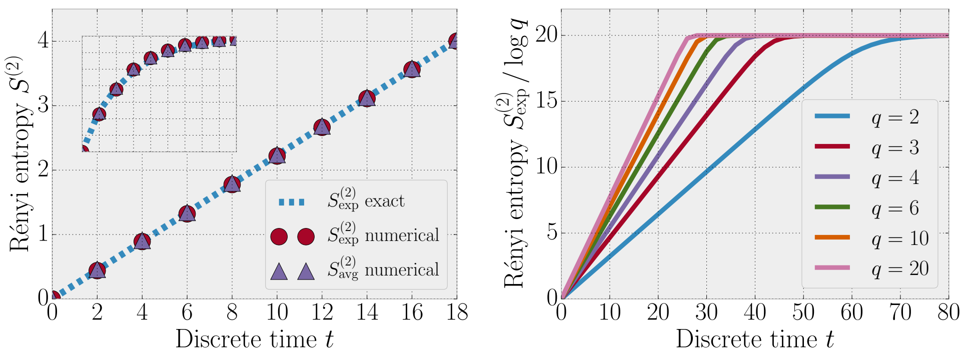

Figure 5.1.: Entanglement growth in the random circuit model. Left: comparing the exact formula, Eq. (5.4), to matrix product state numerics shows that it captures both $S_2^{(a)} = -\log \overline{e^{-S_2}}$, and the average $\overline{S_2}$ of the second Rényi entropy, on the short time scales available to us in the numerics. The main figure shows the time dependence for $L_{\text{A}} = 50$ sites, while the inset is for $L_{\text{A}} = 2$. Right: The entanglement velocity increases with q according to Eq. (5.6) while the saturation regime becomes smaller.

5.2. Alternative calculation and the entanglement membrane

One can also calculate the growth of $S_2^{(a)}$ directly, without using the operator spreading results. This alternative derivation is helpful in formulating a universal, long-wavelength description that can be generalized to other models. In particular, it will prove very useful in extending our calculations to a modified circuit model with conserved quantities in Part II, so we summarize it briefly here, following the discussions of Refs. [253, 260, 278].

The starting point is the so-called 'swap trick', wherein one rewrites the *purity* (the exponentiated 2nd Rényi entropy) as an expectation value in an enlarged Hilbert space as

$$\operatorname{tr}(\rho_A^2) = \operatorname{tr}(\mathcal{F}_A(\rho \otimes \rho)) = \langle \mathcal{F}_A \rangle_{\rho \otimes \rho}. \tag{5.7}$$

Here $\rho \otimes \rho$ is two identical copies of the same quantum state and $\mathcal{F}_A$ is the 'swap' operator, which acts on this doubled Hilbert space, and swaps the two copies inside subsystem A, while acting as the identity on the outside. Te be more precise, consider the two-copy Hilbert space of a single site, spanned by state of the form $|a\rangle \otimes |b\rangle$. Then an on-site swap operator acts as $\mathcal{F}(|a\rangle \otimes |b\rangle) = |b\rangle \otimes |a\rangle$, and $\mathcal{F}_A \equiv \prod_{s \in A} \mathcal{F}_s$. For an illustration, see Fig. 10.3(a,b) below.

One can also think of Eq. (5.7) as an 'overlap' between a pair of two-copy operators, $\mathcal{F}_A$ and $\rho \otimes \rho$. To get the purity of the time evolved state one can then evolve *either* of these objects and then take its overlap with the other. Since these are operators on the doubled

Hilbert space, they evolve in time according to four copies of the unitary U. Schematically, we can write the result as $\langle\mathcal{F}_A|U\otimes U^*\otimes U\otimes U^*|\rho_0\otimes\rho_0\rangle$, where $\rho_0\equiv|\Psi_0\rangle\langle\Psi_0|$ is the initial state. When U is given by a circuit of local gates, one can take four copies of each gate; the purity then looks like a two-dimensional tensor network, where the tensors in the bulk are four-copy versions of the original local gates and they are contracted with tensors on the upper and lower boundaries that encode the two operators $\rho_0\otimes\rho_0$ and $\mathcal{F}_A$, respectively[3]. Formally, this tensor network has the structure of a partition function for a two-dimensional classical spin model, although it might have weights that are negative or complex. However, averaging over the Haar randomness of each gate simplifies the local tensors immensely, leading to a simple classical model with only two possible states per site.

To see this, it is useful to write the fourth moment of an $N\times N$ Haar-random unitary U as

$$\overline{U\otimes U^*\otimes U\otimes U^*}=\frac{1}{N^2-1}\sum_{\sigma=\pm}\left[|\mathcal{I}_\sigma\rangle\langle\mathcal{I}_\sigma|-\frac{1}{N}|\mathcal{I}_\sigma\rangle\langle\mathcal{I}_{-\sigma}|\right],\tag{5.8}$$

where $|\mathcal{I}_\pm\rangle$ are states in the four-copy Hilbert space defined as

$$|\mathcal{I}_+\rangle\equiv\sum_{a,b=1}^{N}|aabb\rangle\qquad\qquad|\mathcal{I}_-\rangle\equiv\sum_{a,b=1}^{N}|abba\rangle.\tag{5.9}$$

In our case, U is a two-site unitary, and $a,b=1,2,\dots,q^2$ go over basis states of the two-site Hilbert space. One can then split these into products of one-site states, $|\mathcal{I}_\sigma\rangle_{s,s+1}=|\sigma\rangle_s|\sigma\rangle_{s+1}$, where

$$|+\rangle\equiv\sum_{\alpha,\beta=1}^{q}|\alpha\alpha\beta\beta\rangle\qquad\qquad|-\rangle\equiv\sum_{\alpha,\beta=1}^{q}|\alpha\beta\beta\alpha\rangle\tag{5.10}$$

are now states from four copies of a single-site Hilbert space. Note that $\langle+|+\rangle=\langle-|-\rangle=q^2$ and $\langle+|-\rangle=q$.

Combining these formulae, each Haar-averaged two-site gate gives rise to a four-leg tensor, which can be written in the form

$$\overline{U\otimes U^*\otimes U\otimes U^*}=\frac{1}{q^4-1}\sum_{\sigma,\tilde\sigma,\sigma',\tilde\sigma'}w_{\sigma\tilde\sigma\sigma'\tilde\sigma'}|\sigma'\rangle|\tilde\sigma'\rangle\langle\sigma|\langle\tilde\sigma|=\frac{1}{q^4-1}\sum_{\sigma,\sigma'}w_{\sigma\sigma'}|\sigma'\rangle|\sigma'\rangle\langle\sigma|\langle\sigma|,\tag{5.11}$$

where in the last step we used that the only non-vanishing elements are those where the two input and the two output indices coincide. The coefficients $w_{\sigma\sigma'}$ (which equal 1 if $\sigma=\sigma'$ and $-1/q^2$ otherwise), together with the overlaps $\langle\sigma|\sigma'\rangle$, can be thought of as local interaction terms of a classical spin model, with spins σ living on sites of a two-dimensional lattice. Contracting all the tensors together defines a partition function for these spins, with boundary conditions fixed by the quantity one wishes to compute. In particular, when calculating the purity, the swap operator $\mathcal{F}_A$ defines a boundary condition $\prod_{s\in A}|-\rangle_s\prod_{s\notin A}|+\rangle_s$. The condition on the other boundary depends on the chosen initial state $|\Psi_0\rangle$. For a product initial state, it reads $\prod_s\frac{|+\rangle_s+|-\rangle_s}{q(q+1)}$,, which corresponds to an equal weight sum over all spin configurations.

Consider now calculating the entanglement between two halves of the chain, where the subsystem A consists of sites $s\leq L_A$. In this case the swap operator corresponds to a domain wall boundary condition $\mathcal{F}_A\equiv\mathcal{F}(L_A)=|-\rangle_1\dots|-\rangle_{L_A}|+\rangle_{L_A+1}\dots|+\rangle_L$. In this case, the ‘interactions’, defined by the (Haar-averaged) local unitaries, result in a

---

[3] Note that one could write down a very similar tensor network representation also for the quantities considered in Chapter 4, with the difference appearing only in the boundary conditions.

particularly simple behavior. If a gate acts somewhere away from the position of the domain wall, it has no effect: $|+\rangle|+\rangle \to |+\rangle|+\rangle$ and $|-\rangle|-\rangle \to |-\rangle|-\rangle$. If the gate crosses the domain wall, it induces a random walk, moving it either to the left or the right by one site, while also picking up a constant prefactor: $|-\rangle|+\rangle \to \frac{2q}{q^2+1}\frac{|-\rangle|-\rangle+|+\rangle|+\rangle}{2}$. Therefore, at time τ, the domain wall evolves to (ignoring finite-size effects, i.e. taking $L_A > \tau$)

$$|\mathcal{F}(L_A,\tau)\rangle = \left(\frac{2q}{q^2+1}\right)^{\tau} \sum_s K(s-L_A,\tau)|\mathcal{F}(s)\rangle, \tag{5.12}$$

where $K(s-L_A,\tau)$ is a random walk kernel describing the probability of a domain wall traveling from initial position L_A to final position s under τ steps of the (unbiased) random walk process induced by the two-site gates. $|\mathcal{F}(s)\rangle$ is now a swap acting on sites $[1,s]$, i.e., it is a domain wall of the same form as the initial condition, located at a different position. As stated above, for a product initial state, the purity is given by the sum of the weights of all the different configurations. Since we normalized the kernel to $\sum_s K(s,\tau) = 1$, this leaves us with only the prefactor, $\overline{e^{-S_2(\tau)}} = \left(\frac{2q}{q^2+1}\right)^{\tau}$, which coincides with our earlier result. One could easily extend this calculation to take into account finite-size effects and reproduce the eventual saturation of the entropy.

A big advantage of this alternative formulation is that it easily generalizes to quantities other than the average purity. As a first step, one could consider similar 'annealed' averages of higher Rényi entropies, related to partition functions of the form $Z_\alpha \equiv e^{-(\alpha-1)S_\alpha}$ for $\alpha = 3,4,\ldots$. After averaging over circuits, these would also lead to similar, albeit more complicated, spin partition functions.. In this case, one has to consider α copies of the density matrix and an appropriately generalized swap operator that performs a cyclic permutation of these copies; this can again be thought of as a domain wall between two different ways of pairing up the different copies. The local interactions are defined by the 2α-th moment of the Haar random unitaries, which results in more complicated Haar-average formulae (see Ref. [278] for details). For example, the resulting statistical models will now possess $\alpha!$ different kinds of domain walls, corresponding to the different possible permutations of the copies. Moreover, one can extend these mappings to calculate directly the quenched averages of various Rényi entropies. This can be done using the so-called *replica trick* (widely used in treating the statistical physics of systems with static disorder [188, 575–577]). One then writes the average Rényi entropy as

$$\overline{S_\alpha} = \frac{1}{1-\alpha}\frac{\partial \overline{Z_\alpha^k}}{\partial k}\bigg|_{k=0}. \tag{5.13}$$

As a result, one needs to evaluate Z_α^k for various k, which is a partition function of a similar form as Z_α itself, now corresponding to αk copies of the system.

In practice, the classical partition functions one needs to evaluate become rather complicated, and an exact analytical solution is no longer possible. However, certain general features can be efficiently extracted from this representation, and controlled calculations are possible near the $q=\infty$ limit. Expanding around this limit, one finds [278] that the leading scaling of $\overline{S_2}$ in time is a linear growth, with an entanglement speed that coincides with Eq. (5.6) up to corrections of order $O(1/q^8 \log q)$. Apart from being suppressed at large q, the leading correction also comes with a numerically small prefactor (1/384), which explains why the two speeds observed at short times in Fig. 5.1 appear to be indistinguishably close. A similar calculation shows that $\overline{S_3}$ also grows linearly, but with a speed that is smaller than that of S_2 at finite q. However, while the leading order behavior is well-described by the annealed average result we calculated, there are important subleading effects, stemming from the fluctuations that are suppressed when we take the average before the logarithm. We will return to these below in Section 5.3.

There are some important conclusions to be drawn from these calculations, which generalize beyond the realm of random circuit models. We reduced the calculation of the purity to following the stochastic dynamics of an ‘entanglement domain wall’. In this calculation, the initial quantum state only appears in the very last step, in the form of the boundary condition that weights the different spin configurations. Therefore, the domain wall picture allows us to consider the entanglement dynamics of *any* initial state simultaneously. This leads to a very appealing description of entanglement growth, in terms of the ‘energy’ of a minimal membrane (or polymer, in one dimension).

To construct this description, consider a partition function with a modified boundary condition: instead of summing over all configurations at the final time, we fix a boundary where there is a domain wall at position x on the boundary[4]. We denote this modified partition function as $Z(x,t)$ (where we changed notation and put the domain wall on the first boundary at position 0; otherwise one would need to replace $x \to x - L_A$): this gives the probability of transitioning from an initial domain wall to another domain wall that has moved x sites. In the above random circuit case this is simply $\left(\frac{2q}{q^2+1}\right)^t K(x,t)$, but we could define the same quantity for any other evolution. We are interested in the scaling limit, where $x/t \equiv v$ is fixed. The random circuit calculation suggests that in this case

$$Z(x,t) = e^{-s_{\text{eq}}\mathcal{E}(v)t}, \tag{5.14}$$

where s_{eq} is the equilibrium entropy density (in our case here, $s_{\text{eq}} = \log q$). The function $\mathcal{E}(v)$ determines the scaling of the ‘free energy’, $\log Z(x,t)$ with the total time. If one imagines the trajectory of the domain wall, $x(t)$, as a polymer in two dimensions, one can think of $\mathcal{E}(v)$ as its *line tension*, proportional to its free energy per unit length. The total free energy associated to a given trajectory is then $\int_0^t \mathrm{d}t'\mathcal{E}(\dot{x}(t'))$. In principle, to calculate the entropy, we have to perform a path integral over all the possible trajectories. However, in a sufficiently coarse-grained limit (at long times and large distances), one might naturally expect that this path integral is dominated by its saddle point, i.e., by the path that minimizes the free energy. Under this assumption, one finds a remarkably simple formula for the half-chain entanglement for a bi-partition at position x at time t:

$$S_2(x,t) = \min_y \left(s_{\text{eq}} \int_0^t \mathrm{d}t'\mathcal{E}(\dot{x}(t')) + S_2(y,0) \right). \tag{5.15}$$

In this picture, computing the entanglement accumulated over time reduces to the problem of finding a polymer with minimal free energy. This is especially simple in the case of spacetime translation invariant dynamics, in which case the minimal curves are straight lines parametrized by a single parameter v. All the details of the microscopic dynamics have been repackaged into line tension function $\mathcal{E}(v)$. One can naturally extend this picture to higher dimensions, where the one-dimensional polymer is replaced by a d dimensional membrane embedded in the $d+1$ dimensional spacetime and characterized by a surface tension $\mathcal{E}(v)$. Note, moreover, that we could rerun the same argument for other Rényi entropies, writing the partition function as $Z_\alpha(x,t) = e^{-s_{\text{eq}}\mathcal{E}_\alpha(v)t}$, where the line/surface tension $\mathcal{E}_\alpha(a)$ now also depends on the Rényi index. One could then extend this minimal cut picture to of the von Neumann entropy, by taking the limit $\alpha \to 1$.

There is an alternative line of reasoning that leads to the same formula for entanglement growth. Imagine trying to write down an equation of motion for the entropy: $\partial_t S(x,t) = \ldots$. One can use a hydrodynamic approximation, analogous to the ones discussed in Section 2.3, to argue that in an appropriately coarse-grained, long-wavelength limit, the

---

[4] In the rest of this section, we use x and y, rather than s or r, to denote lattice positions. Since this is a quite general discussion, the distinction between original and coarse-grained coordinates is not important here.

RHS of the equation can be approximated by some function of the spatial entropy-gradient, $\partial_x S(x,t)$, only. Even though the entropy itself is not a conserved quantity, it makes sense to treat it as a 'slow variable', in the hydrodynamic sense. For example, above we saw that the dynamics of Rényi entropies is closely tied to the motion of a domain-wall object (the half-chain swap operator), whose behavior can be treated similarly to that of a conserved density (see also Ref. [260]). The hydrodynamic equation of motion, in the long-wavelength limit, neglecting higher derivative corrections, then reads

$$\partial_t S = s_{\text{eq}} \Gamma(\partial_x S). \tag{5.16}$$

Here, the dynamics is characterized by the entropy production rate Γ. This depends on the details of the dynamics, but it has to satisfy certain general constraints. In particular, it should vanish in equilibrium, when $\partial_x S = s_{\text{eq}}$, and it should be positive when $|\partial_x S| < s_{\text{eq}}$. By definition, $\Gamma(0)$ is the entanglement velocity v_{E}. One can now define the line tension as the Legendre transform of Γ:

$$\mathcal{E}(v) = \max_s \left(\Gamma(s) + \frac{vs}{s_{\text{eq}}} \right) \qquad\qquad \Gamma(s) = \min_v \left(\mathcal{E}(v) - \frac{vs}{s_{\text{eq}}} \right). \tag{5.17}$$

This definition of $\mathcal{E}(v)$ is equivalent to the previous one, which can be seen by differentiating Eq. (5.15) with respect to t.

From this definition, one can see that $\mathcal{E}(0) = v_{\text{E}}$. However, the minimal cut picture contains far more information than just the entanglement speed; among other things one can also use it to extract the butterfly velocity as the point which satisfies $\mathcal{E}(v_{\text{B}}) = v_{\text{B}}$[5] [277]. The minimal cut picture also provides a simple interpretation of the saturation of entanglement for finite systems: while initially the minimal cut goes through space-time vertically (in the time direction), at late times it becomes increasingly favorable to move horizontally and end up at the closest spatial boundary.

Note that in this latter derivation of the minimal cut picture did not rely on starting from a partition function for the purity, and makes no reference to which particular Rényi entropy we consider. As a matter of fact one could run the same heuristic argument directly for the von Neumann entropy; in fact this is how the membrane picture was originally introduced in Ref. [277]. There, numerical evidence was provided that this 'hydrodynamic' picture for entanglement growth indeed holds, and $\mathcal{E}(v)$ was computed numerically for a particular time-independent chaotic Hamiltonian. This is in complete agreement with an earlier influential study, Ref. [269], which found that S_1 grows linearly in a chaotic Hamiltonian, despite transport being diffusive due to the lack of well-defined quasiparticles. Later, Ref. [578] noted that the same membrane picture can be derived from holographic calculations of entanglement, based on the Ryu-Takayanagi formula [579–581]; this derivation applies specifically for S_1. One would then in principle have a distinct line tension $\mathcal{E}_\alpha(v)$ for each Rényi index α, corresponding for example to the fact that these all have separate entanglement velocities as mentioned before. We indeed expect this to be the case in the random circuit model, or in other systems that have no extensive conserved quantities. However, as we shall show in Part II, this picture is modified drastically in the presence of conserved quantities, such as energy of particle number. For the von Neumann entropy, the above picture still holds for a homogenous initial state, while one

---

[5] One way to motivate this relation is by noting that the partition function $Z(x,t)$ for $x > 0$ is closely related to the right operator weight $R(x,t)$ encountered in Chapter 4. Both correspond to propagation of a domain wall-like object. The difference lies in the fact that in the definition of $R(x,t)$, the two domains are defined asymmetrically, which corresponds to replacing $|-\rangle$ with $q|-\rangle$ in the formulae. This gives $\rho_R(x,t) \sim q^x Z(x,t) = e^{s_{\text{eq}}(v - \mathcal{E}(v))t}$ (compare Eq. (4.14) with Eq. (5.12)). The two terms in the exponent are balanced when $\mathcal{E}(v) = v$, which corresponds to the position of the front; for all other v, we have $\mathcal{E}(v) > v$.

has to consider a generalization of it when encountering inhomogenous initial conditions; in this latter case the line tension will depend on the local, space-time dependent entropy density, and therefore couples to the transport of conserved quantities in a non-trivial way as we detail in Chapter 11. Even more strikingly, for Rényi indices $\alpha > 1$, the minimal cut picture breaks down in the presence of conservation laws, *even for homogenous initial states*. This will be the topic of Chapter 10.

5.3. Effect of noise on entanglement dynamics

As we saw above, the annealed average Rényi entropy shows a perfect linear growth, which is reproduced by the leading behavior of the quenched average (with speeds that remain close to each other even at $q = 2$). However, for any particular realization of the random circuit, there will be a noise term appearing in the dynamics of the bi-partite entropy, resulting in a profile for $S(x,t)$ that depends on space as well as time, even away from the boundaries. The effects of this noise in fact show up in the form of universal sub-leading correction in entanglement growth, and are also present in the spatio-temporal correlations of the evolving entanglement profile.

A simple way to motivate this result is in the entanglement membrane picture developed in the previous section. Taking the noise into account, the entanglement corresponds to the free energy of a polymer in a random environment. This is a problem that has been studied extensively [303, 573, 582, 583] and is well known to be described by the same KPZ equation that we encountered previously in a different context in Section 4.4. This suggests that in an appropriately coarse-grained limit, the equation of motion of $S(x,t)$ becomes

$$\partial_t S(x,t) = v_{\mathrm{E}} + \nu \partial_x^2 S(x,t) + \frac{\lambda}{2}(\partial_x S(x,t))^2 + \zeta(x,t). \tag{5.18}$$

As noted before in Section 4.4, there are various universal exponents that characterize the KPZ universality class. In particular, the surface 'height' grows as $\overline{S(x,t)} \sim v_{\mathrm{E}} t + Bt^{\beta}$ with exponent $\beta = 1/3$, and the fluctuations in the height of the circuit similarly scale as $\overline{S(x,t)^2} \sim t^{2\beta}$ (one can either think of this as the variance taken over realizations of the noisy dynamics at a fixed cut x, or, alternatively, as the variance taken over different cuts in the same realization). Moreover, there is another, distinct exponent, which describes the size of the transverse fluctuations in the size of the polymer, given by $\Delta x(t) \sim t^{1/z}$ with $z = 3/2$ (compare this with the case of a random walk, wherein $z = 2$). This defines a correlation length for the entanglement profile, which therefore obeys a scaling form

$$\overline{[S(x,t) - S(0,t)]^2} = r^{2\alpha} g(x/t^z). \tag{5.19}$$

Here, α is a third exponent (not to be confused with the Rényi index), related to the other two as $\alpha = z\beta = 1/2$. The $1/2$ exponent is consistent with the fact that on scales $x \ll t^z$, the surface resembles the trace of a simple random walk, while its KPZ nature becomes apparent on scales $x \approx t^z$. There are various ways of showing that the problem of entanglement growth in the random circuit is in the KPZ universality class, which we briefly review below. The KPZ scaling has also been observed numerically in a continuous-time noisy Heisenberg chain [566].

The mapping of the entanglement growth problem to the KPZ equation can be performed in various ways. One is to do the replica calculation for $\overline{S_2}$ outlined in the previous section. In this case the noise has been integrated out and is no longer explicitly present, but it appears in the form of interactions between different replicas (in the absence of such interactions, one would get $\overline{Z_2^k} = \left(\overline{Z_2}\right)^k$). This results in a problem of k domain walls with attractive interactions. In the large q limit, one can then show that the resulting stochastic process, after taking a continuum limit, is the same as the one found when performing a similar replica calculation for the free energy of a polymer in a random background potential [278, 584]; the latter is which is known to be in the KPZ universality class. One can in principle extend this calculation to Rényi indices $\alpha \neq 2$.

A more direct way to do the mapping is to write down the partition function $Z(x,t)$ explicitly, without the use of replicas, for a *single* realization of the circuit, as described in Ref. [260]. As outlined in the previous section, in principle one can write down the purity as $\langle \mathcal{F}_A | U \otimes U^* \otimes U \otimes U^* | \rho_0 \otimes \rho_0 \rangle$ for a particular circuit instance U. While, in the absence of the simplifications that come from averaging, this is a very complicated object, one can expand it systematically around the circuit-averaged result. To do this, one has to note that the Haar-average for a single gate is a projector on the four-copy Hilbert space (which follows directly from the defining property of the Haar measure). Denoting this projector as $P_{||}$, and its orthogonal complement by $P_\perp$, one can insert an identity of the form $P_{||} + P_\perp$ in front of every gate in the circuit. The result is a sum has exponential many terms (in the number of gates), which can be organized according to the number of $P_\perp$ insertions. The zeroth order term is exactly the Haar-average result we computed above, while there are terms with $N_\perp = 1, 2, 3, \dots$ insertions. This rewriting is useful when the size of these corrections decays rapidly with $N_\perp$, which can be shown to hold in the large q limit. One can also show, by direct calculation, that the insertion of a singe $P_\perp$ gives rise to a process wherein a domain wall stays at the same position (instead of always moving left or right, as in the Haar-averaged case), with a weight that depends on the local gate at that particular space-time position. One can interpret this as a randomly fluctuating potential for the domain wall, which directly corresponds to a lattice regularized version of a directed polymer in a random medium. We note here, that the same approach of expanding the partition function in orders of $N_\perp$ can be used to treat *deterministic* circuit models, and argue that their behavior can also be described by the entanglement membrane picture, with a line tension $\mathcal{E}$ that is renormalized by the $N_\perp \geq 1$ terms; see Ref. [260] for details.

To further develop some intuition on the KPZ dynamics of entanglement, it is useful to consider a modified circuit model that gives rise to a simple, exact random surface growth evolution for $S(x,t)$. Consider first the $q \to \infty$ limit of a 2-site gate, acting on sites $x, x+1$. In this case, the *concentration of measure* property of the Haar distribution ensures that random fluctuations disappear and the entanglement across the bond evolves as [276]

$$S(x,t+1) = \min(S(x-1,t), S(x+1.t)) + 1 \tag{5.20}$$

(in units of $\log q$). In the $q \to \infty$ limit this update rule is valid fo *all* Rényi entropies. Note, that the same rule is true, with probability 1, for S_0 (the so-called Hartley entropy) at any $q > 1$ [276].

For our brick-wall random circuit, this means that the randomness disappears when the $q \to \infty$ limit is taken and the dynamics becomes trivial, as we have already observed when considering the operator spreading problem in Section 4.2. This corresponds to a pathological limit, where $\mathcal{E}(v)$ becomes completely flat and the entropy production rate Γ develops non-analicities. However, one can fix these issues, while maintaining $q = \infty$, by modifying the structure of the circuit. A simple way to do this is to replace the regular brick-wall geometry of the circuit with a random geometry, for example by choosing a random bond with uniform probability in each step on which to apply a 2-site gate (for an illustration, see Fig. 7.1(b) below). This defines a random surface growth model for the entanglement, wherein the update rule Eq. (5.20) is applied on these randomly chosen bonds. This model is very similar to other random surface growth models, which are known to be in the KPZ universality class [573], and the expected scaling exponents can be easily confirmed by direct numerical simulation in this case. The line tension $\mathcal{E}$ also acquires an intuitive meaning in this model: it simply counts the number of bonds cut (per unit time) in a diagram of the circuit with random geometry. The entanglement is simply the minimal number of bonds cut by a curve with a fixed upper endpoint. We will consider a similar model when we discuss the coupling to diffusive transport in Chapter 11.

It is important to emphasize that while the same $1+1$ dimensional KPZ equation (and its associated universality class) appeared here and in Section 4.4, these two cases are physically unrelated. One describes entanglement growth in one dimension, while the other describes operator spreading in two dimensions. Moreover, while in the present case, the noise inherent in the KPZ description originates from the explicit randomness of the dynamics and is absent in deterministic systems, the noise that appeared in the operator spreading problem stems from quantum fluctuations and is expected to generalize to systems that are invariant under space-time translations.

6. Entanglement spectroscopy after a quench

As we saw above, there are at least two distinct velocity scales (and their associated time scales) that characterize the thermalization process from the standpoint of the scrambling of quantum information: the butterfly velocity v_{B} and the entanglement velocity v_{E} (which we now take to be the – appropriately normalized – growth rate of the von Neumann entropy). In this chapter we take a different perspective, and consider the fine structure of the entanglement for a finite subsystems in a one-dimensional chain. In particular, we argue that one can access the 'scrambling time' (defined as the time needed for the butterfly front to cross the subsystem) by considering the detailed statistics of entanglement eigenvalues. We connect these to Lieb-Robinson light cones, and arrive at an appealing analytical picture, wherein 'chaos' moves up throughout the entanglement spectrum, from small to large eigenvalues of the reduced density matrix. We corroborate this picture by numerical simulations, finding excellent agreement.

The focus of our study will be the full spectrum of the reduced density matrix (RDM) ρ_A of a subsystem A of size $l \gg 1$ in the middle of a chain of size $L \gg l$, concentrating on the intermediate-time regime leading up to thermalization. We will argue that the spectral correlations of ρ_A identify the timescales involved in thermalization. We quantify these correlations via the *entanglement spectrum*, i.e. the eigenvalues of the so-called entanglement Hamiltonian, $H_{\mathrm{ent}} \equiv -\ln \rho_A$. The entanglement spectrum was originally introduced in Ref. [78] as a powerful tool for characterizing ground states; more recently, it has been used in non-equilibrium settings [537, 585–592]. We continue in this vein and explore its post-quench dynamics. Assuming, as we do, that the system thermalizes, H_{ent} at long times should become approximately equivalent to the physical Hamiltonian restricted to the subsystem A, which characterizes the thermal Gibbs state. Since this is the Hamiltonian of thermalizing many-body system, and following the discussion in Section 2.1, it is expected to have level statistics described by random matrix theory (RMT), and in particular, level repulsion. In the following, we explore how this level repulsion develops over time.

After a quench, degrees of freedom near either end of A quickly become entangled with the outside world, but take longer to become entangled with those at the other end of A. We find that this is reflected in the spectrum of ρ_A: its large eigenvalues (i.e., the low-energy part of the entanglement spectrum) correspond to eigenstates that are localized on either end of the system, leading to Poissonian level statistics on short timescales, whereas small eigenvalues of ρ_A (i.e., high-energy part of the entanglement spectrum) couple and become essentially random on much shorter times. We examine the crossover between these two sectors of the entanglement spectrum with time, and link it to the spread of operators and entanglement across the subsystem.

6.1. Analytical argument

We begin by giving an analytical argument, describing how level repulsion develops in the entanglement spectrum during time evolution. We first focus on a simple system which has an *exact* light cone, and argue that this leads to a lack of level repulsion at short times at *all* entanglement energies. We then generalize this to arbitrary locally

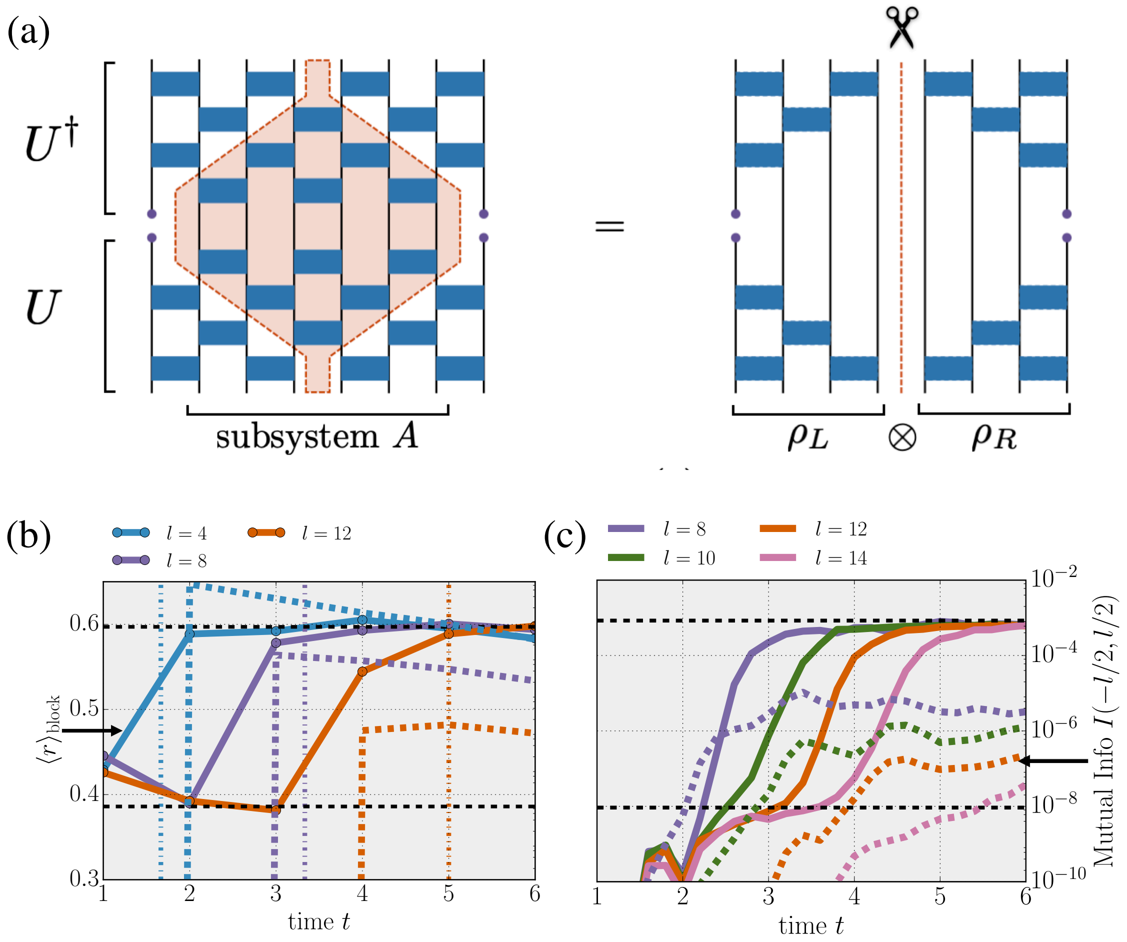

Figure 6.1.: (a) Representation of the reduced density matrix $\rho_{\bar{A}}$ after a few steps of time evolution under a local unitary circuit. Tracing over subsystem A causes unitaries to cancel inside the red shaded region. Consequently, $\rho_{\bar{A}}$ factors as a tensor product, and the entanglement spectrum (ES) decouples into left/right contributions. (b) ES dynamics for a random unitary circuit, showing the linear subsystem-size-dependent crossover from Poisson to RMT level statistics of the ES (solid) and mutual information between spins on either side of subsystem A (dashed); (c) shows similar data for Hamiltonian dynamics of the nonintegrable Ising model (6.7). In both cases the level statistics are computed for entanglement energies $E \leq 10$.

interacting chains, using a combination of Lieb-Robinson bounds and perturbation theory, and argue that level repulsion initially develops at high energies and moves down towards low energies, linearly in time. Eventually, the entire spectrum develops level repulsion, on a time scale set by the Lieb-Robinson speed, which we expect to be equivalent to the infinite temperature butterfly velocity[1].

---

[1] The only distinction between the two speeds is in the definition of norm used in evaluating the 'size' of the commutator of two space-time separated operators. The Lieb-Robinson theorem uses the operator norm, i.e. the largest eigenvalue of the modulus of the commutator. The infinite-temperature butterfly velocity, on the other hand, is defined in terms of the Frobenius norm. It is natural to expect that the two should be governed by the same velocity, although we are not aware of a systematic investigation of this question. Note also that recent results have shown that in long-range interacting systems, there can exist regimes where the butterfly velocity is well defined, while the Lieb-Robinson velocity is not [122].

6.1.1. Strict light cone

For clarity, let us first focus on the random unitary circuit (RUC) model introduced earlier. We begin with a pure product state at $t = 0$ and evolve it to time t by applying a depth-t RUC. The RDM ρ_A of subsystem A is obtained by constructing the density matrix of the whole system, $\rho = |\psi(t)\rangle\langle\psi(t)|$, and then tracing over degrees of freedom outside A. However, since the spectrum of ρ_A is identical (up to zero modes) to that of the RDM of the complement of A (denoted $\rho_{\bar{A}}$), we may instead perform the trace over the degrees of freedom *within* A, corresponding to the circuit on the LHS of Fig. 6.1(a) (where the purple dots denote the degrees of freedom in $\bar{A}$). At early times, after canceling conjugate pairs of gates U and $U^\dagger$, this circuit separates into a tensor product: $\rho_{\bar{A}} = \rho_L \otimes \rho_R$, where L/R denote regions to the left and right of A respectively. Therefore the eigenvalues of $\rho_{\bar{A}}$, and hence those of ρ_A, take the form $\lambda^L_\alpha \lambda^R_\beta$, and the entanglement spectrum is the sum of the spectra of independent random matrices, leading to Poisson level statistics. After an initial non-universal transient (from the singular entanglement spectrum of each edge in the initial state) this behavior is maintained up to time $l/2v_{\mathrm{LC}}$. Note that this discussion only uses the fact that the system has a strict light cone, with correlations exactly vanishing on the outside; none of it actually relies on the choice of gates in the circuit and it would directly carry over for example to the kicked Ising chain (4.22).

Consider now times shortly after $t = l/2v_{\mathrm{LC}}$: canceling pairs of conjugate unitaries no longer partitions the circuit into disjoint pieces, so the RDM no longer factorizes. However, the left and right blocks are initially only weakly entangled, since any entanglement between them is produced only by the few gates between the corners of the light-cone region and the bottom/top of the circuit. This idea can be formalized by considering the *mutual information* between the regions L and R that are left and right of A: $I(L, R) = S_L + S_R - S_{\bar{A}}$. At short times, when the RDM of $\bar{A}$ factorizes, $I(L, R) = 0$. At times only shortly after $l/2v_{\mathrm{LC}}$, the mutual information $I(L, R)$ becomes finite, but it is still much below its upper bound, $2v_{\mathrm{LC}}t - l$. This is due to the fact that in our two-level circuits, the "butterfly velocity" v_B that characterizes the spread of operators, is much slower than v_{LC}, so on times comparable to v_{LC}, only rare low-amplitude operators entangle the two halves of the subsystem, which is thus almost separable. As a consequence of this, level repulsion initially only appears at high energies in the spectrum of H_{ent}, as we discuss in the following subsection.

6.1.2. General case

We now generalize the above argument to the case of arbitrary short-range interacting chains, including Hamiltonian evolution (either time-independent or periodically driven). While generically there is no strict light cone, and therefore the RDM does not factorize into left and right parts, such a factorization still applies *approximately* at short enough times, as can be established using Lieb-Robinson bounds. We then argue that this approximate factorization implies a lack of level repulsion at low entanglement energies, but not at high energies. The edge separating the two regimes in the spectrum moves downwards in time, until the entire spectrum becomes RMT-like. This happens at times when the von Neumann entropy of the subsystem (i.e., the typical entanglement energy) is still far from its equilibrium value.

The starting point of our argument is to approximate the time evolution operator $U(t)$, using the results of Ref. [536], as

$$U = \tilde{U} + \delta U, \tag{6.1}$$

where $\tilde{U}$ is a unitary circuit made up by two layers of unitaries, each acting on vt contiguous spins for some constant v (i.e. each block has size linear in t) and the error term has a small operator norm $||\delta U|| = \epsilon$. Eq. (6.1) illustrated in Fig. 6.2. Note that this approximation is done in the spirit of Lieb-Robinson bounds: there is a smallest possible velocity (which we will identify with the Lieb-Robinson velocity) such that the approximation holds, but one can always increase the accuracy by making v larger and thus decreasing the error ϵ. For systems with a *strict* light cone speed, like the RUC discussed in the previous subsection, this approximation becomes exact ($\epsilon = 0$) for $v \geq v_{\mathrm{LC}}$.

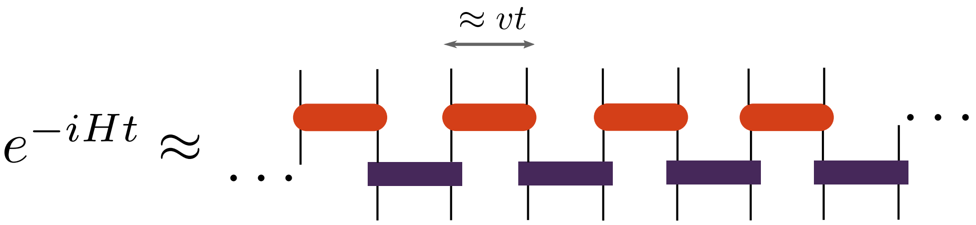

Figure 6.2.: Approximating the time evolution generated by a local Hamiltonian with a two-layer circuit of local unitaries, as described in Ref. [536].

Making use of the above approximation we can write the time evolved state after a quench as

$$|\psi(t)\rangle \equiv U(t)|\psi_0\rangle = |\tilde{\psi}\rangle + \epsilon|\phi\rangle, \tag{6.2}$$

where all the states are normalized to 1 (in principle $|\phi\rangle \equiv \delta U|\psi_0\rangle/\epsilon$ can have some norm ≤ 1 which we could pull out as a prefactor, but for simplicity we set it to 1). The corresponding reduced density matrix of a block A of size l is then

$$\rho_A = \tilde{\rho}_A + \epsilon\delta\rho_1 + \epsilon^2\delta\rho_2; \qquad \delta\rho_1 \equiv \mathrm{tr}_{\bar{A}}\left[|\tilde{\psi}\rangle\langle\phi| + h.c.\right]; \qquad \delta\rho_2 \equiv \mathrm{tr}_{\bar{A}}\left[|\phi\rangle\langle\phi|\right].$$

At times at which the light-cone for the approximate unitary $\tilde{U}$ has not yet penetrated to the middle of the subsystem A, the arguments made in the previous subsection apply, showing that the leading term factorizes as $\tilde{\rho}_A = \rho_L \otimes \rho_R$. The first-order correction, $\delta\rho_1$, involves the overlap of two essentially independent vectors on a subsystem of $L-l$ sites; we expect its matrix elements to be of size $\mathcal{O}(2^{(L-l)/2})$, going to zero in the thermodynamic limit. It is therefore safe to neglect this term in the following and focus on the effect of $\delta\rho_2$ on the spectrum of ρ_A.

Since $\tilde{\rho}_A$ factorizes, its eigenvalues are of the form $\tilde{\Lambda}_\alpha = \lambda_\alpha^L \lambda_\alpha^R$. Ref. [591] showed that the density of states for λ_L is given by $N(\lambda_L) \sim 1/\lambda_L$, and likewise for λ_R. Combining these, we get

$$N(\tilde{\Lambda}) = N(\lambda_L)N(\tilde{\Lambda}/\lambda_L) \sim \int d\lambda \frac{1}{\lambda}\frac{1}{\tilde{\Lambda}/\lambda} \sim \frac{1}{\tilde{\Lambda}}. \tag{6.3}$$

To leading order, the normalization of $N(\tilde{\Lambda})$ is set by the number of nonzero eigenvalues of the RDM, so the density of states at $\tilde{\Lambda}$ is

$$N(\tilde{\Lambda}) \approx 2^{2vt}/\tilde{\Lambda} + \delta(\tilde{\Lambda})(2^l - 2^{2vt}), \tag{6.4}$$

up to terms polynomial in t that we neglect [591].

Let us work in the eigenbasis of $\tilde{\rho}$ and consider the matrix elements of $\delta\rho_2$ in this basis. This takes the form $\langle\alpha|\phi\rangle\langle\phi|\beta\rangle$, where $|\alpha\rangle, |\beta\rangle$ are Schmidt states of $\tilde{\rho}$. We approximate $|\phi\rangle$ as a random state, so its overlap with any basis state is of magnitude $2^{-l/2}$, and consequently the typical matrix element of $\epsilon^2\delta\rho_2$ between two eigenstates of $\tilde{\rho}$ has magnitude $\epsilon^2/2^l$. To see if nearby energy levels hybridize, we compare this typical matrix element to the energy difference between two adjacent eigenstates of the RDM at energy $\tilde{\Lambda}$. Any zero modes in Eq. (6.4) will hybridize by this criterion. For the nonzero eigenvalues, hybridization occurs when $\tilde{\Lambda} \leq \epsilon^2 2^{2vt-l}$.

Turning now to the entanglement spectrum, we estimate that states with unperturbed energy $\tilde{E} \equiv -\ln \tilde{\Lambda}$ will develop random-matrix statistics when

$$\tilde{E} \geq (l - 2vt) \log 2 - 2 \log \epsilon. \tag{6.5}$$

To minimize the error while maintaining the separability of $\tilde{\rho}$ we choose $2vt = l$. Then the error of the approximation takes the form [536] $\epsilon \sim e^{(\kappa - \mu v)t} = e^{\kappa t - \mu l/2}$ for some constants κ, μ. Plugging in this expression, we find that

$$\tilde{E} \geq \mu l - 2\kappa t. \tag{6.6}$$

This suggests the crossover energy scale from Poisson to RMT statistics should drift linearly downwards in energy as a function of time, consistent with our numerical results presented below in Fig. 6.3.

The perturbative argument breaks down whhen ϵ becomes $\mathcal{O}(1)$, which is at times $t \approx l/2v_{\mathrm{LR}}$, where v_{LR} is the Lieb-Robinson speed. This speed should be close to the infinite temperature butterfly velocity, which characterizes operator spreading (see the footnote[1] above). As we have seen, these speeds (v_{LR} or v_B) are generically larger then the 'entanglement velocity' [256, 277], relevant for the growth of von Neumann entropy of a subsystem. Therefore there should exist an intermediate time scale where already the entire spectrum shows level repulsion, but the von Neumann entropy (which is the size of the typical entanglement energy) is still far below its equilibrium value. This is verified below in Fig. 6.4.

The above discussion clarifies that the energy-dependence of the level repulsion captures certain aspects of the shape of the wavefront of an evolving operator. For a sharp, δ-function like wavefront, i.e. $v_B = v_{\mathrm{LC}}$, all enetanglement energies would develop level repulson simultaneously. The fact that there is instead a delay between high and low energies corresponds to the fact that there are exponential tails outside of the wavefront. It remains to be seen whether other details of the front shape, such as its diffusive broadening can also be diagnosed from a more careful analysis of the entanglement spectrum.

Note that our entire discussion is independent of the initial state: it therefore provides a lower bound on the times needed for the entanglement spectrum to become RMT-like. We expect that this is the relevant time scale for e.g. a random product state, while the actual time scale can be different for other initial states. We provide an example of this in Section 11.3, where the time scales increase by a factor of 2 for certain initial states due to a conservation law.

6.2. Numerical Simulations

We now turn to the numerical confirmation of the analytical arguments outlined above. Our dynamical regime of interest consists of not too large subsystems at intermediate times. Since the relevant time evolution only generates modest entanglement, it is feasible to simulate it efficiently using matrix-product state (MPS) techniques. We simulate dynamics using the time-evolving block decimation (TEBD) algorithm [417] on systems of size $L = 60$, and compute the entanglement spectra of subsystems ranging in size from $l = 4$ to $l = 14$. Note that the limiting factor in going to larger l lies in the fact that, unlike in typical applications of MPS technology, we are interested in the entire entanglement spectrum rather than its low-energy sector. We have verified that L is sufficiently large that it does not produce any significant finite-size effects; all finite-size scaling is controlled by l. For RUCs, we draw two-site unitary gates at random from the Haar measure, and average results over 100 realizations. Here, the time t counts the number of full time steps

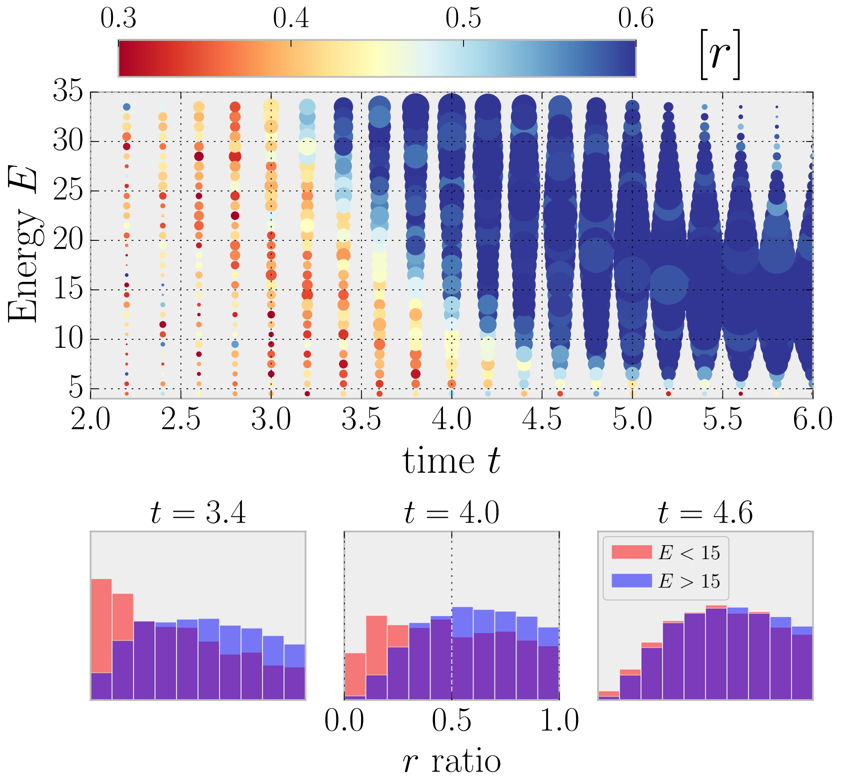

Figure 6.3.: Time evolution of energy-resolved ES level statistics for the non-integrable Ising model shows successively lower-energy states crossing over from Poisson to RMT behavior. The color of each dot corresponds to the r-ratio and the size to the number of states in the energy window of size $\Delta E = 1$. Bottom: histograms of low/high energy parts at representative early, intermediate, and late times.

in which each even and each odd bond is acted upon exactly once by a 2-site gate. For the Hamiltonian case, we study the Ising model in a tilted magnetic field,

$$H = \sum\nolimits_i J_i X_i X_{i+1} + h_i^z Z_i + h_i^x X_i, \tag{6.7}$$

where X, Y, Z are Pauli matrices at lattice site i. We chose $J_i = J = 1$ to be uniform and measure time in units of $1/J$. To avoid dealing with subtleties of thermalization within (translation) symmetry sectors, and to make the two edges of the block inequivalent, we add weak on-site disorder, taking $h^{z,x} \in [\overline{h^{z,x}} - \frac{W}{2}, \overline{h^{z,x}} + \frac{W}{2}]$ and choose their averages to be $\overline{h^z} = 0.9045$, $\overline{h^z} = 0.709$ and the disorder strength $W = 0.05$; the tilted-field Ising chain is known to be ergodic for this choice [269]. We average the results over 50 disorder realizations. For both models, we begin with an initial Néel state $|\Psi(t = 0)\rangle = |\uparrow\downarrow\uparrow\downarrow \ldots\rangle$.

6.2.1. Development of level repulsion

Our main results are presented in Fig. 6.1(b,c) and Fig. 6.3. Figure 6.1(b) shows the time evolution of the level statistics and the mutual information between the two edges for RUCs, while Fig. 6.1(c) shows the same data but for Hamiltonian dynamics (Eq. (6.7)); note the broad similarities between the two sets of data, despite the absence of the strict light cone in the latter.

To succinctly characterize the level statistics via a single parameter, we use the so called r-ratio, defined as the average over the entanglement spectrum and disorder realizations of

$r = \frac{\min(\delta_n, \delta_{n+1})}{\max(\delta_n, \delta_{n+1})}$, where $\delta_n = E_n - E_{n-1}$ is the spacing between consecutive entanglement energy levels [184]. The value r is a measure of level repulsion: for Poisson statistics, $r \approx 0.39$, whereas for random matrices in the Gaussian Unitary Ensemble[2], $r \approx 0.6$. As a proxy for the mutual information between the left and right halves of the outside world, we take the mutual information between two sites just outside the block A on the left/right, which we denote by $I(-l/2, l/2)$.

The level statistics shows a regime of Poisson behavior after the initial transient, but crosses over to RMT behavior at a time that scales linearly with the subsystem size l. Note that for the RUC, which has a strict light cone, the mutual information between the boundary spins remains exactly zero until this time, when it begins to grow. In both Fig. 6.1(b) and (c), we have cut off the high-energy part of the entanglement spectrum when computing r and include only eigenvalues $E < 10$. A more fine-grained picture of entanglement level statistics is provided by studying the time evolution of the energy-resolved r-ratio, takings its average within some small energy window $[E, E+\Delta E]$. For the non-integrable Ising model (Fig. 6.3), high entanglement energies exhibit RMT behavior at relatively short times compared to low ones, with the ‘edge’ between the two moving roughly linearly in time. Representative line-cuts of the data at $t = 3.4, 4.0, 4.6$ are shown in the bottom panel of Fig. 6.3, indicating the cross-over from Poisson to RMT statistics in the low-energy part. We note that the discrete time evolution of RUCs makes their entanglement spectral crossover abrupt and challenging to capture on the relatively modest system sizes considered here, though it is qualitatively similar.

6.2.2. RMT time scale vs. entanglement saturation

In the analytical part we argued that the time needed for the entanglement spectrum (including the lowest energies) to develop level repulsion is parametrically smaller than the time necessary for the block to become fully entangled with the rest of the system. In particular we argued that the first of these time scales should be controlled by the Lieb-Robinson / butterfly velocity, v_{B}, that gives the speed at which local operators spread, while the time for the entanglement of the block to saturate is set by the entanglement velocity, v_{E}, i.e. the rate at which the two sides of a bi-partition become entangled. As noted before, the inequality $v_{\mathrm{E}} < v_{\mathrm{B}}$ is expected on general grounds that [256, 277], so there should be a time window where the spectrum has already acquired RMT statistics but the amount of entanglement between the block and its environment still keeps increasing. Indeed, we find clear numerical evidence for this in the case of the tilted field Ising model.

We take the Hamiltonian as defined in Eq. (6.7) and simulate its dynamics at weak disorder ($W = 0.05$). We compute the average r ratio of the entanglement spectrum, taking only eigenvalues in the low energy part of the spectrum ($E < 10$), and compare their behavior with the von Neumann entropy of the block $S_A = -\mathrm{tr}(\rho_A \ln \rho_A)$. As expected, we find that at the times when the r ratio saturates, S_A is still far from its thermal value, as shown in Fig. 6.4. Moreover, we consider the velocity related to the development of level repulsion (taking the arrival of the front to be the time when the derivative of the r ratio as a function of t is the largest) and compare it to both the butterfly velocity as measured from the endpoint density ρ_R for an initial Z operator, and the entanglement velocity extracted from the slope of the von Neumann entropy at short times. We compute all three for different values of the transverse field h_z in a clean version of the model ($W = 0$), as shown in the right panel of Fig. 6.4. We find that while there

---

[2] This ensemble corresponds to random Hamiltonians without any additional symmetries, as opposed to the so-called Gaussian Orthogonal Ensemble, relevant for systems with time-reversal symmetri. Although the Hamiltonian (6.7) is real, the time-evolved state and hence its entanglement Hamiltonian are generically complex, so the unitary ensemble is the appropriate one here.

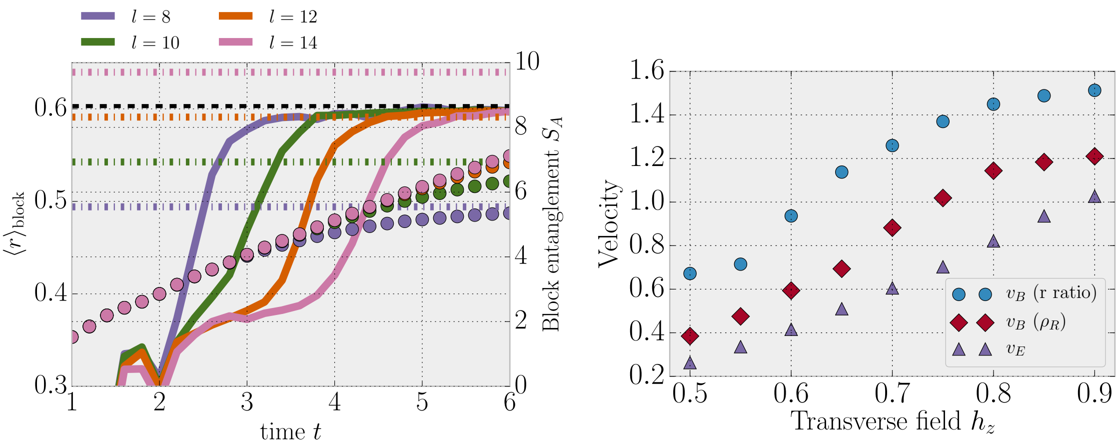

Figure 6.4.: Left: Average r ratio (solid lines) and von Neumann entropy (dots) for blocks of l sites in the tilted field Ising model with weak disorder ($W = 0.05$). The dash-dotted horizontal lines denote the thermal values of the von Neumann entropy S_A at infinite temperature, relevant for the initial Neel state we consider here. At the times when $\langle r \rangle$ saturates to its random matrix value (dashed horizontal line) the total entropy is still far from this thermal value and keeps increasing up to a parametrically longer time scale. Right: comparison of different velocity scales: butterfly velocity v_{B} as extracted from i) the right operator density ρ_R and ii) from the r ratio of the entanglement spectrum vs. the entanglement velocity v_{E}, shown as a function of the transverse field strength at zero disorder. Not only are the first too strictly larger than the latter, they follow a different curve as a function of h_z.

is a constant shift between the first two velocities that we cannot account for[3], they are both larger than v_{E}. Moreover, while the the first two appear to follow the same curve when plotted against h_z, the entanglement velocity has a qualitatively different shape, supporting our claim that the development of level repulsion has more to do with operator spreading than it does with the overall entanglement growth.

6.2.3. Floquet model

To complement the data for random circuits and the tilted field Ising model, we also present some further numerical results on the periodically driven version of the latter. This is the same model introduces previously in Eq. (4.22), except that we now allow for the possibility of spatial disorder in both the transverse and the longitudinal magnetic field (we also switch the roles of X and Z; this should not lead to significant changes):

$$U = e^{-\frac{T}{2}\sum_i h_i^z Z_i} e^{-\frac{T}{2}\sum_i X_i X_{i+1} + h_i^x X_i}. \tag{6.8}$$

The dynamics generated by repeated application of this unitary can be thought of as being half-way between the previous two models. On the one hand it is simply a (periodically) time-dependent version of the Ising chain described in Eq. (2) of the main text, and has no randomness in the time direction. On the other hand it has no conserved quantities and has a strict light cone velocity of 1 site per Floquet period, which makes it similar to the random circuit model (in fact, as noted before, it can be represented exactly as a circuit with the same geometry). The data presented here emphasizes the universality of our result, which apply to any spatially local time evolution in 1D.

---

[3] One possible explanation is that there is in fact a difference between the Lieb-Robinson and the butterfly speeds, and the r ratio measures the former.

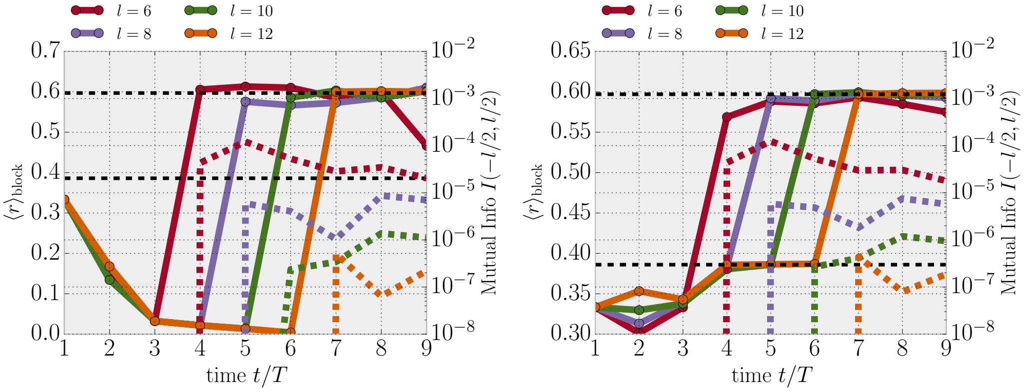

Figure 6.5.: Average r ratio for different block sizes l (solid lines) and mutual information between the two neighboring spins on the left/right side of the block (dashed lines) for the kicked Ising chain defined in Eq. (6.8) with no disorder ($W = 0$, left) and weak disorder ($W = 0.05$, right). The average longitudinal field is $\overline{h^z} = 0.7$ in both cases. In calculationg the r ratio, only eigenvalues of the rediced density matrix with magnitude larger then 10^{-10} are kept. At this cutoff we observe a sharp transition to random matrix statistics when the strict light cone reaches the middle of the block, at $t = l/2$.

We fix $T = 1.6$ and choose the on-site fields according to a box distribution of width W. We take the average longitudinal field to be $\overline{h^x} = 0.809$ and consider different values of the average transverse field $\overline{h^z}$. As we have seen in Section 4.3 for the clean case, changing the transverse field can be used to tune the butterfly velocity [1], between 0 at $h^z = 0$ and $v_{\text{B}} \approx v_{\text{LC}} = 1$ when $h^z \approx 0.9$, and we expect similar dependence on the average transverse field in the weakly disordered case as well. This allows us to explore how the time scales relevant for the block entanglement spectrum change with the butterfly speed and confirm that increasing the latter reduces the time needed to reach random matrix level statistics.

In Fig. 6.5 we show results both for the clean ($W = 0$) and weakly disordered ($W = 0.05$) chains, comparing level statistics and mutual information as we did for the other two models. By applying a weak cutoff (keeping eigenvalues of ρ_A with magnitude $\Lambda > 10^{-10}$) we observe a sharp transition in the level statistics at times $t = l/2$ when the sharp light cone reaches the middle of the block, similarly to the random circuit case. Before this

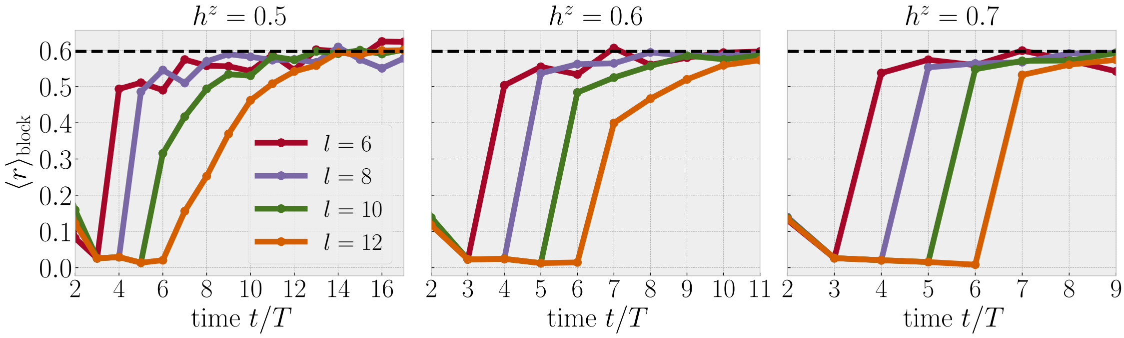

Figure 6.6.: Average r ratio for the clean kicked Ising chain ($W = 0$), keeping RDM eigenvalues $> 10^{-5}$, for different transverse fields $h^z = 0.5, 0.6, 0.7$ (left to right). While the average r ratio starts growing when the strict light cone crosses half the block, the transition is much slower for smaller values of h^z, which we attribute to the decrease in the butterfly velocity.

time the disordered model exhibits Poisson level statistics, also in agreement with our random circuit results. In the clean case, on the other hand, the average r ratio remains close to zero as long as the two edges are uncoupled. This is due to the fact that in this case the entanglement spectra at the two edges of the block are identical, leading to exact degeneracies in the block spectrum. The same behavior occurs also in the Hamiltonian case in the clean limit at short times.

In Fig. 6.6 we show results with a stronger cutoff, keeping only RDM eigenvalues with $\Lambda > 10^{-5}$, for different values of the transverse field h^z. We find that, while the transition in the average r ratio always starts at the same time, set by the light cone velocity, it becomes less and less sharp at smaller transverse fields, and the time it takes for $\langle r \rangle$ to reach the random matrix value increases. This can be interpreted by noting that time needed for the spectrum to become fully random matrix-like even at low energies should be controlled by the butterfly / Lieb-Robinson velocity, as detailed in subsection 6.1.2, which becomes smaller when h^z is decreased as observed previously in Section 4.3.

Part II.

Quantum Information Dynamics in Diffusive Systems

Overview of Part II

In Part II of the thesis, we shift our focus to systems that possess extensive conserved quantities. This includes Hamiltonian systems, where the energy is conserved, but also time-dependent systems with additional symmetries leading to a conservation of some quantity, such as particle number, or magnetization. While much of our discussion will focus on the latter case, as this is the setup where a generalization of our random circuit model is straightforward, we expect many of our main results to hold equally well for Hamiltonian dynamics. This expectation stems from the central role played by the *diffusion* of the conserved quantity in both cases, and we shall support it with numerical evidence below.

Chapter 7: Random circuits with diffusive transport

Chapter 7 serves as an introduction to this part of the thesis. After a brief discussion of the role of diffusion, in Section 7.1 we introduce a modified random circuit model which has a conserved particle number (or magnetization, depending on the interpretation), corresponding to a $U(1)$ symmetry. We also discuss two different ways of generalizing the model to a larger on-site Hilbert space, both of this will play a role in subsequent chapters. In Section 7.2 we show, via direct calculation, that these circuit models exhibit diffusive transport properties on all time scales.

Chapter 8: Operator spreading with diffusion

Chapter 8 contains our treatment of operator spreading and OTOCs in systems with diffusive transport. Most of our discussion relies on the aforementioned random circuit models. For these, we develop a way of calculating average OTOCs by mapping to a two-dimensional tensor network (which we refer to as a 'classical partition function' due to its formal similarities). This is described in subsection 8.1.1. The results of this calculation, presented in subsection 8.1.2, show that OTOCs involving the conserved density have qualitatively new features compared to the case without symmetries that we studied previously in Section 4.2. While diffusive broadening of the operator wavefront is still present, the shape of the OTOC behind the front changes drastically, with the appearance of an algebraically decaying 'hydrodynamic tail'. In subsection 8.1.3 we show numerically, that a similar power law decay is present in a deterministic system with the same symmetries.

Having described the new phenomenology associated with conservation laws, in Section 8.2 we set out the explain them from various perspectives. This includes considering operator spreading in the language previously developed in Section 4.1, but also developing a new description in terms of superoperators. Our discussion culminates in subsection 8.2.3, where we use a coarse-grained version of the circuit to derive the hydrodynamic tails, including the spatial dependence. This calculation leads to an intuitive picture, where the part of the evolving operator that is related to conserved densities acts as a continual source of newer and newer ballistic fronts. We sketch an alternative description of this 'coupler hydrodynamics' in Section 8.2.4, based on Ref. [549].

The existence of a conserved quantity allows us to consider OTOCs at a finite chemical potential (or temperature, in the Hamiltonian case). We do this in Section 8.3. First, we consider their fate at the longest times, deriving formulae for their saturation values as a function of the chemical potential μ in subsection 8.3.1. We then show that while at $\mu \lesssim 1$, the dynamics of OTOCs is largely unchanged from the $\mu = 0$ case (subsection 8.3.2), new interesting features arise for $\mu \gg 1$. In particular, we argue, via a perturbative expansion, that at early times the ballistic front of the OTOC is absent, only appearing at times long compared to the average spacing between particles. This is done in subsection 8.3.3.

Chapter 9: Dissipation-assisted operator evolution

Chapter 9 is something of a detour from our main theme, but closely related to the preceding chapter. Instead of considering the dynamics of quantum information, here we take a closer look of the diffusive transport properties of these systems, and use some of the intuition developed in Chapter 8 to devise a scheme for numerically calculating them. In particular, we rely on the aforementioned splitting of the operator into a conserved, diffusive part and a ballistically spreading part. We construct a non-unitary evolution, which dissipates the latter, while aiming to keep track of processes that contribute to the diffusion constant. This is similar in spirit to the so-called memory matrix formalism, which we review in Section 9.1. Our main new insight is that we can turn this into a concrete numerical scheme, constructed in the language of tensor networks, which we describe in Section 9.2. In Section 9.3 we test this method in two different strongly interacting systems in 1D and find that it provides a reliable way of estimating diffusion constants.

Chapter 10: Entanglement growth for global quenches

In Chapter 10 we turn to the issue of how diffusive transport coupled to entanglement growth. We show that its effects is particularly strong for Rényi entropies with index $\alpha > 1$, which become *sub-ballistic*, as we detail in Section 10.1. We show this both in the random circuit model and, using exact numerics on small systems, for a Hamiltonian system. We explain this finding analytically as being due to the effect of 'rare histories' in the wavefunction, where the conservation law prevents the growth of entanglement. Due to their rarity, these only show up in the few largest eigenvalues of the reduced density matrix, and are thus invisible to the von Neumann entropy, but dominate higher Rényis at long times. We also discuss this phenomenon from a complementary perspective, by constructing a generalization of the minimal polymer picture of entanglement, which we previously discussed in Section 5.2 for circuits without symmetries. We also consider long-time algebraic tails that appear near the saturation of the second Rényi entropy in Section 10.2, and the dynamics of the so-called *charge entropy* in Section 10.3.

Chapter 11: Entanglement growth for inhomogenous quenches

In Chapter 11 we consider a different type of coupling between transport and entanglement, which becomes relevant for initial states with large-scale inhomogeneities. We argue that the growth rate of entanglement (as measured by the von Neumann entropy in this case), becomes space-time dependent, proportional to the local entropy density, which itself is a function of the density of the conserved quantities in a 'fluid cell'. In Section 11.1 we support this intuition by considering the effects of a unitary gate in a coarse-grained version of the random circuit model. We then subsequently use it to motivate a random surface growth model of entanglement dynamics, and study the consequences of various initial states. The cleanest signature of diffusion arises for an initial domain wall state, in which case the behavior of the von Neumann entropy is entirely dominated by diffusion, limiting it to a $\sim \sqrt{t}$ growth. We further test these results by examining various spin-$1/2$ models in Section 11.2.

7. Random circuits with diffusive transport

While Haar random circuits provide a variety of exact results, many of which are expected to be generic for chaotic quantum dynamics, they also differ from Hamiltonian systems in certain crucial ways. One important such aspect, which we emphasized throughout the previous chapters, is the absence of any conservation laws, especially extensive ones that originate from continuous symmetries. As we detailed in Section 2.3, conserved quantities are expected to give rise to the slowest, 'hydrodynamic' modes of the system, and are therefore of utmost importance for understanding the equilibration process. This is quite different from the case we considered above, where the only relevant quantities were those related to the propagation of quantum information, such as OTOCs or Rényi entropies. This is the reason why these quantities were found to satisfy simple closed equations (in the random circuits, or more generally in some coarse-grained limit). Generically, as we shall argue below, one instead needs to take into account the coupling between these quantities and the usual hydrodynamic modes; these couplings can induce qualitative differences in their dynamics, which will be our topic in subsequent chapters.

Energy conservation itself is at odds with the idea of random circuit dynamics, which relies on time-dependent randomness to construct solvable models[1]. Instead, one can retain the random circuit setup, but constrain the circuit elements to enforce certain symmetries, such as a conservation of total particle number – this is the approach we take here. On the one hand, such a model is directly relevant for Floquet systems with the same (in this case, $U(1)$) symmetry. On the other hand, we expect this modified circuit to capture features of the dynamics that pertain also to Hamiltonian systems with energy conservation even *without* any additional symmetries. The reason for this is that as far as the aforementioned hydrodynamic modes are concerned, energy and particle conservation behave almost identically: at the longest time- and distance scales, their behavior is generically expected to be governed by a simple diffusion equation, for the reasons outlined in Section 2.3. As we shall see below, many of the qualitative features of operator spreading and entanglement growth can be understood directly from the existence of such a diffusive mode, independently of whether it describes the transport of energy, particle number or some other extensive conserved quantity. This allows us to use the particle-conserving random circuit model to motivate conjectures about generic Hamiltonian evolution, which can be tested numerically.

7.1. Local random circuit with charge conservation

To investigate the relationship between transport of conserved quantities and the dynamics of quantum information, as measured by OTOCs and entanglement entropies, we turn to a simple minimal model that possesses all the main ingredients: a time evolution which is unitary, local in space, and has a conserved charge that obeys diffusive dynamics. This will be a generalization of the model introduced in Chapter 3, with a similar local circuit structure, but with a modified distribution of the two-site gates to ensure that they all satisfy a $U(1)$ symmetry, which we can interpret as either the total particle number, or

---

[1] One can do calculations for a Hamiltonian drawn from one of the usual ensembles [593], but these have no notion of locality. There are also recent attempts at developing tools for computing dynamics for random *local* Hamiltonians [594, 595]. However, so far these have remained largely intractable.

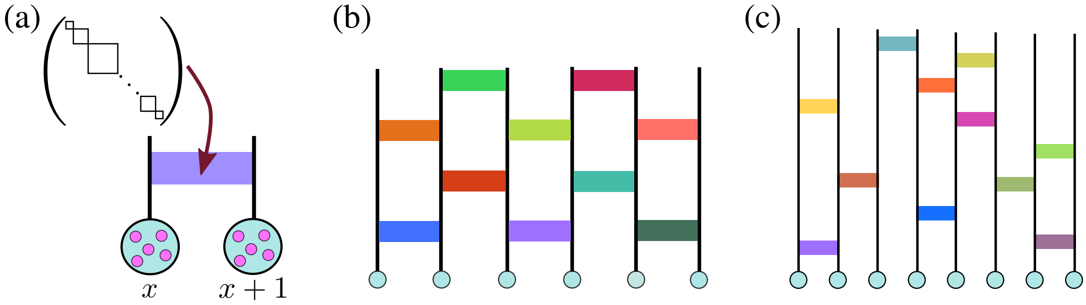

Figure 7.1.: Definition of the charge-conserving random circuit model. (a) A single unitary gate acts on two neighboring cells, each consisting of N qubits, such that the total occupancy of the two cells is conserved. The full time evolution is generated by applying the gates (b) in a regular 'brick wall' pattern or (c) at randomly chosen bonds.

as the total magnetization component in (for example) the z direction. We begin by describing the simplest example, with a $q = 2$ dimensional on-site Hilbert space, and then discuss various ways of generalizing it.

In the simplest case, which we will sometimes refer to as the spin-1/2 circuit, each site hosts a qubit (or spin) with two 'computational' basis states, denoted by $|0\rangle$ (or $|\uparrow\rangle$) and $|1\rangle$ (or $|\downarrow\rangle$). We refer to these as 'empty' and 'filled' - the total number of filled sites is going to be our conserved quantity and we will refer to it as 'charge'. The local charge on site r is measured by the operator $\hat{Q}_r = (1 - \hat{Z}_r)/2$. The qubits are arranged along a d dimensional cubic lattice – our discussion in the following will focus almost exclusively on the one-dimensional case, but we will mention possible generalizations of our results to higher d as we go. We evolve the system in discrete steps, by applying local unitary gates acting on pairs of neighboring sites. We will mostly consider the 'brick-wall' geometry shown in Fig. 7.1(b), but in Section 11.1 we will also consider circuits where the location of each gate is randomly chosen, resulting in the random geometry of Fig. 7.1(c). So far, this is the same as before; the difference arises in the definition of the local gates themselves. We choose these to be block-diagonal in the computational basis, with a two 1×1 blocks (corresponding to the states $|00\rangle$ and $|11\rangle$) and one 2×2 block (acting on the subspace spanned by $|01\rangle$ and $|10\rangle$) (see also Fig. 10.1(b) below). Each block is an independent Haar random unitary (in the case of the 1×1 blocks, just a random phase), but the block structure ensures that the total charge, $\sum_r \hat{Q}_r$ is conserved. As before, we denote averages over the different circuit realizations by $\overline{(\dots)}$.

As we shall see below, the circuit we just defined is not analitically solvable for the quantities we are interested in (OTOCs, Rényi entropies). However, it does lend itself to efficient numerically exact solutions, and investigating the properties of these will be one of our main goals in the following. Nevertheless, it is useful to also have an analytical handle on the problem. As mentioned previously, such a handle is often provided by taking a limit with a large local Hilbert space. There are a number of different ways in which the above model could be extended to include larger on-site Hilbert spaces. One way of achieving this is to consider coarse-grained 'super sites' (or 'cells', in analogy with the notion of a 'fluid cell' in hydrodynamics), each of which contains N different qubits, making its total Hilbert space 2^N dimensional. We can then define the filling of each individual qubit $\hat{Q}_{x,r}$, where $x = 1, \dots, L$ labels the cells in a 1D chain, while $r = 1, \dots, N$ labels the qubits within a cell. On each cell, there are $\eta_n \equiv \binom{N}{n}$ states with charge n. A two-site gate acting on $x, x+1$ would then be block diagonal with blocks labeled by $Q = \sum_r \hat{Q}_{x,r} + \hat{Q}_{x+1,r}$, with a block of size $d_Q = \binom{2N}{Q}$ in the charge Q sector (indicated in Fig. 7.1(a)), each block a different, independently chosen Haar random unitary of size $d_Q \times d_Q$. When $N = 1$

there is only a single qubit on each site and this model reduces to the one defined in the previous paragraph.

While this model is physically motivated, in the sense that we can think of the super-sites as simply a form of coarse-graining the system, and it has its uses as we see below, it remains somewhat complicated even in the large N limit. The reason for this is that, while most of the blocks of a two-site gate become very large in this limit, not all of them do: for example a pair of completely empty cells defines a one-dimensional Hilbert space for any N. At the other end of the spectrum, blocks corresponding to a pair of half-filled sites have a Hilbert space whose dimension grows exponentially with N. In principle, one would need to take into account all the blocks with these vastly different sizes. In certain cases, one can argue that the typical, large blocks are more relevant, and we will discuss calculations that use this intuition later in subsection 8.2.3 and Section 11.1. Nevertheless, it is useful to define an alternative model where *all* blocks can be made large simultaneously. This can be done rather easily, by introducing an auxiliary q-dimensional qudit on each site. This would lead to local basis states $|0,\alpha\rangle$ and $|1,\alpha\rangle$, with $\alpha = 1,\ldots,q$, indicating a Hilbert space $\mathbb{C}^2 \otimes \mathbb{C}^q$. The key point is that the qudits are *not* conserved. A two-site gate has the same block structure as in the spin-1/2 circuit, with four blocks only, labeled by the total charge, but now the blocks with charge $0,1,2$ have sizes $q^2 \times q^2$, $2q^2 \times 2q^2$ and $q^2 \times q^2$ respectively; the spin-1/2 model is recovered at $q = 1$. Therefore, as $q \to \infty$, all blocks become similarly large, which simplifies various Haar averaging formulae to a large extent. We shall rely on such a limit in Section 10.1.3. However, while this model is computationally more tractable than the coarse-grained 'large-N' version of the model, it comes at the expense of introducing non-conserved degrees of freedom, which makes the interpretation of certain results more difficult.

It is worth summarizing here the approach we take in the following chapters, and the advantages of using random circuit models. We will be interested in calculating the same quantities, operator weights, OTOCs and entanglement entropies, as before, for these $U(1)$-symmetric circuits, to see how the symmetry, and its associated diffusive transport, affect them. A key point is that for any of the models defined above, after circuit-averaging, we can map the calculation of the quantities of interest to an effective model that takes the form of a 'classical' partition function in one higher dimension; this mapping is done in a way similar to the one outlined in Section 5.2 and we will describe it in detail for the spin-1/2 charge-conserving circuit below in Section 8.1.1. The resulting effective models, unlike the one in Section 5.2 are generically not analytically solvable; nonetheless, they can be simulated numerically for much longer times than the original quantum problem[2]. These simulations (focusing on the spin-1/2 circuit) will form the backbone of our results below. We will complement these with analytical calculations, taken in the large local Hilbert space limit of one of the models defined above (i.e., either large N or large q). These will provide us with simplified descriptions that help explain some of the main features of our results. Finally, we will perform direct numerical calculations in *deterministic* models – both $U(1)$-symmetric Floquet systems and Hamiltonians with no additional symmetry – to support the universality of the main features uncovered in our random circuit studies.

---

[2] Let us mention here, that even when there is no direct computational advantage (e.g., in calculations of the number entropy in Section 10.3), by averaging over random time evolutions, one might be able to get access to the relevant universal behavior more easily then in any specific microscopic model. For example, as we will show shortly, the random circuit shows diffusion of conserved quantities at all timescales, without the early-time transients that would typically show up in a deterministic system.

7.2. Charge diffusion in the random circuit model

Before attacking the problem of OTOCs and entanglement, we begin our study of the charge-conserving random circuit by showing rigorously that the density of conserved charge diffuses in this system when averaged over different realizations of the circuit; in this sense, our circuit model mimics the expected generic behavior in the high temperature regime of generic quantum systems [279, 285, 553, 554], as we discussed in Section 2.3. We show this by considering directly the time evolution of the local charge operator $\hat{Q}_r$ in the Heisenberg picture, from which results on expectation values or dynamical correlations follow immediately.

To understand the dynamics of $\hat{Q}_r$, let us first understand how a single two-site gate, acting on sites r and $r+1$, evolves a generic operator $\hat{O}$ acting on the same sites. After applying a single two-site random charge-conserving gate on these two sites the operator becomes, on average (see also App. B.1)

$$\overline{\hat{O}(\Delta\tau)} = \overline{\sum_{Q,Q'} \hat{P}_Q U_Q \hat{P}_Q \hat{O} \hat{P}_{Q'} U^\dagger_{Q'} \hat{P}_{Q'}} = \sum_Q \frac{1}{d_Q} \hat{P}_Q \mathrm{tr}\left(\hat{O}\hat{P}_Q\right), \tag{7.1}$$

where $\hat{P}_Q$ projects onto the sector of the two site Hilbert space with $\hat{Q} = Q$ and we used the fact that U decomposes into blocks U_Q, each of which is Haar random. We use $\Delta\tau$ as shorthand for time evolution with a single layer of the random circuit. The diffusion of charge density follows from this algebraic result, but a more elementary argument goes as follows. Note that $\overline{\hat{Q}(\Delta\tau)} = \hat{Q}$ because the Haar ensemble commutes with the total charge on two sites. On the other hand, the ensemble of two-sites gates is invariant under multiplication by the operator swapping sites $r, r+1$, so $\overline{\hat{Q}_r(\Delta\tau)} = \overline{\hat{Q}_{r+1}(\Delta\tau)}$. This allows us to write

$$\overline{\hat{Q}_r\left(\Delta\tau\right)} = \frac{1}{2}\left(\hat{Q}_r + \hat{Q}_{r+1}\right). \tag{7.2}$$

Let us iterate the above formula for a series of two-site gates arranged in the regular gate geometry shown in Fig. 7.1(b). The local charge operator performs a random walk, such that at each application of a two-site gate it ends up on either of the two sites with equal probabilities. It is readily verified that after an even number $2t$ layers of the circuit it becomes

$$\overline{\hat{Q}_r(t)} = \frac{1}{2^{2t}} \sum_{k=0}^{2t-1} \binom{2t-1}{k} \left(\hat{Q}_{2j-2t+2k} + \hat{Q}_{2j+1-2t+2k}\right), \tag{7.3}$$

where $j = \left\lfloor \frac{r+1}{2} \right\rfloor$. At large times, the right hand side behaves like an unbiased diffusion kernel. Note that summing the equation over all r gives $\hat{Q}(t) = \hat{Q}(0)$, which is the global conservation law.

An approximate continuum formulation of the above discrete operator equation is

$$\partial_t \overline{\hat{Q}}(x,t) = D_Q \partial_x^2 \overline{\hat{Q}}(x,t), \tag{7.4}$$

where D_Q is the charge diffusion constant, independent of q[3]. Hence, on average, the local charge density obeys diffusive dynamics. In this sense our random circuit can be thought of as a toy model for a many-body system in the regime of incoherent, diffusive transport. Such behavior is expected also in clean systems at times longer than the coherence time of charged quasi-particle excitations [285, 553, 554] (which can be very short, for example

---

[3] This is in contrast with the diffusion of the operator wavefront discussed in Section 4.2, where the diffusion constant was found to be a decreasing function of the local Hilbert space dimension q. We emphasize that the diffusive broadening of the operator front is physically distinct from the diffusion of conserved charge discussed in this section.

at high temperatures [249]), or in systems that do not possess well defined quasi-particles at all [596]. Note that in our case the diffusion of charge appears directly at the level of operators, without having to refer to any particular state, indicating incoherent charge transport over all time scales. This is consistent with the behavior of the single-particle Green's function, $\langle \hat{\sigma}_0^-(t)\hat{\sigma}_r^+ \rangle$, where $\hat{\sigma}_r^+$ is the operator creating a single charge on site r. Applying formula Eq. (7.1) shows that this Green's function vanishes on average after only a single time step, independently of the state chosen, which is another way of saying that there is no coherent charge transport.

This last point merits a few more words. The simple, exactly solvable evolution here is a consequence of averaging over all random circuit realizations. In the Haar random circuit introduced in Chapter 4, this averaging would make the time-evolved operator completely vanish on average. This is not consistent with the conservation law, hence the non-trivial dynamics in the present case; nonetheless, all more complicated processes, when the operator grows to some larger, multi-site operator, average out due to random phases, resulting in the simple random walk process for the operator. This is quite different from the case of deterministic evolution, or even a single realization of the circuit, where the diffusive behavior only manifests once we consider either expectation values or equilibrium charge-charge correlations, as discussed in Section 2.3. Physically, this is related to the fact that the diffusion in the circuit case originates from the inherent noise of the random unitary dynamics, rather than from interactions as in a deterministic model. Consequently, we are able to determine the diffusion constant almost trivially, by just looking at the 'single-particle' process taking place in the subspace of one-site operators. In a deterministic system, on the other hand, diffusive dissipative transport and spreading to larger operators are inseparable phenomena, and in order to determine the diffusion constant, one necessarily has to take into account processes where the charge density evolves into multi-site operators. We will return to this issue in Chapter 9.

8. Operator spreading with diffusion

In this chapter, we return to the question of operator spreading, previously considered in Chapter 4, and discuss how it is affected by symmetries. As we shall see, the main features uncovered above, encapsulated in the biased diffusion equation, remain valid. However, the conservation law also leads to new universal features, most notably the slow, 'hydrodynamic' decay of operator weights and OTOCs. We provide an understanding of these, starting from the diffusive nature of transport. Furthermore, we discuss the effects of changing the chemical potential.

In our $U(1)$-symmetric setup, we define the out-of-time-ordered correlator between operators $\hat{V}$ and $\hat{W}$ as

$$\mathcal{C}_{\mu}^{WV}(t) = \frac{1}{2}\mathrm{tr}\left(\hat{\rho}_{\mu}\left[\hat{V}(t),\hat{W}\right]^{\dagger}\left[\hat{V}(t),\hat{W}\right]\right), \tag{8.1}$$

where $\hat{\rho}_{\mu} = e^{-\mu\hat{Q}}/\mathrm{tr}\left(e^{-\mu\hat{Q}}\right)$ is a Gibbs state characterized by its chemical potential μ (which sets the average filling fraction). $\hat{\rho}_{\mu}$ accounts for the fact that, unlike the Haar random circuit of Part I, the present model can equilibrate to different states, depending on the expectation value of the total charge in the initial state. This allows for richer physics in the OTOC, which can now have a non-trivial dependence on μ, similar to the Hamiltonian case, where the OTOC can have interesting temperature-dependence [239, 597]. While we focus on the 'infinite temperature' ($\mu = 0$) case for the most part, we will return to the question of the dependence of $\mathcal{C}$ on μ later in Section 8.3

By expanding the commutators we get

$$\mathcal{C}_{\mu}^{WV}(t) = \frac{1}{2}\left(\langle\hat{W}^{\dagger}\hat{V}^{\dagger}(t)\hat{V}(t)\hat{W}\rangle_{\mu} + \langle\hat{V}^{\dagger}(t)\hat{W}^{\dagger}\hat{W}\hat{V}(t)\rangle_{\mu}\right) - -\mathrm{Re}\langle\hat{V}^{\dagger}(t)\hat{W}^{\dagger}\hat{V}(t)\hat{W}\rangle_{\mu}.$$

We will refer to the last term as the out-of-time-ordered part of the OTOC and to the first two terms as its time-ordered part. The interesting physics of the OTOC are captured by the out-of-time-ordered part[1], which we denote

$$\mathcal{F}_{\mu}^{VW}(t) \equiv \mathrm{Re}\langle\hat{V}^{\dagger}(t)\hat{W}^{\dagger}\hat{V}(t)\hat{W}\rangle_{\mu}. \tag{8.2}$$

In the following we will mostly focus on this quantity (a notable exception in subsection 8.3.1 where we discuss the long-time limit of the full OTOC, which is mostly dominated by its time-ordered part). Unless stated otherwise, we assume that $\hat{V}$ and $\hat{W}$ both have trace zero.

It will be convenient to consider operators $\hat{V}, \hat{W}$ with particular charges λ_V, λ_W under the adjoint action of the symmetry, i.e., $[\hat{Q}, \hat{V}] = \lambda_V \hat{V}$. For example, in the $q = 2$ case which we focus on, the one-site operators $\hat{\sigma}^{+}, \hat{\sigma}^{-}, \hat{Z}$ have charges $+1, -1, 0$, respectively (in the following, $\hat{Z}_r$ denotes the Pauli z operator on site r, while the operators $\hat{\sigma}_r^{\pm}$ increase/decrease the local charge by one). As we show below, the behavior of the OTOC can depend strongly on the charges λ_V and λ_W. It is particularly interesting to consider operators with charge $\lambda_V = 0$, which can have a non-vanishing overlap with the conserved

---

[1] In fact, for $q = 2$, even when the time-ordered part is non-trivial (i.e., time dependent), it can be computed exactly on average using Eq. (7.3)

quantity, $\mathrm{tr}(\hat{Q}\hat{V}) \neq 0$. As we argue below, for such operators the diffusion of charge implies a) slow relaxation of the OTOCs and b) non-trivial long-time saturation values at finite μ (see subections 8.1.2, 8.2 and 8.3.1 in particular)[2].

We can reduce the number of distinct OTOCs we need to consider, by noting that there are certain relations between them. For example, we note that

$$\mathcal{F}_\mu^{V^\dagger W^\dagger}(t) = e^{-\mu(\lambda_V+\lambda_W)}\mathcal{F}_\mu^{WV}(t)$$

holds on general grounds, decreasing the number of independent OTOCs. Moreover, in the $q = 2$ case we discuss below, we can also make use of the relation

$$\mathcal{F}_\mu^{\sigma_0^+\sigma_r^-}(t) = e^{-\mu}\mathcal{F}_\mu^{\sigma_0^+\sigma_r^+}(t). \tag{8.3}$$

Therefore we will focus solely on the OTOCs between operators $\hat{Z}\hat{Z}$, $\hat{Z}\hat{\sigma}^+$ and $\hat{\sigma}^+\hat{\sigma}^+$. Note that we can relate $\hat{Z}_r$ to the local charge density $\hat{Q}_r$ as

$$\hat{Z}_r(t) = \hat{\mathbb{1}}_r - 2\hat{Q}_r(t), \tag{8.4}$$

which means that any correlator of the form (8.2) has the same behavior if we replace all occurances of $\hat{Z}_r$ with $\hat{Q}_r$, up to some unimportant contributions that are either time-independent or decay diffusively, as in Eq. (7.3).

8.1. Hydrodynamic tails in the OTOC

In this section, we focus on OTOCs at zero chemical potential. We begin by showing that computing the average value of the OTOC in our random circuit problem is equivalent to evaluating a 'classical' partition function[3]. This allows us to compute the OTOC to significantly longer times than those available to direct numerical calculations. We find that at $\mu = 0$, all OTOCs spread in a ballistic wavefront, wherein the width of the front broadens in time, similarly to the case of random circuits without symmetries. The main new feature is that OTOCs involving the conserved operator $\hat{Z}$ exhibit a slow decay behind their wave front, which we confirm also for a non-random spin chain. We explain this behavior below, in Section 8.2, by building on the results of Section 7.2 and detailing the different ways in which the diffusion of charge effects the dynamics of OTOCs. We give further support to our numerical results in Section 8.2.3 by considering a modified version of the random circuit where we are able to derive analytical predictions for the dynamics of different OTOCs. We return to the question of their behavior at finite chemical potential in Section 8.3.

8.1.1. Mapping from random circuit to a classical partition function

We now outline how to compute OTOCs in the charge-conserving random circuit problem. The properties of the Haar distribution allow us to evaluate the average effect of a single 2-site gate on the OTOC exactly. As we show below, applying this averaging procedure to all the gates in the circuit transforms the problem of computing the average OTOC to the evaluation of a particular classical partition function, similar to the calculation discussed for random circuits without symmetries in Section 5.2. While the classical model we obtain

---

[2] We expect that more generally these conclusions hold for any traceless operator $\hat{V}$ with a finite support that satisfies $\mathrm{tr}(\hat{Q}^m\hat{V}) \neq 0$ for some positive integer m.

[3] We put the word 'classical' in quotation marks, to indicate that while the effective problem we derive has the same structure as a classical partition function, it can have negative weights for certain configurations, as we shall see. Nevertheless, for simplicity, we will just refer to this as a classical partition function in the following.

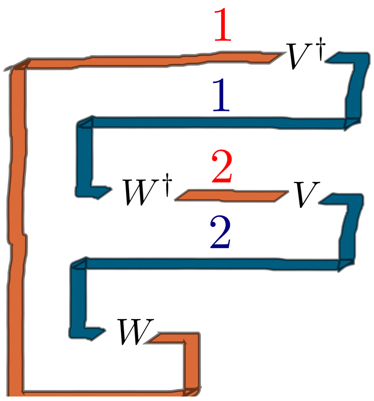

Figure 8.1.: Representation of the OTOC $\langle \hat{V}^\dagger(t)\hat{W}^\dagger\hat{V}(t)\hat{W}\rangle$, as a 'path integral' involving four layers. Each layer corresponds to one of the unitary time evolution operators (blue: U; red: $U^\dagger$) appearing in the correlator. These unitaries are given by a realization of the random circuit, and averaging over them gives rise to interactions between different layers.

has much more structure than the non-symmetric case, and does not allow for an exact closed form solution, it serves as the basis of both numerical calculations and analytical approximations which we present in the rest of this chapter, as well as in Chapter 10.

We begin by observing that one can rewrite the $\mu = 0$ OTOC in the following form (the generalization to finite μ is straightforward, and we shall discuss it later in Section 8.3)

$$\mathcal{F}^{VW}_{\mu=0}(t) \propto U^*_{\beta\alpha}V^*_{\gamma\beta}U_{\gamma\delta}W^*_{\mu\delta}U^*_{\nu\mu}V_{\nu\lambda}U_{\lambda\eta}W_{\eta\alpha} = V^*_{\gamma\beta}V_{\nu\lambda}(U^*\otimes U\otimes U^*\otimes U)_{(\beta\gamma\nu\lambda)(\alpha\delta\mu\eta)}W^*_{\mu\delta}W_{\eta\alpha}, \tag{8.5}$$

where U is the time evolution operator generated by the circuit up to some time t. Therefore, the central quantity one needs to compute in order to obtain the average OTOC is $\overline{U^*\otimes U\otimes U^*\otimes U}$. This is an operator acting on four copies of the original Hilbert space. We can think of this construction as a generalization of the Keldysh contour [245], involving four 'layers', as illustrated in Fig. 8.1. Each of the four operators appearing in the definition of the OTOC connects two of these layers.

Since every gate in the random circuit is independently chosen, we can evaluate the Haar-average for all of the gates (and all of their blocks) individually. For each gate, the Haar averaging results in a four-leg tensor with two incoming and two outgoing legs, one for both of the sites the gate acts on. One leg of this averaged tensor corresponds to four copies of the original Hilbert space. For our $q = 2$ case this would mean in principle 16 states per site of the form $|\alpha\beta\gamma\delta\rangle$ for $\alpha, \beta, \gamma, \delta = 0, 1$. As we argue below, only 6 of these 16 appear in the averaged circuit, and therefore the average OTOC can be calculated in terms of an effective description involving 6 states per site.

In particular, as we show in App. B.1, the average for *a single two-site gate* takes the form

$$\begin{aligned}\overline{U^*\otimes U\otimes U^*\otimes U} = &\sum_{s=\pm}\sum_{Q_1\neq Q_2}\frac{1}{d_{Q_1}d_{Q_2}}|\mathcal{I}^s_{Q_1Q_2}\rangle\langle\mathcal{I}^s_{Q_1Q_2}| \\ &+\sum_{s=\pm}\sum_{Q}\frac{1}{d_Q^2-1}\left[|\mathcal{I}^s_{QQ}\rangle\langle\mathcal{I}^s_{QQ}| - \frac{1}{d_Q}|\mathcal{I}^s_{QQ}\rangle\langle\mathcal{I}^{-s}_{QQ}|\right],\end{aligned} \tag{8.6}$$

where $|\mathcal{I}^\pm_{Q_1Q_2}\rangle$ are states from four copies of the two-site Hilbert space, defined as

$$|\mathcal{I}^+_{Q_1Q_2}\rangle \equiv \sum_{\substack{\alpha\in\mathcal{H}_{Q_1}\\ \beta\in\mathcal{H}_{Q_2}}}|\alpha\alpha\beta\beta\rangle; \qquad |\mathcal{I}^-_{Q_1Q_2}\rangle \equiv \sum_{\substack{\alpha\in\mathcal{H}_{Q_1}\\ \beta\in\mathcal{H}_{Q_2}}}|\alpha\beta\beta\alpha\rangle. \tag{8.7}$$

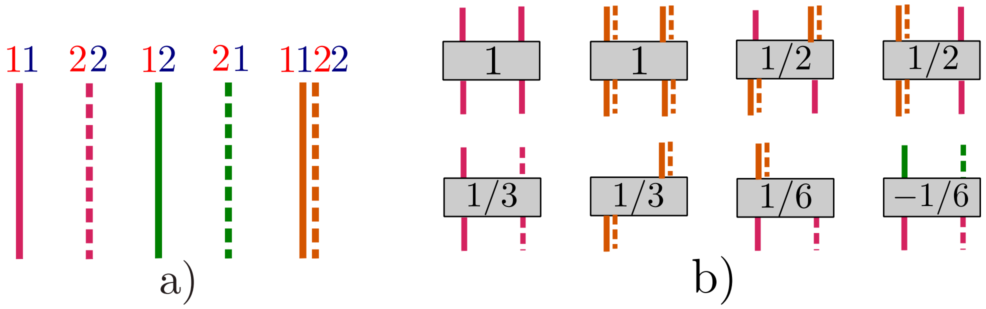

Figure 8.2.: Interpretation of Eq. (8.6) in terms of local states. a) Notation of the five different 'particle types' that can occur: the first four correspond to exactly two of the four layers (shown in Fig. 8.1) being occupied by a charge, while the last one is a bound state, either formed by the first two or the second two particle types. The empty state is not denoted. b) Some possible one- and two-particle processes generated by averaging over a single two-site gate.

$\mathcal{H}_Q$ here is the sector of the two-site Hilbert space with total charge Q, which has dimension d_Q.

The states $|\mathcal{I}^{\pm}_{Q_1 Q_2}\rangle$ cannot be written as products of states on (four copies of) the individual sites[4]. Nevertheless, as we detail in App. B.1, they can all be written in terms of the following six states, living on four copies of a *single site:* $|0000\rangle$, $|1100\rangle$, $|0011\rangle$, $|1001\rangle$, $|0110\rangle$, and $|1111\rangle$ (e.g., $|\mathcal{I}^{-}_{12}\rangle = |1111\rangle_1 |0110\rangle_2 + |0110\rangle_1 |1111\rangle_2$). The first of these is an 'empty' state, wherein all four layers are unoccupied at a given site. We will refer to the states with exactly two layers occupied as having a single 'particle' on a given site, which can belong to four different species, as illustrated in Fig. 8.2 a). The last state then can be thought of as a site being occupied by two particles. In terms of these six states, Eq. (8.6) defines a four-leg tensor that maps each of the 36 possible states on the two sites to a linear combination of the same 36 states with some particular (real, but possibly negative) coefficients. Some of these possible processes are shown in Fig. 8.2 b). All other non-zero coefficients can be obtained from these by swapping the two sites (either on the bottom or the top of the gate) or permuting the different particle types.

To compute the full time evolution we need to contract the four-leg tensors, defined above, according to the geometry of the circuit seen in Fig. 3.1. Thus every layer of the random circuit acts as a transfer matrix, evolving a configuration of particles (in the sense defined above) to a linear combination of different configurations. Finally, in the first and last layers, we need to contract the remaining legs with those of the operators $\hat{V}$ and $\hat{W}$ appearing in the OTOC formula (8.5). We can write the result as the matrix element

$$\overline{\mathcal{F}^{VW}_{\mu=0}}(t) \propto \langle \mathcal{P}_V | \overline{U^* \otimes U \otimes U^* \otimes U} | \mathcal{D}_W \rangle, \tag{8.8}$$

where $|\mathcal{P}_V\rangle$ and $|\mathcal{D}_W\rangle$ are states in the four-copy Hilbert space, defined by $\langle \alpha\beta\gamma\delta | \mathcal{P}_V \rangle = V_{\beta\alpha} V^*_{\gamma\delta}$ and $\langle \alpha\beta\gamma\delta | \mathcal{D}_W \rangle = W_{\delta\alpha} W^*_{\gamma\beta}$ (we give an interpretation of these quantities in terms of superoperators in Section 8.2.2). In this formula, U is the full unitary circuit up to time t. Eq. (8.8), together with Eq. (8.6), can be interpreted as a classical partition function on a two-dimensional lattice, where every site has six possible states. The gates in one layer of the circuit form a transfer matrix of this classical spin problem while the operators $\hat{V}$ and $\hat{W}$ in the definition of the OTOC appear through the boundary conditions, at times 0 and t, respectively. While we are not able to evaluate this partition function exactly (unlike the case with no symmetries), it allows for efficient numerical computations, much

---

[4] Contrast this with the case without symmetries in Eq. (5.9), where the sums go over all states in the two-site Hilbert space and thus factorize [253].

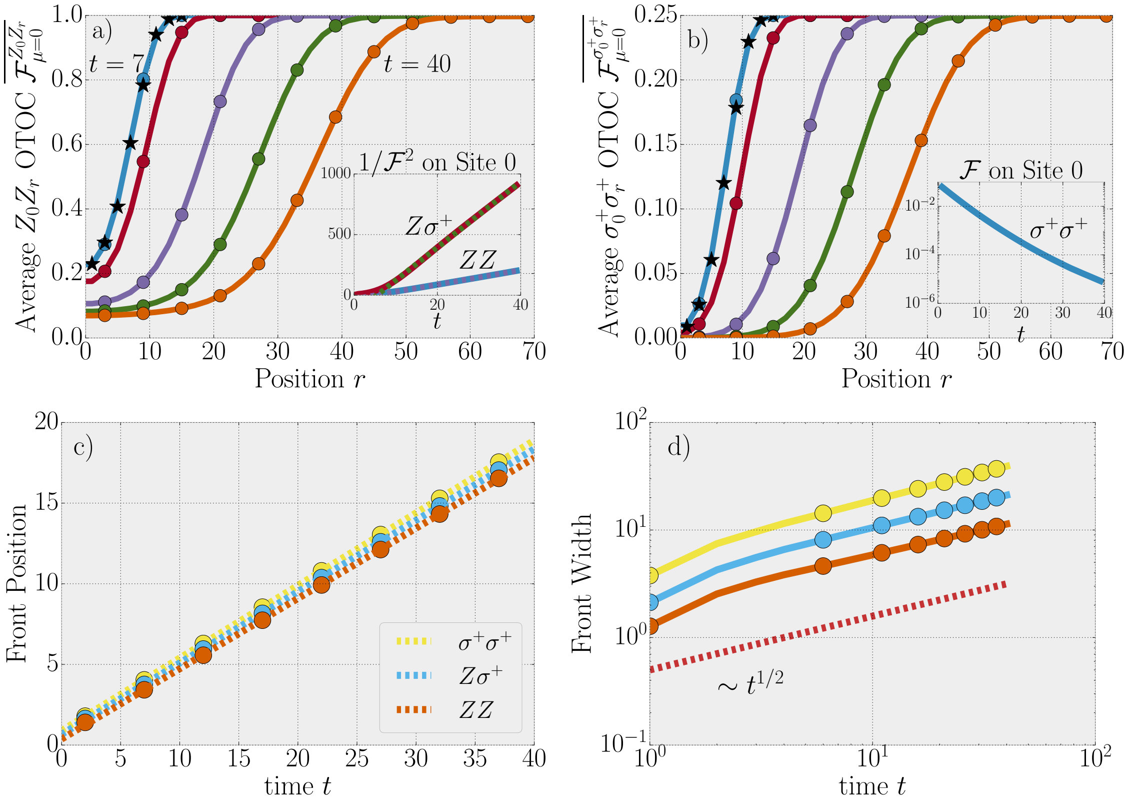

Figure 8.3.: The average OTOC $\mathcal{F}$, defined in Eq. (8.2), at $\mu = 0$, evaluated as a classical partition function. All OTOCs spread in a ballistically propagating front which itself diffusively broadens in time, and saturate to zero behind the front. The shape of the front is shown for a) the $\hat{Z}\hat{Z}$ and b) the $\hat{\sigma}^+\hat{\sigma}^+$ OTOCs for times (from left to right) $t = 7, 10, 20, 30, 40$. The black stars represent data obtained by performing the unitary time evolution with TEBD up to $t = 7$ and averaging over 100 realizations. The insets show the value of $\mathcal{F}$ for different operators at site 0 as a function of time. For OTOCs involving $\hat{Z}$ we find that $1/\mathcal{F}^2$ grows linearly in time, indicating a saturation $\mathcal{F} \propto 1/\sqrt{t}$ at long times, while the $\hat{\sigma}^+\hat{\sigma}^+$ OTOC saturates exponentially fast. The two lower figures show the c) position and d) width of the front as a function of time. The front moves ballistically with the three types of OTOCs having similar front velocities $v_\mathrm{B} \approx 0.45$ in units of the circuit light cone velocity, while they all broaden diffusively. The position and the width are extracted from a curve that smoothly interpolates between the data points: the front position is defined by the point where the OTOC decays to half of its original value, while the width is computed as the inverse of the maximal derivative of this curve near the front.

beyond the time scales attainable otherwise, as well as for some analytical approximations, which we detail below.

8.1.2. OTOCs in the random circuit model

Armed with the mapping to the classical partition function described in Section 8.1.1, we calculate the OTOC up to time $t \approx 40$ (80 layers of the random circuit), which is much beyond what is attainable in simulating the unitary circuit directly. We evaluate the partition function by representing it as a two-dimensional tensor network, built out of

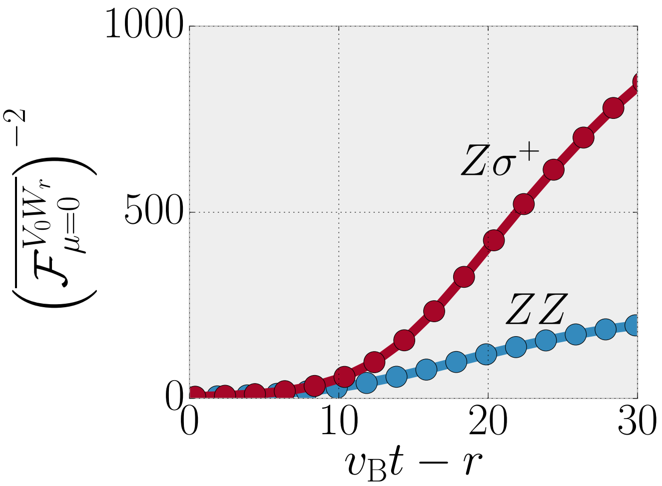

Figure 8.4.: Space-time structure of the wave front in Fig. 8.3 at time $t = 40$ for OTOCs involving the conserved density $\hat{Z}_0$. We plot $\mathcal{F}^{-2}$ at $\mu = 0$ for $\hat{V} = \hat{Z}_0$ and $\hat{W} = \hat{Z}_r, \hat{\sigma}^+_r$ as a function of the distance from the front $v_\mathrm{B}t - r$ and find a linearly growing regime in both quantities, indicating a decay of the form $\mathcal{F} \propto 1/\sqrt{v_\mathrm{B}t - r}$.

the four-legged tensors, defined in Eq. (8.6), that arise when averaging a single gate. We contract these together by representing the boundary condition $|\mathcal{D}_W\rangle$ at $t = 0$ as a matrix product state, which we then propagate forward layer-by-layer, using a method analogous to the TEBD algorithm. The OTOC is then computed by taking the overlap of this MPS with another one that represents the boundary condition $\langle \mathcal{P}_V|$ at time t.

In this section, we focus on the case where $\mu = 0$; the finite μ case is treated in separately in Section 8.3. The results, shown in Fig. 8.3, demonstrate that OTOCs exhibit the same biased diffusion behavior that we described for random circuits without conserved quantities in Chapter 4. In particular, there exists a velocity scale[5] v_B such that the OTOC $\mathcal{F}^{V_0 W_r}_{\mu=0}(t)$ is of $\mathcal{O}(1)$ at $|r| > v_B t$, decreases near the butterfly front'$|r| \approx v_B t$, and saturates to 0 for $v_B t \gg |r|$, as shown in Fig. 8.3. We also observe that the regime over which the OTOCs obtain an $\mathcal{O}(1)$ value (the 'width of the front') broadens diffusively ($\sim \sqrt{t}$) in time (see in particular the last panel of Fig. 8.3), again, in complete agreement with the predictions of the non-symmetric circuit.

Our results indicate that all OTOCs saturate to zero behind the front (this is peculiar to the $\mu = 0$ case considered here: as we argue in subsection 8.3.1 at finite μ certain OTOCs have finite saturation values). Our main new finding is that those OTOCs, $\mathcal{F}^{VW}(t)$, for which at least one of $\hat{V}, \hat{W}$ is the conserved density $\hat{Z}_r$, decay at long times as $\mathcal{F} \propto 1/\sqrt{t}$. We refer to this slow, power-law relaxation as a 'hydrodynamic tail', due to its analogy with similar slow dacay of time-ordered correlation functions in classical and quantum hydrodynamics discussed in Section 2.3. The $\hat{\sigma}^+_0\hat{\sigma}^+_0$ OTOC, on the other hand, decays exponentially with time (using Eq. (8.3), the same is true for the $\hat{\sigma}^+_0\hat{\sigma}^-_0$ OTOC). These results are in contrast with the behavior we observed for random circuits without symmetries, where all OTOCs showed an exponential decay. As we explain in Section 8.2 the hydrodynamic tails we observe here are a natural consequence of the diffusive charge transport discussed in Section 7.2.

Going beyond the decay of the OTOC at a given position, we can ask the question

---

[5] Note that the velocity $v_B \approx 0.45$ observed here numerically is smaller than the butterfly velocity of a random circuit with the no symmetries and the same local Hilbert space dimension, which was derived to be 0.6 in Section 4.2.

of what is the shape of the front at a fixed time. This is shown in Fig. 8.3. Again, for OTOCs involving the conserved density $\hat{Z}$, we find a striking new feature: well behind the butterfly front, we find that the position dependence of the OTOC is well described by $\mathcal{F} \propto 1/\sqrt{v_{\text{B}}t - r}$, i.e. it exhibits power law decay as a function of the distance from the position of the front; this is shown in Fig. 8.4. This particular tail behind the front is our main result in this chapter. In what follows, we will argue that it is a universal feature of OTOCs in diffusive systems and develop a 'hydrodynamic' explanation for it

8.1.3. OTOC tails in deterministic systems

As we argued previously, we expect random unitary circuits, like the one studied in this paper, to capture universal properties of non-noisy, ergodic quantum systems in the strongly interacting, high-temperature regime. This is true for the diffusion of conserved quantities, discussed in Section 7.2, and numerical evidence suggests that it is also the case for the diffusive broadening of the OTOC wavefron (see Section 4.3 and also Refs. [427, 429]). We expect that the OTOC hydrodynamic tails that we observed above – and which, as we argue below, are a direct consequence of charge diffusion – should therefore also be present in non-noisy systems, provided that they exhibit diffusive transport of conserved quantities. Such power law decay of OTOCs in a weakly disordered Hamiltonian system has already been observed numerically in [598]. Here we show that the same phenomena appears also in a system without any randomness. We do this by considering a periodically driven (Floquet) spin-chain, where the total spin z component is conserved, and find that OTOCs involving $\hat{Z}$ show similar diffusive decay to the one seen in the random circuit model, while OTOCs between non-conserved operators decay exponentially.

We consider a one-dimensional chain of spin 1/2 degrees of freedom. A single driving sequence consists of four parts, with the so-called Floquet unitary given by

$$\begin{aligned}
U_{\text{F}} &= e^{-i\tau H_4} e^{-i\tau H_3} e^{-i\tau H_2} e^{-i\tau H_1} \\
H_1 &= J_z^{(1)} \sum_r \hat{Z}_r \hat{Z}_{r+1} \\
H_3 &= J_z^{(2)} \sum_r \hat{Z}_r \hat{Z}_{r+2} \\
H_2 = H_4 &= J_{xy} \sum_r \left(\hat{X}_r \hat{X}_{r+1} + \hat{Y}_r \hat{Y}_{r+1} \right),
\end{aligned} \tag{8.9}$$

where $\hat{X}_r \equiv \hat{\sigma}_r^+ + \hat{\sigma}_r^-$ and $\hat{Y}_r \equiv -i(\hat{\sigma}_r^+ - \hat{\sigma}_r^-)$ are Pauli spin operators on site r, and we take periodic boundary conditions $r \equiv r + L$. Every part of the drive individually conserves the spin z component, $[H_a, \sum_r \hat{Z}_r] = 0$ for $a = 1, 2, 3, 4$. We take the period time to be $T \equiv 4\tau = 1$ and the couplings to be all order 1, namely $J_z^{(1)} = (\sqrt{3} + 5)/6$, $J_z^{(2)} = \sqrt{5}/2$ and $J_{xy} = (2\sqrt{3}+3)/7$. We have found that this Floquet model exhibits diffusive behavior already on the relatively short time scales that we can probe numerically[6]. This makes the model a useful study ground for various phenomena related to diffusive transport, and it has found application in subsequent work by other authors [105, 177].

We compute the OTOC (8.2) at $\mu = 0$ in this system using exact diagonalization methods, up to system size $L = 24$. We do this be approximating the trace in the infinite temperature average by an expectation value in a random state, $|\Psi\rangle$, drawn from the Haar measure over the whole Hilbert space (see also Section 2.4). The OTOC is then calculated as the overlap $\mathcal{F}_{\mu=0}^{VW}(t) \approx \text{Re}\,\langle\Psi_1|\Psi_2\rangle$ where $|\Psi_1\rangle \equiv \hat{W} U_{\text{F}}^{-t} \hat{V} U_{\text{F}}^{t} |\Psi\rangle$ and $|\Psi_2\rangle \equiv U_{\text{F}}^{-t} \hat{V} U_{\text{F}}^{t} \hat{W} |\Psi\rangle$. This overlap approximates the infinite temperature average up to

---

[6] In particular, it appears to be the case that both the next nearest neighbor interactions, and the fact that the drive consists of more than two parts, help with this.

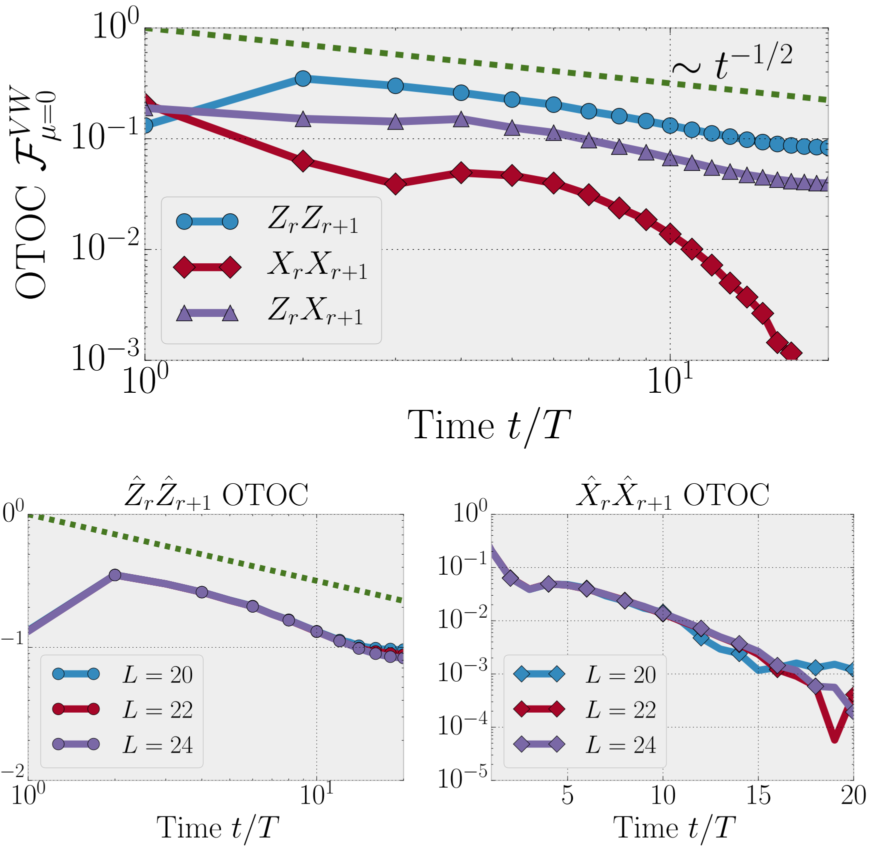

Figure 8.5.: OTOC for different operators on nearest neighbor sites at zero chemical potential in the non-random Floquet model Eq. (8.9) which conserves $\sum_r \hat{Z}_r$. Upper panel: OTOCs on nearest neighbor sites for system size $L = 24$ sites. Both the $\hat{Z}\hat{Z}$ and the $\hat{Z}\hat{X}$ OTOC decay as a power law, approximately as $\sim t^{/1/2}$, while the $\hat{X}\hat{X}$ OTOC decays faster than a power law, as shown by the log-log plot in the upper panel. The lower two panels show a comparison between system sizes $L = 20, 22, 24$ for the $\hat{Z}\hat{Z}$ and $\hat{X}\hat{X}$ OTOCs, respectively. The latter is shown in a lin-log plot and is well approximated by an exponential decay.

an error which is exponentially small in the system size [231] and we indeed find numerically that the deviation of the OTOC between different random states is negligible at the system sizes we consider.

In Fig. 8.5 we show the results for the $\hat{Z}\hat{Z}$, $\hat{X}\hat{X}$ and $\hat{Z}\hat{X}$ OTOCs. The local operator $\hat{X}$ has no overlap with the conserved quantity and is therefore expected to behave similarly to $\hat{\sigma}^+$ discussed above for the random circuit (indeed, it is a simple linear combination of $\hat{\sigma}^+$ and $\hat{\sigma}^-$). We take the OTOC between two operators on nearest neighbor sites such that they all have the same initial value 1. We find numerically that while the decay of the $\hat{Z}\hat{Z}$ and $\hat{Z}\hat{X}$ OTOCs is well described by the diffusive $\propto 1/\sqrt{t}$ behavior, the $\hat{X}\hat{X}$ OTOC decays more quickly, approximately as an exponential. This is all in in agreement with the results found for the random circuit model, and we conjecture that it is the generic behavior for one-dimensional systems with diffusive transport properties. Indeed, we will argue in the following section that these hydrodynamic tails, exhibited by OTOCs involving the conserved density, are a natural consequence of diffusion.

8.2. Explaining the presence and structure of the tails

In Section 7.2 we showed that the presence of a local conservation law leads to a diffusive relaxation of the associated charge. We now discuss how the presence of the same conserved quantity alters the behavior of OTOCs, leading to the hydrodynamic tails observed numerically in the previous section. Our discussion will focus on the random circuit model, but since most of our arguments are based on the diffusion of the conserved quantity, they should apply, with some slight changes, to other systems with diffusive transport, such as the Floquet system introduced in Section 8.1.3 or Hamiltonian systems, such as the one studied in Ref. [598].

First, in Section 8.2.1 and Section 8.2.2 we argue that OTOCs $\mathcal{F}^{VW}(t)$ (with traceless local operators $\hat{V}, \hat{W}$) decay slowly (as a diffusive power law) precisely when at least one of $\hat{V}, \hat{W}$ has nonvanishing overlap with the conserved charge, i.e., $\operatorname{tr}(\hat{Q}\hat{V}) \neq 0$. In the case that neither $\hat{V}, \hat{W}$ have such an overlap, the decay is expected to be exponentially quick, identical to the behavior we observed in random circuits without symmetries. Our arguments in Section 8.2.1 and Section 8.2.2 are not fully controlled analytically. However, they (particularly those in Section 8.2.2) have the merit of being completely analogous to those well established by previous work on hydrodynamical tails in regular observables, both in quantum and classical dynamics [287, 294, 599].

In Section 8.2.3 we provide a more controlled analytical argument which yields the detailed space-time structure of the front in those cases where it is present. For this analysis, we use the 'coarse grained' large-N version of the model, which we introduced in Chapter 7; N controls the size of the local Hilbert space, and provides large parameter which simplifies the calculations. Our conjecture is that such a model should describe the long-time dynamics of the $N = 1$ circuit as well. Indeed, we find in this coarse-grained circuit, OTOCs of conserved densities have the space-time profile $\propto 1/\sqrt{v_B t - x}$, in agreement with the the numerical data presented for the original circuit in Section 8.1.2. Finally, in Section 8.2.4 we summarize an alternative derivation, focusing on operator weights instead of OTOCs, originally discussed in Ref. [549].

8.2.1. Operator spreading explanation for the presence of tails

Consider an OTOC between two local Pauli operators $\hat{\sigma}_0^{\alpha=\mathrm{x,y,z}}, \hat{\sigma}_r^{\beta=\mathrm{x,y,z}}$ on sites 0 and r. At time t, $\hat{\sigma}_0^\alpha$ evolves into a superposition of operators

$$\hat{\sigma}_0^\alpha(t) = \sum_{\boldsymbol{\nu}} \hat{\sigma}^{\boldsymbol{\nu}} c_{\boldsymbol{\nu}}(t), \tag{8.10}$$

where $\hat{\sigma}^{\boldsymbol{\nu}}$ denotes a Pauli string of the form $\bigotimes_{s=1}^L \hat{\sigma}_s^{\nu_s}$, with $\nu_s = 0, x, y, z$. As discussed before, the out-of-time-ordered part of the OTOC at zero chemical potential then takes the form

$$\mathcal{F}^{\alpha\beta}_{\mu=0} = \sum_{\boldsymbol{\nu}} S(\nu_r, \beta) |c_{\boldsymbol{\nu}}(t)|^2, \tag{8.11}$$

where $S(\nu_r, \beta) = \pm 1$ depending on whether $\hat{\sigma}^{\boldsymbol{\nu}}$ commutes or anti-commutes with $\hat{\sigma}_r^\beta$.

To recapitulate, in the case *without* symmetries we found in Section 4.2 that the distribution of $|c_{\boldsymbol{\nu}}(t)|^2$ is strongly dominated by Pauli strings $\boldsymbol{\nu}$ which fill most of the spatial region $[-v_B t, +v_B t]$, while the total weight contained in strings of a fixed length decays exponentially, an observation that follows simply from the fact that there are exponentially more long operators than short ones. Since the operator norm is conserved, the average weight on a single string is $|c_{\boldsymbol{\nu}}|^2 \sim q^{-4 v_B t}$. Assuming $|c_{\boldsymbol{\nu}}|^2$ is largely independent of ν_r for typical strings when $|r| \ll v_B t$, the sum in Eq. (8.11) would average to 0, as the positive and negative contributions cancel. In practice not all strings have the same

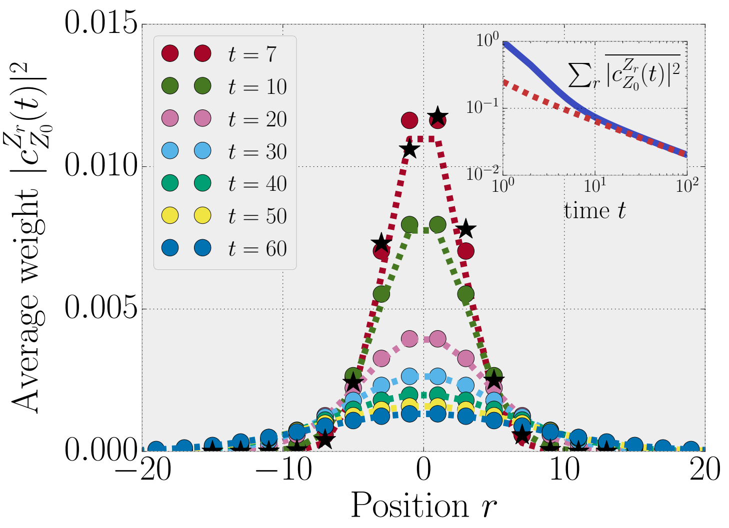

]t!]

Figure 8.6.: Average weights of single-site $\hat{Z}$ operators, $\overline{|c_{Z_0}^{Z_r}(t)|^2}$ (dots), compared to their lower bound given by the squares of the average coefficients $\left(\overline{|c_{Z_0}^{Z_r}(t)|}\right)^2$ (dashed lines). The weights approach the lower bound at times $t \approx 10$. The weight are computed using the classical partition function formalism of subsection 8.1.1, and for comparison we show TEBD data averaged over 100 circuit realizations at time $t = 7$ (black stars). Inset: the total weight contained in single-site $\hat{Z}$ operators decays in time at the rate set by the diffusion of the coefficients $c_{Z_0}^{Z_r}(t)$, as $t^{-1/2}$ at long times.

weight, but we expect such fluctuation to be suppressed (by the law of large numbers) as $\mathcal{O}(\sqrt{1/q^{-4v_B t}})$. Accounting for these fluctuations, and exponentially small contributions from Pauli strings well behind the front, we were able to prove exponential decay of the OTOC, $\mathcal{F}_{\mu=0}^{\alpha\beta} \sim \mathcal{O}(e^{-at})$.

The presence of conserved charges constrains some of the operator spread coefficients and alters the above argument significantly. In particular, expressions of the form $\mathrm{tr}(f(\hat{Q})\hat{\sigma}_0^{\alpha}(t))$ are independent of time, due to charge conservation, for any function f. One immediate consequence for the operator $\hat{Z}_0(t)$ is that its operator spread coefficients on single-site $\hat{Z}_r$ operators, defined as $c_{Z_0}^{Z_r}(t) \equiv q^{-L}\mathrm{tr}(\hat{Z}_r\hat{Z}_0(t))$, satisfy $\sum_r c_{Z_0}^{Z_r}(t) = 1$ at all times, where r ranges over all sites in the forward light cone of $\hat{Z}_0$. Indeed, as we have shown in Section 7.2, the coefficients decay on average as $t^{-1/2}$, rather than exponentially as they would without conservation laws. Using $\overline{|c_{\boldsymbol{\nu}}|^2} \geq \overline{|c_{\boldsymbol{\nu}}|}^2$ and Eq. (7.3), and summing over all sites r, implies that the total weight on single-site $\hat{Z}$ operators is lower bounded by a value that decays as $\sim t^{-1/2}$. We observe numerically that while this weight initially decays faster, it approaches this lower bound at times ≈ 10 (see Fig. 8.6). Based on these numerical results, we expect that at longer times $\sum_r \overline{|c_{Z_0}^{Z_r}|^2}(t) \sim 1/\sqrt{t}$. In contrast, recall that the same weight is expected to decay exponentially quickly for circuits without a conserved charge.

The above argument shows that if we pick $\alpha = z$ in Eq. (8.11) there is an anomalously large, slowly (diffusively) decaying positive contribution to the OTOC, coming from the $|c_{Z_0}^{Z_l}(t)|^2$ coefficients discussed above. This suggests that OTOCs involving $\hat{Z}$ relax to their long-time value as $\sim 1/\sqrt{t}$ at leading order in t, in agreement with the numerical evidence in Fig. 8.3. We expect similar behavior for the relaxation of OTOCs in Hamiltonian systems for operators that have a non-vanishing overlap with the local energy density, an effect already observed numerically in Ref. [598]. One can also understand the more detailed shape of the wavefront from similar arguments, which has been done in Ref. [549]. We will summarize their results later in subsection 8.2.4, after presenting a more rigorous argument of our own which leads to the same result.

8.2.2. Diffusive tails in a superoperator formalism

An alternative, possibly more general way of understanding the effects of charge conservation on operator spreading is possible using the language of superoperators.

Superoperator formalism

First we show that the objects defined in the formalism of Section 8.1.1 have a natural interpretation as superoperators that act on the operators of the original spin chain. This provides a general language for describing OTOCs which we will use for the 'hydrodynamic' interpretation of our results on OTOC dynamics in the rest of this subsection as well as in subsection 8.3.1 where we show that the long-time limit of OTOCs can be understood by generalizing the notion of thermalization to the space of operators (rather than states). We expect these concepts to be useful in the future study of scrambling.

As described in subsection 8.1.1, the quantities $|\mathcal{P}_V\rangle$ and $|\mathcal{D}_W\rangle$, appearing in Eq. (8.8), have four indices, i.e. they live in a Hilbert space which comprises four copies of the original system. We can naturally interpret this as the space of superoperators acting on the spin chain. This identification goes as follows. Let us first note that an operator $\hat{O}$ of the original system can be though of as a state $|\hat{O}\rangle \in \mathcal{H}\otimes\mathcal{H}$ in two copies of the original Hilbert space, such that $\langle\alpha\beta|\hat{O}\rangle \equiv \langle\alpha|\hat{O}|\beta\rangle = O_{\alpha\beta}$. Operators thus naturally correspond to states in a doubled space. Iterating this procedure once more we arrive at superoperators[7] $\mathcal{A}$ that map one operator to another, i.e. $\mathcal{A}|\hat{O}\rangle = |\hat{O}'\rangle$. These can then be reinterpreted as states in *four* copies of the original Hilbert space, defined as $\langle\alpha\beta\gamma\delta|\mathcal{A}\rangle \equiv \langle\beta\alpha|\mathcal{A}|\gamma\delta\rangle$.

A natural basis of superoperators is of the form $|\hat{A}\rangle\langle\hat{B}|$. Another way to turn operators into superoperators is via left and right multiplication, defined as $\mathcal{L}_A|\hat{B}\rangle \equiv |\hat{A}\hat{B}\rangle$ and $\mathcal{R}_A|\hat{B}\rangle \equiv |\hat{B}\hat{A}\rangle$. The two states appearing in Eq. (8.8) can then be interpreted as follows. $\mathcal{P}_V = |\hat{V}\rangle\langle\hat{V}|$ is the 'density matrix' corresponding to the state $|\hat{V}\rangle$, while $\mathcal{D}_W = \mathcal{L}_{W^\dagger}\mathcal{R}_W$ corresponds to multiplying from left and right with $\hat{W}^\dagger$ and $\hat{W}$, respectively. The OTOC then has the interpretation of the time evolved expectation value of a superoperator,

$$\mathcal{F}^{VW}_{\mu=0}(t) \propto \langle\mathcal{P}_V|\mathcal{D}_W(t)\rangle = \langle\hat{V}(t)|\mathcal{D}_W|\hat{V}(t)\rangle.$$

As we show in Section 8.3, the OTOC at $\mu \neq 0$ can be written in a similar form, with $\hat{V}$ replaced by a slightly modified operator. As we argue in subsection 8.3.1, the long-time limit of the 'state' $|\hat{V}(t)\rangle\langle\hat{V}(t)|$ can be understood as relaxation to a state analogous to a thermal equilibrium. This is also important for motivating hydrodynamic descriptions of operator spreading (as we will do shortly). Once a notion of 'operator thermalization' has been established, we can also imagine that at intermediate times, we can approximate (at least for certain purposes) $|\hat{V}(t)\rangle\langle\hat{V}(t)|$ with a 'state' that appears locally thermal. Such a local equilibrium approximation is the key assumption behind hydrodynamic theories, as we discussed in Section 2.3. Finally, we note here that the states appearing in Eq. (8.6) also have simple interpretations in the superoperator language as $\mathcal{I}^+_{Q_1Q_2} = |\hat{P}_{Q_1}\rangle\langle\hat{P}_{Q_2}|$ and $\mathcal{I}^-_{Q_1Q_2} = \mathcal{L}_{P_{Q_1}}\mathcal{R}_{P_{Q_2}}$, where $\hat{P}_Q$ are the projectors defined in Eq. (7.1), acting on the two-site Hilbert space.

---

[7] Throughout the text, we use capital calligraphic letters to denote superoperators. Note that the OTOCs, $\mathcal{C}$ and $\mathcal{F}$ are expectation values of superoperators.

OTOC tails are associated with diffusion of $\mathcal{L}_Q$ and $\mathcal{R}_Q$

We now address the issue of tails, and when they appear in OTOCs, in the language of superoperators. Consider, from the preceeding subsection, the superoperators corresponding to left and right multiplication by $\hat{Q}$, namely $\mathcal{L}_Q$ and $\mathcal{R}_Q$. These super-operators are conserved as a function of time,

$$\mathcal{L}_Q, \mathcal{R}_Q \to \mathcal{L}_{U^\dagger QU}, \mathcal{R}_{U^\dagger QU} = \mathcal{L}_Q, \mathcal{R}_Q.$$

Both superoperators are *extensive*, that is, they can be written as sums of local superoperators, e.g., $\mathcal{R}_Q = \sum_r \mathcal{R}_{Q_r}$. Note that the relation $\overline{\mathcal{L}_{Q_r}(t)}, \overline{\mathcal{R}_{Q_r}(t)} = \mathcal{L}_{\overline{Q_r(t)}}, \mathcal{R}_{\overline{Q_r(t)}}$, together with the diffusion of the local charge $\hat{Q}_r$, derived in Eq. (7.3), imply that $\mathcal{L}_{Q_r}, \mathcal{R}_{Q_r}$ diffuse on average as well. Thus, the presence of a diffusing conserved quantity in the original many body problem leads to the presence of two new diffusing conserved quantities in operator space. In a continuum approximation we can write this as

$$\begin{aligned} \partial_t \mathcal{L}_{Q_r(t)} &= D\partial_r^2 \mathcal{L}_{Q_r(t)}; \\ \partial_t \mathcal{R}_{Q_r(t)} &= D\partial_r^2 \mathcal{R}_{Q_r(t)}. \end{aligned} \tag{8.12}$$

We can make use of the conservation of $\mathcal{L}_Q, \mathcal{R}_Q$ to shed new light on the diffusive relaxation of certain OTOCs, discussed previously in Section 8.1.2. There, we noted that the $\hat{Z}\hat{Z}$ and $\hat{Z}\hat{\sigma}^+$ OTOCs have a power law relaxation. We can account for both of these tails in the following way. These two OTOCs can be written in the form $\langle \hat{V}(t) \mid \mathcal{D}_{Z_r} \mid \hat{V}(t)\rangle$ where $\hat{V} = \hat{Z}, \hat{\sigma}^+$. Note that the superoperator in this expression can be rewritten

$$\mathcal{D}_{Z_r} = 1 - 2(\mathcal{L}_{Q_r(t)} - \mathcal{R}_{Q_r(t)})^2$$

This expression is quadratic in $\mathcal{L}_{Q_r} - \mathcal{R}_{Q_r}$, which is a conserved density. In ergodic theories, where diffusive hydrodynamics applies, conserved densities, *and their variances*, are expected to show $1/\sqrt{t}$ relaxation in 1D. The variances in conserved densities show this diffusive behavior even in states with initially spatially homogeneous distributions of the conserved quantity [287]. In the superoperator language, it is thus natural to conclude at $\hat{Z}$-type OTOCs relax as $1/\sqrt{t}$. The presence of hydrodynamic tails can be made even more explicit in the case of the $\hat{Z}\hat{\sigma}^+$ OTOC by noting that the state $|\hat{\sigma}_0^+\rangle$ has an initial imbalance of the conserved quantities of the form $\langle \hat{\sigma}_0^+ | \mathcal{L}_{Q_r} - \mathcal{R}_{Q_r} | \hat{\sigma}_0^+ \rangle = \delta_{r0}$. Since both $\mathcal{L}_Q$ and $\mathcal{R}_Q$ obey diffusion, this imbalance also relaxes diffusively, a fact picked up by the OTOC. The remaining OTOCs do not involve $\hat{Z}$, and also do not show diffusive decay. We attribute this to the fact that the corresponding OTOC operator $\mathcal{D}_{\hat{\sigma}_r^+}$ is orthogonal to any algebraic combination of the only two available local conserved densities, $\mathcal{L}_Q$ and $\mathcal{R}_Q$.

8.2.3. OTOC Hydrodynamics from coarse-graining

Since an exact analytical calculation of the partition function (8.8) is out of reach, we instead consider a modified version of the random circuit which we expect to reproduce the behavior of the original model at long time- and length scales. We use this simplified model to shed light on the hydrodynamic nature of the OTOC dynamics and give an analytical estimate for the shape of the wavefront, reproducing the numerical results of subsection 8.1.2.

To arrive at this approximate description, we consider the 'coarse-grained' version of the circuit, which we introduced previously in Section 7.1. It is defined by increasing the local Hilbert space to have size 2^N, which we think of as N sites comprising a coarse-grained 'super-site' (alternatively, one can think of this as increasing the range of the random unitary gates such that each one acts on $2N$ consecutive sites), as illustrated in Fig. 7.1(a). We change notation slightly, and label individual sites by r and super-sites by x. Time evolution is then described by a brick-wall circuit of random unitary gates acting pairs of super-sites and block diagonal in the total charge on them (with $2N+1$ blocks in total). We find that in the limit $N \gg 1$ the dynamics simplifies considerably, allowing for a closed approximate expression for the OTOC, which we detail below. We consider evolving the operator $\hat{Z}_r$ here and leave the $\hat{\sigma}^+_r$ case for later work.

As noted above, the $\hat{Z}_r$ OTOC superoperator can be decomposed as

$$\mathcal{D}_{Z_r} \sim \mathcal{D}_{\mathbb{1}} - 2\mathcal{L}_{Q_r} - 2\mathcal{R}_{Q_r} + 4\mathcal{L}_{Q_r}\mathcal{R}_{Q_r}, \tag{8.13}$$

where $\mathcal{D}_{\mathbb{1}} \equiv \mathcal{L}_{\mathbb{1}}\mathcal{R}_{\mathbb{1}}$ is a superoperator that acts on an operator by multiplying it from both sides with the identity, which is equivalent to the 'super-identity', obeying $\mathcal{D}_{\mathbb{1}}|\hat{O}\rangle = |\hat{O}\rangle$ for any operator $\hat{O}$. The decomposition (8.13) already suggests that the superoperator $\mathcal{D}_{Z_r}$ should have a diffusive component, since, as we showed previously, $\mathcal{L}_{Q_r}$ and $\mathcal{R}_{Q_r}$ diffuse on average. The main technical aim of this subsection is to understand the average behavior of the non-linear term $\mathcal{L}_{Q_r}\mathcal{R}_{Q_r}$. Let us first evolve $\mathcal{D}_{Z_r}$ with one unitary gate on sites $r, r+1, \dots, r+2N-1$, corresponding to super-sites $x, x+1$. A straightforward application of Eq. (8.6) yields a sum of two terms

$$\mathcal{D}_{Z_r}(\Delta\tau) = \sum_Q \frac{b_Q}{d_Q}\mathcal{I}^{x,x+1}_{Q_1 Q_2} + \frac{1}{N^2}\mathcal{D}_{\frac{1}{2}(\zeta_x+\zeta_{x+1})}, \tag{8.14}$$

where $\hat{\zeta}_x \equiv \sum_{r\in x}\hat{Z}_r$ is the total charge on supersite x, while $\mathcal{I}_{Q_1Q_2} \equiv \mathcal{I}^+_{Q_1Q_2} \equiv |\hat{P}_{Q_1}\rangle\langle\hat{P}_{Q_2}|$ and $\mathcal{D}_{\frac{1}{2}(\zeta_x+\zeta_{x+1})} \equiv \mathcal{L}_{\frac{1}{2}(\zeta_x+\zeta_{x+1})}\mathcal{R}_{\frac{1}{2}(\zeta_x+\zeta_{x+1})}$ are the superoperators (acting on $x, x+1$) introduced in Section 8.1.1, and $b_Q \equiv 1-(1-\frac{Q}{N})^2$. In this equation we neglected terms that are suppressed by at least $1/N^2$. As we argue in App. B.2, the first term in Eq. (8.14) grows ballistically upon applying further layers of unitaries. For the second term, on the other hand, we find that superoperators of the form $\mathcal{L}_{Q_x}\mathcal{R}_{Q_y}$ diffuse, unless super-sites x and y are acted upon by the same gate in the circuit, in which case extra contact terms arise. Summing up these different contributions, and applying some further approximations which we detail in App. B.2, we arrive at the following form of the OTOC operator[8] at time t:

$$\mathcal{D}_{Z_{r\in x}}(t) \approx \frac{1-2N}{2N}\mathcal{P}^{A_x(t)} + \frac{1}{N^2}\mathcal{D}_{\zeta_x(t)} - \frac{1}{2N}\sum_{t'<t}\sum_{y\in t'+2\mathbb{Z}}\left(K_{x,y+1}-K_{x,y}\right)^2(t')\mathcal{P}^{A_y(t-t')}. \tag{8.15}$$

Here $A_x(t) = [x-t, x+t]$ is a ballistically spreading region around x and $\mathcal{P}^A \equiv \mathcal{P}_{\mathbb{1}_A}/\mathrm{tr}(\mathbb{1}_A)$ is a projection unto $\mathbb{1}_A$, the identity operator acting on this region. $K_{x,y}$ denotes the diffusion kernel defined by the right hand side of Eq. (7.3). Note that the time evolution of the OTOC involves summing up contributions from diffusion processes starting at different times t'. This is a consequence of the aforementioned contact terms, wherein the diffusively spreading densities $\mathcal{R}_{Q_r}$, $\mathcal{L}_{Q_r}$ can be converted into ballistically propagating $\mathcal{P}_{\mathbb{1}}$ superoperators. In App. B.2 we derive a more general version of Eq. (8.15) which also involves corrections from finite μ.

The result (8.15) might look intimidating, so let us take a moment to discuss its physical meaning. The first term describes a ballistically spreading operator front, emitted at $t=0$ and propagating at the butterfly speed, which in our simplified model is simply 1 in the

---

[8] While this equation is only heuristically motivated, rather than exactly derived, it passes a number of consistency checks. In particular, it satisfies the condition that when evaluated on the identity operator $\mathbb{1}$, the resulting OTOC $\mathcal{F}^{Z\mathbb{1}}$ is one at all times. Moreover, it is constructed in such a way that the OTOC saturates to the correct long-time value which we derive later in subsection 8.3.1.

appropriate units. This is completely analogous with the result of the non-symmetric circuits in the $q \to \infty$ limit, where $v_{\mathrm{B}} \to 1$ and the front diffusion is suppressed; similarly, we expect that at finite N, this first term, $\mathcal{P}^{A_x(t)}$, would be modified to describe a front spreading with the appropriate v_{B} and broadening in time. The second term, $\mathcal{D}_{\zeta_x(t)}$, on the other hand, describes the diffusive part, comprised of single-site $\hat{Z}$ operators, which evolve according to the random walk process in Eq. (7.3). This can be identified with the contribution we discussed earlier in subsection 8.2.1 in the language of operator spreading; it spreads out diffusively, reflecting the nature of transport in the system.

Most interesting is the last term in Eq. (8.15), which describes the coupling between the diffusive and ballistic parts. It takes the form of a sum over ballistic components, of the exact same form as the first term, $\mathcal{P}^{A_x(t)}$, emitted at different times t' between 0 and t. The probability of emitting one of these fronts at time t' at position y is given by the gradient of the diffusive charge profile; in a continuum notation: $(\partial_y K(y-x,t'))^2$. Given that the charge evolves diffusively, we can equate this with the square of the *charge current* at position y at time t'. At a fixed y, it decays as $\sim (t')^{-2}$, making the total probability of a new front being emitted at time t' scale as $\int \mathrm{d}y\, (\partial_y K(y-x,t'))^2 \sim (t')^{-3/2}$. This compensates the decay of the total operator weight in the diffusive part[9], so we can interpret this as a gradual conversion from the diffusive part to newly emitted ballistic fronts at each time step. This picture is sketched on the left panel of Fig. 8.7

To see what this result implies for the OTOC, we valuate Eq. (8.15) on the operator $\hat{Z}_0$ to get the $\hat{Z}\hat{Z}$ OTOC, which reads

$$\mathcal{F}^{Z_0 Z_x}_{\mu=0} \approx 1 - \delta(x \in A_0(t)) \left[\frac{2N-1}{2N} - \mathcal{Y}(t,x)\right], \tag{8.16}$$

where $\mathcal{Y}(t,x)$ stands for the double sum appearing in Eq. (8.15) evaluated at the operator $\hat{Z}_x$, given by

$$\mathcal{Y}(t,x) = \frac{1}{2N-1} \sum_{t'<t} \sum_{y} \left(K_{0,y+1}(t') - K_{0,y}(t')\right)^2 \times \delta(x \in A_y(t-t')).$$

The formula Eq. (8.16) is plotted in Fig. 8.7. We find that it exhibits a tail behind the front, where the OTOC decays as $(t-x)^{-1/2}$, reproducing the shape found numerically in Section 8.1.2. At the origin, the function $\mathcal{Y}$ relaxes as $at^{-1} + bt^{-1/2}$, consistent with our earlier discussion of power law tails in Section 8.2.

Evaluating Eq. (8.15) on the local operator $\hat{\sigma}^+_x$ gives the result

$$\mathcal{F}^{Z_0 \sigma^+_x}_{\mu=0} \approx \delta(r \in A_0(t)) \left[-\frac{1}{2}\mathcal{Y}(t,x) - \frac{K^2_{0x}(t)}{N^2}\right] + \frac{1}{2}\delta(r \notin A_0(t)).$$

The main contribution that determines the shape of the OTOC front, is given by the same function, $\mathcal{Y}(t,x)$, as for the $\hat{Z}\hat{Z}$ OTOC. This implies that the shape of the tail behind the front is the same as the one seen in Fig. 8.7. This is also in agreement with our numerics on the spin-1/2 circuit as well as the results of Ref. [549].

The results and the formalism of this section marries two notions of hydrodynamics. As we have seen in Section 4.2, the ballistic spreading of OTOCs can be understood to follow from the biased diffusion equation that describes the spatial growth of an initially local operator. The hydrodynamic nature of this equation is related to the emergent conservation law, that of the norm of the evolving operator, which follows from the unitarity of time evoltuion. A second, more conventional, notion of hydrodynamics arises, as detailed in Sections 7.2 and 8.2, due to the presence of the conserved charge $\hat{Q}$, which leads to the

---

[9] As se saw in subsection 8.2.1, the operator weight summed over all local $\hat{Z}_r$ operators decays in time as $\sim t^{-1/2}$, making its time derivative $\sim t^{-3/2}$

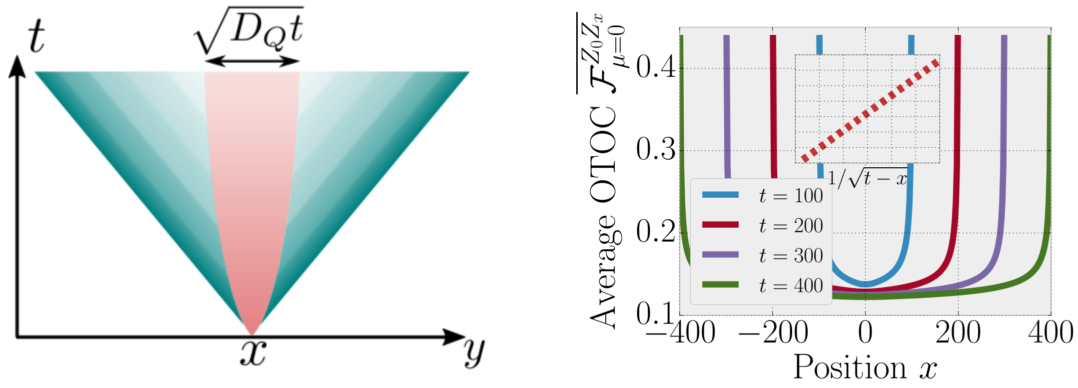

Figure 8.7.: Left: sketch of the OTOC and operator spreading for an initial operator that overlaps with the conserved quantity, based on Eq. (8.16): the diffusive part (red) has a total weight decreasing as $\sim t^{-1/2}$, which is gradually converted into ballistic components. The size of the ballistic component emitted at time t is proportional to the derivative, $\sim t^{-3/2}$. Right: Shape of the resulting OTOC wave fron, arising from the solution Eq. (8.16) of the coarse-grained circuit, substituting $N = 1$. In evaluating the formula we used the continuum form of the diffusion kernel $K_{x,y}(t) = \exp\left[\frac{(x-y)^2}{4t}\right] / \sqrt{4\pi t}$. While the numerical values (for example the saturation value behind the front) have $\mathcal{O}(1/N)$ corrections, the main features of the shape of the OTOC behind the front should be captured by this solution. Notably, we find that the hydrodynamic tail behind the main front is proportional to $(t-x)^{-1/2}$, as illustrated by the inset.

two locally conserved, diffusing, superoperator densities $\mathcal{L}_{Q_r}$ and $\mathcal{R}_{Q_r}$. Our approximate coarse-grained description couples these two types of quantities: Eq. (8.15) includes ballistically spreading terms (namely $\mathcal{P}$), as well as the conserved densities $\mathcal{L}_{Q_r}, \mathcal{R}_{Q_r}$, and couplings between these terms. The couplings lead to a conversion of the conserved densities into ballistically propagating components and all such terms, created at different times $t' < t$, need to be summed up to get the OTOC at time t. This process results in the OTOC decaying as $\sim 1/\sqrt{t-x}$ behind the front, as shown in Fig. 8.7. It the next subsection we make this connection more direct, writing down a set of coupled equations for the various (true and emergent) conserved quantities.

8.2.4. Coupled hydrodynamics for operator densities

The discussion of the previous subsection, especially Eq. (8.15) and its physical interpretation that we put forward, suggest a simple picture of operator dynamics, in which the diffusive component acts as a source of ballistically spreading fronts. One might naturally wonder whether it is possible to turn this picture into an equation of motion for the operator endpoint weights, as a direct generalization of the biased diffusion equation we derived in subsection 4.2.1 for the case with no symmetries. This has been achieved in Ref. [549] and we briefly summarize the results here.

The starting point is to split the time evolved operator into two components, a diffusive part, containing all one-site conserved densities, and a 'ballistic' part[10], that contains all longer operator strings: $\hat{Z}_0(t) = \hat{Z}^{\text{Diff}}(t) + \hat{Z}^{\text{Ball}}(t)$. The right endpoint density (defined

---

[10] The quotation marks refer to the fact that this second part still contains operators that are expected to show some form of diffusive behavior, such as product of the form $\hat{Z}_r \hat{Z}_s$. Nevertheless, it is dominated by long strings of size $\sim v_{\text{B}} t$, so we refer to it as the ballistic part.

previously in Eq. (4.3)) is also a sum of two contributions:

$$\rho_R(r,t) = \rho_R^{\text{Diff}}(r,t) + \rho_R^{\text{Ball}}(r,t) \qquad \rho_R^{\text{Diff}}(r,t) = \left|c_{Z_0}^{Z_r}(t)\right|^2 \equiv |c(r,t)|^2\,, \tag{8.17}$$

where the second equation defines the diffusive component as simply the weight of the one-site $\hat{Z}_r$ operator. The total weight, summed over all r, is still conserved due to unitarity, so any increase in the total ballistic weight has to come from the decrease of the diffusive part. This decrease of the diffusive weight is a manifestation of *dissipation*, a key feature of diffusive transport. In this sense, as Ref. [549] points out, the origin of dissipation can be understood as the effect of an emergent 'bath', provided by the non-local degrees of freedom that make up the ballistic part of the operator (we will have more to say on this later in Chapter 9)

As we noted before in subsection 8.2.1, the total weight in the diffusive part, $\sum_r \rho_R^{\text{Diff}}(r,t)$ decreases slowly in time, as $\sim t^{-1/2}$, as a direct consequence of diffusion. One can also consider this decay locally, without summing over r; in this case, the decrease in ρ_R^{Diff} induced by a two-site gate on sites $r, r+1$ is given by[11] $\left(c(r,t)-c(r+1,t)\right)^2/2$, which is exactly the quantity appearing as the emission rate of a new ballistic component in Eq. (8.15), and as we noted there, it can be interpreted as the square of the local current density. In a scaling limit, where we take $r/t = \kappa$ fixed and t large, both the $\sim\sqrt{t}$ size of the diffusive 'source' region, and the diffusion of the front itself, become negligible. In this case, the value of $\rho_R(\kappa t, t)$ is dominated by the front that was emitted precisely at time $t - r/v_{\text{B}}$. By the above arguments, this is given by the rate of change in the conserved weight at that time, which is $\partial_t \sum_r \rho_R^{\text{Diff}}(r,t) \sim t^{-3/2}$. This suggests that $\rho_R(r,t) \sim (t - r/v_{\text{B}})^{-3/2}$, which is the analogue of the slowly decaying tail we found for the OTOC in Fig. 8.7 (remember that the OTOC was related to the *integrated* weight, $R(x) = \int^x \mathrm{d}y \rho_R(y)$).

These results can be conveniently captured in a set of coupled hydrodynamic equations for ρ_R and the the local conserved density, measured by the coefficient $c(r,t)$. For this, let us now coarse-grain, and replace r with a continuous variable x. Consider first the dynamics of the diffusive part, $\rho_R^{\text{Diff}}(x,t) \equiv |c(x,t)|^2$. The equation of motion follows simply from the diffusion of $c(x,t)$ itself:

$$\partial_t c(x,t) = D_Q \partial_x^2 c(x,t) \rightarrow \partial_t \rho_R^{\text{Diff}}(t) = \partial_t \left|c(x,t)\right|^2 = D_Q \partial_x^2 \rho_R^{\text{Diff}}(x,t) - 2D_Q |\partial_x c(x,t)|^2, \tag{8.18}$$

where D_Q is the diffusion constant of the charge. This equation shows that indeed, the local decay rate is given by the square of the gradient of $c(x,t)$. This decay rate has to be equal to the source term appearing in the equation of motion for ρ_R^{Ball}, which therefore reads

$$\partial_t \rho_R^{\text{Ball}}(x,t) = v_{\text{B}} \partial_x \rho_R^{\text{Ball}}(x,t) + D_\rho \partial_x^2 \rho_R^{\text{Ball}}(x,t) + 2D_Q |\partial_x c(x.t)|^2, \tag{8.19}$$

where we used D_ρ for the diffusion constant associated with the biased diffusion of the operator wavefront. Eqs. (8.18) and (8.19) together provide a closed set of equations, describing the coupled dynamics of the charge[12] and the operator density of the remaining part. This is expected to be, for the same reasons as described before, the leading order hydrodynamic description in some coarse-grained limit, with both equations having further subleading contributions[13]. Finally, we can also combine the above two equations into an

---

[11] To see this, consider.a case of an initial operator $c_1\hat{Z}_1 + c_2\hat{Z}_2$ on some pair of neighboring sites. A two-site gate acting on these sites transforms the coefficients as $(c_1, c_2) \rightarrow (\frac{c_1+c_2}{2}, \frac{c_1+c_2}{2})$. The corresponding change in weights is then $c_1^2 + c_2^2 - 2\frac{1}{4}(c_1+c_2)^2 = \frac{(c_1-c_2)^2}{2}$

[12] More precisely, the infinite temperature charge-charge correlations, captured by $c(x,t) = \langle \hat{Q}(x,t)\hat{Q}(0,0)\rangle_{\beta=0}$.

[13] As discussed in Section 2.3, taking into account corrections to the diffusion equation, one would find that $c(x,t)$ has subleading power laws apart from the leading $t^{-1/2}$. These would translate into subleading corrections in the emission rate of ballistic fronts.

equation of motion for ρ_R itself,

$$\partial_t \rho_R(x,t) = v_\mathrm{B} \partial_x \rho_R^\mathrm{Ball}(x,t) + D_\rho \partial_x^2 \rho_R^\mathrm{Ball}(x,t) + D_Q \partial_x^2 \rho_R^\mathrm{Diff}(x,t), \tag{8.20}$$

which shows that the ballistic part obeys the biased diffusion dynamics we derived previously, while the diffusive part simply diffuses.

Note that while these hydrodynamic equations provide a good description for the spreading of operators that correspond to densities of the conserved quantity, they miss effects that arise for other operators. In particular, for a 'charged' operator, such as σ_0^+, the operator weight ρ_R does not directly couple to the conservation law (ρ_R^Diff, and thus the source term in Eq. (8.19), vanishes at all times), and is therefore expected to behave as in the systems without symmetries we discussed in Part I. Nevertheless, as we have seen, the OTOCs between this operator and a conserved density still picks up the effect of the hydrodynamic tails behind the front, which are hidden in the detailed structure of the operator, and therefore do not appear in ρ_R itself. Instead, they point to the fact that even σ_0^+ only approaches 'local equilibrium' behind the front in an algebraically slow manner. In this sense, OTOCs capture more details of the dynamics than merely the endpoint densities, unlike the case without symmetries, where the fact that the operator behind the front looks almost completely random provided a simple connection between the two quantities.

8.3. Finite chemical potential

One question of great interest is how the behavior of OTOCs changes with temperature. On general grounds it is expected that at higher temperatures many-body systems behave more chaotically as there is effectively more states to scramble over. In Ref. [239] a temperature dependent upper bound was derived for the growth rate of OTOCs (the 'quantum Lyapunov exponent') which is known to be saturated in certain holographic models. However, as we have seen in Chapter 4, for systems with local interactions and finite on-site Hilbert spaces, the Lyapunov exponent seems to vanish quite generically; as such, not much is known about the detailed dependence of out-of-time-ordered correlators on temperature in these systems [249]. While temperature is not well-defined for the random circuits we study, due to the lack of energy conservation, it is plausible that the chemical potential μ can play a similar role, setting the equilibrium entropy density of the system and thus effectively limiting the size of the Hilbert space available for the dynamics. For example, taking the $\mu \to \infty$ limit projects it down to a single stationary state, analogous to $T \to 0$ in conventional systems. On the other hand, $\mu \to 0$ is equivalent to the infinite temperature limit.

Motivated bu this, in this section we extend our discussion from the properties of OTOCs in the infinite temperature state $\mu = 0$, discussed so far, to the case of a finite chemical potential $\mu > 0$. Our results are as follows. i) We show how the finite chemical potential affects the long-time saturation value of the OTOC and use the superoperator formalism developed above in Section 8.2.2 to interpret this as a form of thermalization on the space of operators. ii) We confirm our prediction for the saturation values in the random circuit model and show that the hydrodynamic tails observed at $\mu = 0$ are also present at small but finite chemical potential. iii) We examine the limit $\mu \to \infty$, and find that in this case the OTOC spreads out diffusively as a function of space and time, as opposed to having a ballistic light-cone seen in previous sections. In this somewhat special limit, the OTOC can exhibit a double plateau structure: it initially relaxes to a value different from the one predicted in i), only decaying to its final saturation value on time scales $\mathcal{O}(L^2)$; we refer to this initial relaxation as a 'prethermal plateau'. iv) Through a perturbative expansion, we show that the $\mu \to \infty$ results, including the diffusive space-time behavior and double plateau structure, can survive at finite μ to times $t \sim \mathcal{O}(e^{2\mu})$.

We begin our discussion by rewriting the OTOC, originally defined in Eq. (8.2), as

$$\langle \hat{V}^\dagger(t)\hat{W}^\dagger\hat{V}(t)\hat{W}\rangle_\mu = e^{\frac{\mu}{2}(\lambda_V+\lambda_W)}\frac{\mathrm{tr}\left(\tilde{V}^\dagger(t)\hat{W}^\dagger\tilde{V}(t)\hat{W}\right)}{\mathrm{tr}\left(e^{-\mu\hat{Q}}\right)}, \tag{8.21}$$

where we defined $\tilde{V} \equiv e^{-\frac{\mu}{4}\hat{Q}}\hat{V}e^{-\frac{\mu}{4}\hat{Q}}$ (this is similar to the regularized version of the OTOC introduced in Ref. [239]). Thus we see that the effect of finite chemical potential can be incorporated entirely into modifying the boundary conditions of the partition function defined in Eq. (8.8); the $\mu > 0$ boundary conditions penalize states (of the four-layer system) with large total charges. We can therefore easily generalize the calculation of the classical partiton function, originally introduced in Section 8.1.1, to the case with finite μ.

8.3.1. Long-time saturation of OTOCs

Before examining the time evolution of OTOCs at finite μ, we derive some analytical results on their expected long-time behavior. For the purposes of this subsection, we return to the definition of the OTOC in terms of the squared commutator (8.1). We will show that the saturation value that the OTOC approaches as $t \to \infty$ depends non-trivially on both the chemical potential and the type of operators considered (i.e., their charges $\lambda_{V,W}$). Notably, we will show that the out-of-time-ordered part has a non-zero saturation value for $\mu > 0$ if either $\lambda_V = 0$ or $\lambda_W = 0$.

As a starting point of this calculation, we will assume that over vast time scales, well in excess of the system size, our local random unitary dynamics for the OTOC becomes indistinguishable from non-local dynamics with the same conserved quantity $\hat{Q}$. An analogous statement is known to hold for a random circuit without symmetries [600, 601], which approximate finite moments of the Haar-distribution at long times, and therefore it is natural to assume that the same would happen in our case for each symmetry sector. Thus we will estimate the long time value of Eq. (8.1) by taking $\hat{V}(t) = U^\dagger(t)\hat{V}U(t)$ where U is a unitary that conserves $\hat{Q}$, but which is otherwise completely Haar random in each symmetry block, without any notion of locality. Averaging the OTOC over such unitaries should yield the saturation values $\overline{\mathcal{C}_\mu^{VW}}(t_\infty)$. In the limit of large system size, provided $\hat{V}, \hat{W}$ are operators with subextensive charge (which automatically holds in the case of interest, where $\hat{V}, \hat{W}$ are local) this approach yields:

$$\overline{\mathcal{C}_\mu^{VW}}(t_\infty) = \frac{1}{2}e^{\mu\lambda_V}\langle\hat{W}_\perp^\dagger\hat{W}_\perp\rangle_\mu\langle\hat{V}_\perp\hat{V}_\perp^\dagger\rangle_\mu + \frac{1}{2}e^{\mu\lambda_W}\langle\hat{W}_\perp\hat{W}_\perp^\dagger\rangle_\mu\langle\hat{V}_\perp^\dagger\hat{V}_\perp\rangle_\mu + \mathcal{O}(1/L), \tag{8.22}$$

where $\hat{W}_\parallel \equiv \sum_Q \frac{\hat{P}_Q}{d_Q}\mathrm{tr}\left(\hat{P}_Q W\right)$ is the part of $\hat{W}$ that is diagonal in charge and $\hat{W}_\perp \equiv \hat{W} - \hat{W}_\parallel$ is the off-diagonal part. The behavior of Eq. (8.22) as a function μ for different OTOCs of interest is shown in Fig. 8.8. Note that Eq. (8.22) indicates that for $\mu \neq 0$, if one of the operators involved in the OTOC has non-zero overlap with $\hat{Q}$, then the out-of-time-ordered part does not saturate to zero, i.e., $\mathcal{F}_{\mu\neq 0}^{VW}(t_\infty) \neq 0$. This fact might also be of relevance for Hamiltonian systems if the operators considered overlap with the local energy density.

We can gain some further insight into the meaning of Eq. (8.22) by relating it to the superoperator formalism developed in Section 8.2.2. As we show in App. B.3, the saturation values, and indeed the long-time value of any superoperator, can be understood as a form of thermalization, wherein the initial state (in operator space), $|\tilde{V}(0)\rangle\langle\tilde{V}(0)|$, for

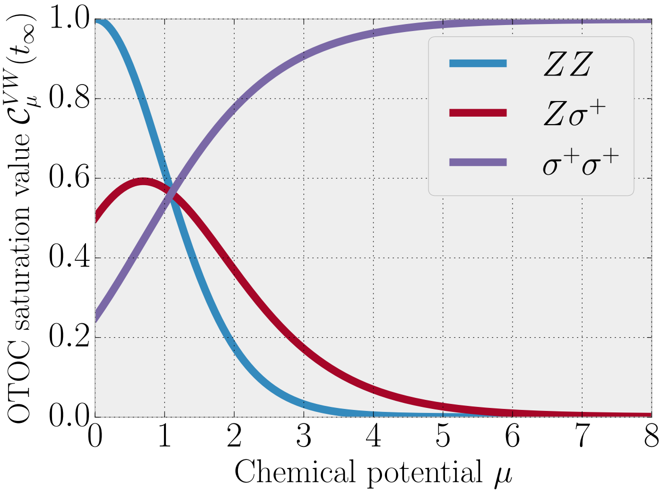

Figure 8.8.: Long-time saturation values of different OTOCs $\mathcal{C}^{WV}$, predicted by Eq. (8.22), as a function of the chemical potential μ.

the operator $\tilde{V} \equiv e^{-\frac{\mu}{4}\hat{Q}}\hat{V}e^{-\frac{\mu}{4}\hat{Q}}$ introduced in Eq. (8.21), becomes at long times locally indistinguishable from the 'thermal' state

$$\overline{|\tilde{V}(t_\infty)\rangle\langle\tilde{V}(t_\infty)|} = \mathrm{tr}\left(\tilde{V}_\parallel^\dagger \tilde{V}_\parallel\right)\frac{|e^{-\frac{\mu}{2}\hat{Q}}\rangle\langle e^{-\frac{\mu}{2}\hat{Q}}|}{Z_\mu} + \mathrm{tr}\left(\tilde{V}_\perp^\dagger \tilde{V}_\perp\right)\frac{e^{-\mu(\mathcal{L}_Q+\mathcal{R}_Q)}}{Z_\mu^2}, \tag{8.23}$$

where $Z_\mu = \mathrm{tr}\left(e^{-\mu\hat{Q}}\right)$. The latter part of this expression in Eq. (8.23) is none other than the Gibbs ensemble with respect to the conserved quantities $\mathcal{L}_Q, \mathcal{R}_Q$ defined in Section 8.2.2. This result suggests (in a manner we detail in App. B.3) that when considering objects like OTOCs or operator weights, the usual notion of thermalization should be supplemented by considering that of equilibration in operator space, as defined above.

The above result relies on averaging over all possible charge-conserving time evolutions without restrictions of locality, which is a valid approximation at time scales long compared to the system size. One might expect that this saturation value is in fact approached on a much shorter, L-independent time scale. This is indeed the case for example at $\mu = 0$ where the OTOCs relax to the above predicted long-time values either exponentially or as a power law, as we showed above. We observe a similar behavior at sufficiently small μ, as we show in Section 8.3.2. In the limit of $\mu \gg 1$, however, we find that the saturation of certain OTOCs can take a time which is proportional to the mean collision time between particles, and in the limit $\mu \to \infty$, the long-time value of the $\hat{\sigma}^+\hat{\sigma}^+$ OTOC in particular deviates from the above prediction by an $\mathcal{O}(1)$ value in an infinite system. For a finite system, this means that the OTOC first saturates to a prethermal plateau and only approaches its final value on a time scale that grows as $\sim L^2$. At $1 \ll \mu < \infty$, the plateau eventually crosses over to the predicted value, but only on time scales that are large compared to the average inter-particle spacing. We discuss this in Section 8.3.3.

8.3.2. Relaxation of OTOCs at $\mu \sim \mathcal{O}(1)$

We now confirm the predictions of the previous subsection regarding the long-time saturation values of OTOCs at finite μ, by computing their time-evolution numerically in the random circuit model. We also show that the relaxation to these long-time values exhibits the same hydrodynamic tails (at least for small μ) as the ones observed previously in Section 8.1.2.

As discussed at the beginning of Section 8.3, the mapping of the average OTOC to the classical partition function problem remains intact in the presence of finite μ, except for some additional Gibbs factors which can be incorporated into either (or both) of the boundary conditions. We can then evaluate the average OTOC using the same tensor network methods that we used at $\mu = 0$. The results for the OTOC between operators $\hat{Z}_0, \hat{Z}_0$ on the same site are shown in Fig. 8.9. We find that the OTOC indeed saturates to the value predicted by Eq. (8.22). Interestingly, for $\mu = 2$, the OTOC first drops below this value and then approaches it from below. Moreover, by plotting the distance from saturation, $\left|\overline{\mathcal{F}_\mu^{Z_0 Z_0}(t)} - \mathcal{F}_\mu^{Z_0 Z_0}(t_\infty)\right|$, we find that the hydrodynamical tail of the form $\left|\overline{\mathcal{F}_\mu^{Z_0 Z_0}(t)} - \mathcal{F}_\mu^{Z_0 Z_0}(t_\infty)\right| \propto t^{-1/2}$ is present also for finite small μ. Namely, we observe that the $\mu = 1/2$ OTOC decays in exactly the same manner as the one at $\mu = 0$, which has diffusive relaxation as discussed at length in the previous sections. We find deviations from the $t^{-1/2}$ behavior for larger chemical potentials, although these might correspond to some intermediate-time behavior. As we discuss in the following subsection, the finite μ behavior of OTOCs at short times can be very different from the one decribed so far in the $\mu = 0$ case.

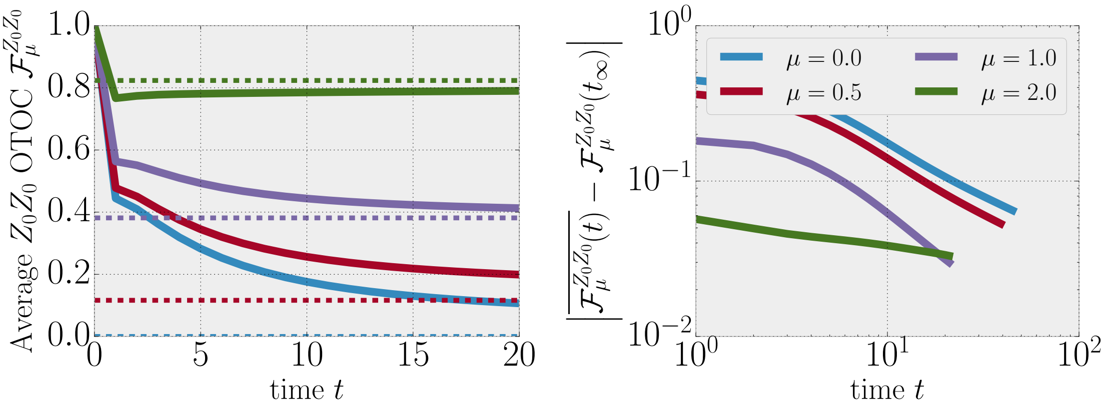

Figure 8.9.: Time evolution of the $\hat{Z}\hat{Z}$ OTOC on site zero for chemical potentials $\mu = 0, 1/2, 1, 2$ in the random circuit model. The left panel shows the OTOC approaching the saturation value predicted by Eq. (8.22) (dashed horizontal lines). For $\mu = 2$ the OTOC tends to the long-time value from below. The right panel shows the distance from this equilibration value as a function of time. The lines for $\mu = 0$ and $\mu = 1/2$ are parallel, indicating that the latter also exhibits the diffusive $t^{-1/2}$ decay discussed in Section 8.2.

8.3.3. $\mu \gg 1$ and OTOC diffusion

We next turn our attention to the behavior of OTOCs at low fillings, or large chemical potentials, and argue perturbatively that there is an additional structure arising in this limit, wherein the ballistic OTOC front does not appear at times that are short compared to $e^{2\mu}$. Moreover, certain OTOCs ($\mathcal{F}^{\sigma^+\sigma^+}$ in particular) can initially relax to a value different from the one predicted in subsection 8.3.1, only approaching their long-time limit at $t \gg e^{2\mu}$.

As discussed in Part I, and in Sec. Section 8.2.1, in the infinite temperature ensemble, i.e., at $\mu = 0$, OTOCs are closely related to the problem of operator spreading, sampling over all coefficients appearing in Eq. (8.10) with equal measures (see Eq. (8.11)). This explains the ballistic spreading of OTOCs, which in this language is a simple consequence of the fact that there are exponentially more long Pauli strings than short ones. However, as μ becomes larger the OTOC will be increasingly dominated by states with a few charges. Here, we set out to explain how this affects their space-time structure and saturation behavior in the limit $\mu \gg 1$. In this limit we can expand the OTOC in powers of $e^{-\mu}$ and find that the terms in this perturbative expansion describe a diffusively, rather than ballistically, spreading OTOC. This diffusive behavior is exhibited by the three lowest orders of the expansion, and we conjecture that it survives up to a time scale $t \sim \mathcal{O}(e^{2\mu})$, at which point the perturbation theory breaks down. While the method is only well controlled in the $\mu \gg 1$ limit, there is excellent qualitative agreement between the results of this section and those from TEBD even when $\mu \approx 3$ (see Fig. 8.11). Thus, we believe the results in this section could be useful in developing a qualitative description of the early time behavior of OTOCs in low temperature strongly coupled systems.

The starting point of the perturbative description is given by expanding the boundary conditions in orders of $e^{-\mu/4}$ as

$$e^{-\frac{\mu}{4}\hat{Q}} = \prod_{r=1}^{L}\left(\hat{P}_r + e^{-\frac{\mu}{4}}\hat{Q}_r\right) \qquad\qquad \hat{P}_r = \mathbb{1} - \hat{Q}_r. \tag{8.24}$$

When expanding this product, the different terms correspond to different number of 'particles', as defined in Section 8.1.1 (see Fig. 8.2 in particular). Since the total number of such particles is conserved during evolution with the circuit, it has to be the same in both boundary conditions. Gathering all terms with the same power of $e^{-\mu}$, we find that the average value of the OTOC can be expanded as a power series of the form

$$\overline{\mathcal{F}_{\mu}^{VW}}(t) \approx \sum_{N} e^{-N\mu}\mathcal{F}_{(N)}^{VW}(t), \tag{8.25}$$

where the $\mathcal{O}(e^{-N\mu})$ term corresponds to initial and final conditions with $2N + \lambda_V + \lambda_W$ particles. $\mathcal{F}_{(N)}^{VW}(t)$ can then be evaluated by considering the same partition function as defined in Section 8.1.1 but with the boundary conditions restricted by the total number of particles, which can therefore be more efficiently calculated, even using exact diagonalization techniques. Note that, since for $\mu \gg 1$ the average density of particles is $n \approx e^{-\mu}$, Eq. (8.25) is effectively an expansion in the charge density.

Here we focus on the $\hat{\sigma}^{+}\hat{\sigma}^{+}$ OTOC which has a non-trivial behavior even at zeroth order; other OTOCs show similar features [3]. The zeroth order contribution can be computed from a random walk problem involving a pair of particles that annihilate upon meeting each other, which has an exact solution as we show in App. B.4. One particularly interesting property of the solution is the absence of a ballistically propagating front. Indeed, as suggested by the formulation of the problem as a two-particle random walk, the spreading of the OTOC front is entirely diffusive, depending only on the combination $r/\sqrt{t}$, where r is the spatial separation of the operators in the OTOC. We demonstrate this in the left panel of Fig. 8.10. This result is in contrast to the behavior seen at $\mu = 0$ in Fig. 8.3 (and general expectations of ballistic propagation), and as we argue below is a property of the perturbative expansion that is in general valid up to a μ-dependent time scale.

Furthermore, if we consider the same OTOC at a fixed distance r as a function of time, we find a double plateau structure: it first saturates to the value $\frac{1}{2} - \frac{1}{\pi}$ on an $\mathcal{O}(r^2/D)$ timescale, where D is the charge diffusion constant defined by Eq. (7.4), and only goes to zero, as predicted by Eq. (8.22), when the particles reach around the whole system, at times $\mathcal{O}(L^2/D)$. This is illustrated on the right panel of Fig. 8.10. As we show in App. B.4, this latter result, the non-commutativity of the $L \to \infty$ and the $t \to \infty$ limits, can be understood from the fact that in an infinite system two random walkers have a finite probability of avoiding each other forever, while they have to meet eventually if the system is finite. Moreover, the mapping from the OTOC to the above random walk

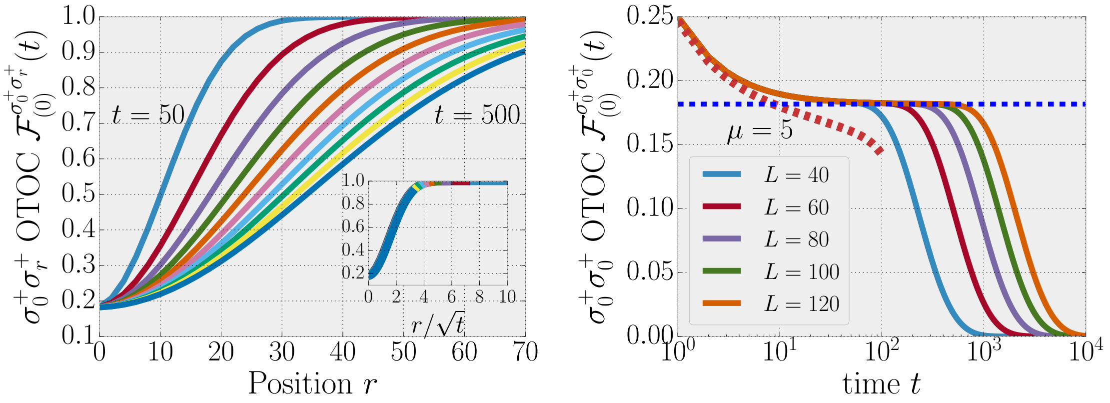

Figure 8.10.: The OTOC $\mathcal{F}$ between $\hat{\sigma}_0^+$ and $\hat{\sigma}_r^+$ at infinite chemical potential. Left: The OTOC as a function of initial distance r for times $t = 50, 100, \dots, 500$ in an infinite system. The OTOC spreads diffusively and saturates to a 'prethermal' plateau behind the front. The inset shows the data collapse when the position is rescaled as $r \to r/\sqrt{t}$. Right: The OTOC first saturates to the aforementioned prethermal value, $\frac{1}{2} - \frac{1}{\pi}$ (dashed horizontal line), as $1/\sqrt{t}$. Then at a later timescale, $t \sim L^2$, it decays to zero. At late times its value decreases as $\exp(-\pi^2 t/L^2)$. The red dashed line shows the next order prediction at $\mu = 5$, which indicates that the plateau survives up to a time scale that diverges with μ.

problem also holds if we consider similar random circuits in higher dimensions, in which case the probability for crossing paths is smaller, and the deviation from the thermal expectation value in the thermodynamic limit is even larger.

Computing the next term, $\mathcal{F}_{(1)}^{\sigma^+\sigma^+}$, which is of order $\mathcal{O}(e^{-\mu})$, we find that it increases as $\sqrt{t}$ up to an $\mathcal{O}(L)$ value, as shown in the inset of Fig. 8.11. Similarly, we find that the ratio $\mathcal{F}_{(2)}^{\sigma^+\sigma^+}/\mathcal{F}_{(1)}^{\sigma^+\sigma^+}$ of the second and first order terms (not shown here) also increases as $\sqrt{t}$. This suggests that the perturbative expansion is valid up to a time scale of order $t \sim e^{2\mu}$, at which point all terms become of comparable size. This time scale has a simple physical interpretation. $e^{\mu} \approx 1/n$ is the average spacing between particles. Since individual particles diffuse, their *mean collision time* scales as quadratically with their distance, making it proportional to $e^{2\mu}$. We thus find that the perturbative expansion breaks down when the interactions between particles become relevant.

While the second order contribution does lead to a speed-up of the spreading of the OTOC compared to the $\mu = \infty$ result shown in Fig. 8.10, it is still diffusive as also illustrated by the same inset. This suggests that the diffusive behavior persists up to the aforementioned $\mathcal{O}(n^{-2})$ time scale, that is up to the mean collision time. Therefore, the $\hat{\sigma}^+\hat{\sigma}^+$ OTOC will saturate to the prethermal plateau seen in Fig. 8.10, if μ is sufficiently large, indicating that the scrambling time [239, 259] associated to saturation of the OTOC is bounded by the time it takes for the particles to interact. While the fact that single-particle physics is diffusive is somewhat particular to our noisy setup, it is natural to expect that in deterministic systems one would also have separate regimes of different OTOC behavior at times short (long) compared to the collision time. Recent results support this conjecture [602].

As shown by Fig. 8.11, the expansion up to $\mathcal{O}(e^{\mu})$ agrees well with numerical TEBD results even for $\mu = 3$ at short times $t \leq 7$. To confirm the results from the perturbative expansion we also computed the $\hat{\sigma}^+\hat{\sigma}^+$ OTOC exactly at different finite μ, using the exact partition function (8.21). We find that by increasing μ, it becomes harder to converge in

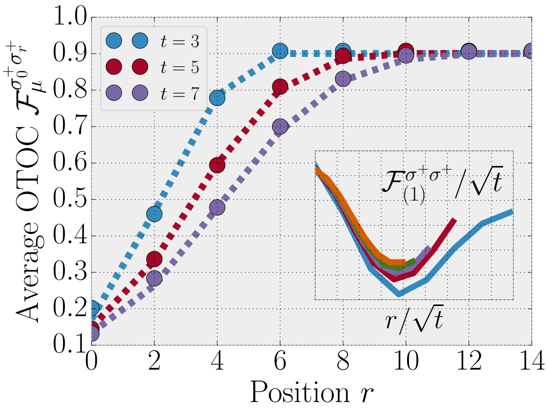

Figure 8.11.: Comparison of the perturbative expansion to TEBD results at short-times for the average $\hat{\sigma}^+\hat{\sigma}^+$ OTOC at chemical potential $\mu = 3$. Dots: TEBD results averaged over 100 circuits; dashed lines: perturbative expansion at $\mathcal{O}(e^{-\mu})$. The perturbative result agrees very well with the TEBD numerics up to the times considered. Inset: the $\mathcal{O}(e^{-\mu})$ correction to the OTOC $\mathcal{F}_{(1)}^{\sigma_0^+\sigma^+}$. We observe an approximate collapse of the data when $\mathcal{F}_{(1)}^{\sigma_0^+\sigma_r^+}/\sqrt{t}$ is plotted as a function of $r/\sqrt{t}$, indicating that the OTOC is still diffusive in nature.

the tensor-network evaluation of the partition function, limiting us to relatively small μ and short times. Nevertheless, we observe a pronounced slow-down of the OTOC spreading even for $\mu = 2$ up to times $t \approx 20$, as shown in Fig. 8.12.

In summary, we find that a variety of intriguing phenomena can occur in OTOCs at early times when the available space for the dynamic is restricted by a finite, large chemical potential. The most robust of these seems to be the initial diffusive spreading of the OTOC at early times. Whether this initial behavior has some bearing on the shape of the OTOC front at later times is an interesting question for further study. Finally, let us comment on the applicability of our results for deterministic dynamics. At high charge densities, or small chemical potentials, we expect that our previous arguments continue to hold, indicating that a strongly interacting deterministic system should appear effectively noisy for the slow variables. Therefore, the result that increasing the chemical potential leads to a decrease in v_B should generalize. This is also consistent with a subsequent paper, Ref. [597], where the authors also find a pronounced slowdown of the butterfly front with decreasing temperature in a Hamiltonian system. The situation is different in the large-μ limit. In this case, at early times, the interactions of the particles are negligible,

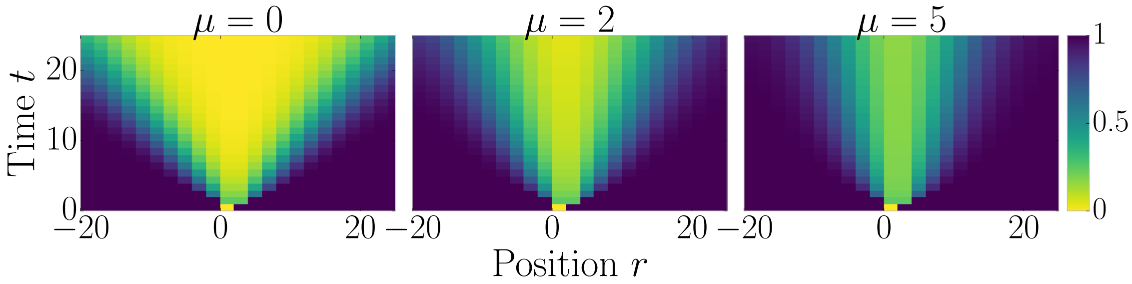

Figure 8.12.: Space-time spreading of the $\hat{\sigma}^+\hat{\sigma}^+$ OTOC $\mathcal{F}_\mu^{\sigma_0^+\sigma_r^+}$ for different the chemical potentials $\mu = 0, 2, 5$. The ballistic light cone observed for $\mu = 0$ slows down and gives way to a diffusively spreading OTOC at large μ.

so the dynamics is dominated by single-particle physics. In our case, individual particles behave diffusively due to the noise inherent in the circuit, which led to the lack of ballistic propagation we observed above. In non-random systems, on the other hand, diffusion originates from interactions, so at early times we expect to see a ballistic front propagating at the single-particle group velocity[14,15]. The behavior of deterministic circuits at finite filling was studied in a recent paper [602]; interestingly, the authors claim that there is an analogue of the early- to late-time cross-over we observed in the random circuit, even in the deterministic case. There, the initial free-particle dynamics eventually crosses over to a late-time regime, dominated by collisions; this latter regime has a much smaller v_B, proportional to the charge density, which becomes arbitrarily small as $\mu \to \infty$, somewhat reminiscent of our random circuit results.

---

[14] Note that, while in such noninteracting systems, a ballistic operator front exists, there is no *scrambing* of the operator, in the sense that it becomes a superposition of only simple, local operators, without populating long, non-local Pauli strings. This manifests in the OTOC $\mathcal{C}$ decaying back to zero after the front has passed, instead of saturating to a finite value as in chaotic systems.

[15] This is true on systems where interaction effects dominate over *disorder*. One can also find diffusive transport in non- (or weakly) interacting systems as a consequence of particles scattering off impurities in three dimensional solids (while Anderson localization suppresses transport altogether in 1 and 2D). It would be interesting to see if our results in this section bear any relevance for these systems.

9. Dissipation-assisted operator evolution

In the previous chapter, we discussed the question of operator spreading, assuming that the underlying transport properties are well-described by diffusion, as was the case in our random circuit models. Here, we shift our attention to the issue of how such dissipative transport emerges from unitary dynamics in the first place. As we saw, non-local operators effectively form a 'bath' that is necessary for dissipation to arise. Here, we aim to shed some light on the internal behavior of this effective bath, and how it effects the details of transport, such as the precise value of the diffusion constant. Our discussion culminates in an explicit numerical scheme for calculating transport properties, which we use to calculate diffusion constants of various deterministic models with a very high precision.

In Section 8.2, we developed a simple picture of the dynamics of a conserved density, such as $\hat{Z}_0(t)$. It splits up into two components, a diffusive part, made up by similar densities $\hat{Z}_r$, and a remaining part which spreads ballistically. The dissipative nature of diffusion manifests itself in a slow conversion of operator weight from the former to the latter. As appealing as this picture is, and while it appears to correctly capture the qualitative features of OTOCs, it certainly misses some important features of diffusive dynamics. Crucial of these is the issue of *backflow*, from longer to shorter operators. In the random circuit, we were able to calculate the behavior of the diffusive part by considering a simple '1-particle' random walk (Eq. (7.2)) in the space spanned by the local densities $\{\hat{Z}_r\}$, without having to consider more complicated processes, where $\hat{Z}_0$ first grows to a multi-site operator and then shrinks back to an on-site density (consider, $\hat{Z}_0 \to \hat{\sigma}_0^+ \hat{\sigma}_1^- \to \hat{Z}_1$, for a simple example). The reason for this simplification in the random circuit case is clear: it is due to phase cancellations. These contributions come with random signs, and therefore quickly average to zero[1].

The situation is quite different in a deterministic system: in that case, the dynamics within the subspace of local densities is coupled to the dynamics of larger operators, due the the aforementioned backflow events. At first sight, it would therefore seem that in order to correctly capture the diffusive transport, one would need to simulate the full many-body dynamics. However, there are physical reasons to believe that this is not the case, and that the effect of backflow is limited to processes where the operator never becomes *too* large. First of all, note that one expect diffusive transport to set in after some initial local thermalization time, t_{loc}, which is an $\mathcal{O}(1)$ quantity in the strongly interacting regime we wish to consider. It therefore stands to reason what the effect of backflow from operators of size $\gg v_{\text{B}} t_{\text{loc}}$ should not play a significant role. One can argue for this, on an intuitive level, using the lessons from the random circuit case. Even if there is no explicit noise in the dynamics, *dephasing* nevertheless arises due to interactions, and leads to cancellations between the contributions from the large number of different possible paths in the space of operators. This discussion is very similar in spirit to the approximations that led to the hydrodynamic equations in Section 2.3: there is a separation of scales between 'slow' and 'fast' processes, the latter being characterized by an autocorrelation time that is set by microscopic scales. One then only needs to consider backflow processes that occur within this relatively small time window. In the following, we will to develop an efficient scheme

---

[1] Note that not only is the average contribution from these processes zero, but their typical size is also very small after some early-time behavior. This can be deduced from the fact that the variance $\overline{\left(c_{Z_0}^{Z_r}(t)\right)^2} - \left(\overline{c_{Z_0}^{Z_r}(t)}\right)^2$ quickly becomes negligibly small; see Fig. 8.6.

for incorporating backflow effects to compute transport properties numerically with high precision. First, however, we make a small detour, and discuss a way of making the intuition more precise.

9.1. The memory matrix formalism

Before discussing our numerical scheme, we first review the memory matrix formalism (also known as projection operator technique) of Zwanzig and Mori [279, 293, 335–337, 339]. While we will not use this directly, it provides a very useful conceptual framework in which to understand the kind of approximations we will make below.

Our goal is to calculate dynamical correlations of the form $C_{ab}(t) \equiv \langle \mathcal{O}_a(t)\mathcal{O}_b\rangle_{\text{eq}}$, evaluated in an equilibrium thermal ensemble with respect to the Hamiltonian H that governs the dynamics. We will be interested in the case when $\mathcal{O}_{a,b}$ are local densities of some conserved quantity; as we saw in Section 2.3, $C_{ab}(t)$ then contains all the information needed to characterize transport in the system, at least in the linear response regime[2].

The starting point is to rewrite the correlation function as a propagator in the space of operators of the form

$$C_{ab}(t) \equiv \langle \mathcal{O}_a(t)\mathcal{O}_b\rangle_{\text{eq}} = \langle \mathcal{O}_b|e^{i\mathcal{L}t}|\mathcal{O}_a\rangle, \tag{9.1}$$

where $\mathcal{L}$ is the Liouvillian superoperator, acting on an operator $\mathcal{O}$ as $\mathcal{L}[\mathcal{O}] \equiv -i\partial_t|\mathcal{O}\rangle = -i[H,\mathcal{O}]$ and we have defined an inner product[3] between operators as $\langle \mathcal{O}_b|\mathcal{O}_a\rangle \equiv \langle \mathcal{O}_b^\dagger\mathcal{O}_a\rangle_{\text{eq}}$.

The next step is to split the space of operators into two parts, one containing 'slow' variables and another containing 'fast' ones. At this point, this distinction is completely arbitrary, except that the $\mathcal{O}_a$ whose correlations we wish to compute should be included among the slow variables. If this is granted, the following formal manipulations go through independently of which other operators we include in the 'slow' subspace. However, as we shall soon see, the formalism is only useful if there is a true separation of scales between the two, with autocorrelations within the fast space decaying much more rapidly. One also wants the slow subspace to be sufficiently small, containing only polynomial in system size many operators. As a simplest example, one could just imagine the slow space being spanned entirely by the conserved densities. We shall return to this question below.

Given a set of slow variables, $\{\mathcal{O}_a\}$, one can define a projection superoperator, $\mathcal{P}$ that projects onto the subspace spanned by them[4]. The fast subspace then corresponds to the projector $\mathcal{Q} \equiv 1-\mathcal{P}$. The key step in deriving the memory matrix formalism is to rewrite the time-evolution as

$$e^{i\mathcal{L}t} = e^{i\mathcal{Q}\mathcal{L}t} + i\int_0^t \mathrm{d}t' e^{i\mathcal{L}t'}\mathcal{P}\mathcal{L}e^{i\mathcal{Q}\mathcal{L}(t-t')}. \tag{9.2}$$

This is an exact operator identity, which can be proven by either taking a time derivative, or by performing a Laplace transformation on both sides. $e^{i\mathcal{Q}\mathcal{L}t}$ describes propagation

---

[2] Note that at infinite temperature, $C_{ab}(t)$ is also the operator spreading coefficient from $\mathcal{O}_b$ to $\mathcal{O}_b$. These correspond to what we called the 'diffusive' part of the operator.

[3] This is indeed an inner product when the equilibrium density matrix has full rank, i.e. at any non-zero temperature. Also, note that in most discussions of memory matrices, a different definition is used, although the two coincide at infinite temperature. At the general level of discussion here, the precise choice of inner product is unimportant.

[4] The observables $\mathcal{O}_a$ will typically be non-orthogonal, as characterized by the overlap matrix $S_{ab} \equiv (\mathcal{O}_b|\mathcal{O}_a) = \langle \mathcal{O}_b^\dagger\mathcal{O}_a\rangle_{\text{eq}}$, given by their thermal correlations. To get the projector $\mathcal{P}_\parallel$ one can instead define the orthonormal basis $|\tilde{\mathcal{O}}_a) \equiv \sum_b (S^{-1/2})_{ab}|\mathcal{O}_b)$, and then define $\mathcal{P}_\parallel \equiv \sum_a |\tilde{\mathcal{O}}_a)(\tilde{\mathcal{O}}_a|$. Note that this contains an implicit temperature-dependence.

entirely within the fast subspace. The intuitive meaning of the above equation is therefore that $t - t'$ is the first time after 0 when the operator comes back into the slow subspace[5].

We can now use Eq. (9.2) to write down an equation of motion for $|\mathcal{O}_a\rangle$. Using also that $\mathcal{P} = \sum_c |\mathcal{O}_c\rangle\langle\mathcal{O}_c|$ (assuming, for simplicity, that we are working with variables that have already been orthogonalized), we arrive at the following key expression:

$$\begin{aligned}
\partial_t|\mathcal{O}_a(t)\rangle &= \sum_c \Omega_{ac}|\mathcal{O}_c(t)\rangle - \sum_c \int_0^t \mathrm{d}t'\,\Gamma_{ac}(t-t')|\mathcal{O}_c(t')\rangle + |f_a(t)\rangle \\
\Omega_{ac} &\equiv \langle\mathcal{O}_c|\partial_t\mathcal{O}_a\rangle \\
\Gamma_{ac}(t-t') &\equiv \langle\partial_t\mathcal{O}_c|\mathcal{Q}e^{i\mathcal{Q}\mathcal{L}\mathcal{Q}t}\mathcal{Q}|\partial_t\mathcal{O}_a\rangle \\
|f_a(t)\rangle &\equiv \mathcal{Q}e^{i\mathcal{Q}\mathcal{L}\mathcal{Q}t}\mathcal{Q}|\partial_t\mathcal{O}_a\rangle.
\end{aligned} \tag{9.3}$$

This equation of motion tells a simple story, especially if we keep in mind the intuition behind the separation of slow and fast variables. Ω describes the intrinsic, non-dissipative dynamics of the slow subspace, and can often be ignored in practice. Γ is the heralded *memory matrix*. It describes processes wherein a slow variable at time t' evolves to another slow variable at time t propagating entirely through the fast subspace. This is exactly what we described by the word *backflow* above. Finally, $|f\rangle$ is a *noise term*, which captures the fluctuating force exerted on the slow variable by the fast degrees of freedom. In this spirit, Eq. (9.3) is also sometimes called a *generalized Langevin equation*. This equation makes clear the intuition behind fast and slow modes: if there is indeed a separation of time scales, then on the times relevant for the dynamics of $\mathcal{O}_a$, the memory matrix will decay rapidly and the dynamics will be well approximated by a Markov process. Notably, the correlations of the noise are also given by the memory matrix,

$$\langle f_c(t')|f_a(t)\rangle = \Gamma_{ac}(t-t'), \tag{9.4}$$

an example of a fluctuation-dissipation relation.

To connect with our previous discussions of diffusion, it is useful to consider a case where the slow subspace contains only local densities of single conserved quantity, $\hat{q}(x,t)$. The label a then simply becomes the spatial coordinate x, which we now treat as a continuum variable for simplicity. Let us take the expectation value of the operator in some unspecified state ρ ($\langle\mathcal{O}\rangle = \langle\rho|\mathcal{O}\rangle$, using the infinite temperature scalar product). The equation of motion then reads (ignoring the Ω term and assuming translation invariance)

$$\partial_t\langle\hat{q}(x,t)\rangle = -\int \mathrm{d}x' \int_0^t \mathrm{d}t'\,\Gamma(t-t', x-x')\langle\hat{q}(x',t')\rangle + \langle f(x,t)\rangle. \tag{9.5}$$

Comparing this with Eq. (2.12), we recognize that $\Gamma(x,t)$ is essentially the space-time dependent diffusion constant $D(x,t)$. After a Fourier transform, the two are related as $\Gamma(k,t) = k^2 D(k,t)$. The diffusion constant that characterizes transport can be obtained by taking appropriate limits of this function. Eq. (9.5) also contains a noisy driving term which we neglected in Eq. (2.12).

Another way to connect Eq. (9.3) to transport is by considering the correlations with which we started. Since by definition, $|f_a(t)\rangle$ lives in the fast subspace, it drops out and one simply finds

$$\partial_t C_{ab}(t) = \sum_c \Omega_{ac} C_{cb}(t) - \sum_c \int_0^t \mathrm{d}t'\,\Gamma_{ac}(t-t') C_{cb}(t'). \tag{9.6}$$

---

[5] One could also write down a slightly modified version of Eq. (9.2) where the order of $e^{i\mathcal{L}(t')}$ and $e^{-i\mathcal{Q}\mathcal{L}(t-t')}$ is exchanged. In that case, we would parametrize the time evolution in terms of the *last* time when the operator is in the slow subspace before t.

This shows that indeed Γ is the key object, that contains all the linear response transport properties of the system.

As emphasized above, the splitting of the space of operators into slow and fast can be done in any number of different ways. The conceptually simplest choice is to make the slow subspace contain the conserved densities and nothing else, but this is not necessarily the best solution in practice. Instead, one would like to make the separation of time scales between the two as large as possible, while keeping the slow subspace small enough to be manageable. One might, for example add *products* of local densities (or, at least, they small momentum components) also to the list of slow variables. This suggests two natural ways of approximating the exact formula (9.6). One is to work with a fixed slow subspace, but truncate the time integral in the memory term at some time $t - t' \leq t_{\mathrm{mem}}$. One would then hope for a quick convergence of the result as a function of increasing t_{mem}. The other option is to fix a relatively small t_{mem}, but gradually increase the size of the slow subspace, until the characteristic time of the memory matrix becomes sufficiently small. In the following, we will explore a combination of these two approaches, albeit in a slightly modified language.

9.2. Dissipation-assisted evolution

While the memory matrix formalism provides a conceptually elegant way of connecting macroscopic transport properties to the underlying microscopic evolution, it does not directly lend itself to *ab initio* calculations, except in particular cases where the system is close to some fine-tuned point [340, 341]. Here, we describe a scheme for numerically approximating dynamical correlation functions for *generic* models in 1D, building on the intuition developed above, regarding backflow and memory effects.

Our method can be thought of as a way of generating approximations to the memory matrix with increasing accuracy, controlled by which contributions to $C_{ab}(t)$ we keep. Based on the notion that the 'fast' degrees of freedom act as a bath for the slow ones, we aim to construct an explicitly non-unitary evolution for initially local operators, designed to correctly capture the parts of this operator that contribute to the hydrodynamic correlations. In particular, our discussion above leads us to believe that the most relevant contributions should come from short Pauli strings, acting on at most a handful of sites. Therefore, we shall attempt to capture these correctly, at the expense of larger operators which we expect to have very short memory times. We will focus on the case of infinite temperature, although we expect the method to work well at finite but large temperatures as well.

9.2.1. Artificial dissipation in operator space

Using the assumption that backflow effects are weak, we aim to apply a truncation that affects non-local operators, without disturbing local ones. Let us denote ℓ_μ the support of a Pauli string σ^μ, i.e., the number of sites where it acts differently from the identity. We shall refer to this as the 'length' of the Pauli string. We introduce an artifical dissipation by discarding non-local operators. This is done by the dissipation super-operator $\mathcal{D}_{\ell^*,\gamma}$, parametrized by a cutoff length ℓ^* and a dissipation strength γ, which acts on a Pauli string as

$$\mathcal{D}_{\ell_*,\gamma}[\sigma^\mu] = \begin{cases} \sigma^\mu & \text{if } \ell_\mu \leq \ell_* \\ e^{-\gamma(\ell_\mu - \ell_*)}\sigma^\mu & \text{otherwise.} \end{cases} \tag{9.7}$$

The cutoff length is introduced to ensure that the physically most relevant local operators, such as conserved densities, are not affected by the dissipator. The strength γ allows this

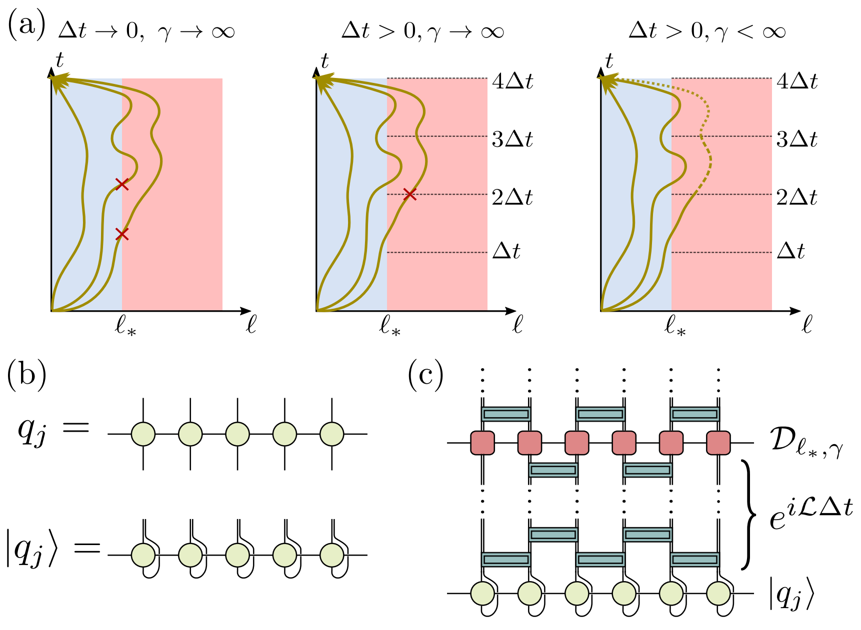

Figure 9.1.: (a) Sketch of the non-unitary evolution defined by Eq. (9.8) as a sum over paths in operator space. In the hard projection limit, $\Delta t \to 0$, $\gamma \to \infty$, all paths that leave the $\ell \leq \ell_*$ subspace at any point are immediately discarded. Keeping $\gamma = \infty$, but making Δt finite, we keep paths that wander off from this subspace but return before the next integer multiple of Δt. Finally, when both Δt and γ are finite, all paths enter the calculation of the correlator, but the weight of those that spend a lot of time outside the 'slow' subspace is gradually reduced. (b): The operator (MPO) q_j can be reinterpreted as a state (MPS) $|q_j\rangle$ on a doubled Hilbert space. (c): One period of the DAOE as a tensor network. $|q_j\rangle$ is evolved with the TEBD algorithm up to time Δt. Then the dissipator $\mathcal{D}_{\ell_*,\gamma}$ is applied as a bond dimension $\ell_* + 1$ MPO.

to be a soft cutoff and lets the operator explore more of the full Hilbert space.

We then define a modified time evolution, by applying the dissipator every Δt time. That is, at time $t = N\Delta t + \delta t$ (for $N \in \mathbb{N}$ and $\delta t < \Delta t$), we consider the time evolved operator

$$|\tilde{q}_j(t)\rangle \equiv e^{i\mathcal{L}\delta t} \left(\mathcal{D}_{\ell_*,\gamma} e^{i\mathcal{L}\Delta t}\right)^N |q_j\rangle, \tag{9.8}$$

where the tilde is meant to denote that we are not dealing with the true, unitarily evolved operator. We name this the *dissipation-assisted operator evolution*, or DAOE for short. In this setup, Δt provides yet another way of tuning the strength of the dissipation, recovering unitary dynamics in the limit $\Delta t \to \infty$. Intuitively, Δt and $1/\gamma$ play a similar role, limiting the amount of time an operator is allowed to spend outside the $\ell \leq \ell^*$ subspace. Indeed, one can show that in the limit $\gamma \ll 1$, the dynamics only depends on the ratio $\gamma/\Delta t$[6] [4].

We can think of DAOE as summing up the contributions of the memory matrix successively, or alternatively, in a path integral language, depicted in Fig. 9.1. ℓ^* functions as the cut-off between slow and fast variables[7], while Δt and $1/\gamma$ restrict the memory time

---

[6] One could also make the dissipation continuous in time, by taking the limit $\Delta t \to 0$ while keeping $\Delta t/\gamma$ fixed. We shall not explore this further here.

[7] In principle, we could further restrict the slow subspace to only contain products of conserved densities; this is easily done in the case of spin/charge conservation, but less so when we consider energy density. Moreover, even in the $U(1)$ case, there are off-diagonal operator that have long-time tails, such as $\sigma_r^+ \sigma_{r+1}^-$, which has a characteristic $t^{-3/2}$ decay. Therefore, we find it better to keep all short operators and only dissipate long ones.

we allow. In the hard projection limit, $\Delta t \to 0$, $\gamma \to \infty$, we are summing up only those paths that never leave the slow subspace; this is analogous to the term Ω in Eq. (9.6)[8]. Making either Δt or γ finite allows for memory effects, or paths that wander out of the slow space. but limiting the time they are allowed to spend there, cutting off the memory matrix at time $t_{\text{mem}} \sim \Delta t/\gamma$.

9.2.2. Tensor network representation

How to calculate $|\tilde{q}_j(t)\rangle$? By making the cut-off soft (as opposed to a hard projection, $\gamma \to \infty$ and $\Delta t \to 0$), we in principle need to work in the full space of operators. As such, it is not immediately obvious whether we have gained anything by introducing the dissipator. However, since the weight associated to large Pauli strings is significantly reduced, we hope that $|\tilde{q}_j(t)\rangle$ can in fact be efficiently compressed, without having to keep track of exponentially many coefficients.

A simple way of going about this, which also allows us to avoid finite-size effects, is to represent it as a matrix product state, which can be obtained from the more natural matrix product operator (MPO) representation, by combining the two physical legs of the local tensors into a single leg (see Fig. 9.1(b)). The unitary evolution of this state can be calculated straightforwardly with standard MPS methodw, for example by an appropriate version (doubling physical Hilbert spaces) of the TEBD algorithm mentioned in Section 2.4. In this language, the dissipator itself becomes an MPO on the enlarged Hilbert space; applying this to an MPS is also straightforward.

$\mathcal{D}_{\ell_*,\gamma}$ in fact has an exact MPO representation with bond dimension $\ell_* + 1$. We label the local basis 'states' by $n = \mathbb{1}, X, Y, Z$ (generalization to higher spin is straightforward). We then write the local MPO tensor, $W_{ab}^{nn'}$, as a matrix acting on the virtual indices $a, b = 0, 1, \ldots, \ell_*$. They read

$$W^{\mathbb{1}\mathbb{1}} = \begin{pmatrix} 1 & & & & \\ & 1 & & & \\ & & \ddots & & \\ & & & 1 & \\ & & & & 1 \end{pmatrix} \qquad W^{XX} = W^{YY} = W^{ZZ} = \begin{pmatrix} 0 & 1 & & & \\ & 0 & 1 & & \\ & & \ddots & \ddots & \\ & & & 0 & 1 \\ & & & & e^{-\gamma} \end{pmatrix}, \tag{9.9}$$

all others being zero. The MPO is contracted with the vector $v_L = (1, 0, \ldots, 0)$ on the left, and $v_R = (1, \ldots, 1, 1)$ on the right. It acts as a 'clock', shifting the virtual index by one for every non-trivial operator, until ℓ_* is reached, and multiplying the factor $e^{-\gamma}$ afterwards. It is easy to check that this reproduces the desired result.

In the MPS language, performing singular value decompositions across various bonds, and throwing away very small singular values (which is already part of e.g. the TEBD algorithm) naturally accomplishes the compression we seek. Of course, this compression will only be approximate, its precision characterized by the size of the singular values we discard. Our key observation is that the dissipator *stops the growth of operator entanglement*, making it possible to follow the evolution of $|\tilde{q}_j(t)\rangle$ to *arbitrary* times, without significant truncation errors.

This requires some explanation. What do we mean by operator entanglement? At this point, the reader has probably gotten used to us treating operator as states in an enlarged Hilbert space, which the notation $|q_j\rangle$ is also meant to emphasize. In this language, it becomes natural to consider Schmidt decompositions of an operator, e.g. between two halves of a one-dimensional chain (this is in fact exactly the aforementioned singular value

---

[8] Previously, we argued that Ω is usually negligible. This is true if we choose the slow subspace to only consist of local densities. As we increase what we include in the slow variables, we shuffle more-and-more contributions from Γ to Ω, making it increasingly important.

decomposition); this is especially natural in the MPO/MPS language of Fig. 9.1(b). From the resulting Schmidt spectrum we can then calculate the Rényi entropies of the operator, $S_\alpha[\tilde{q}_j]$, in much the same way as we would for a state[9]. As an initial local operator grows and becomes increasingly scrambled, its entropies also grow in time. A generalization of the minimal polymer picture [277] suggests that the von Neumann entropy of the operator should grow linearly in generic cases[10]. This implies that evolving operators is just as hard as evolving states, in both cases one has to deal with an exponentially growing complexity, and a finite-χ approximation tends to break down at times $\sim \log \chi$.

However, we find that applying the dissipator *reduces* the operator entanglement, and in fact this effect always becomes dominant at long times. As a result, while $S_1[\tilde{q}_j(t)]$ grows initially, it eventually reaches a peak and starts decreasing, as shown by Fig. 9.2(a). This situation is reminiscent of the entanglement of a quantum state subjected to both unitary dynamics and weak local measurements [543, 604–607]. There, one finds a phase transition, where the entanglement grows unbounded for sufficiently weak measurements, but saturates when the measurements are strong. Our case is different, however, in that the 'measurement' realized by $\mathcal{D}_{\ell^*,\gamma}$ is a *global* (weak) measurement. This means that it reduces the entanglement more strongly than local measurements do, and it eventually always wins over the unitary dynamics that generates the entanglement. A similar effect for operator entanglement of a density matrix was noticed very recently in the context of noisy quantum circuits in Ref. [608].

For our calculations, this means that if we choose our maximal bond dimension such that $\log \chi$ is sufficiently large compared to the size of the peak in the operator entanglement, then we are able to capture the evolution without significant errors up to long times. Of course, the χ one needs will depend on the strength of the dissipation, as characterized by the parameters $\ell^*, \gamma, \Delta t$. This will put a limit to how weak a dissipation we can apply while maintaining a low error threshold. The method is useful is this dissipation is already weak enough to allow us to make predictions about the physical (zero dissipation) limit. We shall demonstrate that this is indeed the case for several models of interest.

Let us make an important comment here. At first glance, it might look tempting to consider the hard cut-off limit, $\Delta t \to 0$, $\gamma \to \infty$. This amounts to replacing the Liouvillian with its restricted form, $\mathcal{L} \to \mathcal{P}_{\ell^*} \mathcal{L} \mathcal{P}_{\ell^*}$, where $\mathcal{P}_{\ell^*} \equiv \lim_{\gamma\to\infty} \mathcal{D}_{\ell^* \gamma}$. This completely restricts the dynamics to a much smaller space of operators[11]. One could then try to gradually increase ℓ^* to converge to physical results. While we believe that such a scheme should work *in principle*, it does not perform well *in practice*. The reason for this is that the projected dynamics is still completely unitary (a manifestation of the *quantum Zeno effect*). Therefore, there is no decrease in entanglement, $S_1[\tilde{q}_j(t)]$ simply saturates to a value that is limited by the projection, but grows rapidly with ℓ^*. As a consequence, making the dissipation *weaker* (by either making Δt or γ finite) actually makes it *easier* to simulate the dynamics: it allows operators to leak outside the $\ell \leq \ell^*$ subspace and be discarded.

---

[9] First, one has to normalize the (squared) Schmidt values as $\Lambda_\alpha \to \Lambda_\alpha / \sum_\alpha \Lambda_\alpha$.

[10] Interestingly, for operators that have power-law decaying autocorrelations, such as conserved densities, the entropies with index $\alpha > 1$ only grow *logarithmically*, as $\log t$, at asymptotic times [603]. This is somewhat reminiscent to our result about entropies of *states*, which we discuss in Chapter 10. The operator case is relatively easy to understand from our discussion of operator spreading: the largest Schmidt values are dominated by the diffusive part of the evolving operator. Nevertheless, the entropies that are important for an accurate MPO/MPS representation are those with index $\alpha \leq 1$, which grow linearly.

[11] Such 'restricted state space' type approximations have been used previously in other contexts, see Refs. [609–611]

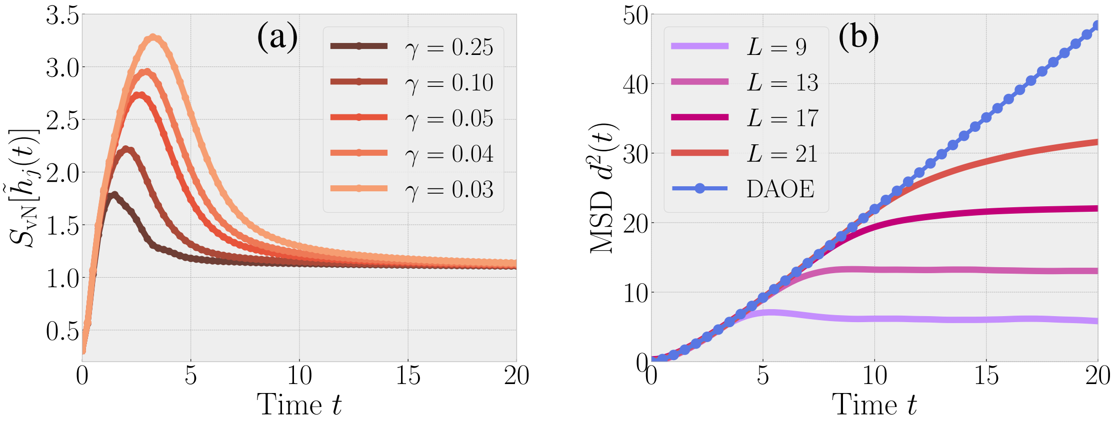

Figure 9.2.: Testing DAOE on the Ising model (9.11). (a) shows how the dissipation (for $\ell_* = 2$, $\Delta t = 0.25$) suppresses operator entanglement (measured in units of $\ln 2$). (b) shows that the MSD (9.10) is correctly captured to long times by the DAOE (same $\ell_*, \Delta t$; $\gamma = 0.03$, using bond dimensions $\chi = 512$), by comparing to exact results on small chains ($L = 9, 13, 17, 21$).

9.3. Results

We use our method to calculate the dynamical correlations between the central site $i = \frac{L+1}{2}$ (we take L odd) and all other positions, $C_j(t) \equiv \mathrm{tr}\left(q_j \tilde{q}_{\frac{L+1}{2}}(t)\right)/\mathcal{N}$. We normalize these such that $\sum_j C_j(0) = 1$. One can characterize the spreading of correlations by the *mean-square displacement* (MSD),

$$d^2(t) \equiv \sum_j C_j(t) j^2 - \left(\sum_j C_j(t) j\right)^2 . \tag{9.10}$$

Diffusive transport manifests itself in a linear growth of the MSD at long times, $d^2(t) \propto t$. This suggests defining a *time-dependent diffusion constant* [196, 286, 612–614] as $2D(t) \equiv \partial_t d^2(t)$. The physical diffusion constant is then $D \equiv \lim_{t\to\infty} D(t)$ (assuming $L \to \infty$ first). Further information about the frequency- and wavevector-dependence of the conductivity can be obtained by looking at space-time dependence of $C_j(t)$ [286, 291, 295].

We study two lattice models. One is the tilted field Ising chain, we met previously in Chapter 6,

$$H = \sum_j h_j \equiv \sum_j \left(g_x X_j + g_z Z_j + \frac{Z_{j-1}Z_j + Z_j Z_{j+1}}{2}\right). \tag{9.11}$$

We fix $g_x = 1.4$ and $g_z = 0.9045$. At these values, we expect the model to be strongly chaotic [269, 615], and hard to simulate exactly, due to fast entanglement growth. Here, h_j is the energy associated to site j. This is the only local conserved density in the model, and its correlations capture energy (or heat) transport [269]. We therefore take $q_j \equiv h_j$ in this case, and evolve $h_{\frac{L+1}{2}}$, as an MPO, according to Eq. (9.8). We perform the unitary part of the dynamics with TEBD, using a small Trotter time-step 0.01. We take large enough systems ($L = 51$) such that finite size effects are negligible at the times we study.

The other system we consider is a spin-1/2 XX model on a two-leg ladder. We denote by $j = 1, \ldots, L$ the rungs of the ladder, and use $a = 1, 2$ for the two legs. Pauli operators on a given site are specified as $X_{j,a}$, etc. The Hamiltonian then reads

$$H = \sum_{j=1}^{L} \sum_{a=1,2} \left(X_{j,a} X_{j+1,a} + Y_{j,a} Y_{j+1,a} \right) + \sum_{j=1}^{L} \left(X_{j,1} X_{j,2} + Y_{j,1} Y_{j,2} \right). \tag{9.12}$$

Besides energy, this model also conserves the spin z component, $\sum_{j,a} Z_{j,a}$. We examine the transport of the corresponding local conserved density $q_j = Z_j \equiv (Z_{j,1} + Z_{j,2})/2$ along the chain. We take a system of $L = 41$ rungs, which is large enough to avoid finite-size effects, up to the times ($t \approx 20$) that we simulate. In the following, we first benchmark the DAOE method in the Ising chain, and confirm some of its properties mentioned above. We then go on to extract diffusion constants for both models.

9.3.1. Benchmarking on the Ising model

First, we confirm the statement made above, that the dissipation leads to a decay of operator entanglement at long times. This is illustrated in Fig. 9.2(a) for the Ising model. The time and height of the peak increase as γ gets smaller, but for any non-zero γ, dissipation dominates at long times. Moreover, we find that after the peak, S_{vN} approaches an $O(1)$ value in units of $\ln 2$, independent of ℓ_* and γ, which indicates that the operator is increasingly dominated by the local densities, $\tilde{h}_{\frac{L+1}{2}}(t) \approx \sum_j C_j(t) h_j$. One can understand this from the operator spreading picture discussed in Section 8.2.4: the remaining ballistic component at time t is mostly made up by operators recently emitted from the diffusive 'core', which did not have time to get dissipated yet. As we have seen, the weight of these decays as $t^{-3/2}$, which is parameterically faster than the weight of the diffusive part, which goes as $t^{-1/2}$ [4].

As we said before, the decay of operator entanglement suggests that the dynamics can be accurately captured with a finite bond dimension even up to long times. We confirm this explicitly in Fig. 9.3. While for small χ, the truncation errors encountered around the peak time are already significant, they decrease (roughly linearly) with χ (Fig. 9.3(a)). This also shows up in the results for the time-dependent diffusion constant, $D(t)$ (Fig. 9.3(b)). While at small χ the truncation effects are clearly visible, the curves quickly converge as χ is increased. Another way of testing the effects of truncation is by looking at whether the conservation law (in this case, of energy) is satisfied. The exact dissipative dynamics would maintain the normalization $\sum_j C_j(t) = 1$ at all times due to energy conservation (assuming ℓ_* is larger than the support of the terms in the Hamiltonian, in this case $\ell_* \geq 2$). This is crucial for correctly capturing transport properties. We find that the errors in the conservation law, as measured by $\left|1 - \sum_j C_j(t)\right|$, quickly decrease as χ becomes larger (Fig. 9.3(c)). We conclude that it is possible to simulate the dissipative dynamics (9.8) up to long times, with a bond dimension that is independent of total system size.

Next, we benchmark that despite the dissipation, our method can correctly capture the spreading of correlations. We do this by comparing it to exact results on small systems, calculated using the canonical typicality approach (see Section 2.4) [113, 389, 390], for up to $L = 21$ sites. In this case, finite-size effects limit the times one can reach to $t \approx 10$. We compare these to the dissipative method for a particular set of parameters, $\ell_* = 2, \Delta t = 0.25, \gamma = 0.03$, which we expect to be close to being converged to the physical diffusion constant (see below). The results for the MSD are presented in Fig. 9.2(b). The curve from the dissipative evolution follows the exact results, and then continues to grow linearly to much longer times, well beyond the reach of exact numerics. This is despite the fact that at these times, the dissipation already had a large effect (as measured, for example, by the decay of S_{vN}), and $\tilde{h}_{\frac{L+1}{2}}(t)$ is far from the true time-evolved operator. This reinforces our assumption that backflow effects remain relatively small. Note that

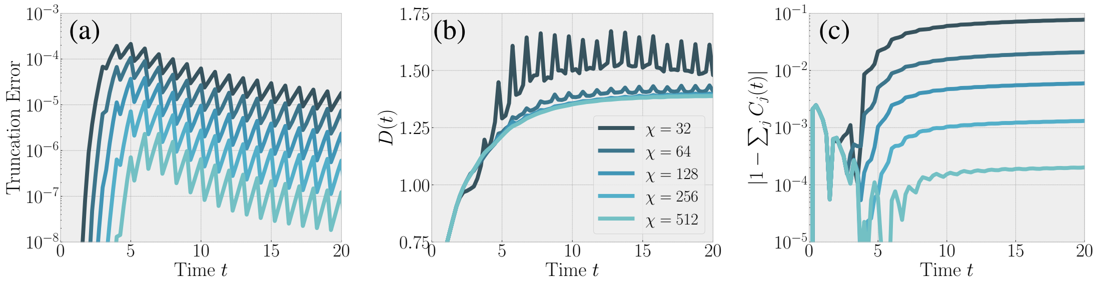

Figure 9.3.: Convergence of results with bond dimension χ in the Ising chain (9.11), for dissipation parameters $\ell_* = 4$, $\Delta t = 1$, $\gamma = 0.2$. (a): Truncation error per TEBD step, summed over all bonds in the chain ($L = 51$ sites). (b) Convergence of results for the time-dependent diffusion constant $D(t)$. (c) Errors in the energy conservation, as measured by the sum of the coefficients of local energy density terms $C_j(t)$.

the dissipation is essential in allowing us to reach long times; for the same bond dimension ($\chi = 512$), TEBD without dissipation starts deviating from the exact results around times $t \approx 7 - 8$ due to truncation errors.

9.3.2. Extracting diffusion constants

Having established the potential of the DAOE method, we now embark on using it to achieve a precise calculation of diffusion constants. Our approach is as follows. We calculate $D(t)$ for the dissipative evolution, and then approach the unitary dynamics by decreasing γ, while keeping Δt and ℓ_* fixed. We decrease γ until we observe signs of convergence, allowing us to extrapolate the results for D back to $\gamma \to 0$. We will estimate the accuracy of this extrapolation by comparing different values of ℓ_*.

As stated above, the value of Δt is in principle irrelevant, as one finds a scaling collapse as a function of $\gamma/\Delta t$ for small γ. However, in practice, Δt should be small enough so that one can follow the full dynamics up to Δt with the given bond dimension. It is also numerically more efficient not to make Δt too small, in order to reduce the number of MPO-to-MPS multiplications we need to perform. We find that $\Delta t \approx 1$ (in units of microscopic couplings) works well.

The results for the Ising chain are shown in Fig. 9.4(a,c), for $\Delta t = 1$ and $\ell_* = 2, 3, 4$. $D(t)$ saturates to a γ-dependent constant. When γ is made sufficiently small, we find that the results converge. The last few data points are well fit by a straight line, which allows us to extrapolate D back to $\gamma = 0$. The extrapolated results for different choices of ℓ_* all agree to within $\approx 1\%$ error, supporting our conclusions that we indeed reached the physical diffusion constant (in this case, $D \approx 1.40$). This constitutes strong evidence that our method can successfully capture transport coefficients to a high precision.

Next, we turn to the XX ladder model Eq. (9.12). Spin transport in this model has been studied in a number of previous works, finding clear evidence of diffusive behavior with a diffusion constant $D \approx 0.95$ [430, 616, 617]. Here we show that our method reproduces this result on much larger systems. We perform the same analysis as in the Ising model, comparing D for different γ and extrapolating back to $\gamma = 0$; the results are shown in Fig. 9.4(b,d). We find that the extrapolated results are all within the range $D \approx 0.96 - 0.98$ (even for $\ell_* = 1$, where energy-conservation is violated). The fact that these values are all very close to one another, and to the previous result, strongly supports the validity of our method.

In this chapter, we introduced a numerical method to extract transport coefficients (diffusion constants) from microscopic lattice models. Our method was inspired by the

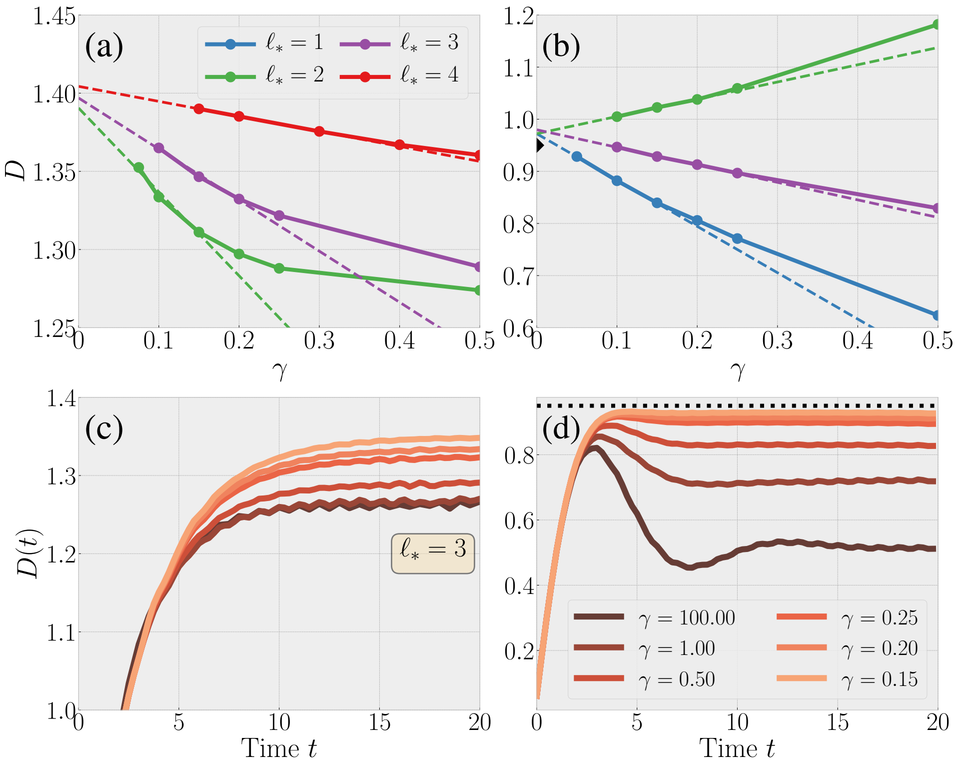

Figure 9.4.: Estimating the diffusion constant for the Ising chain (9.11) (a,c) and for the XX ladder (9.12) (b,d). We fix $\Delta t = 1$ and use bond dimensions up to $\chi = 768$. In (c) and (d) we show results for the time-dependent diffusion constant at a fixed $\ell_* = 3$ for varying γ, showing clear signs of convergence. In (a,b) we show the estimate for D (taken as the average of $D(t)$ in the interval $t \in [15, 20]$). Data for the weakest dissipations is well fit by a linear extrapolation, and results for different ℓ_* give consistent estimates for the physical diffusion constant. In (b) and (d), the black triangle and dotted line represent the estimate $D = 0.95$ from Ref. [616].

results on operator spreading presented in the earlier parts of this chapter, neglecting the non-local, ballistic parts of the evolving operator, but taking into account backflow processes that occur from the ballistic to the diffusive part on short time scales. While testing the method on more models, our results presented here, both for a circuit and a Hamiltonian system, are very encouraging. Moreover, not only can we estimate diffusion constants, our method also offers the possibility of gaining physical understanding of transport in these systems. Since each data point (for a fixed value of ℓ_*, γ) corresponds to summing up a certain subset of contributions to transport, by examining the dependence on these parameters provides a way of probing the importance of different processes.

10. Entanglement growth for global quenches

We now turn to the discussion of entanglement dynamics in the presence of conserved quantities and examine how coupling to the diffusive transport mode manifests in various quantities. In this chapter, we focus on global quenches, i.e., the evolution of initial states with no large-scale inhomogeneities (we still allow inhomogeneities on the lattice scale, such as Néel states). We mostly focus on Rényi entropies of index $\alpha > 1$, for which we argue that the coupling to diffusion is a relevant perturbation, leading to qualitatively new dynamics (this is in contrast with the von Neumann entropy, where the effects of diffusion only become apparent for inhomogenous states, which is the topic of the next chapter). We emphasize that understanding the dynamics of Rényi entropies is a particularly important topic in light of recent experiments [108–110] which have been able to measure S_2 of time-evolving states. As the von Neumann entropy is currently out of reach for experimental detection (except for the smallest subsystems), it is highly desirable to understand the possible differences between these quantities, in order to be able to appropriately interpret experimental results. Our results below, apart from their theoretical interest, are an important contribution to this effort.

10.1. Sub-ballistic growth or Rényi entropies

As we saw in Section 5.2, both the study of random circuit models, and general 'hydrodynamic' considerations lead to an effective long-time, large-wavelength description of entanglement dynamics in terms of the free energy of a minimal polymer (or membrane, in higher dimension) in space-time. One key feature of this is a linear growth of Rényi entropies as $S_\alpha = s_{\text{eq}} v_{\text{E},\alpha} t$ in the thermodynamic limit, with some α-dependent entanglement velocity. This prediction is in agreement with numerical studies of the von Neumann entropy in chaotic Hamiltonian systems [269] and also with general arguments that relate the linear growth of S_2 to ballistic operator spreading [256, 574] (indeed, the latter argument becomes exact, and coincides with the minimal polymer result, in the random circuit as we have shown in Section 5.1). Here we argue that this picture changes drastically in systems exhibiting diffusive transport: we find that $S_{\alpha>1}$ grows *diffusively*, as $\sqrt{t}$, rather than ballistically. S_1, on the other hand, we expect to remain ballistic, in agreement with the numerical results of Ref. [269]. The difference between the two arises because entropies with $\alpha > 1$ are sensitive to the presence of a few anomalously large eigenvalues of the reduced density matrix, while S_1 is dominated by the many exponentially small eigenvalues[1].

10.1.1. Numerical results

First, we consider the spin-1/2 local random unitary circuit, which we have studied in the Chapter 8 (see subsection 8.1.1 in particular). We examine the circuit-averaged purity, $\overline{\mathcal{P}}$, where the purity is $\mathcal{P} \equiv e^{-S_2} = \text{tr}(\rho_A^2)$. This defines the annealed average Rényi

---

[1] The possibility of such qualitative differences was discussed for global cat states in Ref. [277]; here we propose that it arises much more generally, without the need to fine tune the initial state.

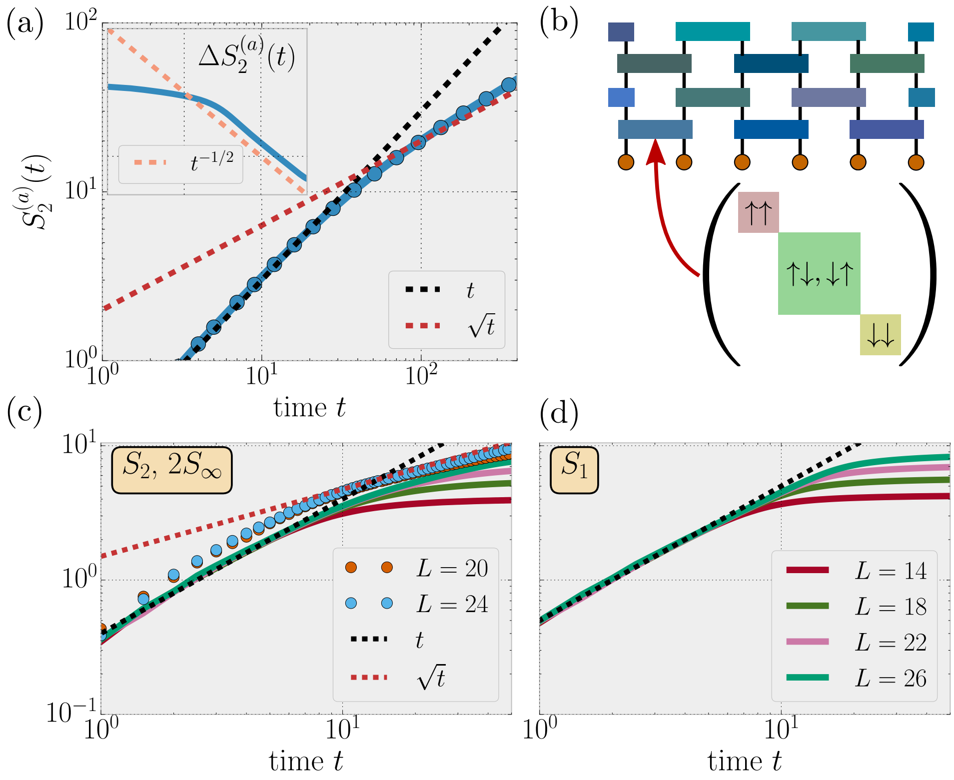

Figure 10.1.: (a) Growth of (annealed average) second Rényi entropy in a spin 1/2, U(1)-symmetric random circuit, averaged over all product states. At long times the growth is diffusive ($\propto \sqrt{t}$). Inset: the discrete time derivative $\Delta S_2^{(a)}(t) \equiv S_2^{(a)}(t+1) - S_2^{(a)}(t)$ decays as $t^{-1/2}$. (b) Geometry of the random circuit and block structure of the gates. (c): Rényi entropies of the tilted field Ising model (10.1), S_2 (solid lines) and $2S_\infty$ (dots) show a similar cross-over to sub-ballistic growth, while (d) the von Neumann entropy grows mostly linearly.

entropy, $S_2^{(a)} \equiv -\log \overline{\mathcal{P}}$, which, as we pointed out before, lower bounds the average, $\overline{S_2} \geq S_2^{(a)}$. $\overline{\mathcal{P}}$ can be represented as a classical partition function, using the mapping derived in subsection 8.1.1. The boundary conditions in this case are modified to capture the purity, as outlined in Section 5.2. In particular, on the bottom layer, the boundary conditions correspond to a string of swap operators acting on subsystem A, and an identity on its complement. On the top layer, they are given by two copies of the initial state, $|\Psi_0\rangle\langle\Psi_0| \otimes |\Psi_0\rangle\langle\Psi_0|$. Note that, unlike the non-symmetric case discussed in Section 5.2, in the $U(1)$-symmetric circuit, different initial product states give different boundary conditions, depending on their local filling, in terms of the six local states that define the classical partition function.

We evaluate the partition function as before, using standard tensor network methods [84, 417], making sure that the results are converged in both system size and bond dimension. Moreover, we average over all initial product states exactly. As shown in Fig. 10.1(a), we find that at long times, the entanglement grows as $S_2^{(a)} \propto \sqrt{t}$. As we have shown in Sections 5.1 and 5.2, in the absence of a conservation law, the same quantity grows linearly; thus we attribute its slow, diffusive growth to diffusive transport. This is the main result of this chapter, and we shall argue that it holds quite generically for chaotic dynamics with a diffusive conserved quantity.

To verify this, we consider the spin 1/2 tilted field Ising model, previously encountered

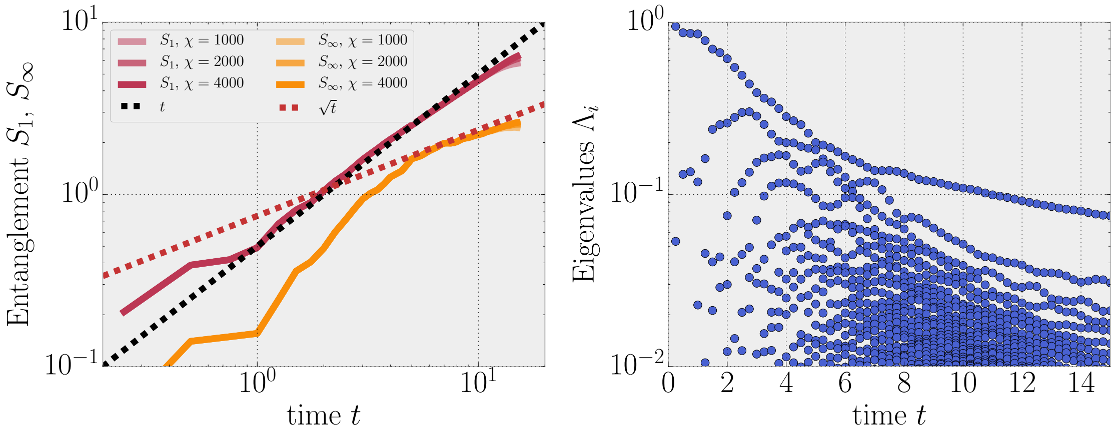

Figure 10.2.: Entanglement growth in the tilted field Ising model, starting from an initial state polarized in the positive Y direction, evolved with the iTEBD algorithm at various bond dimensions χ. We observe a cross-over to sub-ballistic growth in the min-entropy S_∞, as opposed to S_1, which remains ballistic (left). This shows up in the spectrum of the half-chain reduced density matrix, where the largest eigenvalue is separated from the bulk of the spectrum at long times (right).

in Eq. (6.7). Here, we consider the model without spatial disorder, and we add an extra boundary term that helps in reducing finite-size effects[2]

$$H = J\sum_{r=1}^{L-1} Z_r Z_{r+1} + \sum_{r=1}^{L}(h_z Z_r + h_x X_r) - J(Z_1 + Z_L), \tag{10.1}$$

We choose $J = 1$, $h_x = (5+\sqrt{5})/8$, and $h_z = (1+\sqrt{5})/4$, as the same model was previously shown to have diffusive energy transport and linear von Neumann entropy growth [269]. Fig. 10.1(c,d) show the growth of different entropies, averaged over $N = 50$ ($N = 20$) random product states for system sizes $L = 12 - 24$ ($L = 26$). Here we average the entropies, not their exponentials, unlike the random circuit case. We observe a mostly linear growth of S_1, as in Ref. [269]. S_2, however, has a cross-over to sub-linear growth at long times. Although the times we can reach are limited by finite system size, the long-time behavior is consistent with $S_2 \propto \sqrt{t}$. The results become clearer when considering the *min-entropy*, $S_{\alpha\to\infty}$, which provides an upper bound on $S_{\alpha>1} \leq \frac{\alpha}{\alpha-1} S_\infty$. We find that S_∞ is less sensitive to finite size effects, and exhibits a more pronounced cross-over towards $\sqrt{t}$ growth (dots in Fig. 10.1(c)).

Similar results hold also for particular initial states, without averaging, as we now demonstrate for the Ising model. To have a state which is both translation invariant and corresponds to infinite temperature, we take an initial product state which is an eigenstate of the Y Pauli operator on each site with an eigenvalue $+1$. Since both the state and the dynamics are translation invariant, we can time evolve directly in the thermodynamic limit, utilizing the infinite time-evolving block decimation (iTEBD) algorithm [417]. The times obtainable are then limited by the maximal bond dimension χ. We find a behavior analogous to the one observed for random product states: S_1 grows approximately linearly, while S_∞ curves over to an approximately diffusive growth at times $t \approx 10$ (left panel of

---

[2] To be more precise, the reason for adding this term is that otherwise the definition of local energy density is different at the edges compared to the bulk of the system. By modifying the Hamiltonian near the boundary, one can get rid of this difficulty, which makes it easier to observe diffusive energy transport in this system, as pointed out by Ref. [269].

Fig. 10.2). One way to think about this phenomenon is as a separation of scales in the spectrum of the reduced density matrix, whose largest eigenvalues decay as $\Lambda_i \sim e^{-\sqrt{t}}$, while the majority of the eigenvalues are exponentially small, $\Lambda_i \sim e^{-t}$ (right panel of Fig. 10.2). The behavior of the random circuit and Hamiltonian models leads us to conjecture that this separation of scales in the entanglement spectrum is a generic consequence of diffusive hydrodynamic transport. In the following we provide further justification of this conjecture.

10.1.2. Heuristic argument

We interpret our results in terms of the following non-rigorous argument. Let us focus on a Z-conserving, not necessarily random, circuit, with the same brick-wall geometry of 2-site gates as shown in Fig. 10.1(b), acting on an infinite spin-1/2 chain. We write the circuit up to time t as a product of layers, $U(t) = \prod_{\tau<t} U_{\tau,\tau+1}$, and consider the bipartite entanglement at a cut between sites r and $r+1$ at time t. One can insert a resolution of the identity after each layer, to rewrite the time evolved state as a 'sum over histories', $|\psi(t)\rangle = \sum_{\{\sigma(\tau)\}} A(\{\sigma(\tau)\})|\sigma\rangle$, where $A(\{\sigma(\tau)\})$ is the probability amplitude of a world history $\{\sigma(\tau)\}|_{0\leq\tau\leq t}$ in the z basis. We split this sum into two parts: i) histories for which the sites $r, r+1$ have both spins pointing up at *all* times $\tau > t_{\text{loc}}$ for some local equilibration time $t_{\text{loc}} \sim \mathcal{O}(1)$, and ii) all remaining paths. Let $|\phi_0(t)\rangle$ and $|\phi_1(t)\rangle$ denote the normalized states corresponding to i) and ii) respectively. Then $|\psi(t)\rangle = c_0|\phi_0(t)\rangle + c_1|\phi_1(t)\rangle$. By construction, $|\phi_0\rangle$ can only accumulate entanglement across the bond $r, r+1$ at times *before* t_{loc} and therefore has an $\mathcal{O}(1)$ Schmidt rank. Denoting this Schmidt rank by χ, one can then use the *Eckart-Young theorem* [618, 619] to lower bound the largest Schmidt value of $|\psi\rangle$ as[3]

$$\chi\Lambda^{\psi}_{\text{max}} \geq |\langle\phi_0|\psi\rangle|^2 = |c_0 + c_1\langle\phi_0|\phi_1\rangle|^2. \tag{10.2}$$

We will now argue that if transport is diffusive, the RHS is expected to decay slower than exponentially with time.

First, we want to estimate the probability $|c_0|^2$ that the sites $r, r+1$ remain in the state $\uparrow\uparrow$ at all times $t > t_{\text{loc}}$. The simplest approximation is to treat every $\downarrow$ in the system as an independently diffusing particle. For a single particle, starting at position $r' < r$, the probability of staying within the region $[-\infty, r]$ is given by (using a continuum notation for simplicity)

$$\int_{-\infty}^{r} \mathrm{d}r' \frac{e^{-\frac{(r-r')^2}{2Dt}}}{\sqrt{2\pi Dt}} = \frac{1}{2}\left(1 + \operatorname{erf}\left(\frac{r-r'}{\sqrt{2Dt}}\right)\right), \tag{10.3}$$

where D is the diffusion constant. Importantly, when $r' \ll r - \sqrt{2Dt}$, the probability is very close to one[4]. Since we have assumed that the particles are independent, the probability that *all* particles remain in the region left of r is the product of the different probabilities over choices of initial position r'. The dominant contribution comes from the region $r' \gtrsim r - \sqrt{2Dt}$; the result is therefore well approximated by a product of $\mathcal{O}(\sqrt{Dt})$ numbers, which is expected to decay at long times as $|c_0|^2 \propto e^{-\gamma\sqrt{Dt}}$ for some constant γ, which is readily verified by calculating the product numerically. The key element of this calculation was the fact that only particles that are initially within some $\mathcal{O}(\sqrt{Dt})$ distance or r have any significant probability of crossing it. This is a direct consequence of diffusive particle transport, and we therefore we expect the same quanitative scaling of $|c_0|^2$ to hold more generally in diffusive systems. To further support this, we have confirmed by direct

---

[3] As in Chapter 6, Λ_α denotes the eigenvalues of the reduced density matrix (in this case, for a half-chain bi-partition), which are the squares of the Schmidt values.

[4] To leading order, the difference scales as a Gaussian, $\operatorname{erf}(x) = 1 - \frac{e^{-x^2}}{\sqrt{\pi x^2}}$

numerical calculation that the same scaling holds in a system of hard-core interacting random walkers on a lattice, initiated in a Néel state. We therefore expect $|c_0|^2 \sim e^{\gamma\sqrt{Dt}}$ to be the generic behavior dictated by diffusion.

To bound the overlap $\langle\phi_0|\phi_1\rangle$, we can apply the Eckart-Young theorem again, this time for $|\phi_1\rangle$, which gives $|\langle\phi_0|\phi_1\rangle|^2 \leq \chi\Lambda^{\phi_1}_{\text{max}}$. Consequently, if $|\phi_1\rangle$, which corresponds to typical histories, has Rényi entropies $S_{\alpha>1}$ that grow faster than $\sqrt{t}$, then the second term on the RHS of Eq. (10.2) will be negligible at long times compared to c_0, resulting in $\chi\Lambda^{\psi}_{\text{max}} \gtrsim e^{-\gamma\sqrt{Dt}}$. If $\Lambda^{\phi_1}_{\text{max}} \sim e^{-\sqrt{t}}$, then there is in principle a possibility of cancellation between the two terms, such that the RHS of Eq. (10.2) decays faster then $\sim e^{-\sqrt{t}}$; however this would be highly fine-tuned and we see no sign of such cancellation when computing the RHS in the random circuit model. Assuming that there is no such cancellation, Eq. (10.2) implies that $\Lambda^{\psi}_{\text{max}} \gtrsim e^{-\gamma\sqrt{Dt}}$; this can be recast as an upper bound on the min-entropy, $S_\infty \leq \gamma\sqrt{Dt}$. It has been shown subsequently that a similar argument can be used to rigorously prove an upper bound that scales as $S_\infty \lesssim \sqrt{t\log t}$ for a particular set of initial states (product states in the x basis) [619].

This argument implies that at long times, there is a growing distance between the largest Schmidt value, $\Lambda_{\text{max}} \equiv e^{-S_\infty} \sim e^{-\gamma\sqrt{Dt}}$, and typical ones which we still expect to be exponentially small, $\sim e^{-vt}$, in accordance with the linear growth of S_1 [269]. As mentioned previously, the former upper bounds Rényi entropies $S_{\alpha>1} \leq \frac{\alpha}{\alpha-1}S_\infty$. This shows that at long times, $t \gg v^2/D$, all $\alpha > 1$ entropies are controlled by the largest Schmidt value, making their growth diffusive. The time for this sub-ballistic growth to set in depends also on the Rényi index, diverging in the limit $\alpha \to 1$. The von Neumann entropy itself is unconstrained by S_∞, dominated instead by the many exponentially small Schmidt values, leading to its linear growth[5].

We presented the argument in terms of a circuit of 2-site gates. The generalization to circuits involving longer-range gates is trivial, one simply needs to choose the spin-polarized region at the entanglement cut to be of the size of the largest gates; assuming this is $\mathcal{O}(1)$, the argument goes through. For a continuous time, $U(1)$-symmetric Floquet model, which does not have a direct circuit realization, one could generalize the argument by choosing a region of size sufficiently larger than $2v_{\text{LR}}T$, where v_{LR} is the Lieb-Robinson speed an T is the Floquet period. We also expect the argument to generalize to energy conserving systems, in the form of rare events where the time evolved state locally resembles the ground state[6]. This is in agreement with our numerical results in Fig. 10.1(c).

Our argument (as well as that of Ref. [619]) should also generalize to non-diffusive systems, where we expect the behavior of $-\log|c_0|^2$, defined in the same way as above, to be governed by the appropriate power of time, that characterizes the transport properties of the system. In particular, for systems with sub-diffusive transport (for example due to disorder [225–233] or dipole-moment conservation [331–333]), it should grow even slower than $\sim t^{1/2}$. Moreover, in the MBL phase, our argument would suggest that higher Rényi entropies saturate to an *area law*, in contrast with the unbounded logarithmic growth of S_1 that is a characteristic feature of MBL [222]. This question in particular certainly merits further study.

When do the transport properties fail to correctly predict the growth of $S_{\alpha>1}$? The crucial element entering our argument was the existence of regions where no dynamics is

---

[5] It is interesting to note that the difference between S_1 and $S_{\alpha>1}$ is entirely an *interaction* effect. This can be shown by considering non-interacting particles subjected to external noise (e.g. a free fermion version of our random circuit). In this case, the diffusion of particles (which is induced by the noise) dominates *both* entropies, and one finds $S_1 \sim \sqrt{t}$ in 1D [276, 620]. The linear growth in the generic case is due to collisions that generate entanglement dynamically.

[6] The similarity of most apparent in the case of local *frustration free* Hamiltonians, where one can e.g. consider states that are ground states of all local terms within a region.

allowed by the symmetry. This was due to the fact that the smallest (or largest) eigenvalues of the conserved charge corresponded to eigenspaces with only a single, low-entanglement state (i.e., the completely empty/filled states). The heuristic argument clearly doesn't apply if there are some degrees of freedom in the systems that do not carry a conserved charge (as in the finite q random circuit model we study below). Such 'sterile' degrees of freedom can be entangled without transporting charge across a bond. In this case, all symmetry sectors contain many states, and therefore can have non-trivial dynamics. This would mean that the state $|\phi_0\rangle$ defined above will no longer be a low-entanglement state, and our argument breaks down. However, we do not expect this to be relevant for e.g. Hamiltonian systems, where any such 'sterile' degree of freedom by definition would not appear in the Hamiltonian and would therefore have no dynamics.

Finally, let us comment on what our results here tell us about the various approaches to entanglement growth discussed in Chapter 5. First of all, let us emphasize that it is rather surprising that we find a sub-ballistic growth of S_2, *despite* the ballistic spreading of local operators discussed in the previous chapter. This is in contrast with the case without symmetries, where the biased diffusion of operators directly led to the linear growth of $S_2^{(a)}$, as we showed in Section 5.1. Indeed, several other works have suggested previously that the mechanism we discussed there is generic, and that S_2 should grow linearly in typical systems for this reason [256, 574]. Our results show that the presence of a conservation law breaks the central assumption behind such arguments, which is that the operator spreading coefficients are essentially uncorrelated, making the off-diagonal part of Eq. (5.2) vanish due to random signs. Instead, the symmetry imposes subtle correlations between the different coefficients that cannot be neglected. Our result also suggests that the minimal membrane picture of entanglement growth [277] discussed in Section 5.2 does not accurately capture the behavior of $S_{\alpha>1}$[7]. It is natural to ask what replaces the minimal polymer, and how to describe the coupling between $S_{\alpha>1}$ and the conserved charge; this is what we turn to next.

10.1.3. Effective stochastic model in the large q limit

To get a further analytical handle on this problem, we also consider the large-q version of the random circuit, which we introduced in Section 7.1. In this case, a non-conserved, q-state qudit degree of freedom is added to each site. This makes the size of each Haar random unitary larger by a factor of q^2, allowing us to derive an effective model that governs the evolution of $S_2^{(a)}$ in the large q limit. As we shall see, the result decomposes into the sum of two contributions: a $\propto t$ part from the non-conserved degrees of freedom, and a $\propto \sqrt{t}$ part associated to the conserved spins.

Recall, that the purity can be written as the expectation value on the doubled Hilbert space, $\mathcal{P}(r) = \text{tr}(\mathcal{F}(r)[\rho \otimes \rho]) \equiv \langle \mathcal{F}(r) \rangle$, where $\mathcal{F}(r) \equiv \prod_{\leq r} \mathcal{F}$ is a string of swap operators, acting on one half of the entanglement cut (Fig. 10.3(a,b)). We will use the large-q circuit to write down a simplified model for the dynamics of $\mathcal{F}(r)$. The resulting model will shed light on how the minimal polymer picture is modified in the presence of conservation laws and how this leads to the sub-ballistic growth of the Rényi entropy observed above. Among other things, the model we discuss here has the explicit advantage that it leads an actual stochastic process, with only positive weights; the negative weights we encountered at $q = 1$ (see Fig. 8.2 for example) disappear in the large-q limit.

Averaging over a random gate on sites $r, r+1$, to leading order in $1/q$ we find that the

---

[7] The possibility that the minimal membrane might work only for S_1 was pointed out previously in the context of holography in Ref. [578].

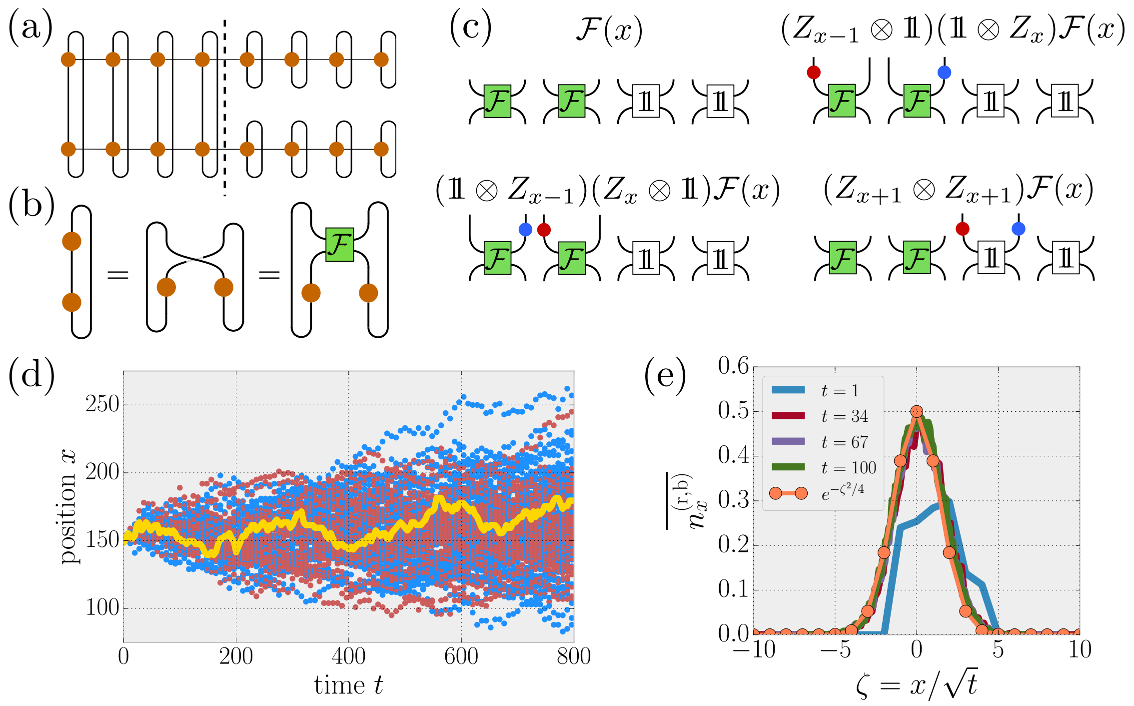

Figure 10.3.: Effective model at $q \to \infty$. (a) The purity $\mathcal{P}$, written in terms of the state ρ as a matrix product operator. (b) This can be rewritten by introducing the swap operator $\mathcal{F}$. (c) Half-chain 'swap-string' $\mathcal{F}(r)$, along with a few of the terms on the RHS of Eq. (10.4), with red and blue particles representing local Z_x operators. (d) These particles obey a random walk with hard core interactions, spreading out diffusively, which (e) leads to a Gaussian density profile.

swap-string evolves as (see App. B.5 for details)

$$\mathcal{F}(r) \to \frac{1}{2q}\sum_{s=r\pm 1}\left(\mathcal{F}(s)+\tilde{\mathcal{F}}_r(s)\right), \tag{10.4}$$

where we have introduced new 'two-copy' operators

$$\tilde{\mathcal{F}}_r(s) \equiv (Z_{r,r+1}\otimes Z_{r,r+1})\mathcal{F}(s), \tag{10.5}$$

with $Z_{r,r+1} \equiv (Z_r + Z_{r+1})/2$, and the tensor product referring to the two copies of the system. These are similar to $\mathcal{F}(r)$, but multiplied by the Z operators that measure the conserved spin on sites near the entanglement cut.

To see how the entanglement evolves, one also needs equations of motion for $\tilde{\mathcal{F}}_r(s)$. This can be done analogously, by averaging over 2-site gates, resulting in the following effective model, which we derive in App. B.5. The operators in Eq. (10.5), and their subsequent circuit-averaged evolution, may be expressed as a sum of dressed swap operators of the form $\prod_s \left(Z_s^{n_s^{(r)}}\otimes Z_s^{n_s^{(b)}}\right)\mathcal{F}(r')$, where $\{n_s^{(r,b)}=0,1\}$. We refer to $\{n_s^{(r,b)}\}$ as configurations of 'red' and 'blue' particles, while r' (the endpoint of the swap string) is called the 'cut position'. Apart from an overall suppression factor of $2/q$ in each step, the circuit-averaged dynamics gives a Markov process on configurations defined by these variables. This effective Markov dynamics has the following properties: away from the cut, the particles independently obey diffusion with hard-core interactions, conserving the number of each species. The cut itself also diffuses, moving one site either to the left or the right, while emitting and absorbing an even number of particles at each step (Fig. 10.3(d)). More

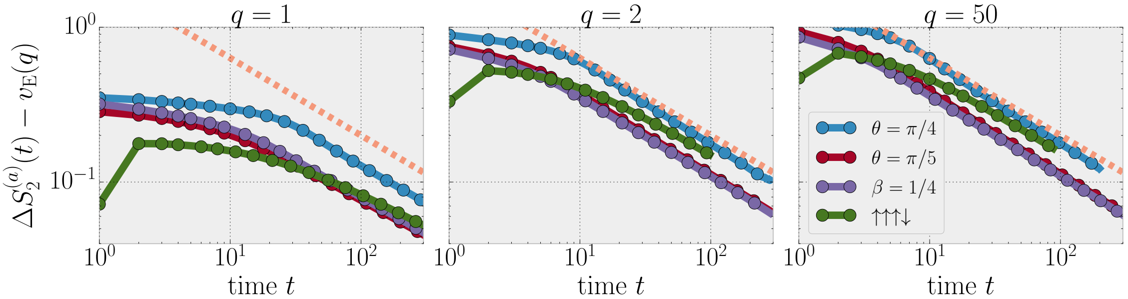

Figure 10.4.: Time derivative of the annealed average Rényi entropy in the random circuit at different values of q, after subtracting the constant term, $v_{\mathrm{E}}(q)$, associated to the non-conserved degrees of freedom. Different curves correspond to different initial states, as described in Section 10.2. All states show a decay of the form $\propto t^{-1/2}$ (dashed line) at long times, indicating diffusive growth.

precisely, whenever the cut 'jumps' across a site, with 1/2 probability it flips the state of red/blue particles on *both* copies simultaneously (from empty to filled and vice versa). This means that the probability of emission vs. absorption decreases with the number of particles on the two sites directly at the cut, changing sign at half filling.

The swap-string and both types of particles evolve as unbiased random walks, therefore, by time t we expect them to occupy a region of width $l(t) \propto \sqrt{t}$. Monte Carlo simulations of the stochastic dynamics show (Fig. 10.3(e)) that the particle densities are Gaussian around r, the original position of the cut. We therefore take a mean field approximation and write the probability of a string ending at site r and a distribution of particles $\{n_s^{(r,b)} = 0, 1\}$ as

$$p(r, n^{(r)}, n^{(b)}) \propto e^{-\frac{r^2}{2l(t)^2}} e^{-\frac{1}{2l(t)^2}\sum_s \left(n_s^{(r)}+n_s^{(b)}\right)s^2} \tag{10.6}$$

if $\sum_s (n_s^{(r)} + n_s^{(b)})$ is even, and zero otherwise. With this ansatz, one can evaluate the half-chain purity at time t. For translation invariant product states, the result reads

$$\mathcal{P}(t) \propto \left(\frac{2}{q}\right)^t \times \prod_s \left(1 - \frac{1-|\langle Z_s\rangle|}{1+e^{s^2/2l(t)^2}}\right)^2 . \tag{10.7}$$

This product has a relevant contributions only from a window of $|s| \lesssim \sqrt{t}$, hence it decays as $e^{-\gamma\sqrt{t}}$. Note that γ is larger when $|\langle Z_s\rangle|$ is smaller. By expanding each term in $e^{-s^2/2l(t)^2}$, we can approximate the product as $\approx e^{-\sqrt{2\pi}(1-|\langle Z\rangle|)l(t)}$, which is in good agreement with Monte Carlo results, at least away from $\langle Z\rangle \approx 0$. Note that Eq. (10.7) looks very similar to the probability of rare events from our heuristic argument in the simplest approximation of independently diffusing particles.

Using Eq. (10.7), at large q we get $S_2^{(a)} = \log(q/2)\, t + a\sqrt{t}$, with $a \sim \mathcal{O}(1)$. Here, $\log(q/2)$ is exactly the large q limit of $v_{\mathrm{E}}(q) = \log\frac{q+1/q}{2}$, the entanglement velocity of a non-symmetric random circuit with q states per site, which we derived in Section 5.1, independently of the initial state. This suggests the following interpretation: there is an entanglement $v_{\mathrm{E}}(q)t$ coming entirely from non-conserved degrees of freedom, while the conserved spins are responsible for the $\propto \sqrt{t}$ term. This is supported by numerical results, presented in Fig. 10.4, which show that $S_2^{(a)}(t) - v_{\mathrm{E}}(q)t$ has only weak q-dependence and grows as $\sqrt{t}$ for any q, including the original model with $q = 1$, where $S_2^{(a)}$ is purely diffusive as we saw above. The same plot also shows that the $\sim \sqrt{t}$ growth appears for a variety of different initial states, including ones that are diagonal in product states in the z-basis (for the definition of the initial states used, see Section 10.2) Our conclusion from this, is that the stochastic model discussed here contains the essential physics of the diffusive growth of S_2 in charge-conserving systems, and can be taken as the appropriate generalization of the minimal polymer picture in this setup. Understanding its properties in more detail, beyond the naive mean-field approximation we used here, and to understand the effect of random fluctuations in this language, are interesting open problems.

Before concluding this section, let us mention that we expect the $\sim \sqrt{t}$ growth of $S_{\alpha>1}$ to hold also in higher dimensions. In this case, the boundary of the subsystem A whose entanglement we consider is a $d-1$ dimensional object of size $|\partial A|$. From the standpoint of our heuristic argument, this means that the probability of maintaining and empty region that encompasses the whole boundary now decays much more rapidly, as $\sim e^{-\gamma|\partial A|\sqrt{Dt}}$. However, this number should be compared with the size of the typical eigenvalue, which decays as $\sim e^{-s_{\text{eq}} v_{\text{E}} |\partial A| t}$, in light of the fact that entanglement is generated along the entire boundary. Therefore, at long times, the first number will still be much smaller than the second, indicating a separation of scales between $\Lambda_{\text{max}} = e^{-S_\infty}$ and $\Lambda_{\text{typical}} = e^{-S_1}$. On the other hand, our effective, large-q model generalizes directly to higher dimensions if we build our d dimensional circuit out of the same 2-site gates. The swap-operator $\mathcal{F}_A(t)$ now acts on a d dimensional region, whose boundary fluctuates due to the application of the gates, while it emits Z_r operators that diffuse on the lattice. The simple mean-field approximation (which might even become better with increasing d) then suggests that $S_2 \propto \sqrt{t}$ still holds. This conjecture recently received support from numerics on $U(1)$-symmetric Clifford circuits [544].

10.2. Long-time tails in Rényi entropies

Diffusive modes also have a strong influence on the long-time behavior of finite subsystems, which we turn to next. The entanglement eventually saturates to an equilibrium value predicted by the appropriate Gibbs ensemble, provided ETH holds and the initial state clusters. We now show that the approach of S_2 to this thermodynamic value is also affected by diffusion and shows long-time hydrodynamic tails, similar to the ones discussed in the context of autocorrelations in Section 2.3. Interestingly, we find that the nature of these tails depends strongly on the initial conditions, leading to the appearance of three different power laws, $t^{-1/2}$, t^{-1} and $t^{-3/2}$. In particular we uncover a difference between states at zero and finite chemical potential (infinite and finite temperature).

We take a spin 1/2 chain and rewrite the reduced density matrix of a small subsystem of l sites by inserting a complete basis of operators σ^μ, given by products of local Pauli operators acting only on the subsystem [574]. This yields $S_2 = l \log 2 - \log\left(1 + \sum_\mu \langle \sigma^\mu \rangle^2\right)$, where the identity is excluded from the sum. Let $\langle \delta\sigma^\mu \rangle \equiv \langle \sigma^\mu \rangle - \langle \sigma^\mu \rangle_{\text{eq}}$ denote the deviation from equilibrium. Then at long times

$$|S_2 - S_{2,\text{eq}}| \propto \sum_\mu \left(2\langle \sigma^\mu \rangle_{\text{eq}} \langle \delta\sigma^\mu \rangle + \langle \delta\sigma^\mu \rangle^2\right). \tag{10.8}$$

Thus the long-time tails that describe how expectation values equilibrate appear directly in the Rényi entropy.

One immediate consequence of Eq. (10.8) is that the hydrodynamic tails can differ between states at half filling and away from half filling. At precisely half filling, the leading order term is $\langle \delta\sigma^\mu \rangle^2$, while away from half filling $\langle \sigma^\mu \rangle_{\text{eq}} \langle \delta\sigma^\mu \rangle$ is expected to dominate. Generically, hydrodynamic observables in d dimension should decay as $t^{-d/2}$ [285, 287, 553, 554], with subleading corrections $\mathcal{O}(t^{-d})$, $\mathcal{O}(t^{-d/2-1})$ etc. Therefore, we generically expect a saturation as $\propto t^{-d}$ for states at half filling (infinite temperature) and $\propto t^{-d/2}$ otherwise. However, this expectation can change for certain initial states, where all hydrodynamic variables have $\langle \delta\sigma^\mu \rangle = 0$ initially. In this case one expects the leading diffusive tail to

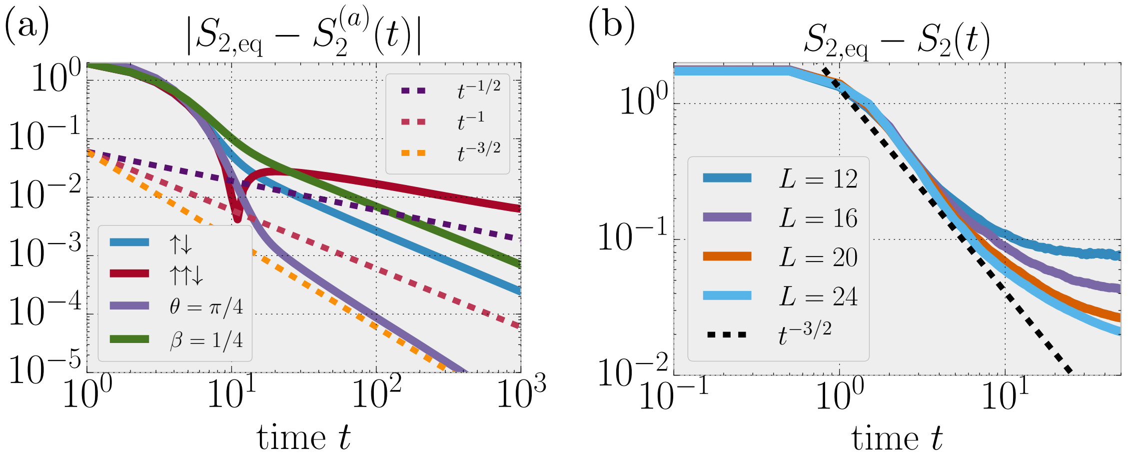

Figure 10.5.: (a) Saturation of $S_2^{(a)}$ for a 4-site subsystem in the spin 1/2 random circuit for different initial states. States away/at half filling generically saturate as $t^{-1/2}, t^{-1}$ respectively. States with hydrodynamic variables in equilibrium at all times saturate with subleading exponent $t^{-3/2}$. (b): The same $t^{-3/2}$ saturation is present for random product states in the tilted field Ising model (10.1) (3-site subsystem, averaged over 50 initial states).

vanish and subleading corrections to take over. In particular, in the 1D random circuit model one can argue that the leading contribution for translation invariant product states should be of order $t^{-3/2}$; we detail this in App. B.6

We observe these three distinct power laws in $S_2^{(a)}$ for the spin 1/2 random circuit, as shown in Fig. 10.5(a). We consider the following types of initial states:

- Néel-like states of the form $|\uparrow\uparrow\downarrow\uparrow\uparrow\downarrow\ldots\rangle$.
- Finitely correlated states: $|\beta\rangle \propto e^{\beta \sum_{r=0}^{L-1} Z_r Z_{r+1}} (|\uparrow\rangle + |\downarrow\rangle)^{\otimes L}$.
- Tilted ferromagnetic states: $|\theta\rangle \equiv e^{i\theta \sum_{r=1}^{L} Y_r} |\uparrow\rangle$.

We find that Néel-like states with less then half filling exhibit an overshooting effect, approaching their equilibrium value *from above*, as $t^{-1/2}$. At half-filling there is no overshooting, and the Rényi entropy of a Néel state approaches its final value as t^{-1}, in accordance with our prediction about the special role of zero chemical potential. Finitely correlated states are similarly at half filling, and consequently saturate as t^{-1}. Tilted ferromagnetic states, on the other hand, belong to the last category, where all diagonal operators take on their equilibrium values at $t = 0$; this results in the aforementioned $t^{-3/2}$ saturation. We also provide evidence of the $t^{-3/2}$ tail for random product states in the tilted field Ising Hamiltonian (10.1), shown in Fig. 10.5(b).

10.3. Logarithmic growth of number entanglement

Before concluding, let us briefly comment on an aspect of entanglement growth after a global quench in a charge-conserving system that is related to the dynamics of the von Neumann entropy . The discussion that follows applies to initial states that are eigenstates of the charge operator $\hat{Q}$, such that there are no fluctuations in the total amount of charge in the system. A simple example of such a state is a Néel state, where exactly every second site is occupied. While this state is not completely homogenous, its charge-density becomes uniformly 1/2 after some quick local equilibration process. The resulting state, however,

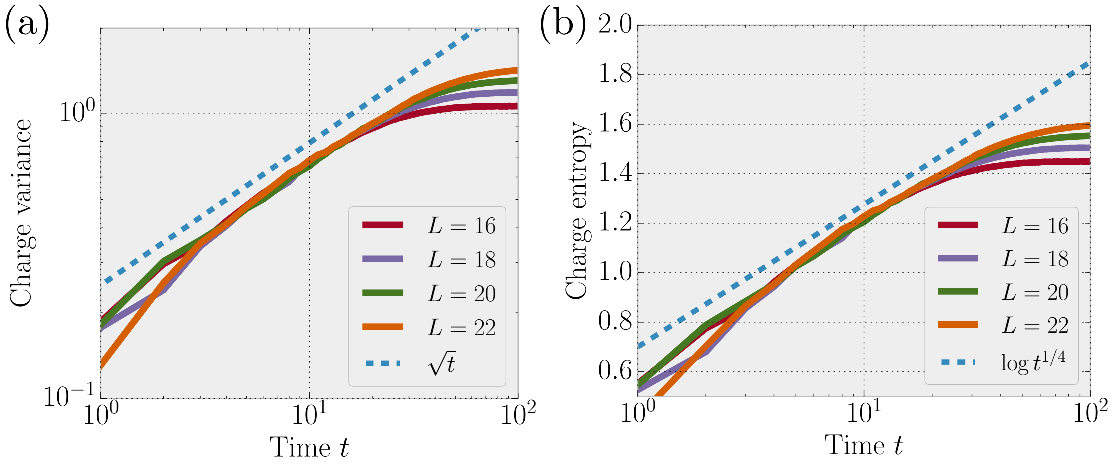

Figure 10.6.: Evolution of the probability distribution of having total charge Q in the left half of a spin chain, initialized in a Néel state and evolved with the random unitary circuit. a) The charge variance $\mathrm{Var}(Q)$ grows as $\propto \sqrt{t}$ and saturates to a volume law. b) The number entropy S_Q grows as the logarithm of the standard deviation, $S_Q = \log t^{1/4} + const.$ and saturates to a value $\log L^{1/2} + const.$

is still far from *global* equilibrium, as indicated, among other things, by the fluctuations in the conserved charge. Consider a subsystem A, containing l sites, and the total charge contained in it, as measured by the operator $\hat{Q}_A \equiv \sum_{r\in A} \hat{Q}_r$. In an equilibrium state, $\rho_A \propto e^{-\mu \hat{Q}_A}$, the charge variance should obey a volume law, $\mathrm{Var}(Q_A) \equiv \langle \hat{Q}_A^2 \rangle - \langle \hat{Q}_A \rangle^2 \propto l$. In a diffusive system, to leading order the evolution of the variance should be governed by diffusion [287] (see also App. B.6), indicating that it takes a time $\propto l^2$ for it to reach its final value. Our goal is to understand how this diffusively slow relaxation affect the dynamics of entanglement.

To see the effects of charge diffusion more clearly, it is worthwhile to write the von Neumann entropy as a sum of two contributions, one of which is related directly to the distribution of total charge in the subsystem. In order to achieve this, note that the conservation of a fixed total charge in the system implies that the reduced density matrix has a block-diagonal structure

$$\rho_A = \sum_{Q_A} p_{Q_A} \rho_A^{(Q_A)}, \tag{10.9}$$

where $\rho_A^{(Q_A)}$ corresponds to the block with total charge Q_A in subsystem A, normalized to have unit trace. With this normalization, the prefactor p_{Q_A} is exactly the probability of having a total number of Q_A charges in A, given by the expectation value $\mathrm{tr}(\rho_A \hat{P}_{Q_A})$ where $\hat{P}_{Q_A}$ is the projector appearing in the spectral decomposition $\hat{Q}_A = \sum_{Q_A} Q_A \hat{P}_{Q_A}$.

With this block-decomposition in hand one can rewrite the von Neumann entropy as [465]

$$S_1[\rho_A] = -\sum_{Q_A} p_{Q_a} \log p_{Q_A} - \sum_{Q_A} p_{Q_A} \mathrm{tr}\left(\rho_A^{(Q_A)} \log \rho_A^{(Q_A)}\right) = S_Q + S_{\mathrm{conf}}. \tag{10.10}$$

The first term is the entropy associated to the probability distribution p_{Q_A}, which we will refer to as the *number entropy*. The second term is the average entropy of the blocks, which, following Ref. [465], we call the configurational entropy, as it is associated to superpositions between different ways of arranging the same number of total charges within the subsystem. Importantly, the number entropy was shown to be an independently measurable quantity in cold atom experiments [465].

For the types of initial states considered here, with roughly homogeneous charge distributions, the mean value of the distribution p_{Q_A} is close to its equilibrium value even after short times. However, this distribution is initially very narrow, with a variance $\mathrm{Var}(Q_A)$ that should grow as $\propto \sqrt{t}$, due to diffusion, as argued we argue in App. B.6. This provides an upper bound on the number entropy, as $S_Q \leq \ln\left(\sqrt{2\pi e \mathrm{Var}(Q_A)}\right) \approx \log t^{1/4} + \text{constant}$. We indeed confirm that the growth of S_Q has this form, by performing the exact random circuit time evolution for a small system, as shown in Fig. 10.6. Note that approximating the entropy as the logarithm of the standard deviation is also consistent with the long-time saturation value, which should be $S_Q(t \to \infty) = \log\sqrt{l} + \text{const.}$ for the binomial distribution. As emphasized earlier, S_Q itself is a measurable quantity and therefore this prediction could be directly confirmed in experiments. We also expect this to manifest as a logarithmically growing component of the full von Neumann entropy (10.10), although in principle it is possible that this contribution is cancelled by some part of the configurational entropy.

11. Entanglement growth for inhomogenous quenches

So far, our discussion of entanglement growth has focused on global quenches, where the initial state is homogenous in space (at least on scales large compared to the lattice spacing). However, quenches starting from *inhomogenous* initial states are of interest on their own right. This is a context where the transport of conserved quantities appears most directly, as they need to be moved across the system in order to reach thermal equilibrium, implying that the time scales needed to fully thermalize, even with respect to local observables, are long compared to the associated wavelengths that characterize the initial state. Here we ask the question of how this slow thermalization manifests itself in the entanglement properties of the evolving state.

An extreme case, which we will discuss in detail below, is that of a domain wall: an initial state where the density of some conserved quantity jumps between two extreme values in the middle of the system. Entanglement growth starting from such a domain wall was investigated for integrable systems, where both logarithmic [621–623] and power law [317, 624] growth have been found for the entanglement. More recently, the quasi-particle picture has been extended to a variety of inhomogeneous initial states, using notions of generalized hydrodynamics, applicable to integrable systems [625–627]. However, the case of generic interacting systems remains largely unexplored.

In this chapter, we develop a general theory of the growth of von Neumann entropy for inhomogenous quenches. Our approach here can be considered as a generalization of the hydrodynamic minimal polymer picture of Section 5.2, modified to take into account the coupling of the entropy to the simpler, diffusive hydrodynamic equations obeyed by the conserved densities such as particle number, energy etc. For homogenous quenches, our theory reduces to the original minimal polymer picture, which is indeed expect to describe the growth of von Neumann entropy after a global quench, even in the presence of conservation laws [277] (this is in contrast with the $\alpha > 1$ entropies, for which this picture needs to be modified, as we saw in the previous chapter).

As before, we use $U(1)$-symmetric random circuits to help develop a general theory. The resulting equations of motion can be interpreted as a surface growth model, similar to the one discussed in Section 5.3, but with a growth rate that is coupled to the diffusive variable. This implies that inhomogeneities in the original charge get imprinted into the growing 'height' profile of the entanglement. In particular, we show that whenever there is a domain wall between two regions with different charge densities, the entanglement entropy near the interface has a component that grows in time as $\sqrt{t}$. The size of the region where this scaling applies also grows in time as $\sqrt{t}$ as the charge density smooths out due to diffusion; this is sketched in Fig. 11.1. For a charge density wave initial state, this process leads to an inhomogeneous entanglement profile across the system with a periodicity that is half the wavelength that characterizes the initial state. At longer times, as the charge distribution flattens, the entanglement profile also smooths out exponentially, but at a timescale that is parametrically larger than the time needed for the charge to equilibrate. We illustrate this general picture on a variety of different initial states, both for a random circuit model and for a deterministic system.

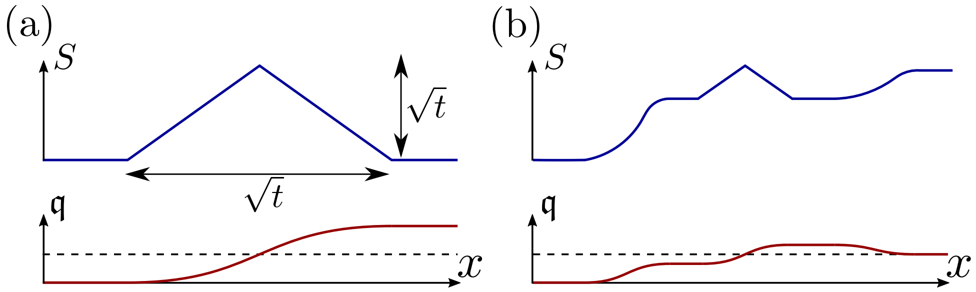

Figure 11.1.: Sketch of the evolving charge density ($\mathfrak{q}$) and entanglement (S) profiles for inhomogenous initial states in a diffusive spin chain. The dashed horizontal lines denote half filling. (a) Starting from a maximally polarized domain wall state, entanglement builds up only in a region of size $\propto \sqrt{t}$ around the initial position of the domain wall, limiting the 'height' of the entanglement profile to also be $O(\sqrt{t})$. (b) For a more generic initial state, with domains of different charge densities, the entanglement grows faster in regions where the charge density is closer to half filling, leading to an inhomogenous profile.

11.1. Stochastic surface growth model

First, to motivate an effective description of entanglement growth in our inhomogenous setup, we turn our attention to the coarse-grained version of the random circuit, which we originally introduced in Section 7.1, and studied previously in subsection 8.2.3 in the context of OTOCs. In this model, each 'super-site' contains N qubits. We imagine working in a large-N limit; the main reason for this is that in this limit, *local fluctuations* of the charge as suppressed, and we can focus on the effect of the inhomogeneities in the *average* charge. We first discuss how the entanglement entropy $S(x)$ across the bond between super-sites $x, x+1$ evolves under the application of a single charge-conserving unitary gate. Based on these considerations, we conjecture a simple random surface growth model to capture certain universal features of entanglement growth. In Section 11.2 we will compare the results of this surface growth model with numerics on various spin-$\frac{1}{2}$ chains.

11.1.1. Effect of a single gate

We begin by considering the effect of a single charge-conserving 2-site gate, and use it to conjecture an effective update rule for the half-chain entanglement across the bond at these two sites. The main feature of this update rule, established using the subadditivity of entropy, is that the growth of entanglement is limited by the local entropy density, corresponding to the density of conserved charge. We also explore the possible interplay between charge density and the gradient of the half-chain entanglement.

We mainly focus on the *half-chain von Neumann entropy*, $S_1(x,t) \equiv -\mathrm{tr}\,(\rho \ln \rho)$, where ρ is the reduced density matrix of the subsystem consisting of all sites $\leq x$, at time t. We mostly focus on S_1 in this chapter, which captures (the logarithm of) the typical eigenvalue of ρ, while later in this subsection we will briefly consider the case of $\alpha = 0$, also known as the *Hartley entropy*, which measures (the logarithm of) the rank of ρ. For this latter quantity, we are able to establish an exact update rule in the case when a charge-conserving gate is applied to a pair of neighboring sites with a fixed amount of total charge. Later on, in subsection 11.2.1, we will also consider S_2, which is more amenable to numerical calculations in the random circuit setting.

Von Neumann entropy S_1

We begin by noting that the growth of S_1 is constrained by the local entropy density, $s_{x,t}$ (the von Neumann entropy of the subsystem consisting of the site x alone), through the subadditivity condition [233],

$$S_1(x, t+1) \leq S_1(x-1, t) + s_{x,t+1}, \tag{11.1}$$

where we used the fact that the entanglement across the bond $x-1, x$ is unchanged by the 2-site gate acting on sites $x, x+1$, so that we can replace $S_1(x-1, t+1)$ with $S_1(x-1, t)$. The same argument holds when replacing $S_1(x-1, t)$ with $S_1(x+1, t)$ and $s_{x,t+1}$ with $s_{x+1,t+1}$, such that

$$S_1(x, t+1) \leq \min\big(S_1(x-1, t) + s_{x,t+1}, S_1(x+1, t) + s_{x+1,t+1}\big). \tag{11.2}$$

What we will conjecture in the following is that replacing the inequality with an equality in Eq. (11.2) provides a good qualitative description of the time evolution of the von Neumann entropy, particularly in situations where the charge has locally equilibrated. After local equilibration, we also expect that $s_{x,t+1} \approx s_{x+1,t+1} \approx s_{x,t}$, so that it can be pulled out of the min function. The resulting equation is already sufficient to capture the qualitative features we discuss below.

The bound in Eq. (11.2) can be improved in certain circumstances, through the following line of reasoning, although there does not appear to be a sharp qualitative change in the physics in considering these subtler effects. In particular, we can consider a case where the two sites on which our unitary gate acts have a fixed total charge. This is motivated by the fact that if the charge distribution on the two sites in question is tightly peaked (as we would expect it to be at times in excess of the local equilibration time, in the large-N limit), then the von Neumann entropy, which measures the size of typical Schmidt values, should be well approximated by focusing on Schmidt values corresponding to the average charge[1]

Thus, let us assume, for the time being, that the charge on sites $x, x+1$ takes a definite value $Q_{x,x+1} = Q$. In this case, the reduced density matrix on sites $\leq x$ is block diagonal in Q_x, the charge on site x. Let us denote the block with $Q_x = a$ as $p_a \rho_a$, where p_a is the probability of having charge a on site x, and $\mathrm{tr}(\rho_a) = 1$. Then the von Neumann entropy can be written as [465]

$$S_1 = \sum_a p_a S_{1,a} - \sum_a p_a \ln p_a,$$

where $S_{1,a} = -\mathrm{tr}(\rho_a \ln \rho_a)$ is the von Neumann entropy of the density matrix associated to charge a. Note that the last term is upper bounded by $\ln(Q+1)$, since a takes values between 0 and Q, and therefore should be strongly subleading, as the total von Neumann entropy will eventually increase to an extensive value. This means that, to a good approximation, the entropy can be written as a weighted sum over entropies of different charge sectors. One can then apply subadditivity to each block separately

$$S_{1,a}(x, t+1) \leq \min\left(S_{1,a}(x-1, t) + \ln \eta_a, S_{1,a}(x+1, t) + \ln \eta_{Q-a}\right),$$

where $\eta_a \equiv \binom{N}{a}$ is the dimension of the on-site Hilbert space with charge a. Here, the entropies of the neighboring bonds also depend on a, since the projection to a given charge sector can in principle change the entanglement even away from the bond $x, x+1$. However, based on a simple numerical experiment involving a 4-site random MPS, we expect that if there is a gradient $S_1(x+1, t) - S_1(x-1, t)$ in the original state, then there should

---

[1] Note that this is in contrast with Rényi entropies $S_{\alpha>1}$, which are strongly influenced by fluctuations of the conserved charge, as discussed in Chapter 10.

also be a a gradient $S_{1,a}(x+1,t) - S_{1,a}(x-1,t)$ in the projected state as well – albeit one whose magnitude decreases with a. Therefore, one ends up with an upper bound that depends on a particular combination of the charge density and the entropy gradient. The same numerical experiment indicates that this bound is tighter then the bound in Eq. (11.2), at least away from half filling. This suggests that there is a possibility of a more complicated coupling between charge and entanglement, where the growth rate of the latter depends not only on the charge density, but also on the local gradient of $S_1(x,t)$. We will argue more rigorously for such a coupling in the case of S_0 below. However, our numerical experiments suggest that the main qualitative features are already captured by the simpler bound in Eq. (11.2), ignoring these subtler effects.

Parameter counting argument for S_0

The above argument, regarding the coupling between charge and entanglement gradient, can be made more precise if we consider the Hartley entropy, $S_{\alpha=0}$, which equals the logarithm of the number of non-zero Schmidt values. Below we derive an update rule for this quantity under the effect of a generic unitary acting on a generic state with well defined charge on $x, x+1$. While the assumption of fixed local charge is not well motivated in the case of S_0, it is nevertheless useful to consider, as it sheds some light on the nature of the coupling between charge and entanglement gradient mentioned above.

Consider a matrix product state (MPS) with fixed 2-site charge Q on sites $x, x+1$, and a bond dimension $\chi(x) \equiv e^{S_0(x)}$ across this bond. One can then generalize the parameter counting argument of Ref. [276] to estimate the bond dimension $\tilde{\chi}(x)$ across the same bond *after* a charge-conserving unitary has been applied to these two sites[2]. Since Q is conserved, we can label the Schmidt values at $x, x+1$ (after applying the unitary) according to the amount of charge on site x. Let us denote this charge by $Q_x = a$. We will estimate the number of non-zero Schmidt values $\tilde{\chi}_a(x)$ in each a sector separately, by equating the number of parameters in the new MPS tensors on sites $x, x+1$ with the number of equations needed to relate the new MPS to the old one (consider Fig. 2.2 for an illustration).

We want to find new MPS tensors on both x and $x+1$ that describe the state after it has been evolved with the unitary gate on these sites. For a given a, the two MPS tensors have $\chi(x-1)\tilde{\chi}_a(x)\eta_a + \tilde{\chi}_a(x)\chi(x+1)\eta_{Q-a} - \tilde{\chi}_a(x)^2$ parameters in total, where $\chi(x\pm1)$ are the bond dimensions on neighboring bonds and the last term takes into account the gauge freedom in choosing the MPS tensors. The number of parameters has to be sufficiently large to satisfy all the $\chi(x-1)\chi(x+1)\eta_a\eta_{Q-a}$ equations, coming from equating the new tensors with the original MPS evolved by a single 2-site gate. Equating the number of equations with the number of parameters gives a quadratic equation for $\tilde{\chi}_a(x)$. Taking the smaller of the two solutions and adding up the Schmidt values for different a sectors gives the total bond dimension across a bond $x, x+1$ with charge Q, after applying the gate:

$$\chi(x,t+1) = \sum_a \min\left(\chi(x-1,t)\,\eta_a, \chi(x+1,t)\,\eta_{Q-a}\right). \tag{11.3}$$

i.e., in each charge sector we end up with the maximal bond dimension allowed by subadditivity.

Without loss of generality, let $\chi(x+1) = \chi(x-1)e^{2\Delta}$, for some entropy gradient $\Delta \geq 0$ going across the bond (note that $e^{2\Delta} \leq d_Q$, due to subadditivity of entanglement). Then, we get the update rule for the Hartley entropy, $S_0(x,t) \equiv \log\chi(x,t)$, as

$$S_0(x,t+1) = \min\left(S_0(x-1,t), S_0(x+1,t)\right) + f_N(Q,\Delta), \tag{11.4}$$

---

[2] While this parameter counting argument is not rigorous, in the sense that fine-tuned states or unitaries could violate it, it is expected to hold for generic states, which we indeed find numerically for random MPS.

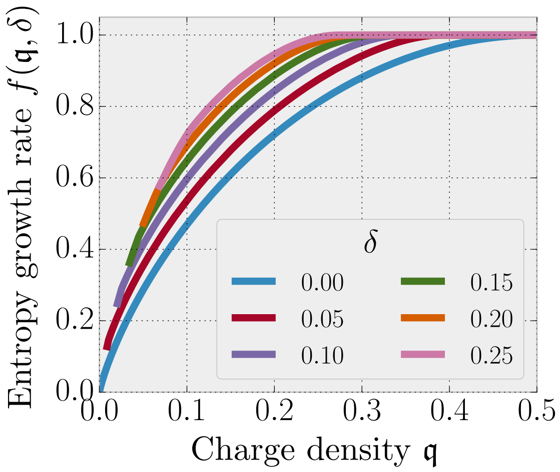

Figure 11.2.: The entropy growth function $f(\mathfrak{q},\delta)$, appearing in the RHS of Eq. (11.4), in $N\to\infty$ limit, using rescaled variables $\mathfrak{q}\equiv Q/(2N)$ and $\delta=\Delta/N$.

where $f_N(Q,\Delta)\equiv\log\left(\sum_{a=0}^{Q}\min(\eta_a,\eta_{Q-a}e^{2\Delta})\right)$, and we measure logarithms base 2^N. Therefore, we find a result that has more structure then the simple subadditivity bound in Eq. (11.2): the entropy increase depends not only on the local entropy, but also on the spatial derivative of $S_0(x,t)$ across the bond. This arises due to the fact that after fixing $Q_{x,x+1}$, we can count the entropy for each charge sector separately: having a gradient Δ across the bond allows for putting more charge on one site in order to increase the total entropy.

To get a sense of the behavior of the term $f_N(Q,\Delta)$ in Eq. (11.4), we take its large-N limit. In this case, $\eta_a=\binom{N}{a}\to e^{Nh_2(a/N)}$, using the binary entropy function, $h_2(\xi)\equiv-\xi\ln\xi-(1-\xi)\ln(1-\xi)$. Defining rescaled variables, $\xi\equiv a/N$, $\mathfrak{q}\equiv Q/2N$ and $\delta=\Delta/N$, the condition $\eta_a=\eta_{Q-a}e^{2\Delta}$ translates to $h_2(\xi)=h_2(2\mathfrak{q}-\xi)+2\delta$. Let $\xi_*(\mathfrak{q},\delta)$ denote the solution to this equation when it exists, and $\xi_*=2\mathfrak{q}$ otherwise. The sum over a in the definition of f_N can then be replaced by a pair of integrals over ξ, on intervals $[0,\xi_*]$ and $[\xi_*,2\mathfrak{q}]$. In the limit $N\to\infty$ these integrals can be approximated by the maximal value inside the interval, giving the result

$$f(\mathfrak{q},\delta)\equiv f_{N\to\infty}(2N\mathfrak{q},N\delta)=\begin{cases}\frac{h_2(\xi_*)}{\ln 2} & \text{if } \xi_*\leq 1/2\\ 1 & \text{if } \xi_*>1/2.\end{cases}\tag{11.5}$$

Fig. 11.2 shows the resulting function $f(\mathfrak{q},\delta)$ as a function of the charge density $\mathfrak{q}$ for a variety of δ. Its most notable feature is that for $\delta>0$ it becomes constant for sufficiently large values of $\mathfrak{q}$.

The arguments above, in particular the result (11.4), indicate a complicated coupling between charge and entanglement entropy, where the local growth rate of the bipartite entanglement depends on a particular combination of local charge density and the entropy gradient. However, in the physical situations we consider in the next subsection, we find that this dependence on the entropy gradient does not change the qualitative features of entanglement growth, and in practice one can replace the constant term in the RHS with just the on-site entropy $h_2(\mathfrak{q})$, which is the original subadditivity bound in Eq. (11.2). As we argue below, in subsection 11.1.2, this can be understood from the fact that in a coarse-grained continuum description the difference only shows up in the form of higher order subleading corrections. Nevertheless, it would be interesting to understand whether there are physical situations where such a coupling can still play an important role.

11.1.2. Surface growth in a space-time dependent background

The equation of motion in Eq. (11.4) is a direct generalization of the local update rule for a non-symmetric random gate, Eq. (5.20). The only difference is that the constant growth term on the RHS now depends on space and time, through the local charge density $\mathfrak{q}$, and also potentially on the entropy gradient. We can then construct an effective, 'surface growth' model of entanglement growth, along the same lines as in Ref. [276]: in each time step we apply the update rule on a randomly chosen bond (see Fig. 7.1(c)), using the function $f(\mathfrak{q}, \delta)$ derived in Eq. (11.5), to update the half-chain entanglement $S(x,t)$ (the 'height'). At the same time we update the local charge densities $\mathfrak{q}(x) \equiv Q_x/N$ as $\mathfrak{q}(x), \mathfrak{q}(x+1) \to (\mathfrak{q}(x)+\mathfrak{q}(x+1))/2$. This leads to a coupled stochastic evolution between $\mathfrak{q}(x)$ and the entropy $S(x,t)$. Below, we investigate the behavior of this stochastic model, which we compare to simulation of quantum systems in Section 11.2.

General considerations

As stated before, we find numerically that the coupling between the charge and the entropy gradient does not affect the main qualitative features of the evolution, therefore in practice, at least in the situations we consider below, one can replace $f(\mathfrak{q}, \delta)$ with $f(\mathfrak{q}, 0) = h_2(\mathfrak{q})$, the local binary entropy associated to the charge density. This leads to a simplified update rule

$$S(x, t+1) = \min\left(S(x-1,t), S(x+1,t)\right) + h_2(\mathfrak{q}). \tag{11.6}$$

In the continuum limit this corresponds to a KPZ equation for the entanglement (as in Section 5.3), but now coupled to the diffusion equation for the charge as

$$\begin{aligned} \partial_t S(x,t) &= \nu \partial_x^2 S - \frac{\lambda}{2}(\partial_x S)^2 + s(x,t)(v_{\mathrm{E}} + \zeta(x,t)); \\ \partial_t \mathfrak{q}(x,t) &= D\partial_x^2 \mathfrak{q} + \zeta_{\mathfrak{q}}(x,t) \end{aligned} \tag{11.7}$$

where $s(x,t) \equiv h_2(\mathfrak{q}(x,t))$ is the entropy density, $\zeta(x,t)$ is uncorrelated white noise and $\zeta_{\mathfrak{q}}(x,t)$ is a noise field consistent with charge conservation (model B dynamics in the language of Ref. [551]). Note that is we kept the function $f(\mathfrak{q}, \delta)$ in Eq. (11.6) (instead of replacing it with $f(\mathfrak{q}, 0) = h_2(\mathfrak{q})$), the highest order terms we would need to add to the continuum description would be of the form $(\partial_x \mathfrak{q})^2 (\partial_x S)^2$, which are subleading in the long wavelength limit, therefore we are justified in dropping them.

The above random surface growth model also admits an interpretation as a directed polymer problem, along the lines discussed in Section 5.2. As shown there, on the longest length and time scales, the entanglement resulting from Eq. (11.6) can be rewritten as the energy of a minimal energy polymer, characterized by an 'entanglement line tension' $\mathcal{E}(v)$, with v being the slope of the polymer, representing a space-tim cut through the unitary circuit. Since our update rule differs from the one in Ref. [276] by having a constant term $s(x,t)$, rather then 1, on the RHS, one has to rescale $S \to S/s$ to get the same physics locally. This implies that the line tension gets rescaled as $\mathcal{E}(v) \to s(x,t)\mathcal{E}(v)$. Therefore the calculation of entanglement growth becomes that of finding a polymer with minimal energy in a space-time dependent background, where the background itself contains a deterministic evolving part, governed by the diffusion equation, as well as random noise. In particular, parts of the systems with very low/high fillings act as bottlenecks for the entanglement growth of nearby regions[3]. On the other hand, the charge density itself undergoes diffusion, tending toward a more homogenous distribution. The entropy density follows the charge distribution, leading to a speed-up of entanglement growth in regions where it gets closer to half filling and vice versa.

---

[3] This is similar to the mechanism proposed in Ref. [233] for entanglement growth in disordered Griffith phases, where the bottleneck is provided by localized regions which act as 'weak links'.

We expect this generalized minimal cut picture to apply also to systems without noise, much like its original version which did not take conservation laws into account [277]. In our case, this would correspond to an equation of motion analogous to Eq. (11.7), but with the noise terms omitted. The original minimal cut picture can also be generalized to higher spatial dimensions, replacing the polymer with a 'membrane' [276, 277, 578]. We expect that the model we consider here similarly generalizes, with a minimal membrane whose local surface tension depends on the entropy density at a given position and time.

Application to various initial states

To see the effect that the diffusion of charge has on entanglement growth, let us first consider the paradigmatic example of a maximally polarized domain wall initial state, wherein all sites on the left half of the chain are empty ($\mathfrak{q}(x \leq 0, t = 0) = 0$) and all sites on the right half are filled ($\mathfrak{q}(x > 0, t = 0) = 1$). We imagine working in the thermodynamic limit, so that $x \in \mathbb{Z}$ and we can ignore boundary effects. At long times and large distances we expect the charge profile $\mathfrak{q}(x, t)$ to be well approximated by the solution of the continuum diffusion equation, which for these initial conditions reads $\mathfrak{q}(x, t) = \left(1 + \mathrm{erf}(x/\sqrt{Dt})\right)/2$, where $\mathrm{erf}(x)$ is the error function.

The important property of the solution of the diffusion equation is that the width of the domain wall scales with time as $\propto \sqrt{t}$, and consequently the local entropy density $s(x, t)$ is also a function solely of $x/\sqrt{Dt}$. This, via Eq. (11.6), indicates that significant entanglement growth can only occur within a region of order $\mathcal{O}(\sqrt{Dt})$ around the origin. At long times this diffusive growth is very slow compared to the linear growth of the entanglement surface that one would get for a homogeneous charge distribution. This means that the charge diffusion acts as a bottleneck for the entanglement growth: for the entanglement in the middle to grow further, it first has to 'wait' for the width of the domain wall to increase. As a consequence, the height itself grows as $S(0, t) \propto \sqrt{t}$, as sketched in Fig. 11.1(a). In fact, the upper bound $S_1(0, t) \lesssim \mathcal{O}(\sqrt{t})$ in this case follows simply from combining subadditivity with the assumption of local equilibrium, see below in Eq. (11.8).

By performing the stochastic surface growth numerically, we find a scaling collapse of the form $S(x, t) = \sqrt{Dt}\, f(x/\sqrt{Dt})$ for some function f, as shown in Fig. 11.3(a). At long enough times, $Dt \gg 1$ (in units of the lattice spacing), the surface profile is always close to being saturated to the maximum value allowed by the charge distribution, with a distance between the two becoming constant. This also means that there is no allowed 'space' for the surface to develop large random fluctuations, which would be present for a flat surface - such KPZ fluctuations are suppressed by the slow dynamics of the charge that is coupled to the surface growth.

While the domain wall constitutes an extreme case, where the charge densities at the two infinities take the two extreme values, 0 and 1, a similar behavior occurs more generally if we take an initial state with a jump in the average charge at the origin. The simplest generalization is to take an initial state where $\mathfrak{q}(x \leq 0) = n$ and $\mathfrak{q}(x > 0) = 1 - n$ for some $0 < n < 1/2$. In this case, far from the origin, at positions $x \gg \sqrt{Dt}$, the dynamics of entanglement is the same as for a homogenous state with charge density n, i.e., it grows linearly with the rate set by n and exhibits KPZ fluctuations. However, in a diffusively growing region around the origin, where the charge density has started equalizing, the entanglement grows faster and exhibits a 'bump' on top of the linearly growing background. Both the spatial size and the height of this bump is once again increasing as $\sqrt{t}$ (see Fig. 11.3(c)) and the KPZ fluctuations are suppressed in this region. This is shown in Fig. 11.3(b).

Another, slightly different, scenario where the diffusion plays an important role, is an

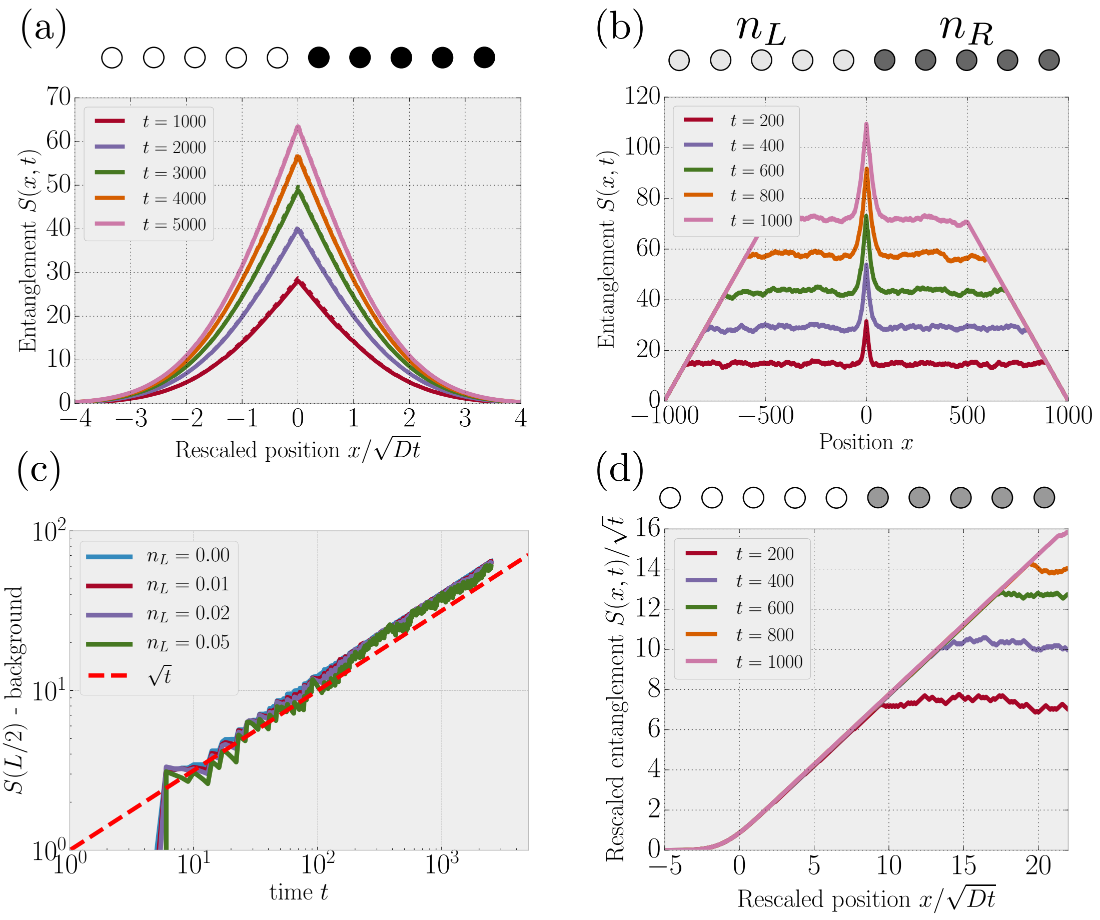

Figure 11.3.: Entanglement growth generated by applying the update rule (11.6) to a randomly chosen bond at each step. (a) For an initial domain wall state, entanglement grows as $\propto \sqrt{t}$ and is close to the maximum value allowed by subadditivity (dashed lines). As a consequence, random fluctuations are strongly suppressed. (b) For a generalized domain wall, with charge densities n_L and $n_R = 1 - n_L$ on the two sides, the 'bump' appears on top of a linearly growing background where KPZ fluctuations are present. (c) Subtracting the average height of this background, we observe that the size of the bump itself always grows as $\propto \sqrt{t}$. (d) For an asymmetric domain wall, $n_L = 0$, $n_R = 1/2$, there is a region with $\propto \sqrt{t}$ entanglement interpolating between the two bulk regions.

interface between two regions with different entropy densities. An extreme example of this is when a region at half filling, such as a Néel state, expands into empty space. In this case, in the middle of the half-filled region, far from the interface, we once again get linear growth with the usual KPZ fluctuations. Far on the other side of the interface, the charge density vanishes and so does the entanglement. Near the interface there is a diffusively growing region that interpolates between these two extremes, where the entanglement obeys the scaling $S(x,t) = \sqrt{Dt}\; g(x/\sqrt{Dt})$ for some scaling function g. The middle region where this scaling is valid then penetrates linearly into the half-filled region. This is shown in Fig. 11.3(d). A similar situation would occur if the average charge densities on the two halves of the chain are initially $0 < n_L < n_R < 1 - n_L$. In this case there is linear growth on both sides, but with different growth rates, so that there are two plateaus of different heights with an interpolating region in-between.

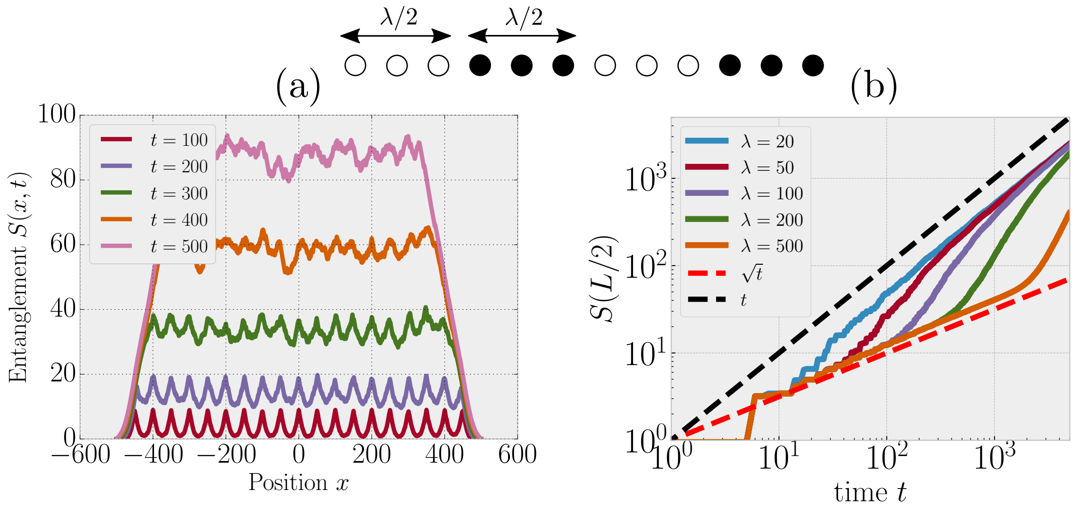

Figure 11.4.: Entanglement growth from the random surface growth model with charge density wave initial state of equally spaced domain walls at a distance $\lambda/2$ sites. (a) the initial melting of the domain walls creates an inhomogenous entanglement profile (shown for $\lambda = 100$ sites). This subsequently smooths out once the charge has equilibrated. At the same time KPZ behavior takes over, with fluctuations growing in time. (b) Consequently, the overall growth rate at a domain wall has a cross-over from $\propto \sqrt{t}$ to $\propto t$ at a time $\propto \lambda^2$, when the domain walls melt into each other (shown for $L = 5000$).

The initial states described above all have charge-imbalances between the left and right halves of the chain, such that in the thermodynamic limit it would take an infinite amount of time for them to become homogeneous. We can also consider initial states which have charge-inhomogeneities on some parametrically smaller length scale, $1 \ll \lambda \ll L$. An example of such a state is a step-like charge density wave (CDW), consisting of domains of $\lambda/2$ filled sites followed by $\lambda/2$ empty ones in a regular pattern. At short times, $t \ll \lambda^2/4D$, each domain wall in the initial state evolves independently, in the way described above, while far from the domain walls there is no dynamics. This results in an entanglement profile with peaks separated by a distance $\lambda/2$ from one another, whose width and height grow as $\sqrt{t}$. Once the peaks start to overlap, at times $t_Q \sim \mathcal{O}(\lambda^2/4D)$, i.e., when the domain walls start to melt together, the bottleneck disappears and the entanglement growth speeds up from $\sqrt{t}$ to linear in t (see Fig. 11.4(b)). At the same time the entanglement profile starts to smooth out: the difference between the top and the bottom of a peak, $\Delta S \equiv S(0,t) - S(\lambda/4,t)$, decreases to zero, as shown by Fig. 11.4. We find numerically (see Fig. 11.5) that the average size of the peaks in the entanglement profile decreases exponentially, as $\Delta S \propto e^{-\frac{4\pi^2}{\lambda^2}t}$. We associate this with the first (diffusive) term on the right hand side of the first equation in Eq. (11.7).

Using the results above we can associate two distinct time scales to the evolution of the entanglement starting from a CDW, made out of regions of different charge densities of typical size λ. First there is the aforementioned time scale $t_Q \sim \lambda^2/D$, until which each domain wall evolves independently. By this time, the entanglement profile develops peaks of size $\Delta S \propto \sqrt{Dt_Q} \propto \lambda$. At times $t \approx t_Q$ a second time regime begins, wherein the entanglement features smooth out exponentially as $\Delta S \propto \lambda e^{-8\pi^2\frac{t-t_Q}{t_Q}}$. The time needed for the entanglement profile to become sufficiently smooth, i.e., $\Delta S \ll 1$, is therefore $\frac{t-t_Q}{t_Q} \gg \log\lambda$, or equivalently $t \gg \frac{\lambda^2}{D}(1 + \log\lambda)$. Note that this is parametrically larger

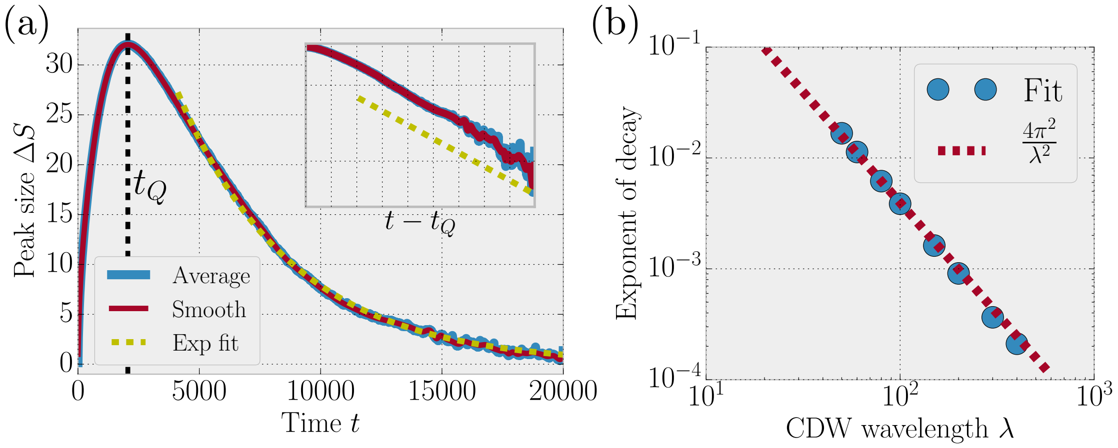

Figure 11.5.: Smoothing out of the inhomogeneities of $S(x,t)$, starting from a charge density wave initial state. We calculate the size of the peaks due to the initial inhomogenous growth (see Fig. 11.3(b)), averaged over all peaks in a system and over 10 realizations of the stochastic dynamics. a) We find that the size of the peaks grows up to some timescale t_Q (denoted by the dashed vertical line), at which point the different domains melt together and the profile starts smoothing out exponentially. Data is shown for a chain with $L = 40000$ sites and CDW wavelength $\lambda = 400$. The thick blue curve is numerical data for the average peak size ΔS, relative to the linearly growing background; the thin red curve is a numerically smoothened extrapolating curve and the dashed yellow line is an exponential fit. The inset shows the same data as a function of $t - t_Q$ with a logarithmic scale on the vertical axis. b) Exponents from the exponential fit for different wavelengths λ. We find that a decay $\propto e^{-\frac{4\pi^2}{\lambda^2}t}$.

than the time scale it takes for the charge-distribution to become approximately flat, which merely requires $\frac{t-t_Q}{t_Q} \gg 1$.

To summarize our findings in this subsection, let us consider a rather broad set of initial states, that consist of different domains of typical size λ, each domain roughly homogeneous with some specific average charge density. For such a state, we can distinguish four different time scales. I) There is some short initial time scale t_{loc} associated to reaching local equilibrium. II) This is followed by the transport of charge from domains of high density to neighboring regions of lower density. In the middle of the domains, the entanglement grows linearly at the rate set by the local entropy density of the region. At the interfaces of different domains, the transport of charge is accompanied by the appearance of 'bumps' in the entanglement profile. These bumps grow as $\sqrt{t}$ with respect to the entanglement in the middle of the domains which they separate (the one with the smaller entropy density if those are different). III) This bumpy entanglement profile develops up to times $t_Q \sim \mathcal{O}(\lambda^2/D)$, at which point the domains start to melt completely into one another. The entanglement growth at the domain walls speeds up to linear in time and the entanglement profile smooths out. There is another timescale associated to this smoothing which scales as $t_Q(1 + \log \lambda)$. IV) Eventually there is a fourth time regime, when the entanglement stops growing and saturates to its equilibrium value (assuming the system is finite). Note that the III) regime is only present if there is a separation of scales $\lambda \ll L$. If the initial inhomogeneities are on the scale of the entire system then equilibration of the charge density and the saturation of the entanglement profile happens simultaneously.

Befor moving on, we mention that there is a potentially important aspect of noisy dynamics that is not captured by our surface growth model presented here, related to the fact that noise can generate small-scale random inhomogeneities in the charge profile even if the initial distribution is homogenous. This effect would be present in the continuum model of Eq. (11.7), but not in the discrete update rule we consider. In this sense, our model would rather correspond to a particular type of noise that is diagonal in the conserved quantity, such as in Refs. [565, 566]. A similar stochastic model that *does* capture such local random inhomogeneities in the charge was recently investigated in a different context [628] (that of classical chaos)[4]. The results of Ref. [628] suggest that, while adding these effects is not expected to affect the overall growth of entanglement for inhomogenous states, which is our main concern here, they *would* lead to qualitatively new features in the scaling of random fluctuations even within homogenous regions, driving them away from the KPZ universality. We leave a more complete exploration of this to future work.

11.2. Spin-$\frac{1}{2}$ chains

We now compare the predictions of the simple effective model of the previous subsection with results on spin-$\frac{1}{2}$ chains. We first take the a version of the $N = 1$ random circuit model defined in Section 7.1, one where the arrangement of random gates follows a regular brick-wall pattern (Fig. 7.1(b)). In this case, the quantity we can compute efficiently is the annealed average of the 2nd Rényi entropy. While, as shown in the previous chapter, $\alpha > 1$ Rényi entropies have very different dynamics from the von Neumann entropy in the case of a *global* quench, we find that the effects associated to charge inhomogeneities are similar to those predicted by our surface growth model. In particular, for a domain wall initial state, we find a scaling collapse of the entanglement profile of the form $S(x,t) = \sqrt{t} f(x/\sqrt{t})$. In subsection 11.2.2 we compare to exact results on a non-random, periodically driven spin chain.

11.2.1. Spin-$\frac{1}{2}$ circuit model

The simplified model of the previous subsection relied on ignoring local fluctuations of the charge, and using only the average local density as the only relevant variable. Here we show that the features associated with inhomogeneities are quite similar even if we consider the spin-$\frac{1}{2}$ random circuit, where we expect fluctuations in the local charge density to be non-negligible. We take now a circuit where the unitary gates are applied in the regular 'brick wall' pattern, and each site contains a single conserved spin ($N = 1$).

We consider the annealed average of the second Rényi entropy, $S_2^{(a)} \equiv -\ln\left(\overline{\mathrm{tr}(\rho_A^2)}\right)$, and calculate it by mapping to the effective 2D partition function as outlined previously (see subsection 8.1.1 in particular). Note that the annealed average Rényi entropy provides a lower bound on the von Neumann entropy, $S_2^{(a)}(t) \leq \overline{S_2(t)} \leq \overline{S_{\mathrm{vN}}(t)}$. As we now show, several of the features predicted by our surface growth model in Section 11.1.2 appear also in the dynamics of $S_2^{(a)}$, when computed for inhomogenous initial states.

We once again start by considering a domain wall initial state. As argued before in subsection 11.1.2, since the charge density obeys the diffusion equation, it has a profile $\langle \hat{Q}_x(t) \rangle$ that depends only on the combination $x/\sqrt{Dt}$, where for the present case the diffusion constant is $D = 1/2$. Assuming local equilibration, i.e., that the on-site reduced density matrix takes the form $\rho_x(t) \propto e^{-\mu(x,t)\hat{Q}_x}$ for some local chemical potential $\mu(x,t)$ (which, as we show in App. B.7, indeed holds after some short-time relaxation process),

---

[4] We thank David Huse for bringing this to our attention.

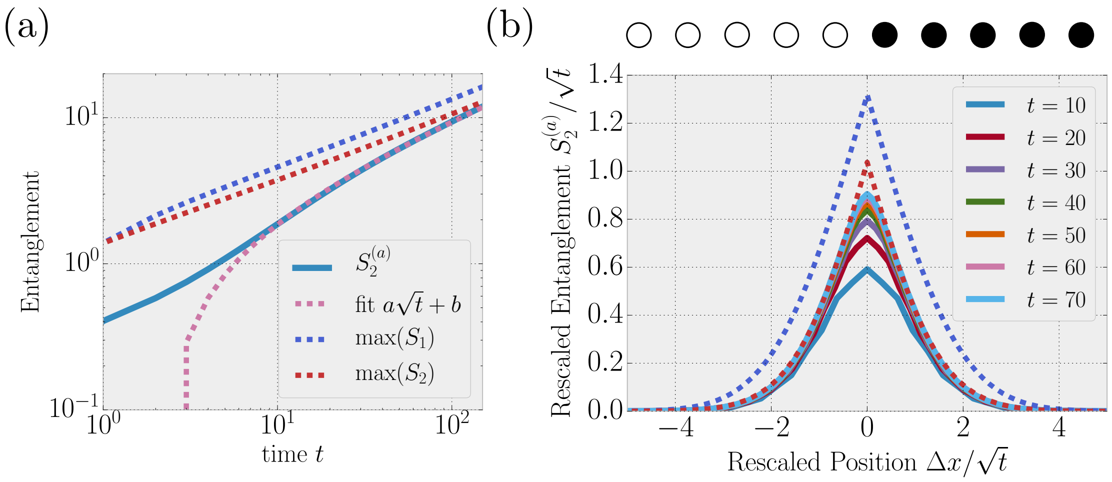

Figure 11.6.: Entanglement growth for an initial domain wall in the random circuit with $N = 1$. The solid lines are data obtained from numerically evaluating the annealed average of S_2, which provides a lower bound for $\overline{S_1}$ and $\overline{S_2}$. (a) Growth of entanglement in the middle of the domain wall, computed numerically for a chain of $L = 400$ sites, is well described by $\sim \sqrt{t}$ asymptotically. The dashed blue line is the upper bound from Eq. (11.8), given by the cumulative sum of the on-site von Neumann entropies associated to the average local charge density. The red dashed line is the cumulative sum of the local second Rényi entropies, which gives a good approximation of the behavior of the annealed average at long times. (b) shows the profile of entanglement over a chain of 200 sites, which at long times exhibits a scaling collapse, when both the position x and the entanglement $S_2^{(a)}$ are rescaled by $\sqrt{t}$. Dashed lines again indicate the cumulative sum of on-site entropies.

one can use subadditivity to upper bound for the von Neumann entropy as

$$S_1(x,t) \leq \sum_{x' \leq x} s(x',t) = \sqrt{Dt}\, f\left(\frac{x}{\sqrt{Dt}}\right), \tag{11.8}$$

where $s(x',t)$ is the one-site von Neumann entropy of site x' at time t. Therefore, the von Neumann entropy cannot grow faster than $\sqrt{t}$. Clearly the same upper bound applies to all higher index Rényi entropies, as well as to $S_2^{(a)}$.

The annealed average, $S_2^{(a)}$, on the other hand, provides a *lower bound* for both $\overline{S_1}$ and $\overline{S_2}$. Therefore if $S_2^{(a)}$ also grows as $\propto \sqrt{t}$ then it follows that all of these quantities have to have the same diffusive growth. This is exactly what we find by evaluating the annealed average numerically: after some initial short-time dynamics its behavior at $x = 0$ is well described by $S_2^{(a)}(0,t) = a\sqrt{t} + b$ for some constants a, b, as shown in Fig. 11.6. In fact we find that the profile of $S_2^{(a)}(x,t)$ is well approximated by the sum of the second Rényi entropies of the local one-site density matrices, $\sum_{x' \leq x} s_2(x,t)$, where $s_2(x,t) = -\log(1 - 2\mathfrak{q} + 2\mathfrak{q}^2)$ is the Rényi entropy density associated to a state in local equilibrium, parametrized by the charge density $\mathfrak{q} = \mathfrak{q}(x,t) \equiv \overline{\langle \hat{Q}_x(t) \rangle}$. That is, despite the fact that S_2 does not obey subadditivity, its annealed average behaves as if it satisfied a modified version of the inequality in Eq. (11.8), where we replace the von Neumann entropy density with that of the second Rényi entropy.

11.2.2. Deterministic Floquet spin chain

While random circuits have many advantages, we also wish to compare our predictions to deterministic models of unitary dynamics. While the KPZ fluctuations mentioned in Section 11.1.2 are particular to noisy dynamics, we expect that the imprints of charge transport, such as the $\sqrt{t}$ growth of entanglement for a domain wall, do generalize to the deterministic setting. We expect this to be the case, since many of the arguments discussed above follow largely from the diffusive dynamics of conserved quantities, which is generic at high temperatures [249, 279, 285, 553, 554].

To this end, we also perform calculations in a Floquet (periodically driven) spin chain, which we introduced in Eq. (8.9), where it was shown to exhibit clear diffusive tails in the OTOCs. Considering such a driven system has the advantage of simplicity; U(1) spin is the only conserved quantity. We leave it to future studies to consider other models, in particular those with energy conservation, and the appropriate generalizations of CDWs and domain walls in that context.

As emphasized in the previous subsection, the scaling observed for domain wall-like initial states, where both the size and the width of the features in the entanglement profile grow as $\propto \sqrt{t}$, is a direct consequence of diffusive transport. In particular, the upper bound derived above in Eq. (11.8) only relies on the assumptions of a) local equilibration and b) diffusive charge transport, both of which are expected to apply to generic many-body systems at high temperatures [249, 279, 285, 553, 554]. While this is only an upper bound, and in principle slower than $\sqrt{t}$ growth is possible, we do not expect this to be the case unless there are some further constraints on the dynamics[5]. Indeed, evolving a domain wall initial state with the Floquet unitary (8.9) we find that the entanglement entropy across the middle of the chain grows slower than ballistically[6], approximately as $t^{0.5-0.6}$. This result, shown in Fig. 11.7, reinforces our expectation that the asymptotic growth should be $\propto \sqrt{t}$.

Considering the full entanglement profile, however, we do not observe the scaling collapse seen previously for the random circuit (i.e. a $\propto \sqrt{t}$ width). Our interpretation for this is the following. While the deterministic model we consider is expected to show diffusive transport at 'high temperatures', or, in this case, at finite filling fractions, this is not the case when the filling is very small (or very close to 1), which is the case far from the middle of the domain wall. In these regions there are very few particles (or very few holes), which therefore propagate without many scattering events. This suggest that in the deterministic model there should be two distinct regimes: near the origin, where the domain wall has sufficiently melted and the average density is close to 1/2, the diffusive scaling should apply, while at the tails of the domain wall, where the filling is close to (but different from) 0 or 1, there is a ballistic region [6].

11.3. Entanglement level statistics for a domain initial state

Finally, we return to the calculation of level statistics in the entanglement spectrum of finite regions, which we discussed previously in Chapter 6. Recall, that there we shows that level repulsion develops initially at very high entanglement energies (the smallest eigenvalues of the reduced density matrix), and propagates linearly downwards, until the entire spectrum becomes chaotic at times set by the Lieb-Robinson velocity. A particular aspect of our proof was that it did not depend on the initial state in question, providing instead a universal lower bound. A natural question then is how the time scale needed

---

[5] Such is the case of integrable systems, which can exhibit logarithmic growth of the entanglement [622, 623], even though their transport properties are typically *faster* than diffusive.

[6] Note that even in the random circuit results at $N = 1$, shown in Fig. 11.6, the $\sqrt{t}$ growth is only true asymptotically and at short times a slightly faster growth is observed.

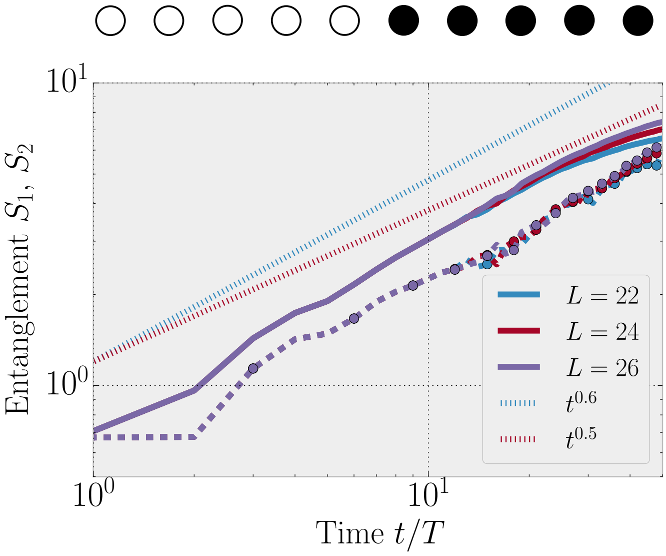

Figure 11.7.: Entanglement growth between two halves of a domain wall, evolved with the Floquet unitary (8.9). Solid lines represent the von Neumann entropy S_1 while dashed lines are the second Rényi S_2. Computed using exact diagonalization for system sizes $L = 22, 24, 26$.

to observe level repulsion depends on the initial state. While for a global quench corresponding to infinite temperature, the bound we derived might very well be tight, for other initial states one might need much longer times. Here we address this question for one particular initial state, one with a block of charges surrounded by empty regions in a $U(1)$-symmetric chain.

In a spin-language, we consider a domain initial state where all spins within region A are up, and all those outside of it are down. We evolve this state with the spin-1/2 $U(1)$-symmetric random circuit. Fig. 11.8(a) shows the resulting entanglement spectrum dynamics, as well as the boundary-spin mutual information. Observe that the time scale for the transition towards RMT behavior as seen in the r-ratio continues to coincide with the onset of non-zero mutual information between the boundary spins, and both remain linear in l, despite the diffusive charge dynamics. However, we see that the scale for the Poisson-RMT crossover is now increased by a factor of 2 relative to the non-conserving case, from $t = l/2v_{\mathrm{LC}}$ to $t = l/v_{\mathrm{LC}}$.

To understand why this is the case, first observe that for times $0 \leq t \leq l/2v_{\mathrm{LC}}$, we may simply use the same sequence of arguments as for the non-conserving case (see Fig. 6.1(a)). For times $l/2v_{\mathrm{LC}} \leq t \leq l/v_{\mathrm{LC}}$, the disentangled region constructed by the backward lightcone argument does not partition the circuit into disjoint regions and so for a generic circuit the density matrix does not factorize. However, the local conservation law strongly constrains the dynamics, as each 2-site gates only entangles spins if they are anti-parallel. It follows from this that that the dynamics deep within region A must be essentially trivial at early times, and can only multiply the system by an overall phase. Accordingly, the lightly shaded gates in Fig. 11.8(b) do not contribute to the entanglement, and may be ignored. Evidently, this picture allows us to construct a 'forward disentangled region' where the gates act trivially, drawing lightcones inward from the ends of subsystem A to the point $(x, t) = (l/2, \leq l/2v_{\mathrm{LC}})$. Combining these, we see that the entanglement spectrum factorizes as long as the two disentangled regions intersect, i.e. for all times $t \leq l/v_{\mathrm{LC}}$. Intuitively, this is the time for the lightcone emanating from one edge to reach the opposite edge. For times longer than this, the two regions no longer intersect, and

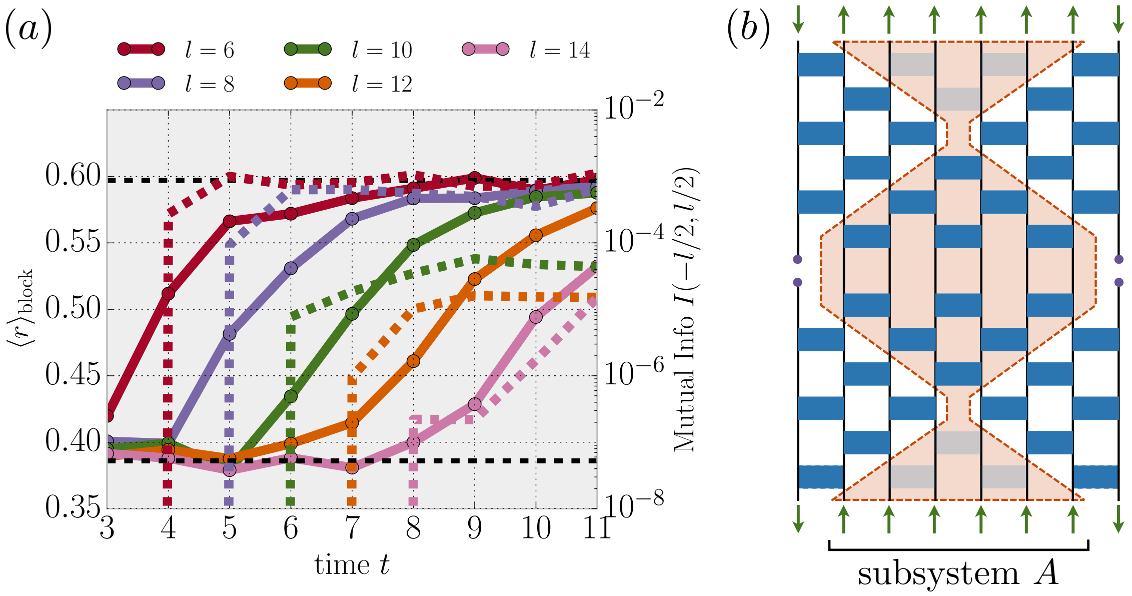

Figure 11.8.: (a) Evolution of entanglement level statistics (for entanglement energies $E < 10$) and boundary-spin mutual information in the charge-conserving random circuit, starting in an domain initial state where the l sites in the subsystem A are occupied (up) and all other sites are empty (down). The time scale of the transition towards random matrix statistics remains linear in l, despite completely diffusive charge transport. However, the time scale increases by a factor of 2 compared to e.g. a Neel initial state. (b) This can be understood by an argument similar to that for the non-conserving case, by noting that there is an additional cancellation from the fact that the state inside the domain is an eigenstate of time evolution, so that the lightly shaded gates are pure phase gates that produce no entanglement.

the gates that lie in the waist between them will spoil the factorization and drive RMT behavior of the entanglement spectrum. We note that the timescale needed for the high entanglement energies to develop level repulsion remains linear, despite the fact that the entanglement growth at the edges of the domain is initially sub-ballistic, as we have shown above. However, we observe that the later stage of the process, namely the approach to RMT level statistics, is slower than for the non-conserving case (cf. Fig. 6.1(b); we attribute this to the slow mode associated with charge diffusion in the conserving circuit.

We point out here, that the same argument would go through with little modifications, in a Hamiltonian system, where we prepare region A to be in an eigenstate of the Hamiltonian restricted to this region, and the state in $\bar{A}$ to be an eigenstate at a different energy density. Then one would again find a similar cancellation of unitaries in the circuit-representation of the time evolution (e.g., in the form of Fig. 6.2).

Our result here shows that the RMT time scale can indeed have a strong dependence on the initial-state. Understanding the nature of this for more generic states is an interesting open problem for future work.

12. Conclusions and outlook

In this thesis, we discussed various topics in quantum many-body dynamics, with particular focus on aspects of the dynamics of quantum information. The two main tools we used to characterize the spreading of quantum information were Rényi entanglement entropies S_α and out-of-time-ordered correlations (OTOCs), which capture the spreading of local operators. Our main goal was throughout was to elucidate the underlying principles that govern the dynamics of these quantities and extract universal features that pertain to wide classes of strongly interacting quantum systems.

In Part I, we focused on systems with no conventional conserved quantities. We constructed a minimal model, build from Haar random local unitary transformations, to capture the universal features in this class. As we showed, this model provides particularly simple descriptions for both type of quantity, and argued in the spirit of hydrodynamics that these should apply, on sufficiently long time- and length scales, to generic models as well. The highlight of this part is our derivation of a simple hydrodynamic description for operator spreading, which takes the form of a biased diffusion in one dimension. This led us to realize a previously unappreciated feature, the diffusive broadening of the operator wavefront, which we also confirmed numerically in a deterministic model.

In Part II we turned our attention to systems that exhibit diffusive transport of some conserved quantity, and studied in detail the effects of such diffusive modes on the dynamics of quantum correlations. Our main tool was a modified random circuit model, with $U(1)$ symmetry. Using this model, we extended our hydrodynamic description of operator spreading to include the coupling to conserved densities. From this, we found that OTOCs of the conserved density exhibit a slowly decaying tail behind their wavefront, which originates from the gradual conversion from the conserved to the non-conserved part of a time-evolving operator. We also discussed in detail the behavior of entanglement in diffusive systems. As a striking result of our investigations, we found that diffusion completely modifies the behavior of $\alpha > 1$ Rényi entropies, leading to sub-ballistic growth.

Chapter 9 stands somewhat apart from the rest of the thesis, focusing on conventional hydrodynamic transport, rather than more exotic topics, such as operator spreading. However, we found that understanding the latter can actually shed new light on the former. It allowed us to devise an innovative new numerical scheme, that managed to capture transport properties with unprecedented accuracy.

In the remainder of this concluding chapter, we contemplate possible future directions moving forward. The results established in this thesis provide a firm starting ground for exploring many more intriguing properties of quantum many-body dynamics. This includes developing a more comprehensive understanding of the hydrodynamic theories of quantum information, as well as their extension to new situations, beyond their current scope. Moreover, our numerical method developed in Chapter 9 invites many potential applications.

12.1. Effective field theory for OTOCs and entanglement

In this thesis, we used random circuit models to arrive at simple descriptions for the evolution of both OTOCs and entanglement entropies. However, the results bore all the hallmarks of a hydrodynamic theory, which suggests that one should be able to rely on the existing vast literature on hydrodynamic transport [279, 280] to motivate and refine them. A generalization of the memory matrix formalism, which we discussed briefly in Section 9.1, to study operator spreading and entanglement growth is currently under development[1] [629] Such a theory, for example, could shed further light on the stability of the biased diffusion theory for operator spreading, and provide a more microscopic understanding of the constants v_{B} and D_ρ.

A related research direction is to understand the nature of corrections to these coarse-grained hydrodynamic theories. This would amount to developing a full theory of *nonlinear fluctuating hydrodynamics* [296–299] for these quantities. From this, one could deduce the various subleading power laws that characterize their dynamics, and identify potential instabilities that could lead to new dynamical universality classes. In particular, it would be interesting to understand whether momentum conservation leads to any new effects, as it is known to make regular diffusion unstable in low dimensions [291, 298–302], giving rise to anomalous transport instead. An attempt to understand these various effects might benefit from the recent results in developing a fully consistent effective field theory description of hydrodynamic transport [281, 295].

Developing such a full theory is already an interesting, and non-trivial problem in the case where the only relevant slow variables are entanglement or operator weights (that is, in the universality class discussed in Part I of this thesis). Including effects of diffusive transport, to arrive at a full effective field theory / nonlinear hydrodynamics treatment of the effects we studied in Part II is even more challenging, but potentially also more rewarding.

12.2. Other universality classes

Here, we studied what are arguably the two simples 'universality classes' for unitary many-body quantum dynamics: systems with no conservation laws and systems with a single diffusive mode. Many other universality classes remain to be explored. The simplest generalization of the results of Part II would be to consider systems with *multiple* diffusive modes, for example ones where both energy and particle number are conserved. While these give rise to new transport phenomena, such as thermoelectric effects, we do not expect them to qualitatively change the results for operator spreading and entanglement growth we derived here. Nevertheless, a more explicit study would be desirable.

More interesting to consider are cases with qualitatively new types of conservation laws. One of these was mentioned just above: momentum conservation in systems that live in the continuum, rather than on a lattice. Momentum plays a crucial role in usual hydrodynamics, manifesting in ballistic sound modes, among other things. As mentioned in Section 2.3, in low dimensions momentum conservation can also completely destabilize diffusive transport. Understanding its effects of the dynamics of quantum information is therefore a very interesting open problem, one with applications to cold atomic experiments, and potentially also to high energy physics, where OTOCs and entanglement in continuum field theories have been a topic of intense study recently [246, 256].

Other classes of systems worth examining in the future include those with non-Abelian symmetries, such as isotropic spin chains, and higher moment conservations. According to recent arguments, these generically have super-diffusive [310, 311], and sub-diffusive [331–333] transport, respectively. Coupling of the new types of hydrodynamic modes that arise in these cases to entanglement and OTOCs is yet to be understood. Moreover, while the dynamics of entanglement in integrable models has received a lot of attention [106, 131, 264, 266–268], results on higher Rényi entropies are relatively rare [630, 631]. It would

---

[1] See also Ref [260] for a similar approach.

be interesting to see whether their qualitative differences compared to S_1, which were the main topic of Chapter 10, could show up in in these systems.

Finally, another hugely important universality class that remains unexplored when it comes to the dynamics of quantum information, is that of systems with spontaneously broken continuous symmetries. Spontaneous symmetry breaking is known to lead to the emergence of new hydrodynamic slow modes [279] (essentially, the Goldstone modes). This naturally brings up the question of how this new, richer type of hydrodynamics coupled to the quantities studied in this thesis. This provides an extremely challenging task, due to the lack of such symmetry breaking in one-dimensional systems; however, models with long-range interactions might provide a way forward [632].

12.3. Entanglement dynamics with noise and measurements

The theories of entanglement growth developed in Chapters 10 and 11 provide many possibilities for future extensions. In particular, we believe that the generalized minimal membrane picture introduced in subsection 10.1.3 is worth developing further. Among other things, this could provide a way to study the effects of noise. Since the leading order behavior of S_2 is modified drastically, for linear to sub-linear, by the presence of conservation laws, the universal features of noisy fluctuations are also likely to be different and no longer by captured by the KPZ equation; as of yet, there is no theory for these. On another note, as mentioned at the end of Section 11.1, even for the von Neumann entropy, where ballistic growth remains valid for global quenches, there is good reason to believe that the coupling to diffusion can drive the behavior of fluctuations from KPZ to a different universality class. This, and its connection to the $\alpha > 1$ case, is worth examining more closely.

In another front, recent years saw a burst of activity in studying the dynamics of entanglement in circuits where unitary evolution is periodically interrupted by local (weak) measurements [543, 604–607, 633–640]. The main finding of these studies is the existence of a phase transition, as a function of measurement strength, between two types of long-time steady states. For sufficiently weak measurements, the steady state is similar to that of the purely unitary evolution, in that its entanglement satisfies a *volume law*:. When measurements are strong, one finds the state saturating to an *area law* instead. The two cases are separated by a phase transition, whose universality class is an intriguing problem in itself[2] [604, 635–637]. These studies have all focused on circuits without any additional symmetries. Examining the phase transition in $U(1)$-symmetric circuits remains an open problem. In particular, it would be interesting to examine whether the qualitative differences between S_1 and $S_{\alpha>1}$, which we observed in the absence of measurements, translate into different transition points for these quantities, or potentially into different universality classes for the transition.

12.4. Information dynamics at finite temperatures

One of the downsides of our random circuit approach is that it cannot directly access Hamiltonian evolution. While we nevertheless believe that many of the conclusions we derived on Part II remain valid in this case, due to the similarity between energy and particle diffusion, it would be highly desirable to develop new tools that apply to the Hamiltonian case and can potentially uncover new features that are specific to energy-conserving systems. One can study Hamiltonians drawn from one of the standard random ensembles [593], but these lack any notion of locality. Recent papers have developed tools

---

[2] Recently, it was shown that this transition is closely related to classical simulation 2D unitary circuits *without* measurements [530]; a problem that is very relevant for demonstrating quantum supremacy [514].

to address Hamiltonians composed of randomly drawn *local* terms [594]. However, so far these calculations have proven intractable, except in the simplest (and still quite non-local) cases [595]. Developing them further, with an eye towards calculating OTOCs or entanglement, is an interesting problem for future study.

One of the important aspects of the Hamiltonian problem is understanding the role of temperature. While we argued in Section 8.3 that finite chemical potential can capture *some* of its effects, this is clearly not the whole story. For example, as discussed there, in a true Hamiltonian system, lowering the temperature also leads to a change in the diffusion constant, and in most cases an appearance of a ballistic transport regime at early times. Explaining these phenomena from an operator-spreading perspective would enrich our understanding of quantum transport. On the other hand, systems where transport remains incoherent even at the lowest temperatures are of particular interest, and have indeed driven much of the early work on OTOCs in condensed matter systems [198, 559, 562]. Developing a more comprehensive theory for these remains a challenge.

12.5. Applications and extensions of DAOE

In Chapter 9, we introduced a new numerical technique for simulating diffusive transport properties in quantum chains, combining ideas from operator spreading with tensor network techniques. We demonstrated that this approach can be used to calculate diffusion constants in the high temperature, strongly interacting regime, with a very high precision. We therefore believe that it will be a fruitful method for studying transport in various systems in the future.

On the technical side, there are several ways of potentially improving the performance of our algorithm. One could, for example, utilize the truncation scheme developed in Ref. [361] to ensure that conservation laws are represented appropriately; we expect that this would lead to better convergence of our results with the bond dimension, and could extend the parameter regimes we can reliably simulate. Another approach would be to apply the algorithm in momentum space, evolving a Fourier transform of the local density [641]. This would allow one to study the system directly in the thermodynamic limit.

Regarding applications, there is a large variety of physical problems one could tackle with this method. One that naturally comes to mind is transport at finite temperatures. We expect that at sufficiently high temperatures, where correlations are sufficiently short-ranged [399, 642–646], the algorithm should continue to work, and could be used to shed light on the temperature-dependence of the diffusion constant, among other things. At low temperatures, the method should eventually break down as increasingly non-local components of the operator become relevant; understanding when and how this happens is itself a physically interesting question. We also note that the temperature-dependent notion of ‘operator size’, introduced in [647], might be useful for developing a modified algorithm tailored towards finite-temperature studies.

Other potential applications include disordered systems, where diffusive transport is expected to give way to sub-diffusion [225–233], and eventually localization [93, 96, 183–185], as well as isotropic quantum magnets [310, 311], which also have direct experimental relevance [648]. Another direction would be to study long-range interacting systems, which have their own intriguing transport properties, and can become super-diffusive in certain regimes [649]. Finally, and rather ambitiously, one could extend our method to higher spatial dimensions; this research could build on recent developments in two-dimensional tensor network algorithms [650].

Appendices

A. Additional calculations for the Haar random circuit

In this appendix we gather some further calculations related to the Haar random circuit model, discussed in Chapters 4 and 5 of the main text. We begin by stating some important formulae regarding Haar averages, which are used for these calculations. We first use these to describe time-dependent correlation functions in the model, verifying our claim that it eventually relaxes to an infinite temperature state. We then describe a direct calculation of all the average operator spreading weights for an initial local operator – these complement the results of the main text where we focused on more coarse-grained quantities, such as the endpoint density. Finally, we provide the derivations of some of the formulae that appeared in the text.

A.1. Haar Identities

We start by stating the first two non-vanishing moments of a Haar random unitary U of size $d \times d$, which are used to calculate various quantities throughout the main text. The first non-vanishing moment is

$$\int d_H U \times U_{i_1 i_2} U^*_{\bar{i}_1 \bar{i}_2} = \frac{1}{d} \delta_{i_1 \bar{i}_1} \delta_{i_2 \bar{j}_2}. \tag{A.1}$$

This is used in calculating averages of time-ordered correlations, which are therefore identically zero for all $\tau > 0$ for traceless operators.

The following higher moment is needed for the derivation of the average square operator spread coefficients, and therefore the dynamics of ρ_R fiscussed in Section 4.2; it is also main ingredient that defines the local interactions in the classical partition function representation discussed in Section 5.2:

$$\begin{aligned} \int d_H U \times U_{i_1^1 i_2^1} U^*_{\bar{i}_1^1 \bar{i}_2^1} U_{i_1^2 i_2^2} U^*_{\bar{i}_1^2 \bar{i}_2^2} = {} & \frac{1}{d^2 - 1} \left(\delta_{i_1^1 \bar{i}_1^1} \delta_{i_1^2 \bar{i}_1^2} \times \delta_{i_2^1 \bar{i}_2^1} \delta_{i_2^2 \bar{i}_2^2} + \delta_{i_1^1 \bar{i}_1^2} \delta_{i_1^2 \bar{i}_1^1} \times \delta_{i_2^1 \bar{i}_2^2} \delta_{i_2^2 \bar{i}_2^1} \right) \\ & - \frac{1}{d(d^2 - 1)} \left(\delta_{i_1^1 \bar{i}_1^2} \delta_{i_1^2 \bar{i}_1^1} \times \delta_{i_2^1 \bar{i}_2^1} \delta_{i_2^2 \bar{i}_2^2} + \delta_{i_1^1 \bar{i}_1^1} \delta_{i_1^2 \bar{i}_1^2} \times \delta_{i_2^1 \bar{i}_2^2} \delta_{i_2^2 \bar{i}_2^1} \right). \end{aligned} \tag{A.2}$$

This can be more elegantly expressed as a sum over elements of permutation group S_2:

$$\begin{aligned} \int d_H U \times U_{i_1^1 i_2^1} U^*_{\bar{i}_1^1 \bar{i}_2^1} U_{i_1^2 i_2^2} U^*_{\bar{i}_1^2 \bar{i}_2^2} &= \sum_{\sigma, \eta \in S_2} \mathrm{Wg}(\eta) R(\eta\sigma)^{i_1^1 i_1^2}_{\bar{i}_1^1 \bar{i}_1^2} R(\sigma)^{i_2^1 i_2^2}_{\bar{i}_2^1 \bar{i}_2^2} \\ \text{where, } \mathrm{Wg}_d(\eta) &\equiv \frac{1}{d^2 - 1} \left(\frac{-1}{d} \right)^{\delta_{\eta = (1,2)}} \end{aligned} \tag{A.3}$$

This last formula can be generalized to higher moments, where for the N-th moment, the permutation group S_N appears [259, 651–653]. This is relevant in deriving classical partition function representations for more complicated quantities, in particular in performing the replica trick to calculate quenched averages of Rényi entropies. This is detailed in Ref. [278].

A.2. Long time correlations

In Chapter 3 we anticipated that random unitary circuits should ‘heat to infinite temperature’, much like ergodic Floquet circuits. Here we back up this claim by examining the long time behaviour of various time-ordered correlations functions, demonstrating that they relax to their expected infinite temperature values. For simplicity we consider 1 and 2 point functions for specific 1-site Pauli operators of form σ_0^α – although most of the results below follow for more general operators as well. Fix any initial state ω and times t_2, t_1. We find that

$$\overline{\langle \sigma_0^\alpha(t_2)\sigma_s^\beta(t_1)\rangle_\omega} = 0\,.$$

This follows from two observations. First, the operator in the expectation value can be written $U_{01}U_{12}\sigma_0^\alpha U_{21}\sigma_s^\beta U_{10}$ where $U_{ij} = U_{ji}^{-1}$ is shorthand for the unitary evolutions between times t_i and t_j. Now U_{12} is statistically independent from U_{01}, so we can average over these disjoint circuits independently. Provided $t_1 \neq t_2$ and $\alpha \neq 0$ it is straightforward to see from Eq. (A.1) that the Haar average $\overline{U_{12}\sigma_0^\alpha U_{21}} = 0$. This can be re-expressed succinctly as $\overline{c_\mu^\alpha(t)} = 0$ for all $t = t_2 - t_1 \neq 0, \alpha \neq 0$. Note that this result is independent of the initial state ω and the value β – in particular we can recover the behavior of 1-point functions by setting $\beta = 0$.

While the above correlation functions disappear on average, we may also quantify how their variance behaves at long times. Indeed, the variance decays exponentially in time, at least for random initial product states ψ. The variance is

$$\overline{\langle \sigma_0^\alpha(t_2)\sigma_s^\beta(t_1)\rangle_\omega^2} = \sum_\mu \overline{|c_\mu^\alpha(t)|^2}|\langle \sigma^\mu(t_1)\sigma_s^\beta(t_1)\rangle_\omega|^2\,.$$

We argue that this variance vanishes as we increase $t \to \infty$ while fixing t_1. We can show this rigorously for an infinite temperature state in App. A.2.1.

For a random product state we have a less rigorous argument which proceeds as follows. First, given any $\epsilon > 0$, it will be true that for sufficiently long times t, all of the weight of α is invested in strings μ with left/right endpoints $l < -(v_\mathrm{B} - \epsilon)t, r > (v_\mathrm{B} - \epsilon)t$ respectively, up to exponentially small corrections in t. These statements follow from Eq. (4.10). Second, as α is a 1-site operator, $\overline{|c_\mu^\alpha(t)|^2}$ only depends on the endpoints of μ rather than the detailed internal structure (See the discussion under Eq. (4.16)). Hence, up to exponentially small corrections in time, $\sigma_0^\alpha(t)$ is made up of an equal amplitude superposition of all operators μ with left/right endpoints near $\mp v_\mathrm{B} t$ respectively. The vast majority of such strings contain an extensive $O(v_\mathrm{B} t)$ number of Pauli operators. The expectation values of such strings on a random product states is exponentially decaying in the number of Pauli operators. As a typical μ string contains $O(v_\mathrm{B} t)$ Pauli operators, we find $|\langle \sigma_0^\mu \sigma_s^\beta\rangle_\omega|^2 \sim e^{-\zeta v_\mathrm{B} t}$ for some constant ζ. Hence for t_1=0, $\overline{\langle \sigma_0^\alpha(t_2)\sigma_s^\beta(0)\rangle_\psi^2} \sim e^{-\zeta v_\mathrm{B} t}$. For t_1 nonzero, we expect even more marked decay $\overline{\langle \sigma_0^\alpha(t_2)\sigma_s^\beta(t_1)\rangle_\psi^2} \sim e^{-\zeta v_\mathrm{B}(t+t_1)}$ because the support of $\sigma_0^\mu \sigma_s^\beta$ is further increased under time evolution.

A.2.1. Infinite temperature results

Consider the variance of the infinite temperature expectation value function

$$\overline{\mathrm{tr}(2^{-L}(\sigma_0^\alpha(t_2)\sigma_s^\beta(t_1))^2} = \sum_\mu \overline{|c_\mu^\alpha(t)|^2}|2^{-L}\mathrm{tr}(\sigma_0^\mu \sigma_s^\beta)|^2 = \overline{|c_{\beta_s}^\alpha(t)|^2}\,. \tag{A.4}$$

This is a Haar averaged single site weight. In the large t, $s/t \to 0$ limit, we have an expression for this quantity (in the coarse grained lattice basis). It is approximately equal to Eq. (A.8) using $x = s/2, y = x + 1, \tau = 2t$. Asymptotically then the variance in the infinite temperature average decays exponentially as $\sim \left(\frac{2q}{q^2+1}\right)^{4t}$.

A.3. Exact operator spreading coefficients

In what follows, we give an exact expression for the averaged operator spread coefficients, $\overline{|c_{\vec{\mu}}^{\vec{\nu}}(t)|^2}$ and a sketch of the derivation. The averaged operator spread coefficients are defined as

$$\overline{|c_{\vec{\mu}}^{\vec{\nu}}(t)|^2} = \int \left[\prod_{\tau=1}^{t,\leftarrow} \prod_{j=1}^{L} d_{\text{Haar}} W(2j+p_\tau, \tau) \right] \times \left| \frac{1}{q^M} \text{tr}\left(\sigma^{\vec{\nu}\dagger} U^\dagger(t) \sigma^{\vec{\mu}} U(t) \right) \right|^2 . \tag{A.5}$$

The Haar-averaging can be performed explicitly using the identity (A.3) in App. A.1. After averaging, each two-site gate can be represented by a classical, Ising-like variable, which takes only two possible values. Due to the geometry of the circuit, these Ising variables form a triangular lattice (see Fig. A.1 and also Ref. [253]). Eq. (A.5) becomes a classical partition function, i.e. a sum over all possible spin configurations, similar to the one discussed in Section 5.2, but with modified boundary conditions that depend on the operators $\sigma^{\vec{\mu}}$ and $\sigma^{\vec{\nu}}$. The bulk part which is independent of the Pauli strings considered, and is the same as the one discussed in Section 9.1 in relation to calculating the average purity. Due to the Haar-averaging, the only information that remains in the partition function about the strings $\vec{\mu}$ and $\vec{\nu}$ is which sites they act on non-trivially. The bulk transfer matrix enforces a light cone structure on the spin variables. A light cone with velocity $v_{\text{LC}} = 1$ emanates from the two endpoints of the string $\vec{\nu}$ such that all spins outside of the light cone have to point up (otherwise the configuration has zero weight in the partition function for $\overline{|c_{\vec{\mu}}^{\vec{\nu}}(t)|^2}$).

In the case of an initial Pauli operator acting on a single site the partition function for the operator spreading can be evaluated exactly. In this case the fact that $\vec{\mu}$ acts on one site only yields a boundary condition for the partition function wherein in the first row there is a single spin pointing down while all others point up. The partition function then becomes a sum over all possible ways this initially one-site domain can spread within the light cone, as shown in Fig. A.1. Furthermore, the bulk interaction terms are only non-trivial at the boundary between the two domains and consequently give the same contribution for all domain configurations with the same depth. Thus the calculation simplifies to counting the possible domain configurations which can be done by considering it as a two-particle random walk for the two endpoints of the domain.

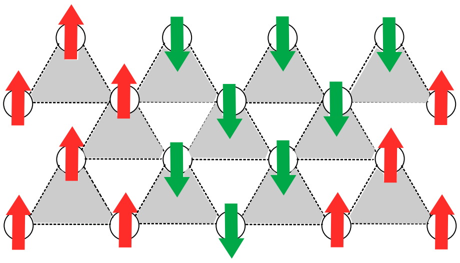

Figure A.1.: Example of a classical spin configuration contributing to the operator spreading coefficients of an initial one-site Pauli operator. All such configurations have a single domain of down spins spreading inside the light cone and each of these configurations contributes equally to $\overline{|c^{\vec{\nu}}(t)|^2}$.

The calculation outlined above yields all average squared coefficients $\overline{|c_{\vec{\mu}}^{\vec{\nu}}(t)|^2}$ where $\mu_j = 0$ if $j \neq 0$. In the following we simplify the notation by dropping the first index and denoting these as $\overline{|c^{\vec{\nu}}(t)|^2}$. The exact formula for these squared coefficients is given in Eq. (A.6). A surprising property of this formula only depends on the positions of the right and left endpoints l, r of the Pauli string $\vec{\nu}$, and not on more detailed information concerning the internal structure of the string i.e., $\overline{|c^{\vec{\nu}}(t)|^2} = h(l, r)$. This is a consequence of the Haar averaging which in each step washes out all memory of the internal structure.

Let us form a circuit with where the number of layers $2t$ is even. Number the spaces between the two site unitaries in the last layer $-t, 1-t, \dots t$. The support of an operator string $\vec{\nu}$ can be represented by $x, y \in \{-t, 1-t, \dots t\}$ with $x < y$. The average square coefficient is obtained by plugging x, y into the formula.

$$\begin{aligned}\overline{|c^{\vec{\nu}}|^2} =& \frac{1}{(1+q^{-2})^{2(2t-1)}} \frac{q^{-2(y-x)-4t}}{1-q^{-4}} \mathcal{J}(x,y,t),\\ \mathcal{J}(x,y,t) \equiv& \sum_{0\le a\le t+x} \sum_{0\le b\le t-y} \binom{2t}{t-b-y} \times \binom{2t}{t-a+x} q^{-2a-2b} \frac{b+y+a-x}{2t}.\end{aligned} \tag{A.6}$$

Note that this expression depends only on x, y and q so we also denote it as $\overline{|c^{\mu_1}_{\vec{\nu}}|^2} = h(x, y, D)$ where we drop the q dependence for simplicity. These expressions are of-course complicated. We note as an aside that this formula has a slightly neater expression in terms of hypergeometric functions.

A.3.1. Useful limits

Let us calculate the weight on an operator with endpoints x, y, in the large t limit, starting from Eq. (A.6). We re-express the weight as

$$\begin{aligned}\overline{\left|c^{\mu_1}_{\vec{\nu}}\right|^2} &= q^{-4t} \times \frac{1}{(1+q^{-2})^{2(2t-1)}} \frac{1}{1-q^{-4}} \mathcal{G}\left(x,y,t\right),\\ \mathcal{G}\left(x,y,t\right) &\equiv \sum_{0\le a\le t+x} \times \sum_{0\le b\le t-y} q^{-2b-2y} q^{-2a+2x} \times \binom{2t}{t-b-y} \binom{2t}{t-a+x} \frac{b+y+a-x}{2t}.\end{aligned}$$

Then define:

$$\begin{gathered}\mathcal{H}(x,y,t) \equiv q^{-4t}(1+q^2)^{4t} v_t(t+x) v_t(t-y),\\ \text{where } v_t(\Delta) \equiv (1+q^2)^{-2t} \sum_{j=0}^{\Delta} \binom{2t}{j} q^{2j}.\end{gathered}$$

Combining these definitions, we find that

$$\frac{\mathrm{d}\mathcal{H}(x,y,t)}{\mathrm{d}q} = -\frac{2t}{q} \mathcal{G}(x,y,t).$$

Putting this altogether, we have

$$h(x,y,t) = -\frac{1}{4t} \frac{q^{-4t}}{(1+q^{-2})^{2(2t-1)}} \frac{1}{1-q^{-4}} \times \frac{\mathrm{d}}{\mathrm{d}\log q}[q^{-4t}(1+q^2)^{4t} v_t(t+x) v_t(t-y)]. \tag{A.7}$$

For fixed x, y taking the large t limit, the v_t functions can be approximated as (using the same reasoning as in Eq. (4.13)):

$$v_t(t+x) \sim \sqrt{\frac{1}{\pi t}} \frac{q^{2(x+1)} \left(\frac{2q}{q^2+1}\right)^{2t}}{q^2-1}.$$

Plugging in this approximation, we find

$$h(x,y,t) \sim \left(\frac{2q}{q^2+1}\right)^{4t} \times \frac{(q^2+1)((q^2-1)(y-x)+2) q^{2(x-y+2)}}{4\pi t^2 \left(q^2-1\right)^4}. \tag{A.8}$$

So, fixing x, y, the weight on an operator with endpoints x, y decays exponentially quickly $\left(\frac{2q}{q^2+1}\right)^{4t}$ with large t.

A.4. Derivation of operator spreading and OTOC

In the remainder of this Appendix, we provide further details on the derivation of some of the equations presented in the main text, both for the right weight of an evolving operator, and for the OTOC.

A.4.1. Validity of Eq. (4.13)

It suffices to work in coarse grained co-ordinates t, x. Recall that

$$\overline{R}(x) = \sum_{y \leq x} \overline{\rho_R}(y) \qquad\qquad \overline{\rho_R}(x,t) = \frac{q^{2(t+x)}}{(1+q^2)^{2t}} \binom{2t}{t+x}.$$

Our task is to justify the formula Eq. (4.13), which can be more carefully phrased as follows: In the limit, $t \to \infty$, with $|x - v_{\mathrm{B}} t|/t = \varepsilon$ held to be a fixed nonzero number, the integrated operator density obeys

$$\frac{\overline{R}(x)}{\overline{\rho_R}(x)} = c_0 \text{ for } -1 < \kappa < v_{\mathrm{B}} \tag{A.9}$$

$$\frac{1-\overline{R}(x)}{\overline{\rho_R}(x)} = c_1 \text{ for } v_{\mathrm{B}} < \kappa < 1 \tag{A.10}$$

where $c_{0,1}$ are positive numbers, bounded in the $t \to \infty$ limit, and we defined $\kappa \equiv x/t$ and work in units where $v_{\mathrm{LC}} = 1$. Define

$$Q_x \equiv \frac{\overline{\rho_R}(x+1,t)}{\overline{\rho_R}(x,t)} = q^2 \frac{1-\kappa}{1+\kappa+\frac{1}{t}}. \tag{A.11}$$

The quotient Q_x is always positive. It is easy to verify that for $-1 < \kappa < v_{\mathrm{B}}$ the quotient is greater than 1, and an increasing function of x. On the other hand, for $v_{\mathrm{B}} < \kappa < 1$, this quotient is less than 1, and a decreasing function of x.

When $-1 < \kappa < v_{\mathrm{B}}$ we use these facts to bound

$$\overline{R}(x) \leq \overline{\rho_R}(x,t)(1 + Q_x^{-1} + Q_x^{-2} \dots) = \overline{\rho_R}(x,t) \frac{1}{1-Q_x^{-1}} \tag{A.12}$$

At the same time, it is immediate that $\overline{R}(x) \geq \overline{\rho_R}(x,t)$. Noting that in the large t limit $Q_x = \frac{(1+v_{\mathrm{B}})(1-\kappa)}{(1-v_{\mathrm{B}})(1+\kappa)}$; we then find that

$$\left| \frac{\overline{R}(x,t)}{\overline{\rho_R}(x,t)} - 1 \right| \leq \frac{Q_x^{-1}}{1-Q_x^{-1}} = \frac{(1+\kappa)(1-v_{\mathrm{B}})}{2\varepsilon}. \tag{A.13}$$

Hence $c_0 \leq 1 + \frac{(1+\kappa)(1-v_{\mathrm{B}})}{2\varepsilon}$is an $O(1)$ constant.

Similarly we consider $v_{\mathrm{B}} < \kappa < 1$. Using $1 = \sum_y \rho_R(y,t)$ it follows that $\overline{R}(x) = 1 - \sum_{y>x} \rho_R(y,t)$. In the present case, $Q_x < 1$ and is straightforward to derive a similar bound

$$\left| \frac{1-\overline{R}(x,t)}{\overline{\rho_R}(x,t)} - 1 \right| \leq \frac{Q_x}{1-Q_x} = \frac{(1-\kappa)(1+v_{\mathrm{B}})}{2\varepsilon}. \tag{A.14}$$

Hence $c_1 \leq 1 + \frac{(1-\kappa)(1+v_{\mathrm{B}})}{2\varepsilon}$ is an $O(1)$ number in the large t limit. Note that near the edge of the light cone, $\kappa = \mp 1$, the results Eq. (A.9) become increasingly exact as each of the bounds Eq. (A.13) and Eq. (A.14) become tighter. On the other hand, as we approach the front $\varepsilon \to 0$ the bounds become looser and Eq. (A.9) is less reliable – in this regime, the near front expansion Eq. (4.11) becomes more useful.

A.4.2. Application to OTOC

Following Section 4.2.2, the quantity $f(s,\tau) \equiv 1 - \overline{\mathcal{C}}(s,\tau)$ can be written as

$$f(s,\tau) = \sum_{\mu} \overline{|c^{\mu}(\tau)|^2} \cos\theta_{\mu,Z_s},$$

where $e^{i\theta_{\mu,Z_s}}$ is a q^{th} root of unity acquired by commuting σ^{μ} past Z_s. We can reparameterize this by summing over the left right endpoints of the Pauli string μ

$$f(s,\tau) = \sum_{l=-t}^{t-1} \sum_{r=-t}^{t-1} h(l,r) \sum_{\mu \in \mathfrak{F}(l,r)} \cos\theta_{\mu,Z_s}, \tag{A.15}$$

where $h(l,r)$is simply the average $\overline{|c^{\mu}(\tau)|^2}$ for a Pauli string μ with left/right endpoint – recall that this value does not depend on the internal structure of μ (see below eqnref or above in App. A.3), only on the endpoints of μ. Here $\mathfrak{F}(l,r) \equiv \{\mu : \operatorname{supp}(\mu) = [l,r]\}$. Those intervals $[l,r]$ such that $s \in (l,r)$ do not on net contribute to this sum, because the sum over q^{th} roots of unity disappears:

$$h(l,r) \sum_{\mu \in \mathfrak{F}(l,r)} \cos\theta_{\mu,Z_s} = 0.$$

There are also contributions to (A.15) which arise when s is on the left and/or right edge of an interval i.e., $s = l$ or $s = r$.

First, we perform the sum over μ in (A.15) for the case $r = s > l$:

$$\sum_{\mu \in \mathfrak{F}(l,s)} \cos\theta_{\mu,Z_s} = -(q^{-2}\delta_{l<s-1} + \delta_{l=s-1,s}(q^2-1)^{-1}) \, |\mathfrak{F}(l,s)| \,.. \tag{A.16}$$

Next, perform the sum over μ in (A.15) for the case $l = s < r$:

$$\sum_{\mu \in \mathfrak{F}(s,r)} \cos\theta_{\mu,Z_s} = -(q^{-2}\delta_{r>s+1} + \delta_{r=s,s+1}(q^2-1)^{-1} \, |\mathfrak{F}(s,r)|) \,.. \tag{A.17}$$

Combining these sum identities, Eq. (A.16) and Eq. (A.17), back into Eq. (A.15) yields (after some rearrangement)

$$\begin{aligned} f(s,\tau) = &\left(\sum_{l \le r \le s-1} + \sum_{s+1 \le l \le r} - \sum_{r=s} \sum_{l \le s} q^{-2} - \sum_{l=s} \sum_{r \ge s} q^{-2} \right) \times h(l,r) \, |\mathfrak{F}(l,r)| \\ &+ \frac{1}{q^2} \left(-(q^2-1)(h(s-1,s) + h(s,s+1)) + \left(q^2-2\right) h(s,s) \right) \end{aligned}$$

The first line is

$$f_{1^{\text{st}}}(s,\tau) = \overline{R}(s-1) + \overline{L}(s+1) - q^{-2} \left(\overline{\rho_R}(s) + \overline{\rho_L}(s) \right).$$

It is readily verified using Eq. (A.8) that the second line disappears exponentially quickly in τ, as $(2q/(q^2+1))^{2\tau}$, for any s. Hence, in the $\tau \to \infty$ fixed s/τ limit, we can approximate

$$\begin{aligned} f(s,\tau) &\approx f_{1^{\text{st}}}(s,\tau) \\ &= \overline{R}(s-1,\tau) - q^{-2}\overline{\rho_R}(s,\tau) \\ &\quad + \overline{R}(-s-2,\tau) - q^{-2}\overline{\rho_R}(-s-2,\tau) \end{aligned} \tag{A.18}$$

where we used the fact $\overline{L}(s+1) = \overline{R}(-s-2)$ and $\overline{\rho_L}(s+1) = \overline{\rho_R}(-s-2)$. For $0 < s < \tau/v_{\mathrm{LC}}$, and for any q, we can use Eq. (4.11) and Eq. (4.14) to argue that the second line is suppressed by a factor of $\sim q^{-s}$ relative to first line. Therefore, provided $\kappa > 0$ in the $\tau \to \infty$ limit, the OTOC behaves as

$$f(s,\tau) \approx \overline{R}(s-1,\tau) - q^{-2}\overline{\rho_R}(s,\tau)$$

up to exponentially small corrections in τ.

B. Additional calculations for $U(1)$ random circuits

Here, we gather various results about $U(1)$ symmetric random circuit models, which were omitted in the main text. We begin with a more complete discussion of the action of a single gate, which is used to build the partition function in Section 8.1.1. We then give detailed derivation of various results stated throughout Chapters 8, 10 and 11. In Section B.6, we provide a derivation of the long-time hydrodynamic tails that appear in expectation values and correlation functions; apart from being of interest on its own, this calculation is useful in understanding the results on Rényi entropies presented in Section 10.2. In the last part of this Appendix, we provide some numerical evidence that the local equilibrium approximation, which is the key element entering a hydrodynamic description, is satisfied at long times when quenching from an initial domain wall.

B.1. Average effect of a single gate

In this Appendix we derive Eq. (8.6) that describes the average effect of a single 2-site gate on four copies of the Hilbert space (i.e., on the time evolution of superoperators), relevant for calculation of average OTOCs and purities. Let us start by examining the simpler problem of the average time evolution of an operator, already discussed in Eq. (7.1), and re-derive the result in a slightly different language. An operator $\hat{O}$ evolves under the effect of the unitary U as

$$(U^\dagger \hat{O} U)_{\alpha\beta} = U^*_{\gamma\alpha} O_{\gamma\delta} U_{\delta\beta} = O_{\gamma\delta}(U^* \otimes U)_{(\gamma\delta)(\alpha\beta)}, \tag{B.1}$$

i.e. we can think of it as being evolved by the superoperator $U^* \otimes U$. Now let us imagine that U is a 2-site unitary, with the block-diagonal structure $U = \sum_Q U_Q$, where U_Q acts on states with total charge Q. We can then use the fact that the blocks are independent Haar-random matrices to evaluate the average. For an $n \times n$ random unitary matrix u, the properties of the Haar-distribution imply that $\overline{u} = 0$ and $\overline{u^* \otimes u} = \frac{1}{n}|\hat{\mathbb{1}}\rangle\langle\hat{\mathbb{1}}|$, where $|\hat{\mathbb{1}}\rangle\langle\hat{\mathbb{1}}| \equiv \mathcal{P}_{\mathbb{1}}$ is a superoperator projecting (up to a normalization constant) on the identity, using the notation of Section 8.2.2. We conclude that

$$\overline{U^* \otimes U} = \sum_{Q_1,Q_2} \overline{U^*_{Q_1} \otimes U_{Q_2}} = \sum_{Q} \overline{U^*_Q \otimes U_Q} = \sum_Q \frac{1}{d_Q}|\hat{P}_Q\rangle\langle\hat{P}_Q|, \tag{B.2}$$

where $\hat{P}_Q$ are projectors acting on the two-site Hilbert space. The above expression acts on an operator as $\hat{O} \to \sum_Q \frac{1}{d_Q}\mathrm{tr}(\hat{P}_Q\hat{O})\hat{P}_Q$.

For evaluating OTOCs (or purities) we need to know how to average the time evolution on four, rather than two copies of the Hilbert space. For this four-layer case we have three distinct ways of pairing up the unitaries which gives

$$\begin{aligned}\overline{U^*\otimes U\otimes U^*\otimes U} = &\sum_{Q_1\neq Q_2}\left(\overline{U^*_{Q_1}\otimes U_{Q_1}\otimes U^*_{Q_2}\otimes U_{Q_2}}+\overline{U^*_{Q_1}\otimes U_{Q_2}\otimes U^*_{Q_2}\otimes U_{Q_1}}\right)\\ &+\sum_{Q}\overline{U^*_{Q}\otimes U_{Q}\otimes U^*_{Q}\otimes U_{Q}}. \end{aligned} \tag{B.3}$$

For the $Q_1\neq Q_2$ terms, where each block only appears at most twice, we can use the result of Eq. (B.2). In the simplest case this gives

$$\overline{U^*_{Q_1}\otimes U_{Q_1}\otimes U^*_{Q_2}\otimes U_{Q_2}} = \frac{1}{d_{Q_1}}(|\hat{P}_{Q_1}\rangle\langle\hat{P}_{Q_1}|)\otimes\frac{1}{d_{Q_2}}(|\hat{P}_{Q_2}\rangle\langle\hat{P}_{Q_2}|)\equiv\frac{1}{d_{Q_1}d_{Q_2}}|\mathcal{I}^+_{Q_1Q_2}\rangle\langle\mathcal{I}^+_{Q_1Q_2}|, \tag{B.4}$$

where we defined $|\mathcal{I}^+_{Q_1Q_2}\rangle\equiv\sum_{\alpha\in\mathcal{H}_{Q_1}}\sum_{\beta\in\mathcal{H}_{Q_2}}|\alpha\alpha\beta\beta\rangle$. The second term in Eq. (B.3) corresponds to swapping the second and fourth copies and thus gives

$$\overline{U^*_{Q_1}\otimes U_{Q_2}\otimes U^*_{Q_2}\otimes U^*} = \frac{1}{d_{Q_1}d_{Q_2}}|\mathcal{I}^-_{Q_1Q_2}\rangle\langle\mathcal{I}^-_{Q_1Q_2}|, \tag{B.5}$$

where $|\mathcal{I}^-_{Q_1Q_2}\rangle\equiv\sum_{\alpha\in\mathcal{H}_{Q_1}}\sum_{\beta\in\mathcal{H}_{Q_2}}|\alpha\beta\beta\alpha\rangle$.

For the last term we need to apply the Haar identity for the fourth moment of U. The result can be evaluated using Eq. (A.2), which gives

$$\begin{aligned}&\overline{U^*_{Q}\otimes U_{Q}\otimes U^*_{Q}\otimes U_{Q}}\\ &=\frac{1}{d_Q^2-1}\left[\left(|\mathcal{I}^+_{QQ}\rangle\langle\mathcal{I}^+_{QQ}|+|\mathcal{I}^-_{QQ}\rangle\langle\mathcal{I}^-_{QQ}|\right)-\frac{1}{d_Q}\left(|\mathcal{I}^+_{QQ}\rangle\langle\mathcal{I}^-_{QQ}|+|\mathcal{I}^-_{QQ}\rangle\langle\mathcal{I}^+_{QQ}|\right)\right].\end{aligned} \tag{B.6}$$

Combining Eqs. (B.4)-(B.6) we get the full result for the average of a single gate in the four-layer system given in Eq. (8.6).

A significant difficulty of this charge-conserving circuit, compared to the one without symmetries, is that the states that appear when averaging over a two-site gate do not factorize into independent states on the two sites. If we want to write them in terms of such single-site states (living on four copies of a single site) they become

$$\begin{aligned}|\mathcal{I}^+_{Q_1Q_2}\rangle &= \sum_{\alpha\beta\gamma\delta}|\alpha\alpha\beta\beta\rangle_1|\gamma\gamma\delta\delta\rangle_2\,\delta_{\alpha+\gamma=Q_1}\delta_{\beta+\delta=Q_2},\\ |\mathcal{I}^-_{Q_1Q_2}\rangle &= \sum_{\alpha\beta\gamma\delta}|\alpha\beta\beta\alpha\rangle_1|\gamma\delta\delta\gamma\rangle_2\,\delta_{\alpha+\gamma=Q_1}\delta_{\beta+\delta=Q_2}.\end{aligned} \tag{B.7}$$

Let us focus on the case of only two states, $|0\rangle$ and $|1\rangle$, on each site site. A possible basis of operators on a single sites is then given by $\hat{Q}=|1\rangle\langle 1|$, $\hat{P}\equiv\mathbb{1}-\hat{Q}=|0\rangle\langle 0|$, $\hat{\sigma}^+=|1\rangle\langle 0|$ and $\hat{\sigma}^-=|0\rangle\langle 1|$. We can then write Eq. (B.7) in terms of the following six local states:

$$\begin{aligned}&|0\rangle\equiv|0000\rangle=|\hat{P}\rangle\langle\hat{P}|=\mathcal{L}_P\mathcal{R}_P && |1\rangle\equiv|1111\rangle=|\hat{Q}\rangle\langle\hat{Q}|=\mathcal{L}_Q\mathcal{R}_Q\\ &|A\rangle\equiv|1100\rangle=|\hat{Q}\rangle\langle\hat{P}|=\mathcal{L}_{\sigma^+}\mathcal{R}_{\sigma^-} && |B\rangle\equiv|0011\rangle=|\hat{P}\rangle|\hat{Q}\rangle=\mathcal{L}_{\sigma^-}\mathcal{R}_{\sigma^+}\\ &|C\rangle\equiv|1001\rangle=|\hat{\sigma}^+\rangle\langle\hat{\sigma}^+|=\mathcal{L}_Q\mathcal{R}_P && |D\rangle\equiv|0110\rangle=|\hat{\sigma}^-\rangle\langle\hat{\sigma}^-|=\mathcal{L}_P\mathcal{R}_Q,\end{aligned} \tag{B.8}$$

where we have included their interpretation as superoperators, using the definitions of Section 8.2.2. The states appearing in the tensor corresponding to a single two-site gate can then be written in terms of the above states on each site as

$$\begin{aligned}
&|\mathcal{I}^+_{00}\rangle = |\mathcal{I}^-_{00}\rangle = |0\rangle|0\rangle && |\mathcal{I}^+_{22}\rangle = |\mathcal{I}^-_{22}\rangle = |1\rangle|1\rangle \\
&|\mathcal{I}^+_{02}\rangle = |A\rangle|A\rangle && |\mathcal{I}^-_{02}\rangle = |C\rangle|C\rangle \\
&|\mathcal{I}^+_{20}\rangle = |B\rangle|B\rangle && |\mathcal{I}^-_{20}\rangle = |D\rangle|D\rangle \\
&|\mathcal{I}^+_{01}\rangle = |0\rangle|A\rangle + |A\rangle|0\rangle && |\mathcal{I}^-_{01}\rangle = |0\rangle|C\rangle + |C\rangle|0\rangle \\
&|\mathcal{I}^+_{10}\rangle = |0\rangle|B\rangle + |B\rangle|0\rangle && |\mathcal{I}^-_{10}\rangle = |0\rangle|D\rangle + |D\rangle|0\rangle \\
&|\mathcal{I}^+_{21}\rangle = |1\rangle|A\rangle + |A\rangle|1\rangle && |\mathcal{I}^-_{21}\rangle = |1\rangle|C\rangle + |C\rangle|1\rangle \\
&|\mathcal{I}^+_{12}\rangle = |1\rangle|B\rangle + |B\rangle|1\rangle && |\mathcal{I}^-_{12}\rangle = |1\rangle|D\rangle + |D\rangle|1\rangle \\
&|\mathcal{I}^+_{11}\rangle = |0\rangle|1\rangle + |1\rangle|0\rangle + |A\rangle|B\rangle + |B\rangle|A\rangle && |\mathcal{I}^-_{11}\rangle = |0\rangle|1\rangle + |1\rangle|0\rangle + |C\rangle|D\rangle + |D\rangle|C\rangle,
\end{aligned} \tag{B.9}$$

where the two states on the right hand side correspond to the two neighboring sites on which the gate acts. Based on these we can compute all the matrix elements of the form $\langle IJ|\overline{U^*\otimes U\otimes U^*\otimes U}|KL\rangle$ for $I,J,K,L = 0,A,B,C,D,1$ which give us the transition coefficients illustrated in Fig. 8.2. Applying these for each gate in the circuit, and contracting with the appropriate boundary conditions defined by the operators $\hat{V}$, $\hat{W}$ and the chemical potential μ, give the 2D partition function one needs to evaluate to compute the OTOC $\mathcal{F}^{VW}_\mu$. The same partition function, with appropriately modified boundary conditions, gives the average purity, used in Chapter 10 and Section 11.2.1.

We end this section by noting that the above formula for the average effect of the 2-site gate can be written in somewhat more compact form by introducing the states $|\mathcal{J}_{Q_1Q_2}\rangle \equiv |\mathcal{I}^-_{Q_1Q_2}\rangle - \frac{\delta_{Q_1Q_2}}{d_{Q_1}}|\mathcal{I}^+_{Q_1Q_2}\rangle$ and renaming $|\mathcal{I}^+_{Q_1Q_2}\rangle \to |\mathcal{I}_{Q_1Q_2}\rangle$. Using this notation Eq. (8.6) becomes

$$\overline{U^*\otimes U\otimes U^*\otimes U} = \sum_{Q_1,Q_2} \frac{1}{d_{Q_1}d_{Q_2}}|\mathcal{I}_{Q_1Q_2}\rangle\langle\mathcal{I}_{Q_1Q_2}| + \sum_{Q_1,Q_2} \frac{1}{d_{Q_1}d_{Q_2} - \delta_{Q_1Q_2}}|\mathcal{J}_{Q_1Q_2}\rangle\langle\mathcal{J}_{Q_1Q_2}|. \tag{B.10}$$

We will use this version of the formula in the following section to derive Eq. (8.15).

B.2. Derivation of Eq. (8.15)

In this section, we detail the derivation that leads us to the conjectured long-time form of the OTOC presented in Eq. (8.15). Here we consider a more general version of the equation of motion in Eq. (8.14), where we also take into account effects of finite chemical potential. We do this by considering a modified superoperator

$$\mathcal{D}_{\mu,V} \equiv \mathcal{L}_{\omega_\mu V \omega_\mu} \mathcal{R}_{\omega_\mu V^\dagger \omega_\mu}, \tag{B.11}$$

where we introduced the notation $\hat{\omega}_\mu \equiv e^{-\frac{\mu}{4}\hat{Q}}$. Similarly, it is useful to define a generalized version of the projection superoperators as

$$\mathcal{P}^x_\mu \equiv \frac{|e^{-\mu\hat{Q}_x}\rangle\langle e^{-\mu\hat{Q}_x}|}{\mathrm{tr}(e^{-\mu\hat{Q}_x})}, \tag{B.12}$$

where $\hat{Q}_x$ is the total charge within a single ‘supersite’ x, consisting of M individual qubits[1], as shown in Fig. 7.1(a).

---

[1] Here we use a different notation compared to the main text, denoting the number of quibts per supersite by M, rather than N.

The superoperator defined in Eq. (B.11) becomes, on average, after a single application of a unitary gate on $2M$ sites,

$$\begin{aligned}\mathcal{D}_{\mu,Z_0}\left(\Delta\tau\right) = & \sum_Q \frac{1}{d_Q}\mathcal{I}^{x,x+1}_{QQ} e^{-\mu Q} b_Q & :\blacklozenge \\ & + \frac{1}{M^2}\mathcal{L}_{\omega_\mu \frac{1}{2}(\zeta_x+\zeta_{x+1})\omega_\mu}\mathcal{R}_{\omega_\mu \frac{1}{2}(\zeta_x+\zeta_{x+1})\omega_\mu}. & :\bigstar,\end{aligned}$$

where $b_Q \equiv 1-(1-\frac{Q}{M})^2$. In the main text we argued that the $\blacklozenge$ term is mainly responsible for ballistic spreading, while the $\bigstar$ term is more complicated and involves diffusion of conserved superoperator densities. We detail these arguments below. The resulting solution for the OTOC superoperator is

$$\mathcal{D}_{\mu,Z_x}\left(t\right) \approx \alpha_\mu\, \mathcal{P}_\mu^{A_x(t)} + \frac{1}{M^2}\mathcal{D}_{\mu,\zeta_x(t)} + \frac{\alpha_\mu}{2M-1}\sum_{t'<t}\sum_{y\in t'+2\mathbb{Z}} \left(K_{x,y+1}-K_{x,y}\right)^2(t')\mathcal{P}_\mu^{A_y(t-t')}, \tag{B.13}$$

where $\alpha_\mu \equiv \frac{1-2M}{2M}\cosh^{-2}(\mu/2)$ and $\mathcal{P}_\mu^A \equiv \bigotimes_{x\in A}\mathcal{P}_\mu^x$ for the ballistically growing region $A_x(t) = [x-t, x+t]$.

B.2.1. Ballistic expansion of $\blacklozenge$

The operator $\blacklozenge$, defined above, occupies two supersites, $x, x+1$. Considered as a superoperator on the 2^{2M} dimensional Hilbert space on these two sites, the individual terms give typical expectation values on local operators of size $d_Q e^{-\mu Q}$. Such summands are, for large M, dominated by $\overline{Q}$ in a small window around $2M/(1+e^\mu)$. The most significant term is therefore

$$\left(|\hat{P}_{\overline{Q}}\rangle\langle\hat{P}_{\overline{Q}}|\right)^{x,x+1} = \sum_{e_L+e_R=\overline{Q}}\ \sum_{f_L+f_R=\overline{Q}} |\hat{P}^x_{e_L}\hat{P}^{x+1}_{e_R}\rangle\langle\hat{P}^x_{f_L}\hat{P}^{x+1}_{f_R}|,$$

where $e_{L,R}$ and $f_{L,R}$ are local charges on the two sites and $\hat{P}^x_e$ is a projection unto that charge on site x. This term is similarly dominated by those terms with $e_{L,R} = f_{L,R} \approx \overline{Q}/2$. Taking the approximations together gives

$$\blacklozenge \approx \frac{\alpha_\mu}{d_{\overline{Q}}} e^{-\mu\overline{Q}} |\hat{P}^x_{\overline{Q}/2}\hat{P}^{x+1}_{\overline{Q}/2}\rangle\langle\hat{P}^x_{\overline{Q}/2}\hat{P}^{x+1}_{\overline{Q}/2}|, \tag{B.14}$$

where $\alpha_\mu \equiv \frac{1-2M}{2M}\cosh^{-2}(\mu/2)$.

We will probe the dynamics of Eq. (B.14) under unitary dynamics on $x+1, x+2$. At this point it is useful to remember that the OTOC operator was originally defined on the whole Hilbert space as $\mathcal{L}, \mathcal{R}$ superoperators being pre- and post-multiplied by thermal factors as in Eq. (B.11). Taking into account these additional factors coming from site $x+2$ we get

$$\begin{aligned}\blacklozenge &= \frac{e^{-\mu\overline{Q}}}{d_{\overline{Q}}} |P^x_{\overline{Q}/2}P^{x+1}_{\overline{Q}/2}\rangle\langle P^x_{\overline{Q}/2}P^{x+1}_{\overline{Q}/2}|\mathcal{L}_{e^{-\mu Q_{x+2}/2}}\mathcal{R}_{e^{-\mu Q_{x+2}/2}} \\ &= \frac{e^{-\mu\overline{Q}}}{d_{\overline{Q}}} \mathcal{P}^x_{\overline{Q}/2}\mathcal{P}^{x+1}_{\overline{Q}/2}\mathcal{L}_{e^{-\mu Q_{x+2}/2}}\mathcal{R}_{e^{-\mu Q_{x+2}/2}},\end{aligned}$$

where $\mathcal{P}^x_Q \equiv |\hat{P}^x_Q\rangle\langle\hat{P}^x_Q|$ is a local projector on the space of operators.

A straightforward but tedious application of Eq. (B.10) gives two contributions to the expression for $\blacklozenge(\Delta\tau) = \blacklozenge(\Delta\tau)_1 + \blacklozenge(\Delta\tau)_2$, corresponding to the first and second terms in

Eq. (B.10), respectively. We detail the calculation of both of these separately below. The first we can write, making similar large M approximations as above, as

$$\blacklozenge(\Delta\tau)_1 \approx e^{-3\mu\overline{Q}}\frac{\alpha_\mu}{\left(\mathcal{Z}^1_\mu\right)^3}|\hat{P}^x_{\overline{Q}/2}\hat{P}^{x+1}_{\overline{Q}/2}\hat{P}^{x+2}_{\overline{Q}/2}\rangle\langle\hat{P}^x_{\overline{Q}/2}\hat{P}^{x+1}_{\overline{Q}/2}\hat{P}^{x+2}_{\overline{Q}/2}| \approx \mathcal{P}^{x,x+1,x+2}_\mu,$$

where we have defined $\mathcal{Z}^1_\mu$ as the partition function of a singe supersite, which is peaked at charge $\overline{Q}/2$. The second term, $\blacklozenge(\Delta\tau)_2$, is obtained by applying the second term in Eq. (B.10); it is sub-leading by a factor at least $\mathcal{O}(1/d_Q)$, which is typically exponentially small in Q.

On net, considering the full Hilbert space, we can iterate the above procedure to argue that

$$\blacklozenge(t) = \alpha_\mu \bigotimes_{x\in A(t)} \mathcal{P}^x_\mu \bigotimes_{x\notin A(t)} \mathcal{L}_{e^{-\mu Q_x/2}}\mathcal{R}_{e^{-\mu Q_x/2}},$$

where $A(t)$ is a region that ballistically spreads out from initial site 1 at a velocity of $2M$. We anticipate that there are $\mathcal{O}(1/M)$ errors involved in this approximation associated with neglecting fluctuations in the charge arguments of the projectors $\mathcal{P}$. We leave a more thorough accounting of these errors to other works.

Computing $\blacklozenge(\Delta\tau)_1$

Here we apply the first line of Eq. (B.10) to $\blacklozenge$. We act on supersites $x+1, x+2$. For the sake of the calculation it is useful to define the local superoperators $\mathcal{I}^x_{ef} \equiv |\hat{P}_e\rangle\langle\hat{P}_f|$, acting on a single supersite. Using these we can write

$$\begin{aligned}
&\langle\mathcal{I}^{x+1,x+2}_{Q_1Q_2}|\mathcal{P}^{x+1}_{\overline{Q}/2}\mathcal{L}_{e^{-\mu Q_{x+2}/2}}\mathcal{R}_{e^{-\mu Q_{x+2}/2}}\rangle = \\
&= \sum_{e_L+e_R=Q_1}\sum_{f_L+f_R=Q_2}\langle\mathcal{I}^{x+1}_{e_Lf_L}\mathcal{I}^{x+2}_{e_Rf_R}|\mathcal{P}^{x+1}_{\overline{Q}/2}\mathcal{L}_{e^{-\mu Q_{x+2}/2}}\mathcal{R}_{e^{-\mu Q_{x+2}/2}}\rangle \\
&= \sum_{e_L+e_R=Q_1}\sum_{f_L+f_R=Q_2}\langle\mathcal{I}^{x+1}_{e_Lf_L}|\mathcal{P}^{x+1}_{\overline{Q}/2}\rangle\langle\mathcal{I}^{x+2}_{e_Rf_R}|\mathcal{L}_{e^{-\mu Q_{x+2}/2}}\mathcal{R}_{e^{-\mu Q_{x+2}/2}}\rangle \\
&= \sum_{e_L+e_R=Q_1}\sum_{f_L+f_R=Q_2}\chi_{\overline{Q}/2}\chi_{\overline{Q}/2}\delta_{e_L\overline{Q}/2}\delta_{f_L\overline{Q}/2}e^{-\mu e_R}\delta_{e_Rf_R}\chi_{e_R} \\
&= \delta_{Q_1Q_2}\left(\chi_{\overline{Q}/2}\right)^2 e^{-\mu(Q_1-\overline{Q}/2)}\chi_{(Q_1-\overline{Q}/2)},
\end{aligned}$$

where χ_Q is the size of the 1-supersite Hilbert space with charge Q. Now we put this back into the first line of the evolution equation to get

$$\begin{aligned}
\blacklozenge(\Delta\tau)_1 &= \sum_{Q_1,Q_2}\frac{1}{d_{Q_1}d_{Q_2}}\mathcal{I}^{x+1,x+2}_{Q_1Q_2} \times \frac{\alpha_\mu e^{-\mu\overline{Q}}}{d_{\overline{Q}}}\mathcal{P}^x_{\overline{Q}/2} \times \delta_{Q_1Q_2}\left(\chi_{\overline{Q}/2}\right)^2 e^{-\mu(Q_1-\overline{Q}/2)}\chi_{(Q_1-\overline{Q}/2)} \\
&= \left(\chi_{\overline{Q}/2}\right)^2 \alpha_\mu e^{-\mu\overline{Q}}\sum_{Q_1}\frac{\mathcal{P}^x_{\overline{Q}/2}}{d_{\overline{Q}}}\frac{\mathcal{I}^{x+1,x+2}_{Q_1Q_1}}{d^2_{Q_1}} \times e^{-\mu(Q_1-\overline{Q}/2)}\chi_{Q_1-\overline{Q}/2}.
\end{aligned}$$

Note that when we take expectation values of this quantity, we should find a value of size χ^3 where χ is the typical value of χ_Q in the thermal ensemble, which is exponentially large in M for large system size. As a function of Q_1 the norm of the terms is peaked around

$Q_1 = \overline{Q}$ giving

$$\begin{aligned}
\blacklozenge(\Delta\tau)_1 &\approx \left(d^1_{\overline{Q}/2}\right)^3 \alpha_\mu e^{-3\mu\overline{Q}/2} \frac{\mathcal{P}^x_{\overline{Q}/2}\mathcal{P}^{x+1}_{\overline{Q}/2}\mathcal{P}^{x+2}_{\overline{Q}/2}}{d^3_{\overline{Q}}} \\
&\approx \alpha_\mu \frac{1}{\left(Z^1_\mu\right)^3} |e^{-\mu\left(\hat{Q}_x+\hat{Q}_{x+1}+\hat{Q}_{x+1}\right)}\rangle\langle e^{-\mu\left(\hat{Q}_x+\hat{Q}_{x+1}+\hat{Q}_{x+1}\right)}| \\
&= \alpha_\mu \mathcal{P}_{x,x+1,x+2}\left(\mu\right),
\end{aligned}$$

where $\mathcal{Z}^1_\mu$ is the 1-site partition function.

Computing $\blacklozenge(\Delta\tau)_2$

We now apply the second line of Eq. (B.10) to $\blacklozenge$ i.e., to calculate $\blacklozenge(\Delta\tau)_2$. The main object of interest is

$$\begin{aligned}
&\langle \mathcal{L}_{P_{Q_1}} \mathcal{R}_{P_{Q_2}} | \mathcal{P}^{x+1}_{\overline{Q}/2} \mathcal{L}_{e^{-\mu Q_{x+2}/2}} \mathcal{R}_{e^{-\mu Q_{x+2}/2}} \rangle \\
&= \sum_{e_L+e_R=Q_1} \sum_{f_L+f_R=Q_2} \langle \mathcal{L}_{P^{x+1}_{e_L}} \mathcal{R}_{P^{x+1}_{f_L}} | \mathcal{P}^{x+1}_{\overline{Q}/2} \rangle \langle \mathcal{L}_{P^{x+2}_{e_R}} \mathcal{R}_{P^{x+2}_{f_R}} | \mathcal{L}_{e^{-\mu Q_{x+2}/2}} \mathcal{R}_{e^{-\mu Q_{x+2}/2}} \rangle \\
&= \sum_{e_L+e_R=Q_1} \sum_{f_L+f_R=Q_2} \delta_{e_L \overline{Q}/2} \delta_{f_L \overline{Q}/2} \chi_{\overline{Q}/2} \times e^{-\mu(f_R+e_R)/2} \chi_{e_R} \chi_{f_R} \\
&= \chi_{\overline{Q}/2} \times e^{-\mu\left(Q_1+Q_2-\overline{Q}\right)/2} \chi^1_{Q_1-\overline{Q}/2} \chi^1_{Q_2-\overline{Q}/2}.
\end{aligned}$$

We also need to calculate

$$\frac{\delta_{Q_1Q_2}}{d_{Q_1}} \langle \mathcal{I}^{x+1,x+2}_{Q_1Q_1} | \mathcal{P}^{x+1}_{\overline{Q}/2} \mathcal{L}_{e^{-\mu Q_{x+2}/2}} \mathcal{R}_{e^{-\mu Q_{x+2}/2}} \rangle \approx \frac{\delta_{Q_1Q_2}}{d_{Q_1}} (\chi_{\overline{Q}/2})^2 \times \chi_{Q_1-\overline{Q}/2} e^{-\mu(Q_1-\overline{Q}/2)}.$$

Now by putting everything together we arrive at

$$\begin{aligned}
\blacklozenge(\Delta\tau)_2 \approx \sum_{Q_1,Q_2} \frac{1}{d_{Q_1}d_{Q_2} - \delta_{Q_1Q_2}} \frac{\alpha_\mu e^{-\mu\overline{Q}}}{d_{\overline{Q}}} \mathcal{P}^x_{\overline{Q}/2} \left(\mathcal{L}^{x+1,x+2}_{P_{Q_1}} \mathcal{R}^{x+1,x+2}_{P_{Q_2}} - \frac{\delta_{Q_1Q_2} \mathcal{I}^{x+1,x+2}_{Q_1Q_1}}{d_{Q_1}} \right) \\
\times \left(\chi_{\overline{Q}/2} \times e^{-\mu\left(Q_1+Q_2-\overline{Q}\right)/2} \chi_{Q_1-\overline{Q}/2} \chi_{Q_2-\overline{Q}/2} - \frac{\delta_{Q_1Q_2}}{d_{Q_1}} (\chi_{\overline{Q}/2})^2 \times \chi_{Q_1-\overline{Q}/2} e^{-\mu(Q_1-\overline{Q}/2)} \right).
\end{aligned}$$

Note that expectation values here will take values of order $O(\chi)$ on local product operators. For the Q of interest, this is a factor of $O(\chi^2)$ smaller than $\blacklozenge(\Delta\tau)_1$. So we ignore $\blacklozenge(\Delta\tau)_2$.

B.2.2. Evolution of ★

Evolve $\frac{1}{M^2}\mathcal{L}_{\zeta_x}\mathcal{R}_{\zeta_x}$ on sites $x, x+1$

We now investigate the evolution of the $\frac{1}{M^2}\mathcal{L}_{\zeta_x}\mathcal{R}_{\zeta_x}$ term under a unitary gate on $x, x+1$. Label the two lines of the OTOC evolution in Eq. (B.10) as ▲ and ■, respectively. Consider ▲ first:

$$\blacktriangle = \frac{1}{M^2} \langle \mathcal{I}^{x,x+1}_{Q_1Q_2} | \mathcal{L}_{\zeta_x} \mathcal{R}_{\zeta_x} \rangle = \delta_{Q_1Q_2} \sum_{e_L} \left(1 - \frac{2e_L}{M}\right)^2 \chi_{e_L} \chi_{Q_1-e_L},$$

where we have used

$$\mathrm{tr}_x \left(\hat{\zeta}_x \hat{P}^x_{f_L} \hat{\zeta}_x \hat{P}^x_{e_L} \right) = \mathrm{tr}_x \left(\left(1 - \frac{2\hat{Q}_x}{M}\right) \hat{P}^x_{f_L} \left(1 - \frac{2\hat{Q}_x}{M}\right) \hat{P}^x_{e_L} \right) = M^2 \left(1 - \frac{2e_L}{M}\right)^2 \chi_{e_L} \delta_{e_L f_L}.$$

Hence

$$\blacktriangle = \sum_{Q_1,Q_2} \frac{1}{d_{Q_1}^2} \mathcal{I}^{x+1,x+2}_{Q_1Q_1} \sum_{e_L} \left(1-\frac{2e_L}{M}\right)^2 \chi_{e_L}\chi_{Q_1-e_L}.$$

Now we estimate $\blacksquare$ as

$$\frac{1}{M^2}\langle \mathcal{L}_{P^{x,x+1}_{Q_1}} \mathcal{R}_{P^{x,x+1}_{Q_2}} - \frac{\delta_{Q_1Q_2}\mathcal{I}^{x,x+1}_{Q_1Q_1}}{d_{Q_1}} | \mathcal{L}_{\zeta_x}\mathcal{R}_{\zeta_x}\rangle \approx d_{Q_1}d_{Q_2}\left(1-\frac{Q_1}{M}\right)\left(1-\frac{Q_2}{M}\right).$$

We can drop the second term in the last line because it is a factor of $\mathcal{O}(d_Q^2)$ smaller than the first — this translates into being exponentially smaller in M as our final expressions for OTOCs are dominated by Q for which d_Q^2 is exponentially large in M at finite chemical potential. This leads to

$$\blacksquare \approx \sum_{Q_1,Q_2} \frac{1}{d_{Q_1}d_{Q_2}-\delta_{Q_1Q_2}} \left(\mathcal{L}_{P^{x,x+1}_{Q_1}} \mathcal{R}_{P^{x,x+1}_{Q_2}} - \frac{\delta_{Q_1Q_2}\mathcal{I}^{x,x+1}_{Q_1Q_1}}{d_{Q_1}}\right) d_{Q_1}d_{Q_2}\left(1-\frac{Q_1}{M}\right)\left(1-\frac{Q_2}{M}\right).$$

Combining the two terms $\blacksquare + \blacktriangle$ and dropping further terms of relative size $\mathcal{O}(1/d_Q^2)$ gives

$$\begin{aligned}&\sum_{Q_1,Q_2} \frac{1}{d_{Q_1}d_{Q_2}} \mathcal{L}_{P^{x,x+1}_{Q_1}} \mathcal{R}_{P^{x,x+1}_{Q_2}} \left(1-\frac{Q_1}{M}\right)\left(1-\frac{Q_2}{M}\right)\\ &+\sum_{Q_1} \frac{1}{d_{Q_1}^2}\mathcal{I}^{x,x+1}_{Q_1Q_1}\left(\sum_{e_L}\left(1-\frac{2e_L}{M}\right)^2 \chi_{e_L}\chi_{Q_1-e_L} - d_{Q_1}\left(1-\frac{Q_1}{M}\right)^2\right).\end{aligned}$$

The former is readily expressed as $\frac{1}{M^2}\mathcal{L}_{\frac{\zeta_x+\zeta_{x+1}}{2}}\mathcal{R}_{\frac{\zeta_x+\zeta_{x+1}}{2}}$. The latter term requires more work. Note first that we can exactly evaluate

$$\sum_{e_L}\left(1-\frac{2e_L}{M}\right)^2 d^1_{e_L}d^1_{Q_1-e_L} - d_{Q_1}\left(1-\frac{Q_1}{M}\right)^2 = \frac{Q_1}{M^2}\left(1-\frac{Q_1}{2M}\right)\left(\frac{1}{1-\frac{1}{2M}}\right)d_{Q_1},$$

so that in total we get

$$\begin{aligned}&\frac{1}{M^2}\mathcal{L}_{\frac{\zeta_x+\zeta_{x+1}}{2}}\mathcal{R}_{\frac{\zeta_x+\zeta_{x+1}}{2}} + \frac{1}{M}\left(\frac{1}{1-\frac{1}{2M}}\right)\sum_{Q_1}\frac{1}{d_{Q_1}}\mathcal{I}^{x,x+1}_{Q_1Q_1}\frac{Q_1}{M}\left(1-\frac{Q_1}{2M}\right)\\ =&\frac{1}{M^2}\mathcal{L}_{\frac{\zeta_x+\zeta_{x+1}}{2}}\mathcal{R}_{\frac{\zeta_x+\zeta_{x+1}}{2}} + \frac{1}{2M-1}\sum_{Q_1}\frac{1}{d_{Q_1}}\mathcal{I}^{x,x+1}_{Q_1Q_1}b_Q.\end{aligned}$$

B.2.3. Evolve $\frac{1}{M^2}\mathcal{L}_{\zeta_{x+1}}\mathcal{R}_{\zeta_x}, \frac{1}{M^2}\mathcal{L}_{\zeta_x}\mathcal{R}_{\zeta_{x+1}}$ on sites $x, x+1$

The result of such an evolution can be obtained from that of $\frac{1}{M^2}\mathcal{L}_{\zeta_x}\mathcal{R}_{\zeta_x}(\Delta\tau)$ in the previous section by noting $\frac{1}{M^2}\mathcal{L}_{\zeta_{x+1}}\mathcal{R}_{\zeta_x} = \frac{1}{M^2}\mathcal{L}_{\zeta_{x+1}+\zeta_x}\mathcal{R}_{\zeta_x} - \frac{1}{M^2}\mathcal{L}_{\zeta_x}\mathcal{R}_{\zeta_x}$ and that $\zeta_{x+1}+\zeta_x$ is conserved on $x, x+1$ for the gate considered. As a result,

$$\begin{aligned}\frac{1}{M^2}\mathcal{L}_{\zeta_{x+1}}\mathcal{R}_{\zeta_x}(\Delta\tau) &= \frac{1}{M^2}\mathcal{L}_{\zeta_{x+1}+\zeta_x}\mathcal{R}_{\frac{1}{2}(\zeta_x+\zeta_{x+1})} - \frac{1}{M^2}\mathcal{L}_{\zeta_x}\mathcal{R}_{\zeta_x}(\Delta\tau)\\ &= \frac{1}{M^2}\mathcal{L}_{\frac{1}{2}(\zeta_{x+1}+\zeta_x)}\mathcal{R}_{\frac{1}{2}(\zeta_x+\zeta_{x+1})} - \frac{1}{2M-1}\sum_{Q_1}\frac{1}{d_{Q_1}}\mathcal{P}^{x,x+1}_{Q_1}b_Q.\end{aligned}$$

The result is the same for $\frac{1}{M^2}\mathcal{L}_{\zeta_x}\mathcal{R}_{\zeta_{x+1}}(\Delta\tau)$.

v_r	$\langle v_r \rangle$	$\left\langle v_r^\dagger v_x \right\rangle$	$\frac{1}{M^2}\left\langle v_r^\dagger \zeta_x(t) v_r \zeta_x(t) \right\rangle$	
1	1	1	$\left(f^2 + \frac{\sum_y K_{xy}^2(t)}{M}\left(1-f^2\right)\right)$	
Z	f	1	$\left(f^2 + \frac{\sum_y K_{xy}^2(t)}{M}\left(1-f^2\right)\right)$	
$\sigma^\pm$	0	$\frac{1\mp f}{2}$	$\frac{1}{2}(1\pm f)\left[\frac{1}{M^2}\left\langle\zeta_x(t)\zeta_x(t)\right\rangle - K_{x[r]}\frac{2}{M}f^2 - K_{x[r]}^2\frac{2}{M^2}\left(1-f^2\right)\right]$	

Table B.1.: Useful expectation values for manipulating OTOC.

Summing up contact terms

Let us start by evolving the purely diffusive term at time t by one time step. Using our results earlier in this section, we obtain a sum of contact terms in addition to the expected purely diffusive term:

$$
\begin{aligned}
&\frac{1}{M^2}\mathcal{L}_{\zeta_x(t)}\mathcal{R}_{\zeta_x(t)} = \frac{1}{M^2}\sum_{yy'} K_{xy'}K_{xy}\mathcal{L}_{\zeta_y}\mathcal{R}_{\zeta_{y'}} \\
&\to \frac{1}{M^2}\mathcal{L}_{\zeta_x(t+1)}\mathcal{R}_{\zeta_x(t+1)} + \frac{1}{2M-1}\sum_{y:y=t \mod 2}\left(K_{x,y}^2(t) + K_{x,y+1}^2(t)\right)\sum_{Q_1}\frac{1}{d_{Q_1}}\mathcal{P}_{Q_1}^{y,y+1} b_{Q_1} \\
&\quad - \frac{1}{2M-1}\sum_{y:y=t \mod 2} 2K_{x,y}K_{x,y+1}(t)\sum_{Q_1}\frac{1}{d_{Q_1}}\mathcal{P}_{Q_1}^{y,y+1} b_Q \\
&\to \frac{1}{M^2}\mathcal{L}_{\zeta_x(t+1)}\mathcal{R}_{\zeta_x(t+1)} + \frac{1}{2M-1}\sum_{y:y=t \mod 2}\left(K_{x,y+1} - K_{x,y}\right)^2(t)\sum_{Q_1}\frac{1}{d_{Q_1}}\mathcal{P}_{Q_1}^{y,y+1} b_{Q_1},
\end{aligned}
$$

where $\zeta_x(t) = \sum_y K_{xy}\zeta_y$ and K_{xy} is the diffusion kernel of Eq. (7.3).

B.3. Equilibration in operator space

In this appendix, we use the superoperator formalism, developed in Sec. 8.2.2, to show that the expectation values of local superoperators, e.g. OTOCs, are at long times determined by a Gibbs ensemble on operator space, which reproduces the results established in Sec. 8.3.1. Consider a spin system with L sites, each with on-site Hilbert space dimension $q = 2$ (for concreteness). We want to time evolve the 'density matrix' corresponding to a pure state in the space of operators, $\mathcal{P}_V(t) = |\hat{V}(t)\rangle\langle\hat{V}(t)|$. It is convenient to consider initial operators which include a Gibbs factor, e.g., take an operator of form $\hat{V} = \hat{\omega}_\mu \hat{O}_0 \hat{\omega}_\mu$ where $\hat{O}_0 = \hat{Z}_0, \hat{\sigma}_0^\pm$ is a local Pauli matrix on site 0 and $\hat{\omega}_\mu \equiv e^{-\frac{\mu}{4}\hat{Q}}$. This is useful for our purposes because the out-of-time-order part of the OTOC (the focus of our study) can be expressed as an expectation value of a local superoperator with respect to such a $\mathcal{P}_V$ as

$$
\langle \mathcal{P}_V(t)|\mathcal{L}_{W_r^\dagger}\mathcal{R}_{W_r}\rangle = \langle\hat{V}(t)|\mathcal{L}_{W_r^\dagger}\mathcal{R}_{W_r}|\hat{V}(t)\rangle = \operatorname{tr}\left(\hat{\omega}_\mu\hat{O}_0^\dagger\hat{\omega}_\mu\hat{W}_r^\dagger(t)\hat{\omega}_\mu\hat{O}_0\hat{\omega}_\mu\hat{W}_r(t)\right). \tag{B.15}
$$

If we apply local two site U(1) random unitaries to such a spin system for a very long time, we expect the system to scramble completely, such that the time evolution is essentially a non-local random unitary operator with conserved U(1) charge. Hence, at long times, we expect the average density matrix to be that obtained by plugging $\mathcal{P}_V$ into Eq. (8.6) for a unitary that acts on the whole chain. The result is a Haar averaged 'density matrix' (on operator space) of the form

$$\mathcal{P}_V\left(t_\infty\right) = |\hat{V}_\parallel\rangle\langle\hat{V}_\parallel| + \sum_{Q_1Q_2} \mathrm{tr}\left(\hat{P}_{Q_1}\hat{V}_\perp\hat{P}_{Q_2}\hat{V}_\perp^\dagger\right) \times \frac{\mathcal{L}_{P_{Q_1}}\mathcal{R}_{P_{Q_2}} - \frac{\delta_{Q_1Q_2}}{d_{Q_1}}\mathcal{P}_{Q_1}}{d_{Q_1}d_{Q_2} - \delta_{Q_1Q_2}},$$

where we have separated $\hat{V}$ into two orthogonal components $\hat{V} = \hat{V}_\parallel + \hat{V}_\perp$, with $\hat{V}_\parallel \equiv \sum_Q \frac{\hat{P}_Q \mathrm{tr}\left(\hat{P}_Q\hat{V}\right)}{d_Q}$ and $\hat{V}_\perp = \hat{V} - \hat{V}_\parallel$, and used the notation $\mathcal{P}_Q \equiv |\hat{P}_Q\rangle\langle\hat{P}_Q|$. In what follows, we consider the expectation value of a local superoperator – for concreteness we will take a superoperator $\mathcal{L}_{W_r}\mathcal{R}_{W_r^\dagger}$ where $\hat{W}_r$ is a local operator. When evaluated in the 'state' $\mathcal{P}_V(t)$, this will have two separate contributions form the $\parallel, \perp$ components respectively. Let us deal first with the $\parallel$ component,

$$\begin{aligned}\mathrm{tr}\left(\mathcal{P}_{V_\parallel}\left(t_\infty\right)\mathcal{L}_{W_r}\mathcal{R}_{W_r^\dagger}\right) &= \mathrm{tr}\left(\hat{\omega}_{2\mu}\hat{O}_\parallel^\dagger\hat{W}_r\hat{\omega}_{2\mu}\hat{O}_\parallel\hat{W}_r^\dagger\right)\\ &= \sum_{Q_1Q_2} e^{-\frac{\mu}{2}(Q_1+Q_2)}\mathrm{tr}\left(\hat{O}_\parallel^\dagger\hat{P}_{Q_1}\hat{W}_r\hat{P}_{Q_2}\hat{O}_\parallel\hat{W}_r^\dagger\right).\end{aligned}$$

It is readily verified by example that for two local observables, $\hat{O}$ and $\hat{W}_r$, this sum is for large L sharply peaked for $Q_{1,2} = \overline{Q} + \mathcal{O}(1)$ where $\overline{Q} = L/(1+e^\mu)$. (The key observation here is that local operators have $\mathcal{O}(1)$ charge under the adjoint action of $\hat{Q}$). This justifies replacing $\mathcal{P}_{V_\parallel}\left(t_\infty\right)$ with essentially any other distribution peaked in the same position. A particularly simple choice is.

$$\mathcal{P}_{V_\parallel}\left(t_\infty\right) \to \mathrm{tr}\left(\hat{V}_\parallel^\dagger\hat{V}_\parallel\right)\frac{|e^{-\frac{\mu}{2}\hat{Q}}\rangle\langle e^{-\frac{\mu}{2}\hat{Q}}|}{Z_\mu},$$

where $Z_\mu = \mathrm{tr}\left(e^{-\mu\hat{Q}}\right)$.

The $\perp$ part of the density matrix takes form

$$\mathcal{P}_{V_\perp}\left(t_\infty\right) = \sum_{Q_1Q_2} \mathrm{tr}\left(\hat{P}_{Q_1}\hat{V}_\perp\hat{P}_{Q_2}\hat{V}_\perp^\dagger\right) \times \frac{\mathcal{L}_{P_{Q_1}}\mathcal{R}_{P_{Q_2}} - \frac{\delta_{Q_1Q_2}\mathcal{P}_{Q_1}}{d_{Q_1}}}{d_{Q_1}d_{Q_2} - \delta_{Q_1Q_2}}.$$

We again consider the expectation values of local superoperators (e.g., $\mathcal{L}_{W_r}\mathcal{R}_{W_r^\dagger}$). Once again, the sum is sharply peaked around $Q_{1,2} = \overline{Q} + \mathcal{O}(1)$ in the large L limit, i.e.

$$\mathcal{P}_{V_\perp}\left(t_\infty\right) \sim \mathrm{tr}\left(\hat{V}_\perp^\dagger\hat{V}_\perp\right)\frac{\mathcal{L}_{P_{\overline{Q}+\lambda_V}}\mathcal{R}_{P_{\overline{Q}}}}{d_{\overline{Q}+\lambda_V}d_{\overline{Q}}}$$

As before, this justifies replacing $\mathcal{P}_{V_\perp}\left(t_\infty\right)$ with a similar distribution peaked at the same charge,

$$\mathcal{P}_{V_\perp}\left(t_\infty\right) \to \mathrm{tr}\left(\hat{V}_\perp^\dagger\hat{V}_\perp\right)\frac{e^{-\mu\left(\mathcal{L}_Q+\mathcal{R}_Q\right)}}{Z_\mu^2}.$$

We reiterate that the above approximations are also only expected to hold weakly (i.e., when we calculate the expectation values of observables with an $\mathcal{O}(1)$ charge).

In summary, our late time operator density matrix takes the form

$$\mathcal{P}_V\left(t_\infty\right) = \mathrm{tr}\left(\hat{V}_\parallel^\dagger\hat{V}_\parallel\right)\frac{|e^{-\frac{\mu}{2}\hat{Q}}\rangle\langle e^{-\frac{\mu}{2}\hat{Q}}|}{Z_\mu} + \mathrm{tr}\left(\hat{V}_\perp^\dagger\hat{V}_\perp\right)\frac{e^{-\mu\left(\mathcal{L}_Q+\mathcal{R}_Q\right)}}{Z_\mu^2}. \tag{B.16}$$

This form, particularly the latter $\perp$ term, is nothing other than a Gibbs ensemble for the superoperator conserved quantities $\mathcal{L}_Q, \mathcal{R}_Q$. In fact, we could motivate Eq. (B.16) using the language standard to discussions of equilibration to the Gibbs ensemble. Having identified $\mathcal{L}_Q, \mathcal{R}_Q$ as the conserved local densities, we could have proposed an obvious ansatz of Gibbs form for the late time density matrix

$$\mathcal{P}_V^{\text{ansatz}} = \operatorname{tr}\left(\hat{V}_\parallel^\dagger \hat{V}_\parallel\right) \frac{|e^{-\frac{1}{2}\eta_\parallel^{(1)}\hat{Q}}\rangle\langle e^{-\frac{1}{2}\eta_\parallel^{(2)}\hat{Q}}|}{Z_{\frac{1}{2}\eta_\parallel^{(1)}+\frac{1}{2}\eta_\parallel^{(2)}}} + \operatorname{tr}\left(\hat{V}_\perp^\dagger \hat{V}_\perp\right) \frac{e^{-\eta_\perp^{(1)}\mathcal{L}_Q-\eta_\perp^{(2)}\mathcal{R}_Q}}{Z_{\eta_\perp^{(1)}} Z_{\eta_\perp^{(2)}}}, \tag{B.17}$$

and determined $\eta_{\perp,\parallel}^{(1,2)}$ via the conditions depending on the initial state,

$$\frac{\langle \hat{V}_\perp | \mathcal{L}_Q | \hat{V}_\perp \rangle}{\langle \hat{V}_\perp | \hat{V}_\perp \rangle} = \mathring{\operatorname{tr}}\left(\frac{e^{-\eta_\perp^{(1)}\mathcal{L}_Q-\eta_\perp^{(2)}\mathcal{R}_Q}}{Z_{\eta_\perp^{(1)}} Z_{\eta_\perp^{(2)}}} \mathcal{L}_Q\right), \tag{B.18}$$

$$\frac{\langle \hat{V}_\parallel | \mathcal{L}_Q | \hat{V}_\parallel \rangle}{\langle \hat{V}_\parallel | \hat{V}_\parallel \rangle} = \mathring{\operatorname{tr}}\left(\frac{e^{-\eta_\parallel^{(1)}\mathcal{L}_Q-\eta_\parallel^{(2)}\mathcal{R}_Q}}{Z_{\frac{1}{2}\eta_\parallel^{(1)}+\frac{1}{2}\eta_\parallel^{(2)}}} \mathcal{L}_Q\right), \tag{B.19}$$

and an otherwise identical pair of equations for $\mathcal{R}_Q$. It is readily verified that for the choice of initial operator $\hat{V} = \hat{\omega}_\mu \hat{O}_0 \hat{\omega}_\mu$, we get $\eta_{\perp,\parallel}^{(1,2)} = \mu$ as required, agreeing with our final result Eq. B.16.

These results point to an extension of the principle of thermalization to operator space. Recall that for the usual notion of thermalization, if the time evolution U is completely ergodic (save the presence of $U(1)$ symmetry), we expect (and have indeed argued in previous sections for random U) that local observables equilibrate according to

$$\left\langle \hat{O}\left(t \to \infty\right)\right\rangle_\psi = \frac{\operatorname{tr}\left(e^{-\mu_\psi \hat{Q}} \hat{O}\right)}{\operatorname{tr}\left(e^{-\mu_\psi \hat{Q}}\right)} \tag{B.20}$$

in the thermodynamic limit. Here μ_ψ is determined for a given state ψ by balancing this equation for $\hat{O} = \hat{Q}$. As we have found above, a similar notion of ETH occurs in operator space. One uses the ansatz Eq. (B.17), and determines the chemical potentials $\eta_{\parallel,\perp}^{(1,2)}$ by ensuring that the superoperator charge densities in the initial state agree with that of the final state (see Eq. (B.18) and Eq. (B.19)). The analogy is especially apparent for the $\perp$ terms, where the ensemble is precisely a Gibbs distribution with respect to the superoperators.

B.4. Solution of $\sigma^+\sigma^+$ OTOC in the $\mu = \infty$ limit

In this appendix we show how the OTOC $\mathcal{F}_{\mu=\infty}^{\sigma_0^+\sigma_r^+}$ (the only non-trivial OTOC in the $\mu \to \infty$ limit) can be understood in terms of a two-particle random walk of absorbing particles, and how this description gives rise to the two important qualitative features (double plateau structure and lack of ballistic light cone) shown in Fig. 8.10. The considerations of this appendix apply also for higher dimensional random circuits, which should therefore also exhibit the same qualitative features.

As described in Section 8.3.3, the OTOC $\mathcal{F}_{\mu=\infty}^{\sigma_0^+\sigma_r^+}$, which is the zeroth order term in the perturbative expansion, is given by a process wherein the partition function is evaluated between boundary conditions that contain 2 particles. These boundary conditions are the following (using the notation of Fig. 8.1):

- At time 0 there is a particle on site 0 on layers 21 and a second particle on site $s \neq 0$ on layers 22
- At time t there is a particle on site 0 on layers 22 and a second particle on site $s' \neq r$ on layers 21.

As long as the two particles in the initial state do not meet they each perform a random walk process of the type described in Eq. (7.2). Upon meeting each other the two particles annihilate, since there is no matrix element with this specific set of incoming particles (see, e.g., Fig 8.2). This means that the computation of the OTOC reduces to the following problem:

Given two random walkers, one that has to start at site 0*, and another which has to end up at site* r *at time* t*, what is the probability that their paths avoid each other?*

The solution to this problem can be easily formulated in terms of single-particle transition probabilities, by noting that there is a one-to-one mapping between crossing paths of the two particles with a fixed set of starting and endpoints and *arbitrary* paths where the two endpoints at time t are interchanged. This mapping is simply given by reinterpreting the paths of the two particle by changing the last crossing into a reflection or vice versa (this is a simple case of the Lindström-Gessel-Viennot Lemma, see Ref. [654] and the references therein)[2]. Using this trick, the solution is given by

$$\overline{\mathcal{F}_{\mu=\infty}^{\sigma_0^+\sigma_r^+}}(t) = \left(\sum_{s'<r} \sum_{s>0} + \sum_{s'>r} \sum_{s<0} \right) \left[K_{0,s'}(\tau) K_{s,r}(\tau) - K_{0,r}(\tau) K_{s,s'}(\tau) \right], \tag{B.21}$$

where $K_{r_1,r_2}(t)$ is the probability of a single random walker travelling from site r_1 to r_2 in time t

The problem of calculating the OTOC thus reduces to solving a single-particle diffusion problem. This is easily done in an infinite system, with the result already stated in Eq. (7.3). Plugging this formula into Eq. (B.21) yields a solution shown in the right panel of Fig. 8.10, which is a function of $r/\sqrt{t}$ and saturates to the value $\frac{1}{2} - \frac{1}{\pi}$ as $t^{-1/2}$. This saturation value is non-zero because in an infinite systems there is a finite probability that the two particles avoid each other for arbitrarily long times, i.e. by travelling in opposite directions. Note that the mapping of the $\mu = \infty$ OTOC to the random walk problem defined above is not restricted to 1D and we would end up with a similar counting of non-crossing paths for random circuits in higher dimensions. This means that the saturation value (which equals the probability of non-crossing paths) is even larger in those cases, as random walkers in higher dimensions have a larger probability of avoiding each other.

To get the full form of the OTOC, with eventual saturation to the second plateau at zero, one needs to solve the diffusion problem in a finite system with either periodic or reflecting boundaries. For a finite system of size L, and for times $t \gg L^2/D$ (where D is the diffusion constant which is of $\mathcal{O}(1)$ in our case) the paths of the two particles have to cross eventually, and as a result the OTOC decays to zero. Here we focus on the case of reflecting boundaries, where the above way of counting crossing paths remains valid, although we checked numerically that the the results are similar for closed boundaries (the time signalling the end of the prethermal plateau is numerically larger in the case with open boundaries, reflecting that fact that particles can evade each other for longer). Instead of giving an exact solution on the lattice (which is nevertheless possible), we solve the same problem in the continuum, substituting the single particle transition probabilities

---

[2] Note that this mapping works for an infinite system or a finite system with open boundaries. The calculation is more complicated if we take closed boundary conditions, although this does not affect the results qualitatively.

with the solution of the continuum diffusion equation with reflecting boundaries,

$$\begin{aligned}\partial_t K(x,t) &= D\partial_x^2 K(x,t); \\ \partial_x K(x,t)|_{x=0,L} &= 0,\end{aligned} \tag{B.22}$$

where we defined $K(x,t) \equiv K_{0,x}(t)$. This equation can be solved by doing an eigen-decomposition of the operator $-D\partial_x^2$, using eigenstates with the appropriate boundary conditions, resulting in the single-particle propagator

$$K_{x,y}(t) = \frac{1}{L}\sum_{n\in\mathbb{Z}} e^{-\frac{\pi^2 Dtn^2}{2L^2}} \cos\frac{\pi nx}{L} \cos\frac{\pi ny}{L}. \tag{B.23}$$

We can then approximate the OTOC by plugging this formula into Eq. (B.21). At short times, when $Dt \ll L^2$ the resulting curve follows the result in an infinite system (which can be seen explicitly ba applying the Poisson summation formula the the above expression and then looking at the lowest order term in $\frac{L^2}{Dt}$) while at times $Dt \gg L^2$ it goes to zero as $\propto \exp(-\frac{\pi^2 Dt}{2L^2})$.

B.5. Circuit-averaged purity dynamics

We first re-derive the mapping to the classical partiton function described in Section 8.1.1 and App. B.1 using a modified notation, generalizing it to the finite-q model described in Chapter 7 in the process. This mapping provides the basis for an efficient method for calculating the average purity of the time evolved state, which we make us of in our numerical calculations. Furthermore, we take the $q \to \infty$ limit to arrive at the rules of the effective model presented in Chapter 10.

We are interested in evaluating the partition with an on-site Hilbert space decomposing into the product of a conserved spin-1/2 and a non-conserved qudit with q states, $\mathbb{C}^2 \otimes \mathbb{C}^q$, described in Ref. Chapter 7 (see also Ref. [549]). In what follows, Z_x denotes the local value of the conserved spin, which is an operator acting only on the $\mathbb{C}^2$ component of the on-site Hilbert space. It will not be necessary to construct an explicit operator basis for the $\mathbb{C}^q$ degrees of freedom. For arbitrary pairs of operators u, v, acting on a single site in the original Hilbert space $\mathbb{C}^2 \otimes \mathbb{C}^q$, we can assign the following operators acting on the doubled Hilbert space

$$\Lambda^-_{u|v} \equiv u \otimes v \qquad\qquad \Lambda^+_{u|v} \equiv (u \otimes v)\,\mathcal{F}, \tag{B.24}$$

where $\mathcal{F} = \sum_{ij} e_{ij} \otimes e_{ji}$ is the on-site swap operator, with i labeling an arbitrary on-site orthonormal basis. The tensor multiplication implicit in the second part of the above expressions is $(u \otimes v)(u' \otimes v') = uu' \otimes vv'$. The notion of Frobenius inner product between operators generalizes naturally to this two-copy space and yields

$$\langle \Lambda^{\pm}_{u|v} \mid \Lambda^{\pm}_{u'|v'} \rangle = \mathrm{tr}\left(u^\dagger u'\right) \mathrm{tr}\left(v^\dagger v'\right) \qquad \langle \Lambda^{\mp}_{u|v} \mid \Lambda^{\pm}_{u'|v'} \rangle = \mathrm{tr}\left(v^\dagger v' u^\dagger u'\right). \tag{B.25}$$

The ‘purity operator’ for the half-chain containing sites $\leq x$ then reads $\mathcal{F}(x) \equiv \Lambda^{\leq x,+}_{1|1} \otimes \Lambda^{>x,-}_{1|1}$.

Consider now the effect of a U(1)-symmetric two-site unitary gate, acting on sites $x, x{+}1$. The two-site Hilbert space decomposes into three subspaces, labeled by the total charge $Q = 0, 1, 2$, corresponding to total spin-z components $+2, 0, -2$ respectively. Let P_Q denote the projector onto the two-site Hilbert spaces with charge $Q = 0, 1, 2$, which have dimension $d_Q = q^2, 2q^2, q^2$ respectively. Averaging over four moments of the random gate yields an effective two-site evolution operator (equivalent to Eq. (8.6) above),

$$\overline{U^* \otimes U \otimes U^* \otimes U} \equiv \mathfrak{T}_{x,x+1} = \sum_{\sigma,\mu=\pm 1} \sum_{e_1 e_2} \frac{w_{\sigma\mu}(e_1,e_2)}{d_{e_1} d_{e_2} - \delta_{e_1 e_2}} \mid \Lambda^{\sigma}_{P_{e_1}|P_{e_2}} \rangle \langle \Lambda^{\mu}_{P_{e_1}|P_{e_2}} \mid \tag{B.26}$$

where $w_+ = 1$ and $w_- = -\delta_{e_1 e_2} d_{e_1}^{-1}$. The terms appearing in this effective evolution are two-copy operators acting on the pair of sites $x, x+1$. In order to contract the tensor network one then needs to split them up to a sum of single-site two-copy operators, which in principle can be done in a many different ways, depending on the choice of local basis; one such choice was described in Eq. (B.9). Given such a local basis choice, the computation of the average purity reduces to contracting $2t$ layers of such two-site tensors, along with the boundary conditions defined by $\rho_0 \otimes \rho_0$ (where ρ_0 is the initial density matrix) and $\mathcal{F}(x)$. The contraction can be done in a variety of ways. In our numerical calculations we use a boundary MPS method [84], wherein the boundary tensors defined by $\mathcal{F}(x)$ are written as a matrix product state (MPS) and evolved layer-by-layer as in the Time Evolving Block Decimation (TEBD) algorithm [417]. Calculting the purity then amounts to taking the overlap of this time evolved MPS with another one that represents $\rho_0 \otimes \rho_0$. A further adventage of this method is that one can average over all product states analytically and incorporate the result into the boundary conditions, which yields the curve shown e.g. in Fig. 10.1a.

B.5.1. Large q limit

While Eq. (B.26) yields an effective evolution that is numerically efficient, it is not analytically solvable, unlike the case of a random circuit without symmetries discussed in Section 5.2. One can, however, simplify the equations by taking the $q \to \infty$ limit, which yields

$$\mathfrak{T}_{x,x+1} \left[\Lambda^{+,x}_{1|1} \otimes \Lambda^{-,x+1}_{1|1} \right] = \frac{2}{q} \times \frac{1}{2} \sum_{\sigma=\pm} \frac{1}{2} \left(\Lambda^{\sigma}_{1|1} + \Lambda^{\sigma}_{Z_{x,x+1}|Z_{x,x+1}} \right) + \mathcal{O}(q^{-3}). \tag{B.27}$$

The terms $\Lambda^{\pm}_{Z_{x,x+1}|Z_{x,x+1}}$ are defined according to $Z_{x,x+1} = 2^{-1}(Z_x + Z_{x+1})$ and Eq. B.24; they are identical to $\tilde{\mathcal{F}}_{x\mp 1}(x \pm 1)$ introduced in Eq. (10.5) of the main text. Applied to the purity operator, the above equation then yields

$$\mathfrak{T}_{r,r+1} \left[\mathcal{F}(x) \right] = \delta_{x \neq r} \mathcal{F}(x) + \delta_{x,r} \frac{1}{2q} \sum_{\sigma} \left(\mathcal{F}(x+\sigma) + \sum_{z,w=x,x+1} \frac{1}{4} \mathcal{F}_{z,w}(x+\sigma) \right) + \mathcal{O}(q^{-3}), \tag{B.28}$$

where we have defined

$$\mathcal{F}_{\tau,\upsilon}(x) = \prod_i \Lambda^{(-1)^{\delta_{x<i}}}_{Z_i^{\tau_i}|Z_i^{\upsilon_i}}. \tag{B.29}$$

Here, $\tau_i, \upsilon_i = 0, 1$ indicate the positions of the z operators which we refer to as the positions of red and blue particles in the main text, as in Fig. 10.3(c,d). x is the position of the entanglement cut. We have abbreviated a special case of such an operator with notation $\mathcal{F}_{y,z}(x)$ where x, y, z simply denote the position of the cut, and y, z are the positions at which a single τ, υ is nonzero. Eq. (B.28) is exactly the result stated in Eq. (10.4). It is illustrated in terms of the red and blue particle picture in Fig. B.1

Before moving on to derive equations of motion for these operators, let us try to gain some intuition about their physical meaning. When evaluated in a pure state they give, focusing on the simplest case,

$$\langle \tilde{\mathcal{F}}_{x-1}(x) \rangle \equiv \langle \tilde{\mathcal{F}}_{x-1}(x) \mid \rho \otimes \rho \rangle = \left\| \mathrm{tr}_{\leq x} \left(\hat{P}_0^{x-1,x} \rho - P_2^{x-1,x} \rho \right) \right\|^2, \tag{B.30}$$

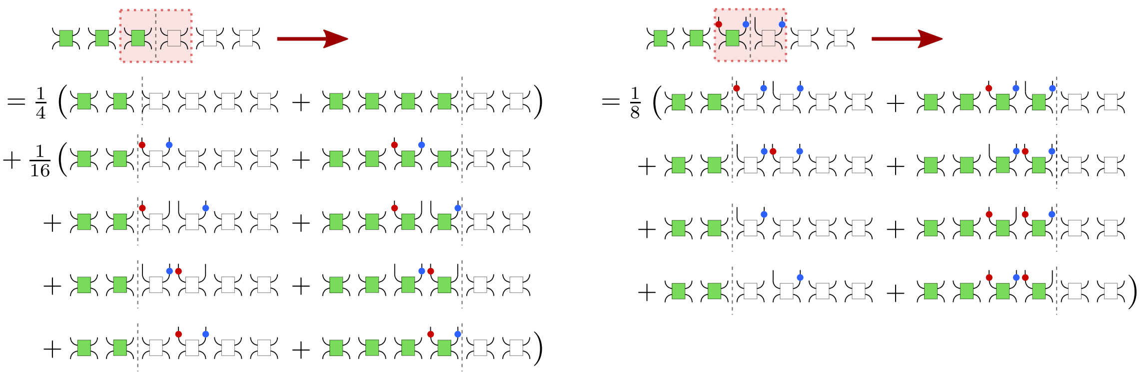

Figure B.1.: Illustration of some of the two-site update rules in the large q effective model. Left: evolution of a swap-string, given by Eq. (B.28). The two-site gate (red dotted line) moves the string by one site, while producing spin-operators on both copies of the Hilbert space, denoted by red and blue particles respectively. Right: evolution of a more complicated configuration, with several particles already present near the endpoint of the string.

where $P_Q^{x-1,x}$ is a projector that projects onto eigenstates of the two-site charge operator $\hat{Q}_{x-1,x}$ with eigenvalue Q. This expression is a direct measure of how distinguishable the positive matrices $\hat{P}_0\rho\hat{P}_0$ and $\hat{P}_2\rho\hat{P}_2$ are through measurements purely on the subsystem consisting of sites to the right of x. It is therefore directly related to local quantum fluctuation of the charge density on these two sites. In particular they are sensitive to the sort of 'rare configurations' discussed in our heuristic argument, where the neighborhood of the entanglement cut if completely empty/filled.

To find the equations of motion for the terms $\mathcal{F}_{\tau,v}(y)$, it is necessary and sufficient to determine the dynamics of various two site operators of form $\Lambda^{\pm,x}_{a|b} \otimes \Lambda^{\pm,x+1}_{a'|b'}$ and $\Lambda^{\pm,x}_{a|b} \otimes \Lambda^{\mp,x+1}_{a'|b'}$ where $a, b, a', b = 1, Z$. To begin, the following operators are exactly invariant under $\mathfrak{T}_{x,x+1}$

$$\Lambda^{\pm,x}_{1|1} \otimes \Lambda^{\pm,x+1}_{1|1} \qquad \Lambda^{\pm,x}_{Z_x|1} \otimes \Lambda^{\pm,x+1}_{Z_{x+1}|1} \qquad \Lambda^{\pm,x}_{1|Z_x} \otimes \Lambda^{\pm,x+1}_{1|Z_{x+1}} \qquad \Lambda^{\pm,x}_{Z_x|Z_x} \otimes \Lambda^{\pm,x+1}_{Z_{x+1}|Z_{x+1}}.$$

These correspond to the statement that, far away from the cut, there are no dynamics for red (blue) particles if the pair of sites in question are empty or fully occupied with red (blue) particles.

The following superoperators have very simple evolutions under $\mathfrak{T}_{x,x+1}$ which follow immediately from Haar averaging.

$$\begin{aligned}
\Lambda^{\pm,x}_{Z_x|1} \otimes \Lambda^{\pm,x+1}_{1|1}, \Lambda^{\pm,x}_{1|1} \otimes \Lambda^{\pm,x+1}_{Z_{x+1}|1} &\to \frac{1}{2}\left(\Lambda^{\pm,x}_{Z_x|1} \otimes \Lambda^{\pm,x+1}_{1|1} + \Lambda^{\pm,x}_{1|1} \otimes \Lambda^{\pm,x+1}_{Z_{x+1}|1}\right) \\
\Lambda^{\pm,x}_{1|Z_x} \otimes \Lambda^{\pm,x+1}_{1|1}, \Lambda^{\pm,x}_{1|1} \otimes \Lambda^{\pm,x+1}_{1|Z_{x+1}} &\to \frac{1}{2}\left(\Lambda^{\pm,x}_{1|Z_x} \otimes \Lambda^{\pm,x+1}_{1|1} + \Lambda^{\pm,x}_{1|1} \otimes \Lambda^{\pm,x+1}_{1|Z_{x+1}}\right) \\
\Lambda^{\pm,x}_{Z_x|Z_x} \otimes \Lambda^{\pm,x+1}_{1|Z_{x+1}}, \Lambda^{\pm,x}_{1|Z_x} \otimes \Lambda^{\pm,x+1}_{Z_{x+1}|Z_{x+1}} &\to \frac{1}{2}\left(\Lambda^{\pm,x}_{Z_x|Z_x} \otimes \Lambda^{\pm,x+1}_{1|Z_{x+1}} + \Lambda^{\pm,x}_{1|Z_x} \otimes \Lambda^{\pm,x+1}_{Z_{x+1}|Z_{x+1}}\right) \\
\Lambda^{\pm,x}_{Z_x|Z_x} \otimes \Lambda^{\pm,x+1}_{Z_{x+1}|1}, \Lambda^{\pm,x}_{Z_x|1} \otimes \Lambda^{\pm,x+1}_{Z_{x+1}|Z_{x+1}} &\to \frac{1}{2}\left(\Lambda^{\pm,x}_{Z_x|Z_x} \otimes \Lambda^{\pm,x+1}_{Z_{x+1}|1} + \Lambda^{\pm,x}_{Z_x|1} \otimes \Lambda^{\pm,x+1}_{Z_{x+1}|Z_{x+1}}\right)
\end{aligned}$$

We also meet more four more involved products

$$\begin{aligned}
\Lambda^{\pm,x}_{Z_x|Z_x} \otimes \Lambda^{\pm,x+1}_{1|1}, \Lambda^{\pm,x}_{1|1} \otimes \Lambda^{\pm,x+1}_{Z_{x+1}|Z_{x+1}} &\to \Lambda^{\pm}_{Z_{x,x+1}|Z_{x,x+1}} + \frac{1}{2q^2}\Lambda^{\mp}_{\frac{1-Z_xZ_{x+1}}{2}|\frac{1-Z_xZ_{x+1}}{2}} + \mathcal{O}(q^{-4}) \\
\Lambda^{\pm,x}_{Z_x|1} \otimes \Lambda^{\pm,x+1}_{1|Z_{x+1}}, \Lambda^{\pm,x}_{1|Z_x} \otimes \Lambda^{\pm,x+1}_{Z_{x+1}|1} &\to \Lambda^{\pm}_{Z_{x,x+1}|Z_{x,x+1}} - \frac{1}{2q^2}\Lambda^{\mp}_{\frac{1-Z_xZ_{x+1}}{2}|\frac{1-Z_xZ_{x+1}}{2}} + \mathcal{O}(q^{-4}).
\end{aligned}$$

The $\mathcal{O}(q^{-2})$ terms on the second line are subleading, and introduce a new entanglement cut at the next time step, which will accrue additional suppressing $\mathcal{O}(q^{-1})$ factors. We henceforth ignore these terms, working in the large q limit; understanding their effect at finite q is an interesting open problem. We note that the above 16 mappings reflect the statement that, far from the cut and at leading order, red and blue particles undergo single-file diffusion (i.e., random walk with hard-core interactions).

We have listed all the possible products on one site of a cut. Finally, we meet products involving sites near the entanglement cut, such as

$$\begin{aligned}
\Lambda^{\pm,x}_{1|1} \otimes \Lambda^{\mp,x+1}_{1|1} &\to \frac{2}{q} \times \frac{1}{2} \sum_{\sigma=\pm} \frac{1}{2} \left(\Lambda^{\sigma}_{1|1} + \Lambda^{\sigma}_{Z_{x,x+1}|Z_{x,x+1}} \right) + \mathcal{O}(q^{-3}) \\
\Lambda^{\pm,x}_{Z_x|1} \otimes \Lambda^{\mp,x+1}_{Z_{x+1}|1} &\to \frac{2}{q} \times \frac{1}{2} \sum_{\sigma=\pm} \frac{1}{2} \left(\Lambda^{\sigma}_{Z_x Z_{x+1}|1} + \Lambda^{\sigma}_{Z_{x,x+1}|Z_{x,x+1}} \right) + \mathcal{O}(q^{-3}) \\
\Lambda^{\pm,x}_{1|Z_x} \otimes \Lambda^{\mp,x+1}_{1|Z_{x+1}} &\to \frac{2}{q} \times \frac{1}{2} \sum_{\sigma=\pm} \frac{1}{2} \left(\Lambda^{\sigma}_{1|Z_x Z_{x+1}} + \Lambda^{\sigma}_{Z_{x,x+1}|Z_{x,x+1}} \right) + \mathcal{O}(q^{-3}).
\end{aligned}$$

The first mapping above shows that the cut can create red and blue particles from nothing in pairs, and is indeed equivalent to Eq. B.28. The second and third equation shows that the particles created can correlate with the direction of motion of the cut. We have further related equations showing that the cut can scatter a red to a blue particle and vice versa:

$$\begin{aligned}
&\Lambda^{\pm,x}_{Z_x|1} \otimes \Lambda^{\mp,x+1}_{1|1}, \Lambda^{\mp,x}_{1|1} \otimes \Lambda^{\pm,x+1}_{Z_{x+1}|1} \\
&\qquad \to \frac{1}{2q} \left(\Lambda^{\pm}_{Z_{x,x+1}|I} + \Lambda^{\pm}_{Z_x Z_{x+1}|Z_{x,x+1}} + \Lambda^{\mp}_{Z_{x,x+1}|I} + \Lambda^{\mp}_{I|Z_{x,x+1}} \right) + \mathcal{O}(q^{-3}), \\
&\Lambda^{\pm,x}_{1|Z_x} \otimes \Lambda^{\mp,x+1}_{1|1}, \Lambda^{\mp,x}_{1|1} \otimes \Lambda^{\pm,x+1}_{1|Z_{x+1}} \\
&\qquad \to \frac{1}{2q} \left(\Lambda^{\pm}_{I|Z_{x,x+1}} + \Lambda^{\pm}_{Z_{x,x+1}|Z_x Z_{x+1}} + \Lambda^{\mp}_{I|Z_{x,x+1}} + \Lambda^{\mp}_{Z_{x,x+1}|I} \right) + \mathcal{O}(q^{-3}).
\end{aligned}$$

Note also that

$$\begin{aligned}
&\Lambda^{\pm,x}_{Z_x|Z_x} \otimes \Lambda^{\mp,x+1}_{1|1}, \Lambda^{\mp,x}_{1|1} \otimes \Lambda^{\pm,x+1}_{Z_{x+1}|Z_{x+1}} \\
&\qquad \to \frac{1}{2q} \left(\Lambda^{\pm}_{Z_x Z_{x+1}|Z_x Z_{x+1}} + \Lambda^{\pm}_{Z_{x,x+1}|Z_{x,x+1}} + \Lambda^{\mp}_{1|1} + \Lambda^{\mp}_{Z_{x,x+1}|Z_{x,x+1}} \right) + \mathcal{O}(q^{-3}), \\
&\Lambda^{\pm,x}_{Z_x|1} \otimes \Lambda^{\mp,x+1}_{1|Z_{x+1}}, \Lambda^{\mp,x}_{1|Z_x} \otimes \Lambda^{\pm,x+1}_{Z_{x+1}|1} \\
&\qquad \to \frac{1}{2q} \left(\Lambda^{\pm}_{Z_x Z_{x+1}|1} + \Lambda^{\pm}_{Z_{x,x+1}|Z_{x,x+1}} + \Lambda^{\mp}_{1|Z_x Z_{x+1}} + \Lambda^{\mp}_{Z_{x,x+1}|Z_{x,x+1}} \right) + \mathcal{O}(q^{-3}),
\end{aligned}$$

the first of which shows that the cut can destroy particles in pairs as well. Finally,

$$\begin{aligned}
&\Lambda^{\pm,x}_{Z_x|Z_x} \otimes \Lambda^{\mp,x+1}_{Z_{x+1}|Z_{x+1}} \\
&\qquad \to \frac{1}{2q} \sum_{\sigma=\pm} \left(\Lambda^{\sigma}_{Z_x Z_{x+1}|Z_x Z_{x+1}} + \Lambda^{\sigma}_{Z_{x,x+1}|Z_{x,x+1}} \right) + \mathcal{O}(q^{-3}), \\
&\Lambda^{\pm,x}_{Z_x|Z_x} \otimes \Lambda^{\mp,x+1}_{Z_{x+1}|1}, \Lambda^{\mp,x}_{Z_x|1} \otimes \Lambda^{\pm,x+1}_{Z_{x+1}|Z_{x+1}} \\
&\qquad \to \frac{1}{2q} \left(\Lambda^{\pm}_{Z_x Z_{x+1}|Z_{x,x+1}} + \Lambda^{\pm}_{Z_{x,x+1}|Z_x Z_{x+1}} + \Lambda^{\mp}_{Z_x Z_{x+1}|Z_{x,x+1}} + \Lambda^{\mp}_{Z_{x,x+1}|I} \right) + \mathcal{O}(q^{-3}), \\
&\Lambda^{\pm,x}_{Z_x|Z_x} \otimes \Lambda^{\mp,x+1}_{1|Z_{x+1}}, \Lambda^{\mp,x}_{1|Z_x} \otimes \Lambda^{\pm,x+1}_{Z_{x+1}|Z_{x+1}} \\
&\qquad \to \frac{1}{2q} \left(\Lambda^{\pm}_{Z_{x,x+1}|Z_x Z_{x+1}} + \Lambda^{\pm}_{Z_x Z_{x+1}|Z_{x,x+1}} + \Lambda^{\mp}_{Z_{x,x+1}|Z_x Z_{x+1}} + \Lambda^{\mp}_{I|Z_{x,x+1}} \right) + \mathcal{O}(q^{-3})
\end{aligned}$$

Note that each of the last 16 terms involves the action of the circuit in the vicinity of the cut, and are correspondingly suppressed by a factor of $2/q$. Otherwise, these equations exhibit a rich set of behaviors. For example, the cut can create and absorb particles in pairs, and can convert a red particle to a blue particle and vice versa.

The full set of two site calculations above show that, up to $\mathcal{O}(q^{-2})$ corrections, the Haar averaged dynamics are closed in the space of operators spanned by $\mathcal{F}_{\tau,\upsilon}(x)$ (see Eq. B.29) where τ, υ denote the possible configurations of red and blue particles alluded to in the text. Moreover, saving for the overall factor of $2/q$ at each global time step, the induced dynamics on this restricted space of operators is in fact Markovian leading to a stochastic process on the configuration space of cuts and blue and red particle configurations $\{x, \{\tau_y\}, \{\upsilon_y\}\}$; i.e., ignoring the $2/q$ factor, the RHS coefficients in all the mappings listed below Eq. B.30 add up to unity.

To summarize, the rules of this Markoc process are the following. Away from the entanglement cut, the red and blue particles perform independent and unbiased random walks, with hard-core intra-species interactions. The cut itself also performs an unbiased random walk, moving one bond to the left or right with equal probabilities. On the site that it crosses, it has a probability $1/2$ of swapping the state of *both* red and blue particles (from empty to filled or vice versa) simultaneously.

The result of the Markov process is a probability distribution $p(x, \{\tau_y\}, \{\upsilon_y\})$. As stated in the main text, one can take the mean field approximation

$$p(x, \{\tau_y\}, \{\upsilon_y\}) \propto e^{-\frac{x^2}{2l(t)^2}} e^{-\frac{1}{2l(t)^2}\sum_y (\tau_y + \upsilon_y) y^2}, \tag{B.31}$$

with $l(t)^2 = \kappa t$. Using this, and the definition of $\mathcal{F}_{\tau,\upsilon}(x)$, one find that the purity of an arbitrary initial state reads

$$\frac{\prod_y \left(1 + \langle Z_y \rangle e^{-\frac{y^2}{2l(t)^2}}\right)^2 + \prod_y \left(1 - \langle Z_y \rangle e^{-\frac{y^2}{2l(t)^2}}\right)^2}{\prod_y \left(1 + e^{-\frac{y^2}{2l(t)^2}}\right)^2 + \prod_y \left(1 - e^{-\frac{y^2}{2l(t)^2}}\right)^2}. \tag{B.32}$$

For translation invariant product states, this expression simplifies to Eq. (10.7) in the main text.

B.6. Hydrodynamic tails in the spin $1/2$ random circuit

In this section we describe the behavior of various correlation functions in the U(1) conserving random circuit model, lifting intuition from our studies of operator spreading in Chapter 8. Our results are in line with the standard lore of hydrodynamics: the space of local observables splits into an orthogonal sum of hydrodynamic and non-hydrodynamic variables. In a short range correlated initial state, the former can decay according to a power law at long times and have diffusive spatiotemporal behavior, while the latter always decay exponentially quickly. An advantage of our approach, compared to the usual scaling arguments [287], is that we are able to make statements about the differences in behavior for different homogenous initial states; something we expect to be of independent interest.

We start with an exact rewriting of the circuit evolved Z_r operator

$$Z_r(t) = D_r(t) + B_r(t), \tag{B.33}$$

where $D_r(t) = \sum_{r'} K_{rr'}(t)\, Z_{r'}$ and $K_{rr'}(t)$ is a lattice diffusion kernel, and where

$$B_r(t) = \frac{1}{2}\sum_{\tau=1}^{t} \sum_{x=\tau \mod 2} (\partial_x K_{rx}(\tau))\, \Gamma_x(t;\tau), \tag{B.34}$$

with $\Gamma_x(t;\tau) \equiv (Z_x - Z_{x+1})(t;\tau)$. No approximations have been made thus far. The operator weight in D_r is $\sum_{r'} K^2_{rr'} = O(t^{-1/2})$, while that in B_r is $1-O(t^{-1/2})$, as discussed in Chapter 8. We will assume that $\Gamma_x(t;\tau)$ grows ballistically, so that it is effectively a random superposition of operators of typical radius $v_B\,(t-\tau)$. This assumption can only be an approximation to the full story, in part because $Z_x - Z_{x+1}$ is itself a hydrodynamical variable. However, it turns out that the expectation values of this tail is either exactly zero (θ-states) or decays exponentially in time (Néel-like states), so we are justified in ignoring it.

In considering the growth of fluctuations, we also consider operators of the form $Z_r(t)Z_s(t)$. These we may similarly write exactly as

$$Z_r(t)Z_s(t) = \sum_{r's'} K^{r's'}_{rs}(t) Z_{r'}Z_{s'} + B_{rs}(t). \tag{B.35}$$

The random circuit calculation demonstrates that, under averaging, the two operators engage in single file diffusion, which we take to have kernel $K^{r's'}_{rs}(t)$. $B_{rs}(t)$ is again assumed to be a ballistically spreading and effectively random superposition of operators. In the following we explain how to estimate the various correlation functions presented in Table B.2, using operator spreading intuition.

One point functions The average behavior of $\langle Z_r(t)\rangle$ is simple to compute for various states through substitution of Eq. B.33. This leads to two expressions $\langle D_r(t)\rangle$ and $\langle B_r(t)\rangle$. The former is independent of time for translation invariant states, and determined by the filling, while for the Neel state it decays exponentially with t because $\sum_{r'}(-1)^{r'}K_{rr'}(t) \sim e^{-\frac{\pi^2 t}{2}}$. The B_r term is more involved, but on average expected to be zero because $\Gamma_x(t;\tau)$ is a superposition of operators with random signs.

Fluctuations in one point functions The average behavior of $\overline{\langle Z_r(t)\rangle\langle Z_s(t)\rangle}$ can also be computed using B.33. Using the results in the previous paragraph, two terms survive the noise averaging, $\langle D_r(t)\rangle\langle D_s(t)\rangle$ and $\overline{\langle B_r(t)\rangle\langle B_s(t)\rangle}$. The former term can be calculated using the paragraph above, while the latter require a more involved discussion. Using

$$\overline{\langle B_r(t)\rangle\langle B_s(t)\rangle} = \frac{1}{2}\sum_{,\tau'\tau=1}^{t}\ \sum_{x,y=\tau \mod 2} \partial_x K_{rx}(\tau)\partial_y K_{sy}(\tau)\overline{\langle\Gamma_x(t;\tau)\rangle\langle\Gamma_y(t;\tau)\rangle} \tag{B.36}$$

To approximate this sum, we first note that, as $\Gamma_y(t;\tau)$ tends to grow ballistically, its expectation value on a short range correlated state will tend to decay exponentially quickly (a string of operators of length R has a typical expectation value $e^{-\alpha R}$ on a product state). So the sum is dominated by τ, τ' near t. Moreover, due to the spatial randomness of the circuit, the sign of the expectation values $\langle\Gamma_{x/y}(t;\tau)\rangle$ are uncorrelated unless $x=y$. Hence we approximate Eq. B.36 by restricting the sum to $\tau', \tau = t-1, x=y$. At large times $t \gg |r-s|^2/D$, the distinction between r, s becomes unimportant, and the contribution goes as $\int dx\,(\partial_x K_{rx})^2 \sim t^{-3/2}$.

Two point functions In order to compute $\overline{\langle Z_r(t)Z_s(t)\rangle}$ we substitute in Eq. B.35 and assume the ballistic terms source random signs that cancel on averaging. This leads to precisely one contribution $\sum_{r's'} K^{r's'}_{rs}(t)\langle Z_{r'}Z_{s'}\rangle$ where $K^{r's'}_{rs}(t)$ is the single file lattice diffusion propagator. This is independent of time for translation invariant states, but remarkably is found to decay as $\sim \frac{1}{\sqrt{t}}$ for the Neel state. In the case of ϵ states we substitute $\langle Z_{r'}Z_{s'}\rangle \sim e^{-|r'-s'|/\xi}$; for finite ϵ, this will have the effect of restricting $|r'-s'| \leq \xi$ in the sum above. The leading behavior is obtained by setting $r'=s'$, which gives $\sum_{r'} K^{r'r'}_{rs}(t) \sim t^{-1/2}$.

State	$\overline{\langle \delta Z_r \rangle}$	$\overline{\langle \delta Z_r \rangle \langle \delta Z_s \rangle}$	$\overline{\delta(\langle Z_r Z_s \rangle)}$	$\lvert \delta S_2 \rvert$
↑↓	$O(e^{-\pi^2 t/2})$	$O(t^{-3/2})$	$O(t^{-1/2})$	$O(t^{-1})$
↑↑↓	$O(e^{-\pi^2 t/3})$	$O(t^{-3/2})$	$O(t^{-1/2})$	$O(t^{-1/2})$
θ-state	0	$O(t^{-3/2})$	0	$O(t^{-3/2})$
β-state	0	$O(t^{-3/2})$	$O(t^{-1/2})$	$O(t^{-1})$

Table B.2.: Summary of the saturation behavior of various circuit averaged correlation functions, their moments and the Rényi entropy at large times $t \gg |r-s|^2$ in the spin 1/2 random circuit.

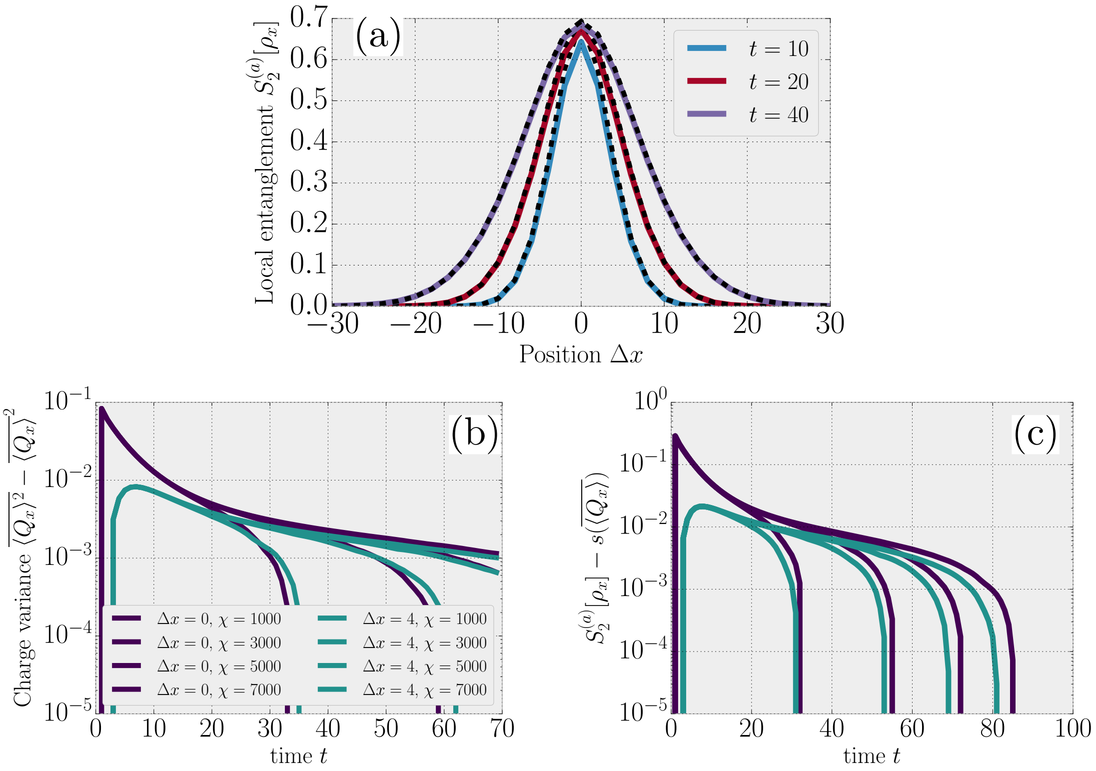

Figure B.2.: Local equilibration for a domain wall state in the random circuit with $N = 1$. (a) The local purity entropy on average is well approximated by the purity of the local equilibrium state associated to the average charge. (b) The distance to the equilibrium value for two different positions as a function of time for different bond dimensions χ shows a decay to zero. (c) the size of the fluctuations between the local charge densities in different circuit realizations (as captured by their variance) similarly decrease in time.

B.7. Local equilibration after a domain wall quench

Our general argument in Chapter 11, putting an upper bound proportional to $\sqrt{t}$ on the growth of von Neumann entropy for a domain wall, relied on the notion of local equilibration. Here we check numerically that this assumption indeed holds in the spin-$\frac{1}{2}$ local random circuit we considered in the main text. This consists of two parts. First of all, in order for local equilibration to $\overline{\langle \hat{Q}_x(t) \rangle}$ to make sense, the circuit-to-circuit fluctuations in $\langle \hat{Q}_x(t) \rangle$ around this average should become small. This means that we can assign a local charge to each site, which should be approximately the same for all realizations of the circuit, making the right hand side of Eq. (11.8) well-defined. Second, we need the one-site density matrices to be close to the Gibbs state defined by this local charge density. As we show in Fig. B.2 both of these requirements are satisfied at sufficiently long times.

To check the first requirement, we compute numerically the statistical variance of the local charge in the random circuit, i.e. the variance between circuit realizations of the quantum expectation value $\langle \hat{Q}_x \rangle$. This variance can be computed as a 2D partition function, similarly to the calculation of other quantities, such as OTOCs and purities, as discussed before. We find that the variance decays in time, as shown by Fig. B.2(b), indicating that at long times it is meaningful to consider locally equilibrated states depending on a circuit-independent average local charge.

To check if the on-site density matrix is indeed locally equilibrated, we compare its annealed average second Rényi entropy with the entropy density expected for an eqilibrium state with the same charge density. Note that since the on-site density matrix only has two parameters, one of which is fixed by the charge density, the equivalence of Rényi entropies is sufficient to establish local equilibrium. We indeed find that the local Rényi entropy tends to its equilibrium value at long times; this is shown in Fig. B.2(c). In both cases we show results for different bond dimensions χ used in the evaluation of these quantities as 2D tensor networks to indicate where the results are converged.

Bibliography

[1] C. W. von Keyserlingk, Tibor Rakovszky, Frank Pollmann, and S. L. Sondhi. Operator hydrodynamics, otocs, and entanglement growth in systems without conservation laws. *Phys. Rev. X*, 8:021013, Apr 2018. doi: 10.1103/PhysRevX.8.021013. URL `https://link.aps.org/doi/10.1103/PhysRevX.8.021013`.

[2] Tibor Rakovszky, Sarang Gopalakrishnan, S. A. Parameswaran, and Frank Pollmann. Signatures of information scrambling in the dynamics of the entanglement spectrum. *Phys. Rev. B*, 100:125115, Sep 2019. doi: 10.1103/PhysRevB.100.125115. URL `https://link.aps.org/doi/10.1103/PhysRevB.100.125115`.

[3] Tibor Rakovszky, Frank Pollmann, and C. W. von Keyserlingk. Diffusive hydrodynamics of out-of-time-ordered correlators with charge conservation. *Phys. Rev. X*, 8:031058, Sep 2018. doi: 10.1103/PhysRevX.8.031058. URL `https://link.aps.org/doi/10.1103/PhysRevX.8.031058`.

[4] Tibor Rakovszky, C. W. von Keyserlingk, and Frank Pollmann. Dissipation-assisted operator evolution method for capturing hydrodynamic transport. ArXiv preprint, 2004.05177, 2020.

[5] Tibor Rakovszky, Frank Pollmann, and C. W. von Keyserlingk. Sub-ballistic growth of rényi entropies due to diffusion. *Phys. Rev. Lett.*, 122:250602, Jun 2019. doi: 10.1103/PhysRevLett.122.250602. URL `https://link.aps.org/doi/10.1103/PhysRevLett.122.250602`.

[6] Tibor Rakovszky, C. W. von Keyserlingk, and Frank Pollmann. Entanglement growth after inhomogenous quenches. *Phys. Rev. B*, 100:125139, Sep 2019. doi: 10.1103/PhysRevB.100.125139. URL `https://link.aps.org/doi/10.1103/PhysRevB.100.125139`.

[7] Tibor Rakovszky, Pablo Sala, Ruben Verresen, Michael Knap, and Frank Pollmann. Statistical localization: From strong fragmentation to strong edge modes. *Phys. Rev. B*, 101:125126, Mar 2020. doi: 10.1103/PhysRevB.101.125126. URL `https://link.aps.org/doi/10.1103/PhysRevB.101.125126`.

[8] Pablo Sala, Tibor Rakovszky, Ruben Verresen, Michael Knap, and Frank Pollmann. Ergodicity breaking arising from hilbert space fragmentation in dipole-conserving hamiltonians. *Phys. Rev. X*, 10:011047, Feb 2020. doi: 10.1103/PhysRevX.10.011047. URL `https://link.aps.org/doi/10.1103/PhysRevX.10.011047`.

[9] Tibor Rakovszky, János K. Asbóth, and Andrea Alberti. Detecting topological invariants in chiral symmetric insulators via losses. *Phys. Rev. B*, 95:201407, May 2017. doi: 10.1103/PhysRevB.95.201407. URL `https://link.aps.org/doi/10.1103/PhysRevB.95.201407`.

[10] Tibor Rakovszky, Márton Mestyán, Mario Collura, Márton Kormos, and Gábor Takács. Hamiltonian truncation approach to quenches in the ising field theory. *Nuclear Physics B*, 911:805 – 845, 2016. ISSN 0550-3213. doi: https://doi.org/10.1016/j.nuclphysb.2016.08.024. URL `http://www.sciencedirect.com/science/article/pii/S0550321316302541`.

[11] Tibor Rakovszky and Janos K. Asboth. Localization, delocalization, and topological phase transitions in the one-dimensional split-step quantum walk. *Phys. Rev. A*, 92: 052311, Nov 2015. doi: 10.1103/PhysRevA.92.052311. URL https://link.aps.org/doi/10.1103/PhysRevA.92.052311.

[12] Asher Peres. *Quantum theory: concepts and methods*, volume 57. Springer Science & Business Media, 2006.

[13] John S Bell and John Stewart Bell. *Speakable and unspeakable in quantum mechanics: Collected papers on quantum philosophy.* Cambridge university press, 2004.

[14] Nicolas Brunner, Daniel Cavalcanti, Stefano Pironio, Valerio Scarani, and Stephanie Wehner. Bell nonlocality. *Rev. Mod. Phys.*, 86:419–478, Apr 2014. doi: 10.1103/RevModPhys.86.419. URL https://link.aps.org/doi/10.1103/RevModPhys.86.419.

[15] Kavan Modi, Aharon Brodutch, Hugo Cable, Tomasz Paterek, and Vlatko Vedral. The classical-quantum boundary for correlations: Discord and related measures. *Rev. Mod. Phys.*, 84:1655–1707, Nov 2012. doi: 10.1103/RevModPhys.84.1655. URL https://link.aps.org/doi/10.1103/RevModPhys.84.1655.

[16] Matthew Saul Leifer. Is the quantum state real? an extended review of -ontology theorems. *Quanta*, 3(1):67, November 2014. doi: 10.12743/quanta.v3i1.22. URL https://doi.org/10.12743/quanta.v3i1.22.

[17] Howard Barnum, Stephanie Wehner, and Alexander Wilce. Introduction: Quantum information theory and quantum foundations. *Foundations of Physics*, 48(8):853–856, July 2018. doi: 10.1007/s10701-018-0188-6. URL https://doi.org/10.1007/s10701-018-0188-6.

[18] Michael A. Nielsen and Isaac L. Chuang. *Quantum Computation and Quantum Information: 10th Anniversary Edition.* Cambridge University Press, USA, 10th edition, 2011. ISBN 1107002176.

[19] Ryszard Horodecki, Paweł Horodecki, Michał Horodecki, and Karol Horodecki. Quantum entanglement. *Rev. Mod. Phys.*, 81:865–942, Jun 2009. doi: 10.1103/RevModPhys.81.865. URL https://link.aps.org/doi/10.1103/RevModPhys.81.865.

[20] Mark M. Wilde. *Quantum Information Theory.* Cambridge University Press, 2016. doi: 10.1017/9781316809976. URL https://doi.org/10.1017/9781316809976.

[21] Ingemar Bengtsson and Karol Życzkowski. *Geometry of quantum states: an introduction to quantum entanglement.* Cambridge university press, 2017.

[22] John Preskill. Quantum computing and the entanglement frontier, 2012.

[23] John Preskill. Quantum Computing in the NISQ era and beyond. *Quantum*, 2: 79, August 2018. ISSN 2521-327X. doi: 10.22331/q-2018-08-06-79. URL https://doi.org/10.22331/q-2018-08-06-79.

[24] Philip Phillips. *Advanced Solid State Physics.* Cambridge University Press, 2009. doi: 10.1017/cbo9781139031066. URL https://doi.org/10.1017/cbo9781139031066.

[25] Piers Coleman. *Introduction to Many-Body Physics.* Cambridge University Press, 2015. doi: 10.1017/cbo9781139020916. URL https://doi.org/10.1017/cbo9781139020916.

[26] Steven M. Girvin and Kun Yang. *Modern Condensed Matter Physics*. Cambridge University Press, February 2019. doi: 10.1017/9781316480649. URL `https://doi.org/10.1017/9781316480649`.

[27] Subir Sachdev. *Quantum Phase Transitions*. Cambridge University Press, 2009. doi: 10.1017/cbo9780511973765. URL `https://doi.org/10.1017/cbo9780511973765`.

[28] Bei Zeng, Xie Chen, Duan-Lu Zhou, and Xiao-Gang Wen. *Quantum Information Meets Quantum Matter*. Springer New York, 2019. doi: 10.1007/978-1-4939-9084-9. URL `https://doi.org/10.1007/978-1-4939-9084-9`.

[29] Lev Pitaevskii and Sandro Stringari. *Bose-Einstein Condensation and Superfluidity*. Oxford University Press, January 2016. doi: 10.1093/acprof:oso/9780198758884.001.0001. URL `https://doi.org/10.1093/acprof:oso/9780198758884.001.0001`.

[30] James F Annett et al. *Superconductivity, superfluids and condensates*, volume 5. Oxford University Press, 2004.

[31] Michael Tinkham. *Introduction to superconductivity*. Courier Corporation, 2004.

[32] J Robert Schrieffer. *Theory of superconductivity*. CRC Press, 2018.

[33] Richard E. Prange and Steven M. Girvin, editors. *The Quantum Hall Effect*. Springer New York, 1990. doi: 10.1007/978-1-4612-3350-3. URL `https://doi.org/10.1007/978-1-4612-3350-3`.

[34] N H D'Ambrumeni. The quantum hall effect: Poincaré seminar (progress in mathematical physics). *Journal of Physics A: Mathematical and Theoretical*, 40 (40):12256–12256, sep 2007. doi: 10.1088/1751-8121/40/40/b02. URL `https://doi.org/10.1088%2F1751-8121%2F40%2F40%2Fb02`.

[35] Ady Stern. Anyons and the quantum hall effect—a pedagogical review. *Annals of Physics*, 323(1):204–249, January 2008. doi: 10.1016/j.aop.2007.10.008. URL `https://doi.org/10.1016/j.aop.2007.10.008`.

[36] David Tong. Lectures on the quantum hall effect, 2016.

[37] M. Z. Hasan and C. L. Kane. Colloquium: Topological insulators. *Rev. Mod. Phys.*, 82:3045–3067, Nov 2010. doi: 10.1103/RevModPhys.82.3045. URL `https://link.aps.org/doi/10.1103/RevModPhys.82.3045`.

[38] Xiao-Liang Qi and Shou-Cheng Zhang. Topological insulators and superconductors. *Rev. Mod. Phys.*, 83:1057–1110, Oct 2011. doi: 10.1103/RevModPhys.83.1057. URL `https://link.aps.org/doi/10.1103/RevModPhys.83.1057`.

[39] B Andrei Bernevig and Taylor L Hughes. *Topological insulators and topological superconductors*. Princeton university press, 2013.

[40] János K. Asbóth, László Oroszlány, and András Pályi. *A Short Course on Topological Insulators*. Springer International Publishing, 2016. doi: 10.1007/978-3-319-25607-8. URL `https://doi.org/10.1007/978-3-319-25607-8`.

[41] Claude N. Cohen-Tannoudji. Nobel lecture: Manipulating atoms with photons. *Rev. Mod. Phys.*, 70:707–719, Jul 1998. doi: 10.1103/RevModPhys.70.707. URL `https://link.aps.org/doi/10.1103/RevModPhys.70.707`.

[42] J. M. Raimond, M. Brune, and S. Haroche. Manipulating quantum entanglement with atoms and photons in a cavity. *Rev. Mod. Phys.*, 73:565–582, Aug 2001. doi: 10.1103/RevModPhys.73.565. URL https://link.aps.org/doi/10.1103/RevModPhys.73.565.

[43] D. Leibfried, R. Blatt, C. Monroe, and D. Wineland. Quantum dynamics of single trapped ions. *Rev. Mod. Phys.*, 75:281–324, Mar 2003. doi: 10.1103/RevModPhys.75.281. URL https://link.aps.org/doi/10.1103/RevModPhys.75.281.

[44] Serge Haroche. Nobel lecture: Controlling photons in a box and exploring the quantum to classical boundary. *Rev. Mod. Phys.*, 85:1083–1102, Jul 2013. doi: 10.1103/RevModPhys.85.1083. URL https://link.aps.org/doi/10.1103/RevModPhys.85.1083.

[45] David J. Wineland. Nobel lecture: Superposition, entanglement, and raising schrödinger's cat. *Rev. Mod. Phys.*, 85:1103–1114, Jul 2013. doi: 10.1103/RevModPhys.85.1103. URL https://link.aps.org/doi/10.1103/RevModPhys.85.1103.

[46] J. S. Bell. On the einstein podolsky rosen paradox. *Physics Physique Fizika*, 1:195–200, Nov 1964. doi: 10.1103/PhysicsPhysiqueFizika.1.195. URL https://link.aps.org/doi/10.1103/PhysicsPhysiqueFizika.1.195.

[47] Stuart J. Freedman and John F. Clauser. Experimental test of local hidden-variable theories. *Phys. Rev. Lett.*, 28:938–941, Apr 1972. doi: 10.1103/PhysRevLett.28.938. URL https://link.aps.org/doi/10.1103/PhysRevLett.28.938.

[48] Alain Aspect, Jean Dalibard, and Gérard Roger. Experimental test of bell's inequalities using time-varying analyzers. *Phys. Rev. Lett.*, 49:1804–1807, Dec 1982. doi: 10.1103/PhysRevLett.49.1804. URL https://link.aps.org/doi/10.1103/PhysRevLett.49.1804.

[49] Gregor Weihs, Thomas Jennewein, Christoph Simon, Harald Weinfurter, and Anton Zeilinger. Violation of bell's inequality under strict einstein locality conditions. *Phys. Rev. Lett.*, 81:5039–5043, Dec 1998. doi: 10.1103/PhysRevLett.81.5039. URL https://link.aps.org/doi/10.1103/PhysRevLett.81.5039.

[50] M. A. Rowe, D. Kielpinski, V. Meyer, C. A. Sackett, W. M. Itano, C. Monroe, and D. J. Wineland. Experimental violation of a bell's inequality with efficient detection. *Nature*, 409(6822):791–794, February 2001. doi: 10.1038/35057215. URL https://doi.org/10.1038/35057215.

[51] B. Hensen, H. Bernien, A. E. Dréau, A. Reiserer, N. Kalb, M. S. Blok, J. Ruitenberg, R. F. L. Vermeulen, R. N. Schouten, C. Abellán, W. Amaya, V. Pruneri, M. W. Mitchell, M. Markham, D. J. Twitchen, D. Elkouss, S. Wehner, T. H. Taminiau, and R. Hanson. Loophole-free bell inequality violation using electron spins separated by 1.3 kilometres. *Nature*, 526(7575):682–686, October 2015. doi: 10.1038/nature15759. URL https://doi.org/10.1038/nature15759.

[52] M. H. Anderson, J. R. Ensher, M. R. Matthews, C. E. Wieman, and E. A. Cornell. Observation of bose-einstein condensation in a dilute atomic vapor. *Science*, 269(5221):198–201, July 1995. doi: 10.1126/science.269.5221.198. URL https://doi.org/10.1126/science.269.5221.198.

[53] K. B. Davis, M. O. Mewes, M. R. Andrews, N. J. van Druten, D. S. Durfee, D. M. Kurn, and W. Ketterle. Bose-einstein condensation in a gas of sodium atoms. *Phys. Rev. Lett.*, 75:3969–3973, Nov 1995. doi: 10.1103/PhysRevLett.75.3969. URL https://link.aps.org/doi/10.1103/PhysRevLett.75.3969.

[54] E. A. Cornell and C. E. Wieman. Nobel lecture: Bose-einstein condensation in a dilute gas, the first 70 years and some recent experiments. *Rev. Mod. Phys.*, 74: 875–893, Aug 2002. doi: 10.1103/RevModPhys.74.875. URL https://link.aps.org/doi/10.1103/RevModPhys.74.875.

[55] Wolfgang Ketterle. Nobel lecture: When atoms behave as waves: Bose-einstein condensation and the atom laser. *Rev. Mod. Phys.*, 74:1131–1151, Nov 2002. doi: 10.1103/RevModPhys.74.1131. URL https://link.aps.org/doi/10.1103/RevModPhys.74.1131.

[56] Albert Einstein. Quantentheorie des einatomigen idealen gases. *SB Preuss. Akad. Wiss. phys.-math. Klasse*, 1924.

[57] Seth Lloyd. Universal quantum simulators. *Science*, 273(5278):1073–1078, 1996. ISSN 0036-8075. doi: 10.1126/science.273.5278.1073. URL https://science.sciencemag.org/content/273/5278/1073.

[58] J. Ignacio Cirac and Peter Zoller. Goals and opportunities in quantum simulation. *Nature Physics*, 8(4):264–266, April 2012. doi: 10.1038/nphys2275. URL https://doi.org/10.1038/nphys2275.

[59] Ehud Altman, Kenneth R. Brown, Giuseppe Carleo, Lincoln D. Carr, Eugene Demler, Cheng Chin, Brian DeMarco, Sophia E. Economou, Mark A. Eriksson, Kai-Mei C. Fu, Markus Greiner, Kaden R. A. Hazzard, Randall G. Hulet, Alicia J. Kollar, Benjamin L. Lev, Mikhail D. Lukin, Ruichao Ma, Xiao Mi, Shashank Misra, Christopher Monroe, Kater Murch, Zaira Nazario, Kang-Kuen Ni, Andrew C. Potter, Pedram Roushan, Mark Saffman, Monika Schleier-Smith, Irfan Siddiqi, Raymond Simmonds, Meenakshi Singh, I. B. Spielman, Kristan Temme, David S. Weiss, Jelena Vuckovic, Vladan Vuletic, Jun Ye, and Martin Zwierlein. Quantum simulators: Architectures and opportunities, 2019.

[60] Immanuel Bloch, Jean Dalibard, and Sylvain Nascimbène. Quantum simulations with ultracold quantum gases. *Nature Physics*, 8(4):267–276, April 2012. doi: 10.1038/nphys2259. URL https://doi.org/10.1038/nphys2259.

[61] R. Blatt and C. F. Roos. Quantum simulations with trapped ions. *Nature Physics*, 8(4):277–284, April 2012. doi: 10.1038/nphys2252. URL https://doi.org/10.1038/nphys2252.

[62] H. P. Büchler, M. Hermele, S. D. Huber, Matthew P. A. Fisher, and P. Zoller. Atomic quantum simulator for lattice gauge theories and ring exchange models. *Phys. Rev. Lett.*, 95:040402, Jul 2005. doi: 10.1103/PhysRevLett.95.040402. URL https://link.aps.org/doi/10.1103/PhysRevLett.95.040402.

[63] Hendrik Weimer, Markus Müller, Igor Lesanovsky, Peter Zoller, and Hans Peter Büchler. A rydberg quantum simulator. *Nature Physics*, 6(5):382–388, March 2010. doi: 10.1038/nphys1614. URL https://doi.org/10.1038/nphys1614.

[64] S. P. Jordan, K. S. M. Lee, and J. Preskill. Quantum algorithms for quantum field theories. *Science*, 336(6085):1130–1133, May 2012. doi: 10.1126/science.1217069. URL https://doi.org/10.1126/science.1217069.

[65] Erez Zohar, J. Ignacio Cirac, and Benni Reznik. Cold-atom quantum simulator for su(2) yang-mills lattice gauge theory. *Phys. Rev. Lett.*, 110:125304, Mar 2013. doi: 10.1103/PhysRevLett.110.125304. URL `https://link.aps.org/doi/10.1103/PhysRevLett.110.125304`.

[66] D. Banerjee, M. Bögli, M. Dalmonte, E. Rico, P. Stebler, U.-J. Wiese, and P. Zoller. Atomic quantum simulation of $\mathbf{U}(n)$ and $\mathrm{SU}(n)$ non-abelian lattice gauge theories. *Phys. Rev. Lett.*, 110:125303, Mar 2013. doi: 10.1103/PhysRevLett.110.125303. URL `https://link.aps.org/doi/10.1103/PhysRevLett.110.125303`.

[67] U.-J. Wiese. Ultracold quantum gases and lattice systems: quantum simulation of lattice gauge theories. *Annalen der Physik*, 525(10-11):777–796, July 2013. doi: 10.1002/andp.201300104. URL `https://doi.org/10.1002/andp.201300104`.

[68] Erez Zohar, J Ignacio Cirac, and Benni Reznik. Quantum simulations of lattice gauge theories using ultracold atoms in optical lattices. *Reports on Progress in Physics*, 79(1):014401, dec 2015. doi: 10.1088/0034-4885/79/1/014401. URL `https://doi.org/10.1088%2F0034-4885%2F79%2F1%2F014401`.

[69] Esteban A. Martinez, Christine A. Muschik, Philipp Schindler, Daniel Nigg, Alexander Erhard, Markus Heyl, Philipp Hauke, Marcello Dalmonte, Thomas Monz, Peter Zoller, and Rainer Blatt. Real-time dynamics of lattice gauge theories with a few-qubit quantum computer. *Nature*, 534(7608):516–519, June 2016. doi: 10.1038/nature18318. URL `https://doi.org/10.1038/nature18318`.

[70]

[71] David P. DiVincenzo. Quantum computation. *Science*, 270(5234):255–261, 1995. ISSN 0036-8075. doi: 10.1126/science.270.5234.255. URL `https://science.sciencemag.org/content/270/5234/255`.

[72] David P. DiVincenzo. The physical implementation of quantum computation. *Fortschritte der Physik*, 48(9-11):771–783, September 2000. doi: 10.1002/1521-3978(200009)48:9/11⟨771::aid-prop771⟩3.0.co;2-e. URL `https://doi.org/10.1002/1521-3978(200009)48:9/11<771::aid-prop771>3.0.co;2-e`.

[73] John Preskill. Reliable quantum computers. *Proceedings of the Royal Society of London. Series A: Mathematical, Physical and Engineering Sciences*, 454(1969):385–410, January 1998. doi: 10.1098/rspa.1998.0167. URL `https://doi.org/10.1098/rspa.1998.0167`.

[74] T. D. Ladd, F. Jelezko, R. Laflamme, Y. Nakamura, C. Monroe, and J. L. O'Brien. Quantum computers. *Nature*, 464(7285):45–53, March 2010. doi: 10.1038/nature08812. URL `https://doi.org/10.1038/nature08812`.

[75] Frank Arute, Kunal Arya, Ryan Babbush, Dave Bacon, Joseph C. Bardin, Rami Barends, Rupak Biswas, Sergio Boixo, Fernando G. S. L. Brandao, David A. Buell, Brian Burkett, Yu Chen, Zijun Chen, Ben Chiaro, Roberto Collins, William Courtney, Andrew Dunsworth, Edward Farhi, Brooks Foxen, Austin Fowler, Craig Gidney, Marissa Giustina, Rob Graff, Keith Guerin, Steve Habegger, Matthew P. Harrigan, Michael J. Hartmann, Alan Ho, Markus Hoffmann, Trent Huang, Travis S. Humble, Sergei V. Isakov, Evan Jeffrey, Zhang Jiang, Dvir Kafri, Kostyantyn Kechedzhi, Julian Kelly, Paul V. Klimov, Sergey Knysh, Alexander Korotkov, Fedor Kostritsa, David Landhuis, Mike Lindmark, Erik Lucero, Dmitry Lyakh, Salvatore Mandrà, Jarrod R. McClean, Matthew McEwen, Anthony Megrant, Xiao

Mi, Kristel Michielsen, Masoud Mohseni, Josh Mutus, Ofer Naaman, Matthew Neeley, Charles Neill, Murphy Yuezhen Niu, Eric Ostby, Andre Petukhov, John C. Platt, Chris Quintana, Eleanor G. Rieffel, Pedram Roushan, Nicholas C. Rubin, Daniel Sank, Kevin J. Satzinger, Vadim Smelyanskiy, Kevin J. Sung, Matthew D. Trevithick, Amit Vainsencher, Benjamin Villalonga, Theodore White, Z. Jamie Yao, Ping Yeh, Adam Zalcman, Hartmut Neven, and John M. Martinis. Quantum supremacy using a programmable superconducting processor. *Nature*, 574 (7779):505–510, October 2019. doi: 10.1038/s41586-019-1666-5. URL https://doi.org/10.1038/s41586-019-1666-5.

[76] Alexei Kitaev and John Preskill. Topological entanglement entropy. *Phys. Rev. Lett.*, 96:110404, Mar 2006. doi: 10.1103/PhysRevLett.96.110404. URL http://link.aps.org/doi/10.1103/PhysRevLett.96.110404.

[77] Michael Levin and Xiao-Gang Wen. Detecting topological order in a ground state wave function. *Phys. Rev. Lett.*, 96(11):110405, 2006.

[78] Hui Li and F. D. M. Haldane. Entanglement spectrum as a generalization of entanglement entropy: Identification of topological order in non-abelian fractional quantum hall effect states. *Phys. Rev. Lett.*, 101:010504, Jul 2008. doi: 10.1103/PhysRevLett.101.010504. URL https://link.aps.org/doi/10.1103/PhysRevLett.101.010504.

[79] Xie Chen, Zheng-Cheng Gu, and Xiao-Gang Wen. Local unitary transformation, long-range quantum entanglement, wave function renormalization, and topological order. *Phys. Rev. B*, 82:155138, Oct 2010. doi: 10.1103/PhysRevB.82.155138. URL http://link.aps.org/doi/10.1103/PhysRevB.82.155138.

[80] Frank Pollmann, Ari M. Turner, Erez Berg, and Masaki Oshikawa. Entanglement spectrum of a topological phase in one dimension. *Phys. Rev. B*, 81(6):064439, February 2010. doi: 10.1103/PhysRevB.81.064439. URL http://link.aps.org/doi/10.1103/PhysRevB.81.064439.

[81] Norbert Schuch, David Pérez-García, and Ignacio Cirac. Classifying quantum phases using matrix product states and projected entangled pair states. *Phys. Rev. B*, 84: 165139, Oct 2011. doi: 10.1103/PhysRevB.84.165139. URL https://link.aps.org/doi/10.1103/PhysRevB.84.165139.

[82] Steven R. White. Density matrix formulation for quantum renormalization groups. *Phys. Rev. Lett.*, 69:2863–2866, Nov 1992. doi: 10.1103/PhysRevLett.69.2863. URL https://link.aps.org/doi/10.1103/PhysRevLett.69.2863.

[83] Steven R. White. Density-matrix algorithms for quantum renormalization groups. *Phys. Rev. B*, 48:10345–10356, Oct 1993. doi: 10.1103/PhysRevB.48.10345. URL https://link.aps.org/doi/10.1103/PhysRevB.48.10345.

[84] F. Verstraete, V. Murg, and J.I. Cirac. Matrix product states, projected entangled pair states, and variational renormalization group methods for quantum spin systems. *Advances in Physics*, 57(2):143–224, 2008. doi: 10.1080/14789940801912366. URL https://doi.org/10.1080/14789940801912366.

[85] Ulrich Schollwöck. The density-matrix renormalization group in the age of matrix product states. *Annals of Physics*, 326(1):96 – 192, 2011. ISSN 0003-4916. doi: https://doi.org/10.1016/j.aop.2010.09.012. URL http://www.sciencedirect.com/science/article/pii/S0003491610001752. January 2011 Special Issue.

[86] Patrick Hayden and John Preskill. Black holes as mirrors: quantum information in random subsystems. *Journal of High Energy Physics*, 2007(09):120, 2007. URL `http://stacks.iop.org/1126-6708/2007/i=09/a=120`.

[87] Daniel Harlow and Patrick Hayden. Quantum computation vs. firewalls. *Journal of High Energy Physics*, 2013(6), June 2013. doi: 10.1007/jhep06(2013)085. URL `https://doi.org/10.1007/jhep06(2013)085`.

[88] Ahmed Almheiri, Xi Dong, and Daniel Harlow. Bulk locality and quantum error correction in AdS/CFT. *Journal of High Energy Physics*, 2015(4), April 2015. doi: 10.1007/jhep04(2015)163. URL `https://doi.org/10.1007/jhep04(2015)163`.

[89] Fernando Pastawski, Beni Yoshida, Daniel Harlow, and John Preskill. Holographic quantum error-correcting codes: toy models for the bulk/boundary correspondence. *Journal of High Energy Physics*, 2015(6), June 2015. doi: 10.1007/jhep06(2015)149. URL `https://doi.org/10.1007/jhep06(2015)149`.

[90] Patrick Hayden, Sepehr Nezami, Xiao-Liang Qi, Nathaniel Thomas, Michael Walter, and Zhao Yang. Holographic duality from random tensor networks. *Journal of High Energy Physics*, 2016(11):9, Nov 2016. ISSN 1029-8479. doi: 10.1007/JHEP11(2016)009. URL `https://doi.org/10.1007/JHEP11(2016)009`.

[91] D. Harlow. Jerusalem lectures on black holes and quantum information. *Rev. Mod. Phys.*, 88:015002, Feb 2016. doi: 10.1103/RevModPhys.88.015002. URL `https://link.aps.org/doi/10.1103/RevModPhys.88.015002`.

[92] Anatoli Polkovnikov, Krishnendu Sengupta, Alessandro Silva, and Mukund Vengalattore. Colloquium: Nonequilibrium dynamics of closed interacting quantum systems. *Rev. Mod. Phys.*, 83:863–883, Aug 2011. doi: 10.1103/RevModPhys.83.863. URL `https://link.aps.org/doi/10.1103/RevModPhys.83.863`.

[93] Rahul Nandkishore and David A. Huse. Many-body localization and thermalization in quantum statistical mechanics. *Annual Review of Condensed Matter Physics*, 6(1):15–38, 2015. doi: 10.1146/annurev-conmatphys-031214-014726. URL `http://dx.doi.org/10.1146/annurev-conmatphys-031214-014726`.

[94] Luca D'Alessio, Yariv Kafri, Anatoli Polkovnikov, and Marcos Rigol. From quantum chaos and eigenstate thermalization to statistical mechanics and thermodynamics. *Advances in Physics*, 65(3):239–362, May 2016. doi: 10.1080/00018732.2016.1198134. URL `https://doi.org/10.1080/00018732.2016.1198134`.

[95] Christian Gogolin and Jens Eisert. Equilibration, thermalisation, and the emergence of statistical mechanics in closed quantum systems. *Reports on Progress in Physics*, 79(5):056001, 2016. URL `http://stacks.iop.org/0034-4885/79/i=5/a=056001`.

[96] Dmitry A. Abanin, Ehud Altman, Immanuel Bloch, and Maksym Serbyn. Colloquium: Many-body localization, thermalization, and entanglement. *Rev. Mod. Phys.*, 91:021001, May 2019. doi: 10.1103/RevModPhys.91.021001. URL `https://link.aps.org/doi/10.1103/RevModPhys.91.021001`.

[97] J. M. Deutsch. Quantum statistical mechanics in a closed system. *Phys. Rev. A*, 43:2046–2049, Feb 1991. doi: 10.1103/PhysRevA.43.2046. URL `https://link.aps.org/doi/10.1103/PhysRevA.43.2046`.

[98] Mark Srednicki. Chaos and quantum thermalization. *Phys. Rev. E*, 50:888–901, Aug 1994. doi: 10.1103/PhysRevE.50.888. URL `https://link.aps.org/doi/10.1103/PhysRevE.50.888`.

[99] Marcos Rigol, Vanja Dunjko, and Maxim Olshanii. Thermalization and its mechanism for generic isolated quantum systems. *Nature*, 452:854–8, 05 2008. doi: 10.1038/nature06838.

[100] Joshua M Deutsch. Eigenstate thermalization hypothesis. *Reports on Progress in Physics*, 81(8):082001, jul 2018. doi: 10.1088/1361-6633/aac9f1. URL https://doi.org/10.1088%2F1361-6633%2Faac9f1.

[101] Takashi Mori, Tatsuhiko N Ikeda, Eriko Kaminishi, and Masahito Ueda. Thermalization and prethermalization in isolated quantum systems: a theoretical overview. *Journal of Physics B: Atomic, Molecular and Optical Physics*, 51(11):112001, may 2018. doi: 10.1088/1361-6455/aabcdf. URL https://doi.org/10.1088%2F1361-6455%2Faabcdf.

[102] Fabien Alet and Nicolas Laflorencie. Many-body localization: An introduction and selected topics. *Comptes Rendus Physique*, 19(6):498 – 525, 2018. ISSN 1631-0705. doi: https://doi.org/10.1016/j.crhy.2018.03.003. URL http://www.sciencedirect.com/science/article/pii/S163107051830032X. Quantum simulation / Simulation quantique.

[103] Marcos Rigol, Vanja Dunjko, Vladimir Yurovsky, and Maxim Olshanii. Relaxation in a completely integrable many-body quantum system: An ab initio study of the dynamics of the highly excited states of 1d lattice hard-core bosons. *Phys. Rev. Lett.*, 98:050405, Feb 2007. doi: 10.1103/PhysRevLett.98.050405. URL https://link.aps.org/doi/10.1103/PhysRevLett.98.050405.

[104] Guifré Vidal. Efficient simulation of one-dimensional quantum many-body systems. *Phys. Rev. Lett.*, 93:040502, Jul 2004. doi: 10.1103/PhysRevLett.93.040502. URL https://link.aps.org/doi/10.1103/PhysRevLett.93.040502.

[105] Sebastian Paeckel, Thomas Köhler, Andreas Swoboda, Salvatore R. Manmana, Ulrich Schollwöck, and Claudius Hubig. Time-evolution methods for matrix-product states. *Annals of Physics*, 411:167998, 2019. ISSN 0003-4916. doi: https://doi.org/10.1016/j.aop.2019.167998. URL http://www.sciencedirect.com/science/article/pii/S0003491619302532.

[106] Pasquale Calabrese and John Cardy. Evolution of entanglement entropy in one-dimensional systems. *Journal of Statistical Mechanics: Theory and Experiment*, 2005(04):P04010, 2005. URL http://stacks.iop.org/1742-5468/2005/i=04/a=P04010.

[107] Nima Lashkari, Douglas Stanford, Matthew Hastings, Tobias Osborne, and Patrick Hayden. Towards the fast scrambling conjecture. *Journal of High Energy Physics*, 2013(4):22, 2013. ISSN 1029-8479. doi: 10.1007/JHEP04(2013)022. URL http://dx.doi.org/10.1007/JHEP04(2013)022.

[108] R Islam, Ruichao Ma, Philipp Preiss, M Eric Tai, Alexander Lukin, Matthew Rispoli, and Markus Greiner. Measuring entanglement entropy through the interference of quantum many-body twins. 09 2015.

[109] Adam M. Kaufman, M. Eric Tai, Alexander Lukin, Matthew Rispoli, Robert Schittko, Philipp M. Preiss, and Markus Greiner. Quantum thermalization through entanglement in an isolated many-body system. *Science*, 353(6301):794–800, 2016. ISSN 0036-8075. doi: 10.1126/science.aaf6725. URL http://science.sciencemag.org/content/353/6301/794.

[110] Tiff Brydges, Andreas Elben, Petar Jurcevic, Benoît Vermersch, Christine Maier, Ben P. Lanyon, Peter Zoller, Rainer Blatt, and Christian F. Roos. Probing rényi entanglement entropy via randomized measurements. *Science*, 364(6437):260–263, 2019. ISSN 0036-8075. doi: 10.1126/science.aau4963. URL `https://science.sciencemag.org/content/364/6437/260`.

[111] Holger Fehske, Ralf Schneider, and Alexander Weiße. *Computational many-particle physics*, volume 739. Springer, 2007.

[112] Anders W. Sandvik, Adolfo Avella, and Ferdinando Mancini. Computational studies of quantum spin systems. AIP, 2010. doi: 10.1063/1.3518900. URL `https://doi.org/10.1063/1.3518900`.

[113] Tjark Heitmann, Jonas Richter, Dennis Schubert, and Robin Steinigeweg. Selected applications of typicality to real-time dynamics of quantum many-body systems, 2020.

[114] M. B. Hastings. Locality in quantum systems, 2010.

[115] Spectral Gap and Exponential Decay of Correlations. *Communications in Mathematical Physics*, 265(3):781–804, 2006. ISSN 1432-0916. doi: 10.1007/s00220-006-0030-4. URL `https://doi.org/10.1007/s00220-006-0030-4`.

[116] Michael Foss-Feig, Zhe-Xuan Gong, Charles W. Clark, and Alexey V. Gorshkov. Nearly linear light cones in long-range interacting quantum systems. *Phys. Rev. Lett.*, 114:157201, Apr 2015. doi: 10.1103/PhysRevLett.114.157201. URL `https://link.aps.org/doi/10.1103/PhysRevLett.114.157201`.

[117] Minh C. Tran, Andrew Y. Guo, Yuan Su, James R. Garrison, Zachary Eldredge, Michael Foss-Feig, Andrew M. Childs, and Alexey V. Gorshkov. Locality and digital quantum simulation of power-law interactions. *Phys. Rev. X*, 9:031006, Jul 2019. doi: 10.1103/PhysRevX.9.031006. URL `https://link.aps.org/doi/10.1103/PhysRevX.9.031006`.

[118] Xiao Chen and Tianci Zhou. Quantum chaos dynamics in long-range power law interaction systems. *Phys. Rev. B*, 100:064305, Aug 2019. doi: 10.1103/PhysRevB.100.064305. URL `https://link.aps.org/doi/10.1103/PhysRevB.100.064305`.

[119] David J. Luitz and Yevgeny Bar Lev. Emergent locality in systems with power-law interactions. *Phys. Rev. A*, 99:010105, Jan 2019. doi: 10.1103/PhysRevA.99.010105. URL `https://link.aps.org/doi/10.1103/PhysRevA.99.010105`.

[120] Tianci Zhou, Shenglong Xu, Xiao Chen, Andrew Guo, and Brian Swingle. Operator lévy flight: Light cones in chaotic long-range interacting systems. *Phys. Rev. Lett.*, 124:180601, May 2020. doi: 10.1103/PhysRevLett.124.180601. URL `https://link.aps.org/doi/10.1103/PhysRevLett.124.180601`.

[121] Chi-Fang Chen and Andrew Lucas. Finite speed of quantum scrambling with long range interactions. *Phys. Rev. Lett.*, 123:250605, Dec 2019. doi: 10.1103/PhysRevLett.123.250605. URL `https://link.aps.org/doi/10.1103/PhysRevLett.123.250605`.

[122] Minh C. Tran, Chi-Fang Chen, Adam Ehrenberg, Andrew Y. Guo, Abhinav Deshpande, Yifan Hong, Zhe-Xuan Gong, Alexey V. Gorshkov, and Andrew Lucas. Hierarchy of linear light cones with long-range interactions, 2020.

[123] Tomotaka Kuwahara and Keiji Saito. Strictly linear light cones in long-range interacting systems of arbitrary dimensions, 2019.

[124] Subir Sachdev and Jinwu Ye. Gapless spin-fluid ground state in a random quantum heisenberg magnet. *Phys. Rev. Lett.*, 70:3339–3342, May 1993. doi: 10.1103/PhysRevLett.70.3339. URL `https://link.aps.org/doi/10.1103/PhysRevLett.70.3339`.

[125] Juan Maldacena and Douglas Stanford. Remarks on the sachdev-ye-kitaev model. *Phys. Rev. D*, 94:106002, Nov 2016. doi: 10.1103/PhysRevD.94.106002. URL `https://link.aps.org/doi/10.1103/PhysRevD.94.106002`.

[126] Vladimir Rosenhaus. An introduction to the SYK model. *Journal of Physics A: Mathematical and Theoretical*, 52(32):323001, jul 2019. doi: 10.1088/1751-8121/ab2ce1. URL `https://doi.org/10.1088%2F1751-8121%2Fab2ce1`.

[127] Elliott H. Lieb and Derek W. Robinson. The finite group velocity of quantum spin systems. *Communications in Mathematical Physics*, 28(3):251–257. ISSN 1432-0916. doi: 10.1007/BF01645779. URL `http://dx.doi.org/10.1007/BF01645779`.

[128] M. B. Hastings. Lieb-schultz-mattis in higher dimensions. *Phys. Rev. B*, 69:104431, Mar 2004. doi: 10.1103/PhysRevB.69.104431. URL `https://link.aps.org/doi/10.1103/PhysRevB.69.104431`.

[129] Bruno Nachtergaele and Robert Sims. Lieb-robinson bounds and the exponential clustering theorem. *Communications in Mathematical Physics*, 265(1):119–130, March 2006. doi: 10.1007/s00220-006-1556-1. URL `https://doi.org/10.1007/s00220-006-1556-1`.

[130] Pasquale Calabrese and John Cardy. Time dependence of correlation functions following a quantum quench. *Phys. Rev. Lett.*, 96:136801, Apr 2006. doi: 10.1103/PhysRevLett.96.136801. URL `https://link.aps.org/doi/10.1103/PhysRevLett.96.136801`.

[131] Pasquale Calabrese and John Cardy. Entanglement and correlation functions following a local quench: a conformal field theory approach. *Journal of Statistical Mechanics: Theory and Experiment*, 2007(10):P10004, 2007. URL `http://stacks.iop.org/1742-5468/2007/i=10/a=P10004`.

[132] M B Hastings. An area law for one-dimensional quantum systems. *Journal of Statistical Mechanics: Theory and Experiment*, 2007(08):P08024–P08024, aug 2007. doi: 10.1088/1742-5468/2007/08/p08024. URL `https://doi.org/10.1088%2F1742-5468%2F2007%2F08%2Fp08024`.

[133] Ehud Altman and Ronen Vosk. Universal dynamics and renormalization in many-body-localized systems. *Annual Review of Condensed Matter Physics*, 6(1):383–409, 2015. doi: 10.1146/annurev-conmatphys-031214-014701.

[134] Pavan Hosur and Xiao-Liang Qi. Characterizing eigenstate thermalization via measures in the fock space of operators. *Phys. Rev. E*, 93:042138, Apr 2016. doi: 10.1103/PhysRevE.93.042138. URL `https://link.aps.org/doi/10.1103/PhysRevE.93.042138`.

[135] James R. Garrison and Tarun Grover. Does a single eigenstate encode the full hamiltonian? *Phys. Rev. X*, 8:021026, Apr 2018. doi: 10.1103/PhysRevX.8.021026. URL `https://link.aps.org/doi/10.1103/PhysRevX.8.021026`.

[136] Giacomo De Palma, Alessio Serafini, Vittorio Giovannetti, and Marcus Cramer. Necessity of eigenstate thermalization. *Phys. Rev. Lett.*, 115:220401, Nov 2015. doi: 10.1103/PhysRevLett.115.220401. URL `https://link.aps.org/doi/10.1103/PhysRevLett.115.220401`.

[137] Lorenzo Campos Venuti and Lawrence Liu. Ergodicity, eigenstate thermalization, and the foundations of statistical mechanics in quantum and classical systems, 2019.

[138] Marcos Rigol. Breakdown of thermalization in finite one-dimensional systems. *Phys. Rev. Lett.*, 103:100403, Sep 2009. doi: 10.1103/PhysRevLett.103.100403. URL `https://link.aps.org/doi/10.1103/PhysRevLett.103.100403`.

[139] Marcos Rigol. Quantum quenches and thermalization in one-dimensional fermionic systems. *Phys. Rev. A*, 80:053607, Nov 2009. doi: 10.1103/PhysRevA.80.053607. URL `https://link.aps.org/doi/10.1103/PhysRevA.80.053607`.

[140] Lea F. Santos and Marcos Rigol. Onset of quantum chaos in one-dimensional bosonic and fermionic systems and its relation to thermalization. *Phys. Rev. E*, 81:036206, Mar 2010. doi: 10.1103/PhysRevE.81.036206. URL `https://link.aps.org/doi/10.1103/PhysRevE.81.036206`.

[141] Marcos Rigol and Lea F. Santos. Quantum chaos and thermalization in gapped systems. *Phys. Rev. A*, 82:011604, Jul 2010. doi: 10.1103/PhysRevA.82.011604. URL `https://link.aps.org/doi/10.1103/PhysRevA.82.011604`.

[142] Lea F. Santos and Marcos Rigol. Localization and the effects of symmetries in the thermalization properties of one-dimensional quantum systems. *Phys. Rev. E*, 82:031130, Sep 2010. doi: 10.1103/PhysRevE.82.031130. URL `https://link.aps.org/doi/10.1103/PhysRevE.82.031130`.

[143] Hyungwon Kim, Tatsuhiko N. Ikeda, and David A. Huse. Testing whether all eigenstates obey the eigenstate thermalization hypothesis. *Phys. Rev. E*, 90:052105, Nov 2014. doi: 10.1103/PhysRevE.90.052105. URL `https://link.aps.org/doi/10.1103/PhysRevE.90.052105`.

[144] W. Beugeling, R. Moessner, and Masudul Haque. Finite-size scaling of eigenstate thermalization. *Phys. Rev. E*, 89:042112, Apr 2014. doi: 10.1103/PhysRevE.89.042112. URL `https://link.aps.org/doi/10.1103/PhysRevE.89.042112`.

[145] Wouter Beugeling, Roderich Moessner, and Masudul Haque. Off-diagonal matrix elements of local operators in many-body quantum systems. *Phys. Rev. E*, 91:012144, Jan 2015. doi: 10.1103/PhysRevE.91.012144. URL `https://link.aps.org/doi/10.1103/PhysRevE.91.012144`.

[146] Rubem Mondaini, Keith R. Fratus, Mark Srednicki, and Marcos Rigol. Eigenstate thermalization in the two-dimensional transverse field ising model. *Phys. Rev. E*, 93:032104, Mar 2016. doi: 10.1103/PhysRevE.93.032104. URL `https://link.aps.org/doi/10.1103/PhysRevE.93.032104`.

[147] Giulio Biroli, Corinna Kollath, and Andreas M. Läuchli. Effect of rare fluctuations on the thermalization of isolated quantum systems. *Phys. Rev. Lett.*, 105:250401, Dec 2010. doi: 10.1103/PhysRevLett.105.250401. URL `https://link.aps.org/doi/10.1103/PhysRevLett.105.250401`.

[148] S. Sorg, L. Vidmar, L. Pollet, and F. Heidrich-Meisner. Relaxation and thermalization in the one-dimensional bose-hubbard model: A case study for the interaction quantum quench from the atomic limit. *Phys. Rev. A*, 90:033606, Sep 2014. doi: 10.1103/PhysRevA.90.033606. URL `https://link.aps.org/doi/10.1103/PhysRevA.90.033606`.

[149] Javier M. Magán. Random free fermions: An analytical example of eigenstate thermalization. *Phys. Rev. Lett.*, 116:030401, Jan 2016. doi: 10.1103/PhysRevLett.116.030401. URL `https://link.aps.org/doi/10.1103/PhysRevLett.116.030401`.

[150] Nima Lashkari, Anatoly Dymarsky, and Hong Liu. Eigenstate thermalization hypothesis in conformal field theory. *Journal of Statistical Mechanics: Theory and Experiment*, 2018(3):033101, mar 2018. doi: 10.1088/1742-5468/aab020. URL `https://doi.org/10.1088%2F1742-5468%2Faab020`.

[151] Nima Lashkari, Anatoly Dymarsky, and Hong Liu. Universality of quantum information in chaotic CFTs. *Journal of High Energy Physics*, 2018(3), March 2018. doi: 10.1007/jhep03(2018)070. URL `https://doi.org/10.1007/jhep03(2018)070`.

[152] Pallab Basu, Diptarka Das, Shouvik Datta, and Sridip Pal. Thermality of eigenstates in conformal field theories. *Phys. Rev. E*, 96:022149, Aug 2017. doi: 10.1103/PhysRevE.96.022149. URL `https://link.aps.org/doi/10.1103/PhysRevE.96.022149`.

[153] Song He, Feng-Li Lin, and Jia ju Zhang. Subsystem eigenstate thermalization hypothesis for entanglement entropy in CFT. *Journal of High Energy Physics*, 2017(8), August 2017. doi: 10.1007/jhep08(2017)126. URL `https://doi.org/10.1007/jhep08(2017)126`.

[154] Madan Lal Mehta. *Random Matrices*. 3rd edition, 2004.

[155] Giacomo Livan, Marcel Novaes, and Pierpaolo Vivo. *Introduction to Random Matrices*. Springer International Publishing, 2018. doi: 10.1007/978-3-319-70885-0. URL `https://doi.org/10.1007/978-3-319-70885-0`.

[156] Eugene P. Wigner. Characteristic vectors of bordered matrices with infinite dimensions. *The Annals of Mathematics*, 62(3):548, November 1955. doi: 10.2307/1970079. URL `https://doi.org/10.2307/1970079`.

[157] M.L. Mehta. On the statistical properties of the level-spacings in nuclear spectra. *Nuclear Physics*, 18:395–419, August 1960. doi: 10.1016/0029-5582(60)90413-2. URL `https://doi.org/10.1016/0029-5582(60)90413-2`.

[158] Norbert Rosenzweig and Charles E. Porter. "repulsion of energy levels" in complex atomic spectra. *Phys. Rev.*, 120:1698–1714, Dec 1960. doi: 10.1103/PhysRev.120.1698. URL `https://link.aps.org/doi/10.1103/PhysRev.120.1698`.

[159] Freeman J. Dyson. Statistical theory of the energy levels of complex systems. i. *Journal of Mathematical Physics*, 3(1):140–156, 1962. doi: 10.1063/1.1703773. URL `https://doi.org/10.1063/1.1703773`.

[160] Eugene P. Wigner. Random matrices in physics. *SIAM Review*, 9(1):1–23, January 1967. doi: 10.1137/1009001. URL `https://doi.org/10.1137/1009001`.

[161] M V Berry. Regular and irregular semiclassical wavefunctions. *Journal of Physics A: Mathematical and General*, 10(12):2083–2091, dec 1977. doi: 10.1088/0305-4470/10/12/016. URL `https://doi.org/10.1088%2F0305-4470%2F10%2F12%2F016`.

[162] Steven W. McDonald and Allan N. Kaufman. Spectrum and eigenfunctions for a hamiltonian with stochastic trajectories. *Phys. Rev. Lett.*, 42:1189–1191, Apr 1979. doi: 10.1103/PhysRevLett.42.1189. URL https://link.aps.org/doi/10.1103/PhysRevLett.42.1189.

[163] G. Casati, F. Valz-Gris, and I. Guarnieri. On the connection between quantization of nonintegrable systems and statistical theory of spectra. *Lettere al Nuovo Cimento*, 28(8):279–282, June 1980. doi: 10.1007/bf02798790. URL https://doi.org/10.1007/bf02798790.

[164] M.V. Berry. Quantizing a classically ergodic system: Sinai's billiard and the kkr method. *Annals of Physics*, 131(1):163 – 216, 1981. ISSN 0003-4916. doi: https://doi.org/10.1016/0003-4916(81)90189-5. URL http://www.sciencedirect.com/science/article/pii/0003491681901895.

[165] O. Bohigas, M. J. Giannoni, and C. Schmit. Characterization of chaotic quantum spectra and universality of level fluctuation laws. *Phys. Rev. Lett.*, 52:1–4, Jan 1984. doi: 10.1103/PhysRevLett.52.1. URL https://link.aps.org/doi/10.1103/PhysRevLett.52.1.

[166] Fritz Haake. *Quantum Signatures of Chaos*. Springer Berlin Heidelberg, 2010. doi: 10.1007/978-3-642-05428-0. URL https://doi.org/10.1007/978-3-642-05428-0.

[167] Alexander Altland and Martin R. Zirnbauer. Nonstandard symmetry classes in mesoscopic normal-superconducting hybrid structures. *Phys. Rev. B*, 55:1142–1161, Jan 1997. doi: 10.1103/PhysRevB.55.1142. URL https://link.aps.org/doi/10.1103/PhysRevB.55.1142.

[168] Pier A. Mello and Narendra Kumar. *Quantum Transport in Mesoscopic Systems*. Oxford University Press, May 2004. doi: 10.1093/acprof:oso/9780198525820.001.0001. URL https://doi.org/10.1093/acprof:oso/9780198525820.001.0001.

[169] C. W. J. Beenakker. Random-matrix theory of quantum transport. *Rev. Mod. Phys.*, 69:731–808, Jul 1997. doi: 10.1103/RevModPhys.69.731. URL https://link.aps.org/doi/10.1103/RevModPhys.69.731.

[170] Andreas P. Schnyder, Shinsei Ryu, Akira Furusaki, and Andreas W. W. Ludwig. Classification of topological insulators and superconductors in three spatial dimensions. *Phys. Rev. B*, 78:195125, Nov 2008. doi: 10.1103/PhysRevB.78.195125. URL https://link.aps.org/doi/10.1103/PhysRevB.78.195125.

[171] Martin Sieber and Klaus Richter. Correlations between periodic orbits and their r?le in spectral statistics. *Physica Scripta*, T90(1):128, 2001. doi: 10.1238/physica.topical.090a00128. URL https://doi.org/10.1238%2Fphysica.topical.090a00128.

[172] Martin Sieber. Leading off-diagonal approximation for the spectral form factor for uniformly hyperbolic systems. *Journal of Physics A: Mathematical and General*, 35(42):L613–L619, oct 2002. doi: 10.1088/0305-4470/35/42/104. URL https://doi.org/10.1088%2F0305-4470%2F35%2F42%2F104.

[173] Sebastian Müller, Stefan Heusler, Petr Braun, Fritz Haake, and Alexander Altland. Semiclassical foundation of universality in quantum chaos. *Phys. Rev. Lett.*, 93:014103, Jul 2004. doi: 10.1103/PhysRevLett.93.014103. URL https://link.aps.org/doi/10.1103/PhysRevLett.93.014103.

[174] Sebastian Müller, Stefan Heusler, Petr Braun, Fritz Haake, and Alexander Altland. Periodic-orbit theory of universality in quantum chaos. *Phys. Rev. E*, 72:046207, Oct 2005. doi: 10.1103/PhysRevE.72.046207. URL https://link.aps.org/doi/10.1103/PhysRevE.72.046207.

[175] Amos Chan, Andrea De Luca, and J. T. Chalker. Solution of a minimal model for many-body quantum chaos. *Phys. Rev. X*, 8:041019, Nov 2018. doi: 10.1103/PhysRevX.8.041019. URL https://link.aps.org/doi/10.1103/PhysRevX.8.041019.

[176] Amos Chan, Andrea De Luca, and J. T. Chalker. Spectral statistics in spatially extended chaotic quantum many-body systems. *Phys. Rev. Lett.*, 121:060601, Aug 2018. doi: 10.1103/PhysRevLett.121.060601. URL https://link.aps.org/doi/10.1103/PhysRevLett.121.060601.

[177] Aaron J. Friedman, Amos Chan, Andrea De Luca, and J. T. Chalker. Spectral statistics and many-body quantum chaos with conserved charge. *Phys. Rev. Lett.*, 123:210603, Nov 2019. doi: 10.1103/PhysRevLett.123.210603. URL https://link.aps.org/doi/10.1103/PhysRevLett.123.210603.

[178] Hrant Gharibyan, Masanori Hanada, Stephen H. Shenker, and Masaki Tezuka. Onset of random matrix behavior in scrambling systems. *Journal of High Energy Physics*, 2018(7), July 2018. doi: 10.1007/jhep07(2018)124. URL https://doi.org/10.1007/jhep07(2018)124.

[179] Pavel Kos, Marko Ljubotina, and Tomaž Prosen. Many-body quantum chaos: Analytic connection to random matrix theory. *Phys. Rev. X*, 8:021062, Jun 2018. doi: 10.1103/PhysRevX.8.021062. URL https://link.aps.org/doi/10.1103/PhysRevX.8.021062.

[180] Bruno Bertini, Pavel Kos, and Tomaž Prosen. Exact spectral form factor in a minimal model of many-body quantum chaos. *Phys. Rev. Lett.*, 121:264101, Dec 2018. doi: 10.1103/PhysRevLett.121.264101. URL https://link.aps.org/doi/10.1103/PhysRevLett.121.264101.

[181] Fabian H L Essler and Maurizio Fagotti. Quench dynamics and relaxation in isolated integrable quantum spin chains. *Journal of Statistical Mechanics: Theory and Experiment*, 2016(6):064002, jun 2016. doi: 10.1088/1742-5468/2016/06/064002. URL https://doi.org/10.1088%2F1742-5468%2F2016%2F06%2F064002.

[182] Toshiya Kinoshita, Trevor Wenger, and David S. Weiss. A quantum newton's cradle. *Nature*, 440(7086):900–903, April 2006. doi: 10.1038/nature04693. URL https://doi.org/10.1038/nature04693.

[183] D. M. Basko, I. L. Aleiner, and B. L. Altshuler. Metal-insulator transition in a weakly interacting many-electron system with localized single-particle states. *Annals of Physics*, 321(5):1126–1205, May 2006. ISSN 0003-4916. doi: 10.1016/j.aop.2005.11.014. URL http://www.sciencedirect.com/science/article/pii/S0003491605002630.

[184] Vadim Oganesyan and David A. Huse. Localization of interacting fermions at high temperature. *Phys. Rev. B*, 75:155111, Apr 2007. doi: 10.1103/PhysRevB.75.155111. URL http://link.aps.org/doi/10.1103/PhysRevB.75.155111.

[185] Marko Žnidarič, Tomaž Prosen, and Peter Prelovšek. Many-body localization in the heisenberg xxz magnet in a random field. *Phys. Rev. B*, 77:064426, Feb 2008. doi: 10.1103/PhysRevB.77.064426. URL https://link.aps.org/doi/10.1103/PhysRevB.77.064426.

[186] Michael Schreiber, Sean S. Hodgman, Pranjal Bordia, Henrik P. Lüschen, Mark H. Fischer, Ronen Vosk, Ehud Altman, Ulrich Schneider, and Immanuel Bloch. Observation of many-body localization of interacting fermions in a quasirandom optical lattice. *Science*, 349(6250):842–845, 2015. ISSN 0036-8075. doi: 10.1126/science.aaa7432. URL http://science.sciencemag.org/content/349/6250/842.

[187] P. W. Anderson. Absence of diffusion in certain random lattices. *Phys. Rev.*, 109:1492–1505, Mar 1958. doi: 10.1103/PhysRev.109.1492. URL http://link.aps.org/doi/10.1103/PhysRev.109.1492.

[188] Ad Lagendijk, Bart van Tiggelen, and Diederik S. Wiersma. Fifty years of anderson localization. *Physics Today*, 62(8):24–29, August 2009. doi: 10.1063/1.3206091. URL https://doi.org/10.1063/1.3206091.

[189] Maksym Serbyn, Z. Papić, and Dmitry A. Abanin. Local conservation laws and the structure of the many-body localized states. *Phys. Rev. Lett.*, 111:127201, Sep 2013. doi: 10.1103/PhysRevLett.111.127201. URL http://link.aps.org/doi/10.1103/PhysRevLett.111.127201.

[190] David A. Huse, Rahul Nandkishore, and Vadim Oganesyan. Phenomenology of fully many-body-localized systems. *Phys. Rev. B*, 90:174202, Nov 2014. doi: 10.1103/PhysRevB.90.174202. URL http://link.aps.org/doi/10.1103/PhysRevB.90.174202.

[191] John Z. Imbrie. On many-body localization for quantum spin chains. *Journal of Statistical Physics*, 163(5):998–1048, 2016. ISSN 1572-9613. doi: 10.1007/s10955-016-1508-x. URL http://dx.doi.org/10.1007/s10955-016-1508-x.

[192] John Z. Imbrie. Diagonalization and many-body localization for a disordered quantum spin chain. *Phys. Rev. Lett.*, 117:027201, Jul 2016. doi: 10.1103/PhysRevLett.117.027201. URL https://link.aps.org/doi/10.1103/PhysRevLett.117.027201.

[193] Wojciech De Roeck and John Z. Imbrie. Many-body localization: stability and instability. *Philosophical Transactions of the Royal Society A: Mathematical, Physical and Engineering Sciences*, 375(2108):20160422, 2017. doi: 10.1098/rsta.2016.0422. URL https://royalsocietypublishing.org/doi/abs/10.1098/rsta.2016.0422.

[194] John Z. Imbrie, Valentina Ros, and Antonello Scardicchio. Local integrals of motion in many-body localized systems. *Annalen der Physik*, 529(7):1600278, 2017. doi: 10.1002/andp.201600278. URL https://onlinelibrary.wiley.com/doi/abs/10.1002/andp.201600278.

[195] Wojciech De Roeck and Fran çois Huveneers. Stability and instability towards delocalization in many-body localization systems. *Phys. Rev. B*, 95:155129, Apr 2017. doi: 10.1103/PhysRevB.95.155129. URL https://link.aps.org/doi/10.1103/PhysRevB.95.155129.

[196] David J. Luitz, Fran çois Huveneers, and Wojciech De Roeck. How a small quantum bath can thermalize long localized chains. *Phys. Rev. Lett.*, 119:150602, Oct

2017. doi: 10.1103/PhysRevLett.119.150602. URL https://link.aps.org/doi/10.1103/PhysRevLett.119.150602.

[197] Pedro Ponte, C. R. Laumann, David A. Huse, and A. Chandran. Thermal inclusions: how one spin can destroy a many-body localized phase. *Philosophical Transactions of the Royal Society A: Mathematical, Physical and Engineering Sciences*, 375(2108): 20160428, October 2017. doi: 10.1098/rsta.2016.0428. URL https://doi.org/10.1098/rsta.2016.0428.

[198] Ionut-Dragos Potirniche, Sumilan Banerjee, and Ehud Altman. Exploration of the stability of many-body localization in $dgt; 1$. *Phys. Rev. B*, 99:205149, May 2019. doi: 10.1103/PhysRevB.99.205149. URL https://link.aps.org/doi/10.1103/PhysRevB.99.205149.

[199] Thorsten B. Wahl, Arijeet Pal, and Steven H. Simon. Signatures of the many-body localized regime in two dimensions. *Nature Physics*, 15(2):164–169, November 2018. doi: 10.1038/s41567-018-0339-x. URL https://doi.org/10.1038/s41567-018-0339-x.

[200] Jae-yoon Choi, Sebastian Hild, Johannes Zeiher, Peter Schauß, Antonio Rubio-Abadal, Tarik Yefsah, Vedika Khemani, David A. Huse, Immanuel Bloch, and Christian Gross. Exploring the many-body localization transition in two dimensions. *Science*, 352(6293):1547–1552, 2016. ISSN 0036-8075. doi: 10.1126/science.aaf8834. URL https://science.sciencemag.org/content/352/6293/1547.

[201] David A. Huse, Rahul Nandkishore, Vadim Oganesyan, Arijeet Pal, and S. L. Sondhi. Localization-protected quantum order. *Phys. Rev. B*, 88:014206, Jul 2013. doi: 10.1103/PhysRevB.88.014206. URL http://link.aps.org/doi/10.1103/PhysRevB.88.014206.

[202] David Pekker, Gil Refael, Ehud Altman, Eugene Demler, and Vadim Oganesyan. Hilbert-glass transition: New universality of temperature-tuned many-body dynamical quantum criticality. *Phys. Rev. X*, 4:011052, Mar 2014. doi: 10.1103/PhysRevX.4.011052. URL http://link.aps.org/doi/10.1103/PhysRevX.4.011052.

[203] Anushya Chandran, Vedika Khemani, C. R. Laumann, and S. L. Sondhi. Many-body localization and symmetry-protected topological order. *Phys. Rev. B*, 89:144201, Apr 2014. doi: 10.1103/PhysRevB.89.144201. URL http://link.aps.org/doi/10.1103/PhysRevB.89.144201.

[204] S A Parameswaran and Romain Vasseur. Many-body localization, symmetry and topology. *Reports on Progress in Physics*, 81(8):082501, jul 2018. doi: 10.1088/1361-6633/aac9ed. URL https://doi.org/10.1088%2F1361-6633%2Faac9ed.

[205] C. W. von Keyserlingk and S. L. Sondhi. Phase structure of one-dimensional interacting floquet systems. i. abelian symmetry-protected topological phases. *Phys. Rev. B*, 93:245145, Jun 2016. doi: 10.1103/PhysRevB.93.245145. URL https://link.aps.org/doi/10.1103/PhysRevB.93.245145.

[206] C. W. von Keyserlingk and S. L. Sondhi. Phase structure of one-dimensional interacting floquet systems. ii. symmetry-broken phases. *Phys. Rev. B*, 93:245146, Jun 2016. doi: 10.1103/PhysRevB.93.245146. URL https://link.aps.org/doi/10.1103/PhysRevB.93.245146.

[207] Dominic V. Else and Chetan Nayak. Classification of topological phases in periodically driven interacting systems. *Phys. Rev. B*, 93:201103, May 2016. doi: 10.1103/PhysRevB.93.201103. URL https://link.aps.org/doi/10.1103/PhysRevB.93.201103.

[208] Vedika Khemani, Achilleas Lazarides, Roderich Moessner, and S. L. Sondhi. Phase structure of driven quantum systems. *Phys. Rev. Lett.*, 116:250401, Jun 2016. doi: 10.1103/PhysRevLett.116.250401. URL https://link.aps.org/doi/10.1103/PhysRevLett.116.250401.

[209] Mark S. Rudner, Netanel H. Lindner, Erez Berg, and Michael Levin. Anomalous Edge States and the Bulk-Edge Correspondence for Periodically Driven Two-Dimensional Systems. *Phys. Rev. X*, 3(3):031005, July 2013. doi: 10.1103/PhysRevX.3.031005. URL http://link.aps.org/doi/10.1103/PhysRevX.3.031005.

[210] Hoi Chun Po, Lukasz Fidkowski, Takahiro Morimoto, Andrew C. Potter, and Ashvin Vishwanath. Chiral floquet phases of many-body localized bosons. *Phys. Rev. X*, 6:041070, Dec 2016. doi: 10.1103/PhysRevX.6.041070. URL https://link.aps.org/doi/10.1103/PhysRevX.6.041070.

[211] Fenner Harper, Rahul Roy, Mark S. Rudner, and S.L. Sondhi. Topology and broken symmetry in floquet systems. *Annual Review of Condensed Matter Physics*, 11(1):345–368, 2020. doi: 10.1146/annurev-conmatphys-031218-013721. URL https://doi.org/10.1146/annurev-conmatphys-031218-013721.

[212] Dmitry A. Abanin, Wojciech De Roeck, and François Huveneers. Theory of many-body localization in periodically driven systems. *Annals of Physics*, 372:1–11, September 2016. doi: 10.1016/j.aop.2016.03.010. URL https://doi.org/10.1016/j.aop.2016.03.010.

[213] Achilleas Lazarides, Arnab Das, and Roderich Moessner. Fate of many-body localization under periodic driving. *Phys. Rev. Lett.*, 115:030402, Jul 2015. doi: 10.1103/PhysRevLett.115.030402. URL http://link.aps.org/doi/10.1103/PhysRevLett.115.030402.

[214] Pedro Ponte, Z. Papić, Francois Huveneers, and Dmitry A. Abanin. Many-body localization in periodically driven systems. *Phys. Rev. Lett.*, 114:140401, Apr 2015. doi: 10.1103/PhysRevLett.114.140401. URL http://link.aps.org/doi/10.1103/PhysRevLett.114.140401.

[215] Pedro Ponte, Anushya Chandran, Z. Papić, and Dmitry A. Abanin. Periodically driven ergodic and many-body localized quantum systems. *Annals of Physics*, 353:196 – 204, 2015. ISSN 0003-4916. doi: http://dx.doi.org/10.1016/j.aop.2014.11.008. URL http://www.sciencedirect.com/science/article/pii/S0003491614003212.

[216] Frank Wilczek. Quantum time crystals. *Phys. Rev. Lett.*, 109:160401, Oct 2012. doi: 10.1103/PhysRevLett.109.160401. URL http://link.aps.org/doi/10.1103/PhysRevLett.109.160401.

[217] C. W. von Keyserlingk, Vedika Khemani, and S. L. Sondhi. Absolute stability and spatiotemporal long-range order in floquet systems. *Phys. Rev. B*, 94:085112, Aug 2016. doi: 10.1103/PhysRevB.94.085112. URL https://link.aps.org/doi/10.1103/PhysRevB.94.085112.

[218] Dominic V. Else, Bela Bauer, and Chetan Nayak. Floquet time crystals. *Phys. Rev. Lett.*, 117:090402, Aug 2016. doi: 10.1103/PhysRevLett.117.090402. URL `https://link.aps.org/doi/10.1103/PhysRevLett.117.090402`.

[219] Soonwon Choi, Joonhee Choi, Renate Landig, Georg Kucsko, Hengyun Zhou, Junichi Isoya, Fedor Jelezko, Shinobu Onoda, Hitoshi Sumiya, Vedika Khemani, Curt von Keyserlingk, Norman Y. Yao, Eugene Demler, and Mikhail D. Lukin. Observation of discrete time-crystalline order in a disordered dipolar many-body system. *Nature*, 543(7644):221–225, March 2017. doi: 10.1038/nature21426. URL `https://doi.org/10.1038/nature21426`.

[220] J. Zhang, P. W. Hess, A. Kyprianidis, P. Becker, A. Lee, J. Smith, G. Pagano, I.-D. Potirniche, A. C. Potter, A. Vishwanath, N. Y. Yao, and C. Monroe. Observation of a discrete time crystal. *Nature*, 543(7644):217–220, March 2017. doi: 10.1038/nature21413. URL `https://doi.org/10.1038/nature21413`.

[221] Vedika Khemani, Roderich Moessner, and S. L. Sondhi. A brief history of time crystals, 2019.

[222] Jens H. Bardarson, Frank Pollmann, and Joel E. Moore. Unbounded growth of entanglement in models of many-body localization. *Phys. Rev. Lett.*, 109:017202, Jul 2012. doi: 10.1103/PhysRevLett.109.017202. URL `https://link.aps.org/doi/10.1103/PhysRevLett.109.017202`.

[223] Maksym Serbyn, Z. Papić, and Dmitry A. Abanin. Universal slow growth of entanglement in interacting strongly disordered systems. *Phys. Rev. Lett.*, 110:260601, Jun 2013. doi: 10.1103/PhysRevLett.110.260601. URL `http://link.aps.org/doi/10.1103/PhysRevLett.110.260601`.

[224] Maksym Serbyn, Z. Papić, and D. A. Abanin. Quantum quenches in the many-body localized phase. *Phys. Rev. B*, 90:174302, Nov 2014. doi: 10.1103/PhysRevB.90.174302. URL `https://link.aps.org/doi/10.1103/PhysRevB.90.174302`.

[225] Ronen Vosk, David A. Huse, and Ehud Altman. Theory of the many-body localization transition in one-dimensional systems. *Phys. Rev. X*, 5:031032, Sep 2015. doi: 10.1103/PhysRevX.5.031032. URL `https://link.aps.org/doi/10.1103/PhysRevX.5.031032`.

[226] Kartiek Agarwal, Sarang Gopalakrishnan, Michael Knap, Markus Müller, and Eugene Demler. Anomalous diffusion and griffiths effects near the many-body localization transition. *Phys. Rev. Lett.*, 114:160401, Apr 2015. doi: 10.1103/PhysRevLett.114.160401. URL `https://link.aps.org/doi/10.1103/PhysRevLett.114.160401`.

[227] Andrew C. Potter, Romain Vasseur, and S. A. Parameswaran. Universal properties of many-body delocalization transitions. *Phys. Rev. X*, 5:031033, Sep 2015. doi: 10.1103/PhysRevX.5.031033. URL `https://link.aps.org/doi/10.1103/PhysRevX.5.031033`.

[228] Yevgeny Bar Lev, Guy Cohen, and David R. Reichman. Absence of diffusion in an interacting system of spinless fermions on a one-dimensional disordered lattice. *Phys. Rev. Lett.*, 114:100601, Mar 2015. doi: 10.1103/PhysRevLett.114.100601. URL `https://link.aps.org/doi/10.1103/PhysRevLett.114.100601`.

[229] David J. Luitz, Nicolas Laflorencie, and Fabien Alet. Extended slow dynamical regime close to the many-body localization transition. *Phys. Rev. B*, 93:060201, Feb 2016. doi: 10.1103/PhysRevB.93.060201. URL https://link.aps.org/doi/10.1103/PhysRevB.93.060201.

[230] Marko Žnidarič, Antonello Scardicchio, and Vipin Kerala Varma. Diffusive and subdiffusive spin transport in the ergodic phase of a many-body localizable system. *Phys. Rev. Lett.*, 117:040601, Jul 2016. doi: 10.1103/PhysRevLett.117.040601. URL https://link.aps.org/doi/10.1103/PhysRevLett.117.040601.

[231] David J. Luitz and Yevgeny Bar Lev. Information propagation in isolated quantum systems. *Phys. Rev. B*, 96:020406, Jul 2017. doi: 10.1103/PhysRevB.96.020406. URL https://link.aps.org/doi/10.1103/PhysRevB.96.020406.

[232] Sarang Gopalakrishnan and S.A. Parameswaran. Dynamics and transport at the threshold of many-body localization. *Physics Reports*, 2020. ISSN 0370-1573. doi: https://doi.org/10.1016/j.physrep.2020.03.003. URL http://www.sciencedirect.com/science/article/pii/S0370157320301083.

[233] Adam Nahum, Jonathan Ruhman, and David A. Huse. Dynamics of entanglement and transport in one-dimensional systems with quenched randomness. *Phys. Rev. B*, 98:035118, Jul 2018. doi: 10.1103/PhysRevB.98.035118. URL https://link.aps.org/doi/10.1103/PhysRevB.98.035118.

[234] Stephen H. Shenker and Douglas Stanford. Black holes and the butterfly effect. *Journal of High Energy Physics*, 2014(3):67, 2014. ISSN 1029-8479. doi: 10.1007/JHEP03(2014)067. URL http://dx.doi.org/10.1007/JHEP03(2014)067.

[235] Stephen H. Shenker and Douglas Stanford. Multiple shocks. *Journal of High Energy Physics*, 2014(12):46, 2014. ISSN 1029-8479. doi: 10.1007/JHEP12(2014)046. URL http://dx.doi.org/10.1007/JHEP12(2014)046.

[236] Stephen H. Shenker and Douglas Stanford. Stringy effects in scrambling. *Journal of High Energy Physics*, 2015(5):132, 2015. ISSN 1029-8479. doi: 10.1007/JHEP05(2015)132. URL http://dx.doi.org/10.1007/JHEP05(2015)132.

[237] Daniel A. Roberts, Douglas Stanford, and Leonard Susskind. Localized shocks. *Journal of High Energy Physics*, 2015(3):51, 2015. doi: 10.1007/JHEP03(2015)051. URL http://dx.doi.org/10.1007/JHEP03(2015)051.

[238] Daniel A. Roberts and Douglas Stanford. Diagnosing chaos using four-point functions in two-dimensional conformal field theory. *Phys. Rev. Lett.*, 115:131603, Sep 2015. doi: 10.1103/PhysRevLett.115.131603. URL https://link.aps.org/doi/10.1103/PhysRevLett.115.131603.

[239] Juan Maldacena, Stephen H. Shenker, and Douglas Stanford. A bound on chaos. *Journal of High Energy Physics*, 2016(8):106, 2016. doi: 10.1007/JHEP08(2016)106. URL http://dx.doi.org/10.1007/JHEP08(2016)106.

[240] Pavan Hosur, Xiao-Liang Qi, Daniel A. Roberts, and Beni Yoshida. Chaos in quantum channels. *Journal of High Energy Physics*, 2016(2):4, 2016. ISSN 1029-8479. doi: 10.1007/JHEP02(2016)004. URL http://dx.doi.org/10.1007/JHEP02(2016)004.

[241] A. I. Larkin and Y. N. Ovchinnikov. Quasiclassical Method in the Theory of Superconductivity. *Soviet Journal of Experimental and Theoretical Physics*, 28:1200, June 1969.

[242] Avijit Das, Saurish Chakrabarty, Abhishek Dhar, Anupam Kundu, David A. Huse, Roderich Moessner, Samriddhi Sankar Ray, and Subhro Bhattacharjee. Light-cone spreading of perturbations and the butterfly effect in a classical spin chain. *Phys. Rev. Lett.*, 121:024101, Jul 2018. doi: 10.1103/PhysRevLett.121.024101. URL https://link.aps.org/doi/10.1103/PhysRevLett.121.024101.

[243] Jordan S. Cotler, Dawei Ding, and Geoffrey R. Penington. Out-of-time-order operators and the butterfly effect. *Annals of Physics*, 396:318 – 333, 2018. ISSN 0003-4916. doi: https://doi.org/10.1016/j.aop.2018.07.020. URL http://www.sciencedirect.com/science/article/pii/S000349161830191X.

[244] Douglas Stanford. Many-body chaos at weak coupling. *Journal of High Energy Physics*, 2016(10):9, 2016. ISSN 1029-8479. doi: 10.1007/JHEP10(2016)009. URL http://dx.doi.org/10.1007/JHEP10(2016)009.

[245] Igor L. Aleiner, Lara Faoro, and Lev B. Ioffe. Microscopic model of quantum butterfly effect: Out-of-time-order correlators and traveling combustion waves. *Annals of Physics*, 375:378 – 406, 2016. ISSN 0003-4916. doi: https://doi.org/10.1016/j.aop.2016.09.006. URL http://www.sciencedirect.com/science/article/pii/S0003491616301919.

[246] Debanjan Chowdhury and Brian Swingle. Onset of many-body chaos in the $o(n)$ model. *Phys. Rev. D*, 96:065005, Sep 2017. doi: 10.1103/PhysRevD.96.065005. URL https://link.aps.org/doi/10.1103/PhysRevD.96.065005.

[247] A. Kitaev. A simple model of quantum holography, kitp strings seminar and entanglement 2015 program.

[248] Joseph Polchinski and Vladimir Rosenhaus. The spectrum in the sachdev-ye-kitaev model. *Journal of High Energy Physics*, 2016(4):1–25, April 2016. doi: 10.1007/jhep04(2016)001. URL https://doi.org/10.1007/jhep04(2016)001.

[249] A Bohrdt, C B Mendl, M Endres, and M Knap. Scrambling and thermalization in a diffusive quantum many-body system. *New Journal of Physics*, 19(6):063001, 2017. URL http://stacks.iop.org/1367-2630/19/i=6/a=063001.

[250] Ivan Kukuljan, Sašo Grozdanov, and Tomaž Prosen. Weak quantum chaos. *Phys. Rev. B*, 96:060301, Aug 2017. doi: 10.1103/PhysRevB.96.060301. URL https://link.aps.org/doi/10.1103/PhysRevB.96.060301.

[251] Vedika Khemani, David A. Huse, and Adam Nahum. Velocity-dependent lyapunov exponents in many-body quantum, semiclassical, and classical chaos. *Phys. Rev. B*, 98:144304, Oct 2018. doi: 10.1103/PhysRevB.98.144304. URL https://link.aps.org/doi/10.1103/PhysRevB.98.144304.

[252] Shenglong Xu and Brian Swingle. Locality, quantum fluctuations, and scrambling. *Phys. Rev. X*, 9:031048, Sep 2019. doi: 10.1103/PhysRevX.9.031048. URL https://link.aps.org/doi/10.1103/PhysRevX.9.031048.

[253] Adam Nahum, Sagar Vijay, and Jeongwan Haah. Operator spreading in random unitary circuits. *Phys. Rev. X*, 8:021014, Apr 2018. doi: 10.1103/PhysRevX.8.021014. URL https://link.aps.org/doi/10.1103/PhysRevX.8.021014.

[254] Pasquale Calabrese and John Cardy. Quantum quenches in extended systems. *Journal of Statistical Mechanics: Theory and Experiment*, 2007(06):P06008–P06008, jun 2007. doi: 10.1088/1742-5468/2007/06/p06008. URL https://doi.org/10.1088%2F1742-5468%2F2007%2F06%2Fp06008.

[255] Pasquale Calabrese, Fabian H L Essler, and Maurizio Fagotti. Quantum quench in the transverse field ising chain: I. time evolution of order parameter correlators. *Journal of Statistical Mechanics: Theory and Experiment*, 2012(07):P07016, jul 2012. doi: 10.1088/1742-5468/2012/07/p07016. URL https://doi.org/10.1088%2F1742-5468%2F2012%2F07%2Fp07016.

[256] Márk Mezei and Douglas Stanford. On entanglement spreading in chaotic systems. *Journal of High Energy Physics*, 2017(5):65, May 2017. ISSN 1029-8479. doi: 10.1007/JHEP05(2017)065. URL http://dx.doi.org/10.1007/JHEP05(2017)065.

[257] Felix M. Haehl, R. Loganayagam, Prithvi Narayan, and Mukund Rangamani. Classification of out-of-time-order correlators. *SciPost Phys.*, 6:1, 2019. doi: 10.21468/SciPostPhys.6.1.001. URL https://scipost.org/10.21468/SciPostPhys.6.1.001.

[258] Arpan Bhattacharyya, Wissam Chemissany, S. Shajidul Haque, and Bin Yan. Towards the web of quantum chaos diagnostics, 2019.

[259] Daniel A. Roberts and Beni Yoshida. Chaos and complexity by design. *Journal of High Energy Physics*, 2017(4):121, Apr 2017. ISSN 1029-8479. doi: 10.1007/JHEP04(2017)121. URL https://doi.org/10.1007/JHEP04(2017)121.

[260] Tianci Zhou and Adam Nahum. The entanglement membrane in chaotic many-body systems, 2019.

[261] Alfréd Rényi. On measures of entropy and information. In *Proceedings of the Fourth Berkeley Symposium on Mathematical Statistics and Probability, Volume 1: Contributions to the Theory of Statistics*, pages 547–561, Berkeley, Calif., 1961. University of California Press. URL https://projecteuclid.org/euclid.bsmsp/1200512181.

[262] C. E. Shannon. A mathematical theory of communication. *Bell System Technical Journal*, 27(3):379–423, July 1948. doi: 10.1002/j.1538-7305.1948.tb01338.x. URL https://doi.org/10.1002/j.1538-7305.1948.tb01338.x.

[263] John Neumann. *Mathematical foundations of quantum mechanics*. Princeton university press, 1955.

[264] Vincenzo Alba and Pasquale Calabrese. Entanglement and thermodynamics after a quantum quench in integrable systems. *Proceedings of the National Academy of Sciences*, 114(30):7947–7951, 2017. doi: 10.1073/pnas.1703516114. URL http://www.pnas.org/content/114/30/7947.abstract.

[265] Pasquale Calabrese. Entanglement and thermodynamics in non-equilibrium isolated quantum systems. *Physica A: Statistical Mechanics and its Applications*, 504:31 – 44, 2018. ISSN 0378-4371. doi: https://doi.org/10.1016/j.physa.2017.10.011. URL http://www.sciencedirect.com/science/article/pii/S037843711731018X. Lecture Notes of the 14th International Summer School on Fundamental Problems in Statistical Physics.

[266] Gabriele De Chiara, Simone Montangero, Pasquale Calabrese, and Rosario Fazio. Entanglement entropy dynamics of heisenberg chains. *Journal of Statistical Mechanics: Theory and Experiment*, 2006(03):P03001, 2006. URL http://stacks.iop.org/1742-5468/2006/i=03/a=P03001.

[267] Maurizio Fagotti and Pasquale Calabrese. Evolution of entanglement entropy following a quantum quench: Analytic results for the xy chain in a transverse magnetic field. *Phys. Rev. A*, 78:010306, Jul 2008. doi: 10.1103/PhysRevA.78.010306. URL https://link.aps.org/doi/10.1103/PhysRevA.78.010306.

[268] Vincenzo Alba and Pasquale Calabrese. Entanglement dynamics after quantum quenches in generic integrable systems. *SciPost Phys.*, 4:17, 2018. doi: 10.21468/SciPostPhys.4.3.017. URL https://scipost.org/10.21468/SciPostPhys.4.3.017.

[269] Hyungwon Kim and David A. Huse. Ballistic spreading of entanglement in a diffusive nonintegrable system. *Phys. Rev. Lett.*, 111:127205, Sep 2013. doi: 10.1103/PhysRevLett.111.127205. URL https://link.aps.org/doi/10.1103/PhysRevLett.111.127205.

[270] V. Balasubramanian, A. Bernamonti, N. Copland, B. Craps, and F. Galli. Thermalization of mutual and tripartite information in strongly coupled two dimensional conformal field theories. *Phys. Rev. D*, 84:105017, Nov 2011. doi: 10.1103/PhysRevD.84.105017. URL https://link.aps.org/doi/10.1103/PhysRevD.84.105017.

[271] Silvia Pappalardi, Angelo Russomanno, Alessandro Silva, and Rosario Fazio. Multipartite entanglement after a quantum quench. *Journal of Statistical Mechanics: Theory and Experiment*, 2017(5):053104, may 2017. doi: 10.1088/1742-5468/aa6809. URL https://doi.org/10.1088%2F1742-5468%2Faa6809.

[272] Vincenzo Alba and Pasquale Calabrese. Quantum information scrambling after a quantum quench. *Phys. Rev. B*, 100:115150, Sep 2019. doi: 10.1103/PhysRevB.100.115150. URL https://link.aps.org/doi/10.1103/PhysRevB.100.115150.

[273] Thomas Hartman and Juan Maldacena. Time evolution of entanglement entropy from black hole interiors. *Journal of High Energy Physics*, 2013(5):14, 2013. ISSN 1029-8479. doi: 10.1007/JHEP05(2013)014. URL http://dx.doi.org/10.1007/JHEP05(2013)014.

[274] Hong Liu and S. Josephine Suh. Entanglement tsunami: Universal scaling in holographic thermalization. *Phys. Rev. Lett.*, 112:011601, Jan 2014. doi: 10.1103/PhysRevLett.112.011601. URL https://link.aps.org/doi/10.1103/PhysRevLett.112.011601.

[275] Hong Liu and S. Josephine Suh. Entanglement growth during thermalization in holographic systems. *Phys. Rev. D*, 89:066012, Mar 2014. doi: 10.1103/PhysRevD.89.066012. URL https://link.aps.org/doi/10.1103/PhysRevD.89.066012.

[276] Adam Nahum, Jonathan Ruhman, Sagar Vijay, and Jeongwan Haah. Quantum entanglement growth under random unitary dynamics. *Phys. Rev. X*, 7:031016, Jul 2017. doi: 10.1103/PhysRevX.7.031016. URL https://link.aps.org/doi/10.1103/PhysRevX.7.031016.

[277] Cheryne Jonay, David A. Huse, and Adam Nahum. Coarse-grained dynamics of operator and state entanglement. 2018.

[278] Tianci Zhou and Adam Nahum. Emergent statistical mechanics of entanglement in random unitary circuits. *Phys. Rev. B*, 99:174205, May 2019. doi: 10.1103/PhysRevB.99.174205. URL https://link.aps.org/doi/10.1103/PhysRevB.99.174205.

[279] Dieter Forster. *Hydrodynamic fluctuations, broken symmetry, and correlation functions*. CRC Press, 2018.

[280] Paul M Chaikin, Tom C Lubensky, and Thomas A Witten. *Principles of condensed matter physics*, volume 10. Cambridge university press Cambridge, 1995.

[281] Hong Liu and Paolo Glorioso. Lectures on non-equilibrium effective field theories and fluctuating hydrodynamics. In *Proceedings of Theoretical Advanced Study Institute Summer School 2017 "Physics at the Fundamental Frontier" — PoS(TASI2017)*. Sissa Medialab, July 2018. doi: 10.22323/1.305.0008. URL https://doi.org/10.22323/1.305.0008.

[282] Benjamin Doyon. Lecture notes on generalised hydrodynamics, 2019.

[283] R. Esposito, J. L. Lebowitz, and R. Marra. On the derivation of hydrodynamics from the boltzmann equation. *Physics of Fluids*, 11(8):2354–2366, August 1999. doi: 10.1063/1.870097. URL https://doi.org/10.1063/1.870097.

[284] François Golse. The boltzmann equation and its hydrodynamic limits. In *Handbook of Differential Equations Evolutionary Equations*, pages 159–301. Elsevier, 2005. doi: 10.1016/s1874-5717(06)80006-x. URL https://doi.org/10.1016/s1874-5717(06)80006-x.

[285] Leo P Kadanoff and Paul C Martin. Hydrodynamic equations and correlation functions. *Annals of Physics*, 24:419 – 469, 1963. ISSN 0003-4916. doi: https://doi.org/10.1016/0003-4916(63)90078-2. URL http://www.sciencedirect.com/science/article/pii/0003491663900782.

[286] B. Bertini, F. Heidrich-Meisner, C. Karrasch, T. Prosen, R. Steinigeweg, and M. Žnidarič. Finite-temperature transport in one-dimensional quantum lattice models, 2020.

[287] Jonathan Lux, Jan Müller, Aditi Mitra, and Achim Rosch. Hydrodynamic long-time tails after a quantum quench. *Phys. Rev. A*, 89:053608, May 2014. doi: 10.1103/PhysRevA.89.053608. URL https://link.aps.org/doi/10.1103/PhysRevA.89.053608.

[288] Lars Onsager. Reciprocal relations in irreversible processes. i. *Phys. Rev.*, 37:405–426, Feb 1931. doi: 10.1103/PhysRev.37.405. URL https://link.aps.org/doi/10.1103/PhysRev.37.405.

[289] P. W. Anderson. Absence of diffusion in certain random lattices. *Phys. Rev.*, 109:1492–1505, Mar 1958. doi: 10.1103/PhysRev.109.1492. URL https://link.aps.org/doi/10.1103/PhysRev.109.1492.

[290] B. J. Alder and T. E. Wainwright. Decay of the velocity autocorrelation function. *Phys. Rev. A*, 1:18–21, Jan 1970. doi: 10.1103/PhysRevA.1.18. URL https://link.aps.org/doi/10.1103/PhysRevA.1.18.

[291] Henk van Beijeren. Transport properties of stochastic lorentz models. *Rev. Mod. Phys.*, 54:195–234, Jan 1982. doi: 10.1103/RevModPhys.54.195. URL https://link.aps.org/doi/10.1103/RevModPhys.54.195.

[292] Wilhelm Brenig. Hydrodynamic long-time tails. In *Statistical Theory of Heat*, pages 149–151. Springer Berlin Heidelberg, 1989. doi: 10.1007/978-3-642-74685-7_30. URL https://doi.org/10.1007/978-3-642-74685-7_30.

[293] Y Pomeau and P Résibois. Time dependent correlation functions and mode-mode coupling theories. *Physics Reports*, 19(2):63 – 139, 1975. ISSN 0370-1573. doi: https://doi.org/10.1016/0370-1573(75)90019-8. URL `http://www.sciencedirect.com/science/article/pii/0370157375900198`.

[294] Subroto Mukerjee, Vadim Oganesyan, and David Huse. Statistical theory of transport by strongly interacting lattice fermions. *Phys. Rev. B*, 73:035113, Jan 2006. doi: 10.1103/PhysRevB.73.035113. URL `https://link.aps.org/doi/10.1103/PhysRevB.73.035113`.

[295] Xinyi Chen-Lin, Luca V. Delacrétaz, and Sean A. Hartnoll. Theory of diffusive fluctuations. *Phys. Rev. Lett.*, 122:091602, Mar 2019. doi: 10.1103/PhysRevLett.122.091602. URL `https://link.aps.org/doi/10.1103/PhysRevLett.122.091602`.

[296] Christian B. Mendl and Herbert Spohn. Dynamic correlators of fermi-pasta-ulam chains and nonlinear fluctuating hydrodynamics. *Phys. Rev. Lett.*, 111:230601, Dec 2013. doi: 10.1103/PhysRevLett.111.230601. URL `https://link.aps.org/doi/10.1103/PhysRevLett.111.230601`.

[297] Herbert Spohn. Nonlinear fluctuating hydrodynamics for anharmonic chains. *Journal of Statistical Physics*, 154(5):1191–1227, February 2014. doi: 10.1007/s10955-014-0933-y. URL `https://doi.org/10.1007/s10955-014-0933-y`.

[298] Vladislav Popkov, Andreas Schadschneider, Johannes Schmidt, and Gunter M. Schütz. Fibonacci family of dynamical universality classes. *Proceedings of the National Academy of Sciences*, 112(41):12645–12650, 2015. ISSN 0027-8424. doi: 10.1073/pnas.1512261112. URL `https://www.pnas.org/content/112/41/12645`.

[299] Herbert Spohn. Fluctuating hydrodynamics approach to equilibrium time correlations for anharmonic chains. In *Thermal Transport in Low Dimensions*, pages 107–158. Springer International Publishing, 2016. doi: 10.1007/978-3-319-29261-8_3. URL `https://doi.org/10.1007/978-3-319-29261-8_3`.

[300] Lorenzo Bertini and Giambattista Giacomin. Stochastic burgers and KPZ equations from particle systems. *Communications in Mathematical Physics*, 183(3):571–607, February 1997. doi: 10.1007/s002200050044. URL `https://doi.org/10.1007/s002200050044`.

[301] Benjamin Doyon. Diffusion and superdiffusion from hydrodynamic projection, 2019.

[302] Marko Medenjak, Jacopo De Nardis, and Takato Yoshimura. Diffusion from convection, 2019.

[303] Mehran Kardar, Giorgio Parisi, and Yi-Cheng Zhang. Dynamic scaling of growing interfaces. *Phys. Rev. Lett.*, 56:889–892, Mar 1986. doi: 10.1103/PhysRevLett.56.889. URL `https://link.aps.org/doi/10.1103/PhysRevLett.56.889`.

[304] Xenophon Zotos. *Journal of Low Temperature Physics*, 126(3/4):1185–1194, 2002. doi: 10.1023/a:1013827615835. URL `https://doi.org/10.1023/a:1013827615835`.

[305] Enej Ilievski and Jacopo De Nardis. Microscopic origin of ideal conductivity in integrable quantum models. *Phys. Rev. Lett.*, 119:020602, Jul 2017. doi: 10.1103/PhysRevLett.119.020602. URL `https://link.aps.org/doi/10.1103/PhysRevLett.119.020602`.

[306] Marko Ljubotina, Marko Žnidarič, and Tomaž Prosen. Kardar-parisi-zhang physics in the quantum heisenberg magnet. *Phys. Rev. Lett.*, 122:210602, May 2019. doi: 10.1103/PhysRevLett.122.210602. URL `https://link.aps.org/doi/10.1103/PhysRevLett.122.210602`.

[307] Enej Ilievski, Jacopo De Nardis, Marko Medenjak, and Tomaž Prosen. Superdiffusion in one-dimensional quantum lattice models. *Phys. Rev. Lett.*, 121:230602, Dec 2018. doi: 10.1103/PhysRevLett.121.230602. URL `https://link.aps.org/doi/10.1103/PhysRevLett.121.230602`.

[308] Jacopo De Nardis, Marko Medenjak, Christoph Karrasch, and Enej Ilievski. Anomalous spin diffusion in one-dimensional antiferromagnets. *Phys. Rev. Lett.*, 123:186601, Oct 2019. doi: 10.1103/PhysRevLett.123.186601. URL `https://link.aps.org/doi/10.1103/PhysRevLett.123.186601`.

[309] Maxime Dupont and Joel E. Moore. Universal spin dynamics in infinite-temperature one-dimensional quantum magnets. *Phys. Rev. B*, 101:121106, Mar 2020. doi: 10.1103/PhysRevB.101.121106. URL `https://link.aps.org/doi/10.1103/PhysRevB.101.121106`.

[310] Vir B. Bulchandani. Kardar-parisi-zhang universality from soft gauge modes. *Phys. Rev. B*, 101:041411, Jan 2020. doi: 10.1103/PhysRevB.101.041411. URL `https://link.aps.org/doi/10.1103/PhysRevB.101.041411`.

[311] Jacopo De Nardis, Marko Medenjak, Christoph Karrasch, and Enej Ilievski. Universality classes of spin transport in one-dimensional isotropic magnets: the onset of logarithmic anomalies, 2020.

[312] S. Langer, F. Heidrich-Meisner, J. Gemmer, I. P. McCulloch, and U. Schollwöck. Real-time study of diffusive and ballistic transport in spin-$\frac{1}{2}$ chains using the adaptive time-dependent density matrix renormalization group method. *Phys. Rev. B*, 79:214409, Jun 2009. doi: 10.1103/PhysRevB.79.214409. URL `https://link.aps.org/doi/10.1103/PhysRevB.79.214409`.

[313] Tomaž Prosen and Marko Žnidarič. Matrix product simulations of non-equilibrium steady states of quantum spin chains. *Journal of Statistical Mechanics: Theory and Experiment*, 2009(02):P02035, feb 2009. doi: 10.1088/1742-5468/2009/02/p02035. URL `https://doi.org/10.1088%2F1742-5468%2F2009%2F02%2Fp02035`.

[314] Robin Steinigeweg and Wolfram Brenig. Spin transport in the xxz chain at finite temperature and momentum. *Phys. Rev. Lett.*, 107:250602, Dec 2011. doi: 10.1103/PhysRevLett.107.250602. URL `https://link.aps.org/doi/10.1103/PhysRevLett.107.250602`.

[315] Marko Žnidarič. Spin transport in a one-dimensional anisotropic heisenberg model. *Phys. Rev. Lett.*, 106:220601, May 2011. doi: 10.1103/PhysRevLett.106.220601. URL `https://link.aps.org/doi/10.1103/PhysRevLett.106.220601`.

[316] Tomaž Prosen and Enej Ilievski. Families of quasilocal conservation laws and quantum spin transport. *Phys. Rev. Lett.*, 111:057203, Aug 2013. doi: 10.1103/PhysRevLett.111.057203. URL `https://link.aps.org/doi/10.1103/PhysRevLett.111.057203`.

[317] Marko Ljubotina, Marko Žnidarič, and Tomaž Prosen. Spin diffusion from an inhomogeneous quench in an integrable system. *Nature Communications*, 8(1), July 2017. doi: 10.1038/ncomms16117. URL `https://doi.org/10.1038/ncomms16117`.

[318] Lorenzo Piroli, Jacopo De Nardis, Mario Collura, Bruno Bertini, and Maurizio Fagotti. Transport in out-of-equilibrium xxz chains: Nonballistic behavior and correlation functions. *Phys. Rev. B*, 96:115124, Sep 2017. doi: 10.1103/PhysRevB.96.115124. URL https://link.aps.org/doi/10.1103/PhysRevB.96.115124.

[319] Sarang Gopalakrishnan and Romain Vasseur. Kinetic theory of spin diffusion and superdiffusion in *xxz* spin chains. *Phys. Rev. Lett.*, 122:127202, Mar 2019. doi: 10.1103/PhysRevLett.122.127202. URL https://link.aps.org/doi/10.1103/PhysRevLett.122.127202.

[320] H. Bethe. Zur theorie der metalle. *Zeitschrift fr Physik*, 71(3-4):205–226, March 1931. doi: 10.1007/bf01341708. URL https://doi.org/10.1007/bf01341708.

[321] Minoru Takahashi. *Thermodynamics of one-dimensional solvable models*. Cambridge university press, 2005.

[322] Bill Sutherland. *Beautiful models: 70 years of exactly solved quantum many-body problems*. World Scientific Publishing Company, 2004.

[323] Giuseppe Mussardo. *Statistical field theory: an introduction to exactly solved models in statistical physics*. Oxford University Press, 2010.

[324] Olalla A. Castro-Alvaredo, Benjamin Doyon, and Takato Yoshimura. Emergent hydrodynamics in integrable quantum systems out of equilibrium. *Phys. Rev. X*, 6:041065, Dec 2016. doi: 10.1103/PhysRevX.6.041065. URL https://link.aps.org/doi/10.1103/PhysRevX.6.041065.

[325] Bruno Bertini, Mario Collura, Jacopo De Nardis, and Maurizio Fagotti. Transport in out-of-equilibrium *xxz* chains: Exact profiles of charges and currents. *Phys. Rev. Lett.*, 117:207201, Nov 2016. doi: 10.1103/PhysRevLett.117.207201. URL https://link.aps.org/doi/10.1103/PhysRevLett.117.207201.

[326] Vir B. Bulchandani, Romain Vasseur, Christoph Karrasch, and Joel E. Moore. Solvable hydrodynamics of quantum integrable systems. *Phys. Rev. Lett.*, 119:220604, Nov 2017. doi: 10.1103/PhysRevLett.119.220604. URL https://link.aps.org/doi/10.1103/PhysRevLett.119.220604.

[327] Vir B. Bulchandani, Romain Vasseur, Christoph Karrasch, and Joel E. Moore. Bethe-boltzmann hydrodynamics and spin transport in the xxz chain. *Phys. Rev. B*, 97:045407, Jan 2018. doi: 10.1103/PhysRevB.97.045407. URL https://link.aps.org/doi/10.1103/PhysRevB.97.045407.

[328] Benjamin Doyon, Takato Yoshimura, and Jean-Sébastien Caux. Soliton gases and generalized hydrodynamics. *Phys. Rev. Lett.*, 120:045301, Jan 2018. doi: 10.1103/PhysRevLett.120.045301. URL https://link.aps.org/doi/10.1103/PhysRevLett.120.045301.

[329] Jacopo De Nardis, Denis Bernard, and Benjamin Doyon. Hydrodynamic diffusion in integrable systems. *Phys. Rev. Lett.*, 121:160603, Oct 2018. doi: 10.1103/PhysRevLett.121.160603. URL https://link.aps.org/doi/10.1103/PhysRevLett.121.160603.

[330] Elmer Guardado-Sanchez, Alan Morningstar, Benjamin M. Spar, Peter T. Brown, David A. Huse, and Waseem S. Bakr. Subdiffusion and heat transport in a tilted two-dimensional fermi-hubbard system. *Phys. Rev. X*, 10:011042, Feb 2020. doi: 10.1103/PhysRevX.10.011042. URL https://link.aps.org/doi/10.1103/PhysRevX.10.011042.

[331] Alan Morningstar, Vedika Khemani, and David A. Huse. Kinetically-constrained freezing transition in a dipole-conserving system, 2020.

[332] Andrey Gromov, Andrew Lucas, and Rahul M. Nandkishore. Fracton hydrodynamics, 2020.

[333] Johannes Feldmeier, Pablo Sala, Giuseppe de Tomasi, Frank Pollmann, and Michael Knap. Anomalous diffusion in dipole- and higher-moment conserving systems, 2020.

[334] David J. Luitz and Yevgeny Bar Lev. Anomalous thermalization in ergodic systems. *Phys. Rev. Lett.*, 117:170404, Oct 2016. doi: 10.1103/PhysRevLett.117.170404. URL `https://link.aps.org/doi/10.1103/PhysRevLett.117.170404`.

[335] Robert Zwanzig. Memory effects in irreversible thermodynamics. *Phys. Rev.*, 124: 983–992, Nov 1961. doi: 10.1103/PhysRev.124.983. URL `https://link.aps.org/doi/10.1103/PhysRev.124.983`.

[336] Hazime Mori. Transport, collective motion, and brownian motion. *Progress of Theoretical Physics*, 33(3):423–455, March 1965. doi: 10.1143/ptp.33.423. URL `https://doi.org/10.1143/ptp.33.423`.

[337] Robert Zwanzig. *Nonequilibrium statistical mechanics.* Oxford University Press, 2001.

[338] Hermann Grabert. *Projection Operator Techniques in Nonequilibrium Statistical Mechanics*. Springer Berlin Heidelberg, 1982. doi: 10.1007/bfb0044591. URL `https://doi.org/10.1007/bfb0044591`.

[339] J. Rau and B. Müller. From reversible quantum microdynamics to irreversible quantum transport. *Physics Reports*, 272(1):1 – 59, 1996. ISSN 0370-1573. doi: https://doi.org/10.1016/0370-1573(95)00077-1. URL `http://www.sciencedirect.com/science/article/pii/0370157395000771`.

[340] P. Jung, R. W. Helmes, and A. Rosch. Transport in almost integrable models: Perturbed heisenberg chains. *Phys. Rev. Lett.*, 96:067202, Feb 2006. doi: 10.1103/PhysRevLett.96.067202. URL `https://link.aps.org/doi/10.1103/PhysRevLett.96.067202`.

[341] Peter Jung and Achim Rosch. Lower bounds for the conductivities of correlated quantum systems. *Phys. Rev. B*, 75:245104, Jun 2007. doi: 10.1103/PhysRevB.75.245104. URL `https://link.aps.org/doi/10.1103/PhysRevB.75.245104`.

[342] Mark R. Dowling, Matthew J. Davis, Peter D. Drummond, and Joel F. Corney. Monte carlo techniques for real-time quantum dynamics. *Journal of Computational Physics*, 220(2):549 – 567, 2007. ISSN 0021-9991. doi: https://doi.org/10.1016/j.jcp.2006.05.017. URL `http://www.sciencedirect.com/science/article/pii/S002199910600249X`.

[343] Giuseppe Carleo, Federico Becca, Marco Schiró, and Michele Fabrizio. Localization and glassy dynamics of many-body quantum systems. *Scientific Reports*, 2(1), February 2012. doi: 10.1038/srep00243. URL `https://doi.org/10.1038/srep00243`.

[344] Giuseppe Carleo, Lorenzo Cevolani, Laurent Sanchez-Palencia, and Markus Holzmann. Unitary dynamics of strongly interacting bose gases with the time-dependent variational monte carlo method in continuous space. *Phys. Rev. X*, 7:031026, Aug 2017. doi: 10.1103/PhysRevX.7.031026. URL `https://link.aps.org/doi/10.1103/PhysRevX.7.031026`.

[345] S De Nicola, B Doyon, and M J Bhaseen. Stochastic approach to non-equilibrium quantum spin systems. *Journal of Physics A: Mathematical and Theoretical*, 52(5): 05LT02, jan 2019. doi: 10.1088/1751-8121/aaf9be. URL https://doi.org/10.1088%2F1751-8121%2Faaf9be.

[346] S De Nicola, B Doyon, and M J Bhaseen. Non-equilibrium quantum spin dynamics from classical stochastic processes. *Journal of Statistical Mechanics: Theory and Experiment*, 2020(1):013106, jan 2020. doi: 10.1088/1742-5468/ab6093. URL https://doi.org/10.1088%2F1742-5468%2Fab6093.

[347] P. Schmidt and H. Monien. Nonequilibrium dynamical mean-field theory of a strongly correlated system, 2002.

[348] J. K. Freericks, V. M. Turkowski, and V. Zlatić. Nonequilibrium dynamical mean-field theory. *Phys. Rev. Lett.*, 97:266408, Dec 2006. doi: 10.1103/PhysRevLett.97.266408. URL https://link.aps.org/doi/10.1103/PhysRevLett.97.266408.

[349] Martin Eckstein, Marcus Kollar, and Philipp Werner. Thermalization after an interaction quench in the hubbard model. *Phys. Rev. Lett.*, 103:056403, Jul 2009. doi: 10.1103/PhysRevLett.103.056403. URL https://link.aps.org/doi/10.1103/PhysRevLett.103.056403.

[350] Hideo Aoki, Naoto Tsuji, Martin Eckstein, Marcus Kollar, Takashi Oka, and Philipp Werner. Nonequilibrium dynamical mean-field theory and its applications. *Rev. Mod. Phys.*, 86:779–837, Jun 2014. doi: 10.1103/RevModPhys.86.779. URL https://link.aps.org/doi/10.1103/RevModPhys.86.779.

[351] Leonid V Keldysh et al. Diagram technique for nonequilibrium processes. *Sov. Phys. JETP*, 20(4):1018–1026, 1965.

[352] Jürgen Berges. Controlled nonperturbative dynamics of quantum fields out of equilibrium. *Nuclear Physics A*, 699(3-4):847–886, March 2002. doi: 10.1016/s0375-9474(01)01295-7. URL https://doi.org/10.1016/s0375-9474(01)01295-7.

[353] Jürgen Berges. Nonequilibrium quantum fields: from cold atoms to cosmology. In *Strongly Interacting Quantum Systems out of Equilibrium*, pages 69–206. Oxford University Press, June 2016. doi: 10.1093/acprof:oso/9780198768166.003.0002. URL https://doi.org/10.1093/acprof:oso/9780198768166.003.0002.

[354] A. Schuckert, A. Piñeiro Orioli, and J. Berges. Nonequilibrium quantum spin dynamics from two-particle irreducible functional integral techniques in the schwinger boson representation. *Phys. Rev. B*, 98:224304, Dec 2018. doi: 10.1103/PhysRevB.98.224304. URL https://link.aps.org/doi/10.1103/PhysRevB.98.224304.

[355] Giuseppe Carleo and Matthias Troyer. Solving the quantum many-body problem with artificial neural networks. *Science*, 355(6325):602–606, 2017. ISSN 0036-8075. doi: 10.1126/science.aag2302. URL https://science.sciencemag.org/content/355/6325/602.

[356] Markus Schmitt and Markus Heyl. Quantum dynamics in transverse-field Ising models from classical networks. *SciPost Phys.*, 4:013, 2018. doi: 10.21468/SciPostPhys.4.2.013. URL https://scipost.org/10.21468/SciPostPhys.4.2.013.

[357] Markus Schmitt and Markus Heyl. Quantum many-body dynamics in two dimensions with artificial neural networks, 2019.

[358] Irene López-Gutiérrez and Christian B. Mendl. Real time evolution with neural-network quantum states, 2019.

[359] Jutho Haegeman, J. Ignacio Cirac, Tobias J. Osborne, Iztok Pižorn, Henri Verschelde, and Frank Verstraete. Time-dependent variational principle for quantum lattices. *Phys. Rev. Lett.*, 107:070601, Aug 2011. doi: 10.1103/PhysRevLett.107.070601. URL https://link.aps.org/doi/10.1103/PhysRevLett.107.070601.

[360] Jutho Haegeman, Christian Lubich, Ivan Oseledets, Bart Vandereycken, and Frank Verstraete. Unifying time evolution and optimization with matrix product states. *Phys. Rev. B*, 94:165116, Oct 2016. doi: 10.1103/PhysRevB.94.165116. URL https://link.aps.org/doi/10.1103/PhysRevB.94.165116.

[361] Christopher David White, Michael Zaletel, Roger S. K. Mong, and Gil Refael. Quantum dynamics of thermalizing systems. *Phys. Rev. B*, 97:035127, Jan 2018. doi: 10.1103/PhysRevB.97.035127. URL https://link.aps.org/doi/10.1103/PhysRevB.97.035127.

[362] Jonathan Wurtz, Anatoli Polkovnikov, and Dries Sels. Cluster truncated wigner approximation in strongly interacting systems. *Annals of Physics*, 395:341 – 365, 2018. ISSN 0003-4916. doi: https://doi.org/10.1016/j.aop.2018.06.001. URL http://www.sciencedirect.com/science/article/pii/S0003491618301647.

[363] C. Krumnow, J. Eisert, and Ö. Legeza. Towards overcoming the entanglement barrier when simulating long-time evolution, 2019.

[364] Vedika Khemani, Frank Pollmann, and S. L. Sondhi. Obtaining highly excited eigenstates of many-body localized hamiltonians by the density matrix renormalization group approach. *Phys. Rev. Lett.*, 116:247204, Jun 2016. doi: 10.1103/PhysRevLett.116.247204. URL https://link.aps.org/doi/10.1103/PhysRevLett.116.247204.

[365] Arijeet Pal and David A. Huse. Many-body localization phase transition. *Phys. Rev. B*, 82:174411, Nov 2010. doi: 10.1103/PhysRevB.82.174411. URL http://link.aps.org/doi/10.1103/PhysRevB.82.174411.

[366] David J. Luitz, Nicolas Laflorencie, and Fabien Alet. Many-body localization edge in the random-field heisenberg chain. *Phys. Rev. B*, 91:081103, Feb 2015. doi: 10.1103/PhysRevB.91.081103. URL https://link.aps.org/doi/10.1103/PhysRevB.91.081103.

[367] Vedika Khemani, S. P. Lim, D. N. Sheng, and David A. Huse. Critical properties of the many-body localization transition. *Phys. Rev. X*, 7:021013, Apr 2017. doi: 10.1103/PhysRevX.7.021013. URL https://link.aps.org/doi/10.1103/PhysRevX.7.021013.

[368] Francesca Pietracaprina, Nicolas Macé, David J. Luitz, and Fabien Alet. Shift-invert diagonalization of large many-body localizing spin chains. *SciPost Phys.*, 5:45, 2018. doi: 10.21468/SciPostPhys.5.5.045. URL https://scipost.org/10.21468/SciPostPhys.5.5.045.

[369] Trithep Devakul and Rajiv R. P. Singh. Early breakdown of area-law entanglement at the many-body delocalization transition. *Phys. Rev. Lett.*, 115:187201, Oct 2015. doi: 10.1103/PhysRevLett.115.187201. URL https://link.aps.org/doi/10.1103/PhysRevLett.115.187201.

[370] Elmer V. H. Doggen, Frank Schindler, Konstantin S. Tikhonov, Alexander D. Mirlin, Titus Neupert, Dmitry G. Polyakov, and Igor V. Gornyi. Many-body localization and delocalization in large quantum chains. *Phys. Rev. B*, 98:174202, Nov 2018. doi: 10.1103/PhysRevB.98.174202. URL https://link.aps.org/doi/10.1103/PhysRevB.98.174202.

[371] Titas Chanda, Piotr Sierant, and Jakub Zakrzewski. Time dynamics with matrix product states: Many-body localization transition of large systems revisited. *Phys. Rev. B*, 101:035148, Jan 2020. doi: 10.1103/PhysRevB.101.035148. URL https://link.aps.org/doi/10.1103/PhysRevB.101.035148.

[372] J. Šuntajs, J. Bonča, T. Prosen, and L. Vidmar. Quantum chaos challenges many-body localization, 2019.

[373] D. A. Abanin, J. H. Bardarson, G. De Tomasi, S. Gopalakrishnan, V. Khemani, S. A. Parameswaran, F. Pollmann, A. C. Potter, M. Serbyn, and R. Vasseur. Distinguishing localization from chaos: challenges in finite-size systems, 2019.

[374] R. K. Panda, A. Scardicchio, M. Schulz, S. R. Taylor, and M. Žnidarič. Can we study the many-body localisation transition? *EPL (Europhysics Letters)*, 128(6): 67003, feb 2020. doi: 10.1209/0295-5075/128/67003. URL https://doi.org/10.1209%2F0295-5075%2F128%2F67003.

[375] André Nauts and Robert E. Wyatt. New approach to many-state quantum dynamics: The recursive-residue-generation method. *Phys. Rev. Lett.*, 51:2238–2241, Dec 1983. doi: 10.1103/PhysRevLett.51.2238. URL https://link.aps.org/doi/10.1103/PhysRevLett.51.2238.

[376] Martin H. Gutknecht. A brief introduction to krylov space methods for solving linear systems. In *Frontiers of Computational Science*, pages 53–62. Springer Berlin Heidelberg, 2007. doi: 10.1007/978-3-540-46375-7_5. URL https://doi.org/10.1007/978-3-540-46375-7_5.

[377] Marlon Brenes, Vipin Kerala Varma, Antonello Scardicchio, and Ivan Girotto. Massively parallel implementation and approaches to simulate quantum dynamics using krylov subspace techniques. *Computer Physics Communications*, 235:477 – 488, 2019. ISSN 0010-4655. doi: https://doi.org/10.1016/j.cpc.2018.08.010. URL http://www.sciencedirect.com/science/article/pii/S0010465518303060.

[378] Seth Lloyd. Pure state quantum statistical mechanics and black holes. 2013.

[379] Sheldon Goldstein, Joel L. Lebowitz, Roderich Tumulka, and Nino Zanghì. Canonical typicality. *Phys. Rev. Lett.*, 96:050403, Feb 2006. doi: 10.1103/PhysRevLett.96.050403. URL https://link.aps.org/doi/10.1103/PhysRevLett.96.050403.

[380] Sandu Popescu, Anthony J. Short, and Andreas Winter. Entanglement and the foundations of statistical mechanics. *Nature Physics*, 2(11):754–758, October 2006. doi: 10.1038/nphys444. URL https://doi.org/10.1038/nphys444.

[381] Peter Reimann. Typicality for generalized microcanonical ensembles. *Phys. Rev. Lett.*, 99:160404, Oct 2007. doi: 10.1103/PhysRevLett.99.160404. URL https://link.aps.org/doi/10.1103/PhysRevLett.99.160404.

[382] Jochen Gemmer, Mathias Michel, and Günter Mahler. *Quantum thermodynamics: Emergence of thermodynamic behavior within composite quantum systems*, volume 784. Springer, 2009.

[383] Sho Sugiura and Akira Shimizu. Canonical thermal pure quantum state. *Phys. Rev. Lett.*, 111:010401, Jul 2013. doi: 10.1103/PhysRevLett.111.010401. URL `https://link.aps.org/doi/10.1103/PhysRevLett.111.010401`.

[384] Alfred Haar. Der massbegriff in der theorie der kontinuierlichen gruppen. *The Annals of Mathematics*, 34(1):147, January 1933. doi: 10.2307/1968346. URL `https://doi.org/10.2307/1968346`.

[385] J. Jaklič and P. Prelovšek. Lanczos method for the calculation of finite-temperature quantities in correlated systems. *Phys. Rev. B*, 49:5065–5068, Feb 1994. doi: 10.1103/PhysRevB.49.5065. URL `https://link.aps.org/doi/10.1103/PhysRevB.49.5065`.

[386] Toshiaki Iitaka and Toshikazu Ebisuzaki. Algorithm for linear response functions at finite temperatures: Application to esr spectrum of $s = \frac{1}{2}$ antiferromagnet cu benzoate. *Phys. Rev. Lett.*, 90:047203, Jan 2003. doi: 10.1103/PhysRevLett.90.047203. URL `https://link.aps.org/doi/10.1103/PhysRevLett.90.047203`.

[387] M. W. Long, P. Prelovšek, S. El Shawish, J. Karadamoglou, and X. Zotos. Finite-temperature dynamical correlations using the microcanonical ensemble and the lanczos algorithm. *Phys. Rev. B*, 68:235106, Dec 2003. doi: 10.1103/PhysRevB.68.235106. URL `https://link.aps.org/doi/10.1103/PhysRevB.68.235106`.

[388] Tarek A. Elsayed and Boris V. Fine. Regression relation for pure quantum states and its implications for efficient computing. *Phys. Rev. Lett.*, 110:070404, Feb 2013. doi: 10.1103/PhysRevLett.110.070404. URL `https://link.aps.org/doi/10.1103/PhysRevLett.110.070404`.

[389] Robin Steinigeweg, Jochen Gemmer, and Wolfram Brenig. Spin-current autocorrelations from single pure-state propagation. *Phys. Rev. Lett.*, 112:120601, Mar 2014. doi: 10.1103/PhysRevLett.112.120601. URL `https://link.aps.org/doi/10.1103/PhysRevLett.112.120601`.

[390] Robin Steinigeweg, Jochen Gemmer, and Wolfram Brenig. Spin and energy currents in integrable and nonintegrable spin-$\frac{1}{2}$ chains: A typicality approach to real-time autocorrelations. *Phys. Rev. B*, 91:104404, Mar 2015. doi: 10.1103/PhysRevB.91.104404. URL `https://link.aps.org/doi/10.1103/PhysRevB.91.104404`.

[391] Satoshi Okamoto, Gonzalo Alvarez, Elbio Dagotto, and Takami Tohyama. Accuracy of the microcanonical lanczos method to compute real-frequency dynamical spectral functions of quantum models at finite temperatures. *Phys. Rev. E*, 97:043308, Apr 2018. doi: 10.1103/PhysRevE.97.043308. URL `https://link.aps.org/doi/10.1103/PhysRevE.97.043308`.

[392] Youhei Yamaji, Takafumi Suzuki, and Mitsuaki Kawamura. Numerical algorithm for exact finite temperature spectra and its application to frustrated quantum spin systems, 2018.

[393] E M Stoudenmire and Steven R White. Minimally entangled typical thermal state algorithms. *New Journal of Physics*, 12(5):055026, may 2010. doi: 10.1088/1367-2630/12/5/055026. URL `https://doi.org/10.1088%2F1367-2630%2F12%2F5%2F055026`.

[394] J. Eisert. Entanglement and tensor network states. 2013.

[395] Román Orús. A practical introduction to tensor networks: Matrix product states and projected entangled pair states. *Annals of Physics*, 349:117 – 158, 2014. ISSN 0003-4916. doi: https://doi.org/10.1016/j.aop.2014.06.013. URL `http://www.sciencedirect.com/science/article/pii/S0003491614001596`.

[396] Johannes Hauschild and Frank Pollmann. Efficient numerical simulations with Tensor Networks: Tensor Network Python (TeNPy). *SciPost Phys. Lect. Notes*, page 5, 2018. doi: 10.21468/SciPostPhysLectNotes.5. URL `https://scipost.org/10.21468/SciPostPhysLectNotes.5`.

[397] Luigi Amico, Rosario Fazio, Andreas Osterloh, and Vlatko Vedral. Entanglement in many-body systems. *Rev. Mod. Phys.*, 80:517–576, May 2008. doi: 10.1103/RevModPhys.80.517. URL `https://link.aps.org/doi/10.1103/RevModPhys.80.517`.

[398] J. Eisert, M. Cramer, and M. B. Plenio. Colloquium: Area laws for the entanglement entropy. *Rev. Mod. Phys.*, 82:277–306, Feb 2010. doi: 10.1103/RevModPhys.82.277. URL `https://link.aps.org/doi/10.1103/RevModPhys.82.277`.

[399] Michael M. Wolf, Frank Verstraete, Matthew B. Hastings, and J. Ignacio Cirac. Area laws in quantum systems: Mutual information and correlations. *Phys. Rev. Lett.*, 100:070502, Feb 2008. doi: 10.1103/PhysRevLett.100.070502. URL `https://link.aps.org/doi/10.1103/PhysRevLett.100.070502`.

[400] F. Verstraete and J. I. Cirac. Matrix product states represent ground states faithfully. *Phys. Rev. B*, 73:094423, Mar 2006. doi: 10.1103/PhysRevB.73.094423. URL `https://link.aps.org/doi/10.1103/PhysRevB.73.094423`.

[401] Daniel Gottesman and M B Hastings. Entanglement versus gap for one-dimensional spin systems. *New Journal of Physics*, 12(2):025002, feb 2010. doi: 10.1088/1367-2630/12/2/025002. URL `https://doi.org/10.1088%2F1367-2630%2F12%2F2%2F025002`.

[402] Itai Arad, Zeph Landau, and Umesh Vazirani. Improved one-dimensional area law for frustration-free systems. *Phys. Rev. B*, 85:195145, May 2012. doi: 10.1103/PhysRevB.85.195145. URL `https://link.aps.org/doi/10.1103/PhysRevB.85.195145`.

[403] Itai Arad, Alexei Kitaev, Zeph Landau, and Umesh Vazirani. An area law and sub-exponential algorithm for 1d systems, 2013.

[404] Fernando G. S. L. Brandão and Michał Horodecki. Exponential decay of correlations implies area law. *Communications in Mathematical Physics*, 333(2):761–798, November 2014. doi: 10.1007/s00220-014-2213-8. URL `https://doi.org/10.1007/s00220-014-2213-8`.

[405] Ian Affleck, Tom Kennedy, Elliott H. Lieb, and Hal Tasaki. Rigorous results on valence-bond ground states in antiferromagnets. *Phys. Rev. Lett.*, 59:799–802, Aug 1987. doi: 10.1103/PhysRevLett.59.799. URL `https://link.aps.org/doi/10.1103/PhysRevLett.59.799`.

[406] M. Fannes, B. Nachtergaele, and R. F. Werner. Finitely correlated states on quantum spin chains. *Communications in Mathematical Physics*, 144(3):443–490, March 1992. doi: 10.1007/bf02099178. URL `https://doi.org/10.1007/bf02099178`.

[407] Stellan Östlund and Stefan Rommer. Thermodynamic limit of density matrix renormalization. *Phys. Rev. Lett.*, 75:3537–3540, Nov 1995. doi: 10.1103/PhysRevLett.75.3537. URL `https://link.aps.org/doi/10.1103/PhysRevLett.75.3537`.

[408] Stefan Rommer and Stellan Östlund. Class of ansatz wave functions for one-dimensional spin systems and their relation to the density matrix renormalization group. *Phys. Rev. B*, 55:2164–2181, Jan 1997. doi: 10.1103/PhysRevB.55.2164. URL `https://link.aps.org/doi/10.1103/PhysRevB.55.2164`.

[409] D. Perez-Garcia, F. Verstraete, M. M. Wolf, and J. I. Cirac. Matrix product state representations. 2006.

[410] Norbert Schuch. Condensed matter applications of entanglement theory. 2013.

[411] Norbert Schuch, Michael M. Wolf, Frank Verstraete, and J. Ignacio Cirac. Entropy scaling and simulability by matrix product states. *Phys. Rev. Lett.*, 100:030504, Jan 2008. doi: 10.1103/PhysRevLett.100.030504. URL `https://link.aps.org/doi/10.1103/PhysRevLett.100.030504`.

[412] Tomaž Prosen. Note on a canonical form of matrix product states. *Journal of Physics A: Mathematical and General*, 39(22):L357–L360, may 2006. doi: 10.1088/0305-4470/39/22/l02. URL `https://doi.org/10.1088%2F0305-4470%2F39%2F22%2Fl02`.

[413] G. Vidal. Classical simulation of infinite-size quantum lattice systems in one spatial dimension. *Phys. Rev. Lett.*, 98:070201, Feb 2007. doi: 10.1103/PhysRevLett.98.070201. URL `https://link.aps.org/doi/10.1103/PhysRevLett.98.070201`.

[414] J Dukelsky, M. A Martín-Delgado, T Nishino, and G Sierra. Equivalence of the variational matrix product method and the density matrix renormalization group applied to spin chains. *Europhysics Letters (EPL)*, 43(4):457–462, aug 1998. doi: 10.1209/epl/i1998-00381-x. URL `https://doi.org/10.1209%2Fepl%2Fi1998-00381-x`.

[415] U. Schollwöck. The density-matrix renormalization group. *Rev. Mod. Phys.*, 77:259–315, Apr 2005. doi: 10.1103/RevModPhys.77.259. URL `https://link.aps.org/doi/10.1103/RevModPhys.77.259`.

[416] Ian P McCulloch. From density-matrix renormalization group to matrix product states. *Journal of Statistical Mechanics: Theory and Experiment*, 2007(10):P10014–P10014, oct 2007. doi: 10.1088/1742-5468/2007/10/p10014. URL `https://doi.org/10.1088%2F1742-5468%2F2007%2F10%2Fp10014`.

[417] Guifré Vidal. Efficient classical simulation of slightly entangled quantum computations. *Phys. Rev. Lett.*, 91:147902, Oct 2003. doi: 10.1103/PhysRevLett.91.147902. URL `https://link.aps.org/doi/10.1103/PhysRevLett.91.147902`.

[418] A J Daley, C Kollath, U Schollwöck, and G Vidal. Time-dependent density-matrix renormalization-group using adaptive effective hilbert spaces. *Journal of Statistical Mechanics: Theory and Experiment*, 2004(04):P04005, apr 2004. doi: 10.1088/1742-5468/2004/04/p04005. URL `https://doi.org/10.1088%2F1742-5468%2F2004%2F04%2Fp04005`.

[419] Steven R. White and Adrian E. Feiguin. Real-time evolution using the density matrix renormalization group. *Phys. Rev. Lett.*, 93:076401, Aug 2004. doi: 10.1103/PhysRevLett.93.076401. URL `https://link.aps.org/doi/10.1103/PhysRevLett.93.076401`.

[420] Michael Zwolak and Guifré Vidal. Mixed-state dynamics in one-dimensional quantum lattice systems: A time-dependent superoperator renormalization algorithm. *Phys. Rev. Lett.*, 93:207205, Nov 2004. doi: 10.1103/PhysRevLett.93.207205. URL https://link.aps.org/doi/10.1103/PhysRevLett.93.207205.

[421] F. Verstraete, J. J. García-Ripoll, and J. I. Cirac. Matrix product density operators: Simulation of finite-temperature and dissipative systems. *Phys. Rev. Lett.*, 93:207204, Nov 2004. doi: 10.1103/PhysRevLett.93.207204. URL https://link.aps.org/doi/10.1103/PhysRevLett.93.207204.

[422] M. B. Hastings. Light-cone matrix product. *Journal of Mathematical Physics*, 50 (9):095207, September 2009. doi: 10.1063/1.3149556. URL https://doi.org/10.1063/1.3149556.

[423] Michael P. Zaletel, Roger S. K. Mong, Christoph Karrasch, Joel E. Moore, and Frank Pollmann. Time-evolving a matrix product state with long-ranged interactions. *Phys. Rev. B*, 91:165112, Apr 2015. doi: 10.1103/PhysRevB.91.165112. URL https://link.aps.org/doi/10.1103/PhysRevB.91.165112.

[424] Hale F Trotter. On the product of semi-groups of operators. *Proceedings of the American Mathematical Society*, 10(4):545–551, 1959.

[425] Masuo Suzuki. Generalized trotter's formula and systematic approximants of exponential operators and inner derivations with applications to many-body problems. *Communications in Mathematical Physics*, 51(2):183–190, June 1976. doi: 10.1007/bf01609348. URL https://doi.org/10.1007/bf01609348.

[426] A. Strathearn, P. Kirton, D. Kilda, J. Keeling, and B. W. Lovett. Efficient non-markovian quantum dynamics using time-evolving matrix product operators. *Nature Communications*, 9(1), August 2018. doi: 10.1038/s41467-018-05617-3. URL https://doi.org/10.1038/s41467-018-05617-3.

[427] Shenglong Xu and Brian Swingle. Accessing scrambling using matrix product operators. *Nature Physics*, 16(2):199–204, November 2019. doi: 10.1038/s41567-019-0712-4. URL https://doi.org/10.1038/s41567-019-0712-4.

[428] Christian B. Mendl. Time evolution of matrix product operators with energy conservation, 2018.

[429] Eyal Leviatan, Frank Pollmann, Jens H. Bardarson, David A. Huse, and Ehud Altman. Quantum thermalization dynamics with matrix-product states, 2017.

[430] Benedikt Kloss, Yevgeny Bar Lev, and David Reichman. Time-dependent variational principle in matrix-product state manifolds: Pitfalls and potential. *Phys. Rev. B*, 97:024307, Jan 2018. doi: 10.1103/PhysRevB.97.024307. URL https://link.aps.org/doi/10.1103/PhysRevB.97.024307.

[431] Bingtian Ye, Francisco Machado, Christopher David White, Roger S. K. Mong, and Norman Y. Yao. Emergent hydrodynamics in floquet quantum systems, 2019.

[432] Immanuel Bloch, Jean Dalibard, and Wilhelm Zwerger. Many-body physics with ultracold gases. *Rev. Mod. Phys.*, 80:885–964, Jul 2008. doi: 10.1103/RevModPhys.80.885. URL https://link.aps.org/doi/10.1103/RevModPhys.80.885.

[433] Tim Langen, Remi Geiger, and Jörg Schmiedmayer. Ultracold atoms out of equilibrium. *Annual Review of Condensed Matter Physics*, 6(1):201–217, March 2015. doi:

10.1146/annurev-conmatphys-031214-014548. URL https://doi.org/10.1146/annurev-conmatphys-031214-014548.

[434] B. P. Lanyon, C. Hempel, D. Nigg, M. Müller, R. Gerritsma, F. Zähringer, P. Schindler, J. T. Barreiro, M. Rambach, G. Kirchmair, M. Hennrich, P. Zoller, R. Blatt, and C. F. Roos. Universal digital quantum simulation with trapped ions. *Science*, 334(6052):57–61, 2011. ISSN 0036-8075. doi: 10.1126/science.1208001. URL https://science.sciencemag.org/content/334/6052/57.

[435] Markus Greiner, Olaf Mandel, Theodor W. Hänsch, and Immanuel Bloch. Collapse and revival of the matter wave field of a bose–einstein condensate. *Nature*, 419 (6902):51–54, September 2002. doi: 10.1038/nature00968. URL https://doi.org/10.1038/nature00968.

[436] S. Hofferberth, I. Lesanovsky, B. Fischer, T. Schumm, and J. Schmiedmayer. Non-equilibrium coherence dynamics in one-dimensional bose gases. *Nature*, 449(7160): 324–327, September 2007. doi: 10.1038/nature06149. URL https://doi.org/10.1038/nature06149.

[437] Yijun Tang, Wil Kao, Kuan-Yu Li, Sangwon Seo, Krishnanand Mallayya, Marcos Rigol, Sarang Gopalakrishnan, and Benjamin L. Lev. Thermalization near integrability in a dipolar quantum newton's cradle. *Phys. Rev. X*, 8:021030, May 2018. doi: 10.1103/PhysRevX.8.021030. URL https://link.aps.org/doi/10.1103/PhysRevX.8.021030.

[438] M. Gring, M. Kuhnert, T. Langen, T. Kitagawa, B. Rauer, M. Schreitl, I. Mazets, D. Adu Smith, E. Demler, and J. Schmiedmayer. Relaxation and prethermalization in an isolated quantum system. *Science*, 337(6100):1318–1322, 2012. ISSN 0036-8075. doi: 10.1126/science.1224953. URL https://science.sciencemag.org/content/337/6100/1318.

[439] T. Langen, R. Geiger, M. Kuhnert, B. Rauer, and J. Schmiedmayer. Local emergence of thermal correlations in an isolated quantum many-body system. *Nature Physics*, 9(10):640–643, September 2013. doi: 10.1038/nphys2739. URL https://doi.org/10.1038/nphys2739.

[440] Tim Langen, Sebastian Erne, Remi Geiger, Bernhard Rauer, Thomas Schweigler, Maximilian Kuhnert, Wolfgang Rohringer, Igor E. Mazets, Thomas Gasenzer, and Jörg Schmiedmayer. Experimental observation of a generalized gibbs ensemble. *Science*, 348(6231):207–211, 2015. ISSN 0036-8075. doi: 10.1126/science.1257026. URL https://science.sciencemag.org/content/348/6231/207.

[441] Immanuel Bloch. Ultracold quantum gases in optical lattices. *Nature Physics*, 1(1): 23–30, October 2005. doi: 10.1038/nphys138. URL https://doi.org/10.1038/nphys138.

[442] Markus Greiner and Simon Fölling. Optical lattices. *Nature*, 453(7196):736–738, June 2008. doi: 10.1038/453736a. URL https://doi.org/10.1038/453736a.

[443] L.-M. Duan, E. Demler, and M. D. Lukin. Controlling spin exchange interactions of ultracold atoms in optical lattices. *Phys. Rev. Lett.*, 91:090402, Aug 2003. doi: 10.1103/PhysRevLett.91.090402. URL https://link.aps.org/doi/10.1103/PhysRevLett.91.090402.

[444] Jonathan Simon, Waseem S. Bakr, Ruichao Ma, M. Eric Tai, Philipp M. Preiss, and Markus Greiner. Quantum simulation of antiferromagnetic spin chains in an optical lattice. *Nature*, 472(7343):307–312, April 2011. doi: 10.1038/nature09994. URL https://doi.org/10.1038/nature09994.

[445] K. Kim, M.-S. Chang, S. Korenblit, R. Islam, E. E. Edwards, J. K. Freericks, G.-D. Lin, L.-M. Duan, and C. Monroe. Quantum simulation of frustrated ising spins with trapped ions. *Nature*, 465(7298):590–593, June 2010. doi: 10.1038/nature09071. URL https://doi.org/10.1038/nature09071.

[446] Waseem S. Bakr, Jonathon I. Gillen, Amy Peng, Simon Fölling, and Markus Greiner. A quantum gas microscope for detecting single atoms in a hubbard-regime optical lattice. *Nature*, 462(7269):74–77, November 2009. doi: 10.1038/nature08482. URL https://doi.org/10.1038/nature08482.

[447] Jacob F. Sherson, Christof Weitenberg, Manuel Endres, Marc Cheneau, Immanuel Bloch, and Stefan Kuhr. Single-atom-resolved fluorescence imaging of an atomic mott insulator. *Nature*, 467(7311):68–72, August 2010. doi: 10.1038/nature09378. URL https://doi.org/10.1038/nature09378.

[448] Herwig Ott. Single atom detection in ultracold quantum gases: a review of current progress. *Reports on Progress in Physics*, 79(5):054401, apr 2016. doi: 10.1088/0034-4885/79/5/054401. URL https://doi.org/10.1088%2F0034-4885%2F79%2F5%2F054401.

[449] Stefan Kuhr. Quantum-gas microscopes: a new tool for cold-atom quantum simulators. *National Science Review*, 3(2):170–172, April 2016. doi: 10.1093/nsr/nww023. URL https://doi.org/10.1093/nsr/nww023.

[450] Manuel Endres, Hannes Bernien, Alexander Keesling, Harry Levine, Eric R. Anschuetz, Alexandre Krajenbrink, Crystal Senko, Vladan Vuletic, Markus Greiner, and Mikhail D. Lukin. Atom-by-atom assembly of defect-free one-dimensional cold atom arrays. *Science*, 354(6315):1024–1027, 2016. ISSN 0036-8075. doi: 10.1126/science.aah3752. URL https://science.sciencemag.org/content/354/6315/1024.

[451] Daniel Barredo, Sylvain de Léséleuc, Vincent Lienhard, Thierry Lahaye, and Antoine Browaeys. An atom-by-atom assembler of defect-free arbitrary two-dimensional atomic arrays. *Science*, 354(6315):1021–1023, 2016. ISSN 0036-8075. doi: 10.1126/science.aah3778. URL https://science.sciencemag.org/content/354/6315/1021.

[452] Marc Cheneau, Peter Barmettler, Dario Poletti, Manuel Endres, Peter Schauß, Takeshi Fukuhara, Christian Gross, Immanuel Bloch, Corinna Kollath, and Stefan Kuhr. Light-cone-like spreading of correlations in a quantum many-body system. *Nature*, 481(7382):484–487, January 2012. doi: 10.1038/nature10748. URL https://doi.org/10.1038/nature10748.

[453] Sebastian Hild, Takeshi Fukuhara, Peter Schauß, Johannes Zeiher, Michael Knap, Eugene Demler, Immanuel Bloch, and Christian Gross. Far-from-equilibrium spin transport in heisenberg quantum magnets. *Phys. Rev. Lett.*, 113:147205, Oct 2014. doi: 10.1103/PhysRevLett.113.147205. URL https://link.aps.org/doi/10.1103/PhysRevLett.113.147205.

[454] P. Jurcevic, B. P. Lanyon, P. Hauke, C. Hempel, P. Zoller, R. Blatt, and C. F. Roos. Quasiparticle engineering and entanglement propagation in a quantum many-body system. *Nature*, 511(7508):202–205, July 2014. doi: 10.1038/nature13461. URL https://doi.org/10.1038/nature13461.

[455] Elmer Guardado-Sanchez, Peter T. Brown, Debayan Mitra, Trithep Devakul, David A. Huse, Peter Schauß, and Waseem S. Bakr. Probing the quench dynamics of antiferromagnetic correlations in a 2d quantum ising spin system. *Phys. Rev. X*, 8:021069, Jun 2018. doi: 10.1103/PhysRevX.8.021069. URL https://link.aps.org/doi/10.1103/PhysRevX.8.021069.

[456] Ulrich Schneider, Lucia Hackermüller, Jens Philipp Ronzheimer, Sebastian Will, Simon Braun, Thorsten Best, Immanuel Bloch, Eugene Demler, Stephan Mandt, David Rasch, and Achim Rosch. Fermionic transport and out-of-equilibrium dynamics in a homogeneous hubbard model with ultracold atoms. *Nature Physics*, 8 (3):213–218, January 2012. doi: 10.1038/nphys2205. URL https://doi.org/10.1038/nphys2205.

[457] J. P. Ronzheimer, M. Schreiber, S. Braun, S. S. Hodgman, S. Langer, I. P. McCulloch, F. Heidrich-Meisner, I. Bloch, and U. Schneider. Expansion dynamics of interacting bosons in homogeneous lattices in one and two dimensions. *Phys. Rev. Lett.*, 110:205301, May 2013. doi: 10.1103/PhysRevLett.110.205301. URL https://link.aps.org/doi/10.1103/PhysRevLett.110.205301.

[458] Matthew A. Nichols, Lawrence W. Cheuk, Melih Okan, Thomas R. Hartke, Enrique Mendez, T. Senthil, Ehsan Khatami, Hao Zhang, and Martin W. Zwierlein. Spin transport in a mott insulator of ultracold fermions. *Science*, 363(6425):383–387, 2019. ISSN 0036-8075. doi: 10.1126/science.aat4387. URL https://science.sciencemag.org/content/363/6425/383.

[459] Peter T. Brown, Debayan Mitra, Elmer Guardado-Sanchez, Reza Nourafkan, Alexis Reymbaut, Charles-David Hébert, Simon Bergeron, A.-M. S. Tremblay, Jure Kokalj, David A. Huse, Peter Schauß, and Waseem S. Bakr. Bad metallic transport in a cold atom fermi-hubbard system. *Science*, 363(6425):379–382, 2019. ISSN 0036-8075. doi: 10.1126/science.aat4134. URL https://science.sciencemag.org/content/363/6425/379.

[460] J. Smith, A. Lee, P. Richerme, B. Neyenhuis, P. W. Hess, P. Hauke, M. Heyl, D. A. Huse, and C. Monroe. Many-body localization in a quantum simulator with programmable random disorder. *Nature Physics*, 12(10):907–911, June 2016. doi: 10.1038/nphys3783. URL https://doi.org/10.1038/nphys3783.

[461] Pranjal Bordia, Henrik P. Lüschen, Sean S. Hodgman, Michael Schreiber, Immanuel Bloch, and Ulrich Schneider. Coupling identical one-dimensional many-body localized systems. *Phys. Rev. Lett.*, 116:140401, Apr 2016. doi: 10.1103/PhysRevLett.116.140401. URL http://link.aps.org/doi/10.1103/PhysRevLett.116.140401.

[462] R. J. Lewis-Swan, A. Safavi-Naini, A. M. Kaufman, and A. M. Rey. Dynamics of quantum information. *Nature Reviews Physics*, 1(10):627–634, August 2019. doi: 10.1038/s42254-019-0090-y. URL https://doi.org/10.1038/s42254-019-0090-y.

[463] Matthew B. Hastings, Iván González, Ann B. Kallin, and Roger G. Melko. Measuring renyi entanglement entropy in quantum monte carlo simulations. *Phys. Rev. Lett.*, 104:157201, Apr 2010. doi: 10.1103/PhysRevLett.104.157201. URL https://link.aps.org/doi/10.1103/PhysRevLett.104.157201.

[464] Dmitry A. Abanin and Eugene Demler. Measuring entanglement entropy of a generic many-body system with a quantum switch. *Phys. Rev. Lett.*, 109:020504, Jul 2012. doi: 10.1103/PhysRevLett.109.020504. URL `https://link.aps.org/doi/10.1103/PhysRevLett.109.020504`.

[465] Alexander Lukin, Matthew Rispoli, Robert Schittko, M. Eric Tai, Adam M. Kaufman, Soonwon Choi, Vedika Khemani, Julian Léonard, and Markus Greiner. Probing entanglement in a many-body–localized system. *Science*, 364(6437):256–260, 2019. ISSN 0036-8075. doi: 10.1126/science.aau0818. URL `https://science.sciencemag.org/content/364/6437/256`.

[466] Brian Swingle, Gregory Bentsen, Monika Schleier-Smith, and Patrick Hayden. Measuring the scrambling of quantum information. *Phys. Rev. A*, 94:040302, Oct 2016. doi: 10.1103/PhysRevA.94.040302. URL `https://link.aps.org/doi/10.1103/PhysRevA.94.040302`.

[467] Martin Gärttner, Justin G. Bohnet, Arghavan Safavi-Naini, Michael L. Wall, John J. Bollinger, and Ana Maria Rey. Measuring out-of-time-order correlations and multiple quantum spectra in a trapped-ion quantum magnet. *Nature Physics*, 13(8): 781–786, May 2017. doi: 10.1038/nphys4119. URL `https://doi.org/10.1038/nphys4119`.

[468] K. A. Landsman, C. Figgatt, T. Schuster, N. M. Linke, B. Yoshida, N. Y. Yao, and C. Monroe. Verified quantum information scrambling. *Nature*, 567(7746):61–65, March 2019. doi: 10.1038/s41586-019-0952-6. URL `https://doi.org/10.1038/s41586-019-0952-6`.

[469] A. Elben, B. Vermersch, M. Dalmonte, J. I. Cirac, and P. Zoller. Rényi entropies from random quenches in atomic hubbard and spin models. *Phys. Rev. Lett.*, 120: 050406, Feb 2018. doi: 10.1103/PhysRevLett.120.050406. URL `https://link.aps.org/doi/10.1103/PhysRevLett.120.050406`.

[470] B. Vermersch, A. Elben, L. M. Sieberer, N. Y. Yao, and P. Zoller. Probing scrambling using statistical correlations between randomized measurements. *Phys. Rev. X*, 9: 021061, Jun 2019. doi: 10.1103/PhysRevX.9.021061. URL `https://link.aps.org/doi/10.1103/PhysRevX.9.021061`.

[471] Manoj K. Joshi, Andreas Elben, Benoît Vermersch, Tiff Brydges, Christine Maier, Peter Zoller, Rainer Blatt, and Christian F. Roos. Quantum information scrambling in a trapped-ion quantum simulator with tunable range interactions, 2020.

[472] T. L. Nguyen, J. M. Raimond, C. Sayrin, R. Cortiñas, T. Cantat-Moltrecht, F. Assemat, I. Dotsenko, S. Gleyzes, S. Haroche, G. Roux, Th. Jolicoeur, and M. Brune. Towards quantum simulation with circular rydberg atoms. *Phys. Rev. X*, 8:011032, Feb 2018. doi: 10.1103/PhysRevX.8.011032. URL `https://link.aps.org/doi/10.1103/PhysRevX.8.011032`.

[473] Hannes Bernien, Sylvain Schwartz, Alexander Keesling, Harry Levine, Ahmed Omran, Hannes Pichler, Soonwon Choi, Alexander S. Zibrov, Manuel Endres, Markus Greiner, Vladan Vuletić, and Mikhail D. Lukin. Probing many-body dynamics on a 51-atom quantum simulator. *Nature*, 551(7682):579–584, November 2017. doi: 10.1038/nature24622. URL `https://doi.org/10.1038/nature24622`.

[474] C. J. Turner, A. A. Michailidis, D. A. Abanin, M. Serbyn, and Z. Papić. Weak ergodicity breaking from quantum many-body scars. *Nature Physics*, 14(7):745–749, May 2018. doi: 10.1038/s41567-018-0137-5. URL `https://doi.org/10.1038/s41567-018-0137-5`.

[475] C. J. Turner, A. A. Michailidis, D. A. Abanin, M. Serbyn, and Z. Papić. Quantum scarred eigenstates in a rydberg atom chain: Entanglement, breakdown of thermalization, and stability to perturbations. *Phys. Rev. B*, 98:155134, Oct 2018. doi: 10.1103/PhysRevB.98.155134. URL `https://link.aps.org/doi/10.1103/PhysRevB.98.155134`.

[476] L. Childress, M. V. Gurudev Dutt, J. M. Taylor, A. S. Zibrov, F. Jelezko, J. Wrachtrup, P. R. Hemmer, and M. D. Lukin. Coherent dynamics of coupled electron and nuclear spin qubits in diamond. *Science*, 314(5797):281–285, 2006. ISSN 0036-8075. doi: 10.1126/science.1131871. URL `https://science.sciencemag.org/content/314/5797/281`.

[477] P. Cappellaro, C. Ramanathan, and D. G. Cory. Simulations of information transport in spin chains. *Phys. Rev. Lett.*, 99:250506, Dec 2007. doi: 10.1103/PhysRevLett.99.250506. URL `https://link.aps.org/doi/10.1103/PhysRevLett.99.250506`.

[478] Ken Xuan Wei, Chandrasekhar Ramanathan, and Paola Cappellaro. Exploring localization in nuclear spin chains. *Phys. Rev. Lett.*, 120:070501, Feb 2018. doi: 10.1103/PhysRevLett.120.070501. URL `https://link.aps.org/doi/10.1103/PhysRevLett.120.070501`.

[479] Jared Rovny, Robert L. Blum, and Sean E. Barrett. Observation of discrete-time-crystal signatures in an ordered dipolar many-body system. *Phys. Rev. Lett.*, 120:180603, May 2018. doi: 10.1103/PhysRevLett.120.180603. URL `https://link.aps.org/doi/10.1103/PhysRevLett.120.180603`.

[480] Soham Pal, Naveen Nishad, T. S. Mahesh, and G. J. Sreejith. Temporal order in periodically driven spins in star-shaped clusters. *Phys. Rev. Lett.*, 120:180602, May 2018. doi: 10.1103/PhysRevLett.120.180602. URL `https://link.aps.org/doi/10.1103/PhysRevLett.120.180602`.

[481] Jun Li, Ruihua Fan, Hengyan Wang, Bingtian Ye, Bei Zeng, Hui Zhai, Xinhua Peng, and Jiangfeng Du. Measuring out-of-time-order correlators on a nuclear magnetic resonance quantum simulator. *Phys. Rev. X*, 7:031011, Jul 2017. doi: 10.1103/PhysRevX.7.031011. URL `https://link.aps.org/doi/10.1103/PhysRevX.7.031011`.

[482] M. V. Gurudev Dutt, L. Childress, L. Jiang, E. Togan, J. Maze, F. Jelezko, A. S. Zibrov, P. R. Hemmer, and M. D. Lukin. Quantum register based on individual electronic and nuclear spin qubits in diamond. *Science*, 316(5829):1312–1316, 2007. ISSN 0036-8075. doi: 10.1126/science.1139831. URL `https://science.sciencemag.org/content/316/5829/1312`.

[483] P. L. Stanwix, L. M. Pham, J. R. Maze, D. Le Sage, T. K. Yeung, P. Cappellaro, P. R. Hemmer, A. Yacoby, M. D. Lukin, and R. L. Walsworth. Coherence of nitrogen-vacancy electronic spin ensembles in diamond. *Phys. Rev. B*, 82:201201, Nov 2010. doi: 10.1103/PhysRevB.82.201201. URL `https://link.aps.org/doi/10.1103/PhysRevB.82.201201`.

[484] Gopalakrishnan Balasubramanian, Philipp Neumann, Daniel Twitchen, Matthew Markham, Roman Kolesov, Norikazu Mizuochi, Junichi Isoya, Jocelyn Achard, Johannes Beck, Julia Tissler, Vincent Jacques, Philip R. Hemmer, Fedor Jelezko, and Jörg Wrachtrup. Ultralong spin coherence time in isotopically engineered diamond. *Nature Materials*, 8(5):383–387, April 2009. doi: 10.1038/nmat2420. URL `https://doi.org/10.1038/nmat2420`.

[485] Joonhee Choi, Soonwon Choi, Georg Kucsko, Peter C. Maurer, Brendan J. Shields, Hitoshi Sumiya, Shinobu Onoda, Junichi Isoya, Eugene Demler, Fedor Jelezko, Norman Y. Yao, and Mikhail D. Lukin. Depolarization dynamics in a strongly interacting solid-state spin ensemble. *Phys. Rev. Lett.*, 118:093601, Mar 2017. doi: 10.1103/PhysRevLett.118.093601. URL `https://link.aps.org/doi/10.1103/PhysRevLett.118.093601`.

[486] G. Kucsko, S. Choi, J. Choi, P. C. Maurer, H. Zhou, R. Landig, H. Sumiya, S. Onoda, J. Isoya, F. Jelezko, E. Demler, N. Y. Yao, and M. D. Lukin. Critical thermalization of a disordered dipolar spin system in diamond. *Phys. Rev. Lett.*, 121:023601, Jul 2018. doi: 10.1103/PhysRevLett.121.023601. URL `https://link.aps.org/doi/10.1103/PhysRevLett.121.023601`.

[487] J. I. Cirac and P. Zoller. Quantum computations with cold trapped ions. *Phys. Rev. Lett.*, 74:4091–4094, May 1995. doi: 10.1103/PhysRevLett.74.4091. URL `https://link.aps.org/doi/10.1103/PhysRevLett.74.4091`.

[488] D. Kielpinski, C. Monroe, and D. J. Wineland. Architecture for a large-scale ion-trap quantum computer. *Nature*, 417(6890):709–711, June 2002. doi: 10.1038/nature00784. URL `https://doi.org/10.1038/nature00784`.

[489] Rainer Blatt and David Wineland. Entangled states of trapped atomic ions. *Nature*, 453(7198):1008–1015, June 2008. doi: 10.1038/nature07125. URL `https://doi.org/10.1038/nature07125`.

[490] C. Monroe and J. Kim. Scaling the ion trap quantum processor. *Science*, 339(6124):1164–1169, 2013. ISSN 0036-8075. doi: 10.1126/science.1231298. URL `https://science.sciencemag.org/content/339/6124/1164`.

[491] Colin D. Bruzewicz, John Chiaverini, Robert McConnell, and Jeremy M. Sage. Trapped-ion quantum computing: Progress and challenges. *Applied Physics Reviews*, 6(2):021314, June 2019. doi: 10.1063/1.5088164. URL `https://doi.org/10.1063/1.5088164`.

[492] C. Monroe, D. M. Meekhof, B. E. King, W. M. Itano, and D. J. Wineland. Demonstration of a fundamental quantum logic gate. *Phys. Rev. Lett.*, 75:4714–4717, Dec 1995. doi: 10.1103/PhysRevLett.75.4714. URL `https://link.aps.org/doi/10.1103/PhysRevLett.75.4714`.

[493] Q. A. Turchette, C. S. Wood, B. E. King, C. J. Myatt, D. Leibfried, W. M. Itano, C. Monroe, and D. J. Wineland. Deterministic entanglement of two trapped ions. *Phys. Rev. Lett.*, 81:3631–3634, Oct 1998. doi: 10.1103/PhysRevLett.81.3631. URL `https://link.aps.org/doi/10.1103/PhysRevLett.81.3631`.

[494] D. Kielpinski, V. Meyer, M. A. Rowe, C. A. Sackett, W. M. Itano, C. Monroe, and D. J. Wineland. A decoherence-free quantum memory using trapped ions. *Science*, 291(5506):1013–1015, 2001. ISSN 0036-8075. doi: 10.1126/science.1057357. URL `https://science.sciencemag.org/content/291/5506/1013`.

[495] Ferdinand Schmidt-Kaler, Hartmut Häffner, Mark Riebe, Stephan Gulde, Gavin P. T. Lancaster, Thomas Deuschle, Christoph Becher, Christian F. Roos, Jürgen Eschner, and Rainer Blatt. Realization of the cirac–zoller controlled-NOT quantum gate. *Nature*, 422(6930):408–411, March 2003. doi: 10.1038/nature01494. URL `https://doi.org/10.1038/nature01494`.

[496] Jonathan P. Home, David Hanneke, John D. Jost, Jason M. Amini, Dietrich Leibfried, and David J. Wineland. Complete methods set for scalable ion trap quantum information processing. *Science*, 325(5945):1227–1230, 2009. ISSN 0036-8075. doi: 10.1126/science.1177077. URL `https://science.sciencemag.org/content/325/5945/1227`.

[497] Norbert M. Linke, Dmitri Maslov, Martin Roetteler, Shantanu Debnath, Caroline Figgatt, Kevin A. Landsman, Kenneth Wright, and Christopher Monroe. Experimental comparison of two quantum computing architectures. *Proceedings of the National Academy of Sciences*, 114(13):3305–3310, 2017. ISSN 0027-8424. doi: 10.1073/pnas.1618020114. URL `https://www.pnas.org/content/114/13/3305`.

[498] Ye Wang, Mark Um, Junhua Zhang, Shuoming An, Ming Lyu, Jing-Ning Zhang, L.-M. Duan, Dahyun Yum, and Kihwan Kim. Single-qubit quantum memory exceeding ten-minute coherence time. *Nature Photonics*, 11(10):646–650, September 2017. doi: 10.1038/s41566-017-0007-1. URL `https://doi.org/10.1038/s41566-017-0007-1`.

[499] Y. Nakamura, Yu. A. Pashkin, and J. S. Tsai. Coherent control of macroscopic quantum states in a single-cooper-pair box. *Nature*, 398(6730):786–788, April 1999. doi: 10.1038/19718. URL `https://doi.org/10.1038/19718`.

[500] Max Hofheinz, H. Wang, M. Ansmann, Radoslaw C. Bialczak, Erik Lucero, M. Neeley, A. D. O'Connell, D. Sank, J. Wenner, John M. Martinis, and A. N. Cleland. Synthesizing arbitrary quantum states in a superconducting resonator. *Nature*, 459(7246):546–549, May 2009. doi: 10.1038/nature08005. URL `https://doi.org/10.1038/nature08005`.

[501] Matthew Neeley, Radoslaw C. Bialczak, M. Lenander, E. Lucero, Matteo Mariantoni, A. D. O'Connell, D. Sank, H. Wang, M. Weides, J. Wenner, Y. Yin, T. Yamamoto, A. N. Cleland, and John M. Martinis. Generation of three-qubit entangled states using superconducting phase qubits. *Nature*, 467(7315):570–573, September 2010. doi: 10.1038/nature09418. URL `https://doi.org/10.1038/nature09418`.

[502] Matteo Mariantoni, H. Wang, T. Yamamoto, M. Neeley, Radoslaw C. Bialczak, Y. Chen, M. Lenander, Erik Lucero, A. D. O'Connell, D. Sank, M. Weides, J. Wenner, Y. Yin, J. Zhao, A. N. Korotkov, A. N. Cleland, and John M. Martinis. Implementing the quantum von neumann architecture with superconducting circuits. *Science*, 334(6052):61–65, 2011. ISSN 0036-8075. doi: 10.1126/science.1208517. URL `https://science.sciencemag.org/content/334/6052/61`.

[503] R. Barends, J. Kelly, A. Megrant, D. Sank, E. Jeffrey, Y. Chen, Y. Yin, B. Chiaro, J. Mutus, C. Neill, P. O'Malley, P. Roushan, J. Wenner, T. C. White, A. N. Cleland, and John M. Martinis. Coherent josephson qubit suitable for scalable quantum integrated circuits. *Phys. Rev. Lett.*, 111:080502, Aug 2013. doi: 10.1103/PhysRevLett.111.080502. URL `https://link.aps.org/doi/10.1103/PhysRevLett.111.080502`.

[504] R. Barends, J. Kelly, A. Megrant, A. Veitia, D. Sank, E. Jeffrey, T. C. White, J. Mutus, A. G. Fowler, B. Campbell, Y. Chen, Z. Chen, B. Chiaro, A. Dunsworth, C. Neill, P. O'Malley, P. Roushan, A. Vainsencher, J. Wenner, A. N. Korotkov, A. N. Cleland, and John M. Martinis. Superconducting quantum circuits at the surface code threshold for fault tolerance. *Nature*, 508(7497):500–503, April 2014. doi: 10.1038/nature13171. URL `https://doi.org/10.1038/nature13171`.

[505] J. Kelly, R. Barends, A. G. Fowler, A. Megrant, E. Jeffrey, T. C. White, D. Sank, J. Y. Mutus, B. Campbell, Yu Chen, Z. Chen, B. Chiaro, A. Dunsworth, I.-C. Hoi, C. Neill, P. J. J. O'Malley, C. Quintana, P. Roushan, A. Vainsencher, J. Wenner, A. N. Cleland, and John M. Martinis. State preservation by repetitive error detection in a superconducting quantum circuit. *Nature*, 519(7541):66–69, March 2015. doi: 10.1038/nature14270. URL `https://doi.org/10.1038/nature14270`.

[506] Nissim Ofek, Andrei Petrenko, Reinier Heeres, Philip Reinhold, Zaki Leghtas, Brian Vlastakis, Yehan Liu, Luigi Frunzio, S. M. Girvin, L. Jiang, Mazyar Mirrahimi, M. H. Devoret, and R. J. Schoelkopf. Extending the lifetime of a quantum bit with error correction in superconducting circuits. *Nature*, 536(7617):441–445, July 2016. doi: 10.1038/nature18949. URL `https://doi.org/10.1038/nature18949`.

[507] Jay M. Gambetta, Jerry M. Chow, and Matthias Steffen. Building logical qubits in a superconducting quantum computing system. *npj Quantum Information*, 3(1), January 2017. doi: 10.1038/s41534-016-0004-0. URL `https://doi.org/10.1038/s41534-016-0004-0`.

[508] S. Rosenblum, Y. Y. Gao, P. Reinhold, C. Wang, C. J. Axline, L. Frunzio, S. M. Girvin, Liang Jiang, M. Mirrahimi, M. H. Devoret, and R. J. Schoelkopf. A CNOT gate between multiphoton qubits encoded in two cavities. *Nature Communications*, 9(1), February 2018. doi: 10.1038/s41467-018-03059-5. URL `https://doi.org/10.1038/s41467-018-03059-5`.

[509] L. Hu, Y. Ma, W. Cai, X. Mu, Y. Xu, W. Wang, Y. Wu, H. Wang, Y. P. Song, C.-L. Zou, S. M. Girvin, L-M. Duan, and L. Sun. Quantum error correction and universal gate set operation on a binomial bosonic logical qubit. *Nature Physics*, 15 (5):503–508, February 2019. doi: 10.1038/s41567-018-0414-3. URL `https://doi.org/10.1038/s41567-018-0414-3`.

[510] M. H. Devoret and R. J. Schoelkopf. Superconducting circuits for quantum information: An outlook. *Science*, 339(6124):1169–1174, 2013. ISSN 0036-8075. doi: 10.1126/science.1231930. URL `https://science.sciencemag.org/content/339/6124/1169`.

[511] G Wendin. Quantum information processing with superconducting circuits: a review. *Reports on Progress in Physics*, 80(10):106001, September 2017. doi: 10.1088/1361-6633/aa7e1a. URL `https://doi.org/10.1088/1361-6633/aa7e1a`.

[512] Morten Kjaergaard, Mollie E. Schwartz, Jochen Braumüller, Philip Krantz, Joel I.-J. Wang, Simon Gustavsson, and William D. Oliver. Superconducting qubits: Current state of play. *Annual Review of Condensed Matter Physics*, 11(1):369–395, March 2020. doi: 10.1146/annurev-conmatphys-031119-050605. URL `https://doi.org/10.1146/annurev-conmatphys-031119-050605`.

[513] Aram W. Harrow and Ashley Montanaro. Quantum computational supremacy. *Nature*, 549(7671):203–209, September 2017. doi: 10.1038/nature23458. URL `https://doi.org/10.1038/nature23458`.

[514] Sergio Boixo, Sergei V. Isakov, Vadim N. Smelyanskiy, Ryan Babbush, Nan Ding, Zhang Jiang, Michael J. Bremner, John M. Martinis, and Hartmut Neven. Characterizing quantum supremacy in near-term devices. *Nature Physics*, 14(6):595–600, April 2018. doi: 10.1038/s41567-018-0124-x. URL `https://doi.org/10.1038/s41567-018-0124-x`.

[515] C. Neill, P. Roushan, K. Kechedzhi, S. Boixo, S. V. Isakov, V. Smelyanskiy, A. Megrant, B. Chiaro, A. Dunsworth, K. Arya, R. Barends, B. Burkett, Y. Chen, Z. Chen, A. Fowler, B. Foxen, M. Giustina, R. Graff, E. Jeffrey, T. Huang, J. Kelly, P. Klimov, E. Lucero, J. Mutus, M. Neeley, C. Quintana, D. Sank, A. Vainsencher, J. Wenner, T. C. White, H. Neven, and J. M. Martinis. A blueprint for demonstrating quantum supremacy with superconducting qubits. *Science*, 360(6385):195–199, 2018. ISSN 0036-8075. doi: 10.1126/science.aao4309. URL `https://science.sciencemag.org/content/360/6385/195`.

[516] Andrew A. Houck, Hakan E. Türeci, and Jens Koch. On-chip quantum simulation with superconducting circuits. *Nature Physics*, 8(4):292–299, April 2012. doi: 10.1038/nphys2251. URL `https://doi.org/10.1038/nphys2251`.

[517] P. Roushan, C. Neill, J. Tangpanitanon, V. M. Bastidas, A. Megrant, R. Barends, Y. Chen, Z. Chen, B. Chiaro, A. Dunsworth, A. Fowler, B. Foxen, M. Giustina, E. Jeffrey, J. Kelly, E. Lucero, J. Mutus, M. Neeley, C. Quintana, D. Sank, A. Vainsencher, J. Wenner, T. White, H. Neven, D. G. Angelakis, and J. Martinis. Spectroscopic signatures of localization with interacting photons in superconducting qubits. *Science*, 358(6367):1175–1179, 2017. ISSN 0036-8075. doi: 10.1126/science.aao1401. URL `https://science.sciencemag.org/content/358/6367/1175`.

[518] Kai Xu, Jin-Jun Chen, Yu Zeng, Yu-Ran Zhang, Chao Song, Wuxin Liu, Qiujiang Guo, Pengfei Zhang, Da Xu, Hui Deng, Keqiang Huang, H. Wang, Xiaobo Zhu, Dongning Zheng, and Heng Fan. Emulating many-body localization with a superconducting quantum processor. *Phys. Rev. Lett.*, 120:050507, Feb 2018. doi: 10.1103/PhysRevLett.120.050507. URL `https://link.aps.org/doi/10.1103/PhysRevLett.120.050507`.

[519] Daniel Loss and David P. DiVincenzo. Quantum computation with quantum dots. *Phys. Rev. A*, 57:120–126, Jan 1998. doi: 10.1103/PhysRevA.57.120. URL `https://link.aps.org/doi/10.1103/PhysRevA.57.120`.

[520] J. R. Petta, A. C. Johnson, J. M. Taylor, E. A. Laird, A. Yacoby, M. D. Lukin, C. M. Marcus, M. P. Hanson, and A. C. Gossard. Coherent manipulation of coupled electron spins in semiconductor quantum dots. *Science*, 309 (5744):2180–2184, 2005. ISSN 0036-8075. doi: 10.1126/science.1116955. URL `https://science.sciencemag.org/content/309/5744/2180`.

[521] B. E. Kane. A silicon-based nuclear spin quantum computer. *Nature*, 393(6681): 133–137, May 1998. doi: 10.1038/30156. URL `https://doi.org/10.1038/30156`.

[522] Ronald Hanson and David D. Awschalom. Coherent manipulation of single spins in semiconductors. *Nature*, 453(7198):1043–1049, June 2008. doi: 10.1038/nature07129. URL `https://doi.org/10.1038/nature07129`.

[523] E. Knill, R. Laflamme, and G. J. Milburn. A scheme for efficient quantum computation with linear optics. *Nature*, 409(6816):46–52, January 2001. doi: 10.1038/35051009. URL `https://doi.org/10.1038/35051009`.

[524] Robert Raussendorf and Hans J. Briegel. A one-way quantum computer. *Phys. Rev. Lett.*, 86:5188–5191, May 2001. doi: 10.1103/PhysRevLett.86.5188. URL https://link.aps.org/doi/10.1103/PhysRevLett.86.5188.

[525] Antonio Acín, Immanuel Bloch, Harry Buhrman, Tommaso Calarco, Christopher Eichler, Jens Eisert, Daniel Esteve, Nicolas Gisin, Steffen J Glaser, Fedor Jelezko, Stefan Kuhr, Maciej Lewenstein, Max F Riedel, Piet O Schmidt, Rob Thew, Andreas Wallraff, Ian Walmsley, and Frank K Wilhelm. The quantum technologies roadmap: a european community view. *New Journal of Physics*, 20(8):080201, aug 2018. doi: 10.1088/1367-2630/aad1ea. URL https://doi.org/10.1088%2F1367-2630%2Faad1ea.

[526] Lukas M. Sieberer, Tobias Olsacher, Andreas Elben, Markus Heyl, Philipp Hauke, Fritz Haake, and Peter Zoller. Digital quantum simulation, trotter errors, and quantum chaos of the kicked top. *npj Quantum Information*, 5(1), September 2019. doi: 10.1038/s41534-019-0192-5. URL https://doi.org/10.1038/s41534-019-0192-5.

[527] Francesco Tacchino, Alessandro Chiesa, Matthew LaHaye, Ivano Tavernelli, Stefano Carretta, and Dario Gerace. Digital quantum simulations of spin models on hybrid platform and near-term quantum processors. *Proceedings*, 12(1):24, July 2019. doi: 10.3390/proceedings2019012024. URL https://doi.org/10.3390/proceedings2019012024.

[528] Eric Chitambar and Gilad Gour. Quantum resource theories. *Rev. Mod. Phys.*, 91:025001, Apr 2019. doi: 10.1103/RevModPhys.91.025001. URL https://link.aps.org/doi/10.1103/RevModPhys.91.025001.

[529] Andrew W. Cross, Lev S. Bishop, Sarah Sheldon, Paul D. Nation, and Jay M. Gambetta. Validating quantum computers using randomized model circuits. *Phys. Rev. A*, 100:032328, Sep 2019. doi: 10.1103/PhysRevA.100.032328. URL https://link.aps.org/doi/10.1103/PhysRevA.100.032328.

[530] John Napp, Rolando L. La Placa, Alexander M. Dalzell, Fernando G. S. L. Brandao, and Aram W. Harrow. Efficient classical simulation of random shallow 2d quantum circuits, 2019.

[531] N Goldman, G Juzeliūnas, P Öhberg, and I B Spielman. Light-induced gauge fields for ultracold atoms. *Reports on Progress in Physics*, 77(12):126401, nov 2014. doi: 10.1088/0034-4885/77/12/126401. URL https://doi.org/10.1088%2F0034-4885%2F77%2F12%2F126401.

[532] Marin Bukov, Luca D'Alessio, and Anatoli Polkovnikov. Universal high-frequency behavior of periodically driven systems: from dynamical stabilization to floquet engineering. *Advances in Physics*, 64(2):139–226, March 2015. doi: 10.1080/00018732.2015.1055918. URL https://doi.org/10.1080/00018732.2015.1055918.

[533] André Eckardt. Colloquium: Atomic quantum gases in periodically driven optical lattices. *Rev. Mod. Phys.*, 89:011004, Mar 2017. doi: 10.1103/RevModPhys.89.011004. URL https://link.aps.org/doi/10.1103/RevModPhys.89.011004.

[534] Takashi Oka and Sota Kitamura. Floquet engineering of quantum materials. *Annual Review of Condensed Matter Physics*, 10(1):387–408, March 2019. doi: 10.1146/annurev-conmatphys-031218-013423. URL https://doi.org/10.1146/annurev-conmatphys-031218-013423.

[535] John Preskill. Quantum shannon theory, 2016.

[536] Tobias J. Osborne. Efficient approximation of the dynamics of one-dimensional quantum spin systems. *Phys. Rev. Lett.*, 97:157202, Oct 2006. doi: 10.1103/PhysRevLett.97.157202. URL https://link.aps.org/doi/10.1103/PhysRevLett.97.157202.

[537] Bruno Bertini, Pavel Kos, and Tomaž Prosen. Entanglement spreading in a minimal model of maximal many-body quantum chaos. *Phys. Rev. X*, 9:021033, May 2019. doi: 10.1103/PhysRevX.9.021033. URL https://link.aps.org/doi/10.1103/PhysRevX.9.021033.

[538] Bruno Bertini, Pavel Kos, and Tomaž Prosen. Exact correlation functions for dual-unitary lattice models in $1 + 1$ dimensions. *Phys. Rev. Lett.*, 123:210601, Nov 2019. doi: 10.1103/PhysRevLett.123.210601. URL https://link.aps.org/doi/10.1103/PhysRevLett.123.210601.

[539] Bruno Bertini, Pavel Kos, and Tomaz Prosen. Operator entanglement in local quantum circuits i: Chaotic dual-unitary circuits, 2019.

[540] Lorenzo Piroli, Bruno Bertini, J. Ignacio Cirac, and Tomaž Prosen. Exact dynamics in dual-unitary quantum circuits. *Phys. Rev. B*, 101:094304, Mar 2020. doi: 10.1103/PhysRevB.101.094304. URL https://link.aps.org/doi/10.1103/PhysRevB.101.094304.

[541] Daniel Gottesman. The heisenberg representation of quantum computers. 1998.

[542] Scott Aaronson and Daniel Gottesman. Improved simulation of stabilizer circuits. *Phys. Rev. A*, 70:052328, Nov 2004. doi: 10.1103/PhysRevA.70.052328. URL https://link.aps.org/doi/10.1103/PhysRevA.70.052328.

[543] Yaodong Li, Xiao Chen, and Matthew P. A. Fisher. Quantum zeno effect and the many-body entanglement transition. *Physical Review B*, 98(20), November 2018. doi: 10.1103/physrevb.98.205136. URL https://doi.org/10.1103/physrevb.98.205136.

[544] Marko Znidaric. Entanglement growth in diffusive systems, 2019.

[545] Sarang Gopalakrishnan and Bahti Zakirov. Facilitated quantum cellular automata as simple models with non-thermal eigenstates and dynamics. *Quantum Science and Technology*, 3(4):044004, aug 2018. doi: 10.1088/2058-9565/aad759. URL https://doi.org/10.1088%2F2058-9565%2Faad759.

[546] Sarang Gopalakrishnan. Operator growth and eigenstate entanglement in an interacting integrable floquet system. *Phys. Rev. B*, 98:060302, Aug 2018. doi: 10.1103/PhysRevB.98.060302. URL https://link.aps.org/doi/10.1103/PhysRevB.98.060302.

[547] V. Alba, J. Dubail, and M. Medenjak. Operator entanglement in interacting integrable quantum systems: The case of the rule 54 chain. *Phys. Rev. Lett.*, 122:250603, Jun 2019. doi: 10.1103/PhysRevLett.122.250603. URL https://link.aps.org/doi/10.1103/PhysRevLett.122.250603.

[548] Jason Iaconis, Sagar Vijay, and Rahul Nandkishore. Anomalous subdiffusion from subsystem symmetries. *Phys. Rev. B*, 100:214301, Dec 2019. doi: 10.1103/PhysRevB.100.214301. URL https://link.aps.org/doi/10.1103/PhysRevB.100.214301.

[549] Vedika Khemani, Ashvin Vishwanath, and David A. Huse. Operator spreading and the emergence of dissipative hydrodynamics under unitary evolution with conservation laws. *Phys. Rev. X*, 8:031057, Sep 2018. doi: 10.1103/PhysRevX.8.031057. URL https://link.aps.org/doi/10.1103/PhysRevX.8.031057.

[550] P. C. Hohenberg and B. I. Halperin. Theory of dynamic critical phenomena. *Rev. Mod. Phys.*, 49:435–479, Jul 1977. doi: 10.1103/RevModPhys.49.435. URL https://link.aps.org/doi/10.1103/RevModPhys.49.435.

[551] U. C. Täuber. *Field-Theory Approaches to Nonequilibrium Dynamics*, pages 295–348. Springer Berlin Heidelberg, Berlin, Heidelberg, 2007. ISBN 978-3-540-69684-1. doi: 10.1007/3-540-69684-9_7. URL https://doi.org/10.1007/3-540-69684-9_7.

[552] Herbert Spohn. *Large scale dynamics of interacting particles*. Springer Science & Business Media, 2012.

[553] N. Bloembergen. On the interaction of nuclear spins in a crystalline lattice. *Physica*, 15(3):386 – 426, 1949. ISSN 0031-8914. doi: https://doi.org/10.1016/0031-8914(49)90114-7. URL http://www.sciencedirect.com/science/article/pii/0031891449901147.

[554] P.G. De Gennes. Inelastic magnetic scattering of neutrons at high temperatures. *Journal of Physics and Chemistry of Solids*, 4(3):223 – 226, 1958. ISSN 0022-3697. doi: https://doi.org/10.1016/0022-3697(58)90120-3. URL http://www.sciencedirect.com/science/article/pii/0022369758901203.

[555] Winton Brown and Omar Fawzi. Decoupling with random quantum circuits. *Communications in Mathematical Physics*, 340(3):867–900, September 2015. doi: 10.1007/s00220-015-2470-1. URL https://doi.org/10.1007/s00220-015-2470-1.

[556] Daniel A. Roberts and Brian Swingle. Lieb-robinson bound and the butterfly effect in quantum field theories. *Phys. Rev. Lett.*, 117:091602, Aug 2016. doi: 10.1103/PhysRevLett.117.091602. URL https://link.aps.org/doi/10.1103/PhysRevLett.117.091602.

[557] Charles Stahl, Vedika Khemani, and David A. Huse. Asymmetric butterfly velocities in hamiltonian and circuit models, 2018.

[558] Yong-Liang Zhang and Vedika Khemani. Asymmetric butterfly velocities in 2-local hamiltonians, 2019.

[559] Yingfei Gu, Xiao-Liang Qi, and Douglas Stanford. Local criticality, diffusion and chaos in generalized sachdev-ye-kitaev models. *Journal of High Energy Physics*, 2017 (5), May 2017. doi: 10.1007/jhep05(2017)125. URL https://doi.org/10.1007/jhep05(2017)125.

[560] David J. Gross and Vladimir Rosenhaus. A generalization of sachdev-ye-kitaev. *Journal of High Energy Physics*, 2017(2), February 2017. doi: 10.1007/jhep02(2017)093. URL https://doi.org/10.1007/jhep02(2017)093.

[561] Sumilan Banerjee and Ehud Altman. Solvable model for a dynamical quantum phase transition from fast to slow scrambling. *Phys. Rev. B*, 95:134302, Apr 2017. doi: 10.1103/PhysRevB.95.134302. URL https://link.aps.org/doi/10.1103/PhysRevB.95.134302.

[562] Aavishkar A. Patel, Debanjan Chowdhury, Subir Sachdev, and Brian Swingle. Quantum butterfly effect in weakly interacting diffusive metals. *Phys. Rev. X*, 7:031047, Sep 2017. doi: 10.1103/PhysRevX.7.031047. URL `https://link.aps.org/doi/10.1103/PhysRevX.7.031047`.

[563] Xiao Chen, Tianci Zhou, and Cenke Xu. Measuring the distance between quantum many-body wave functions. *Journal of Statistical Mechanics: Theory and Experiment*, 2018(7):073101, jul 2018. doi: 10.1088/1742-5468/aace1f. URL `https://doi.org/10.1088%2F1742-5468%2Faace1f`.

[564] Tianci Zhou and Xiao Chen. Operator dynamics in a brownian quantum circuit. *Phys. Rev. E*, 99:052212, May 2019. doi: 10.1103/PhysRevE.99.052212. URL `https://link.aps.org/doi/10.1103/PhysRevE.99.052212`.

[565] Daniel A. Rowlands and Austen Lamacraft. Noisy coupled qubits: Operator spreading and the fredrickson-andersen model. *Phys. Rev. B*, 98:195125, Nov 2018. doi: 10.1103/PhysRevB.98.195125. URL `https://link.aps.org/doi/10.1103/PhysRevB.98.195125`.

[566] Michael Knap. Entanglement production and information scrambling in a noisy spin system. *Phys. Rev. B*, 98:184416, Nov 2018. doi: 10.1103/PhysRevB.98.184416. URL `https://link.aps.org/doi/10.1103/PhysRevB.98.184416`.

[567] Cheryne Jonay, Senior Thesis, unpublished.

[568] Liangsheng Zhang, Vedika Khemani, and David A. Huse. A floquet model for the many-body localization transition. *Phys. Rev. B*, 94:224202, Dec 2016. doi: 10.1103/PhysRevB.94.224202. URL `https://link.aps.org/doi/10.1103/PhysRevB.94.224202`.

[569] Sarang Gopalakrishnan, David A. Huse, Vedika Khemani, and Romain Vasseur. Hydrodynamics of operator spreading and quasiparticle diffusion in interacting integrable systems. *Phys. Rev. B*, 98:220303, Dec 2018. doi: 10.1103/PhysRevB.98.220303. URL `https://link.aps.org/doi/10.1103/PhysRevB.98.220303`.

[570] Murray Eden. A two-dimensional growth process. In *Proceedings of the Fourth Berkeley Symposium on Mathematical Statistics and Probability, Volume 4: Contributions to Biology and Problems of Medicine*, pages 223–239, Berkeley, Calif., 1961. University of California Press. URL `https://projecteuclid.org/euclid.bsmsp/1200512888`.

[571] F Family and T Vicsek. Scaling of the active zone in the eden process on percolation networks and the ballistic deposition model. *Journal of Physics A: Mathematical and General*, 18(2):L75–L81, feb 1985. doi: 10.1088/0305-4470/18/2/005. URL `https://doi.org/10.1088%2F0305-4470%2F18%2F2%2F005`.

[572] A-L Barabási and Harry Eugene Stanley. *Fractal concepts in surface growth*. Cambridge university press, 1995.

[573] Timothy Halpin-Healy and Yi-Cheng Zhang. Kinetic roughening phenomena, stochastic growth, directed polymers and all that. aspects of multidisciplinary statistical mechanics. *Physics Reports*, 254(4-6):215–414, March 1995. doi: 10.1016/0370-1573(94)00087-j. URL `https://doi.org/10.1016/0370-1573(94)00087-j`.

[574] Wen Wei Ho and Dmitry A. Abanin. Entanglement dynamics in quantum many-body systems. *Phys. Rev. B*, 95:094302, Mar 2017. doi: 10.1103/PhysRevB.95.094302. URL `https://link.aps.org/doi/10.1103/PhysRevB.95.094302`.

[575] S F Edwards and P W Anderson. Theory of spin glasses. *Journal of Physics F: Metal Physics*, 5(5):965–974, may 1975. doi: 10.1088/0305-4608/5/5/017. URL https://doi.org/10.1088%2F0305-4608%2F5%2F5%2F017.

[576] Marc Mézard, Giorgio Parisi, and Miguel Virasoro. *Spin glass theory and beyond: An Introduction to the Replica Method and Its Applications*, volume 9. World Scientific Publishing Company, 1987.

[577] Giorgio Parisi. Replica theory and spin glasses. In *Statistical Physics, Optimization, Inference, and Message-Passing Algorithms*, pages 61–94. Oxford University Press, December 2015. doi: 10.1093/acprof:oso/9780198743736.003.0003. URL https://doi.org/10.1093/acprof:oso/9780198743736.003.0003.

[578] Márk Mezei. Membrane theory of entanglement dynamics from holography. *Phys. Rev. D*, 98:106025, Nov 2018. doi: 10.1103/PhysRevD.98.106025. URL https://link.aps.org/doi/10.1103/PhysRevD.98.106025.

[579] Shinsei Ryu and Tadashi Takayanagi. Holographic derivation of entanglement entropy from the anti–de sitter space/conformal field theory correspondence. *Phys. Rev. Lett.*, 96:181602, May 2006. doi: 10.1103/PhysRevLett.96.181602. URL https://link.aps.org/doi/10.1103/PhysRevLett.96.181602.

[580] Shinsei Ryu and Tadashi Takayanagi. Aspects of holographic entanglement entropy. *Journal of High Energy Physics*, 2006(08):045–045, aug 2006. doi: 10.1088/1126-6708/2006/08/045. URL https://doi.org/10.1088%2F1126-6708%2F2006%2F08%2F045.

[581] Veronika E Hubeny, Mukund Rangamani, and Tadashi Takayanagi. A covariant holographic entanglement entropy proposal. *Journal of High Energy Physics*, 2007(07):062–062, jul 2007. doi: 10.1088/1126-6708/2007/07/062. URL https://doi.org/10.1088%2F1126-6708%2F2007%2F07%2F062.

[582] David A. Huse and Christopher L. Henley. Pinning and roughening of domain walls in ising systems due to random impurities. *Phys. Rev. Lett.*, 54:2708–2711, Jun 1985. doi: 10.1103/PhysRevLett.54.2708. URL https://link.aps.org/doi/10.1103/PhysRevLett.54.2708.

[583] Timothy Halpin-Healy. Directed polymers versus directed percolation. *Phys. Rev. E*, 58:R4096–R4099, Oct 1998. doi: 10.1103/PhysRevE.58.R4096. URL https://link.aps.org/doi/10.1103/PhysRevE.58.R4096.

[584] Mehran Kardar. Replica bethe ansatz studies of two-dimensional interfaces with quenched random impurities. *Nuclear Physics B*, 290:582–602, January 1987. doi: 10.1016/0550-3213(87)90203-3. URL https://doi.org/10.1016/0550-3213(87)90203-3.

[585] Daniel Shaffer, Claudio Chamon, Alioscia Hamma, and Eduardo R Mucciolo. Irreversibility and entanglement spectrum statistics in quantum circuits. *Journal of Statistical Mechanics: Theory and Experiment*, 2014(12):P12007, 2014. URL http://stacks.iop.org/1742-5468/2014/i=12/a=P12007.

[586] Claudio Chamon, Alioscia Hamma, and Eduardo R. Mucciolo. Emergent irreversibility and entanglement spectrum statistics. *Phys. Rev. Lett.*, 112:240501, Jun 2014. doi: 10.1103/PhysRevLett.112.240501. URL https://link.aps.org/doi/10.1103/PhysRevLett.112.240501.

[587] Zhi-Cheng Yang, Claudio Chamon, Alioscia Hamma, and Eduardo R. Mucciolo. Two-component structure in the entanglement spectrum of highly excited states. *Phys. Rev. Lett.*, 115:267206, Dec 2015. doi: 10.1103/PhysRevLett.115.267206. URL https://link.aps.org/doi/10.1103/PhysRevLett.115.267206.

[588] Zhi-Cheng Yang, Konstantinos Meichanetzidis, Stefanos Kourtis, and Claudio Chamon. Scrambling via braiding of nonabelions. *Phys. Rev. B*, 99:045132, Jan 2019. doi: 10.1103/PhysRevB.99.045132. URL https://link.aps.org/doi/10.1103/PhysRevB.99.045132.

[589] Maksym Serbyn, Alexios A. Michailidis, Dmitry A. Abanin, and Z. Papić. Power-law entanglement spectrum in many-body localized phases. *Phys. Rev. Lett.*, 117:160601, Oct 2016. doi: 10.1103/PhysRevLett.117.160601. URL https://link.aps.org/doi/10.1103/PhysRevLett.117.160601.

[590] G Torlai, L Tagliacozzo, and G De Chiara. Dynamics of the entanglement spectrum in spin chains. *Journal of Statistical Mechanics: Theory and Experiment*, 2014(6):P06001, jun 2014. doi: 10.1088/1742-5468/2014/06/p06001. URL https://doi.org/10.1088%2F1742-5468%2F2014%2F06%2Fp06001.

[591] Po-Yao Chang, Xiao Chen, Sarang Gopalakrishnan, and J. H. Pixley. Evolution of entanglement spectra under generic quantum dynamics. *Phys. Rev. Lett.*, 123:190602, Nov 2019. doi: 10.1103/PhysRevLett.123.190602. URL https://link.aps.org/doi/10.1103/PhysRevLett.123.190602.

[592] M. Mierzejewski, T. Prosen, D. Crivelli, and P. Prelovšek. Eigenvalue statistics of reduced density matrix during driving and relaxation. *Phys. Rev. Lett.*, 110:200602, May 2013. doi: 10.1103/PhysRevLett.110.200602. URL https://link.aps.org/doi/10.1103/PhysRevLett.110.200602.

[593] Sagar Vijay and Ashvin Vishwanath. Finite-temperature scrambling of a random hamiltonian, 2018.

[594] Siddhardh C. Morampudi and Chris R. Laumann. Many-body systems with random spatially local interactions. *Phys. Rev. B*, 100:245152, Dec 2019. doi: 10.1103/PhysRevB.100.245152. URL https://link.aps.org/doi/10.1103/PhysRevB.100.245152.

[595] Matteo Bellitti, Siddhardh Morampudi, and Chris R. Laumann. Hamiltonian dynamics of a sum of interacting random matrices. *Phys. Rev. B*, 100:184201, Nov 2019. doi: 10.1103/PhysRevB.100.184201. URL https://link.aps.org/doi/10.1103/PhysRevB.100.184201.

[596] Sean A Hartnoll, Andrew Lucas, and Subir Sachdev. *Holographic quantum matter*. MIT press, 2018.

[597] Xizhi Han and Sean A. Hartnoll. Quantum Scrambling and State Dependence of the Butterfly Velocity. *SciPost Phys.*, 7:45, 2019. doi: 10.21468/SciPostPhys.7.4.045. URL https://scipost.org/10.21468/SciPostPhys.7.4.045.

[598] Xiao Chen, Tianci Zhou, David A. Huse, and Eduardo Fradkin. Out-of-time-order correlations in many-body localized and thermal phases. *Annalen der Physik*, 529(7):1600332, 2017. doi: 10.1002/andp.201600332. URL https://onlinelibrary.wiley.com/doi/abs/10.1002/andp.201600332.

[599] D. Belitz, T. R. Kirkpatrick, and Thomas Vojta. How generic scale invariance influences quantum and classical phase transitions. *Rev. Mod. Phys.*, 77:579–632, Jul 2005. doi: 10.1103/RevModPhys.77.579. URL `https://link.aps.org/doi/10.1103/RevModPhys.77.579`.

[600] Aram W. Harrow and Richard A. Low. Random quantum circuits are approximate 2-designs. *Communications in Mathematical Physics*, 291(1):257–302, Oct 2009. ISSN 1432-0916. doi: 10.1007/s00220-009-0873-6. URL `https://doi.org/10.1007/s00220-009-0873-6`.

[601] Fernando G. S. L. Brandão, Aram W. Harrow, and Michał Horodecki. Local random quantum circuits are approximate polynomial-designs. *Communications in Mathematical Physics*, 346(2):397–434, Sep 2016. ISSN 1432-0916. doi: 10.1007/s00220-016-2706-8. URL `https://doi.org/10.1007/s00220-016-2706-8`.

[602] Xiao Chen, Rahul M. Nandkishore, and Andrew Lucas. Quantum butterfly effect in polarized floquet systems. *Phys. Rev. B*, 101:064307, Feb 2020. doi: 10.1103/PhysRevB.101.064307. URL `https://link.aps.org/doi/10.1103/PhysRevB.101.064307`.

[603] Dominik Muth, Razmik G. Unanyan, and Michael Fleischhauer. Dynamical simulation of integrable and nonintegrable models in the heisenberg picture. *Phys. Rev. Lett.*, 106:077202, Feb 2011. doi: 10.1103/PhysRevLett.106.077202. URL `https://link.aps.org/doi/10.1103/PhysRevLett.106.077202`.

[604] Brian Skinner, Jonathan Ruhman, and Adam Nahum. Measurement-induced phase transitions in the dynamics of entanglement. *Phys. Rev. X*, 9:031009, Jul 2019. doi: 10.1103/PhysRevX.9.031009. URL `https://link.aps.org/doi/10.1103/PhysRevX.9.031009`.

[605] Yaodong Li, Xiao Chen, and Matthew P. A. Fisher. Measurement-driven entanglement transition in hybrid quantum circuits. *Phys. Rev. B*, 100:134306, Oct 2019. doi: 10.1103/PhysRevB.100.134306. URL `https://link.aps.org/doi/10.1103/PhysRevB.100.134306`.

[606] Yimu Bao, Soonwon Choi, and Ehud Altman. Theory of the phase transition in random unitary circuits with measurements. *Phys. Rev. B*, 101:104301, Mar 2020. doi: 10.1103/PhysRevB.101.104301. URL `https://link.aps.org/doi/10.1103/PhysRevB.101.104301`.

[607] Soonwon Choi, Yimu Bao, Xiao-Liang Qi, and Ehud Altman. Quantum error correction in scrambling dynamics and measurement induced phase transition, 2019.

[608] Kyungjoo Noh, Liang Jiang, and Bill Fefferman. Efficient classical simulation of noisy random quantum circuits in one dimension, 2020.

[609] Tomaz Prosen. Ruelle resonances in quantum many-body dynamics. *Journal of Physics A: Mathematical and General*, 35(48):L737–L743, nov 2002. doi: 10.1088/0305-4470/35/48/102. URL `https://doi.org/10.1088%2F0305-4470%2F35%2F48%2F102`.

[610] Ilya Kuprov, Nicola Wagner-Rundell, and P.J. Hore. Polynomially scaling spin dynamics simulation algorithm based on adaptive state-space restriction. *Journal of Magnetic Resonance*, 189(2):241 – 250, 2007. ISSN 1090-7807. doi: https://doi.org/10.1016/j.jmr.2007.09.014. URL `http://www.sciencedirect.com/science/article/pii/S109078070700273X`.

[611] Alexander Karabanov, Ilya Kuprov, G. T. P. Charnock, Anniek van der Drift, Luke J. Edwards, and Walter Köckenberger. On the accuracy of the state space restriction approximation for spin dynamics simulations. *The Journal of Chemical Physics*, 135(8):084106, August 2011. doi: 10.1063/1.3624564. URL https://doi.org/10.1063/1.3624564.

[612] R. Steinigeweg, H. Wichterich, and J. Gemmer. Density dynamics from current auto-correlations at finite time- and length-scales. *EPL (Europhysics Letters)*, 88 (1):10004, oct 2009. doi: 10.1209/0295-5075/88/10004. URL https://doi.org/10.1209%2F0295-5075%2F88%2F10004.

[613] R. Steinigeweg, F. Jin, D. Schmidtke, H. De Raedt, K. Michielsen, and J. Gemmer. Real-time broadening of nonequilibrium density profiles and the role of the specific initial-state realization. *Phys. Rev. B*, 95:035155, Jan 2017. doi: 10.1103/PhysRevB.95.035155. URL https://link.aps.org/doi/10.1103/PhysRevB.95.035155.

[614] Yonghong Yan, Feng Jiang, and Hui Zhao. Energy spread and current-current correlation in quantum systems. *The European Physical Journal B*, 88(2), February 2015. doi: 10.1140/epjb/e2014-50797-4. URL https://doi.org/10.1140/epjb/e2014-50797-4.

[615] J. Karthik, Auditya Sharma, and Arul Lakshminarayan. Entanglement, avoided crossings, and quantum chaos in an ising model with a tilted magnetic field. *Phys. Rev. A*, 75:022304, Feb 2007. doi: 10.1103/PhysRevA.75.022304. URL https://link.aps.org/doi/10.1103/PhysRevA.75.022304.

[616] R. Steinigeweg, F. Heidrich-Meisner, J. Gemmer, K. Michielsen, and H. De Raedt. Scaling of diffusion constants in the spin-$\frac{1}{2}$ xx ladder. *Phys. Rev. B*, 90:094417, Sep 2014. doi: 10.1103/PhysRevB.90.094417. URL https://link.aps.org/doi/10.1103/PhysRevB.90.094417.

[617] C. Karrasch, D. M. Kennes, and F. Heidrich-Meisner. Spin and thermal conductivity of quantum spin chains and ladders. *Phys. Rev. B*, 91:115130, Mar 2015. doi: 10.1103/PhysRevB.91.115130. URL https://link.aps.org/doi/10.1103/PhysRevB.91.115130.

[618] C. Eckart and G. Young. The approximation of one matrix by another of lower rank. *Psychometrika*, 1(3):211–218, 1936. doi: 10.1007/BF02288367.

[619] Yichen Huang. Dynamics of renyi entanglement entropy in local quantum circuits with charge conservation, 2019.

[620] Gerg ő Roósz, Róbert Juhász, and Ferenc Iglói. Nonequilibrium dynamics of the ising chain in a fluctuating transverse field. *Phys. Rev. B*, 93:134305, Apr 2016. doi: 10.1103/PhysRevB.93.134305. URL https://link.aps.org/doi/10.1103/PhysRevB.93.134305.

[621] Viktor Eisler, Ferenc Iglói, and Ingo Peschel. Entanglement in spin chains with gradients. *Journal of Statistical Mechanics: Theory and Experiment*, 2009(02):P02011, 2009. URL http://stacks.iop.org/1742-5468/2009/i=02/a=P02011.

[622] Vincenzo Alba and Fabian Heidrich-Meisner. Entanglement spreading after a geometric quench in quantum spin chains. *Phys. Rev. B*, 90:075144, Aug 2014. doi: 10.1103/PhysRevB.90.075144. URL https://link.aps.org/doi/10.1103/PhysRevB.90.075144.

[623] Lev Vidmar, Deepak Iyer, and Marcos Rigol. Emergent eigenstate solution to quantum dynamics far from equilibrium. *Phys. Rev. X*, 7:021012, Apr 2017. doi: 10.1103/PhysRevX.7.021012. URL https://link.aps.org/doi/10.1103/PhysRevX.7.021012.

[624] Vir B. Bulchandani and Christoph Karrasch. Subdiffusive front scaling in interacting integrable models. *Phys. Rev. B*, 99:121410, Mar 2019. doi: 10.1103/PhysRevB.99.121410. URL https://link.aps.org/doi/10.1103/PhysRevB.99.121410.

[625] Vincenzo Alba, Bruno Bertini, and Maurizio Fagotti. Entanglement evolution and generalised hydrodynamics: interacting integrable systems. *SciPost Phys.*, 7:5, 2019. doi: 10.21468/SciPostPhys.7.1.005. URL https://scipost.org/10.21468/SciPostPhys.7.1.005.

[626] Vincenzo Alba, Bruno Bertini, and Maurizio Fagotti. Entanglement evolution and generalised hydrodynamics: interacting integrable systems, 2019.

[627] Márton Mestyán and Vincenzo Alba. Molecular dynamics simulation of entanglement spreading in generalized hydrodynamics. *SciPost Phys.*, 8:55, 2020. doi: 10.21468/SciPostPhys.8.4.055. URL https://scipost.org/10.21468/SciPostPhys.8.4.055.

[628] Henry A. Ando, Junior Paper, unpublished.

[629] Curt von Keyserlingk, Private communication.

[630] Vincenzo Alba and Pasquale Calabrese. Quench action and rényi entropies in integrable systems. *Phys. Rev. B*, 96:115421, Sep 2017. doi: 10.1103/PhysRevB.96.115421. URL https://link.aps.org/doi/10.1103/PhysRevB.96.115421.

[631] Vincenzo Alba. Towards a generalized hydrodynamics description of rényi entropies in integrable systems. *Phys. Rev. B*, 99:045150, Jan 2019. doi: 10.1103/PhysRevB.99.045150. URL https://link.aps.org/doi/10.1103/PhysRevB.99.045150.

[632] Mohammad F. Maghrebi, Zhe-Xuan Gong, and Alexey V. Gorshkov. Continuous symmetry breaking in 1d long-range interacting quantum systems. *Phys. Rev. Lett.*, 119:023001, Jul 2017. doi: 10.1103/PhysRevLett.119.023001. URL https://link.aps.org/doi/10.1103/PhysRevLett.119.023001.

[633] Xiangyu Cao, Antoine Tilloy, and Andrea De Luca. Entanglement in a fermion chain under continuous monitoring. *SciPost Phys.*, 7:24, 2019. doi: 10.21468/SciPostPhys.7.2.024. URL https://scipost.org/10.21468/SciPostPhys.7.2.024.

[634] Michael J. Gullans and David A. Huse. Dynamical purification phase transition induced by quantum measurements, 2019.

[635] Aidan Zabalo, Michael J. Gullans, Justin H. Wilson, Sarang Gopalakrishnan, David A. Huse, and J. H. Pixley. Critical properties of the measurement-induced transition in random quantum circuits. *Phys. Rev. B*, 101:060301, Feb 2020. doi: 10.1103/PhysRevB.101.060301. URL https://link.aps.org/doi/10.1103/PhysRevB.101.060301.

[636] Chao-Ming Jian, Yi-Zhuang You, Romain Vasseur, and Andreas W. W. Ludwig. Measurement-induced criticality in random quantum circuits. *Phys. Rev. B*, 101:104302, Mar 2020. doi: 10.1103/PhysRevB.101.104302. URL https://link.aps.org/doi/10.1103/PhysRevB.101.104302.

[637] Yaodong Li, Xiao Chen, Andreas W. W. Ludwig, and Matthew P. A. Fisher. Conformal invariance and quantum non-locality in hybrid quantum circuits, 2020.

[638] Ruihua Fan, Sagar Vijay, Ashvin Vishwanath, and Yi-Zhuang You. Self-organized error correction in random unitary circuits with measurement, 2020.

[639] Oles Shtanko, Yaroslav A. Kharkov, Luis Pedro García-Pintos, and Alexey V. Gorshkov. Classical models of entanglement in monitored random circuits, 2020.

[640] Ali Lavasani, Yahya Alavirad, and Maissam Barkeshli. Measurement-induced topological entanglement transitions in symmetric random quantum circuits, 2020.

[641] Daniel E. Parker, Xiangyu Cao, Alexander Avdoshkin, Thomas Scaffidi, and Ehud Altman. A universal operator growth hypothesis. *Phys. Rev. X*, 9:041017, Oct 2019. doi: 10.1103/PhysRevX.9.041017. URL `https://link.aps.org/doi/10.1103/PhysRevX.9.041017`.

[642] Huzihiro Araki. Gibbs states of a one dimensional quantum lattice. *Communications in Mathematical Physics*, 14(2):120–157, June 1969. doi: 10.1007/bf01645134. URL `https://doi.org/10.1007/bf01645134`.

[643] Yong Moon Park and Hyun Jae Yoo. Uniqueness and clustering properties of gibbs states for classical and quantum unbounded spin systems. *Journal of Statistical Physics*, 80(1-2):223–271, July 1995. doi: 10.1007/bf02178359. URL `https://doi.org/10.1007/bf02178359`.

[644] M. Kliesch, C. Gogolin, M. J. Kastoryano, A. Riera, and J. Eisert. Locality of temperature. *Phys. Rev. X*, 4:031019, Jul 2014. doi: 10.1103/PhysRevX.4.031019. URL `https://link.aps.org/doi/10.1103/PhysRevX.4.031019`.

[645] Andras Molnar, Norbert Schuch, Frank Verstraete, and J. Ignacio Cirac. Approximating gibbs states of local hamiltonians efficiently with projected entangled pair states. *Phys. Rev. B*, 91:045138, Jan 2015. doi: 10.1103/PhysRevB.91.045138. URL `https://link.aps.org/doi/10.1103/PhysRevB.91.045138`.

[646] Tomotaka Kuwahara, Kohtaro Kato, and Fernando G. S. L. Brandão. Clustering of conditional mutual information for quantum gibbs states above a threshold temperature, 2019.

[647] Andrew Lucas. Operator size at finite temperature and planckian bounds on quantum dynamics. *Phys. Rev. Lett.*, 122:216601, May 2019. doi: 10.1103/PhysRevLett.122.216601. URL `https://link.aps.org/doi/10.1103/PhysRevLett.122.216601`.

[648] F. Xiao, J. S. Möller, T. Lancaster, R. C. Williams, F. L. Pratt, S. J. Blundell, D. Ceresoli, A. M. Barton, and J. L. Manson. Spin diffusion in the low-dimensional molecular quantum heisenberg antiferromagnet Cu(pyz)$(NO_3)_2$ detected with implanted muons. *Phys. Rev. B*, 91:144417, Apr 2015. doi: 10.1103/PhysRevB.91.144417. URL `https://link.aps.org/doi/10.1103/PhysRevB.91.144417`.

[649] Alexander Schuckert, Izabella Lovas, and Michael Knap. Nonlocal emergent hydrodynamics in a long-range quantum spin system. *Phys. Rev. B*, 101:020416, Jan 2020. doi: 10.1103/PhysRevB.101.020416. URL `https://link.aps.org/doi/10.1103/PhysRevB.101.020416`.